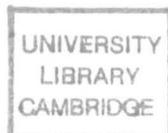# Scale Effects In Tests
On
Footings

by

Chi Keung Lau

A dissertation submitted for the degree of
Doctor of Philosophy
at Cambridge University

Christ's College   October 1988

To My Parents

Preface

I would like to thank my supervisor, Malcolm Bolton for his invaluable guidance, constant support and encouragement throughout the course of this work. I would also like to thank Dr. Dave Airey, Bill Balodis, Dr. Arul Britto, Brian Butler, Steve Chandler, Chris Collison, Dr. Richard Dean, Jim Doherty, John Godlonton, Dr. Janet Gronow, Wally Gwizdala, Trish Hensley, Dr. R.G. James, Roy Julian, Dr. Ryan Phillips, Dave Pittock, Charlie Potter, Prof. Andrew Schofield, Dr. Quen Shi, Dr. Scott Steedman, Kevin Stone, Arthur Timbs, Ralph Ward, Prof. David Wood and all past and present members of the Cambridge Soil Mechanics Group for their technical support, advice, friendship and inspiration.

In particular, I would like to thank Dr. Richard Dean for reading the manuscript and making many useful comments. Dr. Arul Britto made constructive criticisms on chapter 5 and was also responsible for sorting out bugs and implementing new features in CRISP.

Acknowledgements are also due to the Croucher Foundation, the Committee of Vice-Chancellors and Principals of the Universities of the United Kingdom, and the Cambridge University Engineering Department for financial support, without which this work would not have been possible.

I hereby certify that except where specific reference is made in the text to the work of others, the contents of this dissertation are original, and have not been submitted to any other university. This dissertation is the result of my own work, and includes nothing which is the outcome of work done in collaboration. It contains 300 pages as authorized by the Board of Graduate Studies in their letter dated 9 September 1988 (ref. JCH/MT/X/GS. No. 8432701).

C. K. Lau

Summary

This dissertation presents an investigation of the effects of stress, and of absolute and relative particle size, in tests on vertically loaded footings. Two granular materials, namely, a silica rock flour and a Chatelet flint grit, which differed in nominal diameter by a factor of 50 but were otherwise practically similar in all other grain characteristics were used in this work. A comprehensive series of triaxial tests under a wide range of cell pressures was carried out to quantify the stress and absolute particle size effects. Model footing tests were also performed by pushing a rigid circular punch axisymmetrically into the flat surface of a cylindrical soil model either under 1-g (gravity) with surcharge or under elevated g in a centrifuge. The 1-g and centrifuge test series were used to study the scale effects on the surcharge term N_q and the self-weight term N_γ of the Terzaghi bearing capacity equation, respectively. Parameters varied were punch diameter, particle size and surcharge or g level. Two theoretical analyses were attempted based on the finite element method and the method of characteristics. Using the Schofield Soil Model, the finite element analysis can give a reasonable order of magnitude prediction for the settlement of the footing under working load conditions. When the effect of reducing angle of shearing with increasing stress was taken into account together with the change of geometry due to footing penetration, the angles of shearing inferred from the method of characteristics fall within ±2° of those measured in triaxial compression tests. Distortion due to violating the scaling law by not conserving the ratio of particle size to model dimension was not considered to be significant ~~observed~~. Distortion due to violating the constitutive soil behaviour by varying the absolute particle size was found to be significant due to differences in grain crushing, but this can be accounted for effectively by the new style of calculations developed in the thesis.

Keywords: *Finite element method, method of characteristics, modelling distortions, particle crushing, penetration effects, punch indentation, scale effects, soil particle modelling and triaxial tests.*

Contents

Contents

Notation

All stresses are effective stresses unless otherwise stated.

Roman

A	Stress-induced strength reduction constant for sand
AX	axisymmetric
B	width or diameter of footing
B	Skempton's pore pressure parameter $(=\Delta u/\Delta \sigma_{cell})$
B/d_{50}	footing size/particle size ratio
b	intermediate stress parameter $(=(\sigma_2-\sigma_3)/(\sigma_1-\sigma_3))$
CRISP	CRItical State Program
c	cohesion
c^*	Cox's combined cohesion $(=c+\sigma_0\tan\phi)$
D	initial embedment of a footing
D_c	critical depth of a footing
d	diameter of a cylindrical specimen
d_e	equivalent particle diameter of a particle
d_{50}	mean particle size
E	Young's modulus
e	void ratio
e_{cs}	critical state void ratio with p=1kPa
e_{max}	maximum void ratio
e_{min}	minimum void ratio
eps	shear strain
G	shear modulus
G	Cox's dimensionless parameter $(=0.5B\gamma)/c^*$
GDS	digital pressure controller
G_s	specific gravity
g	acceleration due to earth's gravity
H_{tub}	height of tub
I_D	relative density
I_R	relative dilatancy index
K	bulk modulus
K_p	coefficient of passive earth pressure
K_o	coefficient of at rest earth pressure
k	coefficient of permeability

LVDT	linearly variable differential transformer
ln	natural logarithm
N_c	bearing capacity factor (cohesion) (=σ_f/c)
N_q	bearing capacity factor (surcharge) (=σ_f/σ_0)
N_γ	bearing capacity factor (self-weight) (=$\sigma_f/0.5B\gamma$)
$N_{q\gamma}$	combined bearing capacity factor (=$\sigma_f/(\sigma_0+0.5B\gamma)$)
n	linear scaling factor
PPT	pore pressure transducer
PS	plane strain
p	mean stress (=$(\sigma_1+\sigma_2+\sigma_3)/3\approx(\sigma_1+\sigma_3)/2$)
p_c	pre-consolidation pressure
p_{crit}	mean stress at which all dilatancy is suppressed in a triaxial test
p_e	equivalent pre-consolidation pressure
Q	normalized surcharge (=$\sigma_0/0.5B\gamma$)
q	triaxial deviatoric stress (=$\sigma_1-\sigma_3$)
R	roundness
R	normalized radius (=$r/0.5B$)
r	radius
S	sphericity
S	maximum q/p ratio: ϕ_{max} cut-off
S_H	gradient of the Hvorslev surface
s	mean stress (=$0.5(\sigma_1+\sigma_3)$)
t	time
u	back pressure, pore pressure
v	volume
v	terminal velocity
w	workdone
w	settlement
w/B	relative settlement
Greek	
α,β	pair of stress characteristics
β	equivalent relative settlement angle
Γ	specific volume at the critical state line with p=1kPa
γ	engineering shear strain
γ	bulk weight density of soil
γ'	submerged bulk weight density of soil

γ_f	weight density of sedimentation fluid
γ_s	weight density of soil particle
Δ	large increment of ...
δ	small increment of ...
δ	cone/soil friction
$\delta\varepsilon_{ij}$	components of strain increment
$\delta\varepsilon_1, \delta\varepsilon_2, \delta\varepsilon_3$	principal strain increments
ε	strain
ε_a	axial strain
ε_r	radial strain
ε_θ	circumferential strain
ε_s	shear strain ($=2(\varepsilon_1-\varepsilon_3)/3$ for $\varepsilon_2=\varepsilon_3$)
η	stress ratio ($=q/p$)
η_f	dynamic viscosity of fluid
θ	stress rotation
κ	gradient of swelling line
λ	gradient of consolidation line
M	slope of critical state line ($=6\sin\phi/(3-\sin\phi)$)
ν	Poisson's ratio
ν	specific volume ($=1+e$)
ρ_f	mass density of sedimentation fluid
ρ_s	mass density of soil grain
ρ_w	mass density of water
Σ	normalized stress ($\sigma/0.5B\gamma$)
σ	stress
σ_{ij}	components of stress
$\sigma_1, \sigma_2, \sigma_3$	principal stress
σ_c	unconfined compressive strength of a cylindrical specimen
σ_{c50}	unconfined compressive strength of a 50mm dia. cylindrical specimen
σ_e	equivalent surcharge
σ_{cell}	cell pressure
σ_f	bearing capacity
σ_n	normal pressure
σ_o	surcharge
σ_w	working mean pressure

σ_θ	circumferential stress
τ	shear stress
τ_f	shear strength
τ_n	shear stress on plane normal to σ_n
τ_o	shear stress acting on the free equivalent surface
ϕ	secant angle of friction
ϕ_{crit}	critical state angle
ϕ_{en}	angle of local strength envelope decribing the stress characteristics
ϕ_{max}	maximum angle of friction
ϕ_{min}	minimum angle of friction
ϕ_{mob}	mobilized angle of friction
ϕ_{op}	operative angle of friction
ϕ_{tub}	diameter of tub
ψ	orientation of principal stress direction
Ω	superposition factor ($=\sigma_o/0.5B\gamma$)

Subscripts

a	axial
crit	critical state
cs	critical state
en	strength envelope
f	failure
init	initial
max	maximum
min	minium
mob	mobilized
n	normal
op	operative
r	radial
w	working
v	volumetric
z	vertical
θ	circumferential
1	major
2	intermediate
3	minor

1. INTRODUCTION

1.1 Objectives

The purpose of this dissertation is to present the results of a theoretical and experimental investigation of the following aspects of the scale effects in tests on vertically loaded footings:

(1) Stress effects - effects of ambient mean stress level on particle crushing, suppressed dilatancy, compressibility and shear strength.

(2) Absolute particle size effects - effects of particle size alone on particle crushing, compressibility and shear strength.

(3) Relative particle size effects - effects of footing size/particle size ratio on shear band formation and shear strength.

It should be pointed out here that for simplicity, all stresses referred to in this work will be effective stresses unless otherwise stated.

1.2 Background

Due to its wide practical significance, the problem of estimating the ultimate bearing capacity of a footing resting on a bed of soil has over the years consistently attracted immense academic interest. A comprehensive review of the huge body of work in the literature can be found in Vesic (1973). This common interest in a shared problem links the divergent investigations together. It is not surprising, therefore, to find that these explorations have contributed significantly to our understanding of soil mechanics. There remain, however, many uncertainties yet to be resolved.

Terzaghi (1943) has shown that the bearing capacity σ_f of a shallow strip foundation of width B resting on cohesionless materials with a weight density γ can be estimated from the expression

$$\sigma_f = \sigma_o N_q + \frac{1}{2} B \gamma \, N_\gamma \qquad \text{eqn 1.1}$$

where σ_o is the surcharge

N_q is the bearing capacity factor (surcharge)

and N_γ is the bearing capacity factor (self-weight)

Implicitly, Terzaghi's equation relies on the validity of the superposition of the surcharge and self-weight terms.

Prandtl (1920) has obtained a closed-form solution to the above problem for weightless soil. For soil with self-weight, because of the difficulties in computation, numerical methods which involve arbitrary assumptions have to be used. In order to validate the resulting numerical coefficients, tests on footings have to be carried out. Because of the high cost involved in testing large footings, model footings have usually been rather small: typically less than 1 m in width. Notably, Meyerhof (1948, 1951, 1963) has investigated the bearing capacity and failure mechanisms of shallow foundations by carrying out a series of small scale (up to 600 mm in width or diameter) model tests. It has since been commonly accepted that the failure mechanism as depicted in fig 1.1 is applicable to prototype shallow foundations resting on dense sands. Scale effects are usually taken care of by assuming that the mean stress is equal to $\sigma_f/10$ (Meyerhof, 1950).

In foundation engineering practice, it is normally the settlement consideration under working load conditions which dictates the final design decision. This is because conventional settlement criteria for working load conditions turn out to be more critical than the ultimate bearing capacity under an extreme load. This may shield the inadequacy of the existing practice of extrapolating small scale model test results.

1.3 The Problem

According to Terzaghi (1943), the supporting soil will fail by general shear (see fig 1.2) only if soil strain prior to plastic failure is negligibly small. As a result, the footing can not sink into the ground until a state of plastic equilibrium similar to that illustrated in fig 1.1 has been reached. In other words, the soil behaviour approaches that of a rigid-perfectly-plastic material, which may be true for a very small footing (<200 mm in width or diameter) on dense sands.

If on the other hand, failure in the form of plastic flow is preceded by significant strain, the approach to a general shear failure will be associated with gradually increasing settlement. The criterion for the failure of the supporting soil will become uncertain. This type of failure is usually categorized as local shear (see fig 1.2) and progressive failure may, or may not have occurred. It is clear, however, that the mode of failure hinges very much on the relative compressibility of the supporting soil.

De Beer (1965a) has pointed out the effects of scale. De Beer's scale effects can be considered as a reduction of the mass shear strength as a result of higher ambient stress level and progressive failure. Progressive failure, in De Beer's terminology is not

unlike the non-uniform strain effect as discussed by Terzaghi which, in the present context, is defined as a mechanism in which brittle strength components are regionally destroyed due to strain concentration prior to the formation of a global collapse mechanism.

Stress effects have been convincingly demonstrated by De Beer (1965b) in his triaxial tests. Strain concentration prior to failure has been observed by Muhs (1965) in his footing tests. However, the degree of reduction in bearing capacity as a result of progressive failure has yet to be quantified. Kerisel (1972) has suggested the adoption of a lower ϕ_{mob}, perhaps ϕ_{crit}, as a safeguard against the uncertainty of progressive failure. This assumption is acceptable when designing conventional footings but not very useful when designing spudcans, for example.

With the advent of the geotechnical centrifuge, Ovesen (1975) has shown that the stress effects in shallow foundations can be modelled in a geotechnical centrifuge. Yamaguchi et al (1976 & 1977) have gone one step further by including the effects of progressive failure with the assumption that it can be reproduced without modelling the soil particles. With the help of in-flight video photography and post-flight radiography, the plane-strain strain distribution pattern under the footing and slip lines can be established respectively. Progressive failure can therefore be incorporated into the bearing capacity calculation based on the ϕ_{mob} corresponding to the strain observed locally, which is an empirical method of correcting the bearing capacity for strain effects. However, Yamaguchi et al (1976 &1977) have assumed that ϕ is totally independent of the ambient stress level.

Based on some selected data on shallow and deep foundations, Vesic (1969) has concluded that in the case of shallow foundations, the average shear strength along a slip line under the foundation decreases with foundation size. He went on to postulate (Vesic, 1970) that the failure mechanism will change gradually from general to local shear and finally to punching shear (see fig 1.2) as the size of the footing increases. His postulate implies that very large footings on dense sand should fail exclusively in punching shear as apparently all deep foundations do. Vesic arrived at his remark by extrapolating the results from footing tests at small and medium scale (see fig 1.3) which agrees with some other experimental results summarized independently by Meyerhof (1951) in fig 1.4. One plausible explanation is that dense sands become more compressible and appear loose when under high ambient stress level, so that the relative compressibility of dense sands increases with footing size as reported by De Beer (1965a), which according to Terzaghi (1943), determines the mode of failure.

Vesic's postulate has not yet been verified experimentally at full scale because of high cost, while the possible effects of shear band size remains an obstacle yet to be clarified by the centrifuge modellers. The problem of shear band size effects has been highlighted by Palmer and Rice (1973) who postulate the existence of a scale dependent progressive failure effect upon the formation of thin rupture bands. Scarpelli and Wood (1982) have demonstrated empirically the particle size dependent nature of the characteristic length of shear bands in their long shear box tests.

Instead of investigating by direct methods such as those of Scarpelli and Wood, it is equally feasible to investigate indirectly by measuring the reduction in mass shear strength of a soil construction. For example, researches on passive retaining walls (Davis & Auger, 1979) and strip load behind retaining walls (Mak, 1984) have suggested that the behaviour of soil construction may be influenced by the ratio of soil construction size to grain size. Reduction in the particle to model size ratio apparently increases the degree of progressive failure which reduces the mass shear strength of an initially dense soil.

Recently, there is a growing interest shown from the oil exploration industries in shallow foundation design principles. This is a result of the increasing use of spudcan foundations (see fig 1.5) for off-shore oil rigs (LeBlanc, 1981). Like interpretation of penetrometer data, the main point of interest for spudcan design has always been the evaluation of failure loads. It is because spudcans have to be pushed into the seabed to a predetermined depth with ballast on the rig during preloading before unloading the oil rigs to their normal working conditions. This is a safeguard against accidental overloading and scouring of the seabed by under current which may undermine their foundations during their working life. As spudcans can normally reach 14 m in diameter (Hambly, 1985), scale effects have, therefore, emerged as some rather urgent problems to be resolved.

1.4 Methodology

In order to achieve the objectives of this thesis, the problem posed above was tackled on various fronts.

(1) It was decided to acquire two granular materials which differed in nominal diameter by a factor of 50 but which were otherwise practically indistinguishable in all other grain characteristics. The idea was that they could be used as model materials for each other. These two materials had not been used in Cambridge before and therefore a

comprehensive laboratory testing programme was carried out to determine their mechanical properties. The programme included a series of triaxial tests with a wide range of different cell pressures in an attempt to clarify and quantify stress and absolute particle size effects.

(2) Soil models of different sizes were constructed using the same material for both 1-g and centrifuge tests, in order to investigate the relative particle size effects. It has been the common practice in Cambridge (Schofield, 1980) to model a centrifuge model with another centrifuge model at a different scale in order to check their internal consistency. The major disadvantage is that the differences in scale between two such centrifuge models, because of the practical limitations of the centrifuge at Cambridge, are not generally larger than seven.

(3) Soil models were constructed of a particular footing bearing on each of the two model soils of different particle size. The footing size/particle size ratio could then be varied to a much wider extent than in approach (2), while most of the existing laboratory apparatus and equipment could be utilized without much adaptation. This approach inevitably introduced some complications as a result of changing the grain characteristics. In particular, any absolute particle size effects had to be accounted for when interpreting the experimental results.

1.5 Scope Of Work

As it is impossible to solve every aspect of the problem in a work like this, decisions had to be made regarding specific targets. It was decided to restrict the footing tests to the problem of a rigid cylindrical punch indenting axisymmetrically a horizontal bed of dense cohesionless material under drained conditions only (see fig 1.6). The loading of the punch was displacement-controlled and the flat bottom of the punch was rough. To avoid confusion later, it has to be pointed out here that failure of the footing hereafter would refer to the failure of the supporting soil rather than the rigid punch itself.

Bearing capacity is very sensitive to change in ϕ for granular materials and is therefore suitable for the investigation of scale effects. The fact that the punch invokes high stress in its vicinity is an added advantage. From the analysis point of view, this problem also has the advantage of being a relatively simple boundary value problem for both the method of characteristics and the finite element analysis.

The choice of an axisymmetric case was deliberate, because there appear to be more uncertainties here than in the plane strain case. The clarification of any uncertainty can also cast new light on the interpretation of a huge body of existing penetrometer data in the literature. The other benefit is that plate load tests in the field almost always approximate to this condition.

On the practical side, the axisymmetric problem is less vulnerable to side wall friction and the effects of the relative stiffness of the model container than the corresponding plane strain case. This is clearly a significant advantage, as any complications which affect the interpretation of the data should be minimized as far as possible. As opposed to the plane strain problem, however, new techniques have to be developed before the failure mechanism of an axisymmetric problem can be observed.

Two punches, 100 and 14.2 mm diameter were chosen. The bigger one was chosen to facilitate the observation of failure mechanisms under the punch while the smaller one was for providing a wider range of B/d_{50} ratio. The other purpose was for the modelling of models with the maximum possible scale factor of seven in the Cambridge geotechnical centrifuge.

The soil bed under a 1-g condition and with surcharge derives its resistance to the advancing punch solely from the surcharge term of the Terzaghi's equation. This is because its own self-weight at 1-g when compared with surcharge is negligible. For example, when $\sigma_0 > 200kPa$, the soil can practically be regarded as weightless. Under elevated g condition in a geotechnical centrifuge, however, the soil can derive its resistance to the advancement of the punch from its own self-weight alone. In the event that settlement is significant, correction can be made to account for the increase in overburden which may result in an increase in surcharge and other geometric effects. By taking advantage of these considerations, it is possible to uncouple the scale effects on N_q and N_γ

Two parallel series of 1-g and centrifuge footing tests were planned. The 1-g series was primarily designed to investigate the scale effects on N_q (surcharge), and the penetration effects. The centrifuge series was devoted to the investigation of the scale effects on N_γ (self-weight). In addition to the experimental work outlined above, two numerical methods, plastic stress characteristics and finite elements were also developed so that interpretation and comparison could be made in a rational manner.

The choice of an axisymmetric case was deliberate, because there appear to be more uncertainties here than in the plane strain case. The clarification of any uncertainty can also cast new light on the interpretation of a huge body of existing penetrometer data in the literature. The other benefit is that plate load tests in the field almost always approximate to this condition.

On the practical side, the axisymmetric problem is less vulnerable to side wall friction and the effects of the relative stiffness of the model container than the corresponding plane strain case. This is clearly a significant advantage, as any complications which affect the interpretation of the data should be minimized as far as possible. As opposed to the plane strain problem, however, new techniques have to be developed before the failure mechanism of an axisymmetric problem can be observed.

Two punches, 100 and 14.2 mm diameter were chosen. The bigger one was chosen to facilitate the observation of failure mechanisms under the punch while the smaller one was for providing a wider range of B/d_{50} ratio. The other purpose was for the modelling of models with the maximum possible scale factor of seven in the Cambridge geotechnical centrifuge.

The soil bed under a 1-g condition and with surcharge derives its resistance to the advancing punch solely from the surcharge term of the Terzaghi's equation. This is because its own self-weight at 1-g when compared with surcharge is negligible. For example, when $\sigma_0 > 200kPa$, the soil can practically be regarded as weightless. Under elevated g condition in a geotechnical centrifuge, however, the soil can derive its resistance to the advancement of the punch from its own self-weight alone. In the event that settlement is significant, correction can be made to account for the increase in overburden which may result in an increase in surcharge and other geometric effects. By taking advantage of these considerations, it is possible to uncouple the scale effects on N_q and N_γ.

Two parallel series of 1-g and centrifuge footing tests were planned. The 1-g series was primarily designed to investigate the scale effects on N_q (surcharge), and the penetration effects. The centrifuge series was devoted to the investigation of the scale effects on N_γ (self-weight). In addition to the experimental work outlined above, two numerical methods, plastic stress characteristics and finite elements were also developed so that interpretation and comparison could be made in a rational manner.

1.6 Layout Of The Thesis

This opening chapter begins by making statements on the objectives, problem, methodology and scope of work of the thesis.

The next chapter describes the acquisition and manufacture of two granular materials used in the experimental programme. It then covers the detailed investigation of their grain characteristics and mechanical properties, including a comprehensive series of triaxial tests over a wide range of confining cell pressures.

To facilitate the interpretation of experimental data, chapter 3 reviews the background to some existing stress characteristic analyses in the literature. It then shows how a general stress characteristic analysis for constant ϕ which can handle both self-weight and surcharge in both plane strain and axisymmetric strain could be formulated and implemented in a suite of FORTRAN 77 computer programs. The effects of penetration were also quantified. Results were then generated and represented in chart form and as tables for comparing with experimental data later in chapters 6 and 7.

The triaxial test data suggest that ϕ is highly pressure dependent and therefore, a constant-ϕ analysis is not realistic. As a result, chapter 4 is devoted to the modification of the constant-ϕ plastic stress analysis already developed in chapter 3 to include the pressure effects on ϕ. Results relevant to all the corresponding physical model tests were then obtained for later comparison in chapters 6 and 7.

The method of characteristics is unable to model the response of a footing under working load conditions. To supplement the stress analysis covered in chapter 4, chapter 5 describes how a Cam-clay type of constitutive model could be adopted for the two granular materials used in this work based on the triaxial test data. It then goes on to explain how the model was implemented in a finite element analysis using the CRISP program. Results for a number of cases were obtained for later comparison with the experimental data.

The experimental procedures and test results of the 1-g and centrifuge model tests are presented in chapters 6 and 7 respectively. The experimental results are presented by overlaying the experimental data and theoretical predictions obtained from chapter 3. After the effects of penetrations are accounted for, the failure loads measured are compared directly with the predictions obtained in chapter 4.

Chapter 8 attempts to answer some questions raised in chapter 1 in the light of the theoretical and experimental results made available in the previous chapters. Finally, some statements are made regarding the implications of these findings both for the geotechnical centrifuge modeller and the practising engineer.

2. Material Properties

2.1 Material Acquisition

It was decided to acquire two granular materials for the purpose of soil particle modelling. The criterion was that they should differ in particle size (nominal diameter) by a factor of 50 but otherwise be practically similar in all other grain characteristics. The two granular materials chosen for the experimental programmes were:

(1) Washed silica flour. Samples of silica flour were obtained from several silica manufacturers for suitability assessment. The material supplied by Richard Baker Harrison Ltd. of Essex was adopted as their supply turned out to consist of the purest silica among the samples tested. As will be explained below, the silica flour as supplied had to be washed twice in order to remove some of the very fine fraction.

(2) 8/40 wires Chatelet flint grit. A similar search was launched to find the coarse granular material. It was discovered that the 8/40 wires Chatelet flint grit and silica flour as supplied by Richard Baker Harrison Ltd. of Essex were very similar in terms of particle shape and specific gravity (see table 2.1), except that there were proportionally more fines in the silica flour than in the flint grit. By trial and error, it was found that the shape of the silica flour grading curve could be modified by washing the silica flour. The resulting grading curve after a standard washing procedure looked practically the same as the 8/40 wires Chatelet flint grit (see fig 2.1).

2.2 The Standard Washing Procedure

The washing was done in two stages. In the first stage, 100 kg of dry silica flour as supplied by the manufacturer was mixed with de-ionized water in a 400 mm high, 850 mm diameter steel tub until a total volume of 170 litres were reached. The mixtures were then stirred vigorously by a hand-held high speed electric stirrer until no air bubbles were seen surfacing and the silica flour was in a uniform slurry state. This operation normally took 30 minutes. The slurry was then left to settle for one hour. During this time, the coarser fraction settled and formed a cake at the bottom of the tub. The water above the cake which still held most of the finest fraction of the flour was syphoned off. The syphon operation took roughly 20 minutes to complete. The cake of

silica flour so formed was then ready for the second stage washing. De-ionized water was added to the cake again until a total volume of 170 litres were reached. The whole process were then repeated as in the first stage. When complete, the cake of saturated silica flour so formed was removed and stored in plastic containers.

Altogether, 2000 kg of silica flour was processed in this manner. As the grading curve was rather tight, serious segregation of the processed silica flour was not expected. Once the cake of silica flour had been formed, it had to be broken up into tiny fragments by chiselling before they could be transferred from one container to another. This process could actually help to improve the uniformity of the silica flour.

For convenience, from now on, the washed silica flour will simply be known as silt; while the 8/40 wires Chatelet flint grit will simply be known as sand.

2.3 Mineralogy

As preliminary mineralogical identification, only specific gravity tests were conducted. The two materials eventually adopted here have a similar specific gravity which suggests that they are likely to have a similar mineralogy. In order to quantify their purity, Gronow (1987) carried out X-ray diffraction spectrum and chemical analyses on these two materials. The silt was found to contain no less than 99% SiO_2 and the sand no less than 97% SiO_2. Therefore, for the purpose of this work, the two materials can be treated as mineralogically identical.

2.4 Grain Size

The grading curve of the sand was characterized by sieve analysis which represents the grain diameter by the length of the side of a square opening through which the grain particle will just pass. Because of its fine size, the grading curve of the silt was characterized by sedimentation analysis using the pipette method. In this method, the grain diameter is represented by the equivalent diameter of a sphere of the same specific weight and the same terminal settling velocity as the grain particle in water at 25°C. The idea is that particles having a settling velocity greater than that of the size at which separation is desired will settle below the point of withdrawal after elapse of a certain time. The time and depth of withdrawal are predetermined on the basis of Stoke's law.

$$v = \frac{g \, d_e^2 \, (\rho_s - \rho_f)}{18\eta_f}$$ eqn 2.1

where v is the terminal velocity of the soil particle

d_e is the equivalent particle diameter

η_f is the dynamic viscosity of the fluid.

The particle size analysis results were expressed in the form of two cumulative frequency curves in terms of the respective nominal equivalent size used in the analysis (see fig 2.1).

2.5 Roundness And Shape

Particle roundness and shape are two very significant factors on the mechanical properties of the granular materials. Roundness is a measure of the sharpness of the particle edges, regardless of shape. It can be estimated by viewing the particles two-dimensionally and determining the ratio of the average radius of curvature of a particle's corners to the radius of the largest circle that can be inscribed in that particle. Corners are defined as features possessing a ratio smaller than unity; it follows that with the exception of the circle, the roundness defined in this fashion is always less than one.

Shape describes the form of the particle without reference to the sharpness of its edges. The shape of a grain can be expressed in terms of true sphericity which is defined as the ratio of the surface area of the sphere with the same volume as the grain to the surface area of the particle. The difficulty in determining the surface area and volume of small grains led Wadell (1933) to adopt an approximate but more convenient expression for sphericity which is the ratio of the diameter of the circle with an area equal to that of the projection of the grain when it rests on its longest face, to the diameter of the smallest circle circumscribing this projection.

In this work, sphericity and roundness of the two materials were evaluated from the micrographs with the aid of the Rittenhouse (1943) and Krumbein (1941) charts respectively. The results were based on two random samples of 100 samples each. Two typical micrographs of the sand and silt taken under the scanning electron microscope can be seen in plates 2.1 and 2.2.

2.6 Limiting Porosities

Kolbuszewski (1948) has demonstrated quantitatively that the packing of sands by pluviation is influenced most strongly by the pouring rate and velocity at impact. It has also been shown that the relative density is much more useful than the bulk density as a soil parameter (Burmister, 1948).

$$\text{Relative density } I_D = \frac{e_{max} - e}{e_{max} - e_{min}}$$

where e is the void ratio of the soil in question

e_{max} is the maximum void ratio of the same soil

e_{min} is the minimum void ratio of the same soil

In order to obtain relative density, the maximum and minimum porosities of a soil should be measured.

2.6.1 Minimum Porosity

The minimum porosity of the sand was obtained by pluviation at a rate of 1.33 kg/min from a suspended conical hopper via a 600 mm long 28 mm internal diameter plastic hose and at a constant drop height of 600 mm into the tub (see fig 2.2). The tub was 850 mm diameter and 400 mm high. The sand was poured until the target height of the model was slightly passed. A modified vacuum cleaner was used to level the model back down to the target height. The tub was weighed to the nearest 1 kg before and after the sand was placed. When the volume was known, the bulk dry density could be estimated. With this method, e_{min} for sand was found to be 0.60±0.04.

For silt, the material was compacted by vibrating saturated silt inside a 400 mm high 850 mm diameter steel tub by bolting a vibrator onto its wall (fig 2.3). The slurry was introduced into the tub in layers with the vibrator switched on in order to let any trapped air out of the slurry. When the required amount of slurry was in place and no more air bubbles could be be seen escaping through the top of the slurry, which normally took roughly 24 hours to achieve, the top of the silt bed was covered with filter paper before a steel piston weighing 345 kg was put on top. Vibration continued until no further settlement of the piston could be observed. This normally took another 48 hours of continuous vibration. During the compaction process, both top and bottom drainage were provided. The idea is that granular material compacts when subjected to small shear straining cycles which involve rotation of principal stress direction. In order to determine the bulk dry density, the tub was weighed to the nearest 1 kg before and after the

compacted silt was in place. The volume of the silt was calculated by measuring the thickness of the model with the aid of a template at a regular grid of no less than 96 sampling points. With this method, e_{min} for silt was found to be 0.59±0.04.

2.6.2 Maximum Porosity

Quick tilt tests as proposed by Kolbuszewski (1948) were conducted. 1000 g of dry granular material was put inside a 75 mm diameter 2000 ml capacity glass measuring cylinder which was then sealed with a rubber bung. The cylinder was first shaken, turned upside down and then quickly turned over again. The volume of the material when settled was read directly and the void ratio calculated.

Quite consistent results could be obtained for the sand, e_{max}≈ 0.92. However, the silt tended to remain air-borne immediately after tilting. From eqn 2.1, treating air as a sedimentation fluid, it can be seen that the velocity is proportional to the square of the particle diameter which suggests that if fully segregated, the silt will fall much slower than the sand. On the other hand, the silt particles were more likely to stick to each other and fall as a conglomerate of particles rather than as a single grain. This could result in an apparently higher rate of settling. Because of these two opposing effects, the results were quite erratic.

Fortunately, the model tests being carried out were always near their minimum porosities, so the relative densities should in both cases be near one. The inability in determining e_{max} does not, therefore, happen to be a serious handicap.

2.7 Permeability

Permeability of the silt is several thousand times smaller than that of the sand. Permeability tests were, therefore, carried out using two different set-ups. For the sand, a conventional constant head permeameter was used (see fig 2.4) and k was found to be 1.7×10^{-3} m/s. For the silt, because of the difficulty in preparing a very dense specimen in the permeameter, the test was carried out in a modified triaxial cell instead (see fig 2.5). A full size porous disc was used to ensure the uniformity of the hydraulic gradient across the specimen. During the test, a back pressure of 30 kPa above atmospheric pressure was imposed at the base with the top set at atmospheric level. The flow rate was measured by a commercially available GDS controller. The GDS controller is essentially a microcomputer controlled cylinder whose volume or pressure can be controlled or measured by a piston via a stepping motor. The preparation of a triaxial

specimen will be discussed in section 2.8.3. k was found to be 3×10^{-7} m/s for the silt.

2.8 Triaxial Tests

As the triaxial test is one of the commonest test in soil mechanics, only a very brief description of the equipment used and the testing procedures will be given here. Instead, some problem areas of the tests which are directly relevant to the triaxial test programme presented in this work will be covered in more detail , including a description of how the problems were tackled together with an assessment of the accuracy of the measurements.

Although there were many different variations of the triaxial test, basically, the layout of a typical set-up is as shown in fig 2.6. The cylindrical specimen to be tested stands on a pedestal inside the cell with a loading cap sitting on top of the specimen. The specimen has to be completely sealed from the cell fluid by a natural rubber latex sheath and "O" rings. The cell when filled up with cell fluid can be pressurized to provide a range of confining cell pressure. Back pressure and/or pore water drainage are provided through two ports on the cell. One is connected to the loading cap and the second one to the pedestal.

A loading ram passing through a bushing in the cell is used to apply the deviatoric stress on the specimen. The ram can be driven at any pre-determined rate in a strain-controlled manner. The connection between the loading cap and the ram can be rigidly fixed or in the form of a swivel joint. For drained tests, the loading rate should be slow enough so that no excess pore water pressure builds up during any stage of the test.

2.8.1 Some Problem Areas

There are a number of problem areas which have to be overcome before an acceptable overall accuracy can be achieved. They will only be touched upon in general terms here. In the sections covering the actual tests, the strategy actually adopted will be specifically stated.

(1) Ram/cell bushing friction. In order to act as a guide to ensure vertical movement of the loading ram as well as avoiding serious leakage of the cell fluid, the bushing is usually a tight fit. Friction resisting vertical movement of the loading ram through the bushing will become progressively more significant when the cell pressure is low. It can be overcome by either putting the load cell inside the cell, rotating the

bushing continuously and lubricating it with oil, or using a loosely fitting bushing.

(2) Sheath stiffness. The sheath is there to act as a barrier between the cell fluid and the specimen. For low pressure tests, the effects of the stiffness of the sheath will become more significant. The effects have two components.

(i) Axial direction. The sample will appear stronger and stiffer. The sheath stiffness should be measured and then a correction can be applied accordingly (Bishop & Henkel, 1962).

(ii) Radial direction. Except for undrained tests where volumetric strain is zero. A correction to cell pressure has to be made according to whether the specimen dilates or contracts. (a) Dilation. The membrane will be stretched, resulting in an apparent increase in cell pressure on the specimen. (b) Contraction. The membrane will be unstretched and its radial stiffness may take up some of the cell pressure, resulting in an apparent decrease in cell pressure in the specimen.

(3) Volumetric measurement. In a triaxial test, normally the only direct strain measurement is of the axial strain. The volumetric strain is usually measured indirectly by the amount of pore fluid driven in and out of the specimen. The major drawback is that only a fully saturated specimen can be tested in this way. For dry or partially saturated specimens, some form of direct radial strain measurement is required.

(4) Uniformity of strain. The other problem caused by measuring the volumetric strain by the amount of pore fluid driven in and out of the specimen is that we have to assume that the specimen remains cylindrical during the test. Some form of direct strain measurement should be made to justify this assumption. Apart from the error in volumetric strain measurement, non-uniform strain may cause progressive failure resulting in a reduction of peak shear strength.

(5) End friction. At the pedestal and loading cap, the specimen ends are supposed to be subjected to vertical principal stress. However, at the two loading platens, invariably, some friction must exist. This can be ameliorated by putting greased membranes as interfaces between the platens and the specimen. This, however, may introduce some bedding error in the axial strain measurement of the specimen. Judgement is called for to decide which type of error is more significant in a particular situation.

(6) Membrane penetration. The effects are quite different depending on whether the mean effective cell pressure changes or not.

(i) For coarse granular material, when the effective cell pressure increases, the sheath will be stretched and conform more closely to the uneven specimen surface (see fig 2.7). Therefore, any volumetric measurement by metering the amount of water flowing out of the specimen will be over-predicted. For the case of isotropic compression, Roscoe et al (1963) have proposed that by assuming $\Delta V = 3\Delta \varepsilon_a$ and comparing it with ΔV measured indirectly by metering the water pressing out of or sucking into the specimen with a burette, the amount of over-prediction can be estimated (see fig 2.8).

(ii) When mean effective cell pressure remains constant, i.e. $\Delta \sigma_r = 0$, as in a standard drained triaxial compression test. The membrane penetration effects can also manifest themselves in the form of changes in texture or fabric of the skeleton of the specimen. For example, when the specimen dilates, the texture would become coarser and penetration of the rubber membrane into the interstices between the sand particles is more pronounced, resulting in an under-prediction of ΔV (see fig 2.9). If the specimen compacts, the texture would be finer and ΔV will also be underestimated. In this work, a 1 mm thick sheath is used in order to reduce this second kind of penetration error.

2.8.2 Triaxial Test Programme

It was decided to investigate the absolute particle size and stress effects by triaxial tests conducted over a wide range of effective confining cell pressures ranging from 10 to 10000 kPa. In a triaxial test, the stress and strain fields are intended to be uniform, the formation of localized shear in rupture bands is not encouraged at least before ϕ_{max} has been reached.

For practical reasons, such as that a stronger cell is required for the high pressure tests, together with the problem areas commented upon in section 2.8.1, three different set-ups had to be used in order to provide satisfactory results for the full range of tests.

(1) Low pressure set-up (see fig 2.10). This is based on an unconfined compression test rig which has no cell. This feature is good for two reasons. (i) As there would be no cell fluid, the loading ram can have a loosely fitting bushing so that ram friction is also low. (ii) Without the cell, easy physical access to the specimen is

available throughout a test so that radial strain can be measured directly with a pair of vernier calipers. Without the cell fluid, effective cell pressure has to be applied by creating a negative back pressure inside the specimen with a controlled suction. For this reason, the maximum effective confining cell pressure can not exceed one atmospheric pressure i.e.≈100 kPa.

The major task for this set-up is to carry out a test on the dry sand while still being able to monitor crudely the volumetric strain. It can also give some quantitative ideas of how uniform a specimen is before ϕ_{max} is reached. The effective cell pressure was 10, 30, 75 kPa. The suction was monitored by a manometer and controlled by an air-relief valve.

(2) Medium pressure set-up (see fig 2.11). The set-up is a computer controlled system developed in Cambridge by Houlsby (1981) and Airey (1987). The cell is a Geonor cell; back pressure and/or drainage is measured by a GDS controller. Resolution of pressure measurement is 1 kPa and of volume measurement is 1 mm^3. The cell pressure is controlled by a system of mercury pots moving up and down vertical rails by a stepping motor driven winch.

The ram friction was reduced by rotating the bushing at a constant rate using a small auxiliary motor. In order to stop serious leakage of the cell fluid through the ram/cell bushing, oil was introduced into the top of the cell fluid. As the stress path can be programmed into the Sirius computer and data logged automatically via the Orion datalogger, this system is especially useful for very slow tests which last for many hours.

(3) High Pressure Set-up (see fig 2.12). This set-up used a stainless steel cell which could withstand a maximum working cell pressure up to 14000 kPa. In order to stop serious leakage of cell fluid from the bushing under high pressure, oil was used as the cell fluid. Back pressure and/or drainage is measured by a GDS controller. The cell pressure was controlled by a Norgren valve which pressurized the cell fluid through an oil/nitrogen gas interface with a compressed nitrogen gas cylinder. The loading ram was driven by a Wykeham Farrance 3-tonne electric-driven loading frame. The deviatoric stress was monitored via a load cell placed outside the cell. Because of its very high axial load, the ram friction became negligible here.

2.8.3 Sample Preparation

(1) Sand. Triaxial samples were formed by pluviation. The wall of the pedestal was greased before the latex rubber sheath was put on and secured with "O" rings. A 38

mm internal diameter cylindrical split mould was attached to the pedestal and enclosed the sheath. The sheath was then made to conform to the inside of the mould by applying a suction between the sheath and the mould. The net volume of the mould was measured. According to the target density, which in this case is 2.00 g/cm^3, the dry weight of 90 gm of sand was pluviated into the mould at a drop height of 300 mm via a funnel. The top was levelled off by a modified vacuum cleaner. The sand removed was trapped and weighed so that the final void ratio of the specimen could be calculated.

The loading cap, greased on its side was put on top of the specimen. The specimen was then fully enveloped by holding the sheath against the loading cap with "O" rings. The sample was subjected to a negative back pressure via a suction pump before the split mould could be dismantled. Once the mould was off, the height and diameter of the specimen could be measured.

Further steps were necessary when saturated specimens were required. After the cell was fixed and a cell pressure of around 50 kPa was applied, the negative back pressure could be removed. Carbon dioxide was passed into the bottom drain of the specimen to displace the air. The carbon dioxide was then evacuated by a very high suction. De-aired water was later fed into the specimen via the bottom drain and let out from the top. It is believed that the minute amount of carbon dioxide still remaining inside the sample would dissolve readily into the water under a high back pressure. A Skempton B value (Skempton, 1954) of 0.92 or above was achieved for all tests on saturated sand.

(2) Silt. Gentle disturbance of the dry silt causes the segregated particles to become air-borne which indicates that sample preparation by pluviation will not be a suitable method. The air-borne silt can also pose a health hazard. Compaction by vibration is a practical alternative to pluviation as repeated shearing has shown to be able to densify a granular material. This, however, may lead to non-uniformity in density distribution in a soil model (Brand, 1973). As will be demonstrated later in section 2.8.5, this is, nevertheless an acceptable method when a sample near its maximum density (rather than an intermediately dense sample) is required.

The sample preparation used the same compaction method for obtaining e_{min} as described in section 2.6.1. After the vibration was completed, 18 no. 100 mm cubes were excavated from the compacted silt bed. Locations of the cubes are depicted in fig 2.13. As soon as they were excavated, the samples were swiftly sealed with cling film with a view to retaining as much moisture as possible until triaxial tests could be carried out

later.

Immediately before the triaxial test was about to begin, the sample was put on a lathe and trimmed carefully to the required diameter by a sharp cutting edge guided by two vertical straight edges. It was then put on a cradle to be trimmed carefully to the required height before putting inside the triaxial cell for testing. The volume was then measured. The dry weight was measured after each test when the specimen was oven-dried. The retaining of sufficient moisture in the specimen is essential when trimming a cubic specimen into a cylindrical shape triaxial specimen. This is because the specimen relies on suction to hold itself together at this stage. When dried out, the specimen will be weaker and crumble easily if not carefully handled. The trimmed down cylindrical specimen was then completely sealed from the cell fluid by a rubber sheath. The sheath was bound to the loading cap and pedestal by stretched rubber "O" rings. Plumbers' grease was applied between the sheath and the wall of the end platens to improve the effectiveness of the seal.

Top and bottom drains were provided in order to reduce the drainage path by half. By setting back pressures of 400 kPa at the bottom drainage inlet and 350 kPa at the top drainage outlet, most trapped air bubbles should be flushed out eventually at a pressure gradient of 50 kPa per sample height. The idea is that under high isotropic pressure, trapped air may be more likely to dissolve into the water and come out of the specimen together with the pore water. Failing which, the bubbles will reduce in size according to Boyle's law and the smaller the bubbles, the more likely they can be flushed out. Every effort having been made to flush bubbles out prior to the test, it might be assumed that no such movement would affect volume change measurements during the test. Furthermore, the tests were conducted at constant back pressure, so the volume of any residual bubbles should remain constant.

The silt samples achieved a Skempton B value ranging from 0.55 to 0.94 indicating, perhaps, at least 90% saturation (Skempton, 1954). No significant behaviour difference were observed, signifying that the variation in saturation was not significant.

2.8.4 Some Common Features

(1) The end platen frictions were reduced by interfacing both end platens and the specimen with three layers of 0.33mm thick circular latex discs (see fig 2.14). The discs were sandwiched between smears of plumbers' grease. At the centre of the platen where the porous stone was housed, a 6 mm diameter punch hole was made in the latex

discs to allow unhindered passage of water to and from the specimen.

(2) All rubber sheaths used were 1 mm thick and 38 mm external diameter when unstretched. Corrections were made to account for the sheath stiffness in both axial and radial directions.

(3) A cross-sectional area correction was made by assuming that the specimen remained cylindrical which enabled ϕ at large strains to be measured more accurately.

(4) The specimens were about 36 mm diameter and 75 mm high. The slenderness ratio was about 2 for all the tests.

2.8.5 The Role Of Triaxial Tests

The triaxial test data presented in this chapter form a central role in this thesis. The main objectives of this test programme were:

(1) The series of tests on silt were also used to check the density uniformity of the model preparation technique for the silt. Table 2.2 summarizes the void ratio distribution at different locations of the model as depicted in fig 2.13. The void ratio varied from 0.55 to 0.62 with an average of 0.59 when the bulk density suggested that it should be 0.57 ± 0.05. The model preparation method is, therefore, acceptable.

(2) To investigate the absolute particle size effects and to obtain an empirical correlation between ϕ_{max} and the mean effective pressure p ($=(\sigma_1+\sigma_2+\sigma_3)/3$) or s ($=(\sigma_1+\sigma_2)/2$). The difference between p and s is small and they can be regarded as the same for the purpose of this work.

(3) To obtain an empirical correlation between shear modulus G and p.

(4) To compare with direct shear box results so that comments on ϕ_{crit} and progressive failure associated with ruptures can be made.

(5) To obtain parameters for the constitutive model for the finite element analysis in chapter 5.

(6) To check the effects of saturation on a dry sand specimen.

2.8.6 Results

The triaxial test results are presented in fig 2.15 to fig 2.19 as secant angle of friction versus axial strain and volumetric strain versus axial strain. Secant angle of friction is obtained by dropping a tangent from the origin to a single Mohr circle of

stress. ϕ_{max} in general coincides with the maximum rate of dilation. ϕ_{crit} is not reached as dilation continued even after an axial strain of 20%. ϕ_{crit} could be reached, however, when the confining pressure was high enough to suppress all dilation. ϕ_{max} is higher for silt than for sand, and the corresponding rate of dilation is also higher. One interesting observation is that ruptures were obviously formed in the silt samples after ϕ_{max} had been reached, resulting in a sudden decrease in both ϕ and rate of dilation (see fig 2.17). It is obvious that the interference of ruptures was deferred when cell pressure was higher (see fig 2.21). Formation of ruptures was not obvious in the sand specimens. Table 2.3 summarizes the results of all the tests. Fig 2.20 and 2.21 show the pressure effects on secant ϕ and dilatancy of the two materials. Secant ϕ is 4° to 5 ° higher for the silt than sand but the trend of pressure effects is similar. In both cases, the secant angles of friction reduce linearly with the logarithm of mean stresses. The results of sand agree well with Bolton's (1986) empirical correlation for sands as shown in fig 2.22a. Like other sands, the empirical correlation slightly underestimated ϕ for the sand used here at medium pressure range but slightly over-predicted in both low and high pressure range. The deviation is nevertheless smaller than ±2°. The dilatancy is underestimated for the sand at low pressure (see fig 2.22b) probably as a result of membrane penetration as discussed in section 2.8.1.

2.8.7 Soil Stiffness

Each triaxial specimen was isotropically compressed to the target effective confining cell pressure. The isotropic compression lines are shown in fig 2.23 and 2.24. λ is measured from the normally consolidated line at a mean pressure of 8000 kPa and κ from the elastic rebound curve at a mean pressure of 1000 kPa. In some triaxial tests, one unloading and reloading cycle was carried out so that Young's modulus can be measured from the reloading curve as depicted in fig 2.25.

From the theory of elasticity, the following relationship can be established,

$$K = (1 + e)\ p/\kappa$$
$$E = 3K(1 - 2v) \qquad \text{eqn 2.2}$$
$$E = 2G(1 + v)$$

where
      K is the bulk modulus
      E is the Young's modulus
      G is the shear modulus
      v is the Poisson's ratio

From eqn 2.2, K, ν and G can be calculated as κ, p and e are all known. Table 2.4 summarizes the results under different values of p. An empirical fit of $G = 1400p^{0.667}$ was found to fit reasonably well with all the experimental data as shown in fig 2.26. As only pressure effect on soil stiffness was considered, the stiffness parameters are only relevant at the quoted strain level (Jardine et al, 1984). For λ, the axial strain level is about 3% and for G, the axial strain level is about 0.5%.

2.8.8 Discussion

(1) From fig 2.27, it can be seen that a sudden drop from ϕ_{max} coincides with a sudden reduction of overall dilatancy rate consistent with the initiation of a rupture. Ruptures were formed in test FLP3 a bit later than test FLP2. Despite all conditions being essentially the same, ϕ_{max} is also lower in test FLP2 than in test FLP3 probably as a result of the interference of ruptures.

(2) From fig 2.28, it can be seen that tests on dry and saturated sand at an effective cell pressure of 30 kPa follow a similar trend as expected. There does not appear to be any serious difference between dry and saturated specimens.

(3) The diameter of triaxial specimen of tests GLP8, GLP9 and GLP10 was measured directly with a pair of vernier calipers during each test at five different positions. The results are presented in fig 2.29. It can be seen that the assumption that specimens remain cylindrical is valid at least up to an axial strain when ϕ_{max} was mobilized.

(4) The technique of soil particle modelling to determine the shear strength of coarse rock fills for dam construction was reported by Lowe (1964). The maximum size of the rock fills was about 300 mm. In order to use a conventionally sized triaxial shear machine to test the rock fills, a modelled sample of the prototype material was put inside a triaxial shear machine which could test specimen up to 150 mm diameter. The model samples used were made of a certain fraction of the prototype material wherein each particle of the model sample was roughly 1/8 the size of the corresponding particle in the prototype material. Every effort was made to duplicate the shape and mineralogical composition of the prototype material. Implicitly, Lowe assumed that modelling of soil particle does not alter the shear strength of the material. Marachi et at (1969, 1972) have carried out a comprehensive series of tests on rock fill materials with their large diameter triaxial shear machines which suggested that Lowe's technique is unsafe. Fig 2.30 shows the effect of particle size alone on ϕ for crushed basalt. ϕ was found to decrease as

particle size increased. They proposed that the amount of particle breakage increases as the particle size increases, as would be expected from Griffith's crack theory (1921, 1924). Kerisel (1972) attributed the phenomenon to specimen volume effect, i.e. as the volume of soil under test decreases, even though similarity in grain size to specimen size ratio is maintained, the mechanical strength should increase. However, the present triaxial test data have confirmed that the conclusions of Marachi et al (1969, 1972) are more plausible as all the tests display the same phenomenon as observed by Marachi et al even though the volume of the specimen remains constant.

(5) According to Roscoe et al (1963) , the apparent volume change during the increment of effective cell pressure from 35 to 700 kPa as observed from burette readings was about 5 times the estimated volume change of the skeleton according to the assumption that $\Delta V = 3\varepsilon_a$. Because of the bedding error as a result of using latex membranes and grease at both end platens, Roscoe's technique can not be adopted here. However, Marachi et al (1969, 1972) have shown that there is no absolute particle size effect in isotropic compression. By adopting this assumption, λ for sand is found to be overestimated by 80% and κ is overestimated by 65%. In this work, λ and κ measured from the silt tests, being free from membrane penetration error are adopted equally for the sand.

(6) The rate of loading varied between the tests. For the silt a maximum of 2mm/hour was imposed. This rate was based on the work by Airey (1987) which shows that for kaolin which is about 1000 times less permeable than silt, the maximum loading rate for a drained test should be 0.05mm/hour. By simple scaling, the maximum loading rate for silt should not exceed 40mm/hour. Therefore, the adopted rate of 2mm/hour should provide ample margin of safety against inducing unwarranted excess pore water pressures inside a specimen. During one triaxial test on silt (test FHP1), the loading rate was deliberately doubled suddenly from the maximum rate but no observable change in the behaviour can be observed (see fig 2.19). Furthermore, all the tests follow the same trend as expected; therefore the maximum loading rate is deemed slow enough.

(7) Shifting of the grading curves shows that crushing has occured during the triaxial tests for sand under high pressure (see fig 2.31). Visually, some fraction of the sand was found to have been degraded into very fine powder.

(8) Once ϕ_{max} is mobilized, it can be sustained for quite a large strain, i.e. typically 5% axial strain (see fig 2.20 and 2.21). This point is significant as will be explained in section 7.9.

2.9 Direct Shear Box Test

Saturated silt or sand was put inside a 100 mm x 100 mm direct shear box. The shear box was then put on a vibrating table for compaction while the specimen was subjected to a vertical pressure of 500 kPa provided by dead weight. The dry density of each specimen was evaluated by measuring the volume of the shear box occupied by the material and the weight of the oven-dried material after each test. This sample preparation method has highlighted the difficulties in preparing dense granular material by vibration on a conventional vibration table (with vertical cyclic movement). The reason is that the specimen is subjected to cyclic 1-dimensional loading and unloading. This has proved to be far less effective than the repeated shearing of the specimen in the fashion shown in fig 2.3 which may have imposed rotation of stress direction on the specimen. As a result, only 2 drained direct shear tests have been conducted, one on saturated silt and one on saturated sand. A shearing rate of 2.28 mm/hour and 11.52 mm/hour had been adopted for tests on silt and sand respectively. Both tests were carried out under initial normal stresses of 100 kPa. The initial void ratios were 0.78 and 0.74 for the sand and silt respectively. The strain-controlled direct shear box test results are plotted in fig 2.32 as secant ϕ mobilized on the horizontal plane against horizontal displacement. Vertical displacement versus horizontal displacement is also shown. In both cases, it has been assumed that the horizontal plane coincides with the plane of maximum stress obliquity.

$$\text{i.e.} \quad \phi = \tan^{-1} \tau_n / \sigma_n \qquad \qquad *$$

where τ_n is the shear stress
and σ_n is the normal stress on the horizontal shear plane.

Apart from being considered as equipment to measure the basic soil properties in the usual sense, the direct shear box can also be viewed as a special model test which unlike the triaxial test, positively encourages intense stress concentration in the specimen. Although ϕ_{crit} is almost the same for both sand and silt, ϕ_{max} for sand is 4.5° higher than ϕ_{max} for silt. The rate of dilation for sand is consistent with this, being higher than that for silt. This is contrary to the triaxial test data and suggests that progressive failure as a result of varying the model to particle size ratio may be operative here. The other interesting observations are that ϕ_{crit} appears to be independent of apparatus probably because there is no volume change once critical state is reached. Taking ϕ_{crit} as the angle mobilized when all dilatancy are suppressed, both direct shear box tests and stress dilatancy plots (see fig 2.22b) indicated the two soils possessed indentical critical state

* Note taking the stress ratio on the horizontal plane as equal to $\sin \phi$ would give higher value of ϕ.

angles ($=37.5°$). This high value, according to Norris (1977) is typical for angular soils.

2.10 Complications In Soil Particle Modelling

In order to model soil particles successfully, practical steps should be taken to eliminate all complications introduced as a result of scaling the soil particle. The similarity conditions ought to include:

(a) Shape of the grading curve,

(b) Particle shape,

(c) Mineralogy,

(d) ϕ_{crit}

(e) Particle crushing strength.

The relationship between the mean specimen size and breaking strength of rock is well known. For example, Hoek and Brown (1980) have proposed an empirical correlation to account for the rock specimen size effect as

$$\sigma_c = \sigma_{c50} (^{50}/_d)^{0.18}$$

where σ_c is the unconfined compressive strength of a specimen.

σ_{c50} is the unconfined compressive strength of a 50 mm diameter specimen of the same material.

d is the diameter of the cylindrical specimen.

The above-mentioned empirical correlation suggests that between the sand and silt, there should be a difference in strength by a factor of 2 whereas a factor of 4.5 was actually measured.

Consider, for example, a grain of 0.6mm nominal diameter silica sand and a grain of 12µm nominal diameter silica silt. It is likely that the grain of sand, being 125000 times larger in volume than the grain of silt, contains more imperfections than its counterpart. The imperfections may be in the form of numerous cleavages or plane of weakness in the particle at a regular characteristic intervals. Because of its much smaller size, the number of imperfections in the silica silt particle must be statistically fewer. In some extreme cases, the grain of silt may even be in the form of a perfect single crystal provided that the particle is smaller than the characteristic spacing of defects of a particular mineral (see fig 2.33). It is, therefore, believed that the absolute size of a particle alone may have some influence on the crushing strength of the particle. Consequently, the absolute size of a particle alone may change the shear strength of a

material in which the particle forms a part. This may explain why ϕ_{max} in a triaxial test is dependent on d_{50}.

Difficult as it may be in practice, it is theoretically possible to conserve conditions (a) to (d) inclusive when modelling soil particle. However, for particle crushing strength, maintaining a constant value in reduced-scale particle modelling is likely to be impossible. Therefore, an empirical correction has to be made to account for the changes in crushing strength. Alternatively, the coarser material can be modelled by a finer but more crushable mineral instead. It should be pointed out here, however, that by using a weaker material to compensate for the invulnerability of the finer particle to crushing, the mineralogy is no longer conserved, and surface friction may coincidentally be altered, for example.

2.11 Summary

Two silica soils, namely, a sand and a silt, which differed in grain nominal diameter by a factor of 50 but were otherwise indistinguishable in terms of shape, grading and mineralogy were successfully acquired. Triaxial test results demonstrated that the silt was able to maintain a higher peak angle of shearing and rate of dilation than the sand. Under similar void ratio (close to minimum) and confining pressure, ϕ_{max} of the silt is 4 to 5 ° higher than the sand. The extra strength is also associated with extra dilatancy. It can equally be said that the silt is about 4.5 times less stress sensitive than the sand which may be explained by the characteristic spacing of flaws in a quartz mineral. The shear strengths for both soils were found to satisfy a linear relation for secant ϕ_{max} plotted against the logarithm of mean stress. In addition to the strength parameter, stiffness parameters were also measured for serviceability calculations.

3. BEARING CAPACITY - CONSTANT Φ

3.1 Introduction

A theoretical prediction of bearing capacity should be made available, before any definitive statements on scale effects in tests on footings can be made. At present, there are still a number of uncertainties in the prediction of bearing capacity, even when rigid-perfectly-plastic material with constant ϕ is assumed. It is more uncertain for the axisymmetric case than for plane strain.

There are four main methods of analysis:

(1) Limit equilibrium (Terzaghi, 1943, Meyerhof, 1951)

(2) Limit plasticity (Finn, 1967, Chen, 1975)

(3) Method of characteristics (Sokolovski, 1942/1960, Cox et al, 1961, Cox, 1962)

(4) Finite element (Girijavallabhan & Reese, 1968, Griffith, 1982)

In the limit equilibrium method, an arbitrary assumption with regard to the shape of a rupture plane or velocity discontinuity has to be made. As a result, there is no theoretical justification to suggest that the solution is correct. This technique, therefore, always requires validation against collapse limit state events.

Since the upper and lower bound theorems of plasticity have been proved for perfectly-plastic material (Drucker et al, 1951), a great deal of interest has been focussed on the possibility of using plasticity to solve boundary value problems in soil mechanics. The upper bound solution gives a "safe" solution to the task of defining design loads on an earth-moving machine for example. However, a geotechnical engineer who seeks to avoid the earth moving should prefer a lower bound solution to make a conservative design decision. Powerful as it may be, limit analysis at present can only provide solutions for a few very simple cases.[*]

In this work, only the method of characteristics was used. This is because the method can handle slightly more complicated problems. The solutions can be treated as lower bounds if it is possible to extend the stress field throughout the body, without anywhere exceeding the shear strength. The method of characteristics solution can be treated as upper bounds if coincidental velocity characteristics are shown to be kinematically admissible and satisfying the velocity boundary conditions without

[*] Note that strictly those theorems may only be used for frictional materials if normality applies.

involving any negative plastic work. A solution is deemed exact or complete only when it is statically and kinematically admissible. Table 3.1 summarizes a number of cases in the literature which have been solved in this rigorous manner. It is also possible to extend Cox's proof (Cox et al, 1961) for $\phi=20°$ to other cases if so required.

The finite element method is perhaps the most sophisticated and involved technique among the four discussed here. Griffith (1982) has shown that finite element analysis can predict ultimate bearing capacity in close agreement with other published exact and approximate solutions, but it takes considerably more computing effort. Although there is no obvious advantage in using this method to estimate the ultimate bearing capacity, chapter 5 will explain why this method is suitable for predicting the load-settlement response of a footing before collapse.

This chapter starts by reviewing some existing literature on the method of characteristics. Wherever necessary, clarifications and comments are made. The formulation and development of the methods used in this thesis are then presented. In the first instance, N_q and N_γ for both plane strain and axisymmetric cases are obtained for a wide range of ϕ. The effects of superposition are then studied. After that, the effects of embedment are rationalized and quantified. With these calculations made available, an unambiguous method for estimating an equivalent constant ϕ_{max} in the model footing tests in chapters 6 and 7 is proposed.

3.2 The Method Of Characteristics: Review

Sokolovski (1942/1960) has outlined the underlying assumptions and formulation of the method of characteristics for a strip footing. His method was later generalized by Shield (1955) to include the axisymmetric case but only for the Tresca material. Cox et al (1961) include the Mohr-Coulomb material in their analysis but only for weightless soil. Cox (1962) extended the method further by including self-weight in his analysis. He put $c^*=c+\sigma_0\tan\phi$ and introduced a dimensionless parameter G which equals $\gamma B/(2c^*)$. By solving the governing differential equations numerically, Cox's solution can directly take into account any combination of self-weight, cohesion and surcharge without resorting to superposition.

It should be pointed out that Cox et al (1961) and Cox (1962) have defined σ_0 as equal to atmospheric pressure. This assumption is unusual to the geotechnical engineer. However, their subsequent mathematical formulation of the problem does not hinge on this assumption. As a matter of fact, it only renders their solution more general

as σ_0 can be assigned any positive value. Equally, the introduction of a dimensionless parameter G is not central to the formulation either. For example, Larkin (1968) has normalized his stress variables by 0.5Bγ and the co-ordinates by 0.5B. From the numerical point of view, Larkin's approach is actually more straightforward.

Although Cox et al (1961), Cox (1962) and Larkin (1968) have laid down the theoretical foundation for calculating N_q and N_γ for both plane strain and axisymmetric cases, only very limited numerical results are available. Little effort has been made to generate and present the results for a wide range of ϕ which are likely to be encountered in practice. Nor is there any effort to present the results in an immediately understandable fashion. As a result, plane strain bearing capacity coefficient together with empirical shape factors are still widely used when designing axisymmetric footings.

The reason for this is probably due to the unusual assumption made by Cox et al (1961) that a surcharge of $\sigma_0 \approx 100$kPa (i.e. atmospheric pressure) is assumed acting permanently on the soil surface. As for Larkin (1968), his results for plane strain differed by a factor of 2 from the Prandtl (1920) solution which is known to be exact. Hansen and Christensen (1969) suggest that this may have been due to some arithmetic errors. It may also have been due to the adoption of different notation by Cox and Larkin. Unfortunately, this discrepancy remains unexplained to date.

Despite these blemishes, Cox et al (1961), Cox (1962) and Larkin's (1968) formulation of the footing problem is mathematically correct. What is really needed here is some clarification and re-interpretation of their work from the view point of a geotechnical engineer. For example, Cox's published results have always lumped the N_q and N_γ term together which renders it free from any superposition error. Provided that the conservative nature of the superposition technique can be substantiated and quantified, it is by uncoupling the N_γ and N_q factors that their results, and indeed any further results, will become more readily accessible to the engineer.

3.3 Underlying Assumptions

The underlying assumptions of the subsequent analysis are stated as follows:

(1) The material obeys Mohr-Coulomb yield criterion (see fig 3.1). Failure can only take place in the directions of limiting shear stress. This implies that the intermediate principal stress has no influence on the shear strength of the soil.

(2) The circumferential principal stress σ_θ is equal in value to the minor

principal stress. This is a special case of the Haar and Von Karman hypothesis (1909) which states that σ_θ should be equal to either one of the two principal stresses acting in an axial plane (see fig 3.2), i.e. $\sigma_\theta = \sigma_3$.

(3) The material is rigid-perfectly-plastic. It fails at zero strain and at constant yield stress which is dependent on the mean stress (see fig 3.3a), where

$$\tau_f = \sigma \sin\phi \quad \text{and} \quad \sigma = \frac{1}{2}(\sigma_1 + \sigma_3)$$

3.4 Mathematical Formulation

Shi's (1988) mathematical formulation is adopted here, his formulation is essentially similar to Larkin (1968) except that there is some slight difference in mathematical notation. For example, σ is defined as the mean stress here while Larkin defines σ as the radius of the Mohr circle. By considering the equilibrium of a toroidal element in fig 3.4, the equations of equilibrium can be written in cylindrical co-ordinates r, θ and z as

$$\frac{\partial \sigma_r}{\partial r} + \frac{1}{r}\frac{\partial \tau_{r\theta}}{\partial \theta} + \frac{\partial \tau_{rz}}{\partial z} + \frac{\sigma_r - \sigma_\theta}{r} = 0$$

$$\frac{\partial \tau_{rz}}{\partial r} + \frac{1}{r}\frac{\partial \tau_{\theta z}}{\partial \theta} + \frac{\partial \sigma_z}{\partial z} + \frac{\tau_{rz}}{r} = \gamma \qquad \text{eqn 3.1}$$

$$\frac{\partial \tau_{r\theta}}{\partial r} + \frac{1}{r}\frac{\partial \sigma_\theta}{\partial \theta} + \frac{\partial \tau_{\theta z}}{\partial z} + \frac{2\tau_{r\theta}}{r} = 0$$

For axial symmetry, a pair of first order ~~hyperbolic~~ partial differential equations can be obtained,

$$\frac{\partial \sigma_r}{\partial r} + \frac{\partial \tau_{rz}}{\partial z} + \frac{\sigma_r - \sigma_\theta}{r} = 0$$

$$\qquad \text{eqn 3.2}$$

$$\frac{\partial \tau_{rz}}{\partial r} + \frac{\partial \sigma_z}{\partial z} + \frac{\tau_{rz}}{r} = \gamma$$

Assuming that the soil satisfies the Mohr-Coulomb failure criterion, $\tau_f = \sigma \sin\phi$, the four stress components can be expressed in terms of two dependent variables σ and ψ,

$$\sigma_r = \sigma(1 + \sin\phi\cos2\psi)$$

$$\sigma_z = \sigma(1 - \sin\phi\cos2\psi)$$

$$\tau_{rz} = \sigma\sin\phi\sin2\psi)$$

$$\sigma_\theta = \sigma(1 - \sin\phi) = \sigma_3$$

eqn 3.3

where ψ is the angle between the major principal stress direction and the z axis, and $\sigma=0.5(\sigma_1+\sigma_3)$ (see fig 3.3b). Cox et al (1961) have shown that solutions exist if the special case of the Haar and Von Karman hypothesis is assumed, i.e. $\sigma_\theta=\sigma_3$. This assumption is safe since $\sigma_2<\sigma_3$. In chapter 5, a more detailed discussion will be made. New evidence will also be introduced to support this hypothesis.

Differentiating eqn 3.3, we have

$$\frac{\partial\sigma_r}{\partial r} = -2\sigma\sin\phi\sin2\psi\frac{\partial\psi}{\partial r} + (1 + \sin\phi\cos2\psi)\frac{\partial\sigma}{\partial r}$$

$$\frac{\partial\sigma_z}{\partial z} = -2\sigma\sin\phi\sin2\psi\frac{\partial\psi}{\partial z} + (1 - \sin\phi\cos2\psi)\frac{\partial\sigma}{\partial z}$$ eqn 3.4

$$\frac{\partial\tau_{rz}}{\partial z} = -2\sigma\sin\phi\cos2\psi\frac{\partial\psi}{\partial z} + \sin\phi\sin2\psi\frac{\partial\sigma}{\partial z}$$

From eqn 3.3, we can also write $\quad \frac{\partial\tau_{rz}}{\partial r} = -2\sigma\sin\phi\cos2\psi\frac{\partial\psi}{\partial r} + \sin\phi\sin2\psi\frac{\partial\sigma}{\partial r}$

$$\frac{\sigma_r-\sigma_\theta}{r} = \frac{\sigma}{r}\sin\phi(1 + \cos2\psi)$$

Combining the stress conditions at yield (eqn 3.4) with the equations of equilibrium (eqn 3.2), a system of governing equations can be written in terms of σ, ψ, r and z,

$$(1 + \sin\phi\cos2\psi)\frac{\partial\sigma}{\partial r} + \sin\phi\sin2\psi\frac{\partial\sigma}{\partial z}$$

$$+2\sigma\sin\phi[-\sin2\psi\frac{\partial\psi}{\partial r} + \cos2\psi\frac{\partial\psi}{\partial z} + \frac{1}{2r}(1 + \cos2\psi)] = 0$$

eqn 3.5

$$\sin\phi\sin2\psi\frac{\partial\sigma}{\partial r} + (1 - \sin\phi\cos2\psi)\frac{\partial\sigma}{\partial r}$$

$$+2\sigma\sin\phi[\cos2\psi\frac{\partial\psi}{\partial r} + \sin2\psi\frac{\partial\psi}{\partial z} + \frac{1}{2r}\sin2\psi] = \gamma$$

Equations of variation of σ and ψ can also be written as

$$d\sigma = \frac{\partial\sigma}{\partial r} dr + \frac{\partial\sigma}{\partial z} dz$$

$$d\psi = \frac{\partial\psi}{\partial r} dr + \frac{\partial\psi}{\partial z} dz$$

eqn 3.6

Eqn 3.5 and 3.6 can be written in matrix form as $A.b=c$

$$
\begin{bmatrix}
1 + \sin\phi\cos2\psi & \sin\phi\sin2\psi & -2\sigma\sin\phi\sin2\psi & 2\sigma\sin\phi\cos2\psi \\
\sin\phi\sin2\psi & 1 - \sin\phi\cos2\psi & 2\sigma\sin\phi\cos2\psi & 2\sigma\sin\phi\sin2\psi \\
dr & dz & 0 & 0 \\
0 & 0 & dr & dz
\end{bmatrix}
\begin{bmatrix}
\partial\sigma/\partial r \\
\partial\sigma/\partial z \\
\partial\psi/\partial r \\
\partial\psi/\partial z
\end{bmatrix}
$$

$$
=
\begin{bmatrix}
- \dfrac{\sigma}{r} \sin\phi(1 + \cos2\psi) \\[2mm]
- \dfrac{\sigma}{r} \sin\phi\sin2\psi + \gamma \\[2mm]
d\sigma \\[2mm]
d\psi
\end{bmatrix}
$$

For hyperbolic equations such as these, the solution for b is not unique, and the determinant of A is zero. By putting $\det A = 0$, we have

$$\frac{dr}{dz} = \tan(\psi + \eta) \qquad : \qquad \alpha \text{ characteristic}$$

$$\frac{dr}{dz} = \tan(\psi - \eta) \qquad : \qquad \beta \text{ characteristic}$$

where $\eta = \pi/4 - \phi/2$.

Along these two families of characteristics, the governing equations (eqn 3.5) become two ordinary differential equations. They can be obtained by replacing the fourth column of A by c and setting the determinant of the resultant matrix to zero, which gives

$$d\sigma\cos\phi + 2\sigma\sin\phi d\psi + n\frac{\sigma}{r}[\sin\phi\cos\phi dr + (\sin^2\phi - \sin\phi)dz]$$

$$= \gamma(-\sin\phi dr + \cos\phi dz)$$

along an α characteristic given by $\dfrac{dr}{dz} = \tan(\psi + \eta)$

$$d\sigma\cos\phi - 2\sigma\sin\phi\,d\psi + n\frac{\sigma}{r}[\sin\phi\cos\phi\,dr - (\sin^2\phi - \sin\phi)dz]$$

$$= \gamma(\sin\phi\,dr + \cos\phi\,dz)$$

eqn 3.7

along a β characteristic given by $\dfrac{dr}{dz} = \tan(\psi - \eta)$

For the axisymmetric case we must take n=1, while for the plane strain case n=0 (by inspection). Eqn 3.7 can now be written in finite difference form. Before computation can begin, the variables have to be normalized according to some characteristic length (Sokolovski, 1960). Following Larkin (1968), the variables are normalized by putting $\Sigma = \sigma_0/(0.5B\gamma)$, and R and Z are expressed in units of 0.5B. Eqn 3.7 then becomes,

$$R = R_1 + (Z - Z_1)\tan(\psi_1 + \eta)$$

$$R = R_2 + (Z - Z_2)\tan(\psi_2 - \eta)$$

eqn 3.8

and

$(\Sigma - \Sigma_1) + 2\Sigma_1\tan\phi\,(\psi - \psi_1)$

$$= \frac{-2\Sigma_1}{(R + R_1)\cos\phi}\sin\phi\cos\phi(R - R_1) - \frac{(\sin^2\phi - \sin\phi)}{\cos\phi}(Z - Z_1)$$

$$- \frac{\sin\phi}{\cos\phi}(R - R_1) + (Z - Z_1) \quad : \quad \text{along an } \alpha \text{ characteristic}$$

eqn 3.9

$(\Sigma - \Sigma_2) - 2\Sigma_2\tan\phi\,(\psi - \psi_2)$

$$= \frac{-2\Sigma_2}{(R + R_2)\cos\phi}\sin\phi\cos\phi(R - R_2) - \frac{(\sin^2\phi - \sin\phi)}{\cos\phi}(Z - Z_2)$$

$$+ \frac{\sin\phi}{\cos\phi}(R - R_2) + (Z - Z_2) \quad : \quad \text{along a } \beta \text{ characteristic}$$

In order to solve eqn 3.9 which are not in explicit form, Shi (1988) suggested the following substitution,

$$A = \frac{-2\Sigma_1}{(R + R_1)\cos\phi}\sin\phi\cos\phi(R - R_1) \quad \frac{(\sin^2\phi - \sin\phi)}{\cos\phi}(Z - Z_1)$$

$$- \frac{\sin\phi}{\cos\phi}(R - R_1) + (Z - Z_1) + \Sigma_1 + 2\Sigma_1\tan\phi\psi_1$$

$$B = \frac{-2\Sigma_2}{(R + R_2)\cos\phi}\ \sin\phi\cos\phi(R - R_2)\ \frac{(\sin^2\phi - \sin\phi)}{\cos\phi}\ (Z - Z_2)$$

$$+\ \frac{\sin\phi}{\cos\phi}\ (R - R_2) + (Z - Z_2) + \Sigma_2 - 2\Sigma_2\tan\phi\psi_2$$

Eqn 3.9 can now be written as

$$\Sigma + 2\Sigma_1\tan\phi\psi = A$$

$$\Sigma - 2\Sigma_2\tan\phi\psi = B$$

so that

$$\Sigma = \frac{A\Sigma_2 + B\Sigma_1}{\Sigma_1 + \Sigma_2}$$

$$\psi = \frac{B - A}{-2\tan\phi(\Sigma_1 + \Sigma_2)}$$

eqn 3.10

which are now suitable for iteration.

3.5 Organization Of Computation

Eqn 3.8 and 3.10 can now be used to determine Σ and ψ at the point of intersection of the α and β characteristics from either a known boundary condition or from previously computed values at two adjacent points. These two points must not lie on the same characteristic. Proceeding from the known boundary condition along KS (fig 3.5), the entire stress field within KLMO can be determined. To begin with, R was assumed. When the calculation was complete, it should be checked to see if the β characteristic starting from K actually finishes at O. If not, R was adjusted according to whether it is too far or too near. This process was iterated until an acceptable accuracy was achieved.

The algorithm was organized in such a way that the solution for the characteristic field proceeded from initially equally-spaced points on the known boundary, where R, Z, ψ and Σ are known. If at P and Q (see fig 3.6), R_P, Z_P, ψ_P, Σ_P and R_Q, Z_Q, ψ_Q, Σ_Q are known, from eqn 3.8, R and Z at W can be calculated by putting $\psi_1 = \psi_P$ and $\psi_2 = \psi_Q$. ψ and Σ can then be calculated from eqn 3.10. However, in general, the stress characteristics are curved, so that $\psi \neq \psi_W$ and $\Sigma \neq \Sigma_W$. The solution can be improved by solving eqn 3.8 again by putting $\psi_1 = (\psi + \psi_P)/2$ and $\psi_2 = (\psi + \psi_Q)/2$ instead of ψ_P and ψ_Q. By repeating this process, ψ and Σ will eventually converge to ψ_W and Σ_W as the number of iterations increases (Sokolovski, 1960). The iteration

stops when a target accuracy is achieved. A flow chart showing the organization of the program is shown in fig 3.7. This same iteration process can be repeated throughout the whole region. A very coarse mesh as shown in fig 3.5 will be used here to illustrate the marching scheme used in the computer program CONPHI.

(1) Passive zone - The boundary conditions at S, K1, K are known. K2 can be found with K1 and K known; K3 can be found with S, K1 known. Likewise, L can be found from K3 and K2. S, K3, L have now become the known boundary conditions for the fan zone.

(2) Fan zone - Node S can be viewed as a degenerate β characteristic, which is sometimes known as the Prandtl singularity. Being a singularity, it can have the same R, Z, but quite different ψ and Σ. Within the fan zone, the stress should increase exponentially according to the amount of rotation of the principal stress direction. At S, before rotation, ψ and Σ are the known boundary conditions. When the principal stress rotates by θ at S, the boundary condition becomes

$$\Sigma_{(\theta)} = \Sigma\ e^{2\theta\tan\phi}$$

$$\text{and}\quad \psi_{(\theta)} = \psi + \theta$$

Having established this, when $\theta=\pi/4$, L1 can be found with $S_{(\pi/4)}$ and K3 known; L2 can be found with L1 and L known. Likewise, L3 can be found with $S_{(\pi/2)}$ and L1 known; and M can be found with L3 and L2 known. S, L3, M have now become the known boundary conditions for the active zone.

(3) Active zone - At M2 which is in direct contact with the footing, ψ and Z are known as imposed boundary conditions (the value of ψ depending on whether the footing is rough or smooth) but not Σ and R which have to be calculated. The solution of Σ and R at M2 can therefore be determined from the known condition at L3. Once M2 is known, M1 can be determined from M2 and M in the usual manner. Like M2, Σ and R at O can also be determined from known conditions at M1, with ψ and Z as imposed boundary conditions. At this stage, all the variables at O, M2 and $S_{(\pi/2)}$ are known. The bearing pressure σ_z can now be calculated by multiplying Σ with $0.5B\gamma$ to give σ and substituting it together with ψ back to eqn 3.3. The mean bearing pressure σ_f under the footing can now be obtained by integrating σ_z over the whole contact area numerically.

3.6 Principle Of Superposition

As mentioned in section 3.2, Cox (1962) has introduced a dimensionless parameter G which equals $\gamma B/(2c^*)$. For the case of cohesionless soil G becomes $\gamma B/(2\sigma_0 \tan\phi)$. Practically what Cox is saying in Terzaghi's terminology is that the values of N_γ and N_q are not constant but are changing according to the contribution of the self-weight term and that of the surcharge term towards the bearing capacity. For the special case of $\phi=45°$, G becomes $\gamma B/(2\sigma_0)$. For example G=10 is equivalent to saying that the γ term is 10 times that of the q term which represents a very shallow footing. On the other hand, G=0.01 is equivalent to saying that the q term is 1/100 that of the γ term. The condition is now more like the end bearing of a pile foundation.

The conservative nature of superposition has been proved, for example, by Bolton (1988). His argument is that the proof can be divided into two aspects. The first one is equilibrium and the second one is the constitutive relationship. As the resultant of superposing two systems of stresses which are in equilibrium must also be in equilibrium, therefore, the first condition is proved. Referring to an arbitrary surface in fig 3.8, consider two cases of stress represented by vectors $\underset{\sim}{a}$ and $\underset{\sim}{b}$ which are within the Mohr-Coulomb envelope; by inspection, the resultant $\underset{\sim}{c}$ must always lie within the envelope, therefore, superposition must be conservative for material with constant ϕ. It remains to quantify the error margin in any particular case.

Davis and Booker (1971) have discussed the superposition error from the view point of plasticity and concluded that superposition is conservative for the plane strain case. They have also shown that the resulting error is no more than 20% on the safe side when $\phi=20$, 30 and 40°. A similar investigation of the principle of superposition for the case of axisymmetry will be made here. In order to demonstrate the effects of superposition, it is proposed that a new combined bearing capacity factor be defined as

$$N_{q\gamma} = \frac{\sigma_f}{0.5B\gamma + \sigma_0}$$

Where $N_{q\gamma}$ is a function of ϕ and Ω with $\Omega=\sigma_0/(0.5B\gamma)$ which will be known as the superposition factor.

Fig 3.9 and 3.10 depict the effects of Ω on the superposition error for the cases of $\phi=30°$ and 40° respectively. By converting Cox's data into a similar format, it can be seen from the same two figures that the present investigation produces results which are practically the same as Cox's although the numerical solution techniques are slightly different. The maximum superposition error is found to be within 20% and is on the safe

side. The error is at its maximum when Ω is near 1. Fig 3.11 shows the effects of Ω on R. As expected, the results are in complete agreement with Cox's results.

In order to get rid of the superposition error altogether, fig 3.9 and 3.10 can be used to find $N_{q\gamma}$ which is treated as a function of ϕ and Ω. It can therefore be concluded that the "exact" (in the sense that there is no superposition error) solution always gives a higher bearing capacity than those using superposition, provided that N_q and N_γ are obtained for $\Omega \rightarrow 0$ and $\Omega \rightarrow \infty$. A table of N_q and N_γ for both plane strain and axisymmetric cases will therefore be generated in section 3.7 for subsequent comparision with experimental data in this work and also for the benefit of the practising engineer.

Notwithstanding the above, as computers are readily available and increasingly cheap nowadays, it would be quite straight forward to compute the "exact" bearing capacity according to the actual combination of the q and γ terms. This is especially useful, for example, for jack-up spudcan design and penetrometer interpretation when the engineer is more interested in the actual ultimate load than a safe working load.

3.7 Numerical Calculation Of N_q And N_γ

As mentioned earlier, by putting the superposition factor $\Omega \rightarrow \infty$, the N_q solution can be obtained. Likewise, when $\Omega \rightarrow 0$, N_γ can be evaluated. This method of uncoupling N_q and N_γ from $N_{q\gamma}$ is not unlike the technique adopted in the planning of the physical modelling programme described in chapters 6 and 7.

In practice, N_q was obtained with $\Omega=1000$ and N_γ with $\Omega=0.001$. This was because some finite value of surcharge must be used in $\underset{\wedge}{\text{the}}$ this γ analysis for a Mohr-Coulomb material with no cohesion. As further reduction in Ω in the N_γ analysis and further increase in Ω in the N_q analysis did not make any practical difference in the outcome, these estimates were substantiated.

The results of N_q and N_γ are summarized in column 2 to 5 in table 3.2 and those of R^* are summarized in corresponding columns in table 3.3. The footings were assumed flat and smooth. All the analyses were carried out with a mesh consisting of 96 β characteristics and 220 α characteristics. The rotation step of the principal stress direction in the fan zone was $3°$. Fig 3.12, 3.13, 3.14 and 3.15 show the typical stress characteristics and footing pressure distribution for plane strain and axisymmetric cases for both N_q and N_γ at $\phi=40°$. Fig 3.16 shows the case when $\Omega=1$ for the axisymmetric condition at $\phi=40°$.

* R is as defined in fig 3.5.

3.8 Equivalent Surcharge To Replace Self-Weight

It is tempting to find an equivalent surcharge to represent the self-weight so that the bearing capacity can be calculated in terms of N_q alone. The simplest approach is replacing $0.5B\gamma$ by σ_e and assuming $N_q = N_\gamma$ so that

$$\sigma_f = \sigma_e N_q = \frac{1}{2} B\gamma N_q$$

Fig 3.9 and 3.10 show clearly that N_q and N_γ are very different. This assumption is not, therefore, very accurate. Comparing fig 3.12 and 3.13, or fig 3.14 and 3.15, it can be seen that the shear fan zones have drastically contracted due to the effects of self-weight. It is clear that the self-weight in the N_γ analysis has caused the principal stress to rotate in the active zone, so much so that the principal stress in the fan need only rotate the balance of $\pi/2$ instead of the full $\pi/2$ as in the N_q analysis. This may be the reason why the plastic fan region is much smaller in the N_γ case than in the N_q case. For the case when $\Omega=1$, fig 3.16 shows that the plastic fan region falls somewhere between the cases for $\Omega=1000$ (see fig 3.14) and $\Omega=0.001$ (see fig 3.15). It is clear that the size of the fan region is dependent on Ω. The method of equivalent surcharge, therefore, has no general validity.

3.9 Rough Footings

It has been shown (Chen, 1975) that Prandtl's solution is both statically and kinematically admissible for either rough or smooth footings on weightless soil in plane strain. Although no such identity has yet been demonstrated in axisymmetric problems, it will hereafter be assumed that

$$N_{q,rough} = N_{q,smooth}$$

On the other hand, for soil with self-weight, it is anticipated that as the plastic region is bigger in the Prandtl type mechanism than the Hill's mechanism (1950) (see fig 3.17 and 3.12), and more soil means more weight, the bearing capacity should also be bigger. Meyerhof (1955) has experimental evidence to suggest that

$$N_{\gamma,rough} \approx 2 \times N_{\gamma,smooth}$$

published in English

As there is at present no satisfactory solution for rough base footings in an axisymmetric condition,[*] it is proposed to construct an artifice so that an approximate solution can be obtained as follows. In all rough footing analyses for N_γ, a trapped wedge/cone was assumed underneath a rough footing (see shaded area in fig 3.17, 3.18

[*] However see Wojciech Szczepinski (1974)

and 3.19) with $\alpha=\pi/4+\phi/2$ and $\delta=\phi$ where δ is the friction between wedge/cone and soil (see fig 3.19).

This artifice is chosen so that the resultant σ_z including at the tip of the wedge/cone is always vertical. Symmetry can, therefore, be conserved at the centreline. Although there is no rigorous theoretical justification for this assumption, there is experimental evidence to suggest that such a wedge/cone does exist (for example, Ko & Davidson, 1973). Columns 6 and 7 of tables 3.2 and 3.3 summarize $N_{\gamma,rough}$ and R generated with these additional conditions imposed. Fig 3.18 and 3.19 show the stress characteristics and footing pressure distributions for the plane strain case and axisymmetric cases respectively for $\phi=40°$.

3.10 Penetration Effects

When a footing settles, the bearing capacity tends to increase (see fig 3.20), there are three ways to account for this phenomenon. They are:

(1) Additional surcharge due to the overburden.

(2) Shear strength of the overburden being mobilized but there is no additional rotation of principal stress direction in the fan zone.

(3) Shear strength of the overburden being mobilized together with the additional rotation of principal stress direction in the fan zone.

Larkin (1968) attempted to extend Cox's (1962) work to include the shear strength of the overburden in the bearing capacity calculation. He assumed that the principal stress direction should remain horizontal throughout the overburden (see fig 3.21). In other words, there is no further rotation of the principal stress direction upon penetration. Effectively, his assumption is indistinguishable from only taking into account the additional surcharge of the overburden in his solution. As will be shown later in chapter 6, the increase in bearing capacity upon penetration was much higher than could be accounted for solely by the additional surcharge due to the overburden. In order to account for this phenomenon, the stress field must be extended in such a way that the direction of principal stress can actually rotate further so that additional bearing capacity of the magnitude observed experimentally could be mobilized.

Meyerhof (1951) has proposed such an extension based on the work of Prandtl (1920) and Reissner (1924) for footings with initial burial, which can incorporate the shear strength of the overburden as well as the ability to have additional rotation of principal stress direction (see fig 3.22a). The penetration effects of a strip footing on

frictional weightless soil can now be incorporated in

$$\sigma_f = \sigma_o K_P \, e^{2\theta \tan\phi} \qquad\qquad \text{eqn 3.11}$$

where $\theta = \pi/2 + \beta$ and $0 \leq \beta \leq \pi/2$ When $\beta = 0$, the footing is at the surface and $\theta = \pi/2$,

$$\sigma_f = \sigma_o K_P \, e^{\pi \tan\phi}$$

When $\beta = \pi/2$, the footing is at a critical depth D_c, i.e. all additional rotation of principal stress has been exhausted and $\theta = \pi$,

$$\sigma_f = \sigma_o K_P \, e^{2\pi \tan\phi}$$

The above expressions have assumed that the soil within abc of fig 3.22a possesses no shear strength and acts as a hydrostatic fluid. This assumption has greatly simplified the calculation and is also conservative.

It is clear now that for $0 < D < D_c$, the penetration effects can be treated as a problem of gradual additional rotation of principal stress. The bearing capacity equation can now be treated as a simple geometry problem which relates penetration D with the equivalent additional rotation of principal stress direction. By defining bc of fig 3.22a as the equivalent free surface after Meyerhof (1951), we can derive a geometric correlation between D and B in terms of β.

By the sine rule in fig 3.22a

$$r_1 = r \, \frac{\sin(\pi/2 + \phi)}{\sin(\pi/4 - \phi/2)}$$

since

$$D = r_1 \sin\beta$$

$$r = r_o \, e^{\theta \tan\phi}$$

$$r_o = \frac{B}{4\cos(\pi/4 + \phi/2)}$$

we can write

$$D = \frac{B\sin\beta\cos\phi \, e^{\theta \tan\phi}}{4\cos(\pi/4 + \phi/2)\sin(\pi/4 - \phi/2)} \qquad\qquad \text{eqn 3.12}$$

where $\theta = \pi/2 + \beta$. For $D < D_c$, β can be calculated from eqn 3.12 and when substituted in eqn 3.11, σ_f can be found.

For $D \geq D_c$, the footing is at or below a critical depth D_c where $\beta = \pi/2$ and $\theta = \pi$, and any further increase in bearing capacity would be attributed to the additional surcharge of the overburden only.

$$D_c = \frac{B\cos\phi \ e^{\pi\tan\phi}}{4\cos(\pi/4 + \phi/2)\sin(\pi/4 - \phi/2)} \qquad \text{eqn 3.13}$$

D_c may properly be taken as the demarcation between shallow and deep foundation. With this new definition, it can be said that the bearing capacity of a shallow foundation should be corrected for the geometry effects while for deep foundations, the correction for overburden alone is sufficient provided that the rotation in the shear fan is set at π instead of $\pi/2$.

Meyerhof (1951) has demonstrated that the bearing capacity σ_f is not sensitive to the value of the shear stress τ_o assumed. For the case m=1, τ_o is assumed to be fully mobilized. For the case m=0, τ_o is assumed to be zero. The effects of m=0 and 1 have been studied by Meyerhof and are presented in fig 3.22b. There is, therefore, good reason to believe that the assumption of a hydrostatic fluid for the soil within zone abc of fig 3.22a is not only safe but also not unduly conservative. In chapter 6, experimental evidence will be presented to substantiate Meyerhof's method of analysis to account for penetration effects for $\beta<30°$.

3.11 Correlation Between N_q For Axisymmetric And Plane Strain

The discussion of the penetration effect so far has been confined to the plane strain case. By inspecting columns 2 and 3 of table 3.2, a very simple correlation between N_q in plane and axisymmetric strain can be established in which ϕ in the plane strain Prandtl equation is substituted by 1.13ϕ

$$\sigma_f = \sigma_o \frac{[1 + \sin(1.13\phi)]}{[1 - \sin(1.13\phi)]} \ e^{2\theta\tan(1.13\phi)} \qquad \text{eqn 3.14}$$

A very close approximation of N_q for axisymmetric strain can be obtained as shown in table 3.4. The penetration effects can now be generalized empirically to include the axisymmetric condition by replacing eqn 3.11 by eqn 3.14. Consequently, it is not unreasonable to suggest that the geometric relationship between D/B and θ as described by eqn 3.12 should be retained unaltered in the axisymmetric case, leaving the factor of 1.13 on ϕ to calibrate the strength only for the axisymmetric case. N_q in an axisymmetric condition can now be expressed as a function of D/B and ϕ. A series of theoretical curves were generated for use in chapters 6 and 7. An example of the curve is shown in fig 3.23.

3.12 The Effects Of Axisymmetry On The Bearing Capacity

As it is not uncommon to use an empirical shape factor to convert bearing capacity coefficients from plane to axisymmetric case, it is useful here to test its general validity. As discussed in section 3.11, the effects of axisymmetry on N_q is approximately an increase of ϕ effectively by 1.13 times resulting in an increase in bearing capacity by a factor of 2.17 at $\phi=40°$ for example. The most noticeable effect of axisymmetry is the existence of a radial horizontal "body" force due to σ_θ which is roughly inversely proportional to R. Thus, the stress characteristics will be distorted in a manner not unlike the situation in a N_γ analysis under the influence of its own self-weight induced vertical stress gradient. This distortion of the stress characteristics induced by the horizontal "body" force, can increase N_q from 64.18 to 139.56 when $\phi=40°$ for weightless soil, for example. The shape factor ranges from 1.05 at $\phi=5°$ to 3.94 when $\phi=52°$.

The situation is a bit more complicated for N_γ. Only a smooth footing is considered here. From columns 4 and 5 of table 3.2, it can be seen that, instead of an across-the-board increase in N_γ from plane strain to axisymmetric strain, N_γ is smaller in axisymmetric strain than in plane strain when $\phi \leq 33°$ but become higher when $\phi > 33°$. Although the "body" force due to axisymmetry tends to increase the bearing capacity, it will also reduce the plastic region as a result. As can be observed in columns 4 and 5 of table 3.3, the reduction is minute when ϕ is low but will progressively get larger when ϕ increases. Reduction in the plastic region incidentally also reduces the amount of soil involved during failure. For soil with weight, the bearing capacity should therefore tend to decrease. It is clear now that the bearing capacity for soil with weight i.e. N_γ, is the outcome of the interaction of these two opposing effects. The shape factor thus ranges from 0.67 at $\phi=5°$ to 1.82 when $\phi=52°$.* Therefore, adopting any constant shape factor obviously can not cope in general. It can also explain why sometimes the shape factor is found empirically to be less than 1.0.

3.13 Cohesion

Although only cohesionless materials are considered up to now, cohesion can also be taken into account in the analysis described in this chapter. One way of doing this is to view cohesion as an equivalent surcharge so that $\sigma_e = c\cot\phi$ (see fig 3.24).

$$\sigma_f = \sigma_e N_q - \sigma_e$$

$$= c\cot\phi N_q - c\cot\phi \qquad \text{eqn 3.15}$$

* i.e. $\left(\frac{2}{3}\right) \times 1.005$ at $\phi = 5°$ to $\left(\frac{2}{3}\right) \times 2.73$ at $\phi = 52°$.

but $\sigma_f = cN_c$, therefore $N_q = N_c\tan\phi + 1$ and $N_c = (N_q - 1)\cot\phi$. In general, therefore

$$\sigma_f = cN_c + \sigma_o N_q + \frac{1}{2} B\gamma\, N_\gamma$$

$$= \sigma_e \tan\phi\, (N_q - 1)\cot\phi + \sigma_o N_q + \frac{1}{2} B\gamma\, N_\gamma$$

$$= (\sigma_e + \sigma_o) N_q + \frac{1}{2} B\gamma N_\gamma - \sigma_e \qquad \text{eqn 3.16}$$

It should be noted here that σ_e acts everywhere including directly under the punch while σ_o only acts everywhere outside the punch. With $\sigma_e = c\cot\phi$ the analysis outlined in this chapter can be used to solve any problem with constant c, ϕ and γ for both plane strain and axisymmetric strain. Once the total surcharge, which is the summation of the actual and equivalent surcharge, and the dimension of the footing is fixed, bearing capacity can be obtained using table 3.2 and 3.3 with the superposition technique. Alternatively, the superposition factor Ω is calculated and the bearing capacity can be calculated directly with program CONPHI so that bearing capacity free from the superposition error can be obtained.

3.14 Summary

In this chapter, the method of characteristics already published in the literature was reviewed and clarified wherever necessary. The safe nature of the principal of superposition was substantiated and the error margin was also found to be not unduly conservative. Penetration effects were then identified and quantified using a simplified method after Meyerhof (1951). Tables and charts of bearing capacities under a wide range of constant ϕ and different initial burial were then prepared so that footing test data could be interpreted in a rational and unambiguous manner.

4. BEARING CAPACITY - VARIABLE Φ

4.1 Introduction

Triaxial test results presented in chapter 2 have clearly indicated that φ is not a material constant for granular soils but is extremely sensitive to the mean stress level. From the results of the constant-φ analysis presented in chapter 3, it can be seen that the vertical stress distribution in the supporting soil ranges from σ_f when directly under the footing to σ_0 when further away from the footing (see fig 4.1a). Even when directly under the footing, the contact stress distribution is not uniform in general either. The stress tends to be highest at the centre and eases off gradually towards the edge. Constant-φ analysis, as will be shown in chapters 6 and 7, is very useful in interpreting experimental data, it is, however, quite incapable of giving a realistic prediction. A new form of analysis which takes into account the pressure effects on φ will be investigated in this chapter. Essentially, the calculations will use the φ value corresponding to the locally prevailing stress level. As pointed out by Hill (1950), the Mohr-Coulomb envelope is not the most general way to define shear strength for a material when shear strength is pressure sensitive like soil. For example, it is impossible to obtain a shear strength envelope when the rate of change of φ with pressure is above a certain value as shown in fig 4.1b. This is one of the reasons why secant angle of friction, which is more general, is used in this work. The secant angle of friction can be obtained by dropping a tangent from the orgin onto a single Mohr circle of stress.

4.2 Extended Prandtl Equation With Variable Φ

The Prandtl solution for a strip footing on weightless soil is for a frictional material in which rotation of principal stress direction is possible. The solution does not require the exact shape of the various zones to be known. It only depends on the rotation of the principal stress direction. Fig 4.1c shows a stable boundary XX between two adjacent zones **a** and **b**. Jumping across XX would produce an infinitesimal rotation and shift of principal stresses. However, as the boundary is stable, the two zones must also share a common boundary stress (σ_X, τ_X) as shown in fig 4.1d. By sine rule, we have,

$$\frac{ds}{\sin 2d\theta} = \frac{s\sin\phi}{\cos\phi}$$

therefore
$$\frac{ds}{s} = 2\tan\phi d\theta \qquad \qquad \text{eqn } 4.1$$

Eqn 4.1 links the shift in the centre of a train of Mohr circles to the rotation of the direction of the major principal stress. By integrating eqn 4.1 over the limits as shown in fig 4.1e, we have,

$$\int_{s_o}^{s_f} \frac{ds}{s} = \int_0^\theta 2\tan\phi d\theta$$

$$s_f = s_o e^{2\theta\tan\phi}$$

$$\frac{\sigma_f}{1 + \sin\phi} = \frac{\sigma_f}{1 - \sin\phi} e^{2\theta\tan\phi}$$

therefore
$$\sigma_f = K_p e^{2\theta\tan\phi} \qquad \qquad \text{eqn } 4.2$$

For constant ϕ and with $\theta = \pi/2$, eqn 4.2 becomes the Prandtl equation. The discontinuities can be viewed as stress characteristics (see fig 4.2). For example, travelling along characteristic D_1D_1', is equivalent to jumping across a series of the other family of characteristics, i.e. D_2D_2', and vice versa. If ϕ is a function of σ, this additional effect should be included in the general stress rotation equation. By cosine rule, see fig 4.3, we have,

$$ds^2 = s^2\sin^2\phi + (s + ds)^2\sin^2(\phi + d\phi)$$

$$-2s\sin\phi(s + ds)\sin(\phi + d\phi)\cos 2d\theta$$

$$\left(\frac{ds}{s}\right)^2 - 2\left(\frac{ds}{s}\right)\tan\phi d\phi - (4\tan^2\phi d\theta^2 + d\phi^2) = 0$$

$$\frac{ds}{s} = \tan\phi d\phi \pm \sqrt{\sec^2\phi d\phi^2 + 4\tan^2\phi d\theta^2}$$

The general stress rotation equation can now be established as

$$d\theta = \pm \sqrt{\frac{(ds/s - \tan\phi d\phi)^2 - \sec^2\phi d\phi^2}{4\tan^2\phi}} \qquad \qquad \text{eqn } 4.3$$

4.3 Pressure Effects On Φ

In chapter 2, two linear log p ($\approx$ log s) versus ϕ relationships had been established, one for sand and one for silt. Both linear correlations have slopes of 3° but

with quite different cut-offs as shown in fig 4.4. Table 4.1 tabulates the parameters adopted for both materials. The parameters were obtained from the experimental data as shown in fig 2.22a in chapter 2. A subroutine CALPHI was written to implement this pressure effect in the subsequent analyses of these two materials. A flow chart depicting how the subroutine is organized is shown in fig 4.5. $\phi = \phi_{const} - A \ln s$.

4.4 Algorithm To Solve The Extended Prandtl Solution

A FORTRAN 77 Program EXPRAN was written to evaluate N_q for a strip footing with ϕ varying as a function of $\sigma(\approx s)$ in a stepwise manner. A flow chart is shown in fig 4.6 to demonstrate how the calculation is organized. The algorithm commences by calculating ϕ in the passive zone (see fig 4.7). Initially any arbitrary value is assumed so that the mean stress can be written as $\sigma_0/(1-\sin\phi)$. With subroutine CALPHI, a new ϕ can be calculated which may be different from the ϕ assumed initially. Iteration is carried out by using the current ϕ to calculate the next mean stress with improved accuracy. This process continues until ϕ has achieved a target accuracy.

In the fan zone, a loading step of ds=0.1s is imposed. Likewise, the current ϕ is calculated from CALPHI based on the current mean stress. The amount of cumulative rotation of principal stress direction is updated at the end of each loading step by eqn 4.3. The active zone is deemed reached and stress ceases to increase when the rotation of principal stress direction is greater than or equal to $\pi/2$. Typically, the total rotation is overpredicted by 0 to 0.04°. The bearing capacity σ_f can now be established as $s_f(1+\sin\phi_f)$ in the active zone, with $N_q = \sigma_f/\sigma_0$ which is a function of σ_0. Two series of analyses were carried out, one applicable to sand and one to silt. The surcharge ranges from 5 to 200 kPa and the results are summarized in columns 2 and 6 of table 4.2. N_q can be seen to be dependent on σ_0.

4.5 Validation Of The Extended Prandtl Algorithm

An analysis with purely cohesive material, which has a known exact solution (Prandtl, 1920) is selected here as a bench mark to check against the algorithm proposed in section 4.4. The idea is that a purely cohesive material can be viewed as a special case of ϕ varying according to pressure (see fig 4.8b):

$$\phi = \sin^{-1} \frac{c}{s} \qquad\qquad eqn \ 4.4$$

so that the shear strength is constant under all pressure conditions. By replacing CALPHI with eqn 4.4, the algorithm was found to yield $\sigma_f-\sigma_0=5.145c$ which differs from the

exact solution by only 0.07%. Therefore, the algorithm proposed here is suitable for strip footings with weightless soil.

4.6 The Method Of Characteristics With Variable Φ

For cases with self-weight, analytical solutions do not exist and the method of characteristics has to be adopted. Graham and Pollock (1972), and Graham and Hovan (1986) have incorporated ϕ as a stress level dependent variable in their method of characteristics analysis. Although during computation, ϕ is updated according to the mean stress level, they have used the same governing equations formulated by Sokolovski (1960) in which ϕ is treated as a constant. As pointed out by Hill (1950) when ϕ is a function of mean effective stress, a general set of governing equations which treats ϕ as a fifth variable should be formulated instead. Alternatively, geometrical reasoning similar to Mandel (1942) can be used to establish the effects of varying ϕ on the constant-ϕ governing equations.

In order to extend the analysis developed in chapter 3 so that variable-ϕ cases can also be included, an approach similar to Mandel will be adopted. There are actually two effects on the governing equations when ϕ varies. The first is on the stress rotation equation and the second is on the geometry of the characteristic lines. Both effects have to be quantified before computation can begin.

As discussed in section 4.2, when ϕ varies according to stress, the stress rotation equation can be modified as eqn 4.3. From chapter 2, both the sand and silt were found to behave according to

$$d\phi = -\frac{A}{s} ds \qquad \text{eqn 4.5}$$

substitute eqn 4.5 into eqn 4.3, we have,

$$d\theta^2 = \frac{ds^2}{4s^2\tan^2\phi}(1 + 2\tan\phi A - A^2)$$

$$\frac{ds}{s} = \pm \frac{2\tan\phi d\theta}{\sqrt{(1 + 2A\tan\phi - A^2)}}$$

and compare with the stress rotation equation for constant ϕ

$$\text{i.e.} \qquad \frac{ds}{s} = \pm 2\tan\phi_{op} d\theta$$

we can define an operative value ϕ_{op} such that

$$\tan\phi_{op} = \frac{\tan\phi}{\pm\sqrt{(1 + 2A\tan\phi - A^2)}}$$

$$\phi_{op} = \tan^{-1}\frac{\tan\phi}{\pm\sqrt{(1 + 2A\tan\phi - A^2)}} \qquad \text{eqn 4.6}$$

Therefore, if the constant-ϕ governing equations are used in the analysis, ϕ_{op} should be used in the stress rotation equation instead of ϕ. For sand, $A=3I_D$ degrees or $3I_D\pi/180$ radians. When $I_D \approx 1$, $A=3/57.3$.

Equally, the effects of varying ϕ on the angle of intersection of the characteristics can be described in terms of the angle of the strength envelope, as shown in fig 4.9:

$$\sin\phi_{en} = \frac{(s + ds)\sin(\phi + d\phi) - s\sin\phi}{ds}$$

$$= \sin\phi + s\frac{d\phi}{ds}\cos\phi$$

therefore $\qquad \phi_{en} = \sin^{-1}(\sin\phi + s\frac{d\phi}{ds}\cos\phi) \qquad\qquad \text{eqn 4.7}$

As $\qquad\qquad \dfrac{d\phi}{ds} = -\dfrac{A}{s} \qquad\qquad\qquad$ for sands

therefore $\qquad\qquad \phi_{en} = \sin^{-1}(\sin\phi - A\cos\phi)$

Having established ϕ_{op} and ϕ_{en}, the constant-ϕ formulation can now be extended to include variable-ϕ analysis. Subroutine CALPHI was used to calculate ϕ according to the stress level rather than remaining constant. The effects of varying ϕ on the governing equations are then accounted for by converting the current secant ϕ into ϕ_{op} in the general stress rotation equation and ϕ_{en} to represent the local strength envelope.

4.7 Validation Of The Method Of Characteristics With Variable Φ

Before using the analysis to generate predictions for chapters 6 and 7, it is prudent to check the algorithm against known exact solutions. Two cases were checked. The first one is for purely cohesive material in plane strain (Prandtl, 1920). The second one is for purely cohesive material but in axisymmetric strain (Shield, 1955). Following the same spirit as in section 4.5, the purely cohesive soil will be treated in a variable-ϕ analysis with $\phi=\sin^{-1}c/s$, on differentiating, we have

$$d\phi = -\frac{cds}{s^2\cos\phi} \qquad\qquad \text{eqn 4.8}$$

eqn 4.3 can now be written as

$$d\theta^2 = \frac{ds^2}{4s^2\tan^2\phi} \; (1 + \frac{2\tan\phi c}{s\cos\phi} - \frac{c^2}{s^2\cos^2\phi})$$

therefore

$$\frac{ds}{s} = \pm \; 2\sin\phi d\theta$$

Comparing with eqn 4.1

i.e. $$\frac{ds}{s} = \pm \; 2\tan\phi_{op}d\theta$$

we have,

$$\tan\phi_{op} = \sin\phi$$

$$\phi_{op} = \tan^{-1}(\sin\phi)$$

substituting eqn 4.8 in eqn 4.7, we have,

$$\phi_{en} = \sin^{-1}(\sin\phi - \frac{c\,s\cos\phi}{s^2\cos\phi})$$

$$= \sin^{-1}(\sin\phi - \sin\phi) = 0$$

One may appreciated that this particular situation represents an extreme case of pressure effect. In order to make any comparison between this validation analysis with the actual analysis on either sand and silt, a comparable $d\phi/ds$ should be used. From fig 4.10, it can be seen that $d\phi/ds$ is dependent on ϕ which in turn is dependent on σ_0 assumed in the calculation. The equivalent $d\phi/ds$ for purely cohesive soil can be obtained by putting $\phi_{en}=0$ in eqn 4.7, which gives,

$$\frac{d\phi}{ds} = -\frac{\tan\phi}{s}$$

therefore $A = \tan\phi$ for purely cohesive soil

By inspection (see fig 4.10) $\sin^{-1}\dfrac{c}{\sigma_0 + c} = 3°$

Putting $\sigma_0 = nc$, we have $n = 18.107 \approx 18$

The above suggests that by putting $\sigma_0=18c$ in these two validation analyses, we can test the numerical accuracy of the algorithm. Fig 4.11 shows the effects of different σ_0 on the accuracy of the calculations for both plane and axisymmmetric cases. Accuracy is higher when $\sigma_0 \geq 100c$. This is as expected, as higher σ_0 also means less severe pressure induced reduction in ϕ.

In the validation analysis, the superposition factor Ω is put as 1000, so that the analysis is essentially a N_q analysis with $\phi=\sin^{-1}c/s$. σ_0 used is 18c which as mentioned earlier can simulate a comparable rate of strength reduction with pressure for sands. For the plane strain case, the program VARIPHI yields $\sigma_f-\sigma_0=5.14c$ which is practically the same as the exact solution. The stress characteristics and footing pressure distribution are shown in fig 4.12. It can be seen that the log spiral in the shear fan has now degenerated into a circular curve, as required.

For the axisymmetric case, the program yields $\sigma_f-\sigma_0=5.63c$ which differs from Shield's exact solution of 5.69c by 1%. Fig 4.13 compares the distribution of the calculated footing pressure distribution with Shield's solution, which shows that the present calculation gives a similar footing pressure distribution. It also shows that the characteristics are of the same shape as that calculated by Shield. In both cases, R=1.58.

The above validations have demonstrated that with a pressure effect on ϕ equal to the maximum which is likely to be encountered in a dense sand, the algorithm proposed here can yield a very accurate answer. It is, therefore, believed that the algorithm is suitable for application for a wide variety of sands in general.

4.8 Bearing Capacity Prediction From Triaxial Data

With the necessary modification and justification complete, fig 4.14 shows the organization of the computer program VARIPHI which has included subroutine CALPHI so that ϕ varies with pressure. It should also be remembered that ϕ_{op} and ϕ_{en} have to be calculated from ϕ during each iteration. As during the analysis, all stresses are normalized, so when calculating ϕ in CALPHI, the stress has to be restored back to its actual level.

4.8.1 1-g Tests - A Prediction

As mentioned in chapter 3, N_q is thought not to be sensitive to base friction, so although the 1-g tests are on rough base footings, the results can be compared directly with the smooth footing analysis. Table 4.3 summarizes all the predictions for both sand and silt. The analyses were carried out for both plane and axisymmetric strain. The surcharge used in the analyses ranges from 5 to 200 kPa which is also the range used in the 1-g test programme. The superposition factor Ω used is 1000. Contour maps of varying ϕ underneath the footing are presented in fig 4.15 to 4.17.

Although only the axisymmetric case is needed for comparing with experimental data later in chapter 6, the plane strain cases are also considered here so that the extended Prandtl solution outlined in section 4.4 and this present method can be compared. Table 4.2 summarizes the results from these two methods. Variable-ϕ stress characteristic analysis tends to produce solutions which are slightly smaller than the extended Prandtl method. Within the range of surcharge considered, that is 5 to 200 kPa, none of the solutions differ from each other by more than 3%.

4.8.2 Centrifuge Tests - A Prediction

As discussed in chapter 3, N_γ is different for rough and smooth footings. The same artifice of assuming a cone under the footing was, therefore, adopted here as well. As ϕ is no longer constant, an iterative procedure is needed. Initially, α and δ as defined in fig 3.19 are assumed. When the analysis is complete, ϕ at the tip of the cone, i.e. at R=0, is compared with δ. If $\delta \neq \phi$, then α and δ should be changed accordingly. Iteration continues until the difference between δ and ϕ is less than 0.5°. With this procedure, symmetry can be roughly conserved at the centre line.

Table 4.4 summarizes all the results for both sand and silt. The analyses were carried out only for axisymmetric strain. The footing size used in the analysis ranges from 400 mm to 10 m diameter. The superposition factor Ω is 0.001 in this analysis. Contour maps of the varying ϕ underneath the footing are presented in fig 4.18 and 4.19. The predictions generated here will be used to compare with the experimental data in chapter 7.

4.9 Summary

Some simple modifications permit plasticity calculations to deal with variable secant ϕ. This approach was validated by checking two known "cohesion" solutions, i.e. $N_c=5.14c$ for a strip footing and 5.69c for a circular footing. New bearing capacity solutions were then formulated for circular footings on the two dense soils used in this work, taking into account stress level effects. Predictions obtained will be compared with model tests on the same sand and silt in chapters 6 and 7.

5. Settlement Calculations

5.1 Introduction

In order to predict the load/settlement response of a footing under working load conditions, the supporting soils should be treated as an elasto-plastic rather than rigid-plastic material. A Cam-clay type of constitutive model was, therefore, adopted for the two granular materials used, based on the triaxial test data obtained in chapter 2. CRISP, an acronym for CRItical State Program, was used for the finite element analysis. Two types of event will be modelled.

(1) Triaxial event with either perfectly rough or perfectly smooth end platens.

(2) Punch-indentation behaviour before collapse at either 1-g with surcharge or under elevated g level.

The finite element method is a general numerical procedure for obtaining an approximate solution to a field problem. It involves converting the governing differential equations, which must be elliptic, into a set of linear simultaneous equations which can then be assembled and solved. In essence, the method approximates continuum behaviour by discretizing the boundary value problem in question into constitutive elements. Nodes are assigned to each element. Displacements within an element are assumed to vary according to some shape functions. The material behaviour is assumed continuous within each element. The assumptions thus reduce the solution of the problem to the determination of the unknown nodal displacements. Accordingly, its ability to model soil behaviour depends to a very large extent on the adoption of an appropriate constitutive model and how a boundary value problem is discretized. For the case of non-linear behaviour, piece-wise linearization or an iterative technique should be employed. If no iterative technique is used, as in CRISP, the increment step size must be small. As these aspects are so important, they will be discussed individually later in this chapter.

5.2 CRISP

CRISP is a suite of small displacement, small-strain finite element programs first developed by Zytynski (1976) at Cambridge University. Numerous enhancements and modifications to the programs have since been made by various research workers at Cambridge. The most comprehensive treatment of CRISP to date, can be found in Britto and Gunn (1987). Their book covers the mathematical formulation, system design,

application and limitation of CRISP together with a complete listing of the 8000-line standard version of the programs. In this chapter, only some of the salient features of CRISP directly relevant to the analysis in question will be touched upon. Instead, it will concentrate on why some decisions were made in the analysis and how they can be justified in the light of the evidence currently available.

At the outset, some decisions had been made which shaped the general form of the analysis to be carried out.

(1) Like the physical models which will be presented in chapters 6 and 7, the analysis is going to be strain-controlled. Griffiths (1982) has pointed out that the distribution of contact stress on the footing is in general non-uniform. It is, therefore, unrealistic to analyse the performance of a footing by specifying nodal forces on the soil surface. The other reason, which is equally important, is that stress-control analysis can lead to instability in post-peak behaviour.

(2) An elasto-plastic instead of non-linear elastic model was adopted. In plasticity, the principal axes of strain increment and stress coincide which correlates more closely with the experimental evidence (Borin, 1973) than thus elasticity theory in which the increments of stress and strain follow parallel axes (see fig 5.1). The other reason is that elasto-plasticity can handle dilatancy while non-linear elasticity can not. Elasticity does not allow contraction or dilation as a result of changes in deviatoric stress alone.

(3) It was decided to specify an "elastic" shear modulus G as a function only of mean stress p, although it was recognized that in reality there are additional "plastic" strains even in material which is retreating from its plastic yield surface. The particular value of G could be selected to be relevant to the magnitude of soil strain immediately beneath the footing i.e. about 0.5% (Jardine et al, 1984).

5.3 Finite Element Solution

5.3.1 Mesh

In general, improvements in accuracy of the analysis can be achieved by decreasing the size and increasing the number of the elements. As computation time will escalate when the number of elements increase, a graded mesh is usually adopted in practice as a compromise. The idea is to represent areas of concentrated stress and strain by finer sub-division of the continuum locally. Because of this requirement, triangular

elements, which were particularly suitable for this task, were chosen.

In the case of the footing problem, the mesh was made finer in the vicinity of the footing, especially near its edge. It was also decided to form a mesh in such a way that the pattern can, as far as possible, capture any likely failure mechanism. The idea was to arrange nodes along some possible slip line patterns so that if there was strain concentration in the soil model, the analysis could cope with more effectively. It is perhaps appropriate to briefly mention at this stage that before the global stiffness matrix can be assembled, mapping of the triangle element from the local to global co-ordinate system should be carried out. Ideally, the element shape should, therefore, be approaching that of an equilateral triangle. Elongated elements should be avoided to prevent ill-conditioning. Following these principles, the two boundary-value problems were discretized into meshes as shown in fig 5.2b and 5.3a. Because of symmetry about axis x-x, only half of the axisymmetric triaxial specimen was analysed as shown in fig 5.2a.

5.3.2 Element Type

Apart from the mesh, improvement in accuracy can also be achieved by increasing the number of nodes in an element. For an axisymmetric problem, the constraint of no volume change can sometimes lead to "locking" of finite element mesh when low-order elements are used. Sloan and Randolph (1982) have demonstrated that for axisymmetric problems where the constant volume constraint is imposed, cubic strain triangle is the lowest order triangular element which can maintain the necessary kinematic freedom to give good prediction of the collapse load. Although the test in question is not undrained, it is understood that contraction, zero volumetric strain and dilation occur in active, fan and passive zones respectively under the footing. For this reason, the 15-noded cubic strain triangle was chosen for the subsequent analysis.

5.3.3 Element Stiffness

A direct method based on the principle of virtual work can be used to set up the element stiffness equations (Argyris & Kelsey, 1960). As the explicit determination of higher order shape functions for triangular elements is algebraically very tedious, it is usual practice to determine the shape function in terms of the local co-ordinates. As mentioned in section 5.3.1, there are certain restrictions on the shape of the triangle when this type of element is used.

Once the shape function is assumed, the stiffness matrix $\mathbf{K}$ can be obtained by numerical integration using a Gaussian Quadrature scheme. In order to avoid problems in axial symmetry at r=0, CRISP adopts an integration rule where the sampling points are inside the triangle (i.e. not on the edges or corners). For the 15-node cubic strain triangle adopted here, a 16-point integration scheme is employed, which integrates an eighth order polynomial exactly.

5.3.4 Global Stiffness Matrix

Having obtained the stiffness of individual elements, the response of the continuum to external loads and boundary conditions may be obtained by assembling these element stiffnesses to form a global stiffness matrix $\mathbf{K}$ of the continuum. If the external load vector $\mathbf{F}$ and boundary conditions are known or prescribed, the unknown nodal displacement vector $\boldsymbol{\delta}$ corresponding to this condition can easily be obtained by a solution of the equilibrium equations.

$$\mathbf{F} = \mathbf{K} \, \boldsymbol{\delta}$$

From the nodal displacement vector $\boldsymbol{\delta}$, nodal forces can be determined as the body forces, boundary tractions and fixities are already known. This formulation, known as the displacement method, always considers the nodal displacements as the basic unknowns.

5.3.5 Non-linear Technique

For a non-linear constitutive model, the virtual work equation has to be re-written in incremental form. For example, Zienkiewicz (1977) has written the incremental form as

$$\sigma_{i+1} = D \, \delta\varepsilon_i + \sigma_i$$

CRISP does not use iterative technique but uses the incremental tangent stiffness method instead (see fig 5.4). As stiffness is in general a function of stress and strain, the stiffness should, therefore, be repeatedly computed and assembled in each step. This piecewise linearization of the stress strain curve would invariably give a stiffer response (see fig 5.4). In other words, although equilibrium was satisfied throughout the analysis, the yield criterion was not necessarily always satisfied. For strain-control analysis, the error can be reduced by having a fine enough displacement increment.

5.3.6 Efficiency Of Memory Store

In finite element analysis, one of the features which requires a large amount of computer resource is the large memory store needed to solve the huge set of linear simultaneous algebraic equations. CRISP uses the frontal method (Irons, 1970) to overcome this problem. The technique is basically a form of Gaussian elimination whereby elimination of variables takes place during the process of assembling the global stiffness matrix. The reason that this can be achieved is because a node will only contribute non-zero coefficients to equations involving nodes in the same element. Therfore, as soon as all the terms in the stiffness matrix relating to a given node have been assembled, that particular node may be eliminated straight away from all equations except its own, which is then written to store for back substitution later.

5.4 Constitutive Model

The first of the elasto-plastic models which could simulate soft clay reasonably well is due to Roscoe et al (1958). This is essentially an isotropic work hardening model with its yield function written in terms of stress invariants p and q. On the "dry" side, the soil is denser than critical and will dilate during shear; on the "wet" side, the soil is looser than critical and will contract during shear. The term Cam-clay was coined by Schofield and Wroth (1968) for this model. Cam-clay, however, is not very successful in modelling dense sand or very stiff clay because the continuum behaviour is intercepted by shear rupture.

A logical step forward is to find an improved elasto-plastic model which fits the triaxial test data of soil on the dry side of the critical state better. Schofield and Wroth (1968), Atkinson and Bransby (1978) and Schofield (1980) have proposed such a model. Following Taylor (1982) and White (1987), the new model will be known as the Schofield model. The Schofield model combines the Hvorslev surface (Hvorslev, 1937) on the dry side and the Roscoe surface (Roscoe et al, 1958) on the wet side. The Roscoe surface was derived from the work equation

$$dw = p \, dv + q d\varepsilon = M p \, d\varepsilon$$

The Hvorslev surface, however, is empirical. The most convincing triaxial data to support the idea of the Hvorslev surface was Parry's data (Parry, 1960) on Weald clay (see fig 5.5).

5.4.1 Schofield Model

The Schofield model consists of the following main features as depicted in fig 5.6a.

(1) State boundary surface (yield surface) - stress states can never lie outside the yield surface. Within the state boundary surface, the soil behaves elastically, as stress increment which causes the stress state to move inside the yield surface will leave the yield surface unchanged.

(2) Hardening law - when a stress increment causes the stress to move onto the Roscoe surface, the yield surface will work harden by expanding, so much so that the stress state remains on the new yield surface. In other words ~~the~~ stress states outside the yield surface are impossible ~~state~~ and inside it, the soil behaves elastically.

(3) Softening law - on the Hvorslev surface, it is impossible by definition to apply any stress increment probing outwards. Nevertheless, the adoption of negative hardening parameters to cater for softening is not uncommon. For example, Nayak and Zienkiewicz (1972) have included softening in their finite element analysis. Upon closer scruntiny, this is actually a generalization of Drucker's postulate (Drucker, 1950, 1951) on hardening to include softening. The major criticism of the softening law is that by definition, it is impossible to perform any positive load increment which is plastic on the Hvorslev surface (Dean, 1985). This fact is important because the foundation of plasticity hinges upon the validity of Drucker's postulate

$$d\sigma_{ij} d\varepsilon^{p}_{ij} \geq 0 \quad \text{hardening}$$

which is based upon a perturbation at the yield surface in the form of a small stress increment. Without Drucker's restrictions on work hardening, uniquess and normality (i.e. stability) can not be guaranteed. It is possible, however, to adopt an alternative to Drucker's postulate (Iliushin, 1961), which can accomodate softening and hardening as well as perfect plasticity,

$$d\sigma_{ij} d\varepsilon^{p}_{ij} > 0 \quad \text{hardening}$$

$$d\sigma_{ij} d\varepsilon^{p}_{ij} = 0 \quad \text{perfect plastic}$$

$$d\sigma_{ij} d\varepsilon^{p}_{ij} < 0 \quad \text{softening}$$

The alternative postulate ~~which~~ is based on an incremental strain perturbation. As pointed out by Lau (1977), Iliushin's postulate does not affect the widely established concepts of normality. Although uniqueness can only be guaranteed if an additional set of conditions can be

the
satisfied (Prevost and Hoeg, 1975). For example, softening zone must be "contained".

In the current analysis, only monotonic strain-control loading on the triaxial compression plane will be considered. Implicitly, Iliushin's postulate is followed. Once the stress state reaches the Hvorslev surface it will continue to soften, until reaching critical state (see fig 5.7 and 5.8). As the analysis is strain-controlled, the analysis will be stable provided that the displacement increment step is sufficiently small. However, in general, not all the integration points reach the Hvorslev surface at the same time. Therefore, some integration points may experience unloading locally. In CRISP, therefore, when the stress state reaches the Hvorslev surface, the direction of the plastic strain increment was checked so that a decision as to whether the unloading should be treated as strain softening or elastic unloading can be made.

5.4.2 Elastic Properties

In general, the Schofield model assumes non-linear elastic behaviour within the yield surface (see fig 5.8). Plastic strains can only occur on the state boundary surface. In the original Cam-clay model, elastic shear modulus G is assumed to be infinite. Simpson (1973) has pointed out that this assumption will result in a stress jump on the imposition of shear strain as shown in fig 5.9c. Besides, it is common experience that a finite value of G can be measured in a triaxial test.

In this work, the elastic properties were assumed to be isotropic and homogeneous but with non-linear (pressure dependent) bulk modulus K ($=p(1+e)/\kappa$) and shear modulus G. Wroth et al (1979) and Houlsby (1981) suggested that G should vary according to some power law of pressure. For both silt and sand, it has been established empirically in chapter 2 that

$$G = 1400p^{0.667}$$

According to Carter (1977) varying G according to p will result in a phenomenon whereby positive or negative work can occur as a result of stress cycle (see fig 5.9a and 5.9b) depending on the sense of rotation around the cycle. This condition is not "elastic" in the true sense of the word. Errors may become significant after many cycles. The objective of this study is therefore restricted to one loading cycle only by selecting an appropriate shear modulus at a comparable strain level directly from the available data.

5.4.3 Soil Parameters

The parameters adopted here have been derived from the triaxial test data in chapter 2. Table 5.1 summarizes the parameters adopted in the analysis. With ϕ_{crit} already known, M can be obtained using the   relation $M=6\sin\phi/(3-\sin\phi)$. When the maximum stress states were plotted in the p, q space as in fig 5.10a, p_{crit} can be located as the intercept between the Hvorslev surface and the critical state line. p_c, which is the intersection of the Roscoe surface and the hydrostatic stress axis, can be determined as $p_c=2.718p_{crit}$. From fig 5.10b, it can be seen that neither κ or λ is constant. It is also understood that λ may eventually become constant when p is above p_c (Vesic & Clough, 1968). In the present work, λ was taken to be the local tangent of the virgin isotropic compression line at a mean pressure of 8000 kPa. This is an acceptable simplification as all the CRISP analyses fall within this stress level.

All data points on the dry side of the critical state line (see fig 5.10a) will be used to quantify the maximum stress ratio criterion and the Hvorslev surface gradient at a constant v section. It has been assumed that both silt and sand shared the same constitutive relationship apart from stress history (i.e. p_c). In order to arrive at a consistent set of soil parameters, the analysis assumes that at p=100kPa, e_{init}=0.58 for sand and e_{init}=0.56 for silt. With this assumption, both materials have identical critical state lines with Γ=1.80 (see fig 5.10b and 5.12a).

Atkinson and Bransby (1978) suggested that the gradient of the Hvorslev surface S_H can be obtained from a p_{max}, q_{max} plot at a constant v section when normalized by p_e as shown in fig 5.11. The equivalent pre-consolidation pressure p_e (see table 5.2) of the triaxial tests on the dry side can be estimated as explained in fig 5.12b. From the normalized plot (see fig 5.11), a bi-linear curve can be fitted to the data. S=2.25 is equivalent to ϕ_{max}=55° instead of the usual no-tension cut-off of 3, which is equivalent to ϕ_{max}=90°. S_H is found to be 1.4.

As everything is practically similar except particle size between the silt and sand, it warrants an explanation as to why the silt has a larger state boundary than that of the sand. A plausible explanation is that when they were manufactured, the silt should have been subjected to a much more traumatic stress history than the sand (see fig 5.9d). In other words, the stress history experienced by the silt should be more damaging to its grains in order to become finer than the sand. Actually it can be viewed as a corollary to the absolute particle size effect discussed in chapter 2.

A larger state boundary will result in a larger Hvorslev surface and a higher pre-consolidation pressure. It also implies that behaviour within the yield surface becomes relatively more significant. This will inevitably result in a stiffer response. As will be shown later on, all these observations are consistent with the behaviour of silt and sand.

5.4.4 Simplified Schofield Model

Up to now, discussion on the Schofield model is only limited to the triaxial plane. Before finite element analysis on a footing can be carried out, the model should be generalized to 3-dimensions. However, in this work only a simplified version of the Schofield model is generated by rotating the compression triaxial plane about the p axis (see fig 5.6b). It follows automatically that the use of the simplified Schofield model is only justified if the stress path follows a special case of the Haar and Von Karman hypothesis i.e. $\sigma_1 > \sigma_2 = \sigma_3$. Otherwise the shear strength will be over-predicted because the Hvorslev surface is understood to be the Mohr-Coulomb surface.

5.5 CRISP Analysis Results - Part I

Table 5.3 summarizes the details of all the eight analyses. The load (displacement) increment step sizes were chosen such that 0.95<yield ratio<1.05. Yield ratio is defined as the ratio of p_c at the end of the current increment to p_c at the beginning of the current increment. Before analysing the relatively complicated footing problem, it was decided to analyse a standard triaxial test event as a simple check to see whether the various decisions outlined earlier yield any unreasonable results. It can also cast some light on the platen roughness effects on uniformity of strain and progressive failure. All triaxial tests were simulated at an effective cell pressure of 750 kPa. The loading was produced by squashing the specimen with the platens until an axial strain of 5% was reached in 180 increments. Smooth platens were simulated by allowing the interfacing boundary between the soil and platen to move freely in the horizontal direction. Rough platens were simulated by imposing a condition such that no horizontal movement is allowed along the interface.

CRISP1. This analysis is on sand with e_{init}=0.56 and smooth platens. The deformed mesh is shown in fig 5.13, the specimen remaining cylindrical during the whole test. Fig 5.14 shows the stress and strain history during the test. The stress path follows a 3 on 1 slope in the p-q space. Within the state boundary, the specimen was loaded elastically with associated volumetric compression until the Hvorslev was

reached. Thereafter, the specimen softened with accompanying dilation to the critical state. At the critical state, the specimen sheared at constant volume.

CRISP2. This analysis was on silt with e_{init}=0.54 and smooth platens. The deformed mesh is shown in fig 5.15. Fig 5.16 shows the stress strain history during the test. The test behaves in a fashion similar to CRISP1. However, as the state boundary is larger for the silt than for the sand, the maximum stress ratio mobilized was also higher.

CRISP3. This analysis was on sand with e_{init}=0.56 and rough platens. The deformed mesh is shown in fig 5.17, the specimen deformed in a distinctive barrel shape. Fig 5.18 shows the stress and strain history during the test. Initially, the specimen behaved in a similar manner as the smooth counterpart until the Hvorslev surface was reached. Shear strain became more non-uniform as the test progressed as a result of the platen friction. Post-peak, data point 3 (see fig 5.2 for locations) which is near the middle of the sample reach critical state much earlier than data points 1 and 2 which are further away from the middle. Fig 5.19 to 5.21 show the contours of stress and strain at the end of the test.

CRISP4. This analysis is on silt with e_{init}=0.54 and rough platens. All comments made in CRISP3 are all applicable here and will therefore not be repeated. The test results are presented in fig 5.22 to 5.26.

5.5.1 Effects Of Rough Platens On Strength

(a) From fig 5.19, radial stress can be seen to remain roughly the minor principal stress, while from fig 5.20, vertical stress can be seen to remain roughly the major principal stress.

(b) In order to stop the part of the specimen which is in contact with the platens from expanding out radially, additional radial stresses are mobilized in the form of platen friction. Therefore, circumferential stress only remains minor principal stress near the middle half of the specimen (see fig 5.19). Near the end platen, circumferential stress tends to increase beyond σ_3 in order to balance the additional radial stress. The circumferential stress is at its maximum near the edge of the end platen.

(c) The radial stress contour in fig 5.19b suggests that the specimen is, as it were, undergoing a number of triaxial tests at quite different cell pressures at different locations simultaneously. The equivalent effective cell pressure varies from 200 to 1200 kPa.

(d) Stress ratio (q/p) as seen from fig 5.21 remains reasonably uniform throughout the specimen except in a trapped cone near the centre of the end platen, which suggests that as far as shear strength is concerned, end friction does not have a very significant effect on ϕ_{max}. It is understandable because a specimen is only as strong as its weakest link. As the central region mobilized peak shear strength more or less simultaneously, the shear strength of the whole specimen should also roughly peak at the same time.

5.5.2 Effects Of Rough Platens On Stiffness

(a) Mean stress varies as shown in fig 5.21c, stiffness being pressure sensitive may be affected when interpreting the stiffness measured in a test.

(b) Fig 5.21a shows that volumetric strain is uniform only near the middle half of the specimen, so stiffness measured may be affected as an indirect result of only the bulk volumetric strain being measured in an actual test with rough platens.

(c) Shear strain is non-uniform throughout and is highest near the centre of the specimen (see fig 5.21b). As stiffness is strain sensitive, so stiffness too may be affected. As confirmed in fig 5.27, ϕ_{max} is not sensitive to the assumption of end platen friction and is in close agreement with the experimental data obtained in chapter 2. However, stiffness is over-predicted by quite a large margin when $\varepsilon_a > 0.5\%$. It is, therefore, necessary to have some form of direct internal measurement of strain in the specimen (for example, Jardine et al, 1984) if more accurate stiffness parameters are required. For an aspect ratio of 2, the analyses suggest that the middle half should be of sufficient uniformity for strain measurement to be improved significantly.

5.6 CRISP Analysis Results - Part II

Stress and strain history during each test are represented at 6 data points, two each in the active, fan and passive zones respectively, the locations of which are depicted in fig 5.3b. In-situ stress is calculated based on the assumption that $K_o = 1 - \sin\phi_{crit}$. The element sides directly under the punch were given a prescribed incremental values of displacement to simulate the strain-control loading. All tests were analysed with the assumption of a rough footing base, i.e. horizontal movement at the interface with the punch was not allowed. Apart from providing predictions for comparison with the load settlement curves of the physical models in chapters 6 and 7, this exercise can also allow insight to be gained on the stress path experienced by the physical model. To

achieve the above objectives, the following tests were conducted.

CRISP5. This analysis is on sand with e_{init}=0.59 and σ_0=25 kPa at 1-g. The punch was loaded to w/B=16% in 480 increments. The deformed mesh is shown in fig 5.28. Fig 5.29 to 5.31 show the stress and strain history during the test. Fig 5.32 shows the contour of the minor principal stress and circumferential stress. Fig 5.33 shows the mean stress and maximum shear stress distribution. Discussion on the stress path followed by the supporting soil will be made later in section 5.6.2.

CRISP6. This analysis was on silt with e_{init}=0.57 and σ_0=25 kPa at 1-g. The punch was loaded to w/B=15% in 600 increments. The deformed mesh is shown in fig 5.34. Fig 5.35 to 5.37 show the stress and strain history during the test. Fig 5.38 shows the contour of the minor principal stress and circumferential stress. Fig 5.39 shows the mean stress and maximum shear stress distribution. As shown in fig 5.40, silt is stiffer and stronger than sand. These two load/settlement response curves will be used to compare with the experimental data in chapter 6.

CRISP7. This analysis was on sand with e_{init}=0.60 and at 50g. The punch was loaded to w/B=11% in 440 increments. The deformed mesh is shown in fig 5.41. Fig 5.42 to 5.44 show the stress and strain history during the test. Fig 5.45 shows the contour of the minor principal stress and circumferential stress distribution. Fig 5.46 shows the mean stress and maximum shear stress distribution.

CRISP8. This analysis was on silt with e_{init}=0.58 at 50g. The punch was loaded to w/B=10% in 600 increments. The deformed mesh is shown in fig 5.47. Fig 5.48 to 5.50 show the stress and strain history during the test. Fig 5.51 shows the contour of the minor principal stress and circumferential stress distribution. Fig 5.52 shows the mean stress and maximum shear stress distribution. As shown in fig 5.53, silt is stiffer and stronger than sand. These two load/settlement response curves will be used to compare with the experimental data in chapter 7.

5.6.1 Magnitude Of Intermediate Stress

All four tests (for example, fig 5.32) suggest that the circumferential stress is very close to the minor principal stress except in the conical region immediately underneath the punch. This is probably a result of the punch base friction effects as discussed in section 5.5.1.

5.6.2 Stress And Strain History

In the active zones, the stress path first hits the ϕ_{max} cut-off surface (see fig 5.29, for example), then curves round gently to follow the Hvorslev surface and work softens towards a critical state. Critical state can sometimes be reached by a few integration points when punch relative settlement is more than 10%. Because CRISP is not suitable for handling a large strain/large deformation problem, so not everywhere in the active zone reaches critical state at the end of the analysis.

In the fan zone, the stress path hits the ϕ_{max} cut-off (see fig 5.30, for example) and softens to critical state. Among the three zones, the fan zone experiences the most intensive strain. But it is found possible to work harden along the critical state line as the mean pressure is forced to increase as the foundation continues to be loaded.

In the passive zone, the stress path hits the ϕ_{max} cut-off surface and then softens very slowly to a critical state (see fig 5.31, for example). As the shear strain is low in the passive zone compare with the fan zones for a given relative settlement, critical state can only be reached here after a large relative settlement of the punch. As will be explained in section 5.8, this is the reason why work hardening after critical state is possible in the fan zones.

5.7 Haar And Von Karman Hypothesis

In section 5.4.4, it has been emphasized that the simplified Schofield model is only applicable if a special case of the Haar and Von Karman hypothesis holds.

$$\text{i.e. } \sigma_1 > \sigma_2 = \sigma_3$$

The underlying explanation for the hypothesis holding may be illustrated as follows. Assume that the footing problem can be idealized as a semi-spherical cavity expansion problem as shown in fig 5.54. Let u be the radial shift at a radius r and the soil be non-compressible. By compatibility, we have $B^2\pi w/4 = 2\pi r^2 u$, therefore $u = B^2 w/8r^2$. Because circumferential strain $\varepsilon_\theta = u/r = B^2 w/8r^3$ and radial strain $\varepsilon_r = du/dr = B^2 w/4r^3$, therefore $\varepsilon_r = -2\varepsilon_\theta$. By symmetry, the two circumferential strains are equal. By co-axiality, $\sigma_r > \sigma_\theta$, therefore, $\sigma_1 > \sigma_2 = \sigma_3$. In order to further substantiate this argument, intermediate stress parameter b and the major principal stress direction in different region underneath a footing had been sampled and checked for all four CRISP runs on footings

$$\text{where } b = \frac{\sigma_2 - \sigma_3}{\sigma_1 - \sigma_3}$$

if $\sigma_2 = \sigma_3$, b = 0 triaxial compression

and   if $\sigma_2 = \sigma_1$, b = 1 triaxial extension

where $0 \le b \le 1$

Fig 5.55 shows the location of 18 sampling points underneath a footing. Table 5.4 summarizes the variation of b and ψ at the various sampling points. Values of b are found to be very close to zero, so Von Karman hypothesis is realized and that the use of the simplified Schofield model is justified. Although this is not a general proof, it can at least act as an independent substantiation of the assumptions made in chapters 3 and 4 on the validity of the same hypothesis. The other point is that ψ can be higher than 90° in the passive zones when the punch has settled (see table 5.4), further discussion on this point will be made in chapter 6.

5.8 Progressive Failure

Lo (1972) has pointed out that progressive failure can only occur if the following two conditions are met:

(1) The material can strain soften.

(2) A non-uniform stress and strain field should exist inside the model.

Consider the following scenario. During a punch-indentation test, the soil bed is subjected to non-uniform strain. Before a mechanism is formed, yielding soil in the fan zone which has reached a critical state is trapped by non-yielding soil in the active and passive zones while p keeps increasing. The increase in p is due to the continuous loading of the surrounding non-yielding soil in the passive zone. The fact that some integration points work-harden after critical state has been reached, as discussed in section 5.6.2, shows that the first approach to a critical state is not necessarily the final state as it would be in a standard triaxial test. Work hardening may occur even after the critical state has been reached as a result of non-uniform strain effects, leading to the increase of p in trapped zones of shearing soil.

It is perhaps instructive to consider a multi-stage triaxial test here where σ_r can keep increasing in stages. Imagine that at a particular cell pressure, a triaxial specimen is strained to critical state. If at this instant the cell pressure is raised, the triaxial specimen should still be able to work harden to a new critical state under a higher stress level. In other words, progressive failure can either increase or decrease overall shear strength

depending on the pattern of strain non-uniformity.

5.9 Discussion

There are a number of limitations and virtues which are inherent in the finite element analysis carried out here which should be kept in mind when interpreting the results.

(1) The effects of assuming an approximate shape function is to give a stiffer response of the continuum. Consequently, the computed deformations will tend to be underestimated.

(2) The formulation of CRISP is based on small displacement and small strain assumptions, which assumes that both elastic and plastic strain are infinitesimal and that the initial geometry of the deforming body is not altered substantially during the deformation process. This is the reason why the punch test simulations were not carried to the same severe settlement ratios as were the physical model tests. However, the analysis is capable of predicting the load/settlement response under normal working conditions, i.e. when load<0.5 ultimate load.

(3) Near the edge of the punch, p at a number of integration points can sometimes become negative. In order to stabilize the computation p has to be set to zero whenever it becomes negative. The fact that p can be negative suggested that there could be ill-conditioning near the singularity at the edge of the punch. To put p=0 will imply that there is some cohesion in the soil in the vicinity. However, this remedial step is considered to have negligible effects on the overall behaviour of the model because p only becomes negative in a very limited number of integration points (i.e. typically less than 5).

(4) The finite element method is capable of taking into account strain effects, i.e. progressive failure, in an analysis. The incorporation of the Hvorslev surface is equivalent to the incorporation of the pressure effects on ϕ in the analysis. The analysis is also free from any superposition error and finally principal stress directions are free to rotate.

(5) The solution does not require the assumption of the Haar and Von Karman hypothesis. The analysis is good at identifying significant stress paths in an engineering event. For axisymmetric footings the stress path followed is found to be not unlike those of a multi-stage compression triaxial test, so that the special case of the Haar and Von

Karman hypothesis is justified in chapters 3 and 4. In other words, compression triaxial test data are relevant and applicable in the punch-indentation problem in question.

(6) The current investigation has highlighted the importance of accurate direct strain measurement in a triaxial test if good quality stiffness parameters are required.

(7) If Cam-clay is used to model a granular soil, it should be accepted that λ and κ are not necessarily constant but could be functions of stress and strain.

6. 1-g Model Tests

6.1 Introduction

The 1-g test series was designed to investigate scale effects in footing tests on weightless soil. A schematic layout of the test set-up is shown in fig 6.1. The boundary value problem chosen was a cylindrical bed of soil 850mm in diameter and 350mm high. The soil model was either fully submerged in water or dry. The side and bottom of the soil model were assumed to be supported by smooth and rigid boundaries. In order to simulate this smooth condition, the inside of the tub wall was lubricated with plumbers' grease. The top surface of the soil model around the punch was subjected to a constant surcharge pressure ranging from 5 to 200kPa. In this range of surcharge, the superposition factor Ω as defined in chapter 3 ranged from 10 to 2800 so that the soil could practically be treated as weightless. The bottom of the model was a free draining boundary. To achieve this, a 3.2mm thick blanket of grade F Vion supplied by Porvair of King's Lynn was used to line the bottom of the tub. The permeability of this drainage blanket is 7.5×10^{-5} m/s in both vertical and horizontal directions.

During a test, a centrally placed rough, rigid punch of diameter 100mm (or 14.2mm) was pushed axisymmetrically into the soil bed in a displacement-controlled manner. Throughout the indentation process, the average bearing pressure under the footing and settlement of the punch were monitored. Both sand and silt were used; their acquisition and properties were described in chapter 2.

The complete 1-g test programme is summarized in table 6.1. The three variables were B/d_{50}, σ_o and d_{50}. Apart from studying the scale effects, these series of tests were also used to investigate the geometry effects (or w/B effects) on N_q. The 1-g tests are ideal for this task as they are practically free from the interference of change in overburden pressure.

6.2 Test Rig

The soil model was contained inside a modified 850mm internal diameter, 400mm deep standard Cambridge tub originally designed for the Mississippi River Levees project (Schofield, 1980). The modification involves the welding on of four lengths of rolled steel joist section (RSJ) to the bottom plate of the tub (see fig 6.2). With this modification, the loader can be mounted centrally on a loading frame which

straddles the tub as shown in fig 6.3.

The loader was driven by a Parvalux shunt wound D.C. motor at 3000rpm via a 3000:1 Parvalux WS reduction gear box. A Johnson flexible coupler connects this first gear box to a second stage purpose-built gear box and a final ball-screw drive. The drive then converts the rotary motion of the motor into a linear motion. The second gear box is capable of a gear shift whereby either a gear ratio of 25:1 or 1:25 can be engaged. This capability, coupled with the fact that the D.C. motor is powered by a Parvalux thyristor D.C. motor speed controller, enables the loading rate to be regulated from a speed as slow as 0.1mm/min while capable of delivering a maximum load of 60kN.

Two punches (100 and 14.2mm diameter) were used. Each punch was machined from a single dural block. A grooved hardened mild steel bearing plate was used to support the roller bearing where the vertical load was applied (see fig 6.4). For the 14.2mm diameter punch, instead of using a roller, the tip of the loader was machined into a semi-circular shape (see fig 6.5). Before each test, the roller or the loader tip as well as the side of the punch was lubricated with silicon oil. Sand was cemented to the bottom of both punches by araldite in order to simulate a rough base footing (see plate 6.1).

At the outset, it was decided that all the model test should be strain-controlled, to facilitate the investigation of post-peak behaviour and to eliminate any possible dynamic effects. A rig was designed and constructed for the 1-g punch-indentation tests which could withstand a surcharge pressure σ_0 up to 200kPa and a central vertical load of 60kN. The rig was proof test by subjecting it to a surcharge pressure of 300kPa. As it was expected that the most vulnerable part of the rig was the flange of the tub which was bolted to the steel lid via 18 no. high tensile bolts. Fig 6.6 shows the details of the lid. It was possible that the tub wall near the bolt might suffer stress concentration. Therefore, during the proof test, this part of the wall was strain-gauged and which was subsequently shown to be within the elastic range. The loading frame was also loaded to its maximum 60kN capacity and showed no sign of distress. The rig was, therefore, approved as a piece of equipment for its intended function at 1-g. However, apart from using it as a 1-g test rig, the rig was also designed as a centrifuge package working at up to 100g. This aspect will be covered in chapter 7.

6.3 Surcharge Bag

For the purpose of applying surcharge pressure to the model, 2 no. 50mm high and 850mm diameter cylindrical rubber bags each with a different size of central circular opening were made. The two openings were for accommodating the two different punch sizes used in the test programme. For the 100mm diameter opening, a silicon rubber sleeve was inserted in order to reduce the possibility of the bag bursting through the gap between the punch and lid (see fig 6.7). The first requirement for the design of the bags was that there should be very little stress relief around the punch. In other words, the bag had to be a hugging fit to the punch. The second was that the punch must not touch the steel lid so that any spurious vertical load could be minimized. The third and final one was that they should be very flexible so that no significant tensile and shear stresses should be mobilized when the top profile of the soil model deformed. In order to reduce the friction between the silicon rubber sleeve and the 100mm punch or between the latex rubber and the 14.2mm punch, silicon oil was applied.

Before each test, the bag was placed between the soil model and steel lid. The surcharge bag was pressurized by compressed nitrogen regulated roughly first through a Norgren valve and then more accurately by a fine-tune pressure regulating valve. The bag pressure was raised in steps of 10kPa ahead of the punch pressure. This procedure was to avoid any accidental heaving failure of the footing. Before a test started, the whole top surface of the model would be subjected to a constant surcharge including directly under the punch. A blow-off valve set at 250kPa was incorporated in the pressure system as a safeguard against inadvertently overloading the system.

6.4 Instrumentation

The surcharge pressure was monitored throughout each test by a Bell and Howell pressure transducer. As the accuracy of the measurement of surcharge pressure is only ±1kPa, the error margin for a surcharge pressure of 5kPa would be unacceptably high. Therefore, it was decided to apply the 5kPa surcharge pressure using a constant 0.5m head of water via a burette as indicated in fig 6.7.

The axial load was measured by two axial load cells which were essentially two thin walled duralumin (grade HE15) cylinders with strain gauges arranged as a full wheatstone bridge circuit. The cylinder wall was 4mm thick for the 60kN load cell and 1.5mm thick for the 10kN load cell (see fig 6.8). The energizing voltage to both load cells was 10 volts and their outputs were monitored by a high impedance digital volt

meter (DVM). The load cells were calibrated using an Instron 10 tonne calibrator. Both were found to give a linear response throughout their working range with a maximum error due to non-linearity and hysteresis less than ±0.5%.

Settlement of the punches was monitored by dial gauges (see plate 6.2). Two dial gauges were mounted on the lower ends of the loading frame columns with their spindles supported by two metal strips fixed to the top of the punch for the 100mm diameter punch. For the 14.2mm punch, because of its small size, the dial gauges actually monitor the settlement of the load cell instead. As the load cell was in contact with the punch at all times, this arrangement should not make any difference except it was not possible to monitor any tilting experienced by the punch.

Model ground surface movement could not be monitored conveniently in a 1-g test. This was due to the physical presence of the steel lid. The surface profiles could therefore at best be measured before and after each test. In order to measure the bulk dilation and compaction of the model during a test, the amount of water sucking into or pressing out of a saturated soil bed could be monitored if required by a burette connected to the bottom drainage outlet as shown in fig 6.7.

Miniature pore pressure transducers (PPT) manufactured by Druck were used to monitor the pore water pressure inside the silt model. Full scale deflection was about ±40mV and accuracy was within ±5%. The locations of the PPTs are depicted in fig 6.9.

6.5 Model Preparation

As the target density for all the models both at 1-g and in the centrifuge was near their maximum density i.e e≈0.60, therefore, their preparation method was exactly the same as the method of evaluating the minimum porosity. In this section, only deviations from the method described in chapter 2 will be covered. In order to determine the bulk dry density, the tub was weighed to the nearest 1 kg before and after the sands were in place.

6.5.1 Sand

As the grading curve might be slightly different from batch to batch, all the tests were carried out with the same consignment of two tonnes of sand supplied by the manufacturer. After each test only that material underneath the punch which might have suffered particle breakage was discarded. The remaining sand was saved in a container for subsequent reuse. In test 1GT26, layers of coloured sand about 2mm thick were

rained onto the levelled surfaces at regular intervals of 25mm to act as marker bands. The marker bands were about 300mm wide and placed along a diametric line to be sectioned after a test. The sand was dyed with engineers' blue. A technique was developed whereby sugar syrup (1 part sugar: 10 part hot water by weight) was introduced into the model after a test by upward percolation. As soon as the sugar syrup had filled up all the pores in the sand, they were drained out again, leaving behind a coat of syrup on the particle surface. When set by blowing dry and warm air over the model, vertical sectioning of the model through the centre successfully revealed the nature of the failure mechanism, as shown in plate 6.3.

When a saturated model was required, a blank steel lid was put on top of the tub. A vinyl ring was placed between the lid and the tub flange. Plumbers' grease was applied generously as seals to render the lid air-tight. After the lid was in place, the air inside the tub was evacuated by a vacuum pump. Water was then fed through the bottom drainage and percolated through the model from bottom to top. The flow rate was control by a needle valves so that the hydraulic gradient for vertical upward flow was always less than critical so that piping would not occur during the saturation process.

6.5.2 Silt

The procedure for preparing the model was exactly the same as the method stated in chapter 2 for preparing a sample at its maximum density. However, in order to implant the PPTs in the silt model, the model were made in two lifts. After the first lift was compacted, PPTs were placed at the top of the model before the second lift was poured. Otherwise the procedure was exactly the same as before. As the position of the PPTs might drift during the compaction of the second lift of silt slurry, the PPT locations were checked directly by exposing the PPTs by excavation after each test.

In order to determine the bulk density, the tub was weighed to the nearest 1kg before and after the compacted silt model was in place. The volume of the silt was calculated by measuring the thickness of the model at a regular grid of not less than 94 sampling points. This technique of sample preparation has been proved in chapter 2 to be able to produce a silt model with a reasonably uniform density.

As it was extremely difficult to excavate a silt model after each test, the silt model was fluidized by applying a water head at the bottom drainage. Soil at the centre of the model under the punch, which might have suffered particle breakage, was removed and replaced by fresh silt. The model was then vibrated in the usual fashion as

if the silt was prepared from a fresh slurry state.

If so desired, lead threads could be introduced inside the model so that any failure mechanism and/or rupture pattern could be observed after a test. When densification of the silt was completed, a series of vertical holes (1.5mm diameter and 250mm deep) were drilled at a spacing of 36mm centre to centre along a diametrical line. Lead powder mixed thoroughly with a water-solu ble oil was then introduced into the holes with a hypodermic needle. After the test, a 150mm wide middle section of the model was cut away and extruded from the tub for radiography. The radiograph obtained after test 1GT11 is shown in plate 6.4. Although the lead threads for this particular model have not filled up the drilled holes completely as intended, it can still be seen that there is no sign of ruptures in the model.

6.6 Effects Of Saturation On Sand

In order to speed up the turn-round time of the 1-g test programme, most of the tests on sand were carried out in an air-dried condition, so that the drying process after each test could be skipped. At 1-g, the soil could practically be treated as weightless: therefore, it would be immaterial whether the dry density or submerged density was operative as it is believed that, for a drained test, the behaviour of dry and fully saturated models should be the same. In order to substantiate this assumption, tests 1GT17 and 1GT21 were repeated with tests 1GT25 and 1GT23 on saturated sand models instead. As can be seen in fig 6.10, there was no significant difference between them, although the saturated model were slightly weaker than the dry counterparts probably as a result of being slightly looser, therefore the strategy adopted here was justified.

6.7 Test Results

Altogether, 23 1-g tests have been successfully carried out. The test particulars are summarized in table 6.2 and their results are graphically presented in fig 6.11 to 6.14. The effects of surcharge on the load/settlement response are clear. For the tests on silt, only those in which PPTs registered no excess pore water pressure greater than ±2kPa, which indicated that the tests were drained, were included. This aspect will be discussed in section 6.8.

From the volume change plot in fig 6.14, it can be seen that although the punch sank progressively downwards after each loading/unloading cycle, the soil model continued to dilate progressively. However, the dilation tends to diminish slightly after

each loading cycle.

By superposing the theoretical curves based on constant-ϕ analysis on the experimental curves, the constant equivalent ϕ_{max} mobilized can be identified unambiguously from fig 6.15 to 6.17. When compared with the variable-ϕ analysis prediction, the results are all within $\pm 2°$ (see table 6.3). The scatter might come from the variation of void ratio and error in measuring ϕ in a triaxial test. It can therefore be concluded that there~~is no discernable~~ *appears to be no evidence of significant* relative particle size effect for B/d_{50} varies from 24 to 8333. There is also no~~measurable~~ *evidence of significant* chamber effect if $\phi_{tub}/B \geq 8.5$ and $H_{tub}/B \geq 3.5$.

6.8 Loading Rate

As all the tests were assumed to be carried out under drained conditions, a loading rate should have been used which was slow enough for any excess pore water pressure to dissipate. This is particularly important for the silt which was about 6000 times less permeable than the sand. With this in mind, PPTs were implanted inside all the silt models except 1GT4 at different positions underneath the footing, so that any building up of excess pore pressure during the loading of the punch could be detected. All tests were carried out at 0.1mm/min for silt and 0.2mm/min for sand.

In all tests on silt which had pore pressure measurements and with $\sigma_0 > 10kPa$, all PPTs registered only minute negative pore pressurei.e. $< \pm 2kPa$. When $\sigma_0 = 10$ kPa for B=100mm, a slightly higher negative pore pressureswere measured but they were still all within ± 5 kPa. However, when $\sigma_0 = 5kPa$ with B=100mm, the loading rate was obviously not slow enough. Fig 6.18 shows the pore pressure response at position B with punch settlement (see fig 6.9 for location of PPT). Initially, the PPT registered about 0.6kPa positive pore pressure. On further loading, the pore pressure gradually became negative and decreased steadily until it reached -25kPa which coincided with the maximum punch pressure. Test 1GT29 should be less stiff than 1GT11 because it was subjected to a higher surcharge, but as shown in fig 6.18 its negative pore pressure build-up (dilation) has rendered it stiffer than test 1GT11. It is likely that for $\sigma_0 \leq 5$ kPa, the silt has become so dilative that the rate of negative pore pressure build-up became considerably higher than the rate of dissipation of excessive pore water pressure resulting in a gradual increase in negative pore water pressure. Although this negative pore water pressure was small when compared with the actual bearing pressure, it was nevertheless very significant if it was treated as surcharge. Effectively, the surcharge could have become 30 kPa instead of 5 kPa.

It was concluded that for silt a loading rate of 0.1mm/min is deemed adequate, except that this rate was too quick when $\sigma_0 \leq 5$kPa with B=100mm. It appears that the rate of dilation and build-up of negative pore water pressure is faster than the rate of dissipation when $\sigma_0 < 10$kPa. Therefore, for $\sigma_0 \leq 5$kPa with B=100mm, the results have to be discarded.

6.9 Empirical Rule For Finding σ_w

As the variable-ϕ method was found to be able to predict the 1-g model test results to within $\pm 2°$ it is therefore appropriate to establish an empirical rule based on the variable-ϕ analysis so that a working mean pressure in a footing analysis can be estimated. Once the working mean pressure, σ_w, is known, $\phi_{average}$ can be found. Table 6.4 summarizes the results for the variable-ϕ analysis. The empirical correlation of $\sigma_w = 2\sqrt{\sigma_f \sigma_0}$ was found to be able to fit the analysis reasonably well as shown in fig 6.19.

6.10 Stiffness

Fig 6.20 compares the predictions obtained from the finite element analysis with the 1-g test data. The finite element analysis tends to under-estimate the stiffness in the beginning but this will gradually become over-predicted after a relative settlement of 2 to 3%. The reloading curve being elastic, should be able to be estimated from the elastic analysis alone. Poulos and Davis (1974) have established that for a rough, rigid circular punch of diameter B resting on a semi-infinite homogeneous elastic bed as shown in fig 6.21,

$$E = \frac{\sigma_f \pi B}{\delta w 4} (1 - v^2)$$

because $E = 2 G(1+v)$
therefore

$$G = \frac{\sigma_f \pi B}{\delta w 8} (1 - v) \qquad \text{eqn 6.1}$$

It would be interesting to see if G measured from the triaxial test can be used to estimate the stiffness of the reloading curve of a footing. In chapter 2, G was found to be a function of p and so a working mean pressure should be calculated for the estimation. The empirical rule derived in section 6.9 is used here to determine the working mean pressure.

For test 1GT19, from the reloading curve ab in fig 6.22, δw is 2.13 mm.
From empirical rule, $\sigma_w = 2\sqrt{\sigma_f\sigma_o} = 2\sqrt{5000 \times 100} = 1414$ kPa.
From triaxial test data,

$$G_{mean} = 1400(1414/2)^{0.667} = 111350 \text{ kPa}$$

From eqn 6.1 (see table 2.4 for value of ν)

$$\delta w = \frac{\sigma_f \pi B(1-\nu)}{8 G_{mean}} = \frac{5000 \times \pi \times 100 \times (1-0.18)}{8 \times 111350} = 1.45 \text{ mm}$$

The method underestimates settlement by 32%.

For test 1GT4, from the reloading curve ab in fig 6.14, δw is 2.95 mm.
From empirical rule, $\sigma_w = 2\sqrt{\sigma_f\sigma_o} = 2\sqrt{3615 \times 25} = 601$ kPa.
From triaxial test data,

$$G_{mean} = 1400(601/2)^{0.667} = 62929 \text{ kPa}$$

From eqn 6.1 (see table 2.4 for value of ν)

$$\delta w = \frac{\sigma_f \pi B(1-\nu)}{8 G_{mean}} = \frac{3615 \times \pi \times 100 \times (1-0.07)}{8 \times 62929} = 2.10 \text{ mm}$$

The method underestimates settlement by 29%.

w/B is about 2% for both cases which is roughly equivalent to ε_a(average)=0.5% in a triaxial test (see fig 6.21). As G is also obtained from triaxial tests at ε_a(average)=0.5%, this may explain the close agreement obtained here.

6.11 Penetration Effects

Because $\Delta\sigma_0$ was practically zero in each test, the observed $\Delta\sigma_f$ can only be attributed to change in the boundary condition of the model. A plausible explanation put forward by Meyerhof (1951) as discussed in chapter 3 appears to be able to account for the data presented in this chapter very well. In other words, if $w\gamma \ll \sigma_0$, but σ_f keeps increasing with w/B, then a change in σ_f should be due to a change in w/B rather than a change in γw. This has proved to be true as can be seen in fig 6.15 to 6.17: σ_f increases as w/B increases along a constant-ϕ theoretical line.

The argument can similarly be put as follows. As explained earlier, both chamber and relative particle size effects are not operative here. Therefore, tests 1GT18 and 1GT14 which were both subjected to a surcharge of 10 kPa should behave like each other. As showed in fig 6.23, the two tests only look like each other when plotted as σ_f versus w/B but not σ_f versus w. Therefore, it can be concluded that penetration effects involving additional stress rotation as explained in chapter 3 exists.

6.12 Summary

Rough footings of diameter 14.2 and 100 mm were driven very slowly into beds of saturated or dry soil in order to record force against penetration. Tests were conducted under the surcharge of a pressurized rubber bag so that the self-weight of soil was negligible. The new calculation which can account for initial embedment as outlined in chapter 3 was found to be consistent with the experimental data. Comparisons with theoretical prediction obtained from chapter 4 show agreement to within ±2°. For footing with 5kPa<σ_0<200kPa, progressive loss of strength under increased stresses dominated behaviour. Ruptures were not observed. The 350-fold difference in footing/particle size ratio has apparently introduced no _serious_ extraneous effects. The empirical rule for working mean stress $\sigma_w=2\sqrt{\sigma_f\sigma_0}$ can be used to give reasonable G and ϕ value for a footing problem. No ~~measurable~~ _significant_ chamber effects were observed.

7. Centrifuge Model Tests

7.1 Introduction

Chapter 6 has demonstrated how 1-g tests when subjected to a suitable range of surcharge pressures can yield useful information on the scale effects in tests on footings. The main advantage of the 1-g tests is that they can mimic the behaviour of a weightless soil. This advantage, however, becomes its disadvantage when modelling a prototype shallow footing with self-weight. To model correctly, the stresses at homologous points of a scaled-down model should replicate those of a prototype soil construction. This has shown to be possible if the 1/n scale model is subjected to an acceleration field n times that experienced by the prototype. One possible way to achieve this is by the hydraulic gradient method (Zelikson, 1969). This, however, works only when some very strict conditions are satisfied. One condition is that the soil must be saturated and homogeneous. Correct scaling can equally well be achieved approximately but much more generally in a geotechnical centrifuge (Bucky, 1931). As the length of the rotating arm must be finite, the acceleration field would invariably suffer some distortion when compared with the earth's gravitational field. Schofield (1980), however, has demonstrated that the error in stress due to the distortion of the acceleration field for the centrifuge at Cambridge which has a working radius of 4 metres, is under ±2%.

7.2 Geotechnical Centrifuge

This chapter will only briefly describe those aspects of the Cambridge University Geotechnical Centrifuge operations that are directly relevant to the present work. The most comprehensive treatment on this subject to date can be found in Schofield (1980). The Cambridge Centrifuge is a 10m balanced beam construction as shown in fig 7.1. It has a nominal working radius of 4m and driven at its centre by a 225kW motor/drive unit. For a payload of 1 tonne, it can achieve a maximum 155g. The centrifuge package is mounted onto a swinging platform which in turn is fixed via two hinges on the beam. The counter-weight is mounted onto a second identical swinging platform at the other end. When swing-up speed is reached, the swinging platform will swing outward and up. When swing-up is almost complete, further increase in speed would engage two torsion bars which will allow the platform to translate outwards and sit squarely onto the backplate at the end of the beam. This swing-up/swing-down capability enables the direction of the acceleration field to act roughly normal to the

model surface at all times.

There are 60 electrical and 8 hydraulic slip rings at the disposal of the centrifuge user. They can be used for ~~electric power,~~ water/compressed-air supply and electrical signal transmission. All slip rings are connected to the control room where data can be digitized and stored at the data centre. Likewise, electricity and/or water/compressed-air supply to the package can be administered from the control room. During flight, the package can also be continuously monitored visually via a close-circuit video camera mounted near the centre of the beam and pointed outwards at the package.

7.3 Centrifuge Test Programme

The centrifuge series consists of 4 tests. The main objective was to investigate the scale effects in tests on shallow footings and to validate the current modelling practice of using the same prototype material in the scaled model. The physical model chosen was a punch-indentation problem with a boundary condition identical to the 1-g test series except that the stress was due to the self-weight of the soil model rather than as a uniform surcharge. A schematic layout of the test set-up is shown in fig 7.2. The test rig used for the 1-g tests described in chapter 6 was also designed as a centrifuge package. When used in the centrifuge, the top steel lid and surcharge bag have to be replaced by a cross beam for mounting LVDTs. The details of the cross beam are shown in fig 7.3. The cross beam was attached diametrically across the tub. The package can be seen in plate 7.1. The soil bed was fully submerged in water. The soil model was subjected to an elevated acceleration field from 14.2 to 100g in the centrifuge. The whole top surface of the soil model around the punch would be free of any surcharge pressure at all times.

In a centrifuge test, centrally placed rough rigid punch of diameter 100mm (or 14.2mm) was pushed axisymmetrically into a soil bed in a displacement-control manner. The two punches used were the same used in the 1-g series. Throughout the indentation process, the average bearing pressure under the footing and settlement of the punch were monitored. At the same time, heave and settlement of the surface of the model were also monitored at a number of pre-selected check points, the locations of which are shown in fig 7.4.

7.4 Instrumentation

As all the tests were assumed to be carried out under drained conditions, a loading rate which was slow enough for any excess pore pressure to dissipate should have been used. For the silt, in order to make sure that the test was drained, pore pressure at a number of sampling points were checked throughout a test to ensure that no excess pore pressure build-up at any time during the loading of the punch. The sampling points would be in the expected active, fan and passive zones. This information can also be used to establish the top profile of the water table so that the adoption of submerged density can be justified. It was also used to ensure that the specimen was not tending to dry out near the surface. The PPTs used were the same types as the ones used in the 1-g series. The locations of the PPTs are depicted in fig 7.4.

The load cells used were the same as in the 1-g series. Two linearly variable differential transformers (LVDTs) supplied by Sangamo were used to monitor the vertical movements of the punch. The two LVDTs were mounted on the cross beam with the spindles resting on two metal strips fixed to the top of the 100mm diameter punch (see fig 7.3). For the 14.2mm punch, because of its very small size, the LVDTs actually monitor the settlement of the load cell. As the load cell was in direct contact with the punch at all times during a test, this arrangement was quite satisfactory except that it was not possible to monitor any tilt experienced by the punch.

8 to 12 LVDTs were used to monitor the vertical movements of the surrounding soil which had been physically impossible in the 1-g test series. The LVDTs have a full scale deflection output of ±5V with less than ±2% error. In order to avoid indenting the soil bed by the LVDT spindles under its own self-weight at high g condition, each spindle tip was fixed to a 2mm thick 19mm diameter polymer pad.

7.5 Signal Conditioning And Transmission

The output signal from the PPTs was within ±500mV and that from the load cell is ±30mV (60kN maximum) and ±15mV (10kN maximum). Experience in Cambridge has shown that such low level signals will pick up considerable interference when transmitted through the slip rings to the data logging and processing centre. In order to reduce the noise/signal ratio, the PPT output signals were amplified by 10 times and the load cell output signal by 100 times on the package before transmission through the slip rings.

As for the LVDTs, their outputs were relatively high (i.e. within the range of ±5V) and so amplification of signals was deemed unnecessary. However, the LVDT output signals were inherently noisy and they have to pass through an active low pass filter before transmission so that they would not corrupt the other signals transmitted which share the same stack of signal slip rings. The other problem is the 240 volts D.C. power supply to the D.C. motor on the package. As a precaution against interference, the D.C. power supply and all signals were transmitted in two separate stacks of slip rings.

7.6 Centrifuge Test Results

Altogether four centrifuge tests have been carried out from 14.2g up to 100g. Their particulars are summarized in table 7.1. The model preparation method for the centrifuge models was exactly the same as for the 1-g models. Data were logged automatically at the data centre. As an independent check and back-up, data were also manually logged during the test by a digital volt meter (DVM).

7.6.1 Proof Test

As the package was of a new design, it had to be proof tested to 25% above its working stress before it could be commissioned as a standard package. The objectives of the proof test were three-fold. The first was to check the structural integrity of the loading frame and the tub. The second was to test the mechanical performance of the loading system and the electric motor. The third was to check the effectiveness of the power supply strategy and signal conditioning procedure adopted.

During the proof test, the package was gradually taken up to 125g and stayed there for 10 minutes. The deflection of the frame under its own weight was measured and found to be within reasonable agreement to the estimated elastic deflection. The loading frame was tested only under the condition when no load was being applied. This was because when load was applied, the 1-g condition was more critical. This 1-g condition has been proof tested already as discussed in chapter 6. The package was found to be structurally sound up to 125g.

The D.C. motor on the package, however, stalled at about 80g. This problem could have been caused either by the jamming of the second stage gear box due to distortion of the loading frame under its own weight, or by the excessive sagging of the armature spindle of the D.C. motor resulting in contact between the field coil and the armature coil. The centrifuge was, therefore, stopped and the motor was stripped down

for inspection. Scratch marks on the armature were observed and so support the second possibility mentioned above. When the armature dimension was measured, its shape was found to be lop-sided. The armature was therefore trimmed in a lathe. Up to a few thousandths of an inch were machined off before putting it back to the motor housing. Subsequent tests up to 100g have shown that this has cured the problem of stalling. As a precaution against burning out the motor due to stalling, a flag was fixed to the extended armature shaft so that any stalling of the motor could be detected through the close-circuit video system. The slowest rate of the loader was controlled by the stalling speed of the motor, which is 0.1mm/min at a maximum load of 60kN.

During the proof test, signals were logged and it was found that the signal conditioning and transmission strategy adopted had successfully reduced the noise to signal ratio to an acceptable level.

7.6.2 CKL1

The same silt model (e=0.63) used for the proof test was used subsequently for test CKL1. Although the model in this test has been stressed by its own weight up to 125g, it was believed that this 1-dimensional consolidation stress cycle should not have any significant effects on its behaviour for the following reason. At 125g, the soil at the deepest point in the model was subjected to a maximum 1-dimensional compression of around 450kPa. This was very small when compared with the pre-consolidation pressure of 51,650kPa for the silt as discussed in chapter 5.

The test proper commenced by taking the package up to 50g. When the soil bed was fully consolidated as suggested by the PPT and LVDT reading being stabilized, a 100mm diameter punch, modelling a 5m diameter circular footing, was loaded to 20kN and then fully unloaded. The self-weight of the punch being 0.7kN (1.4kg) at 50g was negligibly small when compared with the maximum load of 60kN. Fig 7.5 shows vertical load and movement of check points on the soil surface against time during the test. Fig 7.6 shows the PPT readings against time during the test. This first stress cycle was used to eliminate the bedding error and allow some elastic behaviour to be observed.

The punch was reloaded again until it reached the maximum capacity of the loader, which is 60kN, and was then fully unloaded. Fig 7.7 shows the vertical load versus vertical settlement of the punch. When superimposed on the theoretical curve obtained from chapter 3, the extrapolated load versus displacement curve shows that ϕ_{max} is about 42° (see fig 7.8). The punch was reloaded a third time to 60kN. The load

was kept constant; the g level was gradually reduced while maintaining the vertical load at 60 kN by continuously adjusting the loading rate of the loader. The punch was found to sink steadily into the soil bed at a constant vertical load of 60kN at 30g (see fig 7.5 and 7.7). The punch was then unloaded completely before the centrifuge was stopped. The footing at 30g modelled as a 3m diameter footing. When superposed on the theoretical curves ϕ_{max} is found to be about 43° (see fig 7.9).

Throughout the test, the four PPTs implanted inside the model, apart from the PPT at position A which was faulty, registered only an excess pore pressure of less than ±2kPa. This suggests that the test can be regarded as drained. The PPT at position A was later found to be damaged by the rigid punch. Therefore, in all subsequent tests, PPTs were not placed in direct contact with the punch.

Apart from the two LVDTs which monitored the vertical movement of the rigid punch, eight check points were monitored in this test. All check points first registered settlement and then heave during each loading cycle. The trend was that the closer it was to the punch, the larger also was the heave at the end of the test. As all the check points follow a similar pattern, therefore only the check point with the largest movement is plotted. The rest are presented simply as ratios (see fig 7.5) which show the relative magnitudes compared with the one that is shown.

7.6.3 CKL2

This was a test on saturated sand at a void ratio of 0.61 and with a 100mm diameter punch. The test commenced by taking the package up to 50g with the punch modelling a 5m diameter footing. The punch was then pushed into the soil bed. During this time, the datalogger was logging some spurious LVDT readings which suggested that the footing was rising by about 0.5mm instead of going down. This was thought to be due to slipping of the LVDT relative to its holder. The centrifuge was stopped and all the LVDT holders were tightened up before the test restart again. As a result, the first cycle of LVDT output were lost. However, from the time elapse and rate of loading, the settlement can be estimated.

When the package was taken up to 50g again. The punch was reloaded until a settlement of 30mm was reached. It was then fully unloaded. The test results are presented in fig 7.10 and 7.11b. Fig 7.11a shows the top profile of the model when σ_f was maximum. When superposed on the theoretical curves obtained from chapter 3, the load versus displacement curve shows that ϕ_{max} was about 40° (see fig 7.12).

Apart from the two LVDTs which monitored the vertical movement of the rigid punch, eleven additional check points were also monitored in this test. All check points registered a movement pattern similar to CKL1 except that the heave tended to be higher in magnitude as a result of deeper penetration in this test. Coloured bands of sand were introduced into the model during model preparation. After the centrifuge test, the model was set by sugar solution using the technique described in chapter 6. Vertical sectioning of the model right through the centre revealed the nature of the failure mechanism as shown in plate 7.2. Ruptures were not observed.

7.6.4 CKL3

This was a test on saturated silt at a void ratio of 0.57 and with a 100mm diameter punch. A 1 on 14.2 timber wedge was installed between the package and the swinging platform. Upon swing up, the centreline of the soil model would incline at a gradient of 1 on 14.2 to the centrifugal force direction. When combined with the effects of the earth's gravity, the model would then be subjected to a resultant g force acting along the axis of symmetry of the model. The package was taken up to 14.2g. When all the LVDTs and PPTs readings were stabilized, the loader started pushing the punch modelled as 1.42m diameter footing into the model ground. The punch was loaded up to 17kN and then unloaded (see fig 7.13). The self-weight of the punch being 0.2kN (1.4kg) at 14.2g is negligibly small when compared with the maximum load of 60kN.

In the second cycle, the punch was loaded to 60kN and then unloaded: a very stiff response was recorded (see fig 7.14). It should be noted that although two of the PPTs away from the punch (at position C and D as shown in fig 7.15) registered excess pore pressure less than ±3kPa, the PPT at position A which was in the fan zone gradually built up a suction continuously up to -17kPa. This indicated that strong dilation must had been going on in the supporting soil even at a loading rate of 0.1mm/min. The loading rate was controlled by the stalling speed of the D.C. motor and was already near its minimum. The rate of dilation and negative pore pressure build up appear to be greater than the rate of dissipation of excess pore pressure as indicated by PPTs at position A. This test could not be regarded as fully drained and therefore the results must be treated with caution. Although -17kPa was small when compared with the maximum bearing pressure in the region of 7000kPa, it could be very significant if it was viewed as an additional surcharge of 17kPa. This test was therefore discarded as being influenced by transient pore water pressure. It seems, however, that the silt may be an ideal material for the investigation of loading rate and pore pressure effects in footing tests.

7.6.5 CKL4

This was a test on saturated silt at a void ratio of 0.61 and with a 14.2mm diameter punch. This test was originally designed to act as a modelling of models for CKL3. As CKL3 had to be discarded, this test has to stand on its own now. The test commenced by taking the package up to 100g with the punch modelling a 1.42m diameter footing. When the soil bed was fully consolidated as suggested by the LVDT and PPT readings, the punch was pushed into the soil bed until it reached the peak at about 1kN, softened, and then picked up load again (see fig 7.16). The self-weight of the punch being 0.02kN (21g) at 100g is negligibly small when compared with the maximum load of 1kN. Apart from the two LVDTs which monitored the vertical movement of the rigid punch, twelve check points were monitored by LVDTs during the test. Among the twelve, LVDT13 malfunctioned and its readings had to be discarded. Other LVDTs were in good working order. The punch was loaded to a settlement of 21mm before being unloaded. At the second cycle the punch was reloaded to 28mm before unloaded again. Throughout the test, all three PPTs implanted inside the model registered only an excess pore pressure of less than ±2kPa. This suggested that the test can be regarded as drained (see fig 7.17). Fig 7.18 shows the load/settlement response of the punch. The mean bearing pressure versus relative punch settlement curve shows that ϕ_{max} was about 45.5° (see fig 7.19) when it is superposed on the theoretical curves.

7.6.6 Summary

Table 7.2 summarizes the results of the centrifuge test series. By superposing the theoretical curves based on the constant-ϕ analysis on the experimental curves, the equivalent constant ϕ_{max} mobilized can be identified unambiguously. When compared with the variable-ϕ analysis prediction, the results are all within ±1°. The scatter might be attributed to the variation of void ratio and error in measuring ϕ in a triaxial test. It can therefore be concluded that there appears to be no evidence of serious ~~is no discernable~~ relative particle size effects for B/d_{50} varies from 165 to 8333. There is also no evidence of significant ~~measurable~~ chamber effects when $\phi_{tub}/_B \geq 8.5$ and $H_{tub}/_B \geq 3.5$ which is in general agreement with the results reported by Bagge and Christensen (1977).

7.7 Empirical Rule For Finding σ_w

As the variable-ϕ method presented in chapter 4 was found to be able to predict the centrifuge model test results to within ±1°, it is appropriate to establish an empirical rule based on the variable-ϕ analysis to find a working mean pressure in a footing analysis, so that $\phi_{average}$ can be calculated. Table 7.3 summarizes the results for the

variable-ϕ N_γ analysis. The empirical correlation of $\sigma_w = 9\sqrt{\sigma_f B\gamma}$ was found to be able to fit the theoretical results reasonably well as shown in fig 7.20.

7.8 Stiffness

Fig 7.21 and 7.22 compare the predictions obtained from the finite element analysis with the centrifuge test data. The finite element analysis tends to under-estimate the stiffness in the beginning but this gradually changes and the stiffness is over-predicted after a relative settlement of 2 to 3%. As in chapter 6, the empirical rule derived in section 7.7 is used here to determine the working mean pressure for elastic settlement calculations.

```
For test CKL1, from the reloading curve ab in fig 7.7,
δw is 1.11 mm.
```
From empirical rule, $\sigma_w = 9\sqrt{\sigma_f B\gamma} = 9\sqrt{2546 \times 5 \times 10} = 3211$ kPa.
From triaxial test data,

$$G_{mean} = 1400(3211/2)^{0.667} = 192429 \text{ kPa}$$

From eqn 6.1 (see table 2.4 for value of ν)

$$\delta w = \frac{\sigma_f \pi B (1-\nu)}{8G_{mean}} = \frac{2546 \times \pi \times 100 \times (1-0.17)}{8 \times 192429} = 0.43 \text{ mm}$$

The method underestimates settlement by 61%.

```
For test CKL2, from the reloading curve ab in fig 7.11b,
δw is 1.2 mm.
```
From empirical rule, $\sigma_w = 9\sqrt{\sigma_f B\gamma} = 9\sqrt{1750 \times 5 \times 10} = 2662$ kPa.
From triaxial test data,

$$G_{mean} = 1400(2662/2)^{0.667} = 169807 \text{ kPa}$$

From eqn 6.1 (see table 2.4 for value of ν)

$$\delta w = \frac{\sigma_f \pi B (1-\nu)}{8G_{mean}} = \frac{1750 \times \pi \times 100 \times (1-0.22)}{8 \times 169807} = 0.32 \text{ mm}$$

The method underestimates settlement by 73%.

w/B is about 1% for both cases which is roughly equivalent to ε_a(average)=0.25% in a triaxial test (see fig 6.21). As G is obtained from triaxial tests

when ε_a is about 0.5% which means the strain level experienced by the soil underneath the footing is roughly half that of the triaxial tests. If the fact that G for a triaxial specimen generally deteriorates with increasing strain level (Jardine et al, 1984) is also taken into consideration, the error could even be worse. Nevertheless, the method does provide us with a simple means to predict roughly the settlement on reloading a footing.

7.9 General Observation

There are a number of features common to all the three fully drained centrifuge tests. Instead of repeating them in each individual section, they will be collectively presented here.

(1) All tests commenced by taking the package up to the scheduled g level. Loading of the punch only commenced when the soil bed was fully consolidated. Consolidation was deemed complete when all the LVDTs registered no further noticeable settlement and the pore pressure measured by the PPTs have been stabilized.

(2) All initial zero of the LVDTs were set to the reading when the package was subjected to the scheduled g level, so that all elastic deformation of the rig can be taken into account during each test. For example, the sagging of the LVDT beam had automatically been accounted for before the punch-indentation began.

(3) All punches were subjected to at least two loading/unloading cycles. The first one was to eliminate the bedding error and allow some elastic behaviour to be observed.

(4) All check points settle initially when the punch was loaded and then started to heave upon further loading. It is interesting to note here that the peak load in terms of ϕ_{max} coincides approximately with the maximum rate of heaving. This phenomenon is important for the interpretation of the peak load of a field plate loading test, for example. With the monitoring of the rate of heaving away from the footing, it may be able to identify the load associated with ϕ_{max}.

(5) The closer the check points were to the punch, the larger also was the heave at the end of a test.

(6) By superposing the experimental curve with the theoretical prediction for different ϕ obtained in chapter 3 (see fig 7.19, for example), value of ϕ_{max} were obtained from the experimental curve. The three centrifuge tests consistently yielded

value of ϕ_{max} which were within $\pm 1°$ of the theoretically predicted ϕ_{max} based on the variable-ϕ analysis developed in chapter 4 and the triaxial test data obtained in chapter 2 (see table 7.2).

(7) Strain effects : As observed in chapter 2, once ϕ_{max} was reached, it could be maintained after considerable straining before softening begins (see fig 7.23). This may explain why ϕ_{max} was a good strength parameter for calculating bearing capacity despite the fact that the strain in the supporting soil was very non-uniform. This comment is also applicable to the 1-g test series.

7.10 Summary

The constant-ϕ analysis proposed in chapter 3 which takes into account the penetration effect can facilitate the estimation of ϕ_{max} in a centrifuge test in an unambiguous way (see fig 7.19, for example). The variable-ϕ N_γ analysis proposed in chapter 4 can predict the three centrifuge tests under drained conditions to within $\pm 1°$ based on drained triaxial test data alone. There do̶es̶ not appear to be any evidence of serious relative particle size effects in centrifuge tests on circular footings despite there is a 50-fold (maximum) difference in footing/particle size ratio between the tests. Ruptures were not observed. The finite element analysis using the simplified Schofield Model proposed in chapter 5 was able to predict reasonably the settlement of a shallow foundation under working load condition.

It appears that during a field test, the vertical movement record of soil outside the footing can be very useful. The present series of centrifuge tests suggest that the moment when the supporting soil is mobilizing ϕ_{max} may coincide with the maximum rate of heaving at the soil surface surrounding the footing.

It has been demonstrated that as far as circular footing bigger than 1.42m in diameter is concerned, modelling with the same prototype material is justified. On the other hand, this chapter has also shown that modelling with scaled down soil particle is very promising in investigating a boundary value problem which encourages ruptures provided that triaxial tests are carried out to take the absolute particle size effects into account.

A loading rate of 0.1mm/min is too quick for a footing on silt with B=100mm at 14.2g. It appears that there is no significant chamber effect both in terms of strength and stiffness as long as $\phi_{tub}/_B \geq 8.5$ and $H_{tub}/_B \geq 3.5$. The empirical rule for working mean stress $\sigma_w = 9\sqrt{\sigma_f B \gamma}$ can be used to estimate an average constant ϕ and G for routine calculations.

8. Conclusions

8.1 Summary And Conclusions

This dissertation presents an investigation of scale effects in tests on vertically loaded footings with a view to clarifying the following question in centrifuge modelling. There are two modelling strategies which the centrifuge modeller can choose:

(1) Use the same soil in the centrifuge model as in the prototype soil construction so that the size of particles relative to a characteristic dimension of the construction will be different in model and prototype.

(2) Use scaled down soil particles in the centrifuge model so that the ratio of particle size to a characteristic dimension of the soil construction is the same in both model and prototype, then this may imply that the constitutive behaviours of the soils in model and prototype may be different.

Triaxial test data presented in chapter 2 showed that the effect of absolute particle size and the effect of mean pressure are significant for the quartz silt and sand materials used in this work. Model tests of punch-indentation were conducted at various stress levels either at 1-g with surcharge as reported in chapter 6 or under elevated g level in a centrifuge as reported in chapter 7. Theoretical analyses using the method of characteristics and using CRISP were also carried out. After the effects of pressure and penetration were accounted for, the method of characteristics as developed in chapters 3 and 4 gave good strength predictions in accord with both the 1-g and centrifuge experimental data. The finite element analysis presented in chapter 5 gave predictions of the stiffness which was accurate only to within a factor of about 2.

Modelling distortions associated with using either strategy could then be studied. Effects of not complying with the scaling law for relative particle size was found to be not serious non-operative in a footing problem when $10kPa \leq \sigma_0 \leq 200kPa$ for $24 < B/d_{50} < 8333$. $1.42m \leq B \leq 5.0m$. The effects of not complying with the scaling law for constitutive behaviour (i.e. absolute particle size) was found to be very significant in the sense that the stress-strain properties of the reduced-scale soils were found to be significantly different. Vesic's (1970) postulate on scale effects for footings as outlined in chapter 1 was then rationalized and quantified. This chapter recapitulates what has been clarified by the present work and makes specific comments or recommendations where appropriate.

8.1.1 On Design

The special case of the Haar and Von Karman hypothesis which states that $\sigma_1 > \sigma_2 = \sigma_3$, has been adopted for the footing problem in the plasticity stress analysis in chapters 3 and 4. Although no general proof has yet been found, the finite element analysis reported in chapter 5, which does not make this assumption has shown that for the limited number of cases analysed, the stress condition always approximates to this particular stress condition. The principal of superposition has proved to be safe and also not unduly conservative. Accordingly, the method of characteristics was used to generate bearing capacity factors in the form of tables in chapter 3 for the benefit of the practising engineer. The additional surcharge generated by penetration of the footing alone was found to be not sufficient to account for the steep increase in bearing capacity. The penetration effect is therefore more than an increase in overburden pressure. A plausible explanation is the geometry effect which allows additional rotation of the principal stress to occur in the supporting soil. This explanation is supported by the 1-g test data presented in chapter 6.

There are considerable uncertainties in deciding the failure load of a footing especially when the supporting soil is relatively compressible. If failure is defined as the moment when the supporting soil is mobilizing its highest average ϕ, the constant-ϕ analysis which has taken into account penetration effects can facilitate the determination of the ultimate bearing capacity of a footing in terms of average ϕ_{max} in a clear and unambiguous manner. The constant-ϕ analysis can therefore be used by the practising engineer in interpreting experimental data, in particular, those of the penetrometer.

However, in order to be able to predict, a variable-ϕ analysis should be made available. By modifying the constant-ϕ governing equations to take into account the effects of varying ϕ on the stress rotation equation and the strength envelope, a new style of variable-ϕ analysis can be established which can predict all model footing tests under drained conditions to within $\pm 2°$ based on the drained triaxial test data. For two special cases where exact solutions exist, the new style of calculation reproduces the exact solutions. Encouraged by these close agreements, the variable-ϕ analysis was then used to establish empirical rules to estimate the average working pressure, so that even a constant-ϕ analysis can now give an approximate prediction by using the average ϕ relevant to the average ambient stress level.

By incorporating the Schofield model in CRISP for the two dense reconstituted granular materials used in this work, a simple numerical tool can be formed which

provides a consistent treatment of equilibrium of stresses and compatibility of strains. The analysis has given order of magnitude predictions of the initial stiffness of a number of vertically loaded footings under working load conditions. However, there are still grounds for further improvement, for example, by incorporating the shear strain and stress level effects on stiffness and by more accurate stiffness measurement in a triaxial test. The reloading curve of a footing should theoretically be related to the shear modulus obtained from the reloading curve of a triaxial test using the elastic theory, provided that the average working stress level in the supporting soil of a footing can be estimated. It was discovered that by using the two empirical rules derived from the variable-ϕ analysis, reasonable agreement between the triaxial and model footing data can be found. It is, however, more successful for the 1-g tests than for the centrifuge tests.

Although ϕ_{max} can be measured accurately in a conventional standard triaxial set-up, some form of direct measurement of strain is essential if accurate stiffness parameters are required. In this work, only the standard triaxial plane has been explored. In order to make the Schofield model applicable to more general engineering events, stress space other than on the triaxial plane has to be explored as well.

8.1.2 On Soil Particle Modelling

Soil particle modelling will introduce the complication of modifying the grain crushing strength as a result of changes in the absolute particle size. Particle crushing may result in a reduction in mobilizable shear strength, loss of dilatancy, and increased compressibility. The silt and sand used in this work display quite different stress-strain relations because of their stress history experienced during their formation process. Chapter 5 has shown that this can be looked at in a unified way with the help of the Schofield model. Silt has a larger state boundary than sand and so exhibits more elastic behaviour and is therefore stiffer. The virgin loading curves are different as the silt yields later than the sand. However, on unloading and reloading, the stiffnesses of the two materials are very similar as they both behave quasi-elastically.

It has been demonstrated that it is feasible to model soil particles by taking into account the inevitable complication of varying the particle crushing strength. One possible technique to overcome this complication is by using a weaker material so as to preserve the crushability of the smaller particles. Alternatively, the changes in constitutive behaviour can be corrected by doing a series of triaxial tests to account for any absolute particle size effects.

There is evidence to indicate that although ϕ_{max} measured in a triaxial test shows that silt is stronger than sand, the reverse is true in a direct shear box. This suggests that progressive rupture type of failure may be operative in the direct shear box. It is, therefore, believed that the particle modelling technique developed here may be suitable for the investigation of progressive failure in a class of boundary value problem where ruptures are actively encouraged, e.g. footings under inclined load or active translation of a retaining wall.

8.1.3 On Centrifuge Modelling

For very low surcharges or very small footings subjected to vertical load (e.g. $\sigma_0 \ll 5kPa$ or $B \ll 1.42m$), effects of strain are probably not very significant as the soil is more likely to behave rigid-plastically. From data in chapter 6, it can be said that as surcharge increases, the soil will become more compressible and the effects of penetration of the vertically loaded footing have to be accounted for. At these high surcharge pressures there do not appear to be any non-uniform strain effects on the vertical bearing capacity. This can perhaps be explained by the ability of the soil to mobilize ϕ_{max} over quite a wide range of shear strain (about 5% axial strain in a triaxial test) after ϕ_{max} has been reached. There was no evidence of serious measurable relative particle size effect and ruptures were not observed.

From data in chapter 7, it can be said that as far as modelling a vertically loaded circular footing bigger than 1.42m and smaller than 5m is concerned, modelling with the same prototype material in a centrifuge model will not introduce any measurable distortion. On the other hand, modelling with scaled down soil particles so as to preserve the dimension scaling law is very promising for the investigation of a boundary value problem which encourages ruptures, provided that triaxial tests are carried out to account for any absolute particle size effect.

No evidence of measurable chamber effects both in terms of stiffness and strength were detected when $\phi_{tub}/B \geq 8.5$ and $H_{tub}/B \geq 3.5$. It appears also that during a field footing test, the vertical movement record of soil outside the footing can be instructive, as the present work suggests that the moment when ϕ_{max} (average) in the supporting soil is fully mobilized may coincide with the maximum rate of heaving.

8.2 Suggestions For Further Work

Listed below are a number of areas which may warrant further investigation.

(1) Extend the current work to include a wider variety of granular materials.

(2) Extend the footing problem to other boundary value problems which encourage ruptures, for example, the modelling of footings under inclined load or the modelling of retaining walls to collapse limit states.

(3) The loading rate was found to have very significant effects on stiffness and strength in some of the model tests on silt. It seems that the loading rate begins to have an effect if the rate of negative pore water pressure build-up is faster than the rate of its dissipation. In a full scale spudcan on silt, where the drainage paths are much longer than those in the scaled model, the loading rate effects should become even more serious. As positive pore water pressure may also play a part, further clarification by properly modelling the transient state is needed.

(4) It has been found that conventional triaxial tests did not provide high quality stiffness parameters. New techniques should be developed so that strain can be measured directly and more accurately. When these data were made available, improvement to the finite element analysis can be made by including the effects of shear strain and stress level on the soil stiffness.

(5) The triaxal strength data should ideally be fitted with a curved Hvorslev line instead of a bi-linear line at a constant v section on the compression triaxial plane. The current finite element analysis on footings also indicates that the behaviour of the supporting soil both in the fan and passive zones are dominated by the ϕ_{max} cut-off criterion. Therefore, more high quality low pressure triaxial data are needed to properly define the state boundary of the Schofield model.

(6) Extend the method of characteristics for a surface footing to include initially embedded footings and improve the present method of analysing a rough base footing. One approach to the second problem may be to assume a base friction distribution pattern as an additional boundary condition instead of assuming a trapped rigid cone. The lower bound solution for a rough footing could then be calculated by varying the base friction distribution pattern until a maximum solution is obtained.

REFERENCES

Airey, D. W. (1987). *The computer controlled triaxial testing system - a user guide.* Cambridge University Engineering Department.

Argyris, J. H. & Kelsey, S. (1960). *Energy theorems and structural analysis.* Butterworths (reprinted from Aircraft Eng. 1954-5).

Atkinson, J. H. & Bransby, P. L. (1978). *The mechanics of soils.* MaGraw-Hill, London.

Bagge, G. & Christensen, S. N. (1977). Centrifuge testing on the bearing capacity of circular footings on the surface of sand. In *Dialog 77, 20th anniversary, Danmarks Ingeniorakademi, Bygningsafdelingen, Lyngby,* pp. 337-346.

Bishop, J. F. W. (1953). On the complete solutions to problems of deformation of a plastic rigid material. *J. Mech. Phys. Solids,* Vol. 2, pp. 43-53.

Bishop, A. W. & Henkel, D. J. (1962). *The measurement of soil properties in the triaxial test.* Arnold, London.

Bolton, M. D. (1986). The strength and dilatancy of sands. *Geotechnique* **36** , No. 1, pp. 65-78.

Bolton, M. D. (1988). Lecture notes. In *Advances in the design of earth-retaining structures,* Churchill College, Cambridge.

Borin, D. L. (1973). *The behaviour of saturated kaolin in the simple shear apparatus.* **PhD** thesis, Cambridge University.

Brand, E. W. (1973). Some observations on the control of density by vibration. In *Evaluation of relative density and its role in geotechnical projects involving cohesionless soils.* ASTM Spec. Tech. Publ. 523, pp. 121-132, American Society for Testing and Materials, Philadelphia.

Britto, A. M. & Gunn, M. J. (1987). *Critical state soil mechanics via finite elements.* Ellis Horwood.

Bucky, P. B. (1931). Use of models for the study of mining problems. **AIMME** *Tech. Publ.* No. 425, 3-28.

Burmister, D. M. (1948). The importance and practical use of the relative density in soil mechanics. *Proc*. ASTM 48, pp. 1249-1268.

Carter, J. P. (1977). *Finite deformation theory and its application to elastoplastic soils*. PhD thesis, School of Civil Engineering, University of Sydney.

Chen, W. F. (1975). *Limit analysis and soil plasticity*. Amsterdam: Elsevier.

Corte, J-F. et al (1988). Centrifuge modelling of the behaviour of a shallow foundation - a cooperative test programme. *Proc. of the Int. Conf. on Geotechnical Centrifuge, Paris*. Editor Corte, J-F.

Cox, A. D. (1962). Axially-symmetric plastic deformation in soils - II, Indentation of ponderable soils. *Int. J. Mech. Sci*. Vol. 4, pp. 371-380.

Cox, A. D., Eason, G. & Hopkins, H. G. (1961). Axially symmetric plastic deformations in soils. *Phil. Trans. Roy. Soc. London,* A1036, Vol. 254, pp. 1-45.

Davis, A. G. & Auger, D. (1979). La Butee des Sables: Essais En Vraie Grandeur. *Annales de L'Institut Technique du Batiment et des Travaux Publics, Sols et Fondations,* Vol. 375, No. 166, September, pp. 69-92.

Davis, E. H. & Booker, J. R. (1971). The bearing capacity of strip footings from the standpoint of plasticity theory. *Proc. 1st Aust.-N.Z. Conf. Geomech., Melbourne*. pp. 276-282.

Dean, E. T. R. (1985). *Exterior States* . CUED/D-SOILS/TR 172, Cambridge University.

De Beer, E. E. (1965a). The scale effects on the phenomenon of progressive rupture in cohesionless soils. *Proc. 6th ICSMFE* Vol. 2, Canada.

De Beer, E. E. (1965b). Influence of the mean normal stress on the shearing strength of sand. *Proc. 6th ICSMFE* Vol. 1, Canada.

Drucker, D. C. (1950). Some implications of work hardening and ideal plasticity. *Quart. Appl. Math.* , 7 , pp. 411-418.

Drucker, D. C. (1951). A more fundamental approach to stress-strain relations. *Proc. 1st. U. S. Nat. Cong. for Applied Mech.,* ASME , pp. 487-491.

Drucker, D. C., Prager, W. & Greenburg, H. J. (1951). Extended limit design theorems for continuous media. *Quarterly of Applied Mathematics*, Vol. 9, No. 4, pp.381-389.

Finn, W. D. L. (1967). Applications of limit plasticity in soil mechanics. *J. of the SM&FD*, Proc. of the ASCE, SM5, pp. 101-119.

Girijavallabhan, C. V. & Reese, L. C. (1968). Finite element method for problems in soil mechanics. *J. S. M. & F. Division*, ASCE.

Graham, J. & Hovan, J-M. (1986). Stress characteristics for bearing capacity in sand using a critical state model. *Canadian Geotechnical Journal* **23** , pp. 195-202.

Graham, J. & Pollock, D. J. (1972). Scale dependent plasticity analysis for sand. *Civil Engineering & Public Works Review,* **67** , pp. 245-251.

Griffith, A. A. (1921). The phenomena of rupture and flow in solids. *Phil. Trans. Roy. Soc. of London,* series A, Vol. 221, pp. 163-198.

Griffith, A. A. (1924). The theory of rupture. *1st Int. Cong. in Applied Mechanics,* pp. 55-63.

Griffiths, D. V. (1982). Computation of bearing capacity factors using finite elements. *Geotechnique* **32** , No. 3, pp. 195-202.

Gronow, J. (1987). Private communication.

Hambly, E. C. (1985). Punch-through instability of jack-up on seabed. *J. Geotechn. Eng. Div.* ASCE , Vol. III, No. 4, pp.545-550.

Hansen, B. & Christensen, N. H. (1969). Discussion on theoretical bearing capacity of very shallow footings - by Larkin, L. A., *J. of Soil Mech. & Fdn. Div.* ASCE , Vol. 95, No. SM6, Proc. Paper 6258, pp. 1568-1572.

Haar, A. & Von Karman, Th. (1909). Nachr. Ges. Wiss. Gottingen, pp. 204.

Hill, R. (1950). *The mathematical theory of plasticity.* Oxford: Clarendon Press.

Hoek, E. & Brown, E. T. (1980). Empirical strength criterion for rock masses. *J. Geotech. Engng. Div.* ASCE , Vol. 106, GT9, pp. 1013-1035.

Houlsby, G. T. (1981). *A study of plasticity theories and their applicability to soils.* PhD thesis, Cambridge University.

Hvorslev, M. J. (1937). *Uber die festigkeitseigenshaften gestorter bindinger boden.* Thesis, Copenhagen.

Iliushin, A. A. (1961). On the postulate of plasticity. *Appl. Maths. & Mech.* Vol. 25, pp. 746-752.

Irons, B. M. (1970). A frontal solution program for finite element analysis. *Int. J. Num. Mech. Eng.,* **12** , pp. 5-32.

Jardine, R. J., Symes, M. J. & Burland, J. B. (1984). The measurement of soil stiffness in the triaxial apparatus. *Geotechnique* **34** , pp. 323-340.

Kerisel, J. (1972). The language of models in soil mechanics. *Proc. 5th ICSMFE* , Vol. 2, pp. 9-30 (translated into English from French).

Ko, H. Y. & Davidson, L. W. (1973). Bearing capacity of footings in plane strain. *JSM&FD,* ASCE, Vol. 99, SM1, pp. 1-23.

Kolbuszewski, J. (1948). An experimental study of the maximum and minimum porosities of sands. *2nd Int. Conf.* Vol. 1, pp. 158-165.

Krumbein, W. C. (1941). Measurement and geological significance of shape and roundness of sedimentary particles. *J. of Sedimentary Petrology* , Vol. II, No. 2, pp. 64-72.

Larkin, L. A. (1968). Theoretical bearing capacity of very shallow footings. *Journ. of Soil Mech. & Found. Division,* ASCE **94** (SM6). Proc. paper 6258, pp. 1347-157.

Lau, C. W. (1977). *An analytical investigation of plasticity and strain-softening in geotechniacl engineering.* PhD thesis, London University.

LeBlanc, L. (1981). Tracing the causes of rig mishaps. *Offshore,* , March, pp. 51-62.

Lo, K. Y. (1972). An approach to the problem of progressive failure. *Canadian Geotechnical Journal,* Vol. 9, pp. 407-429.

Lowe, J. (1964). Shear strength of coarse embankment dam materials. *Proc. 8th Int. Cong. Large Dams.* , Edinburgh, pp. 745-761.

Mak, K. W. (1984). *Modelling the effects of a strip load behind rigid retaining walls.* **PhD** thesis, cambridge University.

Mandel, J. (1942). Equilibres par tranches planes des solides (Louis-Jean, Paris), *Proc. 6th Int. Cong. App. Mech.,* Paris.

Marachi, N. D., Chan, C. K., Seed, H. B. & Duncan, J. M. (1969). Strength and deformation characteristics of rockfill materials. *Report No. TE-69-5, Dept. of Civil Eng.,* University of California, Berkeley.

Marachi, N. D., Chan, C. K. & Seed, H. B. (1972). Evaluation and properties of rockfill materials. *J. Soil Mech. Fdn. Div.* **ASCE 98,** SM1, pp. 95-114.

Meyerhof, G. G. (1948). An investigation of the bearing capacity of shallow footings on dry sand. *Proc. 2nd ICSM,* Vol. 1, pp. 237.

Meyerhof, G. G. (1950). *The bearing capacity of sand.* **PhD(Eng)** thesis, London University.

Meyerhof, G. G. (1951). The ultimate bearing capacity of foundations. *Geotechnique* **4** , Vol. 2, pp. 301-332.

Meyerhof, G. G. (1955). Influence of roughness of base and ground water conditions on the ultimate bearing capacity of foundations. *Geotechnique* **5** , Vol. 3, pp. 227-242.

Meyerhof, G. G. (1963). Some recent research on the bearing capacity of foundations. *Canadian Geotechnical Journal.* No. 1, Vol, 1, pp. 16-26.

Muhs, H. (1965). On the phenomenon of progressive rupture in connection with the failure behaviour of footings in sand. Discussion, *Proc. 6th ICSM&FE,* Montreal, Canada, Vol. 3, pp. 419-421.

Nayak, G. C. & Zienkiewicz, O. C. (1972). Elastoplastic stress analysis, a generalization for various constitutive relations including strain softening. *Int. Journ. Numerical Method in Eng.* **5** , pp. 113-135.

Norris, G. M. (1977). *The drained shear strength of uniform quartz sand as related to particle size and natural variation in particle shape and surface roughness.* **PhD** thesis, University of California, Berkeley.

Ovesen, N. K. (1975). Centrifuge testing applied to bearing capacity problems of footings on sand. *Geotechnique* **25** , No 2, pp. 394-401.

Palmer, A. C. & Rice, J. R. (1973). The growth of slip surfaces in the progressive failure of over-consolidated clay. *Proc. Roy. Soc. London.* A332, pp.527-548.

Parry, R. H. G. (1960). Triaxial compression and extension tests on remoulded saturated clay. *Geotechnique* **10** , pp. 166-180.

Poulos, H. G. & Davis, E. H. (1974). *Elastic solutions for soil and rock mechanics.* Wiley, New York.

Prandtl, L. (1920). Uberdie harte plastischer korper. (On the hardness of plastic bodies). *Nachr. Kgl. Ges. Wiss. Gottingen, Math.-Phys. Klasse,* pp. 74-85.

Prevost, J. H. & Hoeg, K. (1975). Soil mechanics and plasticity analysis of strain softening. *Geotechnique* **25** , No. 2, pp. 279-297.

Reissner, H. (1924). Zum Erddruckproblem. In *Proc. 1st Int. Cong. Applied Mech.,* Delft, pp. 295-311.

Rittenhouse, G. (1943). Avisual method of estimating two dimensional sphericity . *J. Sedimentary Petrology,* Vol. 13, No. 2, pp. 79-81.

Roscoe, K. H., Schofield, A. N. & Wroth, C. P. (1958). On the yielding of soils. *Geotechnique* **8** , pp. 22-53.

Roscoe, K. H., Schofield, A. N. & Thurairajah, A. (1963). An evaluation of test data for selecting a yield criterion for soils. *Laboratory shear testing of soils,* ASTM STP 361.

Scarpelli, G. & Wood, D. M. (1982). Experimental observations of shear band patterns in direct shear tests. **IUTAM** *Conf. on Deformation and Failure of Granular Materials,* Delft, pp. 473-483.

Schofield, A. N. (1980). Cambridge geotechnical operations. *Geotechnique* **30** , No. 3, pp. 227-268.

Schofield, A. N. & Wroth, C. P. (1968). *Critical state soil mechanics* , McGraw-Hill.

Shi, Q. (1988). *Centrifugal modelling of surface footings subjected to combined loading.* PhD thesis, Cambridge University.

Shield, R. T. (1955). On the plastic flow of metals under conditions of axial symmetry. *Proc. Roy. Soc. of London*, Vol. 233A, pp. 267-287.

Simpson, B. (1973). *Finite elements applied to problems of plane strain deformation of soils*. PhD thesis, Cambridge University.

Skempton , A. W. (1954). The pore-pressure coefficients A and B. *Geotechnique* **4** , pp. 143-147.

Sloan, S. W. & Randolph, M. F. (1982). Numerical prediction of collapse loads using finite element methods, *Int. J. Num. Anal. Meth. Geomech.*, **6** , pp. 47-76.

Sokolovski, V. V. (1942/1960). *Statics of soil media*. Butterworths, London (translated into English from Russian).

Taylor, R. N. (1982). Not the Schofield model, in *Proc. of workshop on the implementation of critical state soil mechanics in finite element computations*, Cambridge University.

Terzaghi, K. (1943). *Theoretical soil mechanics*. John Wiley & Sons, New York.

Vesic, A. S. (1963). Bearing capacity of deep foundations in sand. *Highway Research Record,* **39** National Academy of Sciences, pp. 112-153.

Vesic, A. S. (1969). Effects of scale and compressibility on bearing capacity of surface foundations. Discussion, *Proc. 7th ICSMFE Mexico City* , Vol. III, pp. 270-272.

Vesic, A. S. (1970). Bearing capacity of shallow foundations. In *Foundation Engineering Handbook,* Ch. 3, Ed. Winterkorn, H. F. & Fang, H. Y. Van Nostrand Reinford Company, pp. 127.

Vesic, A. S. (1973). Analysis of ultimate loads of shallow foundations. *Journ.* ASCE, Vol. 99, No. SM1.

Vesic, A. S. & Clough, G. W. (1968). Behaviour of granular materials under high stresses. *Proc. Am. Soc. Civil Eng.* **94** , SM3, pp. 661-688.

Wadell, H. (1933). Sphericity and roundness of rock particles. *Journ. of Geology,* Vol. 41, pp. 310-331.

White, T. P. (1987). *Finite element calculations involving the yielding of dilatant soils.* **MPhil** thesis, Cambridge University.

Wroth, C. P., Randolph, M. F., Houlsby, G. T. & Fahey, M. (1979). *A review of the engineering properties of soils with particuler reference to the shear modulus.* CUED/D-SOILS TR75.

Yamaguchi, H., Kimura, T. & Fuji-i, N. (1976). On the influence of progressive failure on the bearing capacity of shallow foundations in dense sand. *Soils and Foundations,* Japan, Vol. 16, No. 4, pp.11-22.

Yamaguchi, H., Kimura, T. & Fuji-i, N. (1977). On the scale effect of footings in dense sand. *Proc. 9th ICSMFE,* Vol. 1, Tokyo, pp. 759-798.

Zelikson, A. (1969). Geotechnical models using the hydraulic gradient similarity method. *Geotechnique* **19,** No. 4, pp. 495-508.

Zytynski, M. (1976). *First year research report.* Cambridge University Engineering Department.

Zienkiewicz, O. C. (1977). *The finite element method,* 3rd edition, McGraw-Hill.

Szczepiński, W. (1974). Stany graniczne i kinematyka ośrodków sypkich. Polska Akademia Nauk Instytut Podstawowych Problemów Techniki. p. 207.

Table 2.1 Properties of the two granular materials

	Silt	Sand
Mineralogical make-up	>99% SiO_2	>97% SiO_2
G_s	2.65	2.65
Roundness **R**	0.40	0.41
Sphericity **S**	0.80	0.77
d_{50}	12μm	600μm
k	3×10^{-7}m/s	1.7×10^{-3}m/s
ϕ_{crit}	37.5°	37.5°

Table 2.2 Void ratio variation
in a silt model

Triaxial specimen	location	void ratio
FHP1	T1	0.62
−	T2	0.55
FHP4	T3	−
−	T4	0.56
FHP5	T5	−
−	T6	0.58
FHP2	T7	0.61
FPM1	T8	0.62
FHP3	T9	0.61
FLP2	B1	0.59
−	B2	0.59
−	B3	0.61
FLP6	B4	0.58
FLP3	B5	0.60
FLP4	B6	0.59
FLP5	B7	0.59
−	B8	0.57
FLP1	B9	0.59

Table 2.3 Summary of laboratory tests

Sand

rig	test	e	σ_r	cond.	B	p_{max}	q_{max}	s_{max}	ϕ_{max}	$(^{d\varepsilon_v}/_{\varepsilon_1})_{max}$
low	GLP9	0.58	10	dry	-	30	66	41	53.7	1.00
low	GLP8	0.60	30	dry	-	99	203	132	50.0	0.88
low	GLP10	0.61	75	dry	-	215	411	283	46.4	0.84
med.	GLP4	0.59	30	sat.	0.97	109	227	147	50.2	0.83
med.	GLP5	0.60	100	sat.	0.95	308	613	410	48.4	0.79
med.	GLP2B	0.57	250	sat.	1.00	707	1362	934	46.8	0.61
high	GHP3	0.58	750	sat.	0.92	1835	3254	2377	43.2	0.37
high	GHP4	0.58	2150	sat.	0.93	4673	7540	5930	39.5	0.11
high	GHP6	0.56	4510	sat.	0.96	8996	13459	11240	36.8	-0.04
high	GHP8	0.60	10020	sat.	1.00	18772	26257	23149	34.6	-
high	GHP5	0.56	-	sat.	0.94	Isotropic compression only				
-	GMP1	0.61	-	sat.	-	Permeameter, $k=1.7 \times 10^{-3}$ m/s				

Silt

rig	test	e	σ_r	cond.	B	p_{max}	q_{max}	s_{max}	ϕ_{max}	$(^{d\varepsilon_v}/_{\varepsilon_1})_{max}$
med.	FLP1	0.59	30	sat.	0.94	147	335	186	55.8	1.92
med.	FLP2	0.59	100	sat.	0.90	345	714	464	50.1	1.19
med.	FLP3	0.60	100	sat.	0.84	402	884	549	53.5	1.33
med.	FLP5	0.59	200	sat.	0.73	669	1390	901	50.4	1.10
high	FHP3	0.61	750	sat.	0.63	2190	4319	2910	47.9	1.03
high	FHP1	0.62	2150	sat.	0.55	5386	9709	7015	43.7	0.66
high	FHP2	0.61	4500	sat.	0.65	10035	16606	12793	40.4	0.44
high	FHP5	-	10000	sat.	0.90	20228	30684	25412	37.1	0.18
high	FPM1	0.62	-	sat.	0.60	Permeameter, $k=3.0 \times 10^{-7}$ m/s				

Table 2.4 Summary of elastic properties obtained from triaxial tests

Sand

test	σ_r	p_{mean}	G	K	E	ν
GLP2B	250	433	78125	76987	175000	0.12
GHP3	750	1000	153689	222222	375000	0.22
GHP4	2150	3150	317460	560000	800000	0.26
GHP6	4500	6000	516796	1066667	1333333	0.29
GHP8	10700	13367	713013	2376296	1939394	0.36

Silt

test	σ_r	p_{mean}	G	K	E	ν
FLP5	200	367	77882	65244	166667	0.07
FHP3	750	1417	186473	222222	436364	0.17
FHP1	2150	3843	350000	589630	875000	0.25
FHP2	4500	7000	473485	1185185	1250000	0.32
FHP5	10000	14667	829630	2429689	2240000	0.35

Table 3.1
Summary of some complete solutions in the literature

Plane strain	Axisymmetric strain
Prandtl (1920) $\phi=0$ $c\neq0$	Shield (1955) $\phi=0$ $c\neq0$
Prandtl (1920) Bishop (1953) $\phi\neq0$ $c=0$ $\gamma=0$	Cox et al (1961) $\phi=20°$ $c=0$ $\gamma=0$

Table 3.2 Bearing capacity factors

	N_q		$N_{\gamma, smooth}$		$N_{\gamma, rough}$	
ϕ	PS	AX	PS	AX	PS	AX
5	1.57	1.65	0.09	0.06	0.62	0.68
10	2.47	2.80	0.29	0.21	1.71	1.37
15	3.94	4.70	0.71	0.60	3.17	2.83
20	6.40	8.30	1.60	1.30	5.97	6.04
25	10.66	15.20	3.51	3.00	11.61	13.46
30	18.40	29.50	7.74	7.10	23.59	31.94
31	20.63	34.00	9.10	8.60	27.36	38.32
32	23.18	39.00	10.72	10.30	31.83	46.14
33	26.09	45.00	12.65	12.40	37.14	55.72
34	29.44	52.20	14.97	15.20	43.45	67.62
35	33.29	61.00	17.76	18.20	51.01	82.42
36	37.75	71.30	21.12	22.00	60.09	100.79
37	42.91	82.80	25.23	26.90	70.95	123.89
38	48.92	98.90	30.18	32.60	84.60	153.12
39	55.94	116.40	36.26	40.10	100.60	190.22
40	64.18	139.56	43.74	50.91	120.55	237.60
41	73.88	165.80	52.99	61.70	145.20	298.88
42	85.35	200.40	64.50	77.60	175.71	378.65
43	98.98	241.00	78.92	98.70	213.97	480.48
44	115.26	294.70	97.09	125.40	262.26	619.39
45	134.81	359.30	120.17	160.10	323.72	802.56
46	158.42	443.50	149.71	209.60	402.34	1051.77
47	187.11	550.00	187.77	271.50	504.79	1384.17
48	222.17	686.30	237.43	353.10	638.33	1847.26
49	265.33	864.30	302.36	475.80	815.32	2491.47
50	318.83	1103.30	389.25	621.10	1052.30	3403.38
51	385.69	1427.10	505.33	875.83	1372.52	4710.00
52	469.92	1853.70	662.89	1206.82	1812.31	6627.71
Col.1	2	3	4	5	6	7

Table 3.3 Size of plastic region

φ	R(N_q)		R($N_{\gamma, smooth}$)		R($N_{\gamma, rough}$)	
	PS	AX	PS	AX	PS	AX
5	2.25	1.71	1.16	1.11	2.45	1.90
10	2.57	1.88	1.35	1.24	2.90	2.20
15	2.99	2.09	1.58	1.40	3.50	2.59
20	3.53	2.37	1.90	1.62	4.30	3.09
25	4.26	2.73	2.32	1.90	5.31	3.75
30	5.29	3.21	2.89	2.26	6.70	4.65
31	5.54	3.32	3.03	2.36	7.08	4.86
32	5.81	3.45	3.18	2.45	7.45	5.10
33	6.11	3.59	3.34	2.55	7.85	5.33
34	6.43	3.74	3.50	2.66	8.25	5.60
35	6.77	3.88	3.70	2.78	8.70	5.90
36	7.14	4.05	3.90	2.90	9.20	6.20
37	7.55	4.22	4.15	3.03	9.75	6.50
38	8.00	4.42	4.37	3.18	10.38	6.86
39	8.48	4.62	4.64	3.33	10.95	7.25
40	9.00	4.86	4.90	3.50	11.80	7.70
41	9.60	5.10	5.20	3.69	12.50	8.15
42	10.24	5.37	5.53	3.85	13.38	8.74
43	10.95	5.67	5.90	4.10	14.30	9.30
44	11.74	6.00	6.30	4.34	15.30	9.80
45	12.61	6.35	6.80	4.60	16.50	10.56
46	13.59	6.73	7.30	4.87	17.60	11.30
47	14.68	7.15	7.82	5.20	19.20	12.00
48	15.91	7.65	8.48	5.55	20.70	13.00
49	17.29	8.22	9.11	5.93	22.50	13.90
50	18.86	8.80	9.96	6.37	24.50	15.00
51	20.65	9.49	10.80	6.83	26.80	16.20
52	22.68	10.28	11.80	7.38	29.40	17.70
Col. 1	2	3	4	5	6	7

Table 3.4
N_q at axisymmetric strain

φ	Calculated	Empirical
30	29.50	29.08
31	34.00	33.40
32	39.00	38.53
33	45.00	44.57
34	52.20	51.74
35	61.00	60.31
36	71.30	70.60
37	82.80	83.02
38	98.90	98.10
39	116.40	116.53
40	139.56	139.20
41	165.80	167.29
42	200.40	202.37
43	241.00	246.55
44	294.70	302.69
45	359.30	374.72
46	443.50	468.10
47	550.00	590.54
48	686.30	753.07
49	864.30	971.72
50	1103.30	1270.19
51	1427.10	1684.17
52	1853.70	2268.53

Table 4.1
Parameters used in subroutine CALPHI

	A	ϕ_{max}/degree	s_{max}/kPa	s_{min}/kPa	ϕ_{min}/degree
Silt	3	57.5	130000	50	34
Sand	3	57.5	100000	10	30

Table 4.2
Comparison between solutions by EXPRAN and VARIPHI for N_q at plane strain

	Sand				Silt			
	EXPRAN		VARIPHI		EXPRAN		VARIPHI	
σ_o	N_q	ϕ_{av}	N_q	ϕ_{av}	N_q	ϕ_{av}	N_q	ϕ_{av}
5	290.3	49.5	288.3	49.4	555.2	52.8	538.2	52.6
10	220.6	48.0	218.8	47.9	423.4	51.4	420.1	51.4
25	155.0	45.9	154.3	45.8	288.3	49.4	286.7	49.4
50	120.5	44.3	119.8	44.2	219.1	47.9	217.6	47.9
100	94.4	42.7	93.8	42.6	167.9	46.3	166.9	46.3
200	74.2	41.0	74.0	41.0	129.8	44.7	129.2	44.7
Col.1	2	3	4	5	6	7	8	9

Table 4.3   1-g tests prediction

σ_o	Sand			Silt		
	R	N_q	ϕ_f	R	N_q	ϕ_f
5	6.43	629.70	47.60	7.74	1323.70	50.70
10	5.90	458.40	46.10	7.12	977.80	49.50
25	5.30	305.80	44.20	6.41	626.90	47.60
50	4.92	227.40	42.70	5.90	454.70	46.10
100	4.57	171.10	41.20	5.44	334.30	44.60
200	4.26	129.90	39.60	5.03	248.40	43.10

Table 4.4a
Centrifuge test predictions for sand

Sand, $N_{\gamma, rough}$, AX

B/m	R	α	δ	$\phi_{@tip}$	N_γ	ϕ_{av}
0.40	10.70	64.00	38.00	38.07	711.5	44.5
0.90	9.74	63.50	37.00	37.03	480.3	43.0
1.42	9.15	63.25	36.50	36.34	385.2	42.1
3.00	8.44	62.75	35.50	35.28	267.8	40.5
5.00	7.90	62.25	34.50	34.52	206.6	39.3
10.00	7.28	61.75	33.50	33.45	148.7	37.8

Table 4.4b
Centrifuge test predictions for silt

Silt, $N_{\gamma, rough}$, AX

B/m	R	α	δ	$\phi_{@tip}$	N_γ	ϕ_{av}
0.40	12.77	65.25	40.50	40.38	1577.3	47.4
0.90	11.65	64.50	39.00	39.24	1037.8	45.9
1.42	11.10	64.25	38.50	38.54	837.1	45.1
3.00	10.20	63.75	37.50	37.54	581.3	43.7
5.00	9.63	63.50	37.00	36.89	456.4	42.8
10.00	8.84	63.00	36.00	35.87	323.6	41.3

Table 5.1 Soil parameters used in CRISP

	Sand	Silt
G	$1400p^{0.667}$ kPa	
M	1.53	
$S_H(\phi_H)$	1.4(34.6°)	
P_c	21750 kPa	51650 kPa
K_o	0.39	
e_{cs}	0.80	
ϕ_{crit}	37.5°	
ϕ_{max}	55.0°	
λ	0.029	
κ	0.008	
ρ	2.0×10^{-2}, mN/mm^3	
S	2.25	

Table 5.2

Summary of normalized peak stresses from triaxial tests

Sand

Test	P_e	P_{max}/P_e	q_{max}/P_e
GLP9	2040	0.015	0.032
GLP8	2880	0.034	0.070
GLP10	4065	0.053	0.101
GLP4	4065	0.027	0.056
GLP5	5740	0.054	0.107
GLP2B	8102	0.087	0.168
GHP3	8102	0.226	0.402
GHP4	11440	0.408	0.659

Silt

Test	P_e	P_{max}/P_e	q_{max}/P_e
FLP1	8102	0.018	0.041
FLP2	11438	0.030	0.062
FLP3	11438	0.035	0.077
FLP5	16150	0.041	0.086
FHP3	16150	0.136	0.267
FHP1	24424	0.221	0.398
FHP2	29020	0.346	0.572

Table 5.3 Summary of CRISP analysis

CRISP1	Sand	smooth	triaxial	$\sigma_r = 750$ kPa	$e_{init} = 0.56$	$\varepsilon_a = 5\%$	180incr.
CRISP2	Silt	smooth	triaxial	$\sigma_r = 750$ kPa	$e_{init} = 0.54$	$\varepsilon_a = 5\%$	180incr.
CRISP3	Sand	rough	triaxial	$\sigma_r = 750$ kPa	$e_{init} = 0.56$	$\varepsilon_a = 5\%$	180incr.
CRISP4	Silt	rough	triaxial	$\sigma_r = 750$ kPa	$e_{init} = 0.54$	$\varepsilon_a = 5\%$	180incr.
CRISP5	Sand	rough	1-g model	$\sigma_o = 25$ kPa	$e_{init} = 0.59$	W/B=16%	480incr.
CRISP6	Silt	rough	1-g model	$\sigma_o = 25$ kPa	$e_{init} = 0.57$	W/B=15%	600incr.
CRISP7	Sand	rough	50-g model	$\sigma_o = 0$ kPa	$e_{init} = 0.60$	W/B=11%	440incr.
CRISP8	Silt	rough	50-g model	$\sigma_o = 0$ kPa	$e_{init} = 0.58$	W/B=10%	600incr.

Table 5.4

Intermediate stress parameter b and major principal stress direction ψ

point	b	ψ/degree	point	b	ψ/degree
CRISP5					
a1	0.00	-0.6	b1	0.00	-0.3
a2	-0.02	1.5	b2	0.00	1.9
a3	0.02	5.5	b3	0.04	26.7
a4	0.07	28.3	b4	0.05	31.5
a5	0.13	41.8	b5	0.12	61.1
a6	0.14	73.0	b6	0.06	68.0
a7	0.03	81.9	b7	0.07	80.3
a8	-0.15	93.3	b8	0.01	89.9
a9	-0.21	97.5	b9	-0.02	94.1
CRISP6					
a1	0.01	-4.1	b1	0.00	0.1
a2	-0.03	1.7	b2	0.00	2.0
a3	0.02	5.2	b3	0.03	27.5
a4	0.07	29.2	b4	0.05	32.9
a5	0.13	45.8	b5	0.01	60.1
a6	0.11	71.0	b6	0.02	68.1
a7	0.06	80.8	b7	0.04	80.6
a8	-0.06	84.6	b8	0.01	88.7
a9	-0.13	100.1	b9	0.03	94.0
CRISP7					
a1	0.00	-3.6	b1	0.00	0.1
a2	-0.02	1.4	b2	0.00	1.4
a3	0.02	2.8	b3	0.05	28.4
a4	0.08	28.9	b4	0.06	34.7
a5	0.22	49.8	b5	0.03	61.7
a6	0.09	74.2	b6	0.08	70.7
a7	-0.03	88.1	b7	0.05	81.8
a8	-0.13	92.6	b8	-0.02	87.8
a9	-0.24	93.3	b9	-0.05	91.1
CRISP8					
a1	0.00	-0.3	b1	0.00	0.3
a2	0.04	0.5	b2	0.00	1.7
a3	0.06	0.3	b3	0.04	26.1
a4	0.14	23.5	b4	0.06	32.6
a5	0.20	42.0	b5	0.00	59.2
a6	0.03	66.6	b6	0.02	68.3
a7	-0.03	86.0	b7	-0.01	80.8
a8	-0.10	101.2	b8	0.00	88.4
a9	-0.13	107.1	b9	-0.03	93.7

Table 6.1 Summary of the 1-g test programme

Material type	$d_{50}/\mu m$	B/d_{50} σ_o/kPa	24	167	1183	8333
Silt	12	5			sat. ⊓	sat. ▭
		10			sat. ⊓	sat. (lead thread) ▭
		25			sat. ⊓	sat. ▭
		50			sat. ⊓	
		100			sat. ⊓	
		200			sat. ⊓	
Sand	600	5	sat. ⊓	sat. (colour bands) ▭		
		10	dry ⊓	dry ▭		
		25	dry ⊓	dry/sat. ▭		
		50	dry ⊓	dry/sat. ▭		
		100	dry ⊓	dry ▭		
		200	dry ⊓	dry ▭		
		B/mm	14.2	100	14.2	100

Table 6.2 Particulars of 1-g tests

1GT no.	material	e	B/mm	σ_o/ kPa	condition/comments
4	silt	0.58	100	25	sat./volume change monitored
5	silt	0.63	14.2	100	sat.
6	silt	0.57	14.2	50	sat.
7	silt	0.56	14.2	25	sat.
8	silt	0.57	14.2	10	sat.
9	silt	0.55	14.2	200	sat.
11	silt	0.57	100	10	sat./lead thread(radiograph)
12	sand	0.58	14.2	50	dry
13	sand	0.58	14.2	25	dry
14	sand	0.58	14.2	10	dry
15	sand	0.58	14.2	100	dry
16	sand	0.58	14.2	200	dry
17	sand	0.58	100	25	dry/compare with 1GT25
18	sand	0.58	100	10	dry
19	sand	0.59	100	100	dry
20	sand	0.57	100	200	dry
21	sand	0.57	100	50	dry/compare with 1GT23
23	sand	0.58	100	50	sat./compare with 1GT21
24	sand	0.63	14.2	5	sat.
25	sand	0.64	100	25	sat./compare with 1GT17
26	sand	0.56	100	5	sat./sugar set(colour bands)
28	silt	0.58	14.2	5	sat.
29	silt	0.61	100	5	sat./loading rate too quick

Table 6.3 Calculated and experimental results of the 1-g tests

ϕ	N_q	σ_0/kPa				
		Sand $P_{crit} = 8000$ kPa			Silt $P_{crit} = 40000$ kPa	
		calc.	exp.		calc.	exp.
			B=100	B=14.2		B=14.2
35	61.0					
36	71.3					
37	82.8					
38	98.9					
39	116.4	200				
40	139.6			200		
41	165.8	100				200
42	200.4	50				
43	241.0		25	100	200	100
44	294.7	25		50	100	
45	359.3		10	25		50
46	443.5	10		10	50	25
47	550.0		5	5	25	10
48	686.3	5				
49	864.3				10	5
50	1103.3				5	
51	1427.1					
52	1853.7					
Col. 1	2	3	4	5	6	7

Table 6.4 Summary of results from the variable ϕ analysis at axisymmetric strain for weightless soil

σ_0	σ_f/kPa		$\phi_{average}$/degree		σ_w/kPa	
	sand	silt	sand	silt	sand	silt
5	3149	6619	47.6	50.7	270	480
10	4584	9778	46.1	49.5	450	700
25	7645	15673	44.2	47.6	850	1400
50	11370	22735	42.7	46.1	1400	2200
100	17110	33430	41.2	44.6	2300	3700
200	25980	49680	39.6	43.1	3900	6000

Graphical presentation of Table 6.3
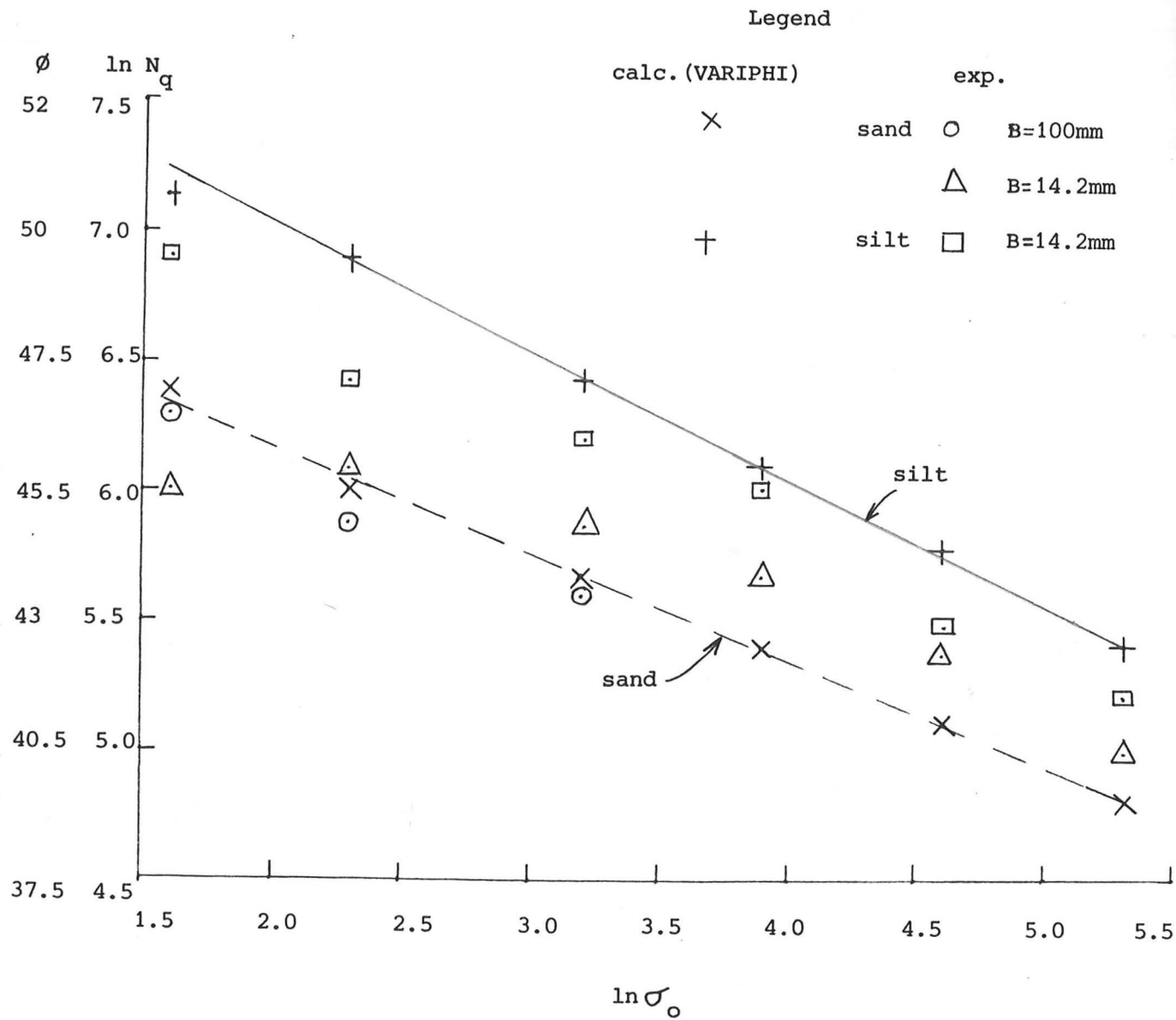
Table 7.1 Summary of the centrifuge test programme
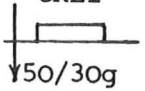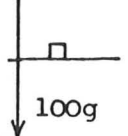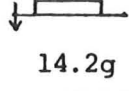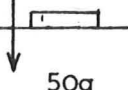
Material type	$d_{50}/\mu m$	B/d$_{50}$ nB/mm	166.7	1183.3	8333.3
Silt	12	5000 & 3000			B=100mm e=0.63 CKL1 ↓50/30g
		1420		B=14.2mm e=0.61 CKL4 100g	B=100mm e=0.57 CKL3 (lead thread) 14.2g
Sand	600	5000	B=100mm e=0.61 (sugar/colour bands) CKL2 50g		

Table 7.2 Calculated and experimental results of the centrifuge tests

		B/m			
		Sand		Silt	
		P_{crit}=8000 kPa		P_{crit}=40000 kPa	
ϕ	$N_{\gamma,rough}$	Calc.	Exp.	Calc.	Exp.
35	82.4				
36	100.8				
37	123.9				
38	153.1	10.00			
39	190.2	5.00			
40	237.6		5.00		
41	298.9	3.00			
42	378.7	1.42		10.00	5.00
43	480.5	0.90		5.00	3.00
44	619.4			3.00	
45	802.6	0.40		1.42	
46	1051.8			0.90	1.42
47	1384.2			0.40	
48	1847.3				
49	2491.5				
50	3403.4				
Col. 1	2	3	4	5	6

Table 7.3 Summary of results for shallow foundations from the variable ϕ analysis at axisymmetric strain

B/m	σ_f/ kPa		$\phi_{average}$/degree		σ_w/ kPa	
	sand	silt	sand	silt	sand	silt
0.40	1423	3155	44.5	47.4	760	1500
0.90	2161	4670	43.0	45.9	1250	2400
1.42	2735	5943	42.1	45.1	1700	3100
3.00	4017	8720	40.5	43.7	2900	5000
5.00	5165	11410	39.3	42.8	4200	6900
10.00	7435	16180	37.8	41.3	7200	11000
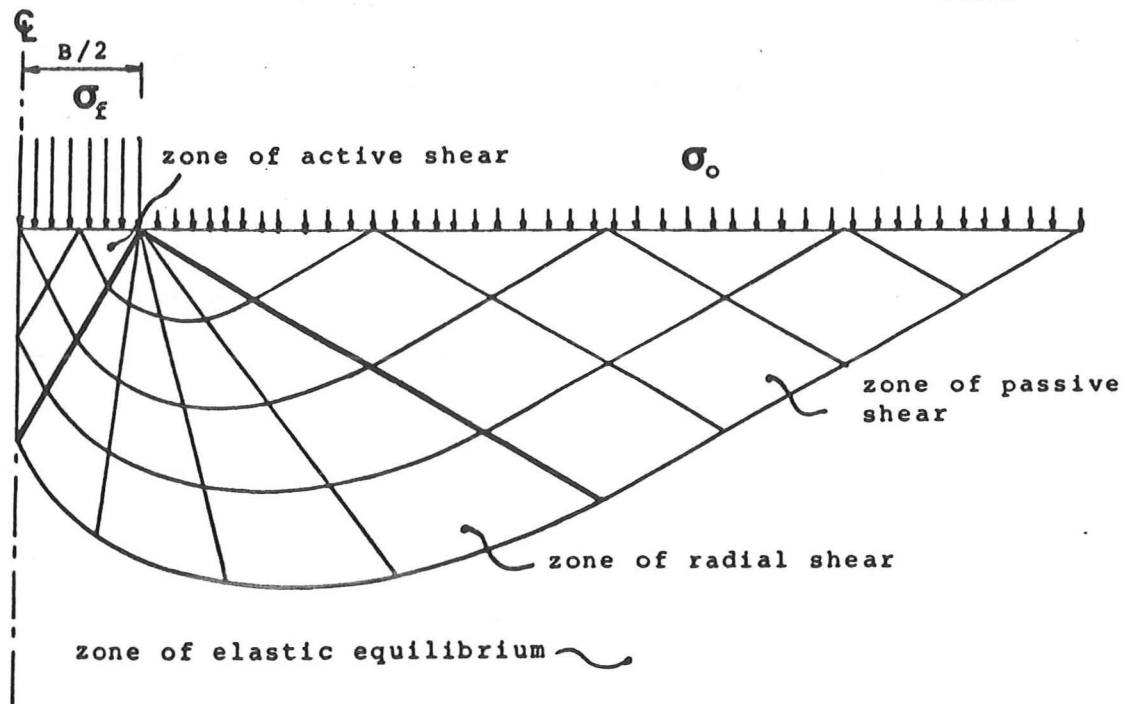
Fig 1.1   Slip line field of a semi-infinite weightless
Mohr-Coulomb material under a strip footing
(After Prandtl, 1920)
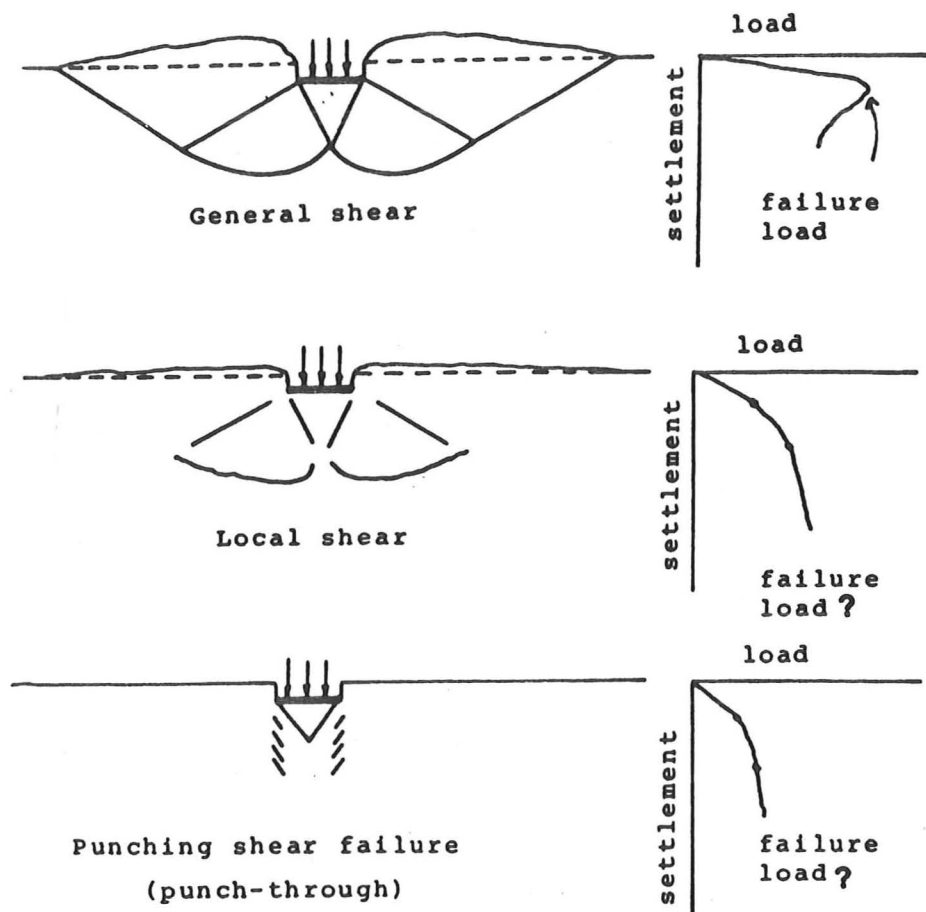
Fig 1.2   Modes of failure mechanism (After Vesic, 1963)
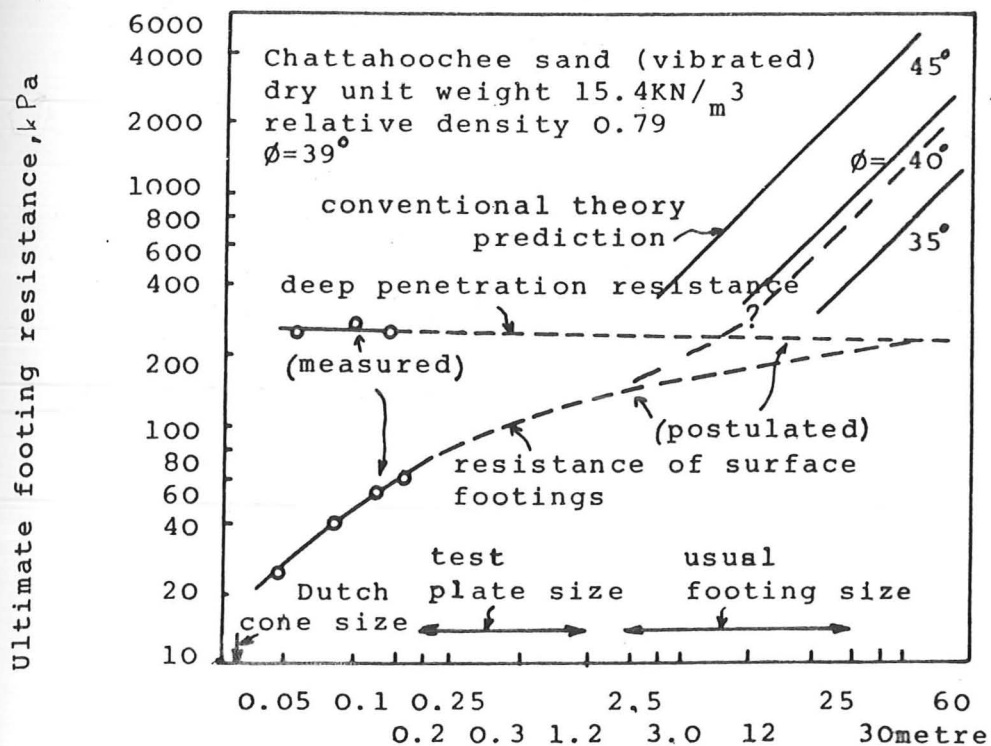
Fig 1.3   Variation of ultimate resistance of circular
           footings with diameter (After Vesic, 1969)
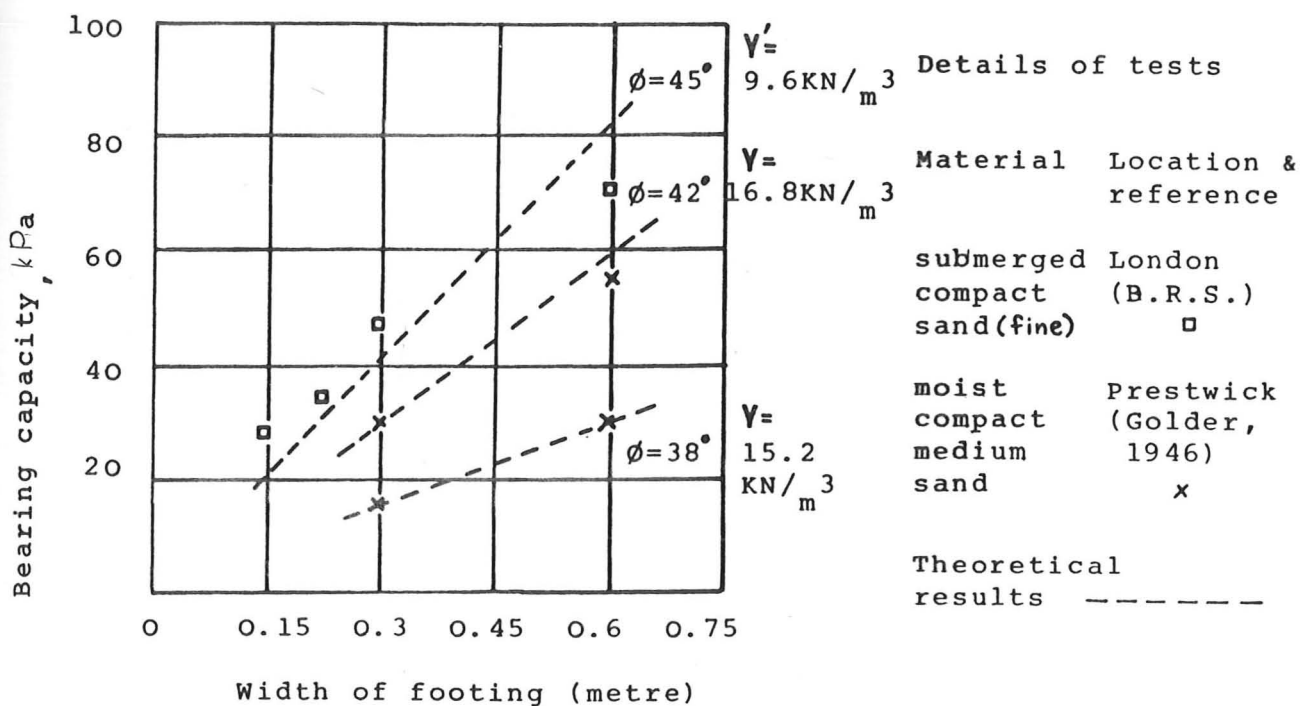
Fig 1.4   Results of field loading tests on footings in sand
           (After Meyerhof, 1951)
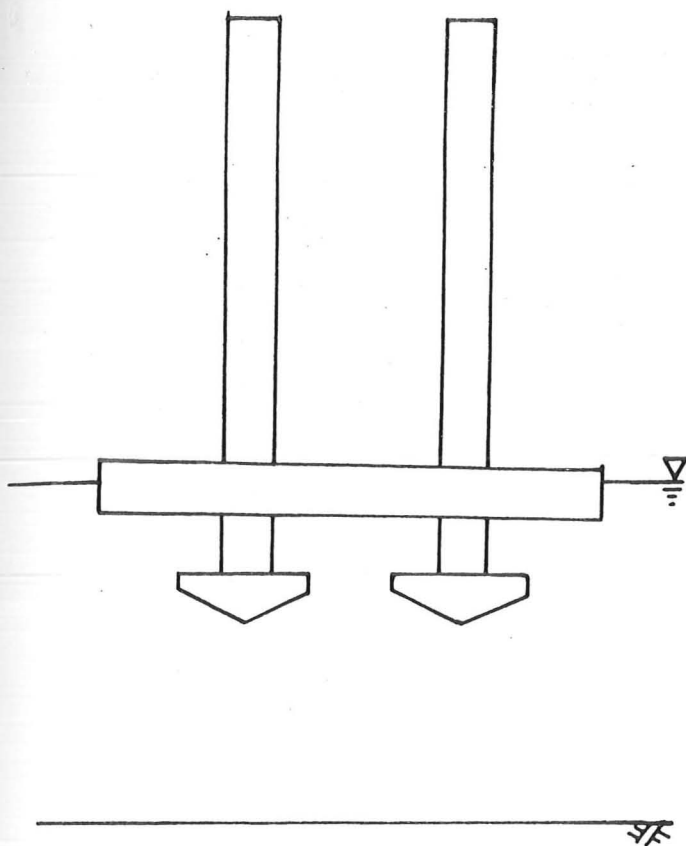
(a) During transportation
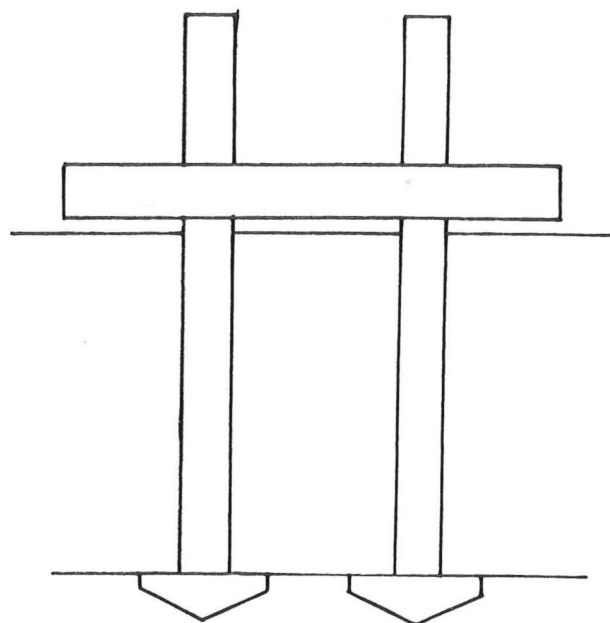
(b) During jack-up with
    pre-loading

wind $\longrightarrow$

wave $\longrightarrow$

current $\longrightarrow$

platform
(hull)

leg
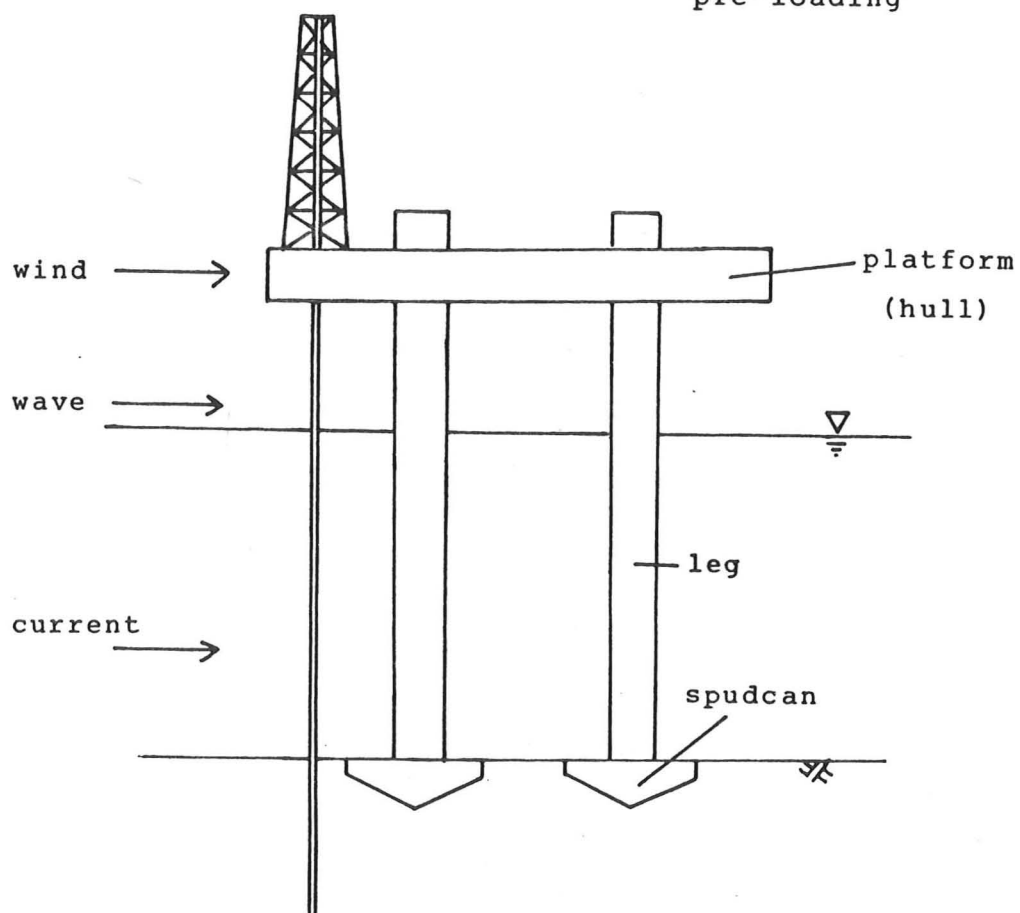
spudcan

(c) Under normal working conditions

Fig 1.5   A typical oil-rig with jack-up spudcans
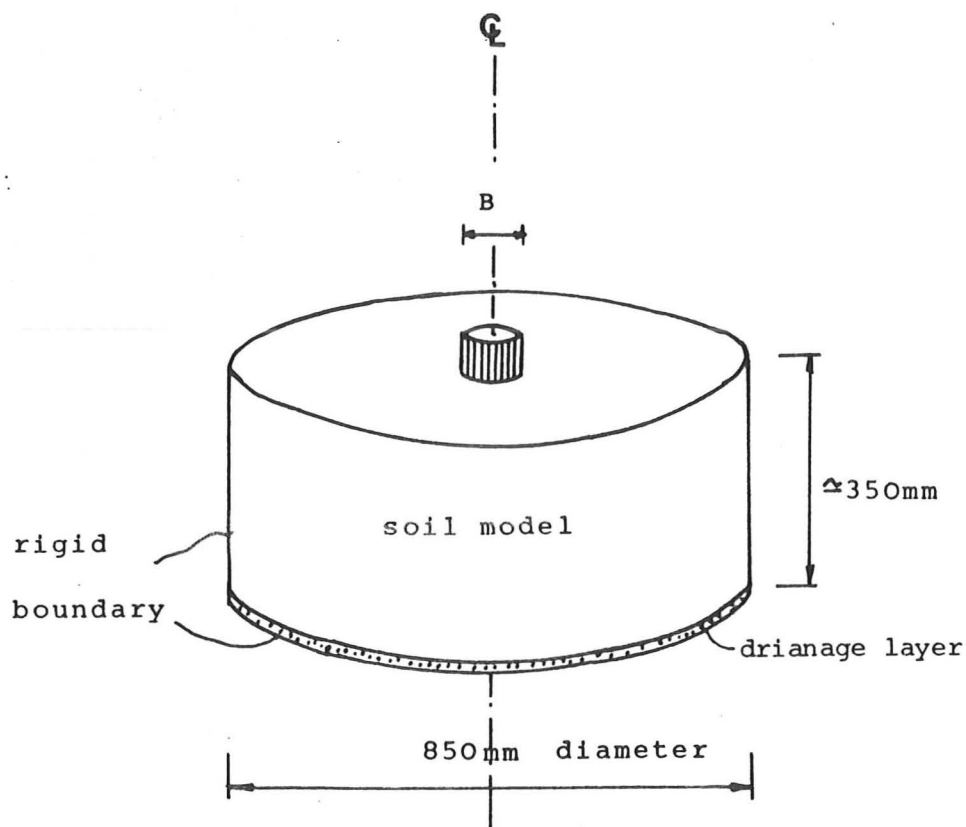
Rigid punch indentation problem
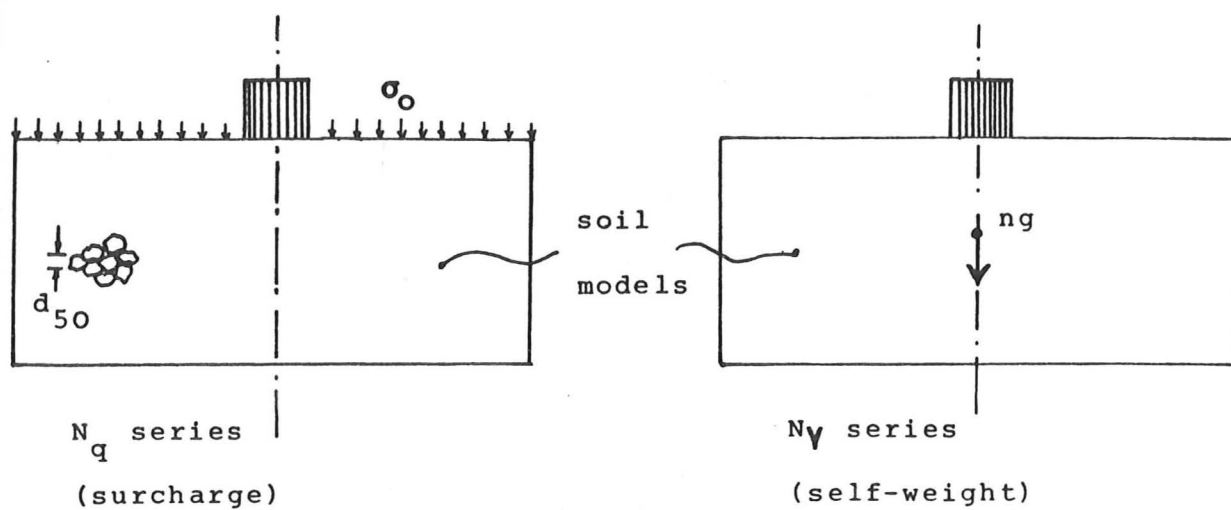
Fig 1.6   Schematic layout of tests on footings
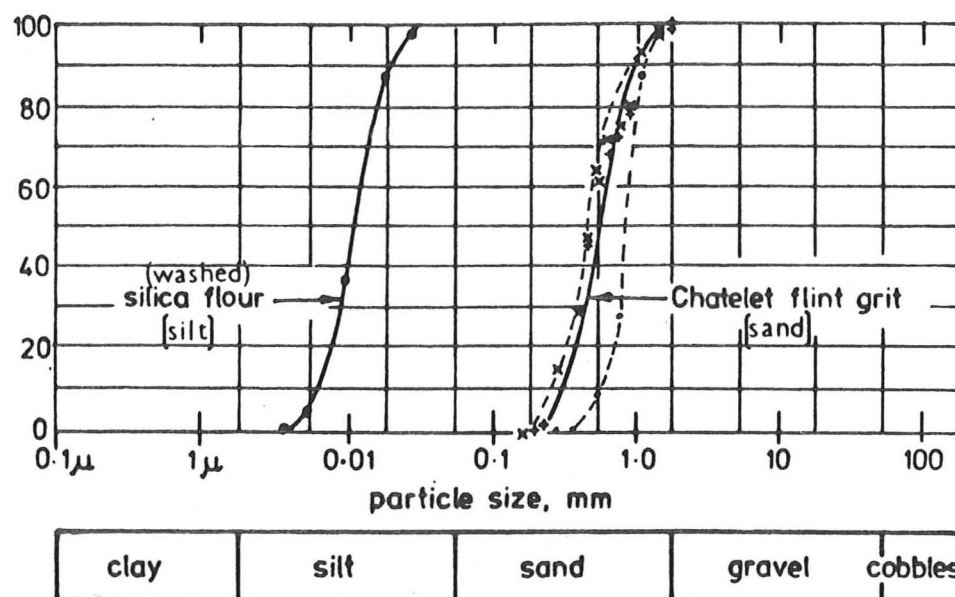
Fig 2.1 Grading curves of the two granular materials
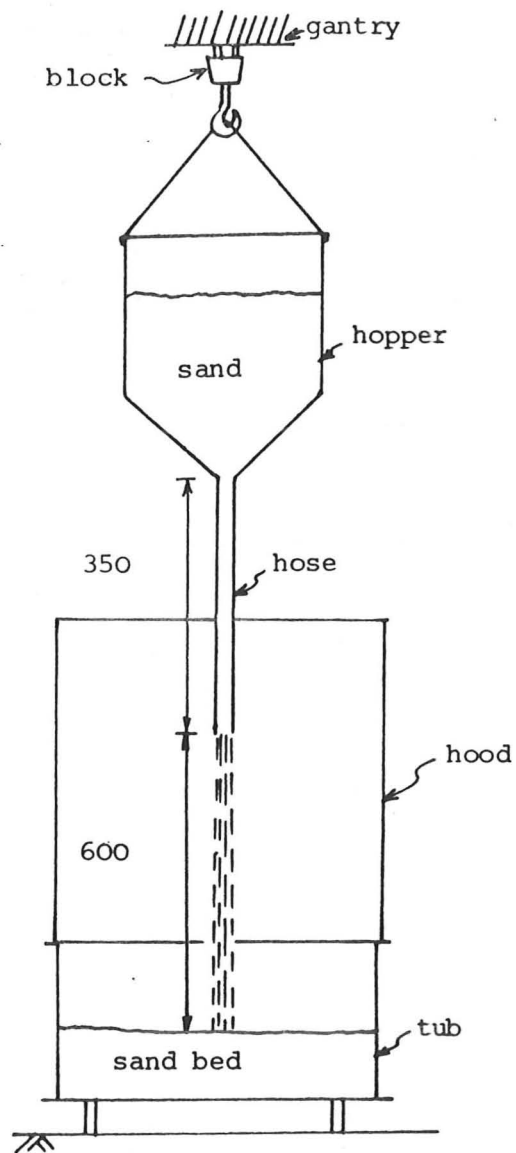
Fig 2.2   Model preparation of sand bed by pluviation
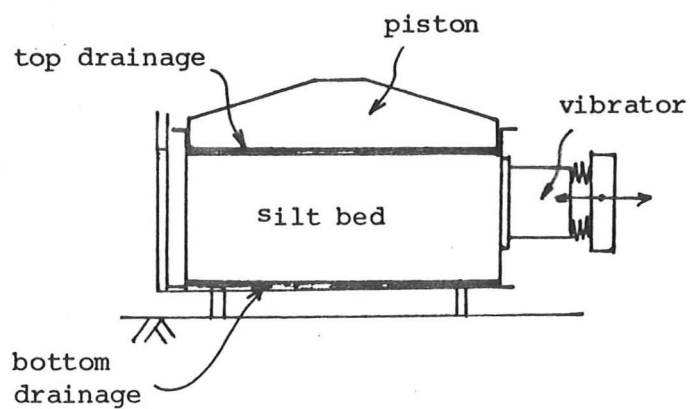
Fig 2.3   Model preparation of silt bed by vibration

constant head
overflow

$\bar{h}$

measuring
cylinder

H=95mm

soil
sample

confining tube
internal area
4754 mm^2

porous material

de-aired
water
supply

flow control
valve
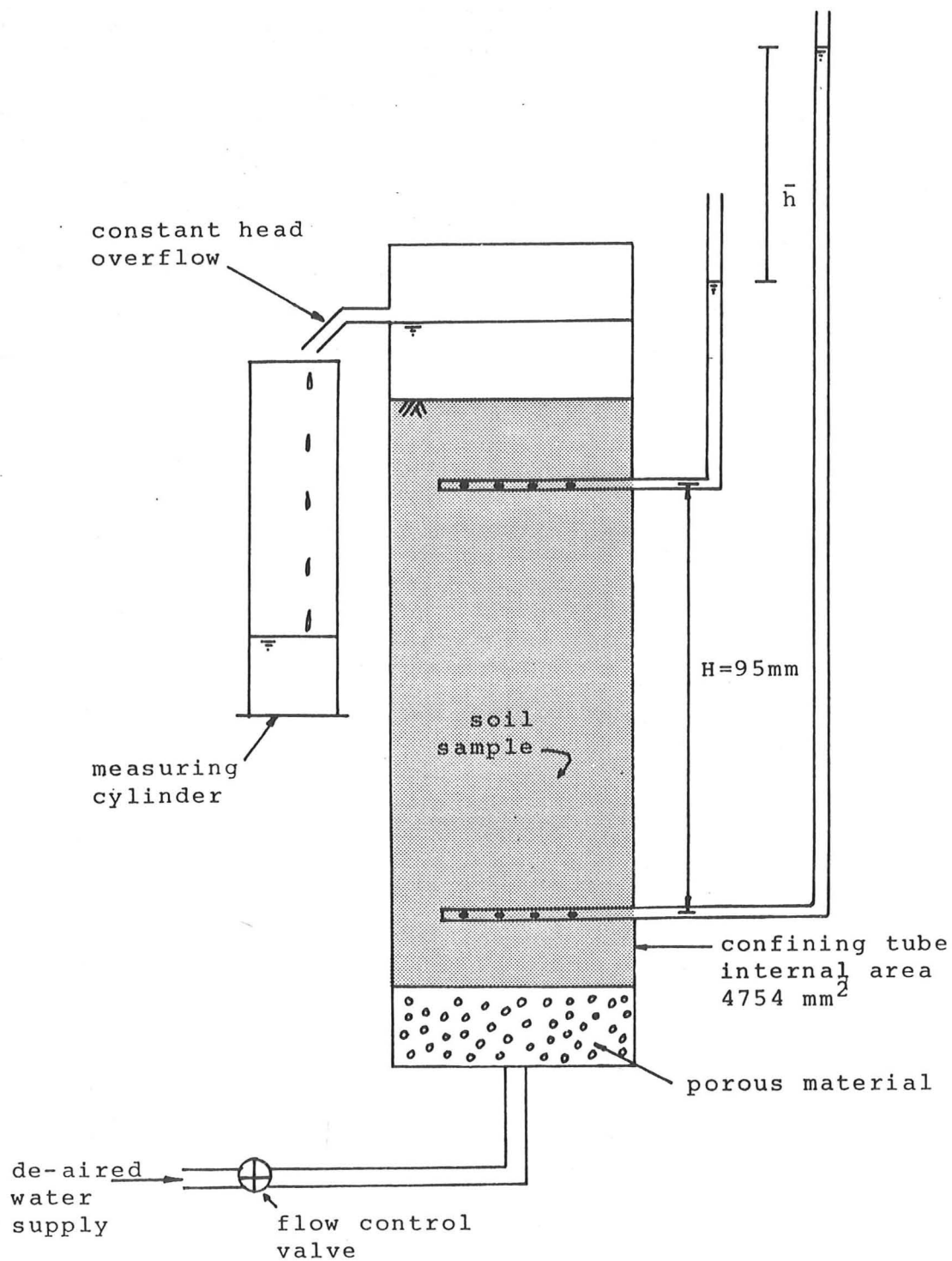
Fig 2.4 Constant head permeameter for sand
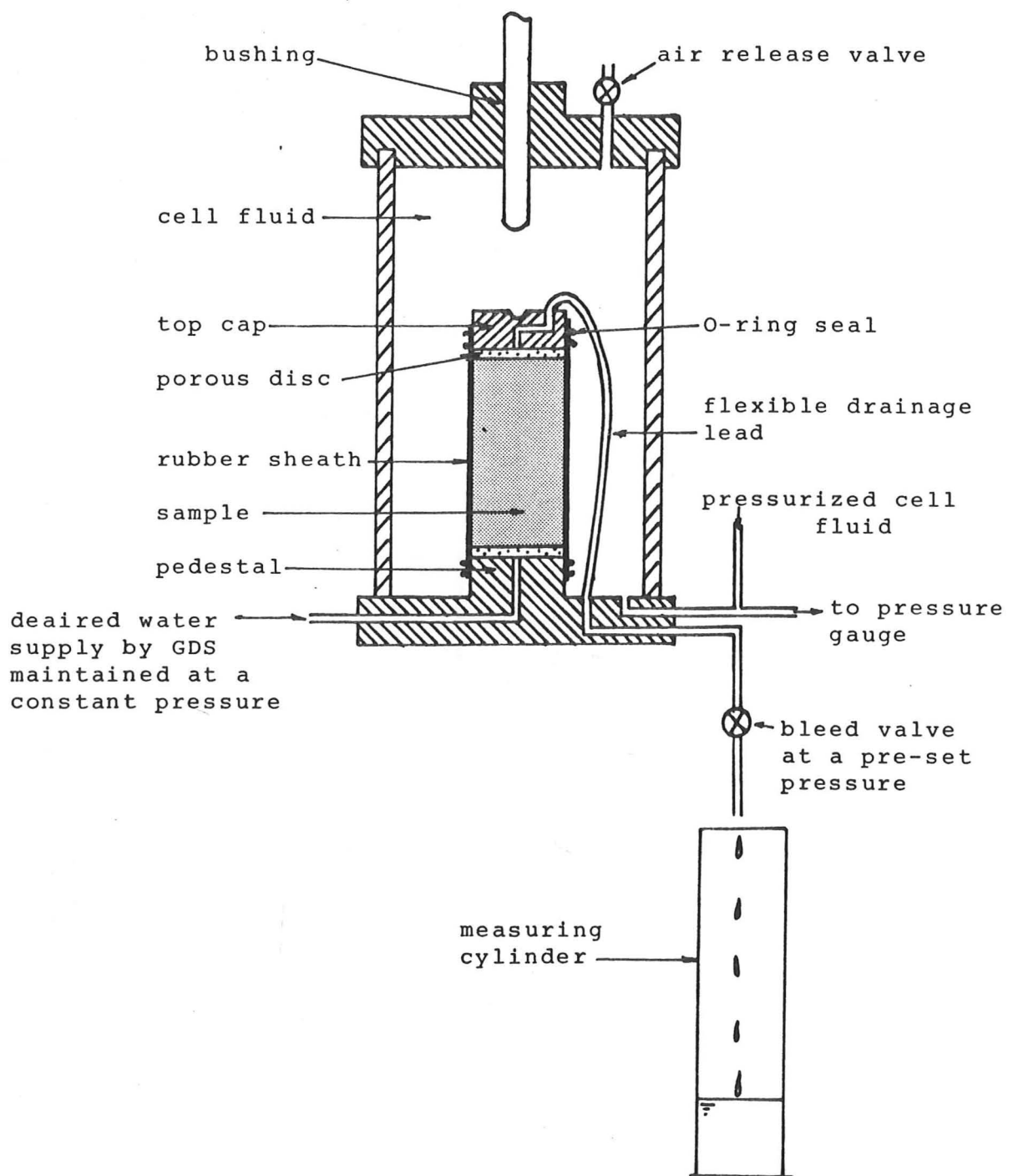
Fig 2.5   Triaxial test equipment modified as a constant
head permeameter for silt
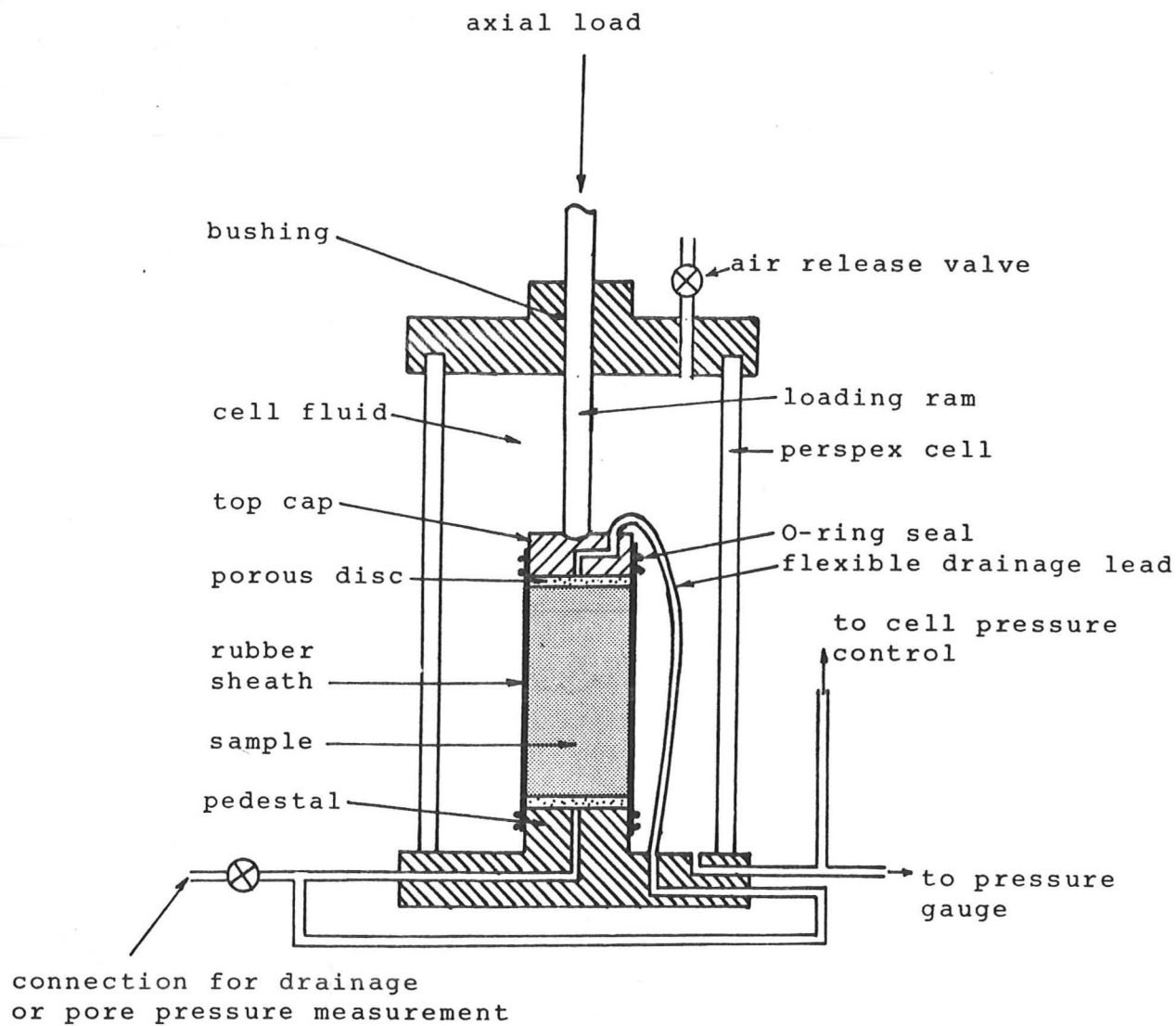
Fig 2.6 Schematic layout of a typical triaxial test rig
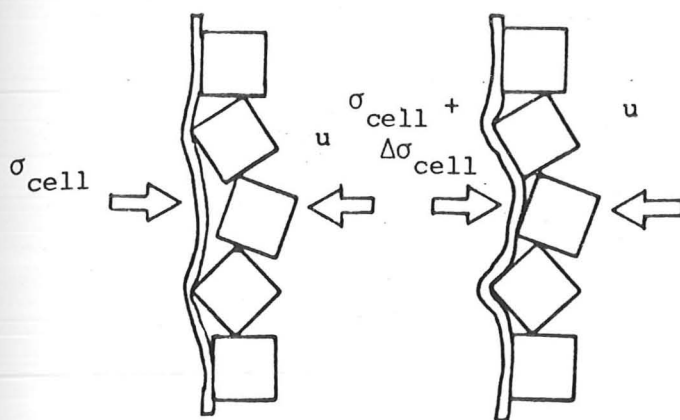
Fig 2.7 Membrane penetration due to change in effective cell pressure

$\Delta V = 3\Delta\varepsilon_a$
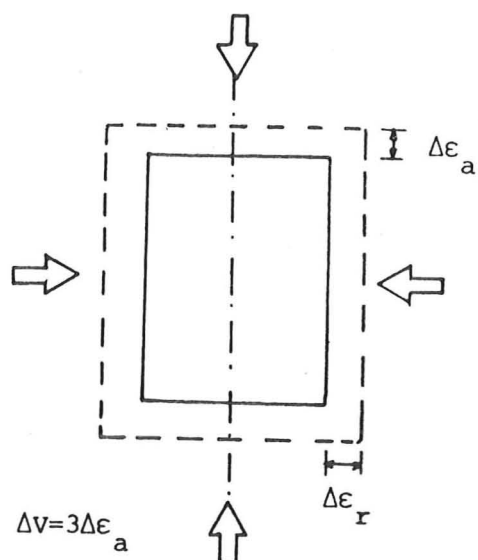
Fig 2.8 Strain increment of triaxial specimen under isotropic compression
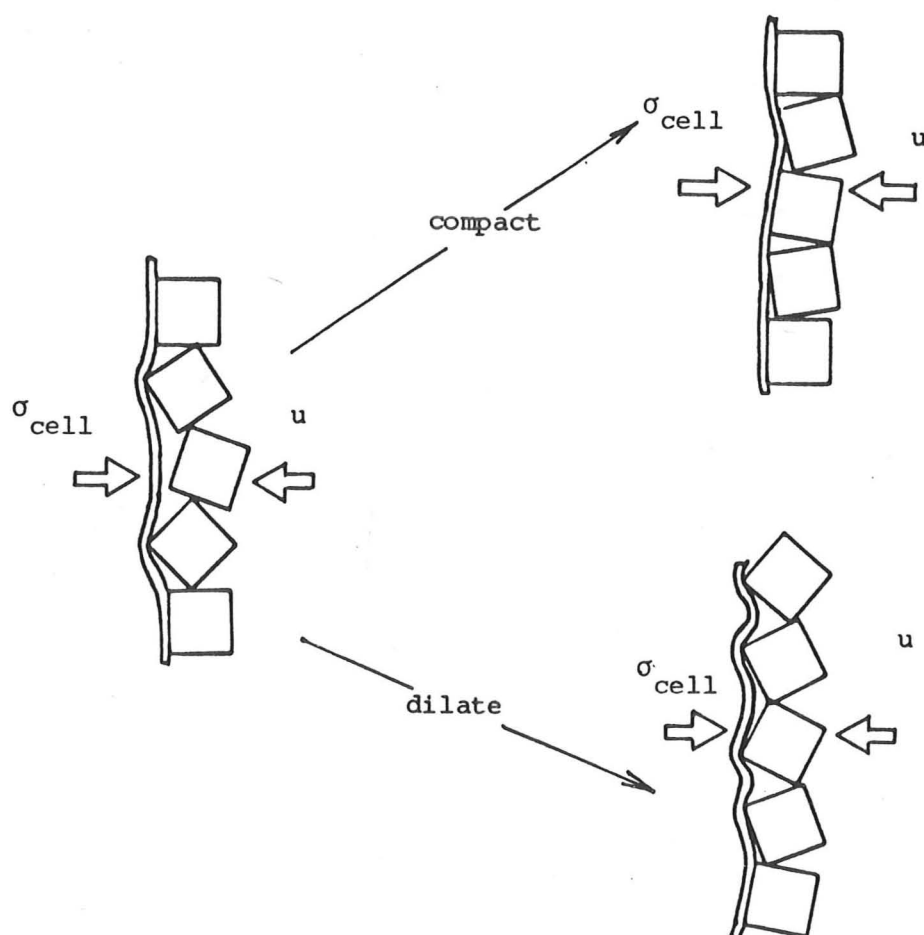
Fig 2.9 Membrane penetration due to change in soil fabric and surface texture of specimen

fixed beam

mechanical load cell

dial gauge

bushing

loading ram

loading cap

O-ring seal

manometer

$\bar{h}$

rubber sheath

sample

mercury

pedestal

to suction pump

vacuum control valve

manual axial drive unit

N.B. Note the absence of cell
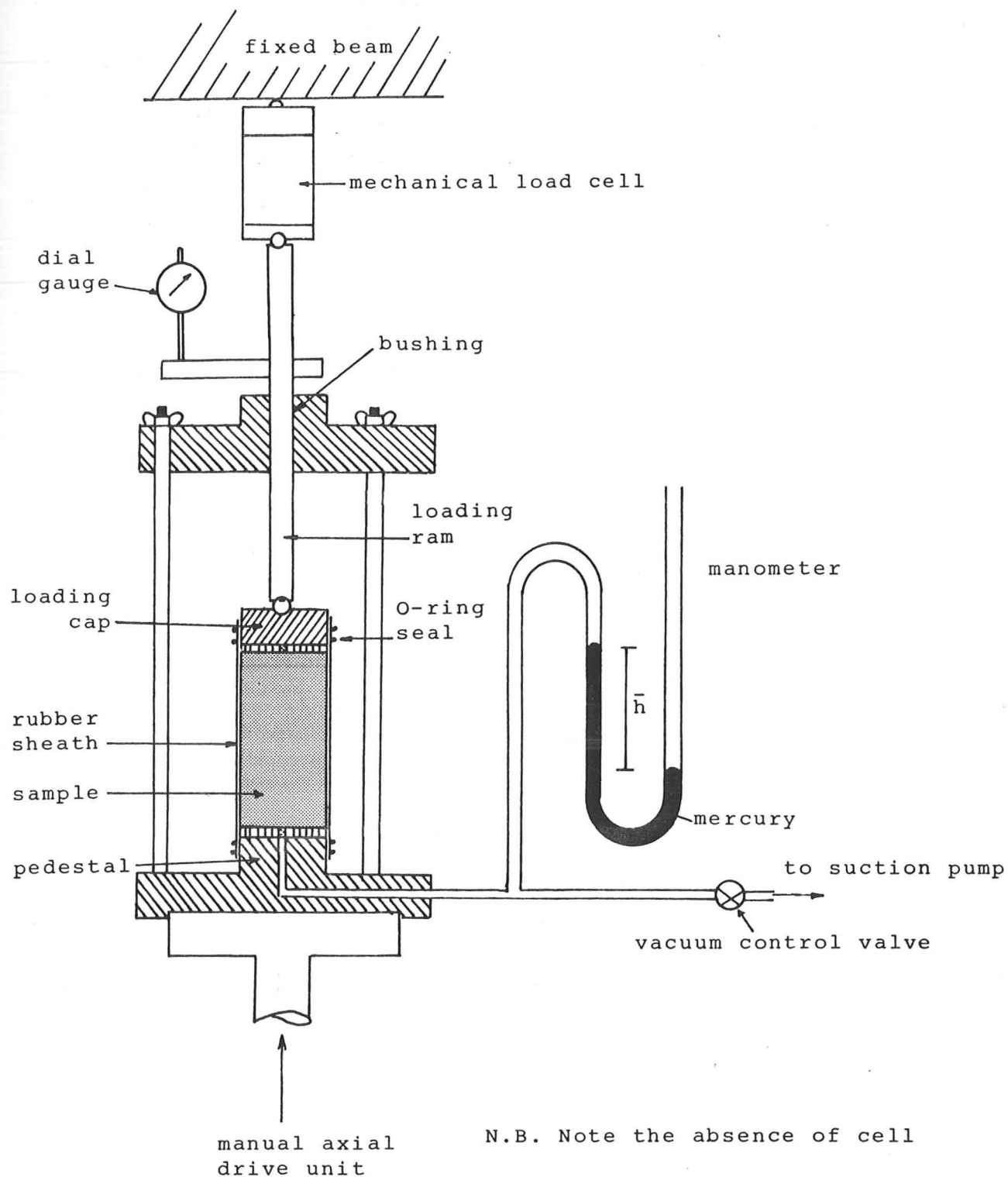
Fig 2.10 Schematic layout of the triaxial set-up at low pressure
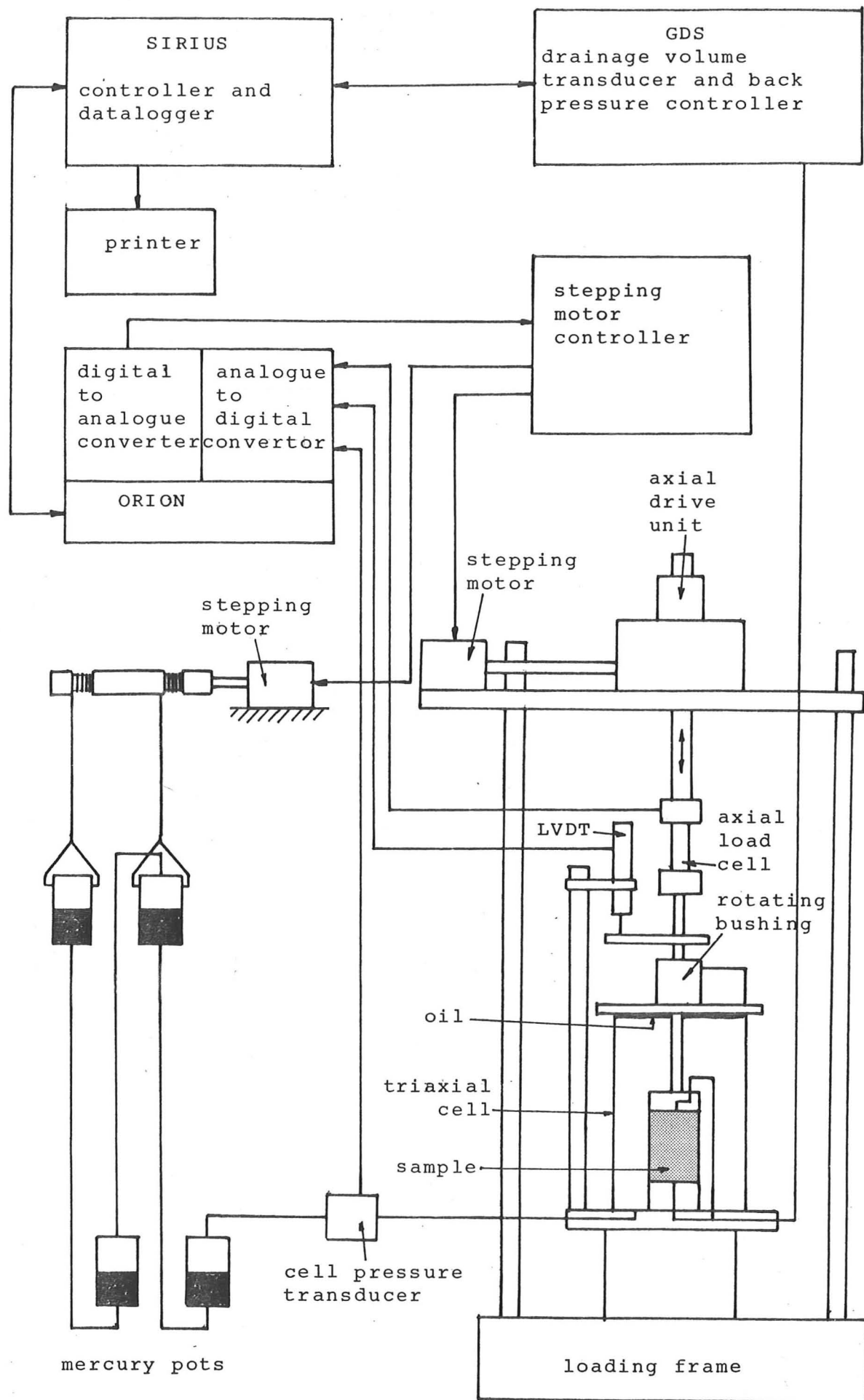
Fig 2.11 Schematic layout of the triaxial set-up at medium pressure
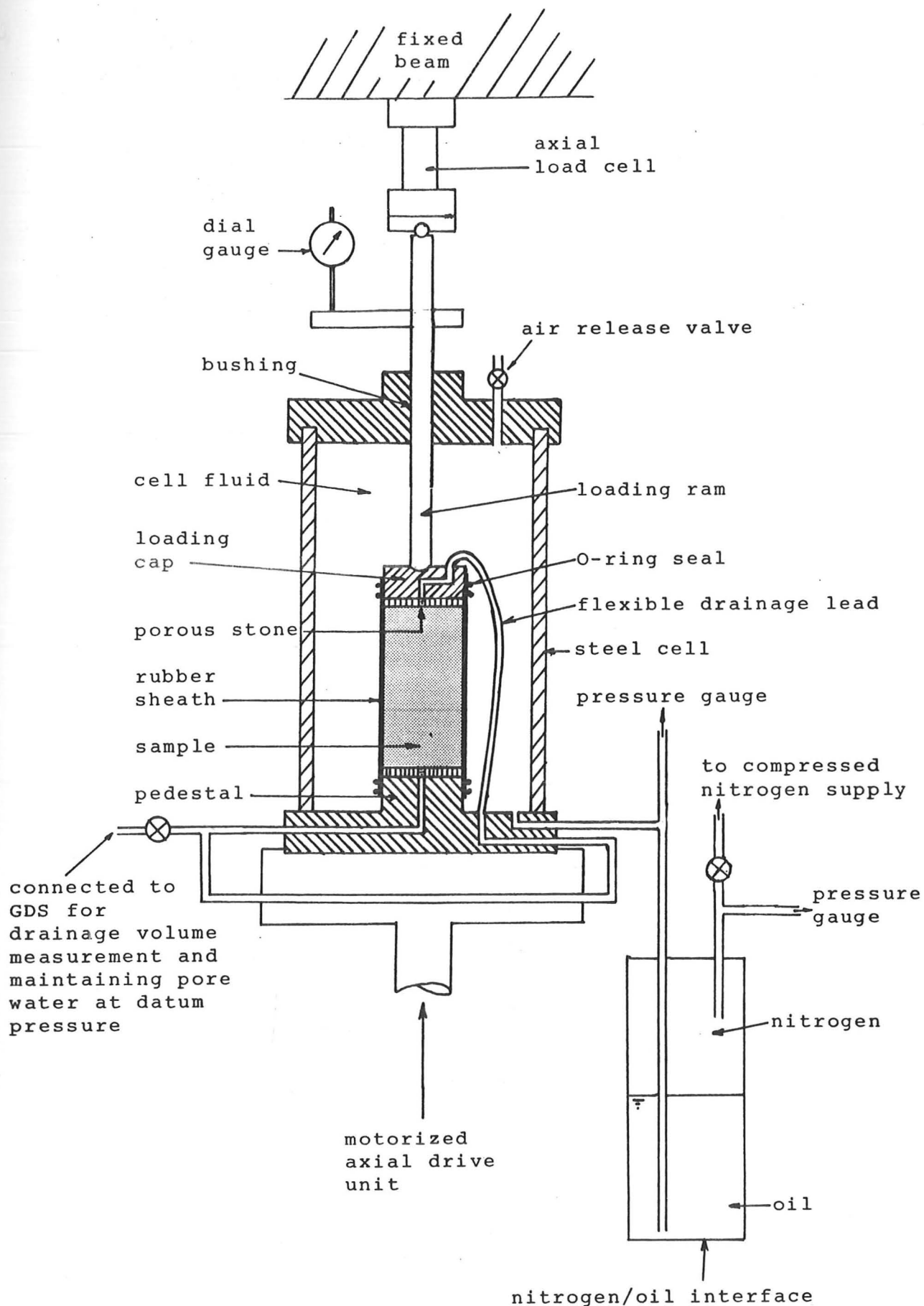
Fig 2.12   Schematic layout of the triaxial set-up at high pressure

TOP (T)

BOTTOM (B)
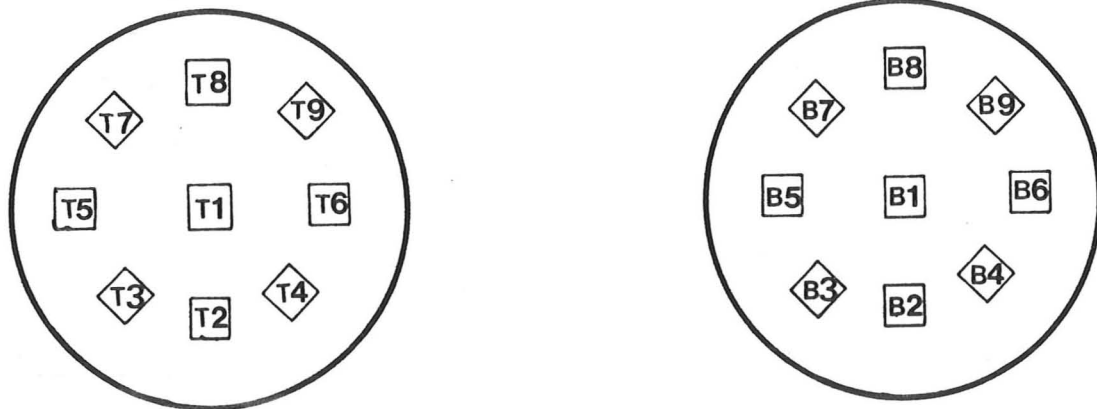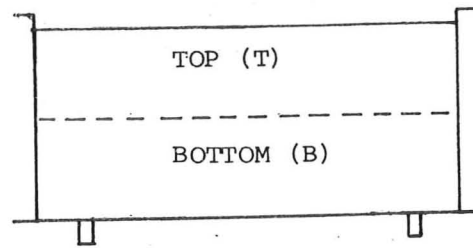
Fig 2.13   Location plan of undisturbed
           cube silt specimen

porous stone

platen

smear of
grease

membrane

sheath

sample
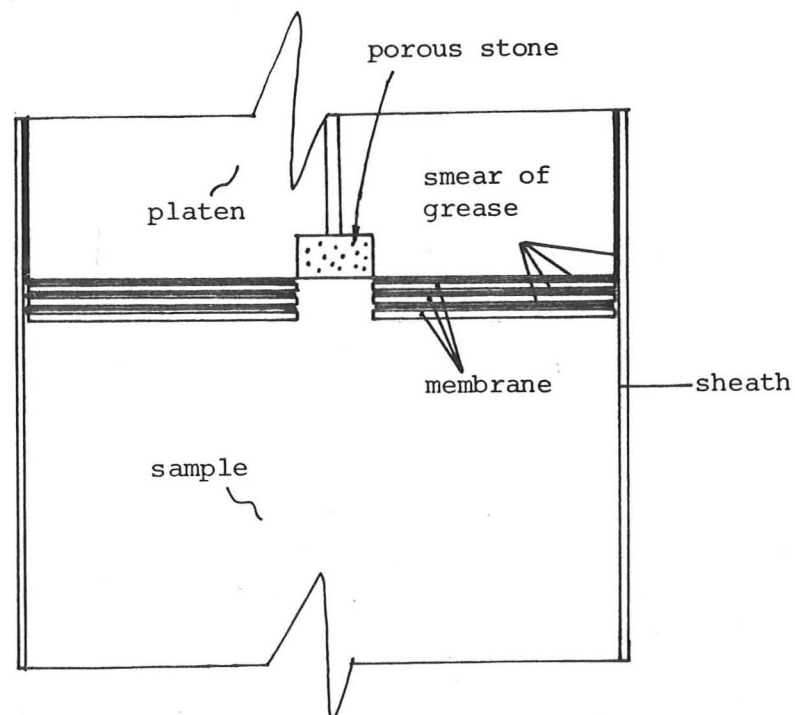
Fig 2.14   Lubrication details of a
           typical end platen
           (not to scale)
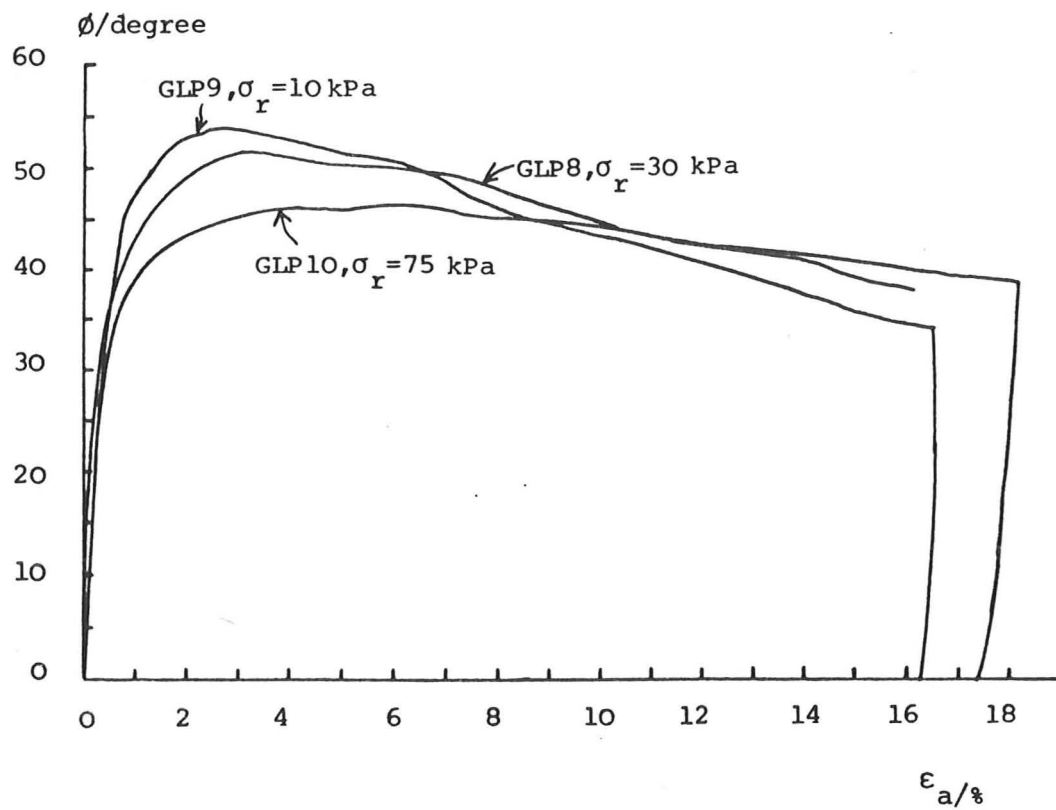
Fig 2.15   Stress-strain behaviour of dry sand in triaxial
compression using the low pressure set-up
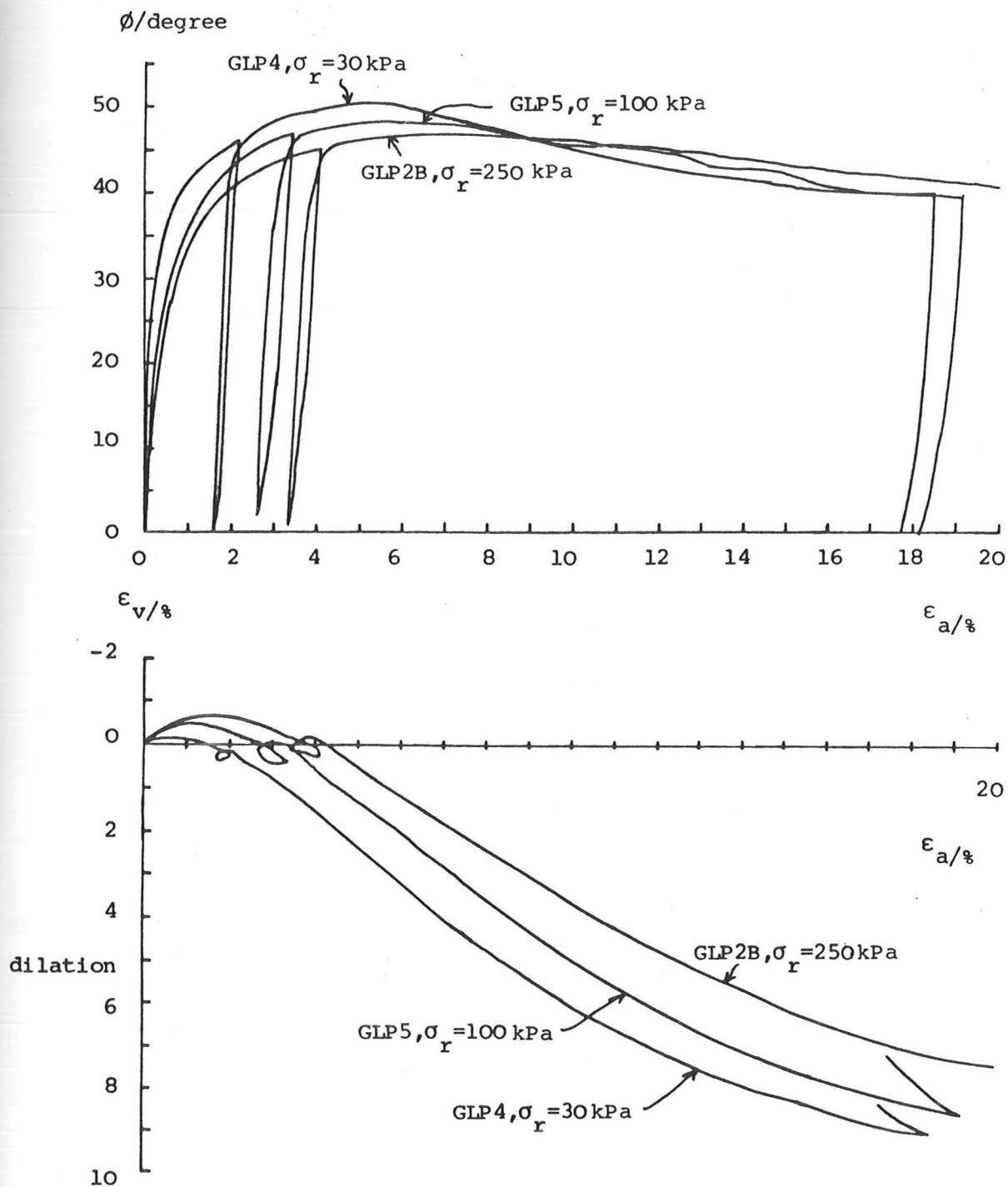
Fig 2.16 Stress-strain behaviour of saturated sand in triaxial compression using the medium pressure set-up
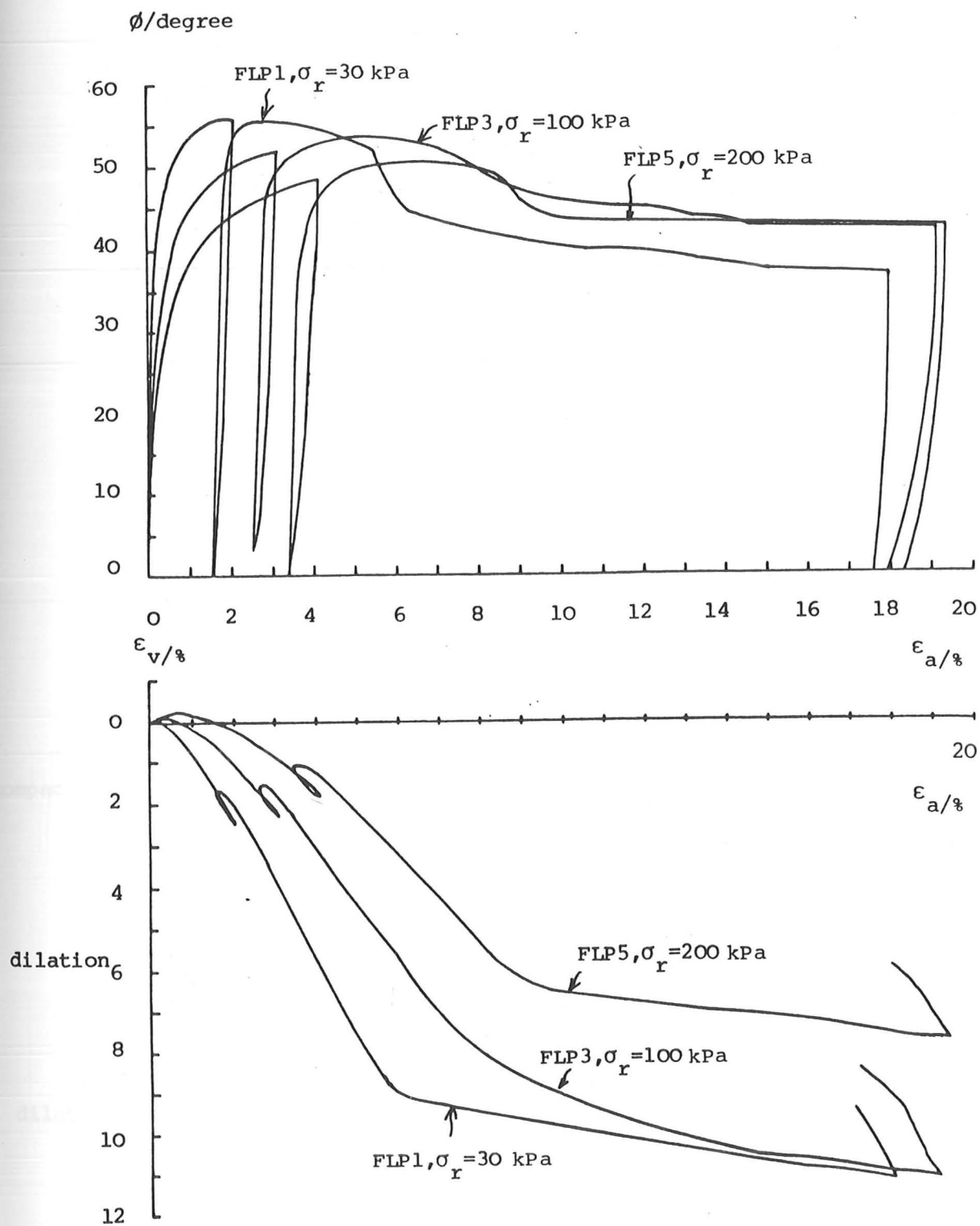
Fig 2.17   Stress-strain behaviour of silt in triaxial compression
using the medium pressure set-up
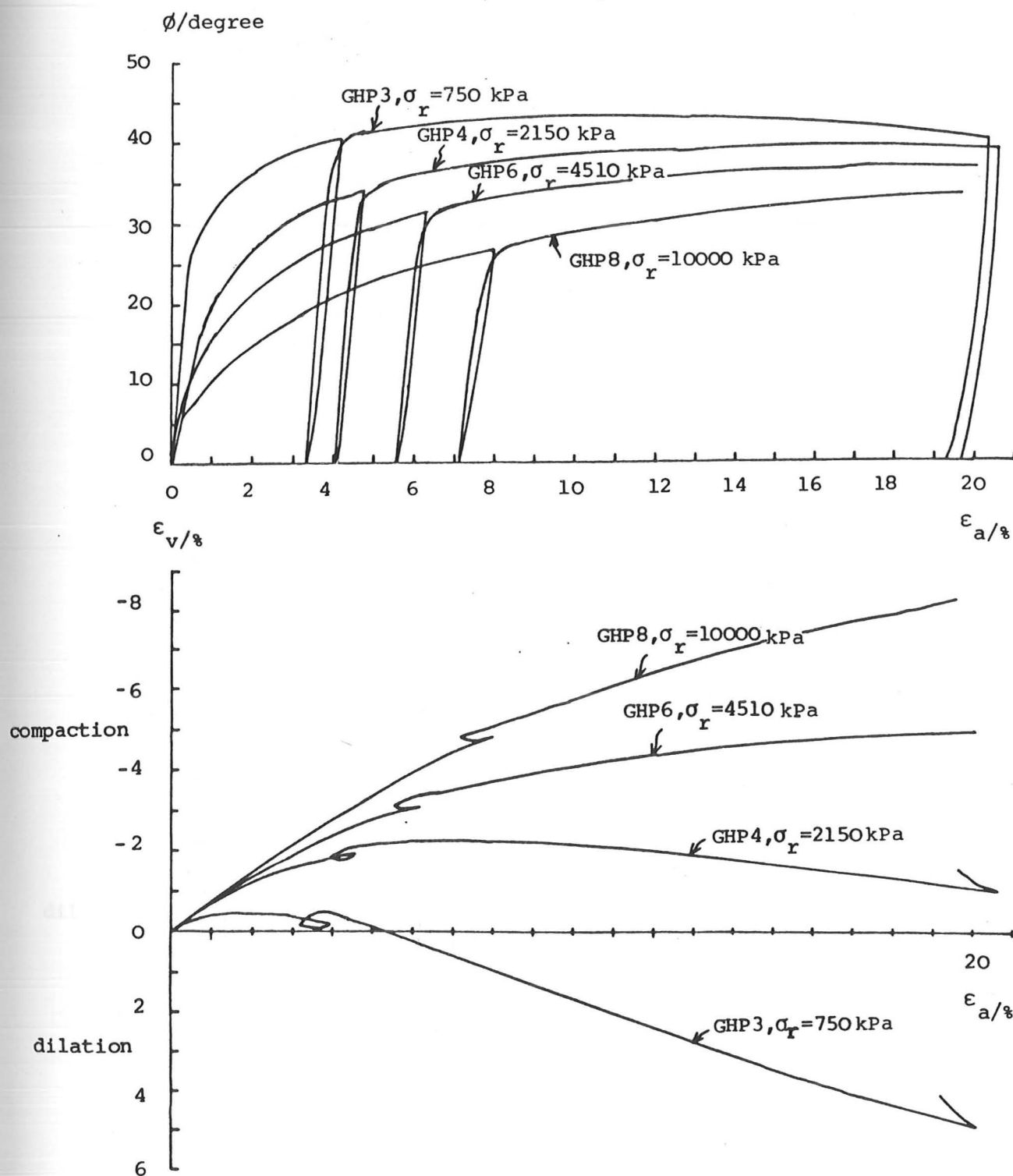
Fig 2.18   Strain-strain behaviour of sand in triaxial compression
           using the high pressure set-up
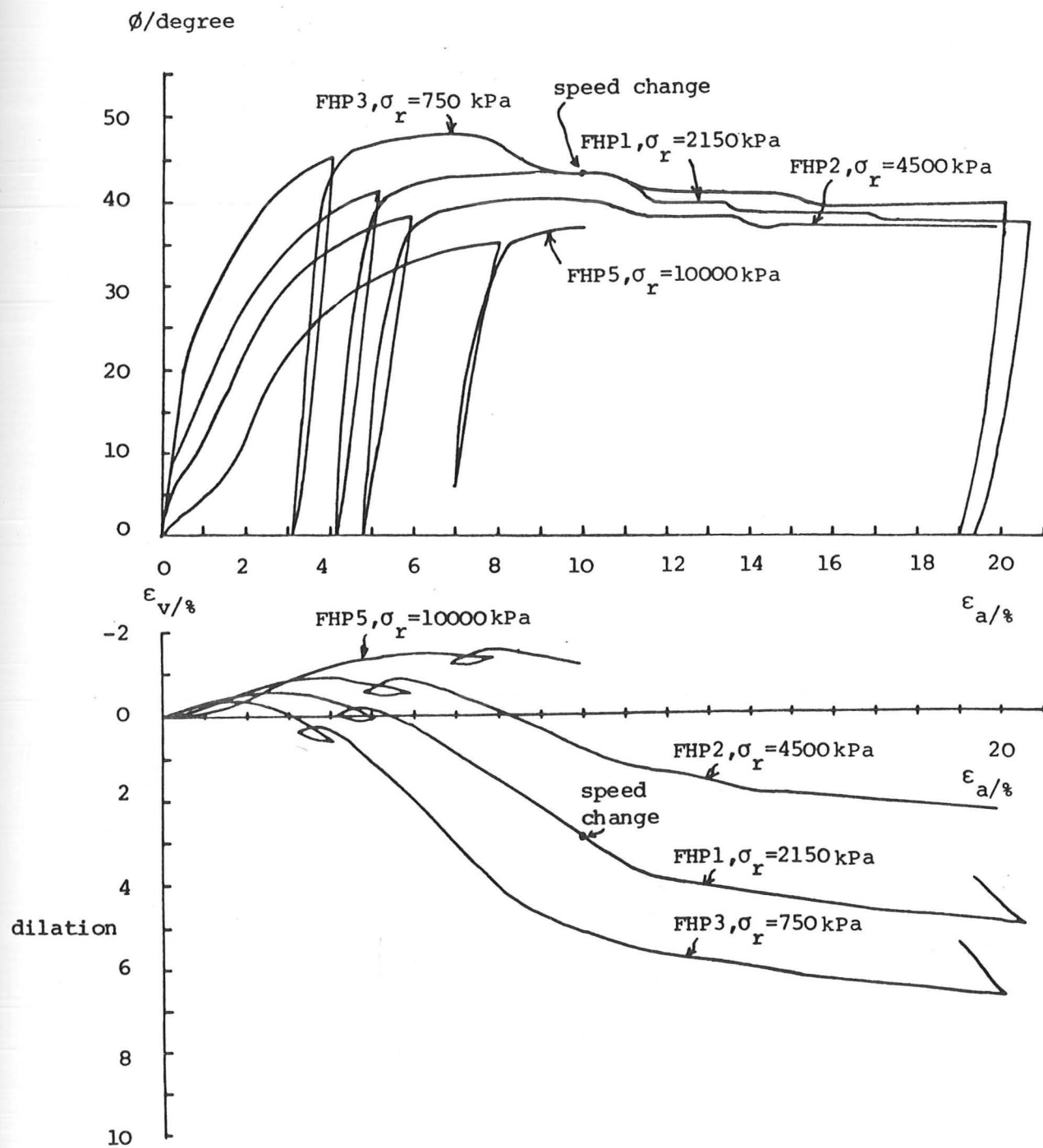
Fig 2.19   Stress-strain behaviour of silt in triaxial compression
using the high pressure set-up
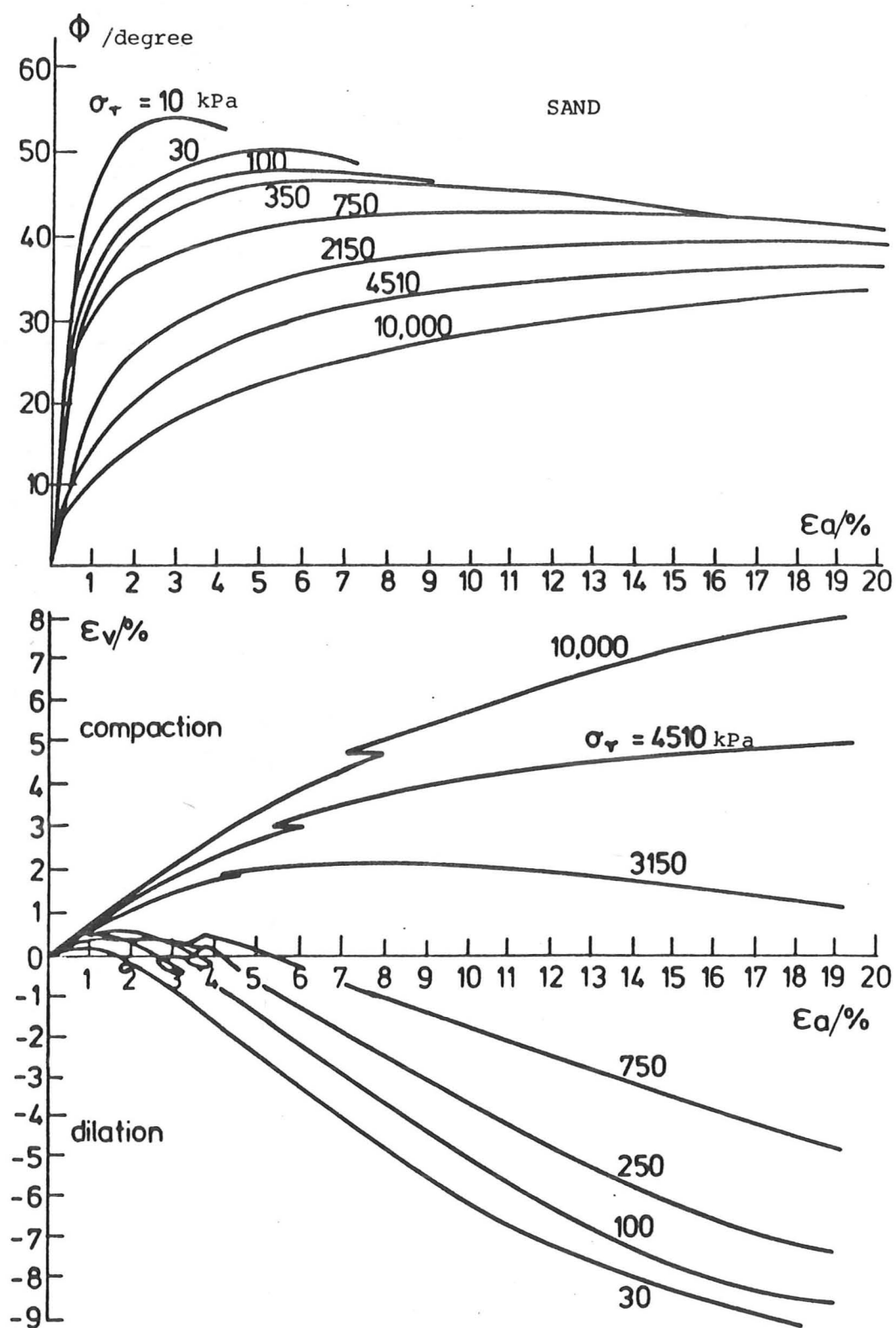
Fig 2.20   Effects of effective cell pressure on the stress-strain
behaviour of sand in triaxial compression
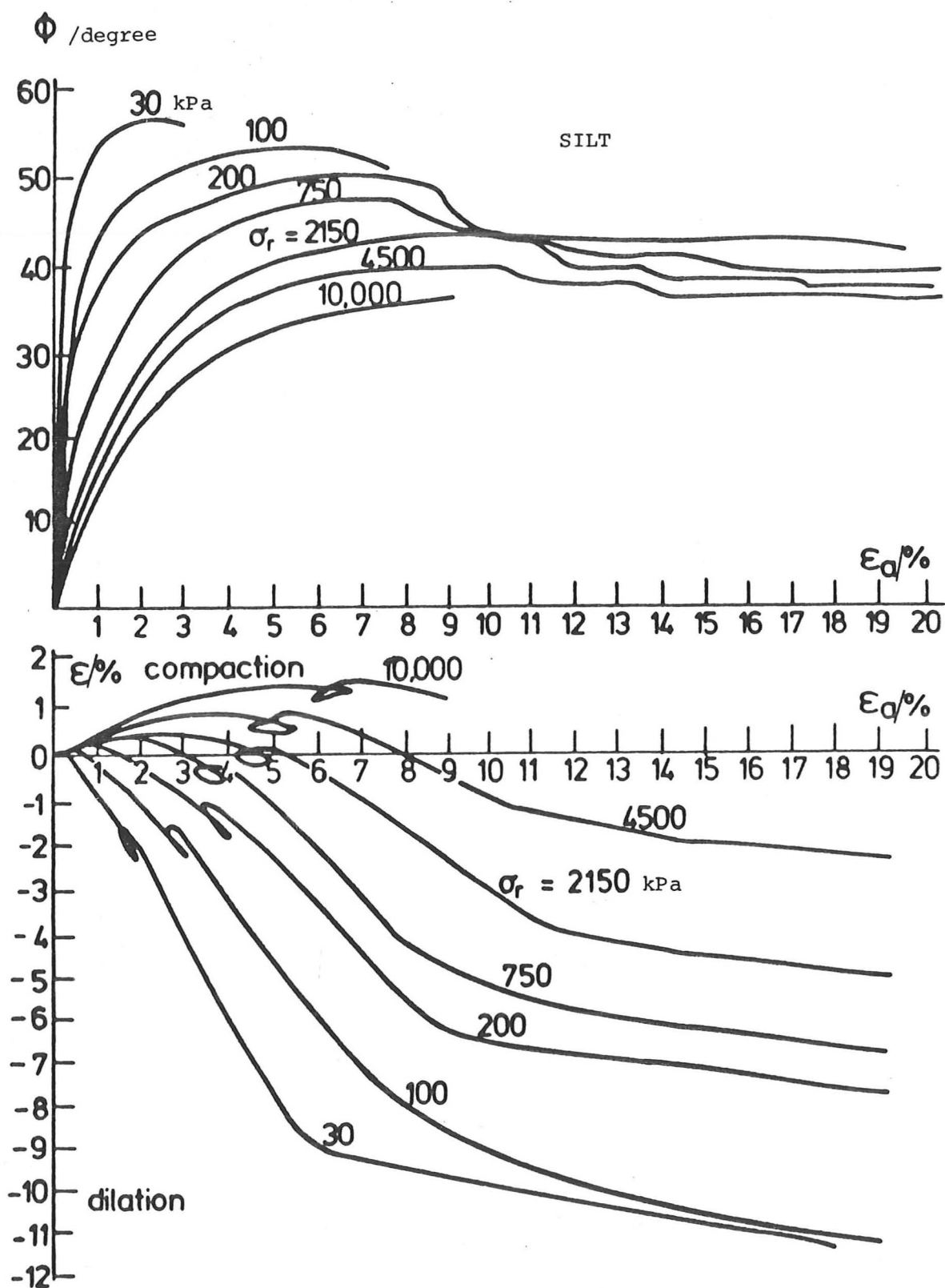
Fig 2.21   Effects of effective cell pressure on the stress–strain
behaviour of silt in triaxial compression
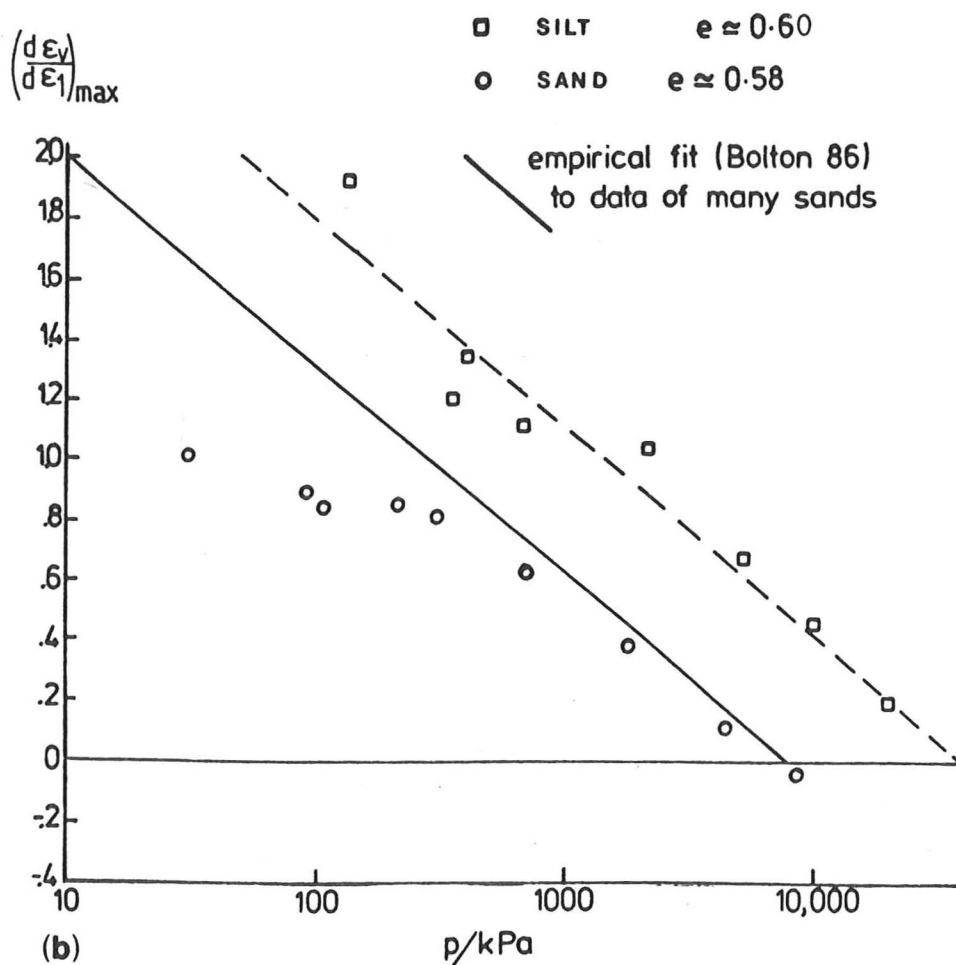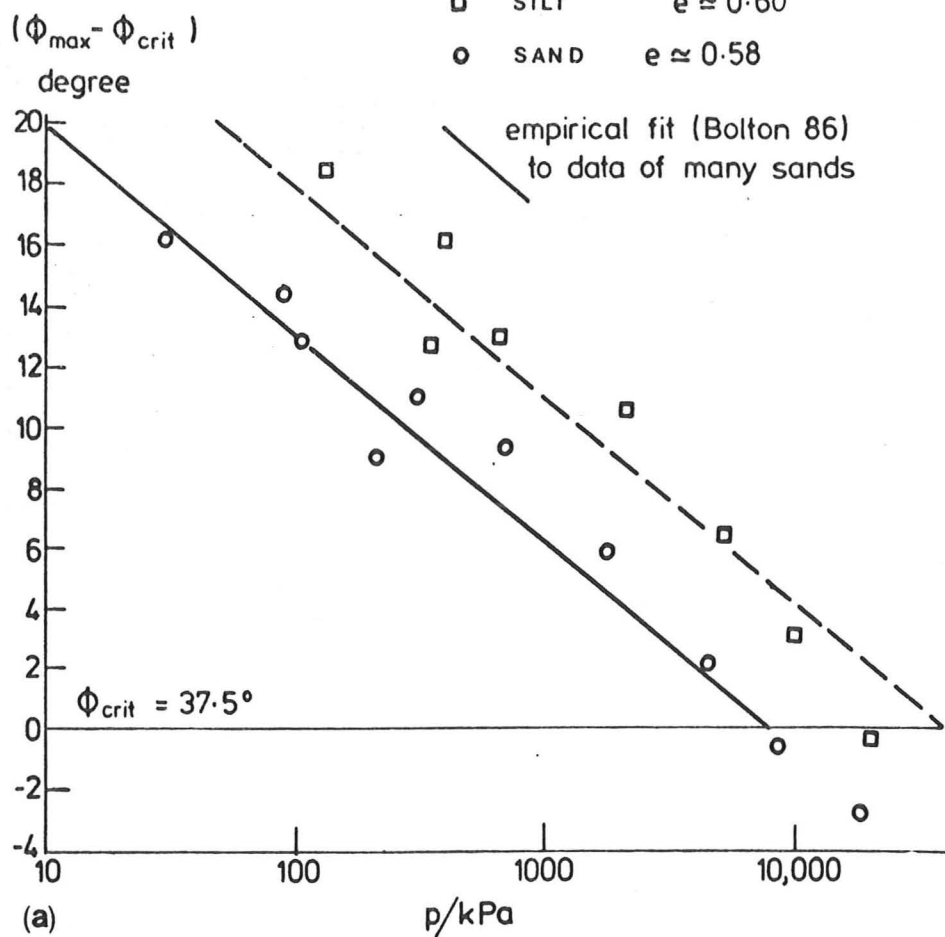
Fig 2.22   Summary of triaxial strength and dilatancy data for the sand and silt under various stress level
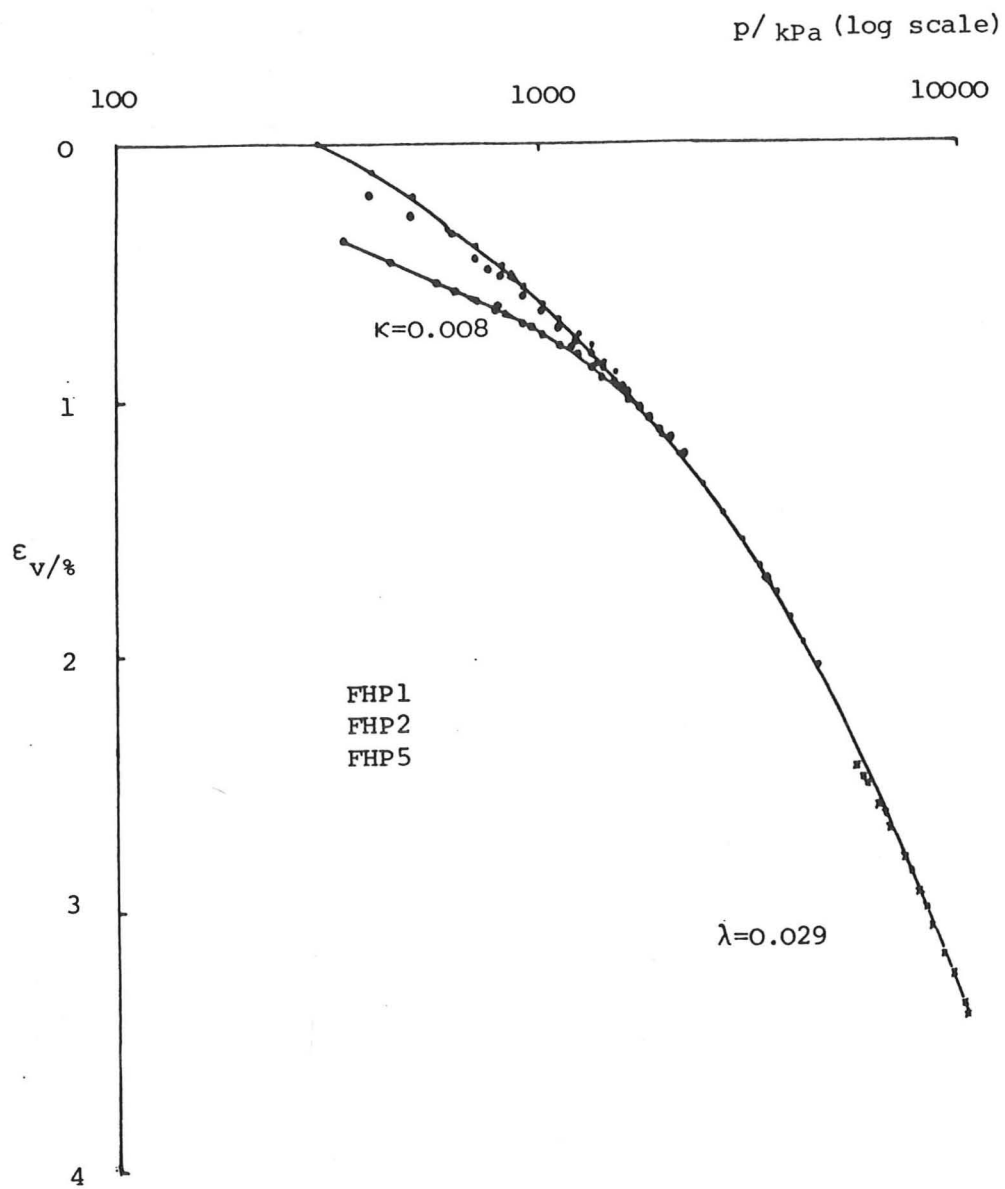
Fig 2.23   Behaviour of silt under isotropic compression
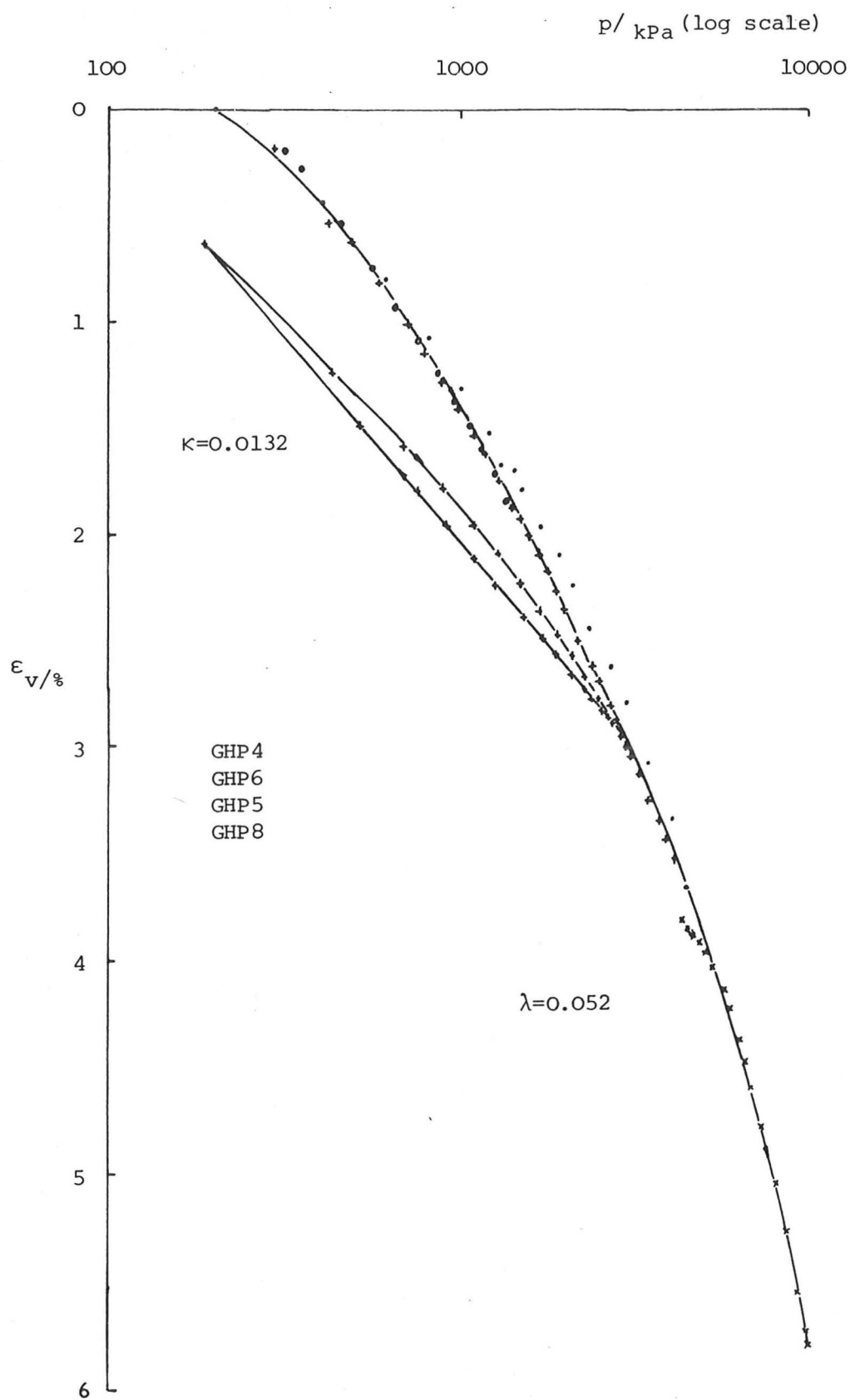
Fig 2.24 Behaviour of sand under isotropic compression

q

$$E = 2G(1+\nu)$$

1

ε_a
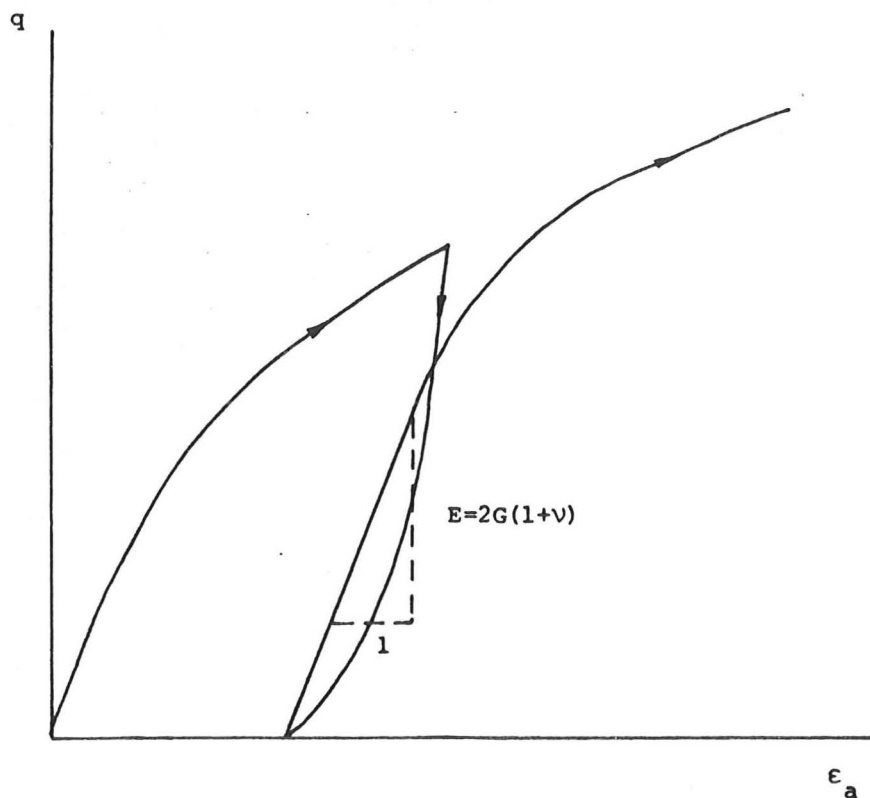
Fig 2.25   Typical unloading/reloading cycle during a
            triaxial test to evaluate the elastic
            parameters

G/kPa

900,000

800,000

700,000

sand ∘
silt ✗

600,000

empirical fit : $G = 1400p^{0.667}$

500,000

400,000

300,000

200,000

100,000

O

0   2000   4000   6000   8000   10,000   12,000   14,000

p/kPa
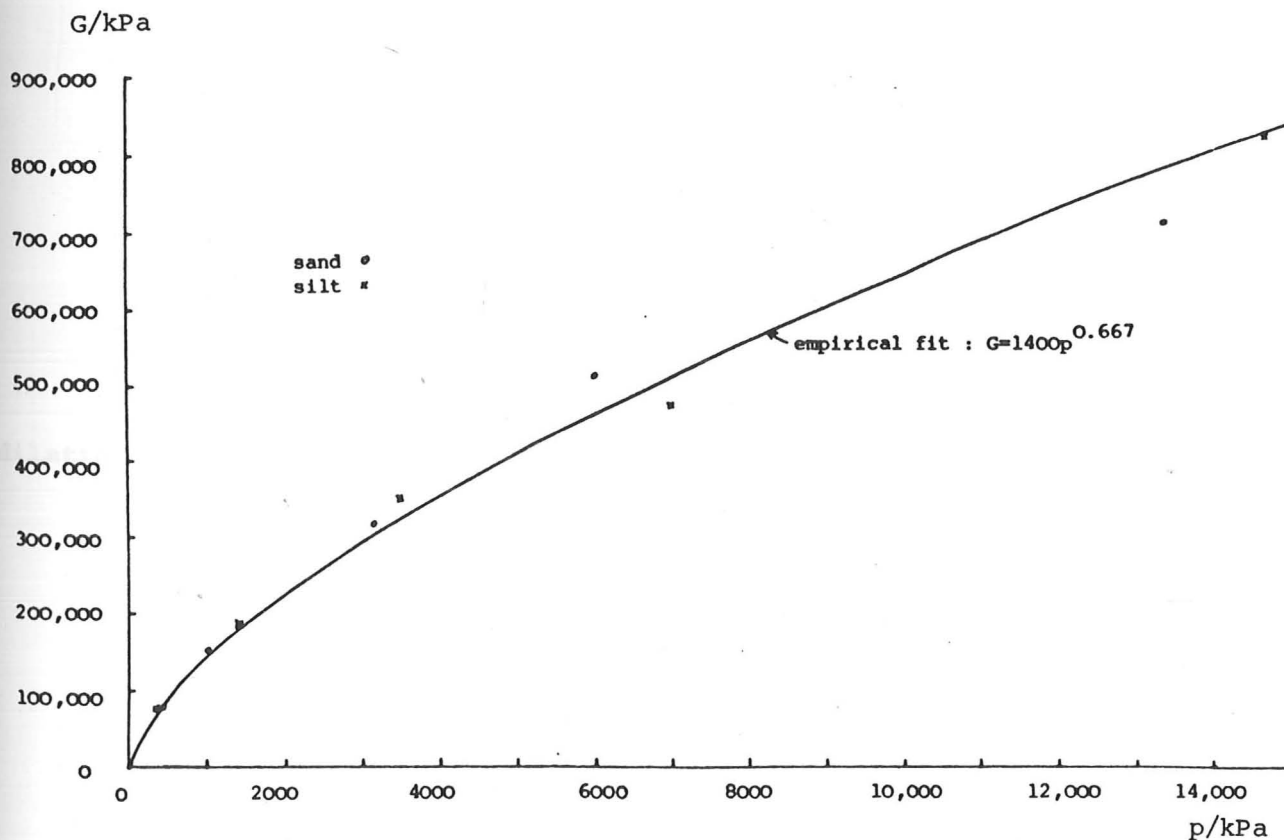
Fig 2.26 Empirical correlation between G and p
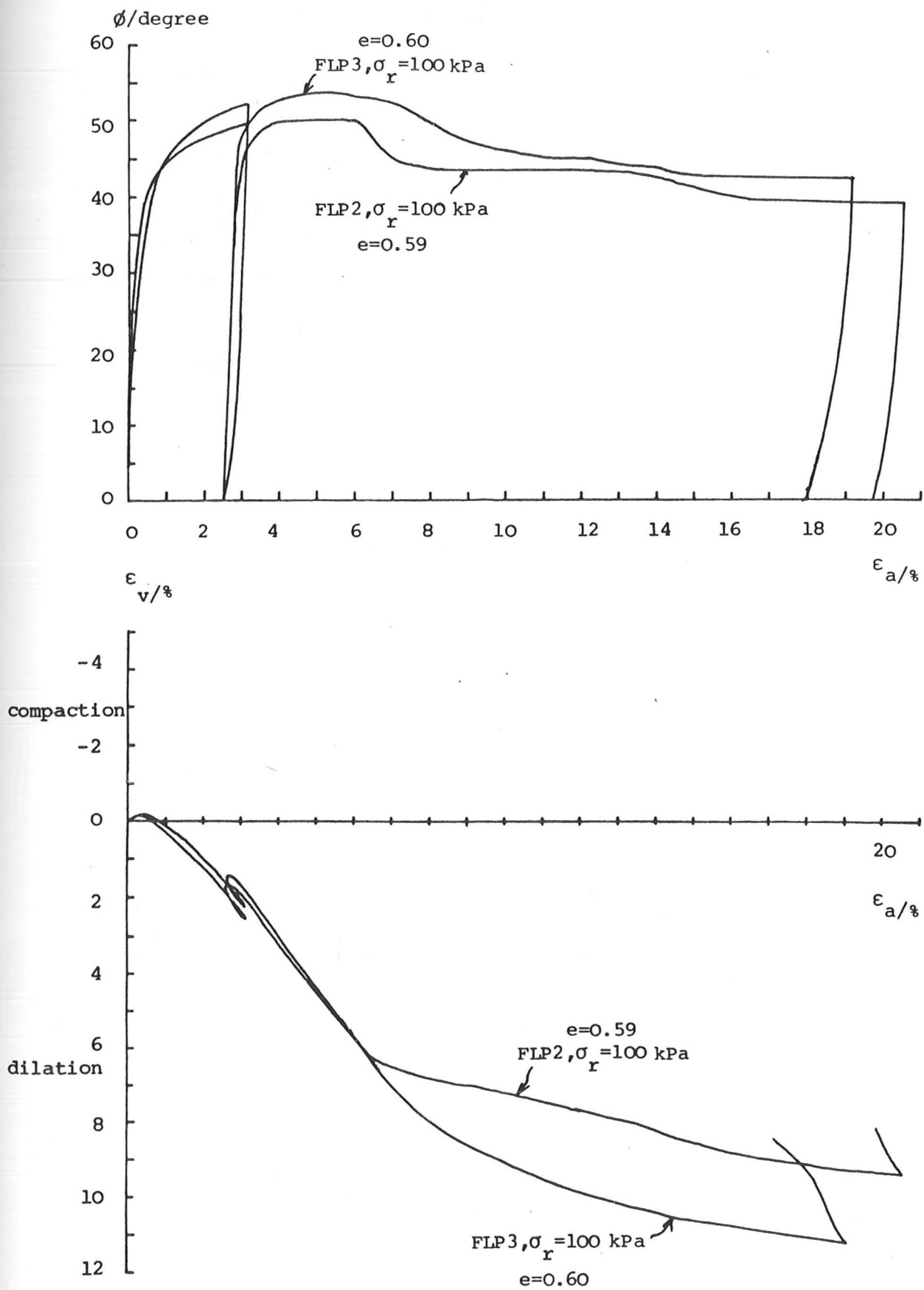
Fig 2.27 Effects of the initiation of ruptures on a triaxial test
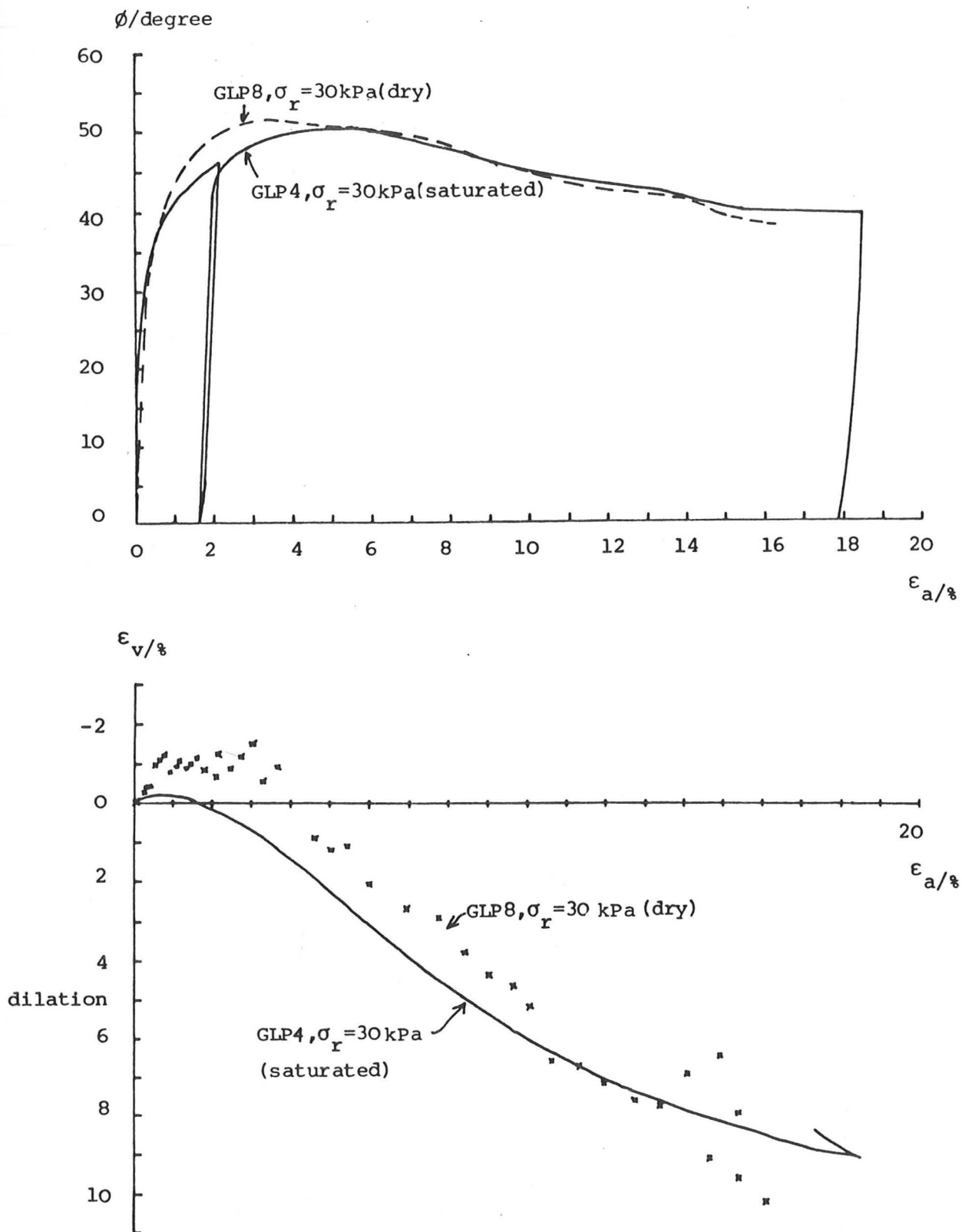
Fig 2.28 Effects of saturation on a dry sand triaxial specimen

38.8		39.0		40.1
38.8		39.2		44.7
38.7		39.3		46.0
38.8		39.3		44.0
38.9		38.9		40.2

$\varepsilon_a = 0\%$ @ 3% $(\emptyset_{max})$ @ 16.6%

GLP9 $\sigma_r = 10$ kPa

38.8		39.0		40.2
38.9		39.1		44.2
38.9		39.1		46.8
38.8		39.2		45.2
38.6		39.1		41.2

$\varepsilon_a = 0\%$ @ 3.5% $(\emptyset_{max})$ @ 17.5%

GLP8 $\sigma_r = 30$ kPa

38.6		39.2		40.2
38.5		39.2		43.0
38.4		39.2		46.2
38.2		39.2		45.7
38.2		39.6		42.8

$\varepsilon_a = 0\%$ @ 4% $(\emptyset_{max})$ @ 17.8%

GLP10 $\sigma_r = 75$ kPa

Fig 2.29   Summary of direct measurement of specimen diameter during tests in the low pressure set-up

Angle of internal
friction in degrees
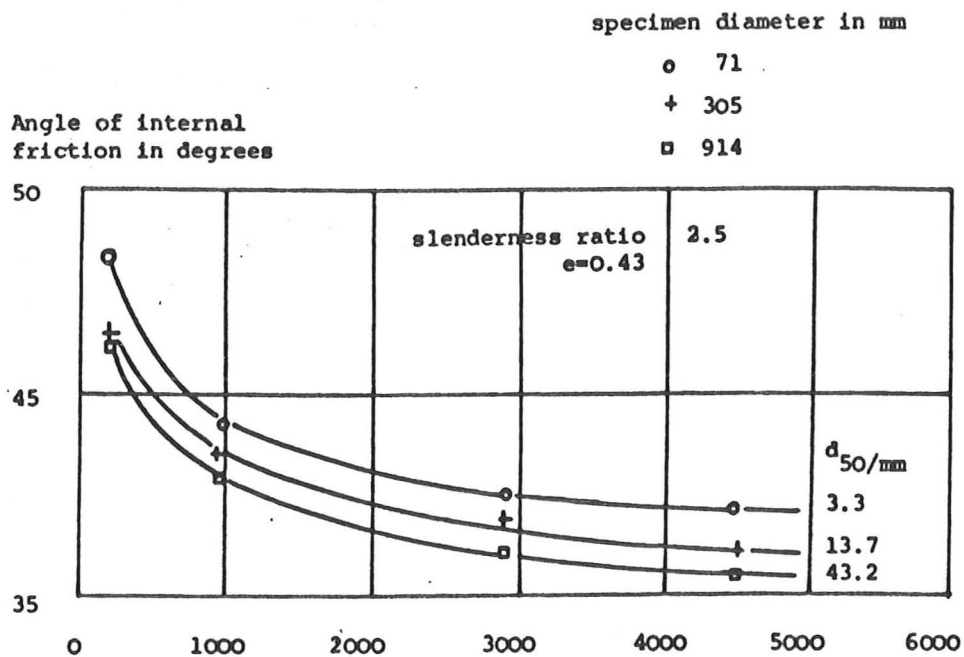
Fig 2.30 Triaxial test results with crushed basalt
(After Marachi et al, 1972)

percentage passing

particle size / mm
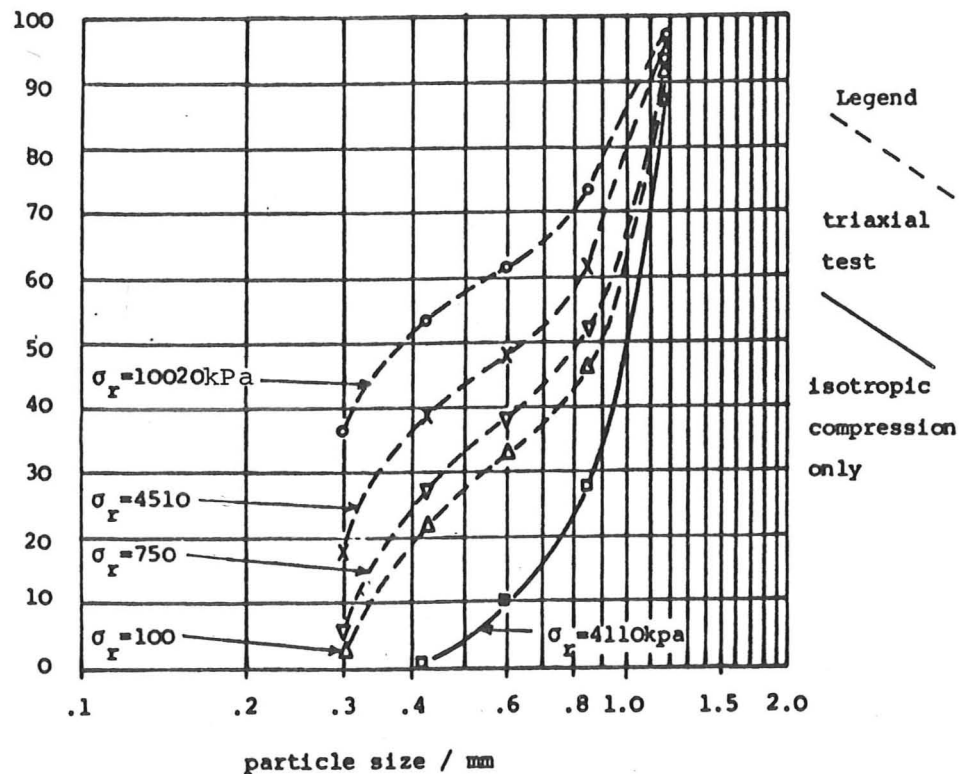
Fig 2.31 Grading curves of sand samples after triaxial tests

secant angle of friction ∅ in degrees

		$\emptyset_{max}$	e	$\sigma_{n/kPa}$	$\emptyset_{crit}$
--------	sand	47.5	0.78	100	38.0
——————	silt	43.0	0.74	100	37.5

vertical displacement/mm
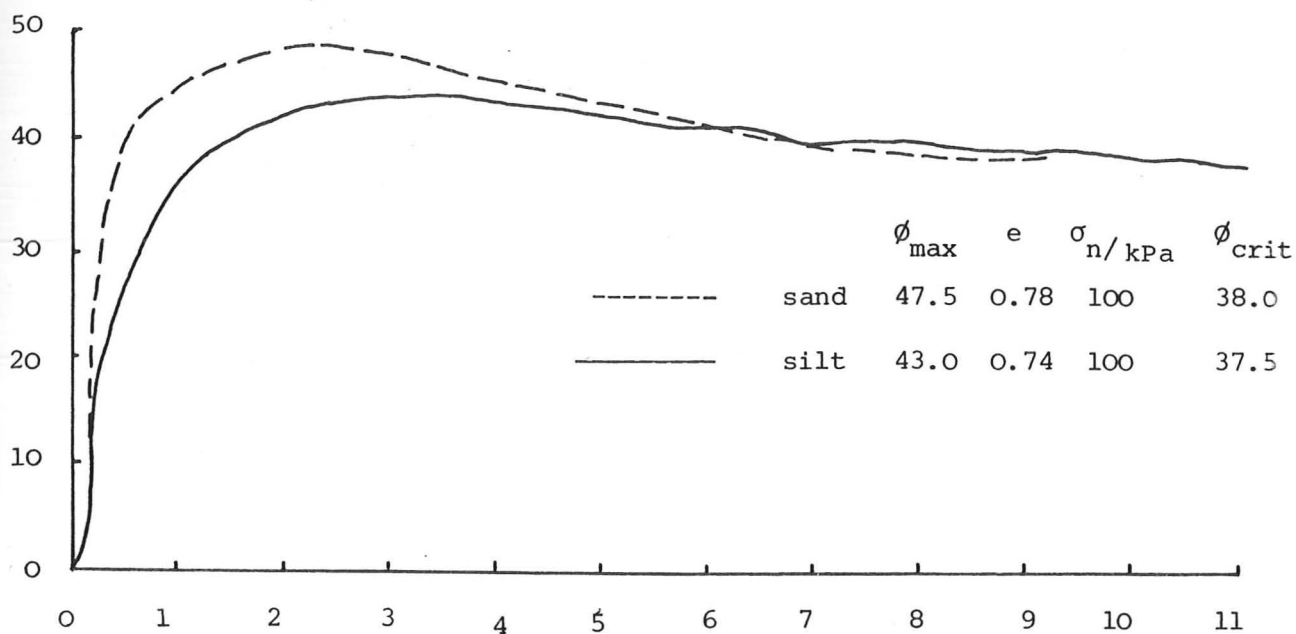
horizontal displacement/mm
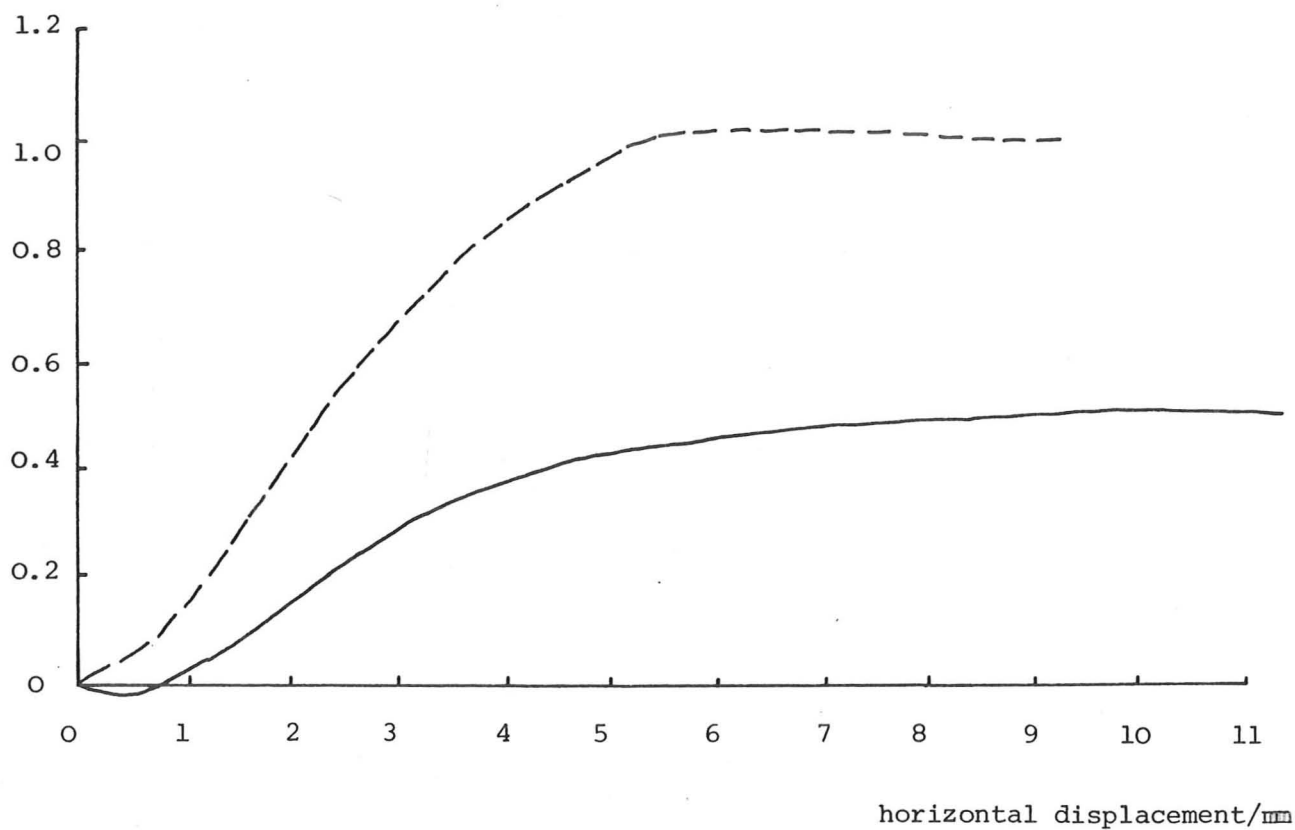
Fig 2.32 Direct shear box data on sand and silt

characteristic
spacing of flaws

sand
(more likely to
have flaws than
silt)

silt
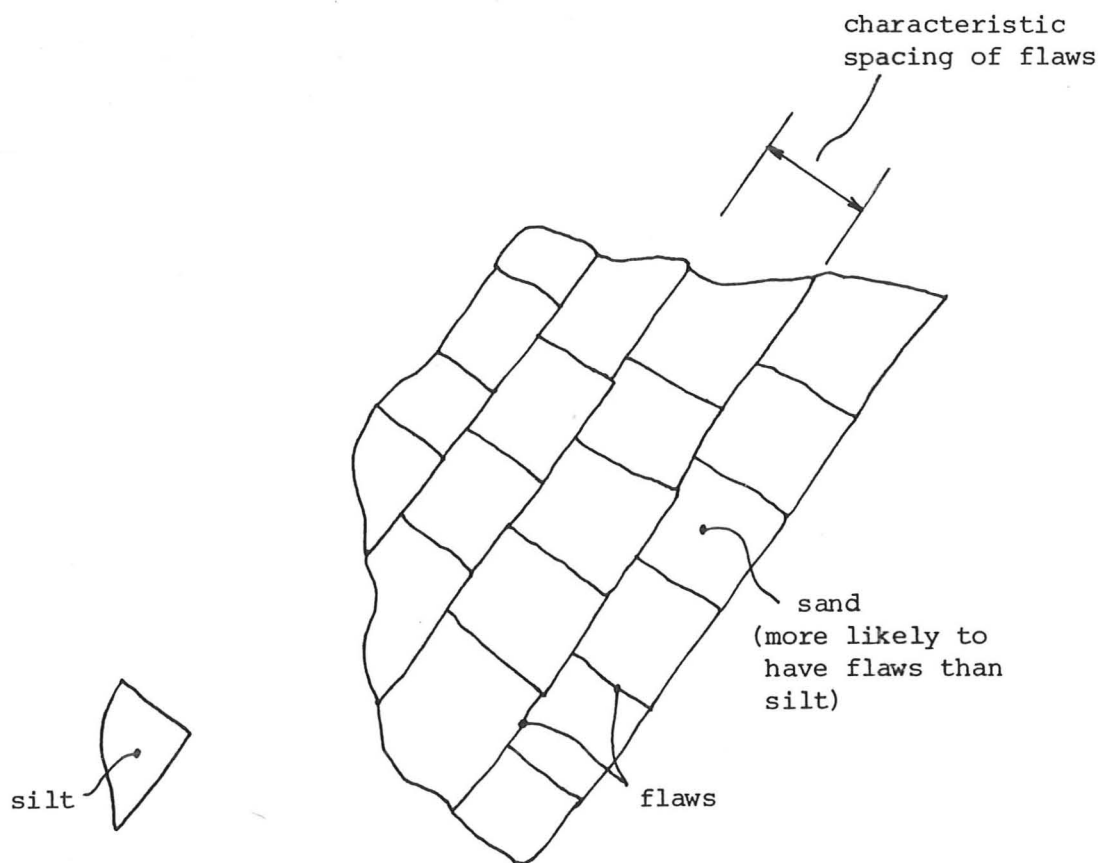
flaws

Fig 2.33 Schematic diagram showing the possible
distribution of flaws in a particle of
quartz sand
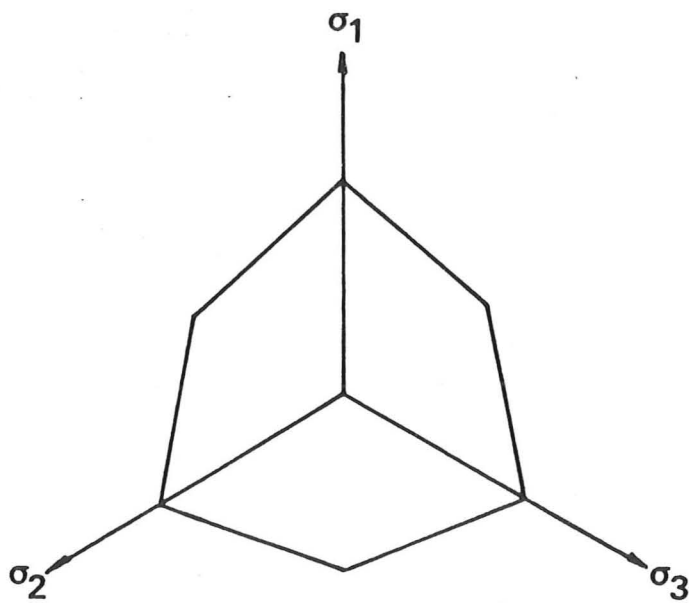
Fig 3.1   Mohr-Coulomb yield surface in an octahedral
(π) plane
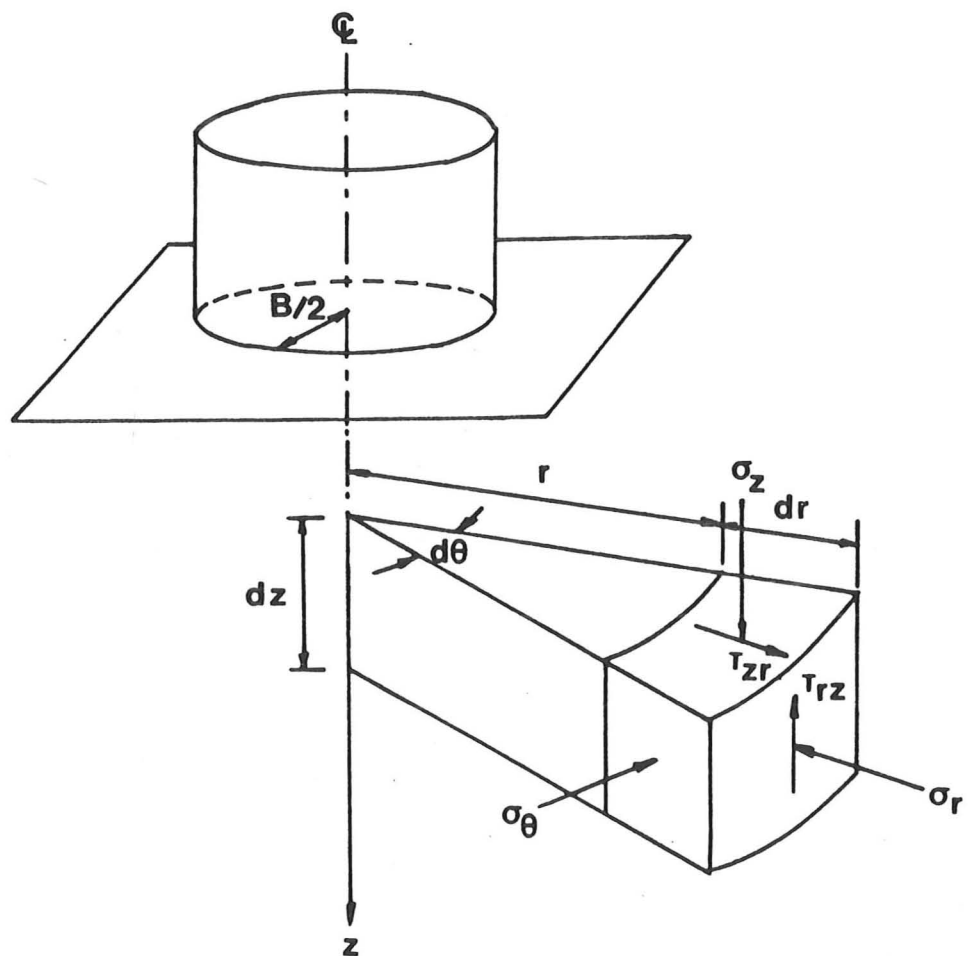
Fig 3.2   Cylindrical co-ordinate system and stress

components
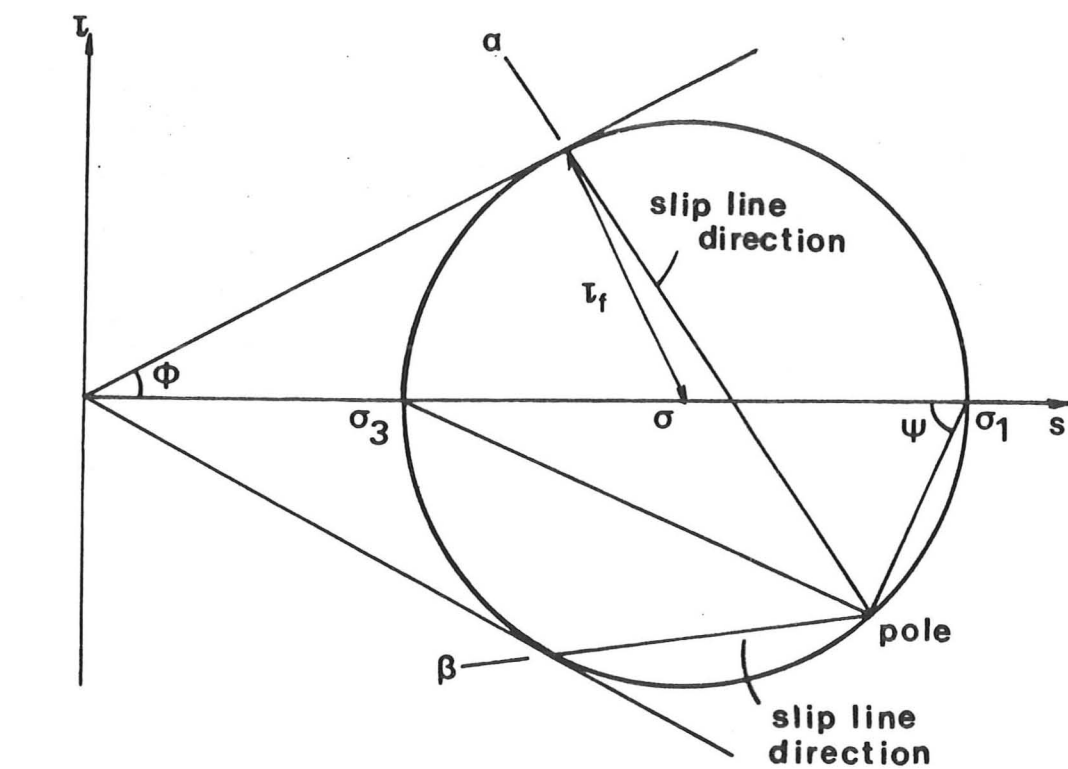
(a) Mohr circle under failure condition
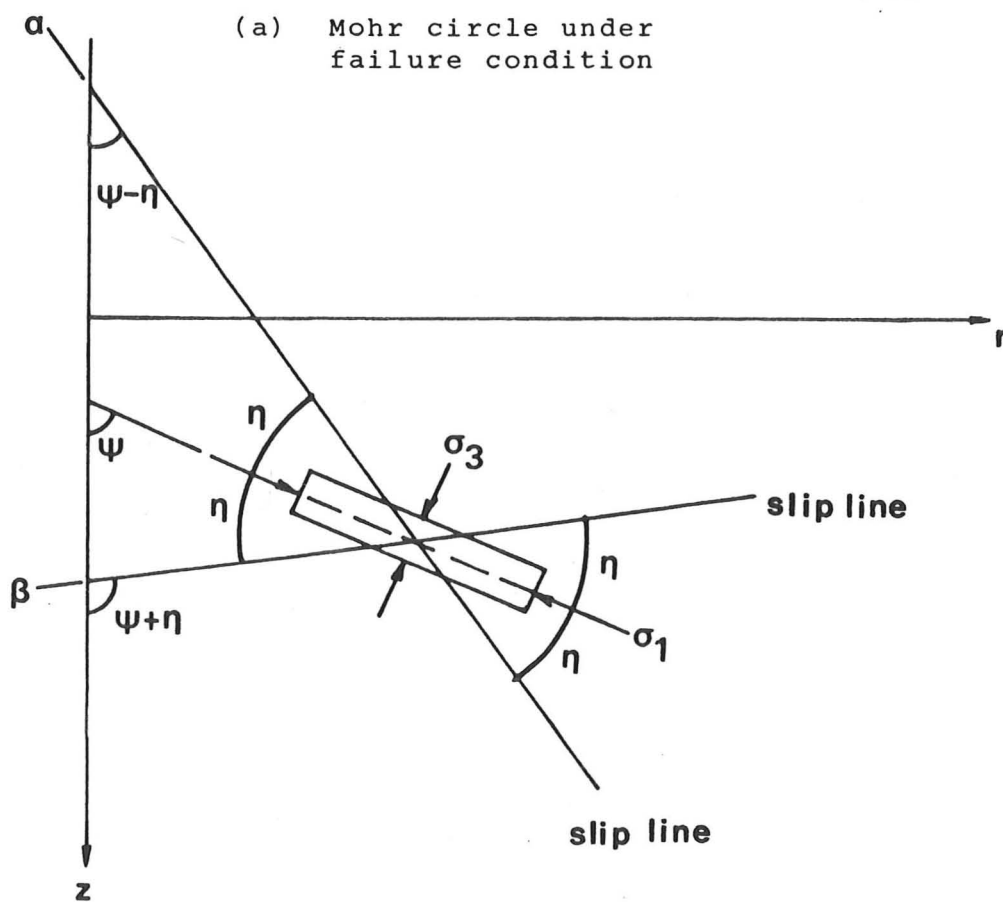
(b) Sign convention and notation

Fig 3.3
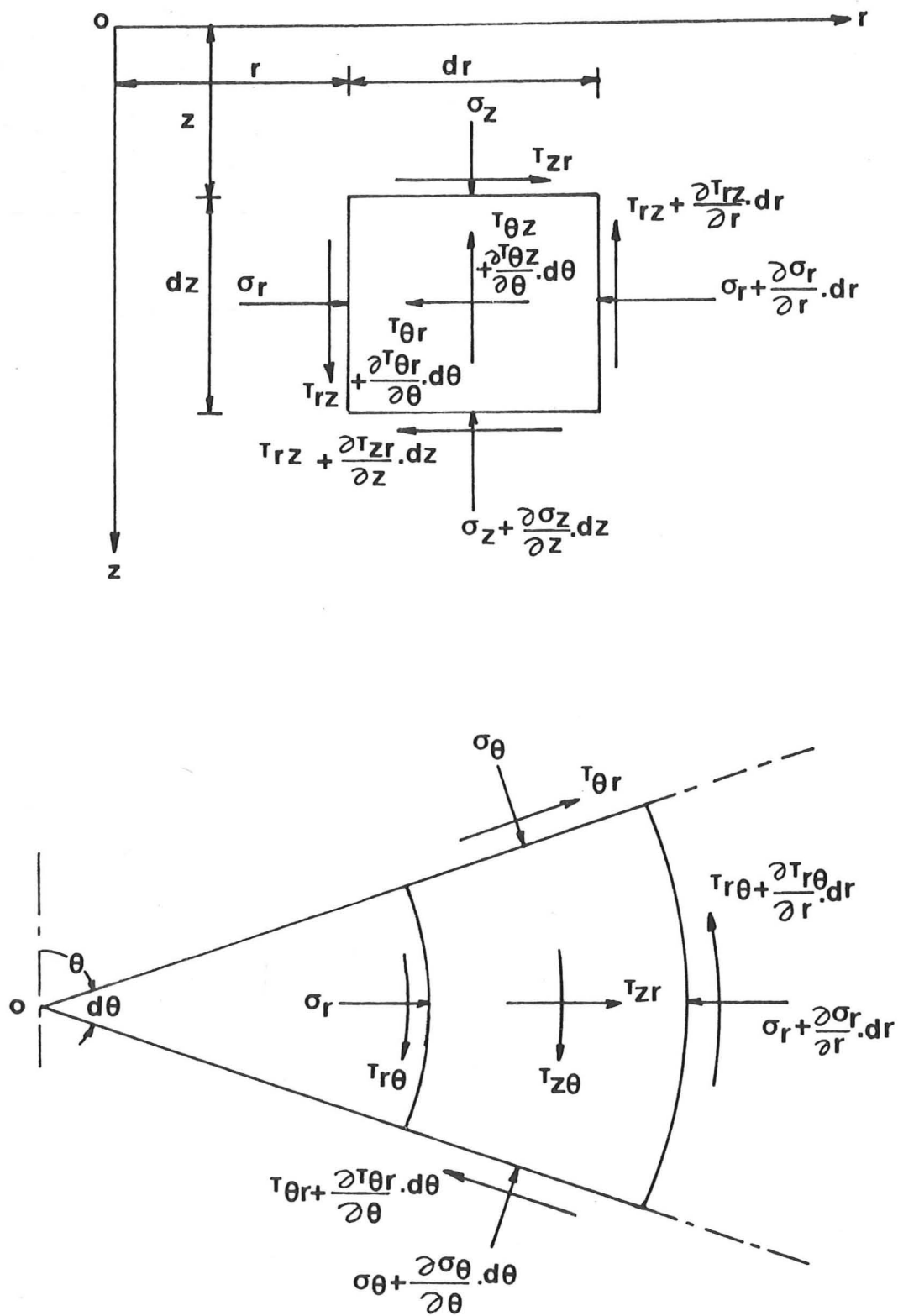
Fig 3.4   General stresses acting on a toroidal
          element under the punch

Fig 3.5   A typical stress characteristic mesh

Fig 3.6   Computation scheme of new point W from known
          points P and Q
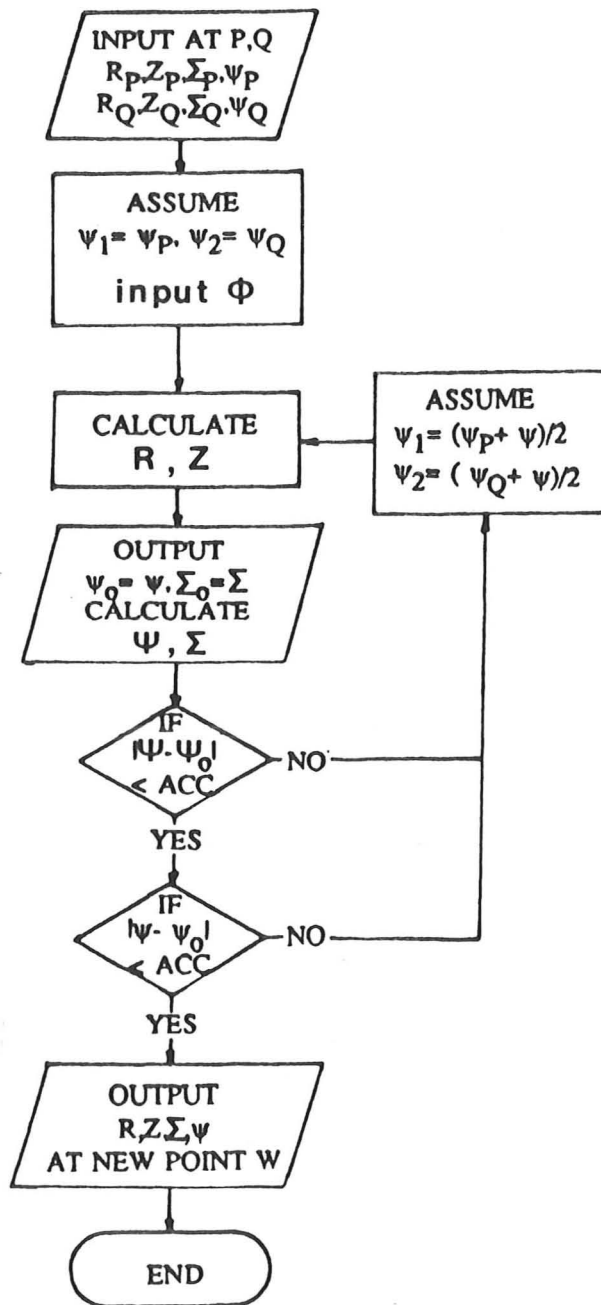
Fig 3.7   Flow chart showing the computation of
R , Z , Ψ and Σ in program CONPHI
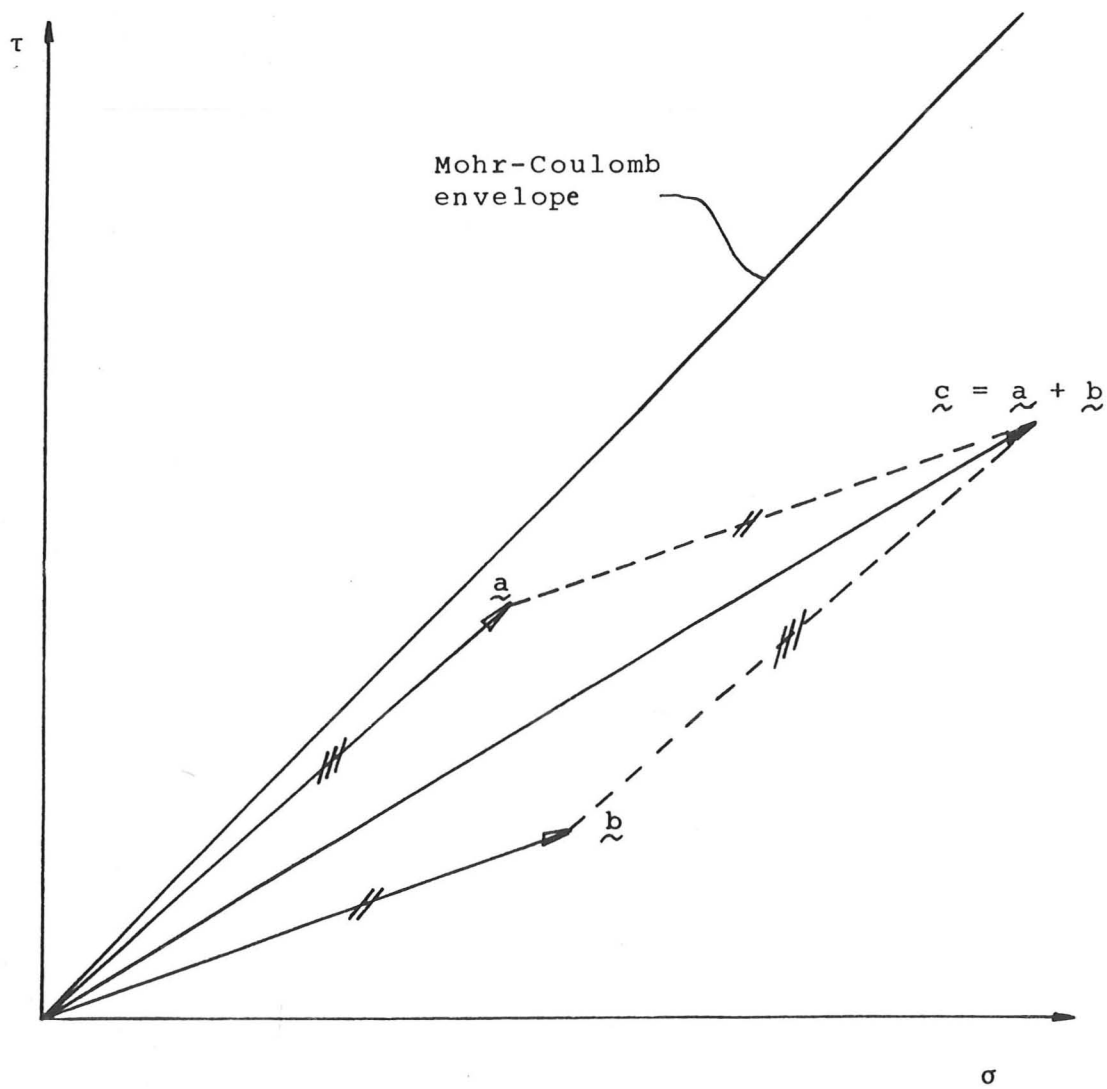
Fig 3.8   Effects of superposition (After Bolton,1988)
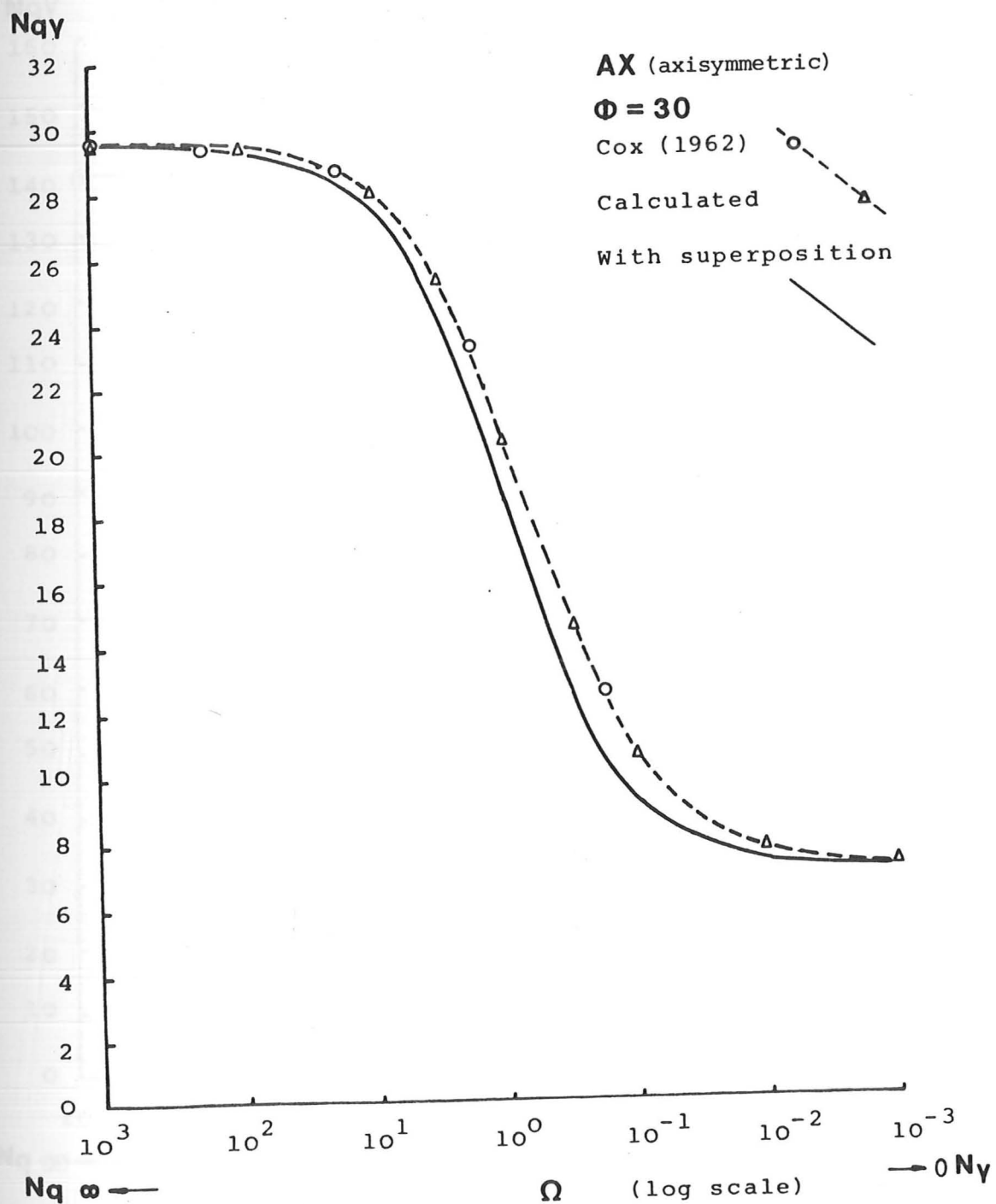
Fig 3.9   Effects of Ω on $N_{q\gamma}$ for smooth circular footing
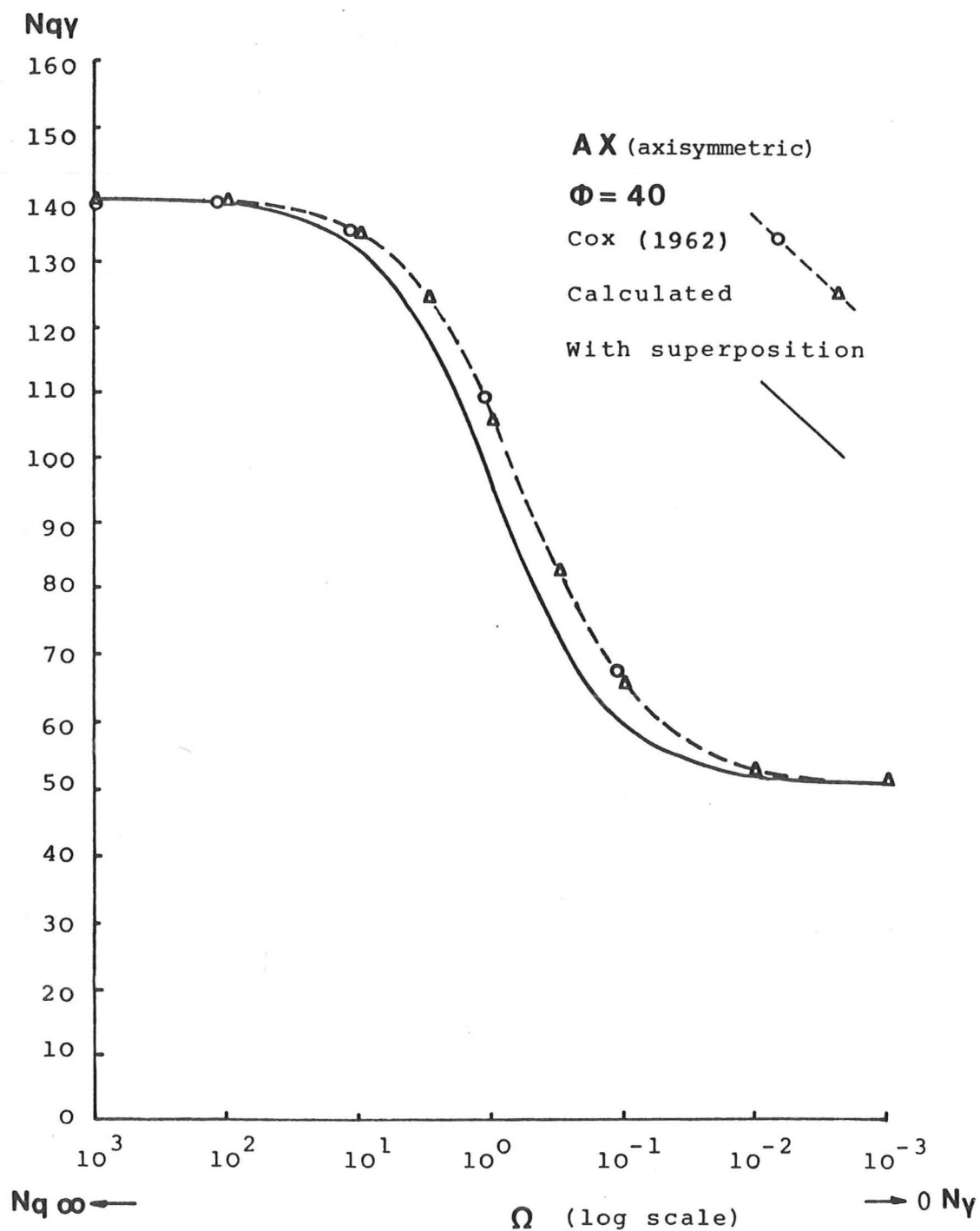
Fig 3.10   Effects of Ω on $N_{q\gamma}$
for smooth circular footing

Fig 3.11 Effects of Ω on R

ps (plane strain)
$\Omega = 10^3$
$\Phi = 40$
smooth
Nq

a Footing pressure distribution

Hill's mechanism
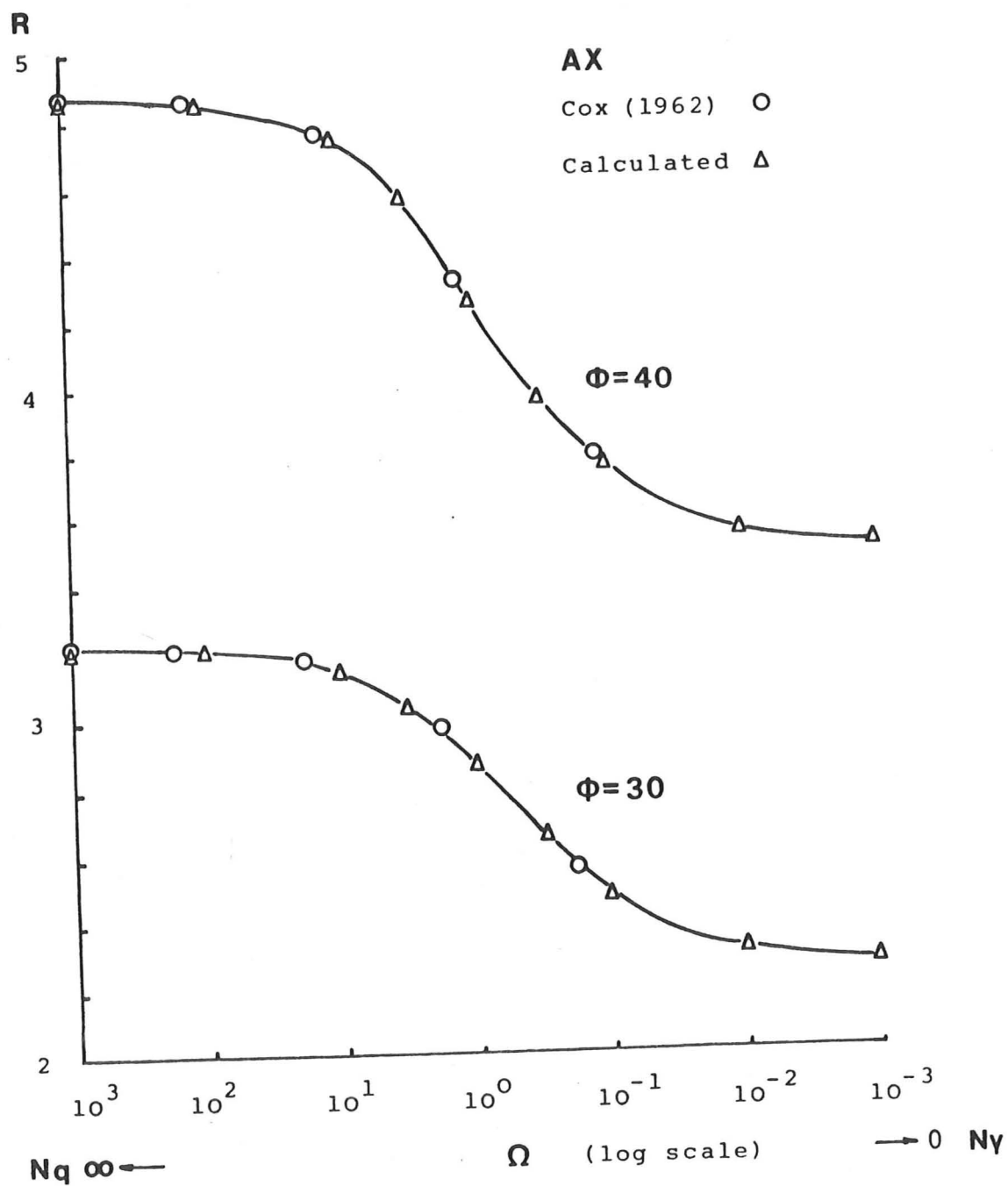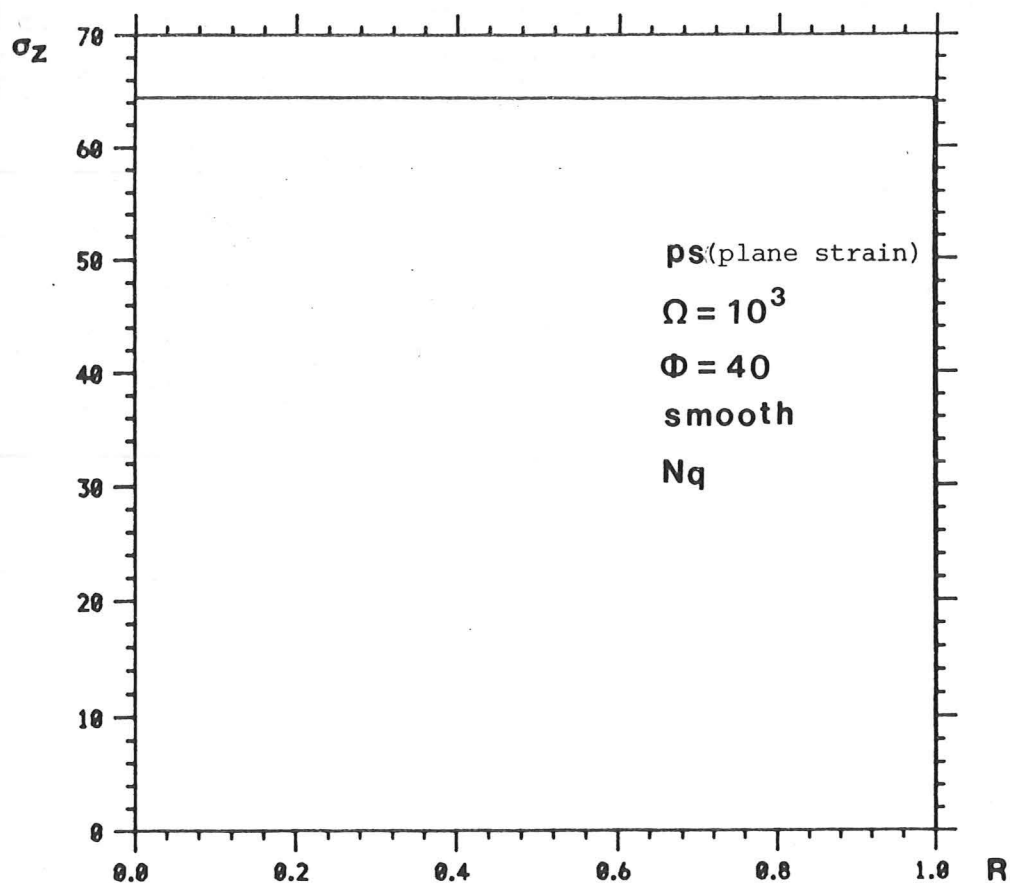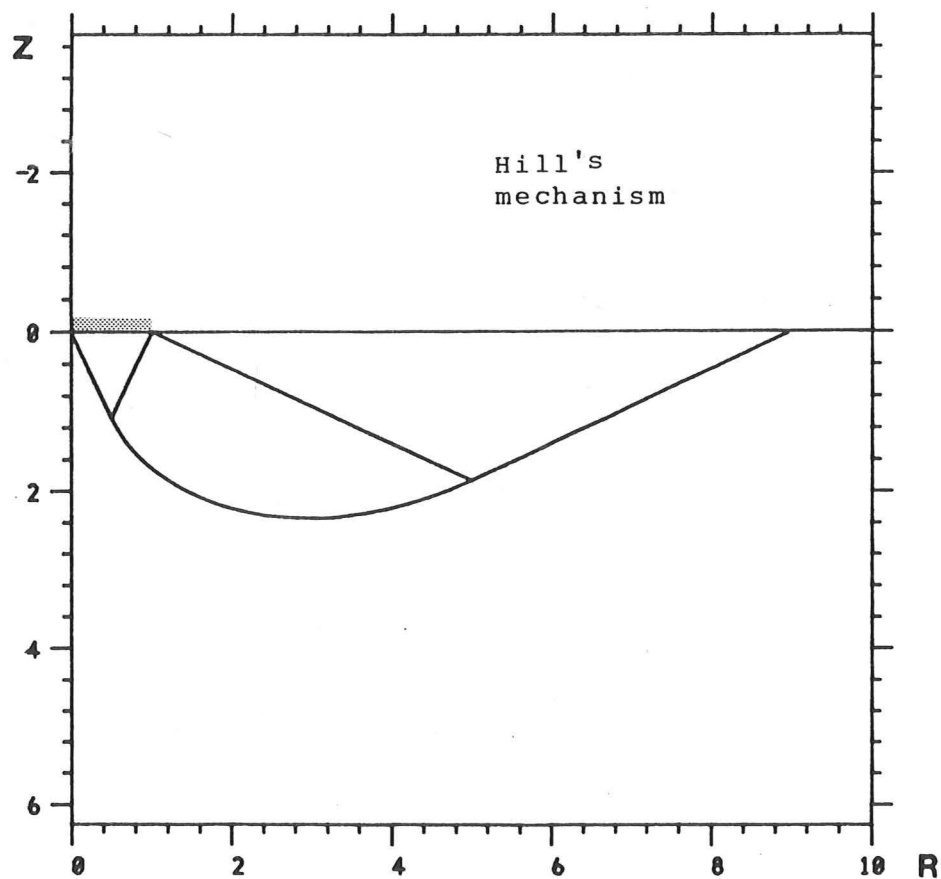
b Stress characteristics

Fig 3.12

ps

$\Omega = 10^{-3}$

$\Phi = 40$

smooth

$N\gamma$

a Footing pressure distribution

b Stress characteristics

Fig 3.13

σ_Z

AX (axisymmetric)
$\Omega = 10^3$
$\Phi = 40$
smooth
Nq
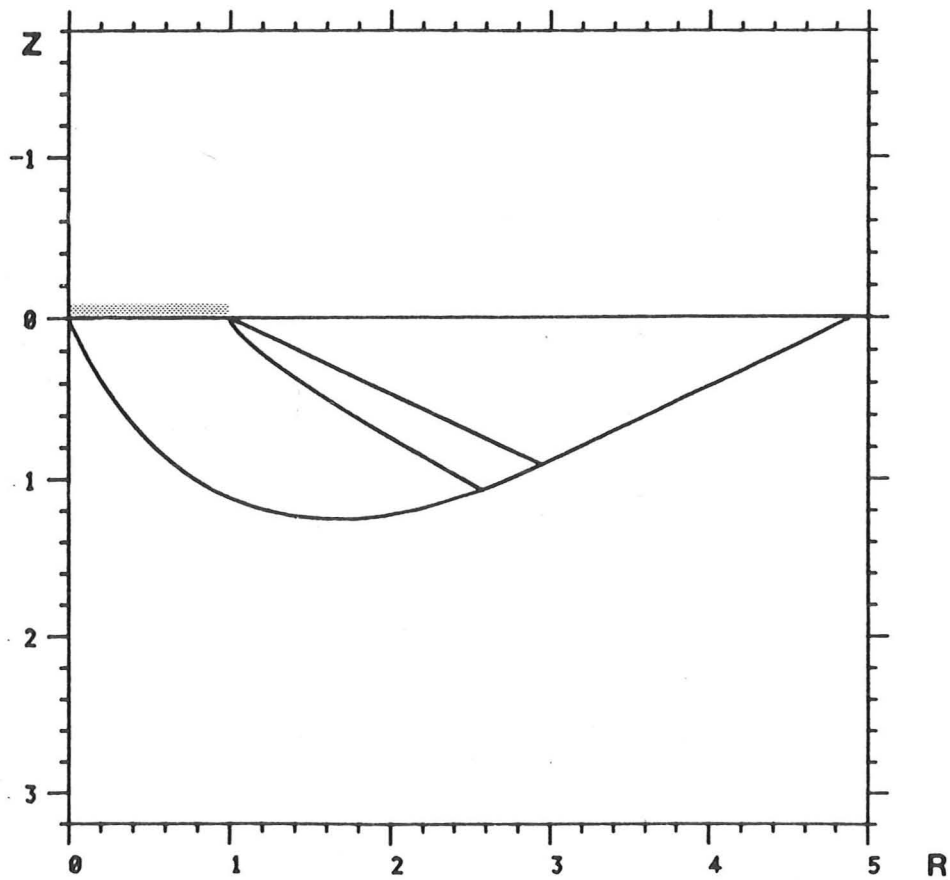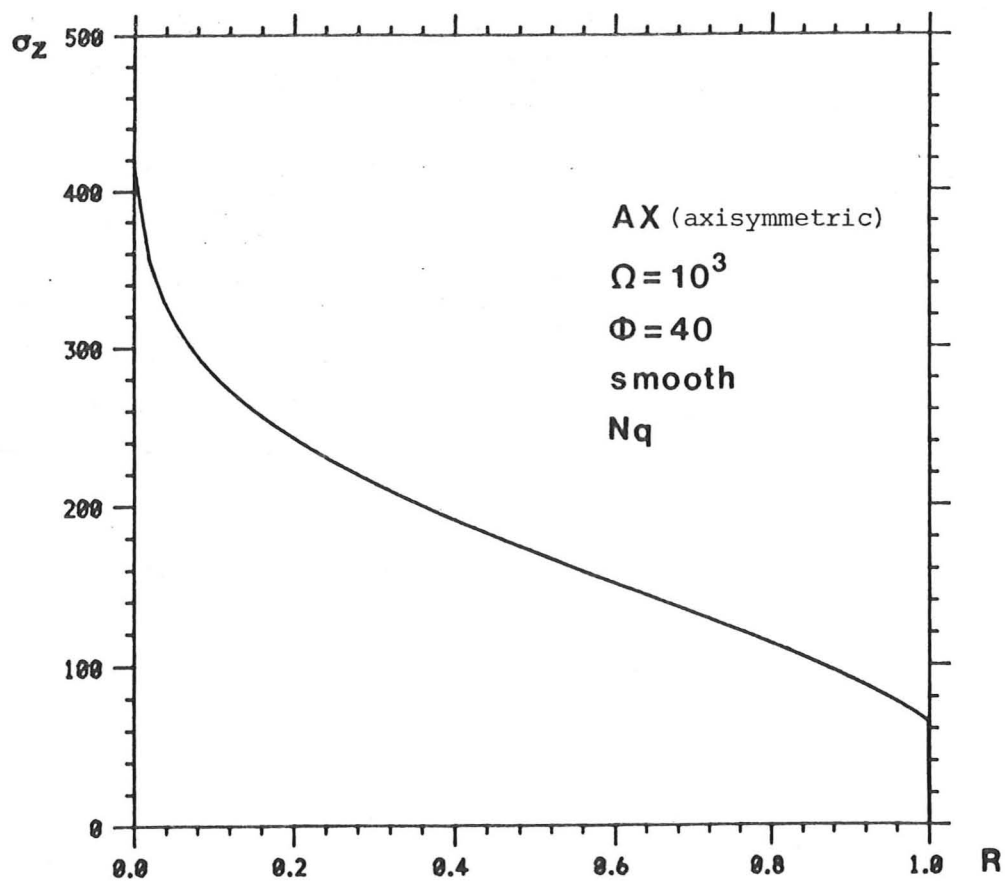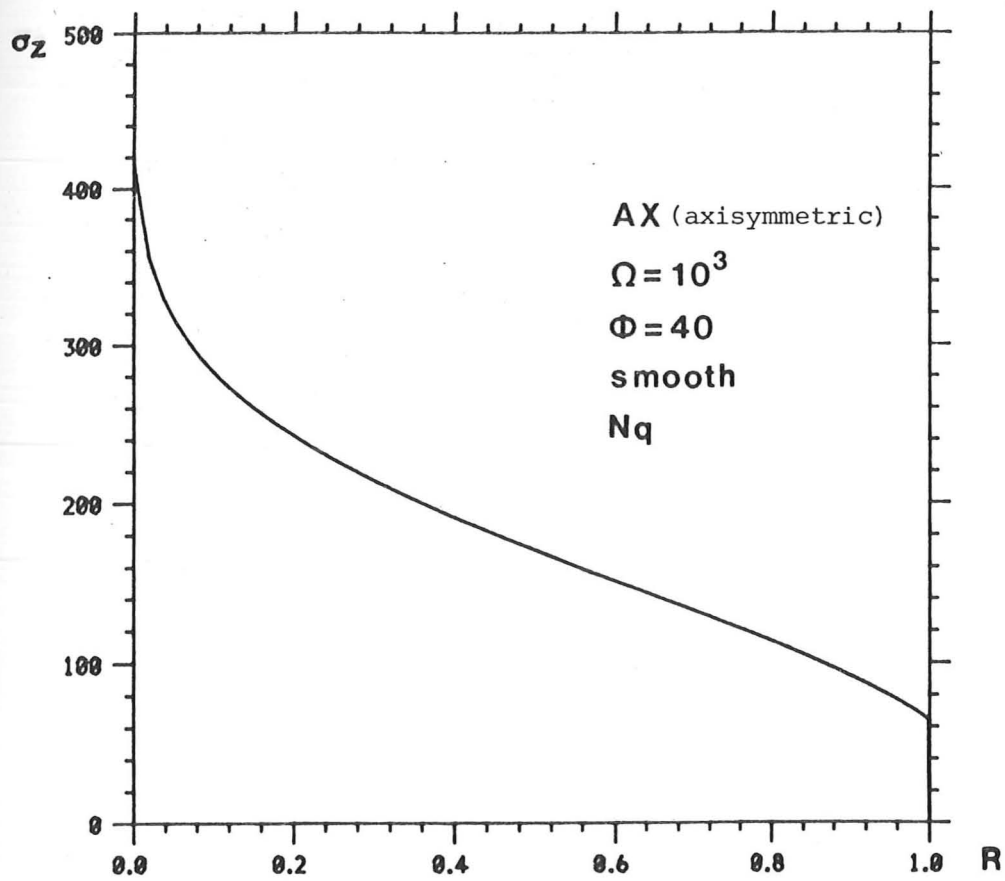
a Footing pressure distribution

b Stress characteristics

Fig 3.14

a   Footing pressure distribution

b   Stress characteristics

Fig 3.14

σ_Z

AX
$\Omega = 10^{-3}$
$\Phi = 40$
smooth
N_γ
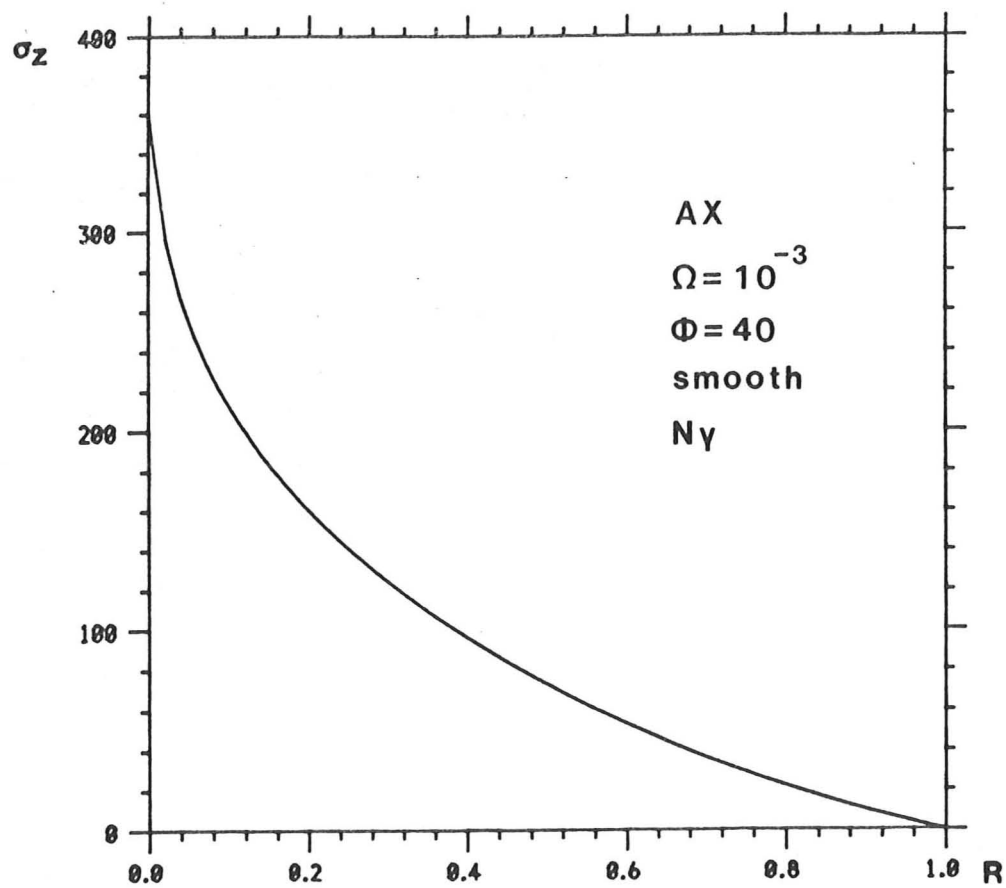
a   Footing pressure distribution
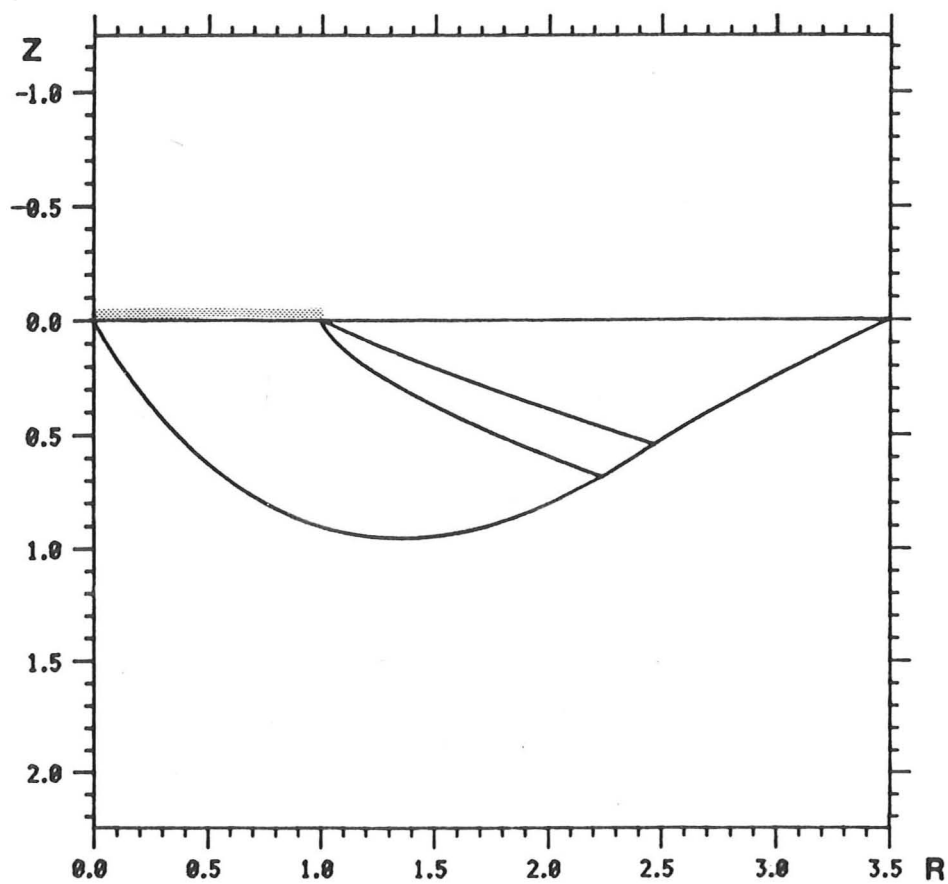
b   Stress characteristics

Fig 3.15
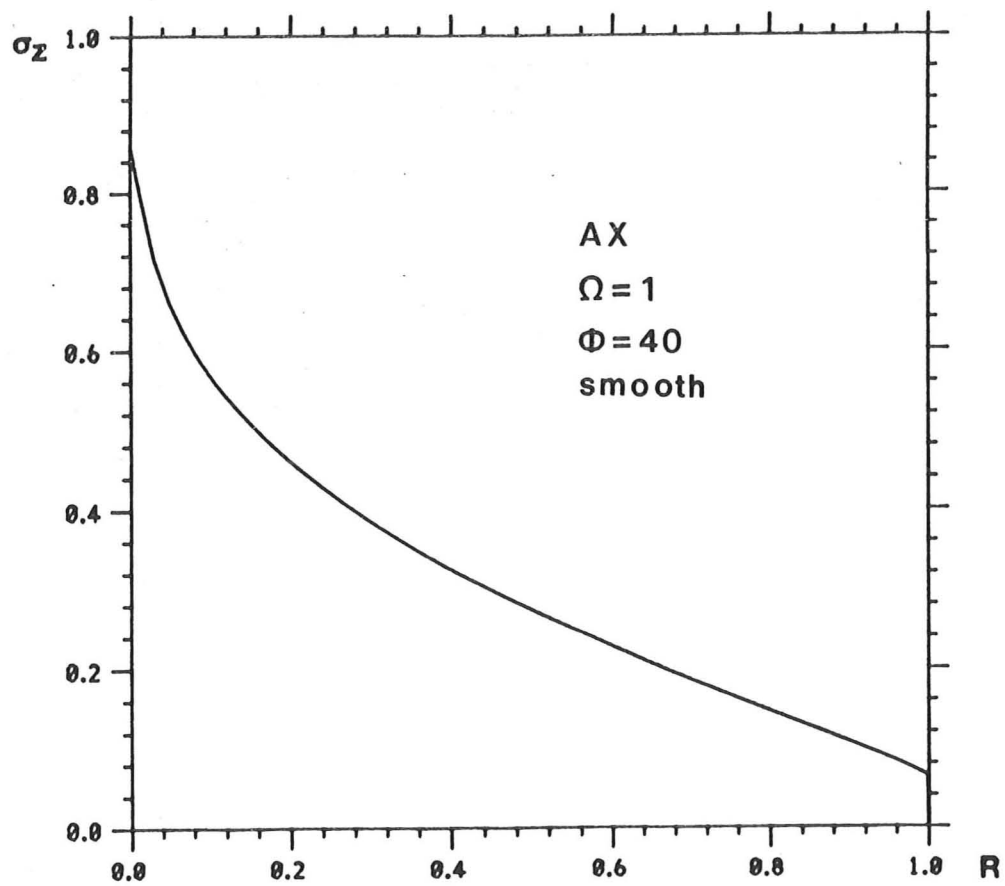
a   Footing pressure distribution
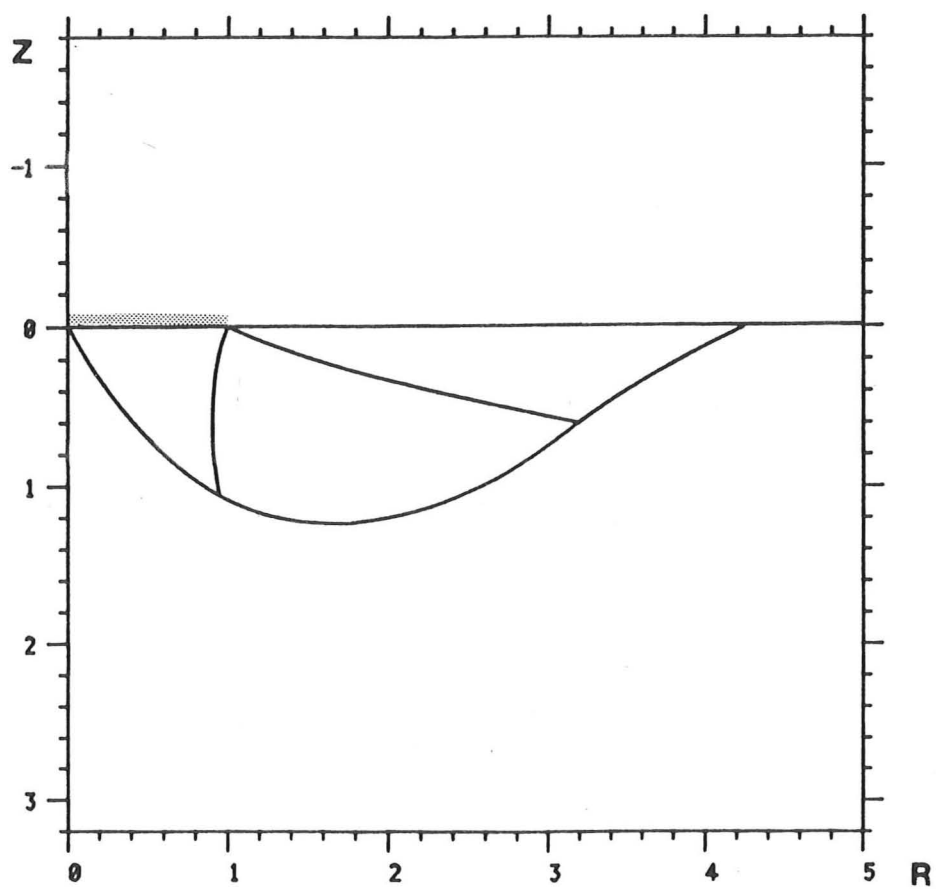
b   Stress characteristics

Fig 3.16
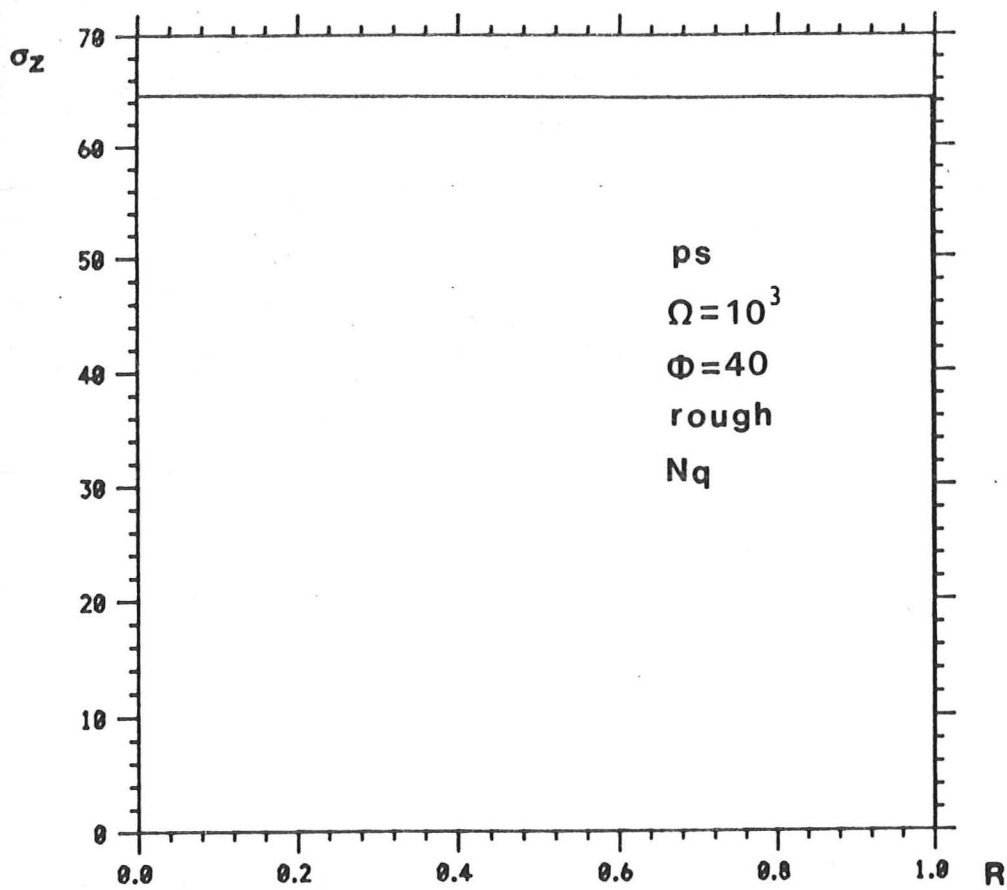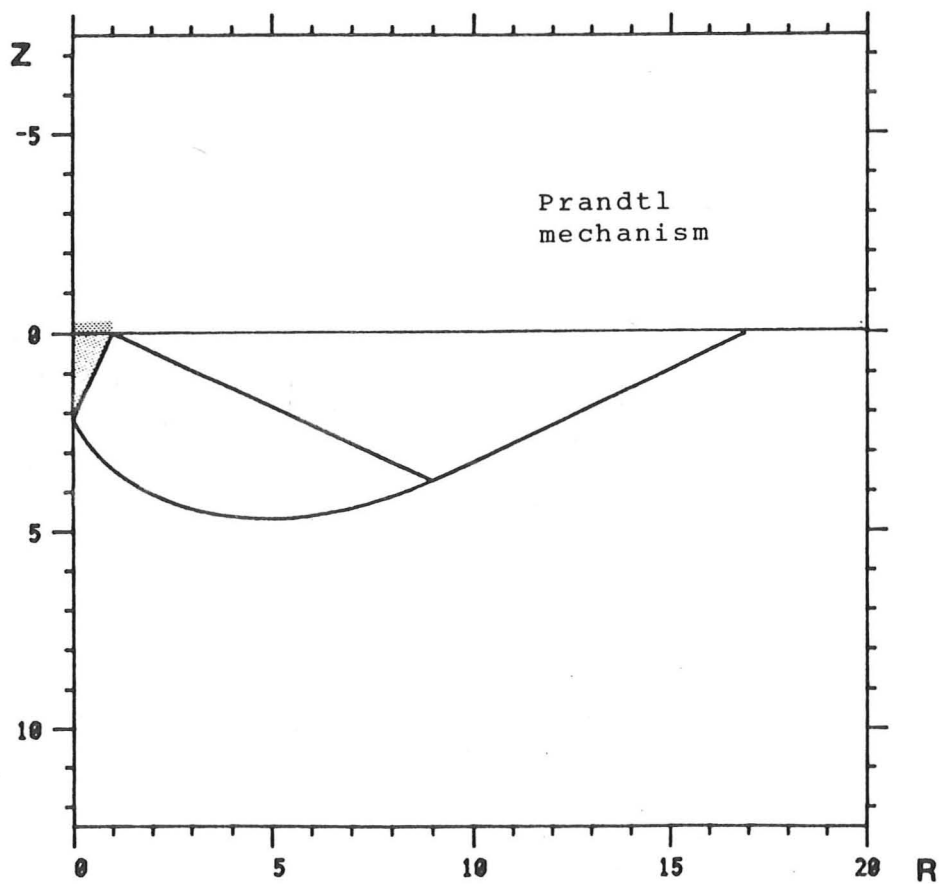
σz

ps
$\Omega = 10^3$
$\Phi = 40$
rough
Nq

a   Footing pressure distribution

Z

Prandtl
mechanism

b   Stress characteristics

Fig 3.17

σ_Z

250

200

150

100

50

0

0.0   0.2   0.4   0.6   0.8   1.0 R

ps

$\Omega = 10^{-3}$

$\Phi = 40$

rough

N_γ

a   Footing pressure distribution

Z -4

-2

0

2

4

6

0   2   4   6   8   10   12 R
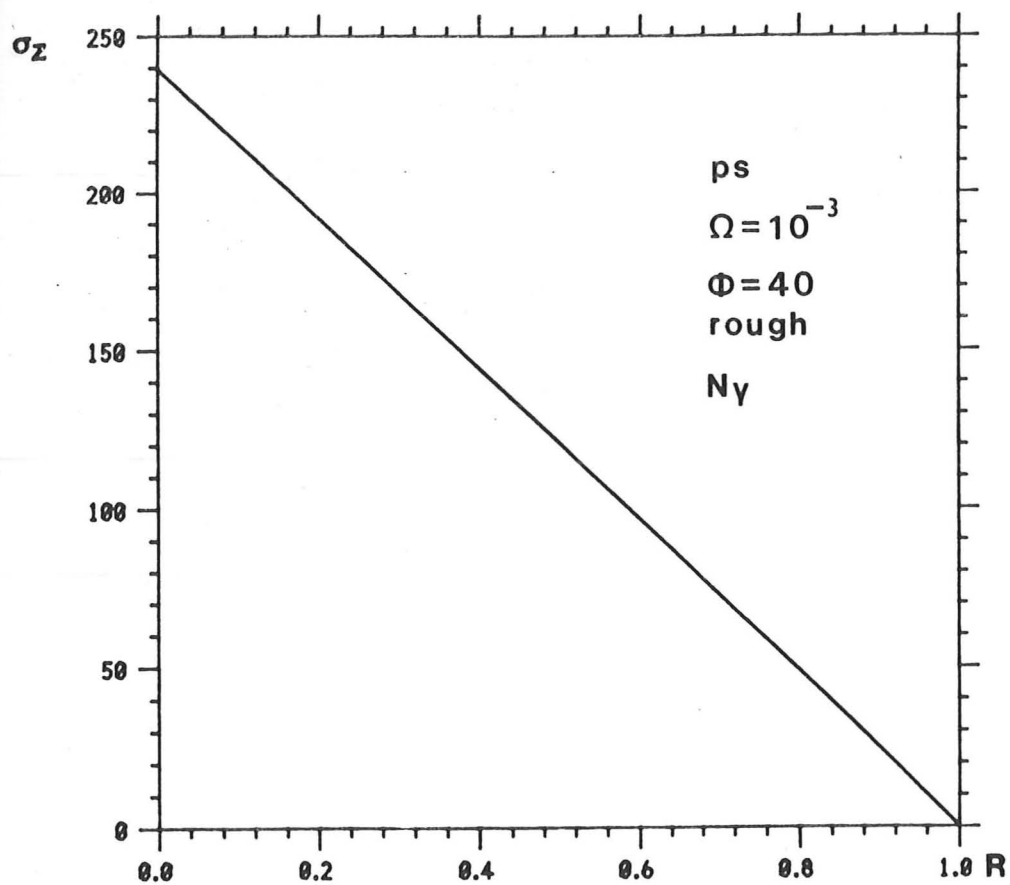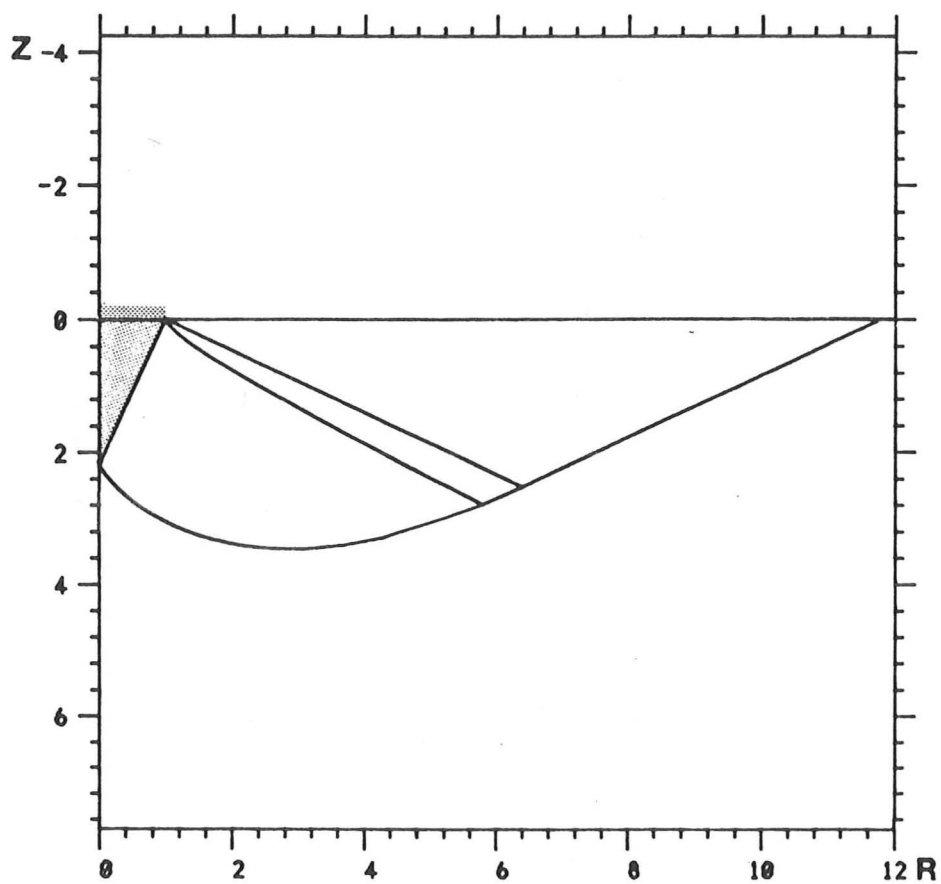
b   Stress characteristics
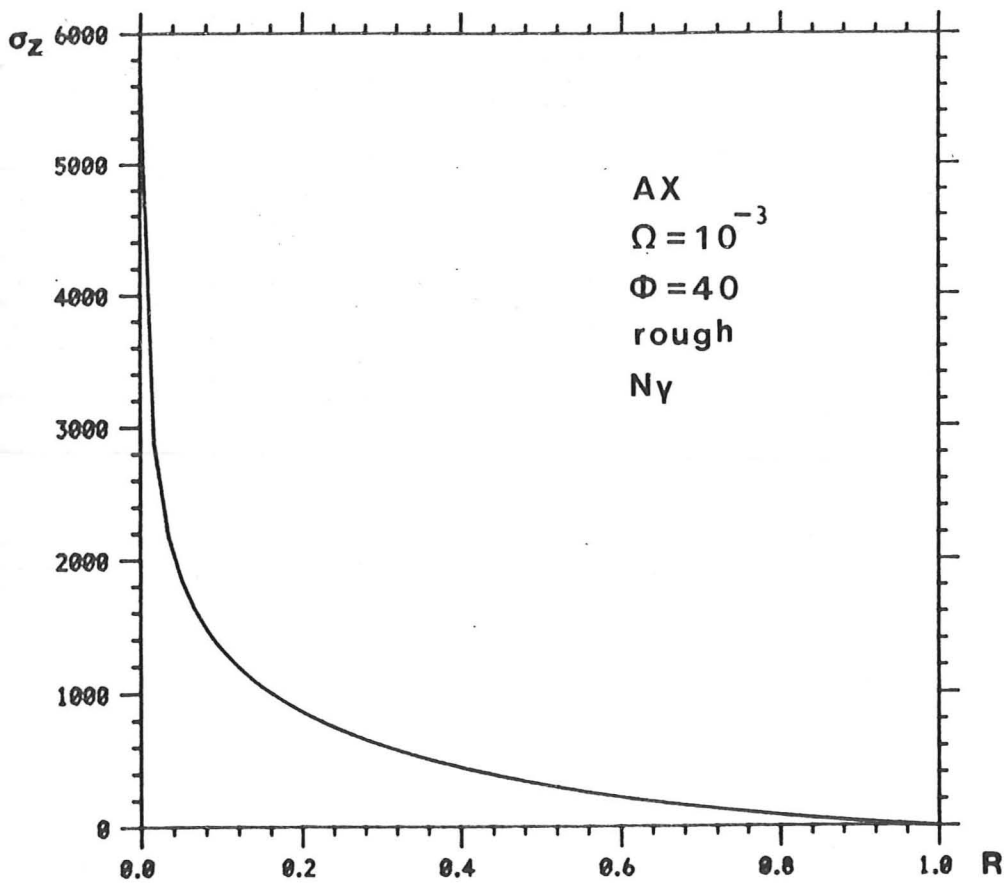
Fig 3.18

a   Footing pressure distribution
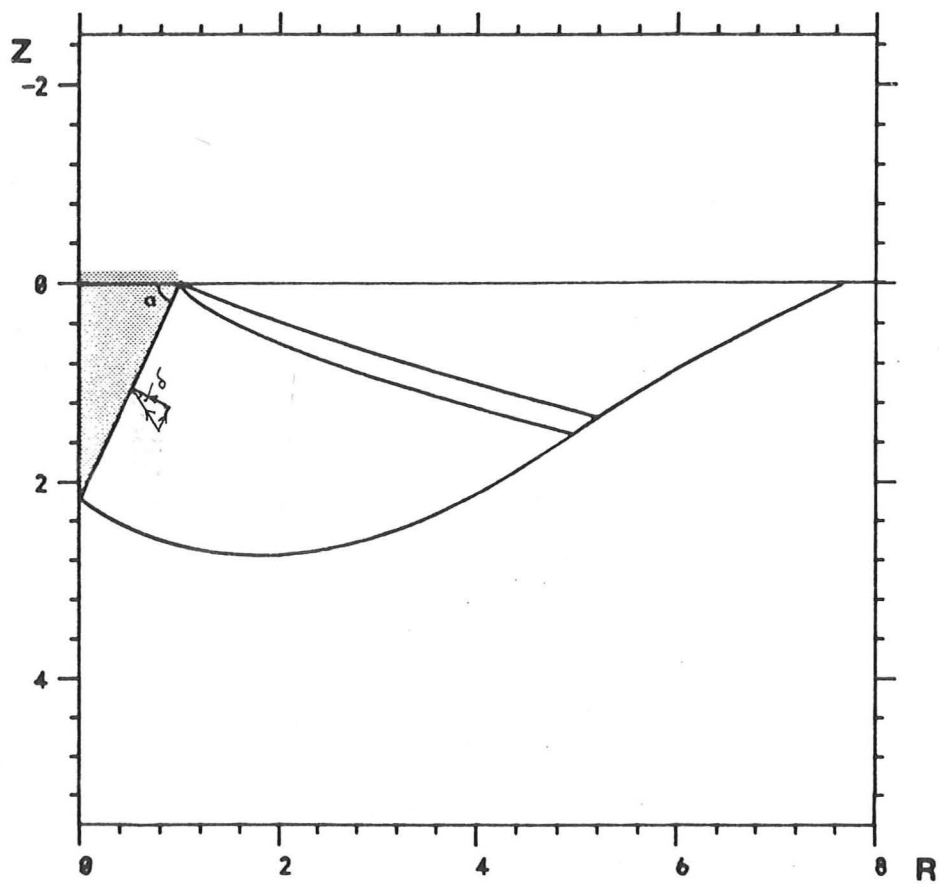
b   Stress characteristics

Fig 3.19
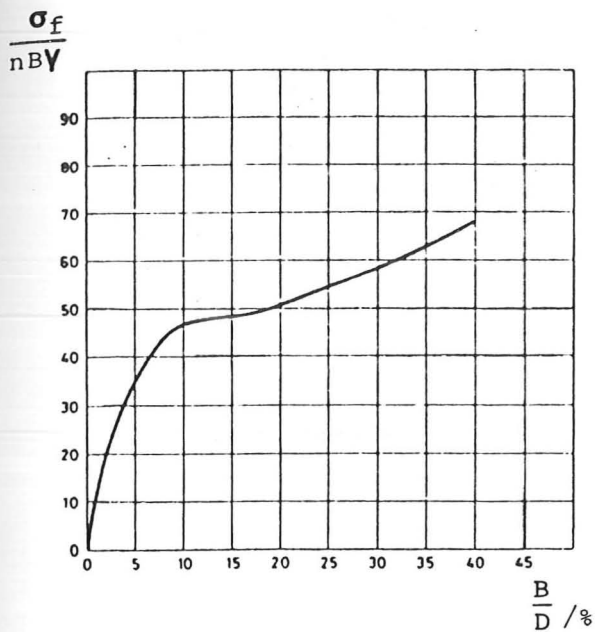
Reference test on saturated
Fontainbleau sand
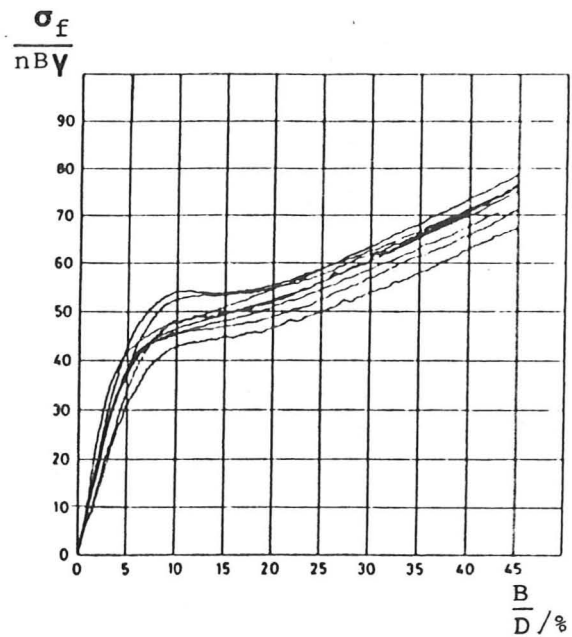
Typical load displacement
curves

Fig 3.20   Typical centrifuge test results on shallow
circular footing (After Corté et al, 1988)
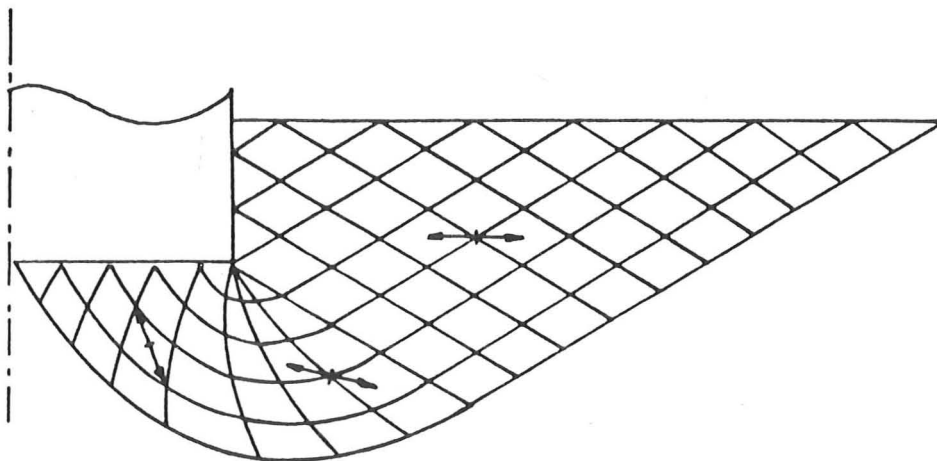
Fig 3.21   Extended stress field to account for
penetration (After Larkin,1968)

(a) Extended stress field to account for penetration

(b) Effects of shear stress on the equivalent free surface on N_q (After Meyerhof, 1951)

(c) Associated Mohr circle diagram
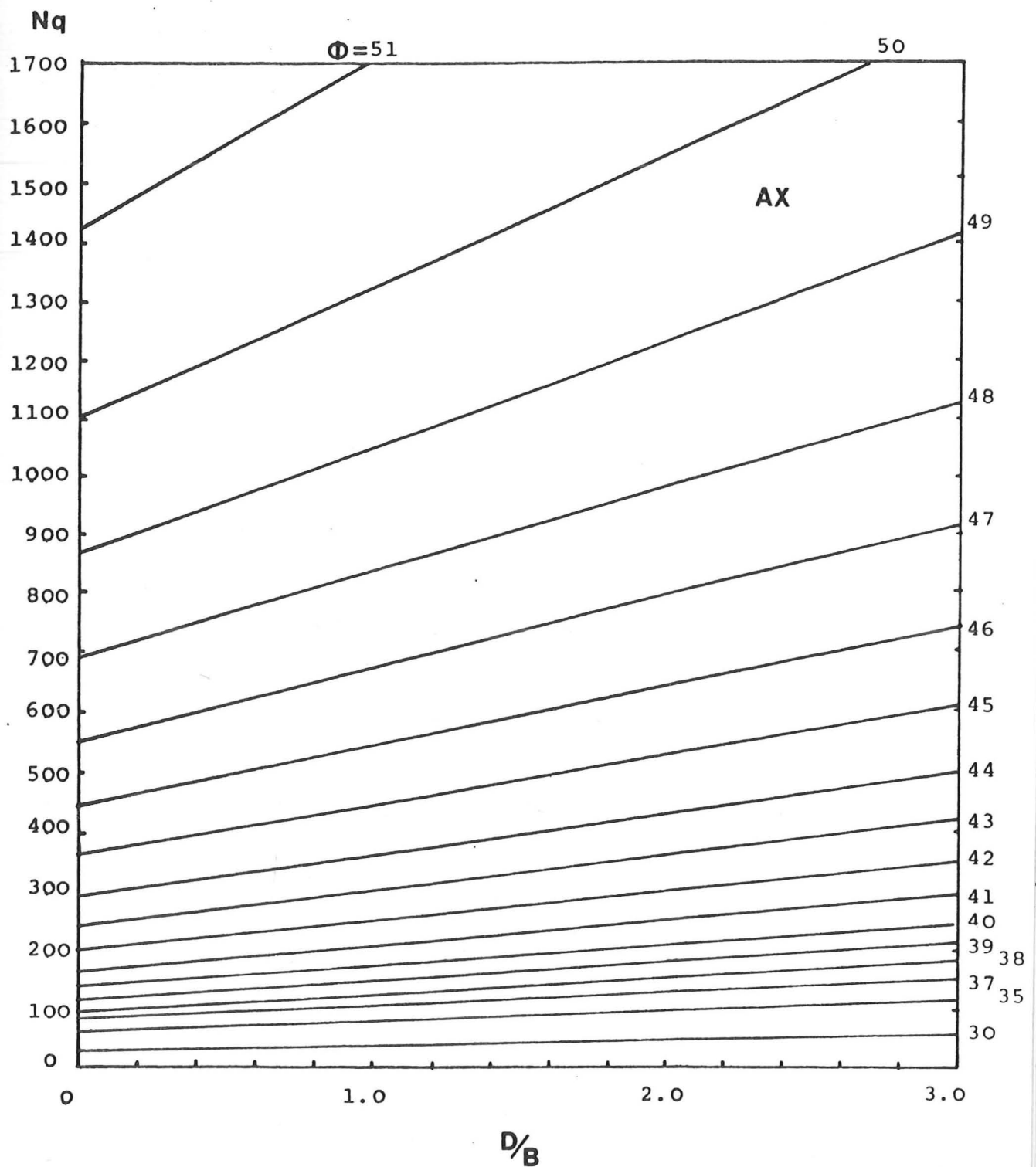
Fig 3.22

Fig 3.23 Theoretical bearing capacity of shallow footing on weightless soil with overburden with shear strength
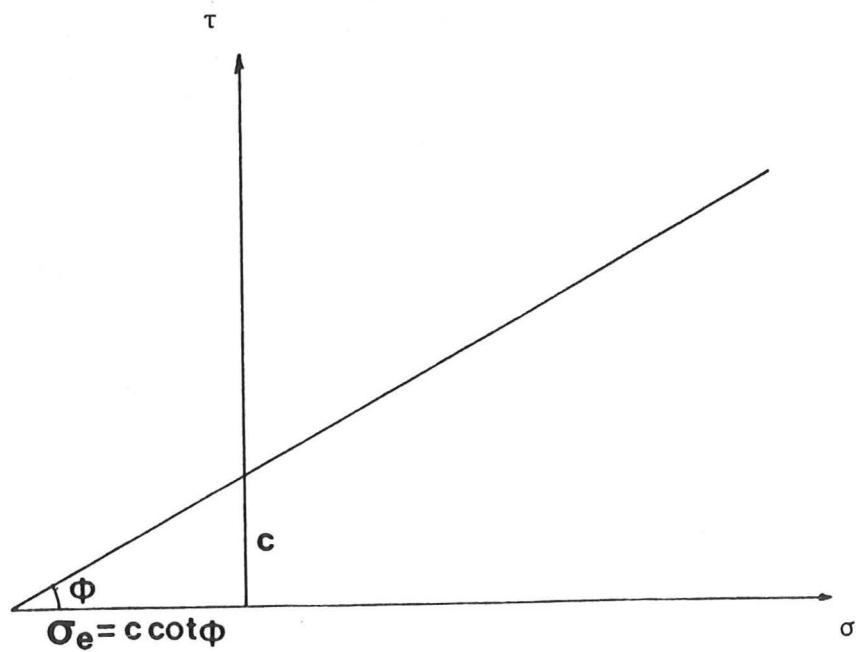
Fig 3.24   Mohr-Coulomb envelope on triaxial
plane

(a) Principal stress directions beneath a collapsing strip footing on weightless soil

(b) Condition when tangent Ø is not applicable

(c) Neighbouring zones of limiting friction

(d) Stresses in equilibrium across boundary XX

(e) Mohr circles of stress beneath a collapsing strip footing
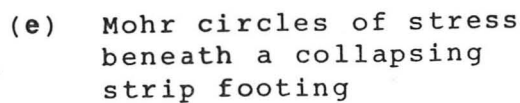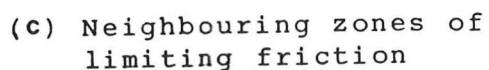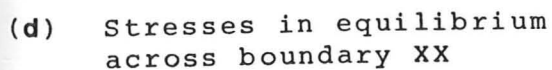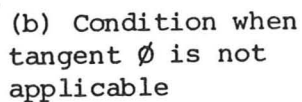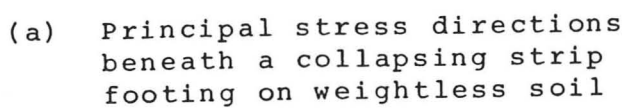
Fig 4.1
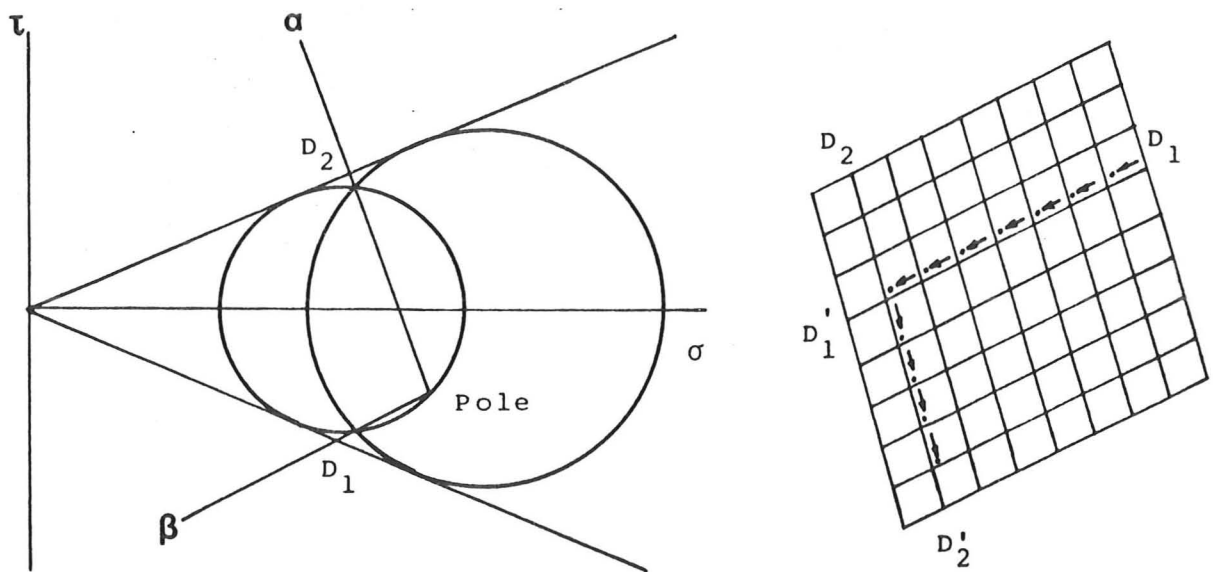
Fig 4.2   Mohr circles of stress across two families
           of discontinuities
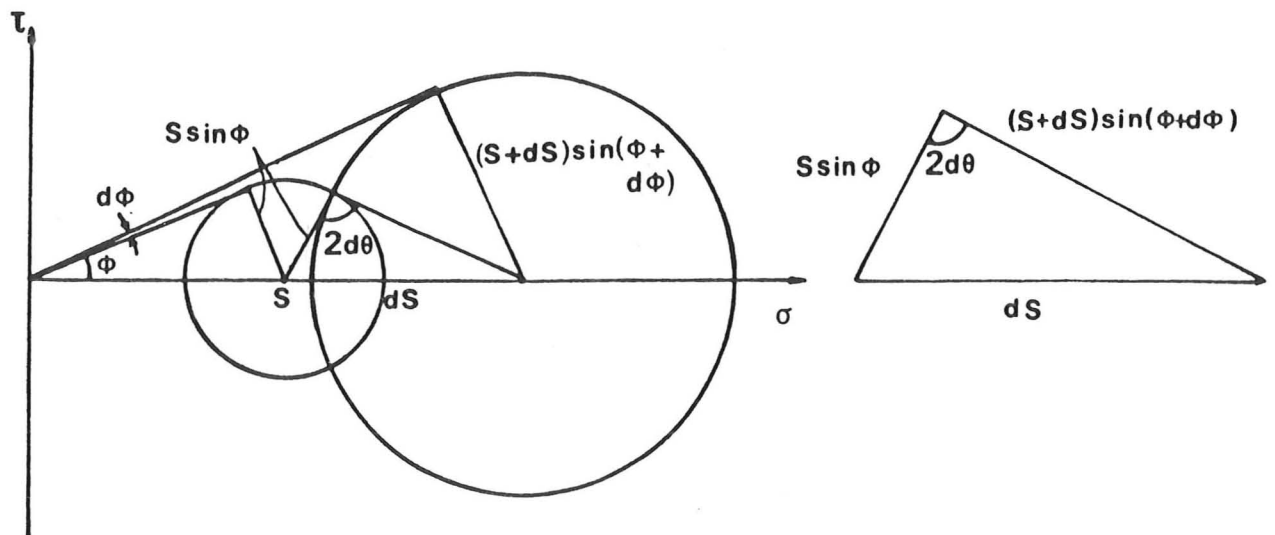
Fig 4.3   Effects of varying ∅ on the stress rotation
           equation
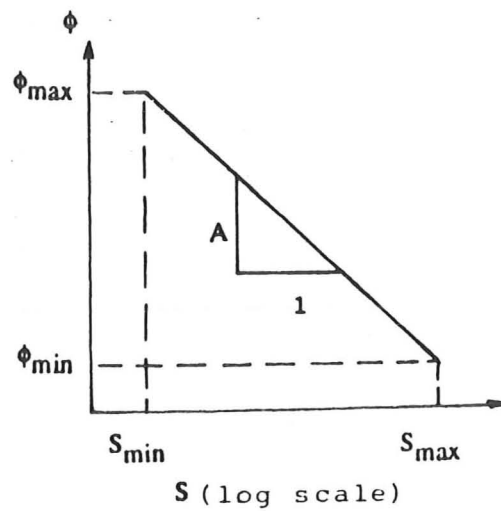
Fig 4.4   Typical effects of pressure on $\emptyset$
for sands

Fig 4.5   Flow chart for subroutine
CALPHI

Fig 4.4   Typical effects of pressure on ϕ
          for sands

Fig 4.5   Flow chart for subroutine
          CALPHI

INPUT σ_o
&
INITIALIZE ϕ

PASSIVE ZONE
$$S = \frac{\sigma_o}{1 - \sin\phi}$$

CALL
CALPHI

IF
$|\phi_i - \phi_{i-1}|$
< 0.01

NO

YES

OUTPUT
$\phi_o = \phi$
$$S_o = \frac{\sigma_o}{1 - \sin\phi_o}$$

FAN ZONE
IMPOSE $\dfrac{dS}{S} = 0.1$
$$S_i = S_{i-1} + dS/2$$

CALL
CALPHI

$$d\theta = \sqrt{\frac{(dS/S - \tan\phi\, d\phi)^2 - \sec^2\phi\, d\phi^2}{4\tan^2\phi}}$$
$$\theta_i = \theta_{i-1} + d\theta$$

IF
$\theta \geq \pi/2$

NO

YES

ACTIVE ZONE
OUTPUT $\phi_f = \phi$
$s_f = s$
$\sigma_f = s_f(1 + \sin\phi_f)$

END
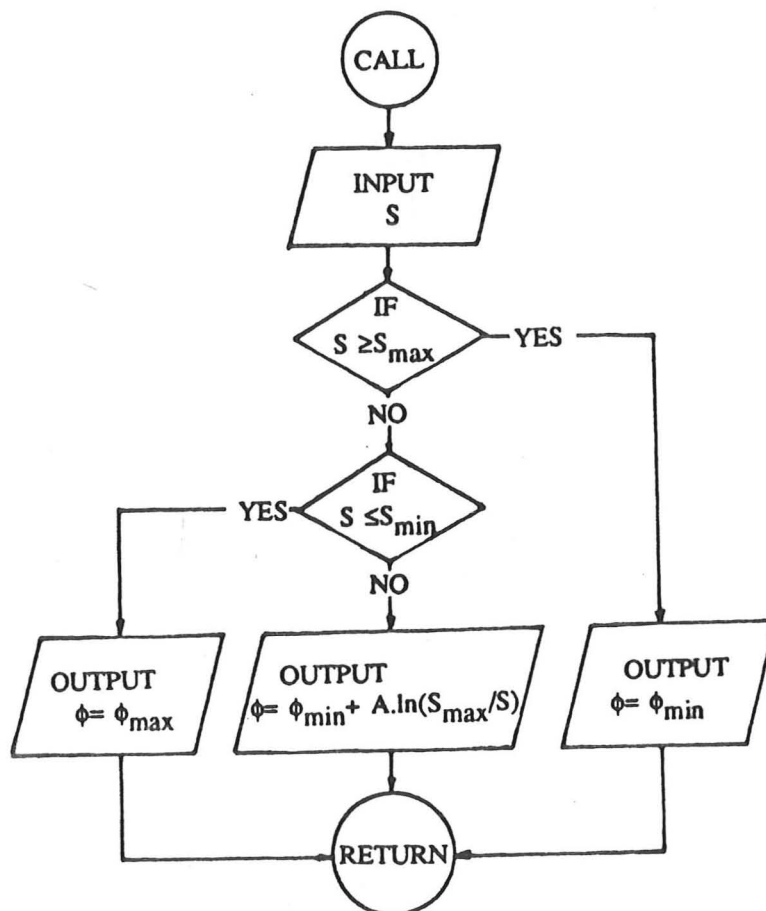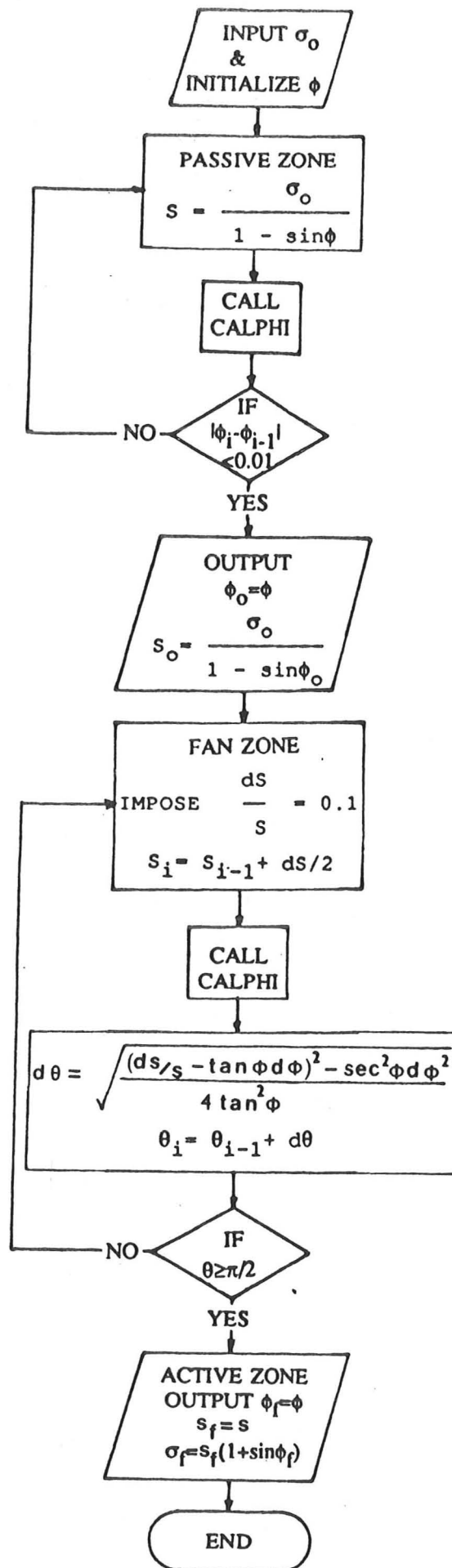
Fig 4.6   Flow chart for program EXPRAN
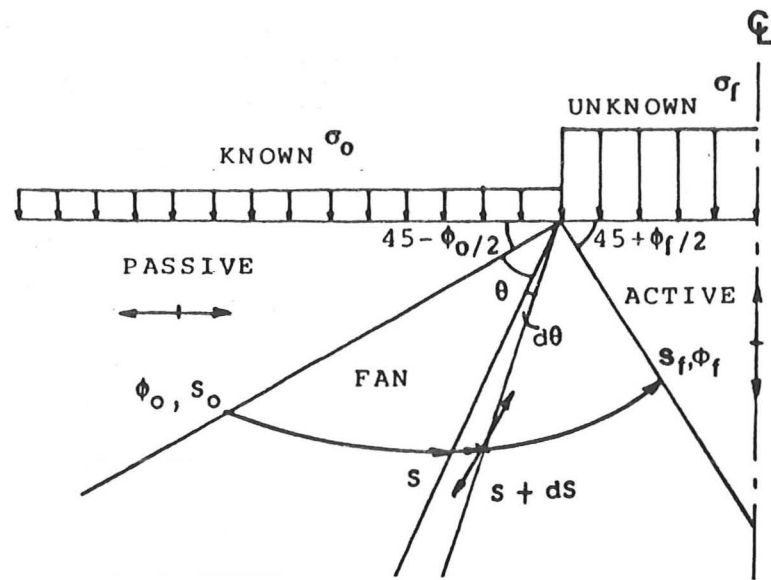
Fig 4.7   Solution scheme for program EXPRAN
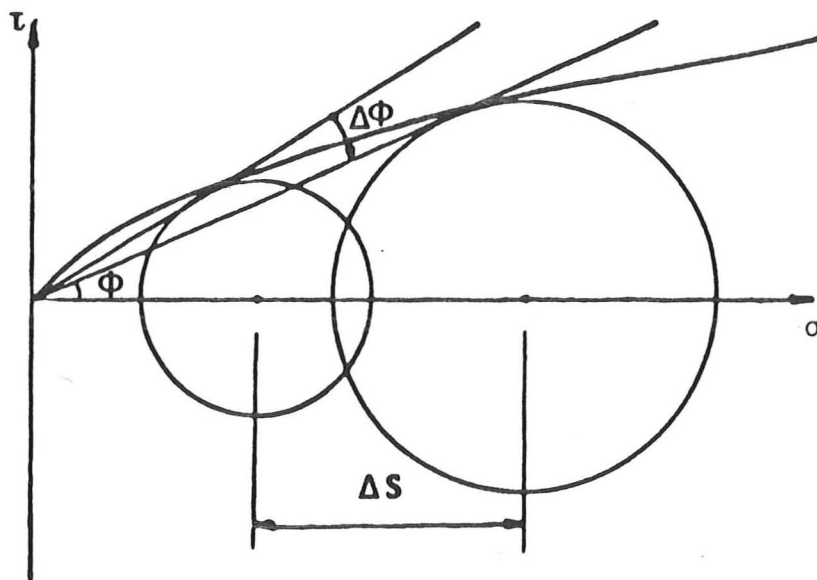
(a)   Typical shear strength for sands
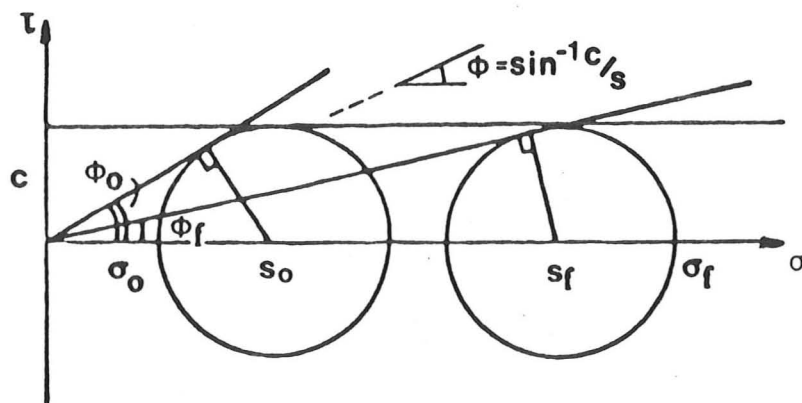
(b)   Cohesion expressed in terms of secant $\emptyset$

Fig 4.8
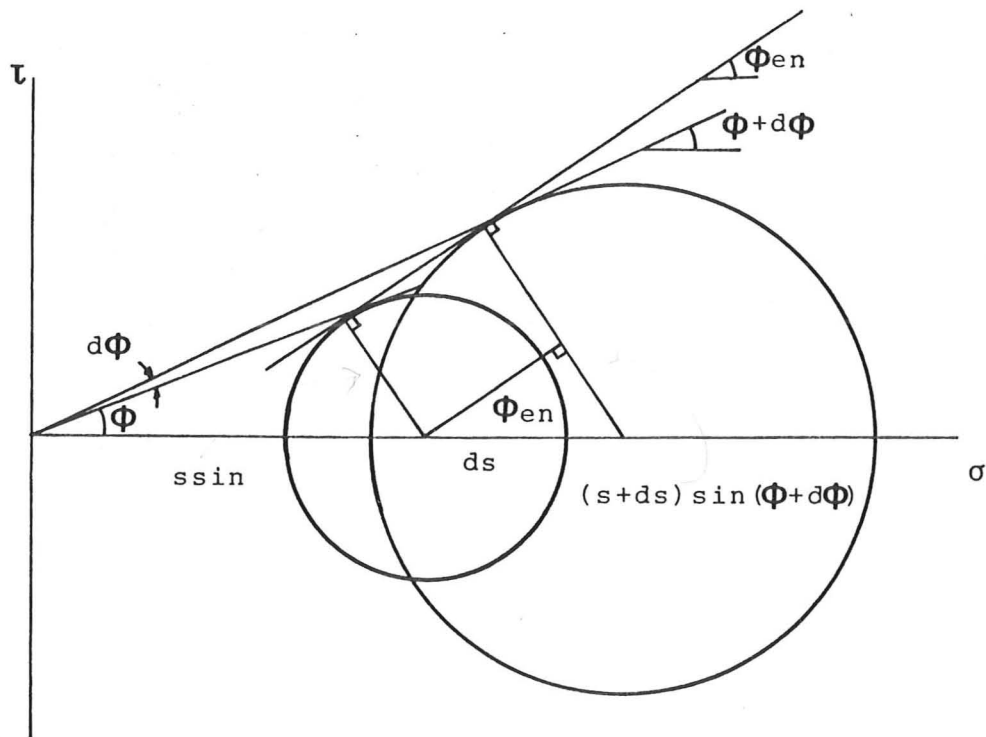
Fig 4.9   Effects of varying ∅ on ∅en
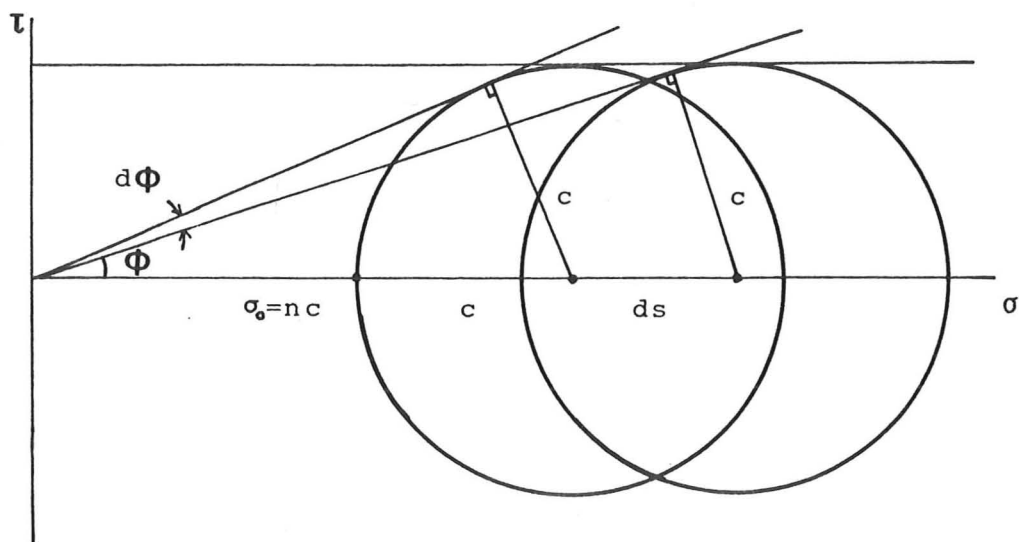
Fig 4.10   Effects of σ_0 on $\dfrac{d\emptyset}{ds}$ for a purely

cohesive material
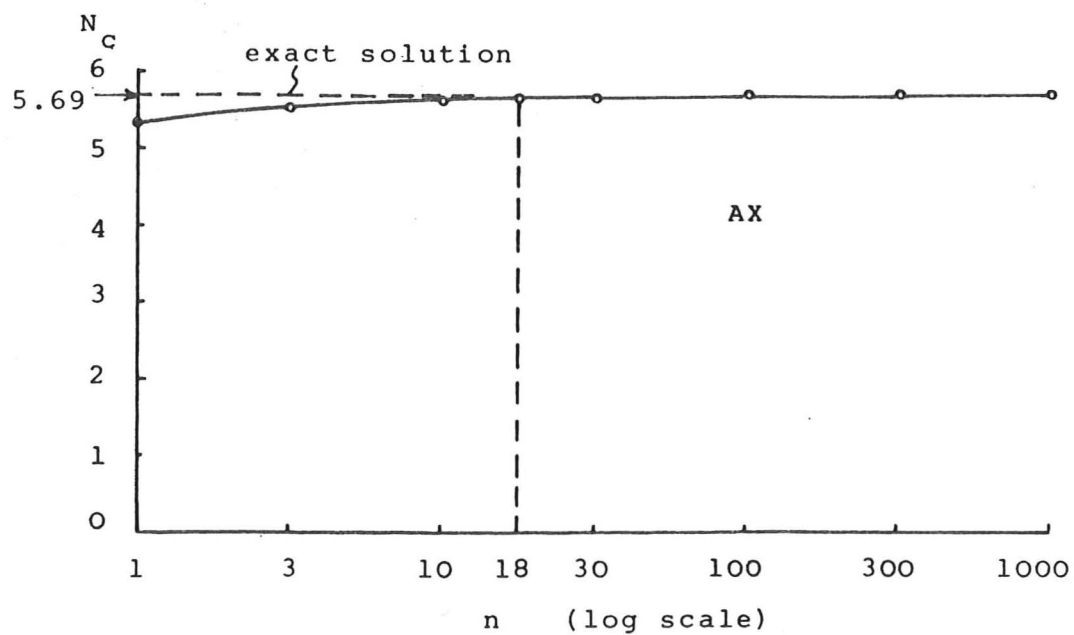
(a) Axisymmetric strain
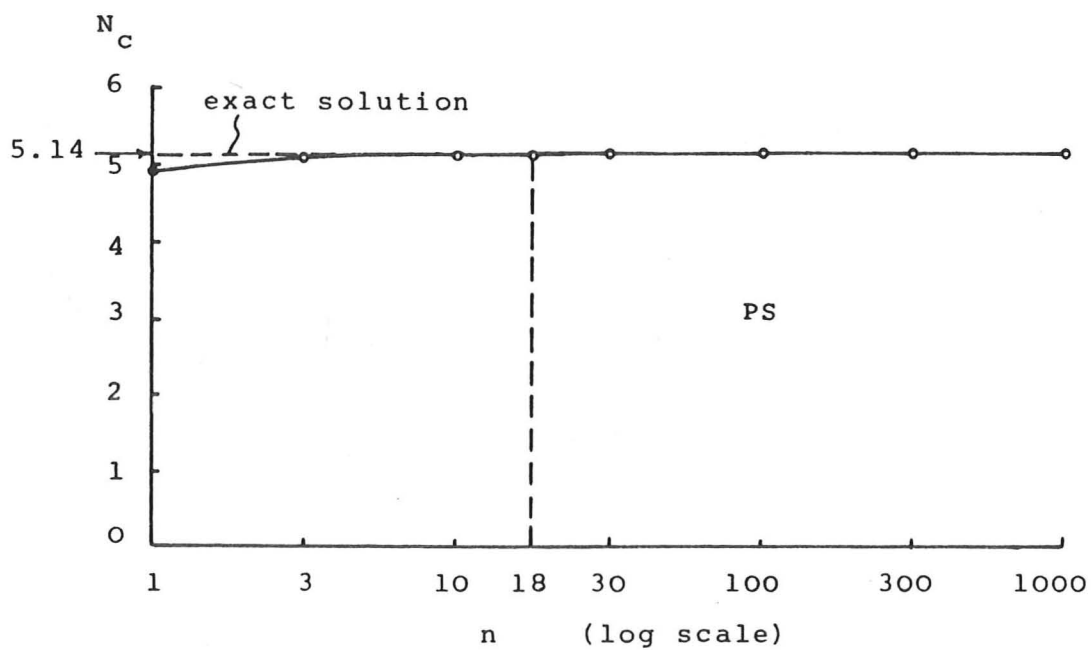
(b) Plane strain

Fig 4.11   Effects of σ_o on N_c

ps
c ≠ 0
Φ = 0
smooth
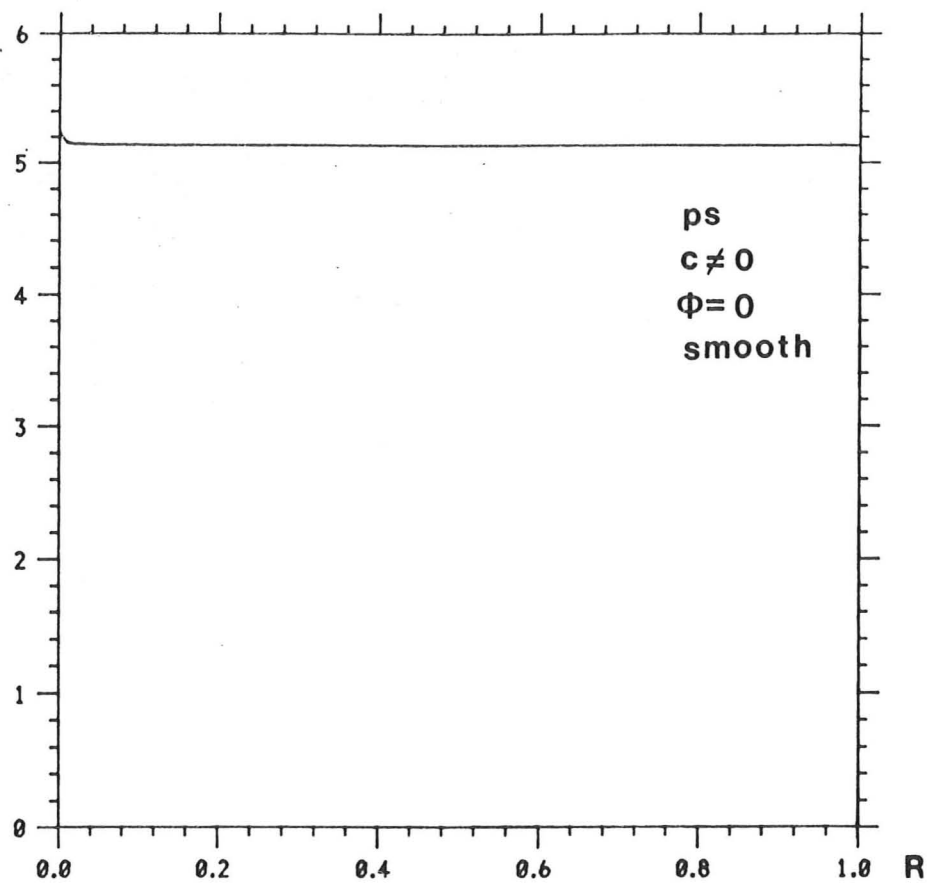
a   Footing pressure distribution
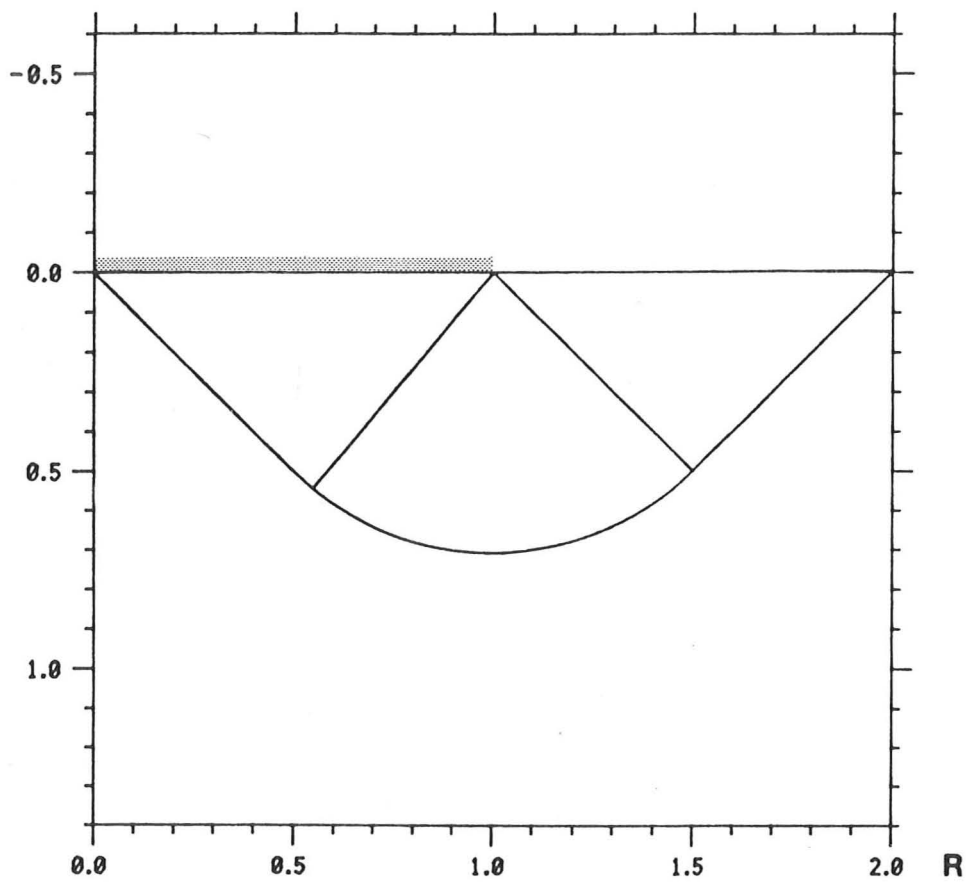
b   Stress characteristics

Fig 4.12
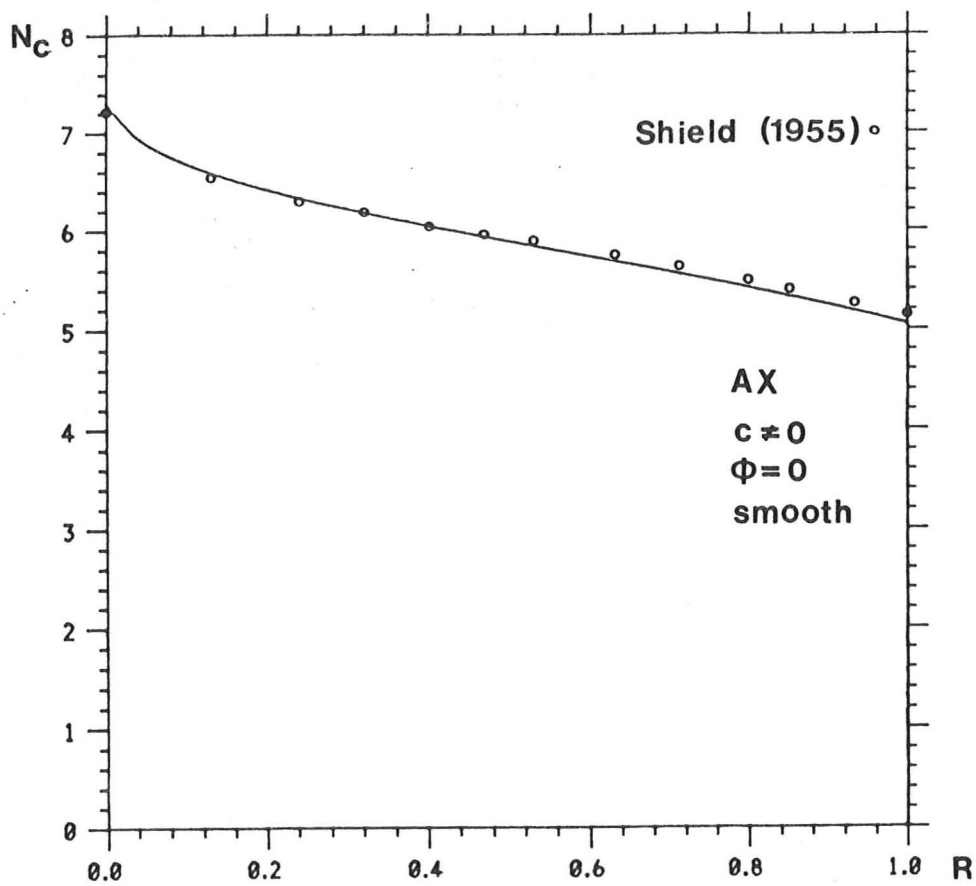
a   Footing pressure distribution
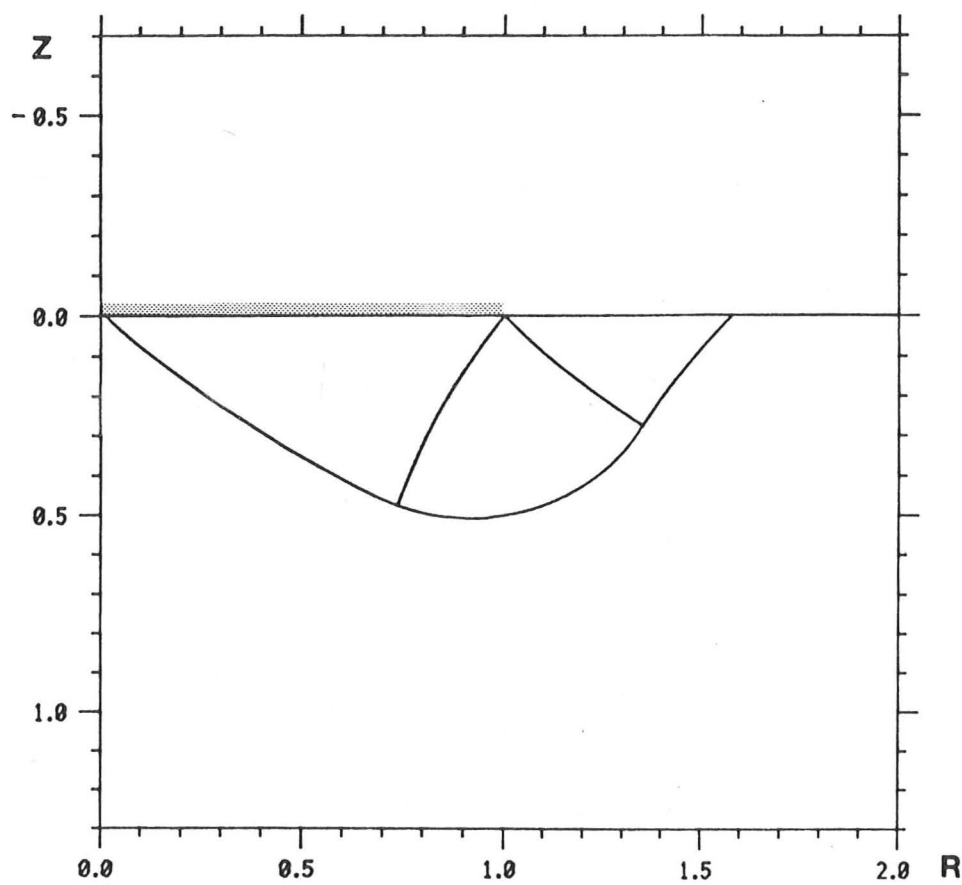
b   Stress characteristics

Fig 4.13
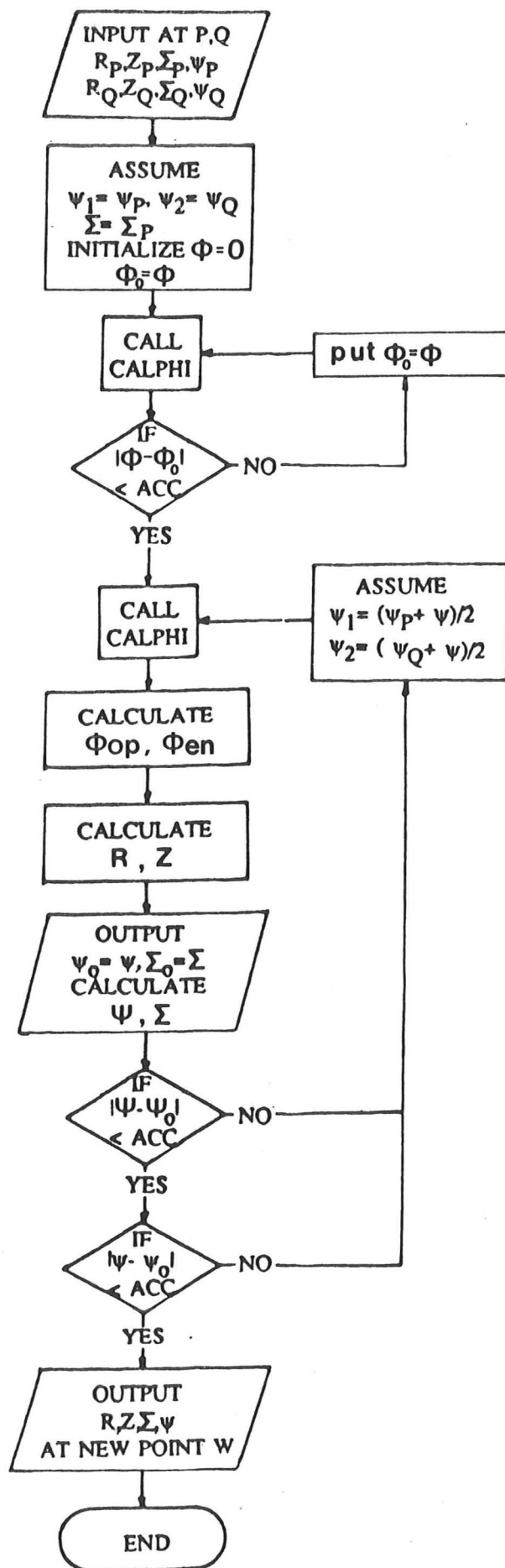
Fig 4.14 Flow chart showing the computation
scheme for R,Z,Ψ and Σ in program
VARIPHI
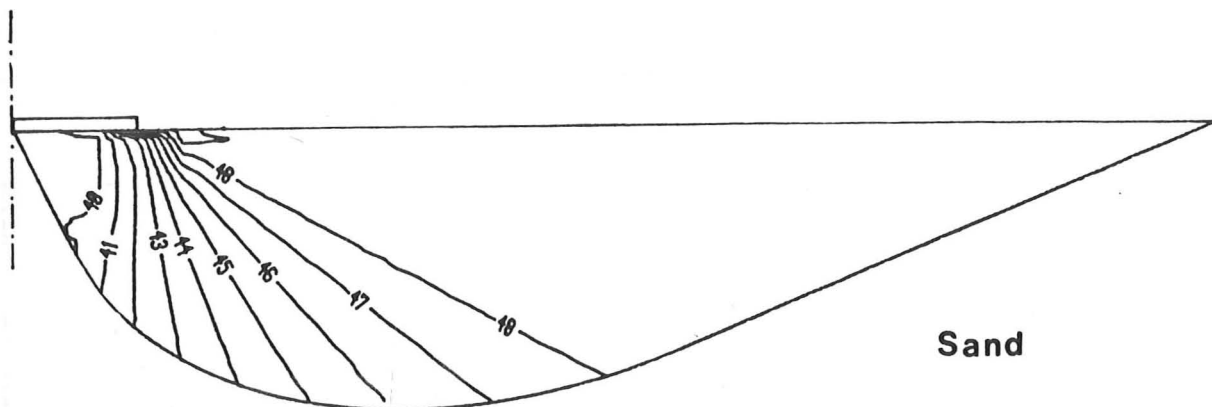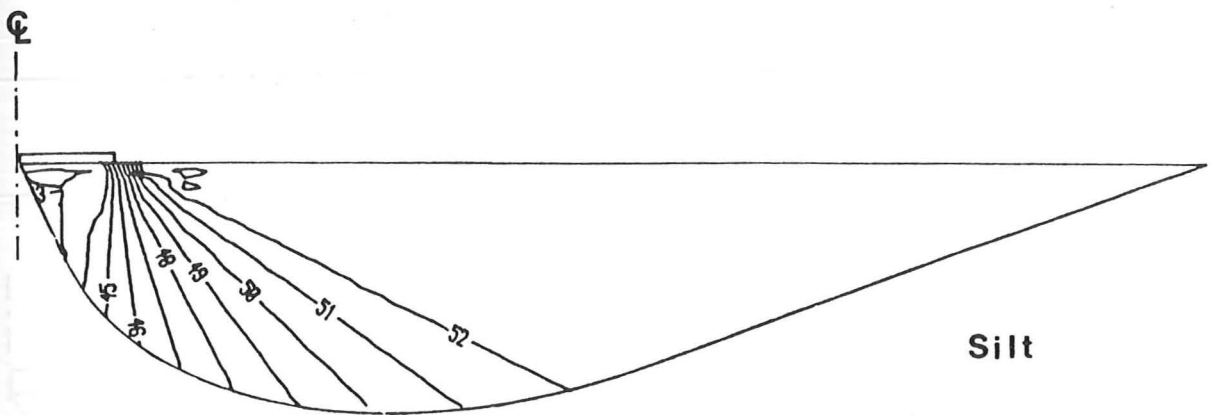
Silt

Sand

PS , N_q , σ_o = 50 kPa

Fig 4.15   Contour map of varying $\emptyset$ under smooth strip
           footing

$\sigma_o = 10\,kPa$

50

200

AX, N_q
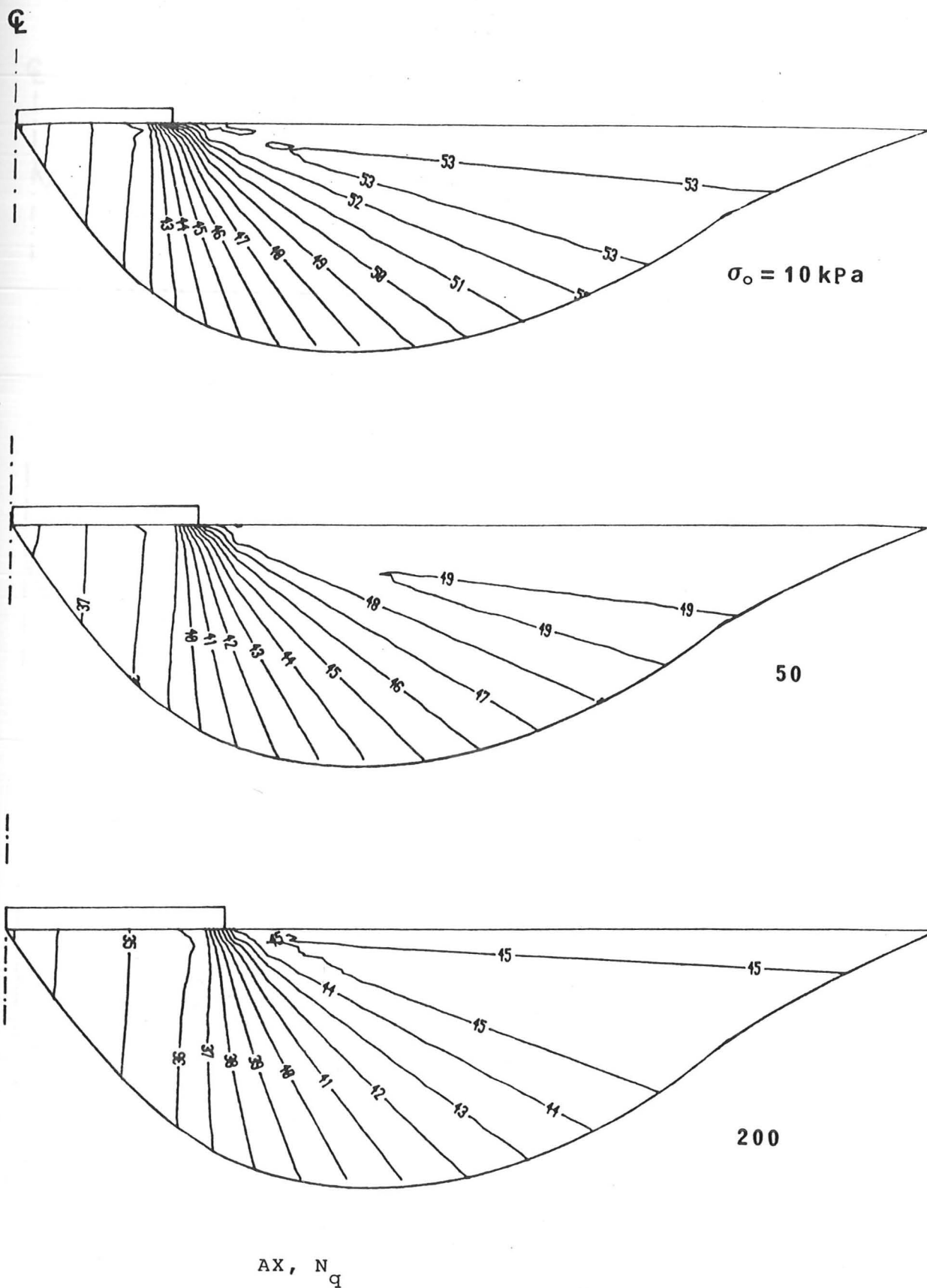
Fig 4.16   Contour map of varying Ø under smooth
circular footing on sand

$\sigma_o = 10\,kPa$

50

200

AX, N_q
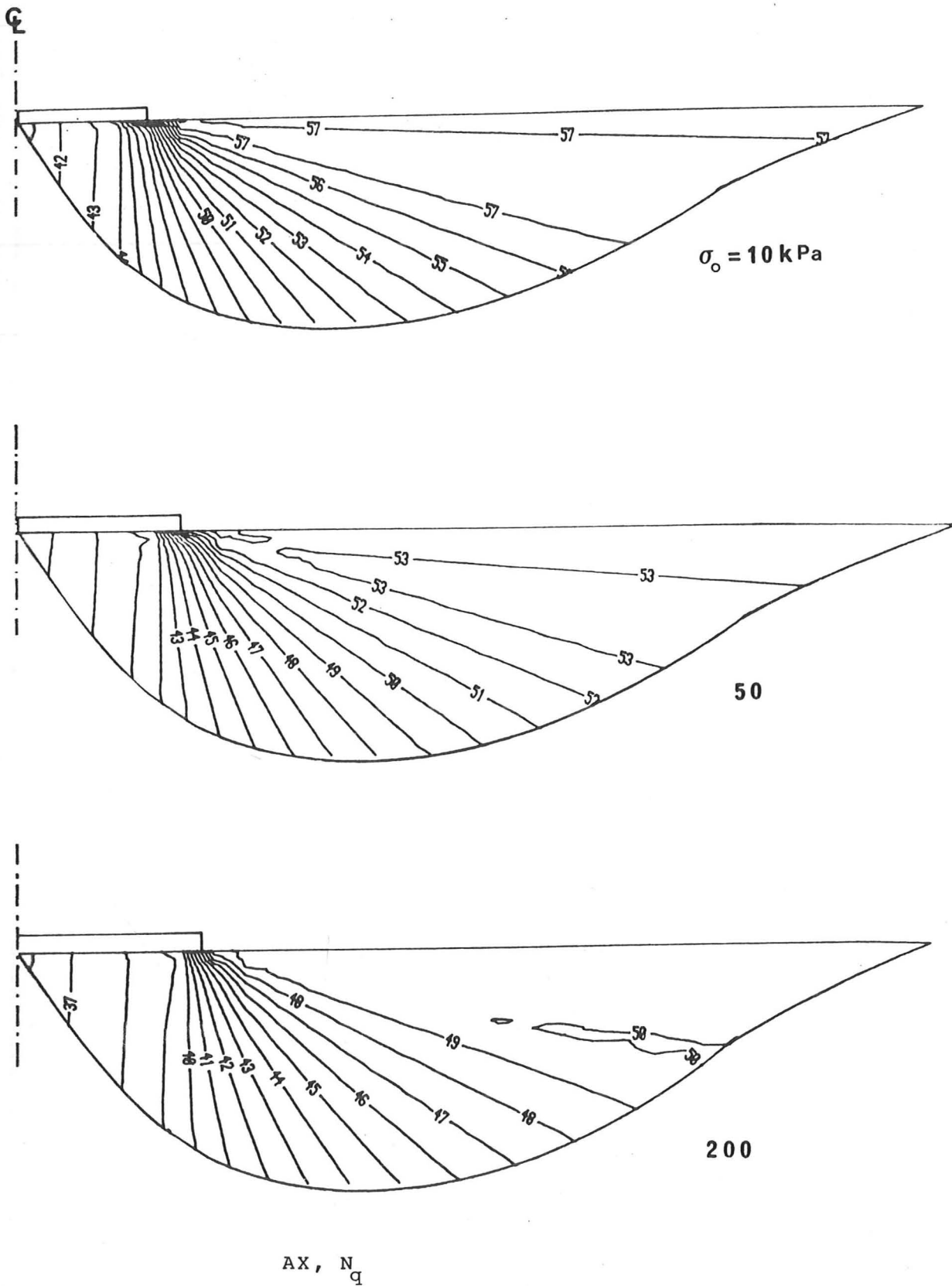
Fig 4.17   Contour map of varying $\emptyset$ under smooth
circular footing on silt

B = 0.4 m

1.42

5.0

AX, Nγ

Fig 4.18   Contour map of varying ∅ under rough
circular footing on sand

B=0.4m

1.42

5.0

AX, Nγ
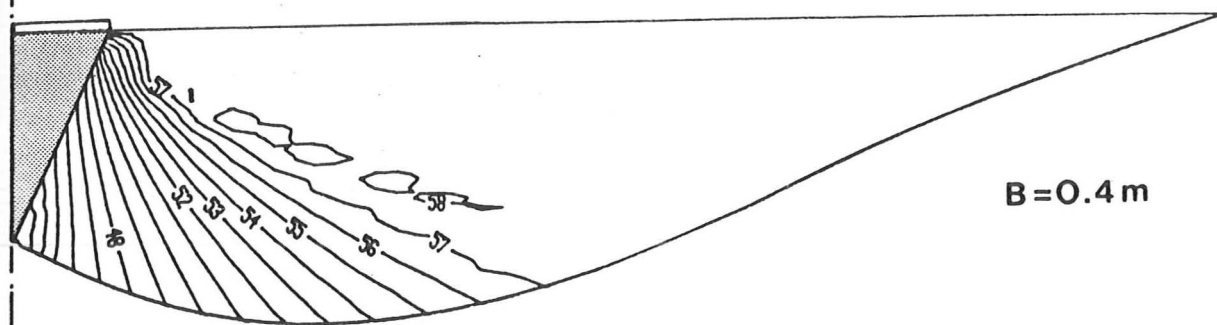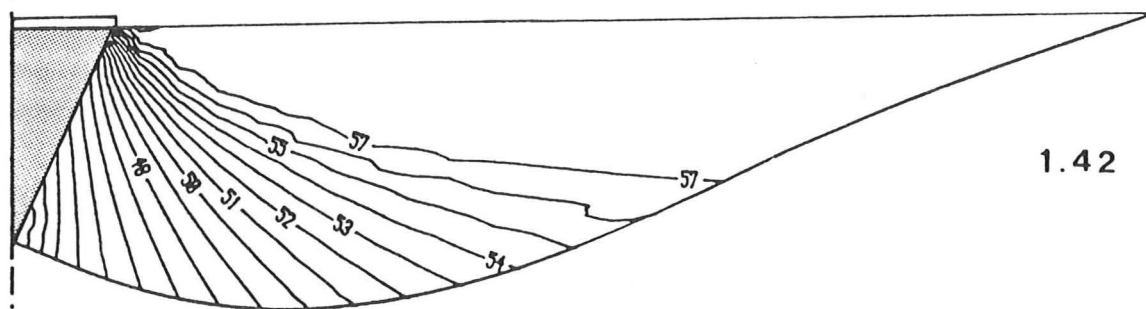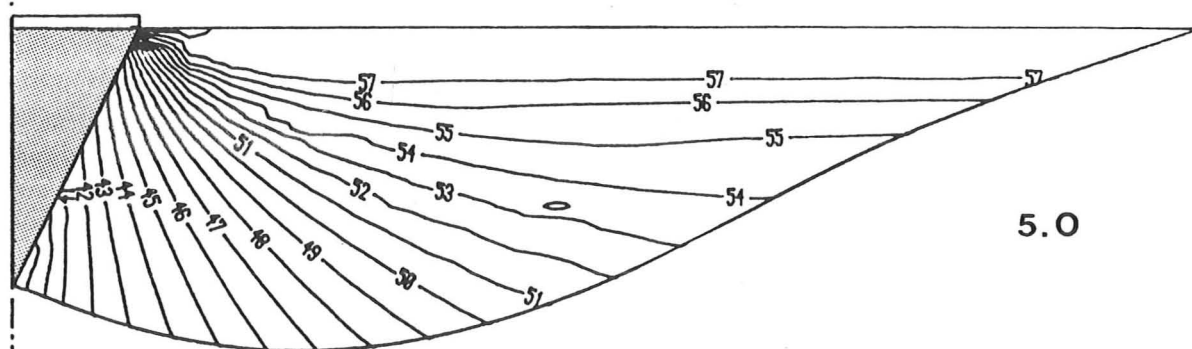
Fig 4.19   Contour map of varying ∅ under rough
circular footing on silt
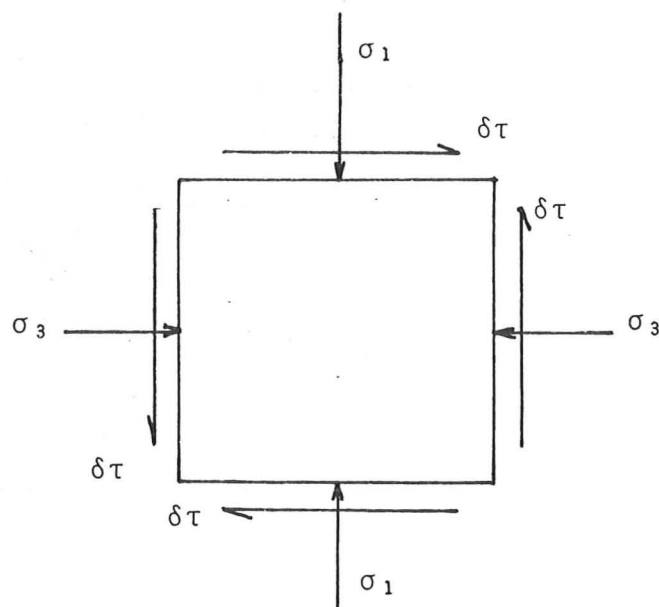
(a) Principal stresses with increment $\delta\tau$
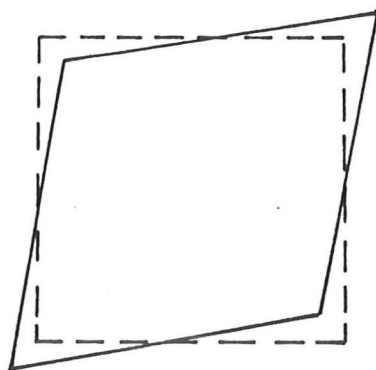
(b) Incremental deformation - non-linear elasticity
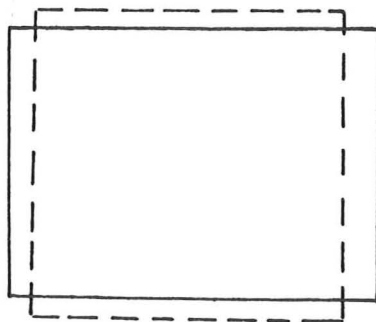
(c) Incremental deformation - plasticity

Fig 5.1
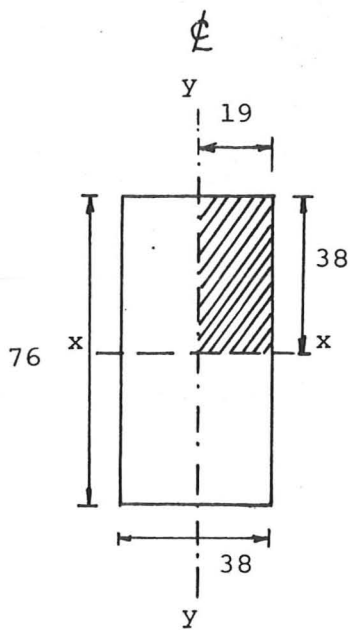
(a) Triaxial specimen

o data points
at which stress-
strain history
shall be looked
at in more
details
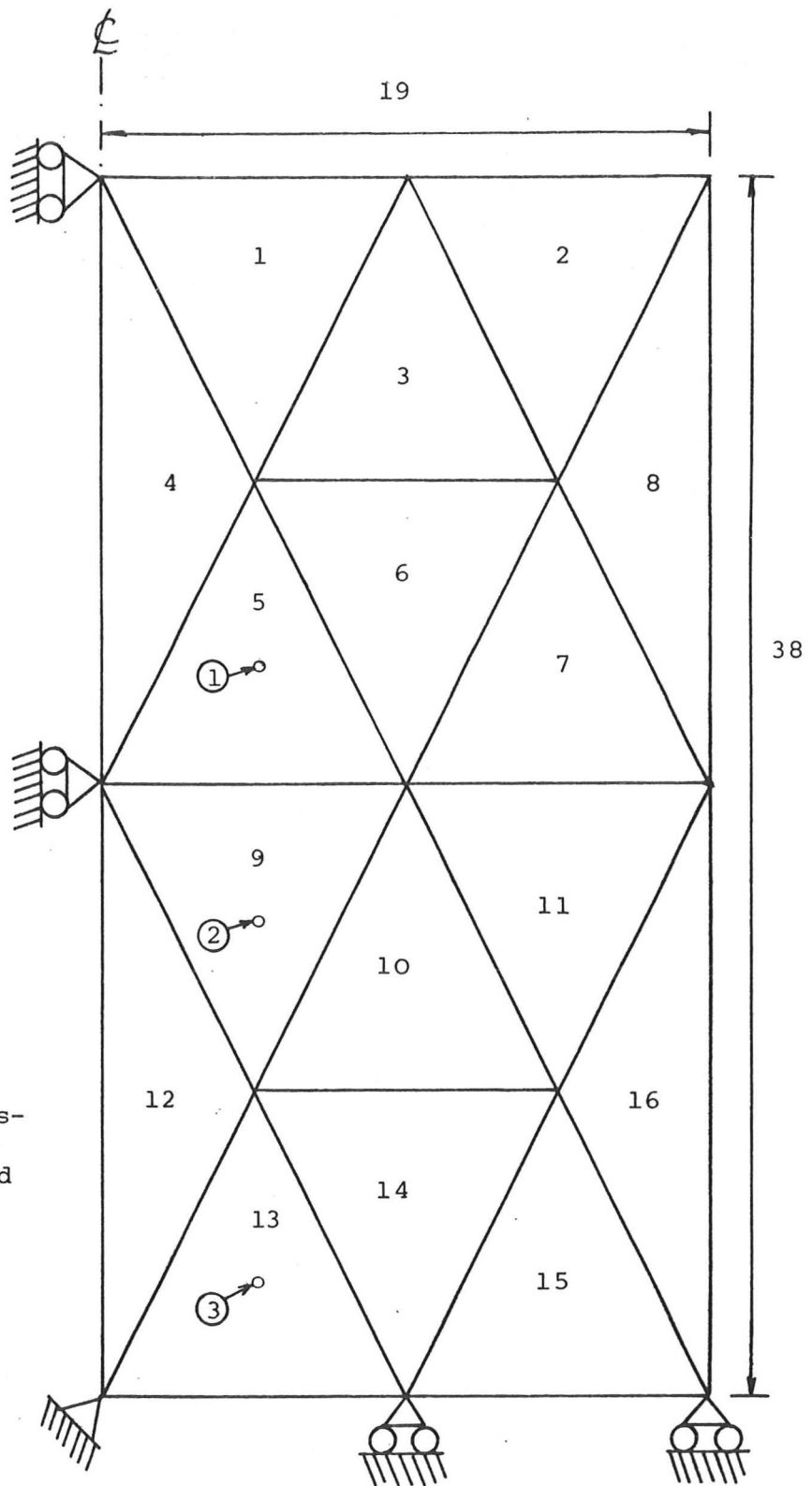
(b) Mesh for the triaxial specimen

Fig 5.2
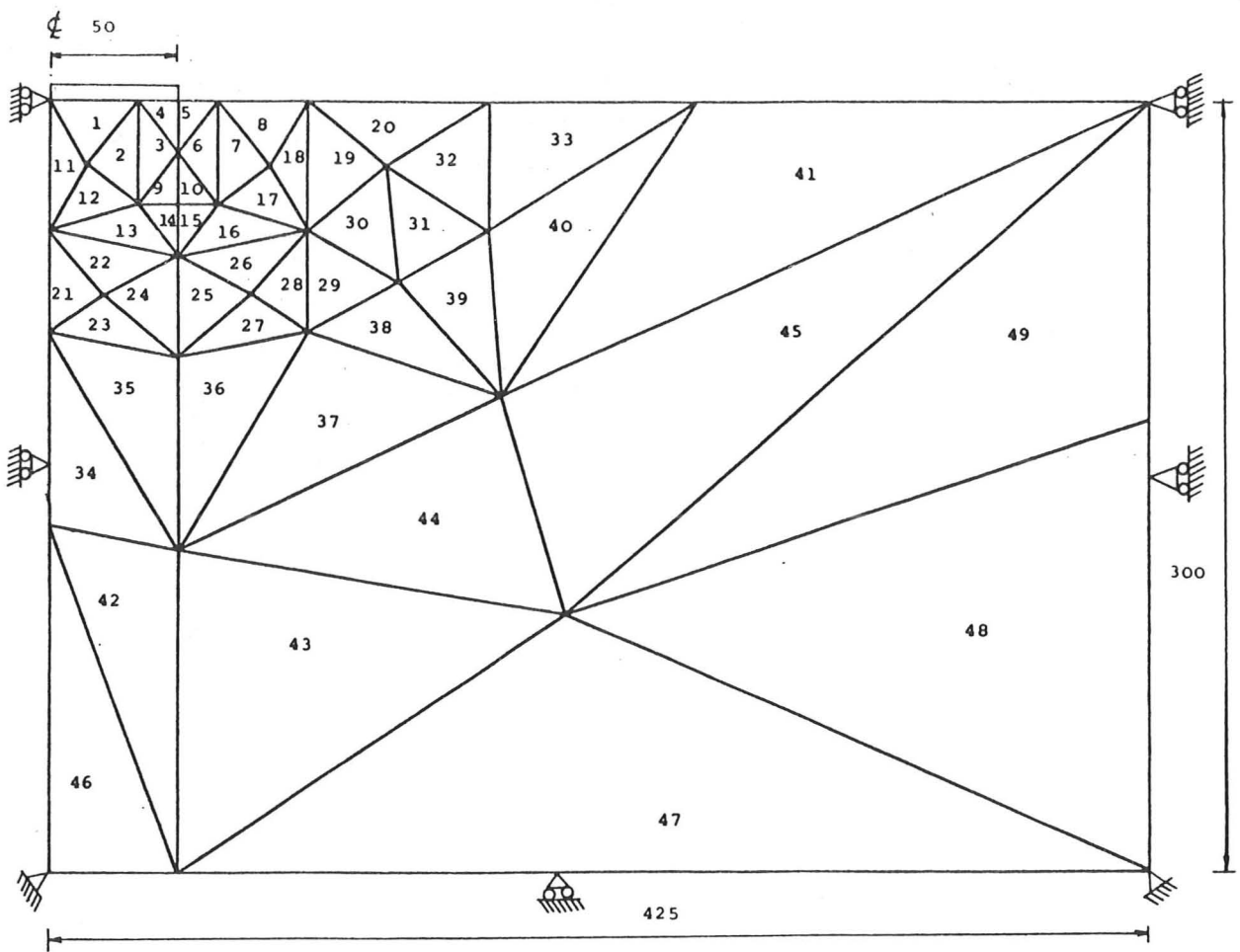
(a) Mesh for the punch-indentation problem
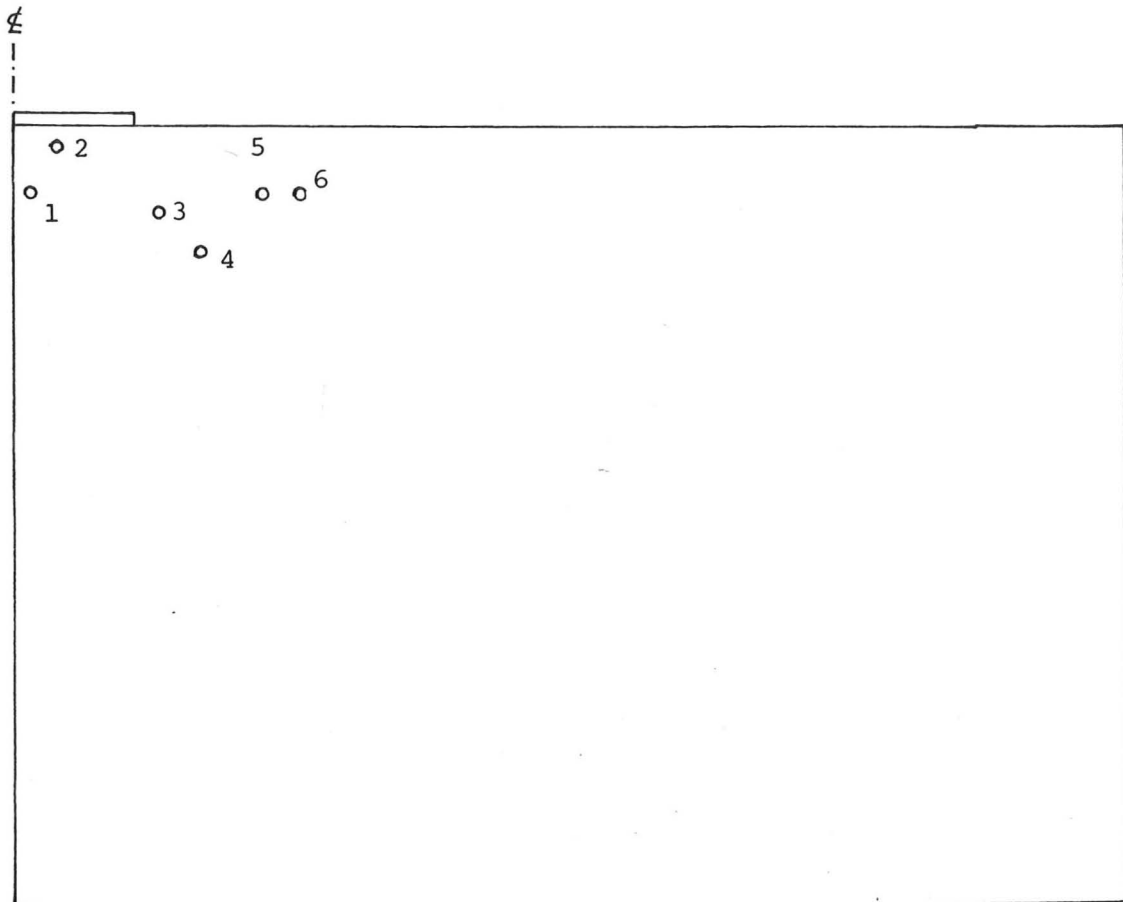
(b) Data points at which stress-strain history shall be looked at
     in more details

Fig 5.3
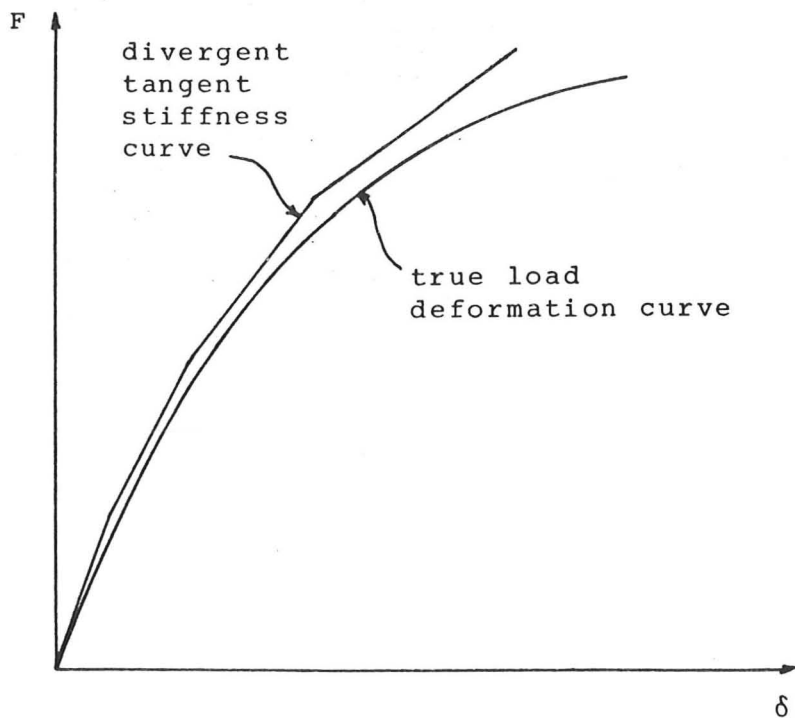
Fig 5.4   Effects of using the incremental tangent
           stiffness method
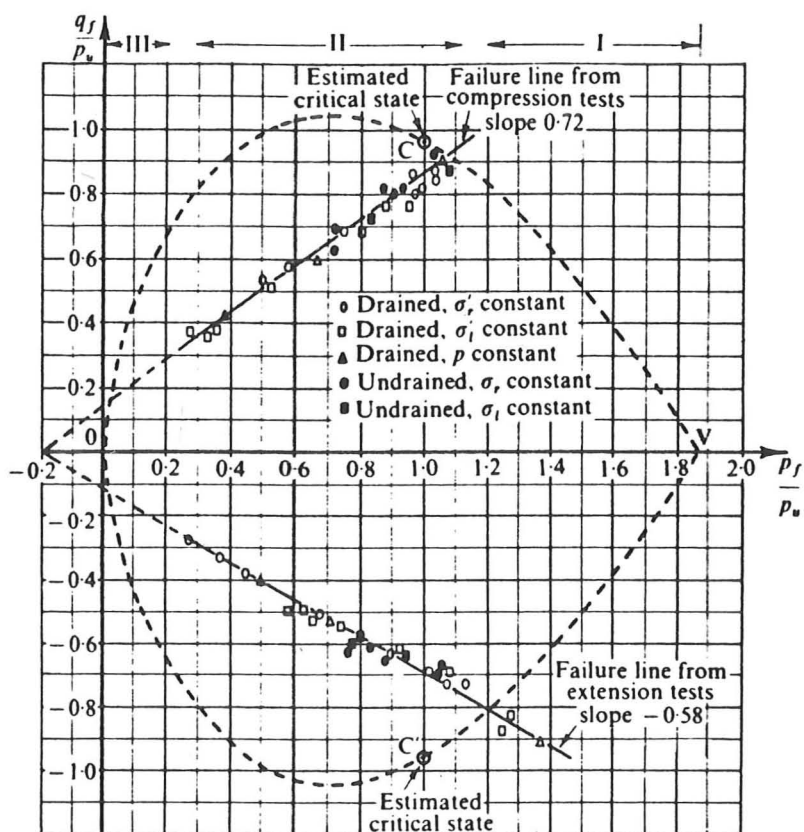
Fig 5.5   Data of failure from tests on Weald clay
           (After Parry, 1960)

q/p_e

impossible
state

critical state

Hvorslev
surface
(rupture)

Roscoe surface
(yield)

possible
state

compression

fracture

extension

p_e/p_e
(equivalent
over-consolidation
pressure)

p
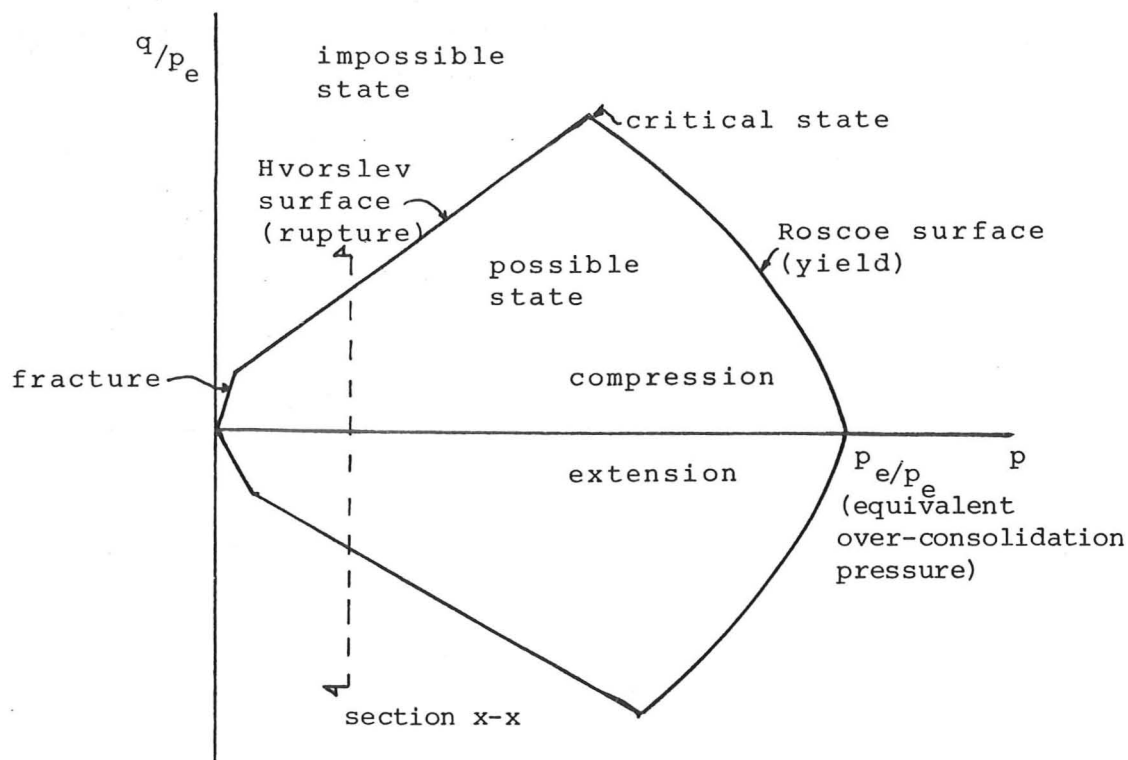
section x-x

(a) Schofield model on the triaxial plane

σ_1/p_e

Hvorslev surface ≜ Mohr-
Coulomb

simplified
Schofield model

σ_2/p_e

σ_3/p_e
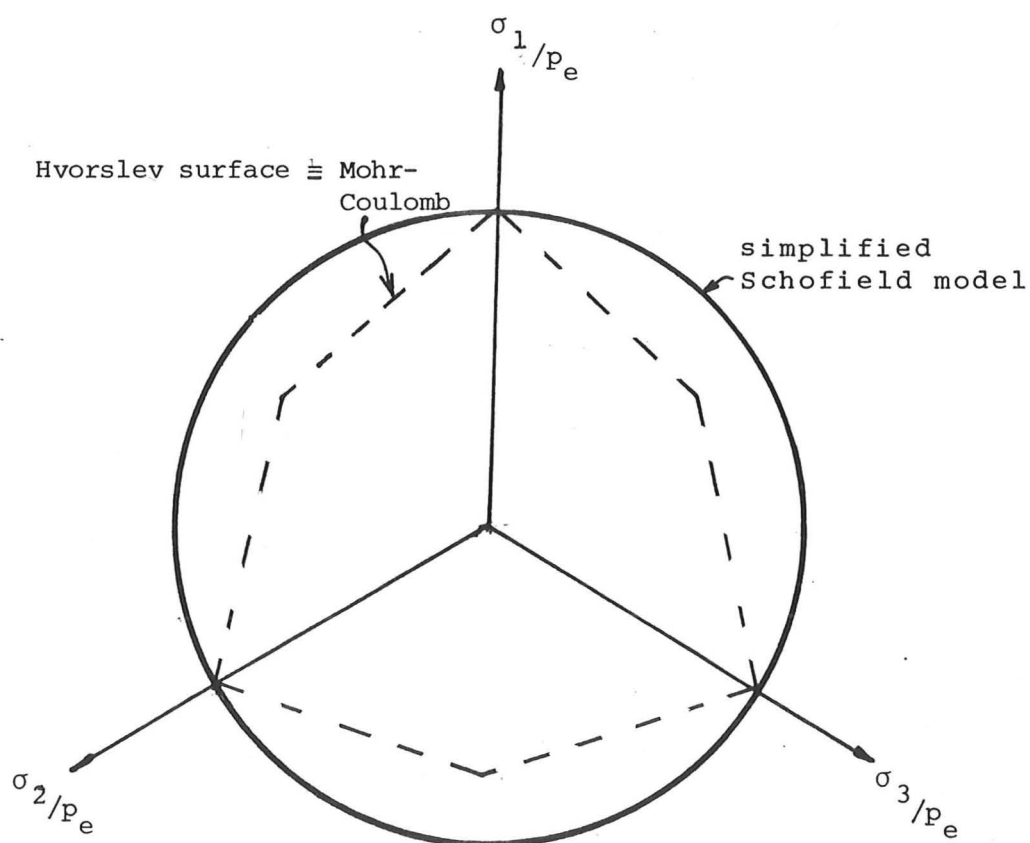
(b) Schofield model on the π plane

(section x-x)

Fig 5.6
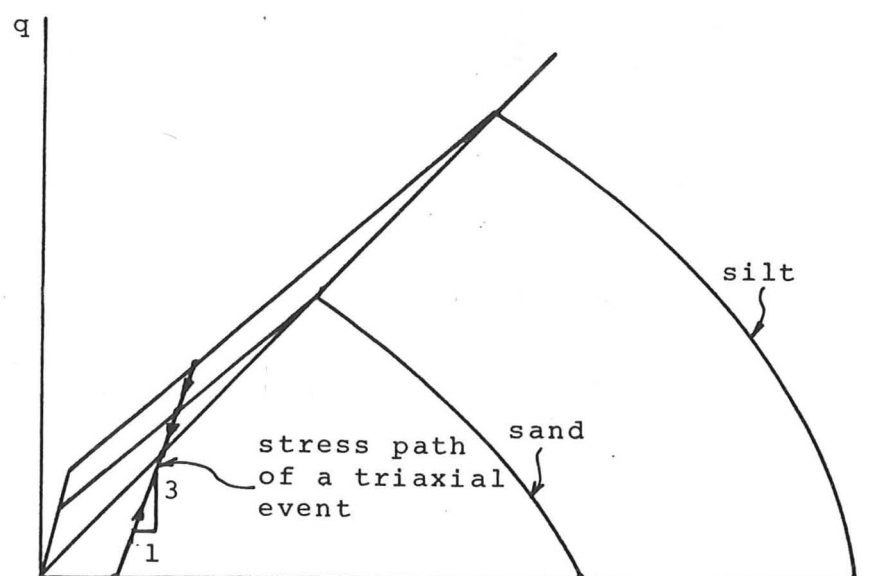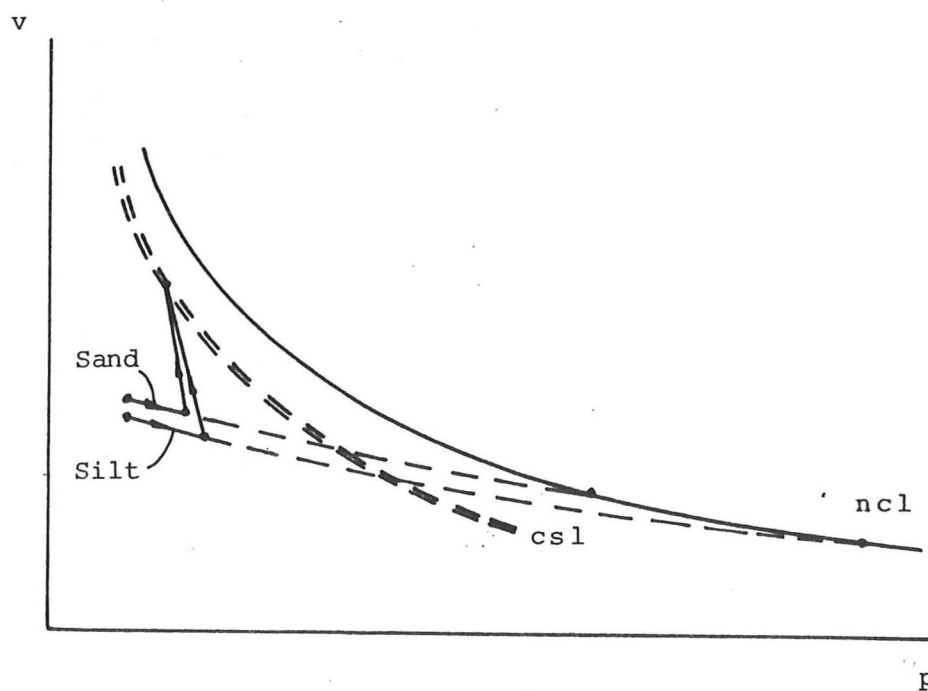
Fig 5.7   Schofield model on the compression triaxial plane
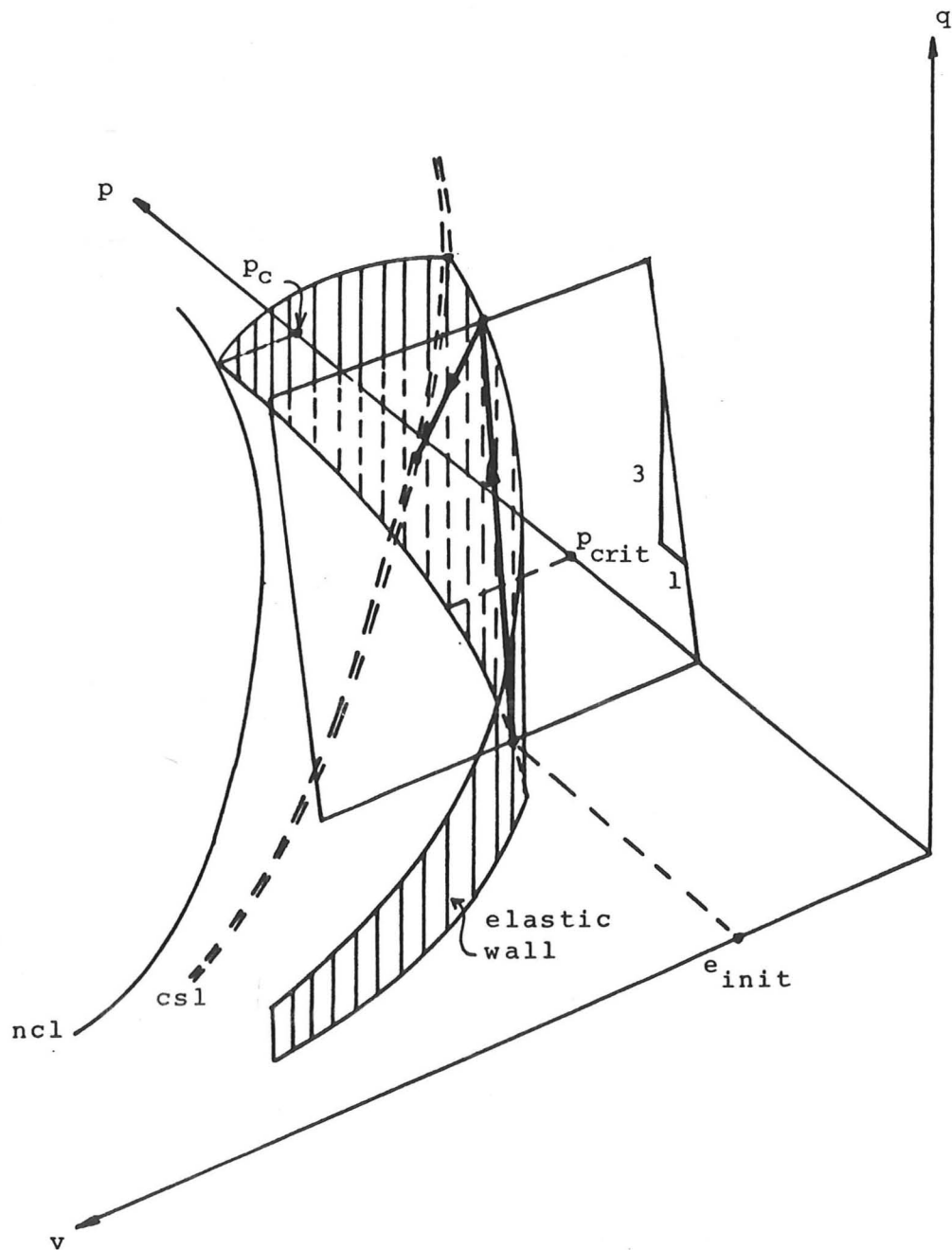
Fig 5.8   Isometric view of the Schofield model
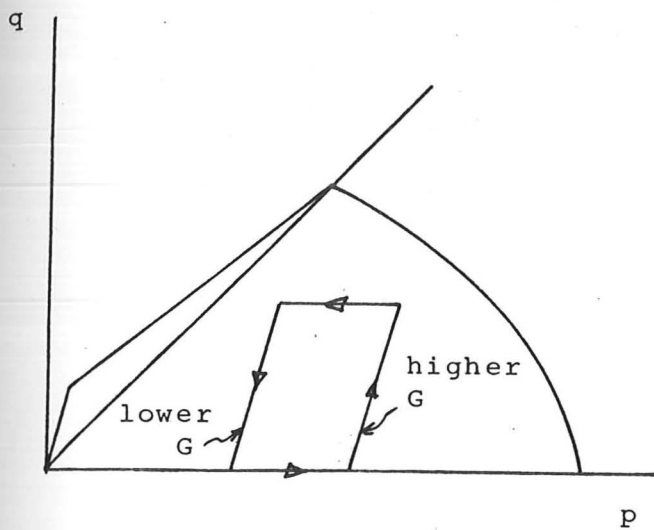
(a) Stress cycle within the state boundary

work $= \dfrac{q}{2}\varepsilon$
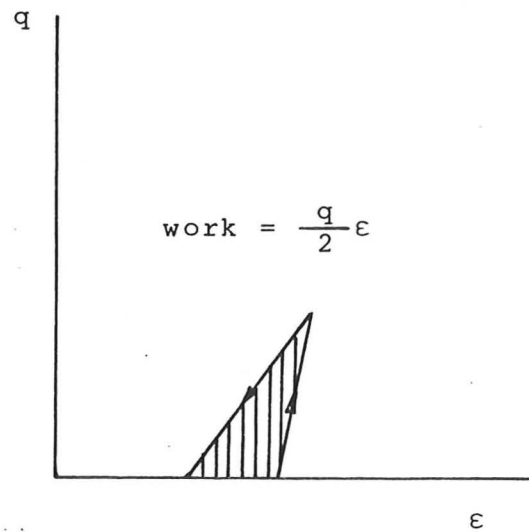
(b) Work done after a stress cycle
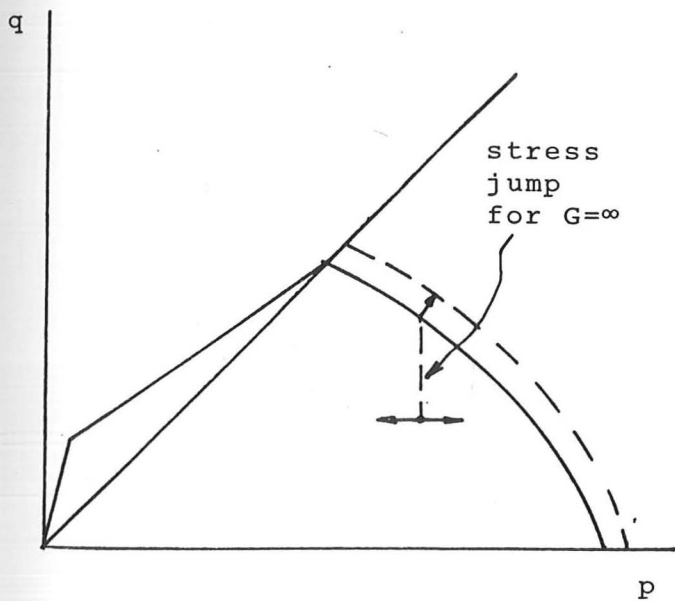
stress jump for $G=\infty$

(c) Stress jump occurs when G is assumed to be infinite
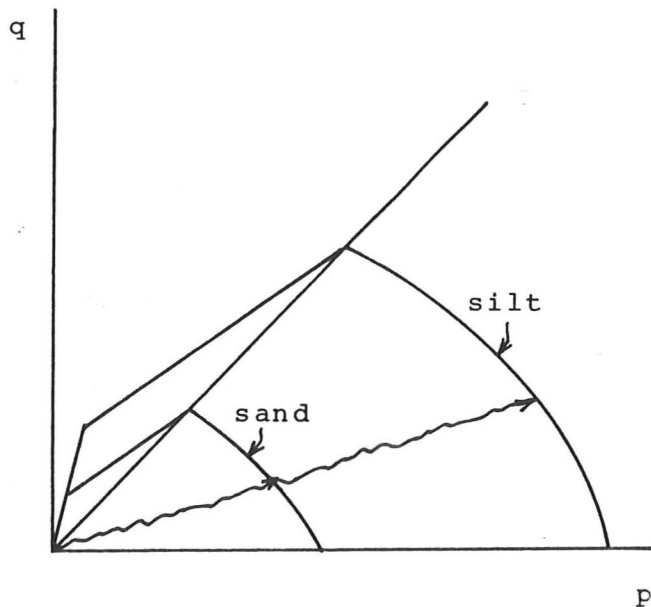
silt

sand

(d) Possible stress path as a result of the crushing process during manufacturing of sand and silt

Fig 5.9
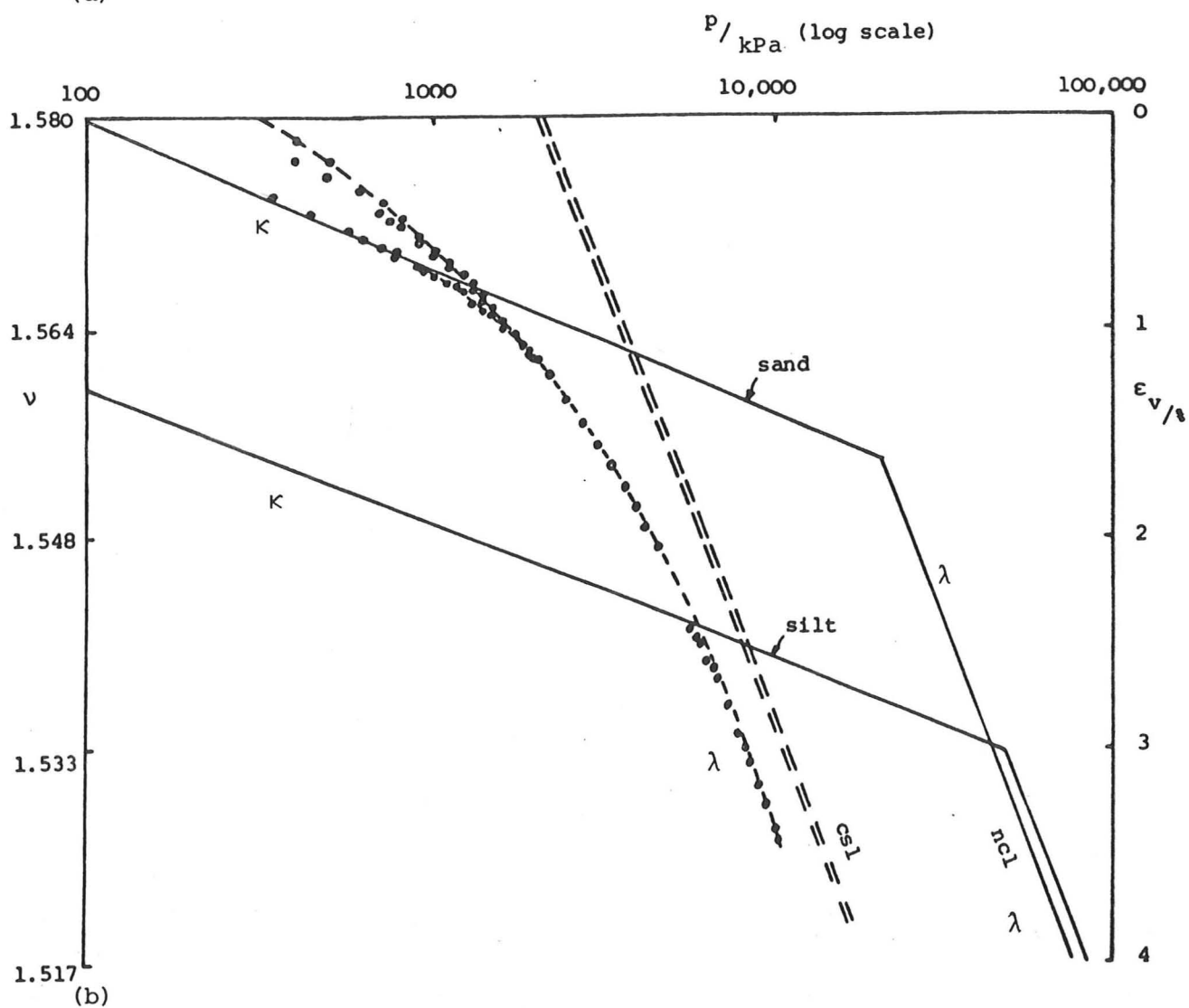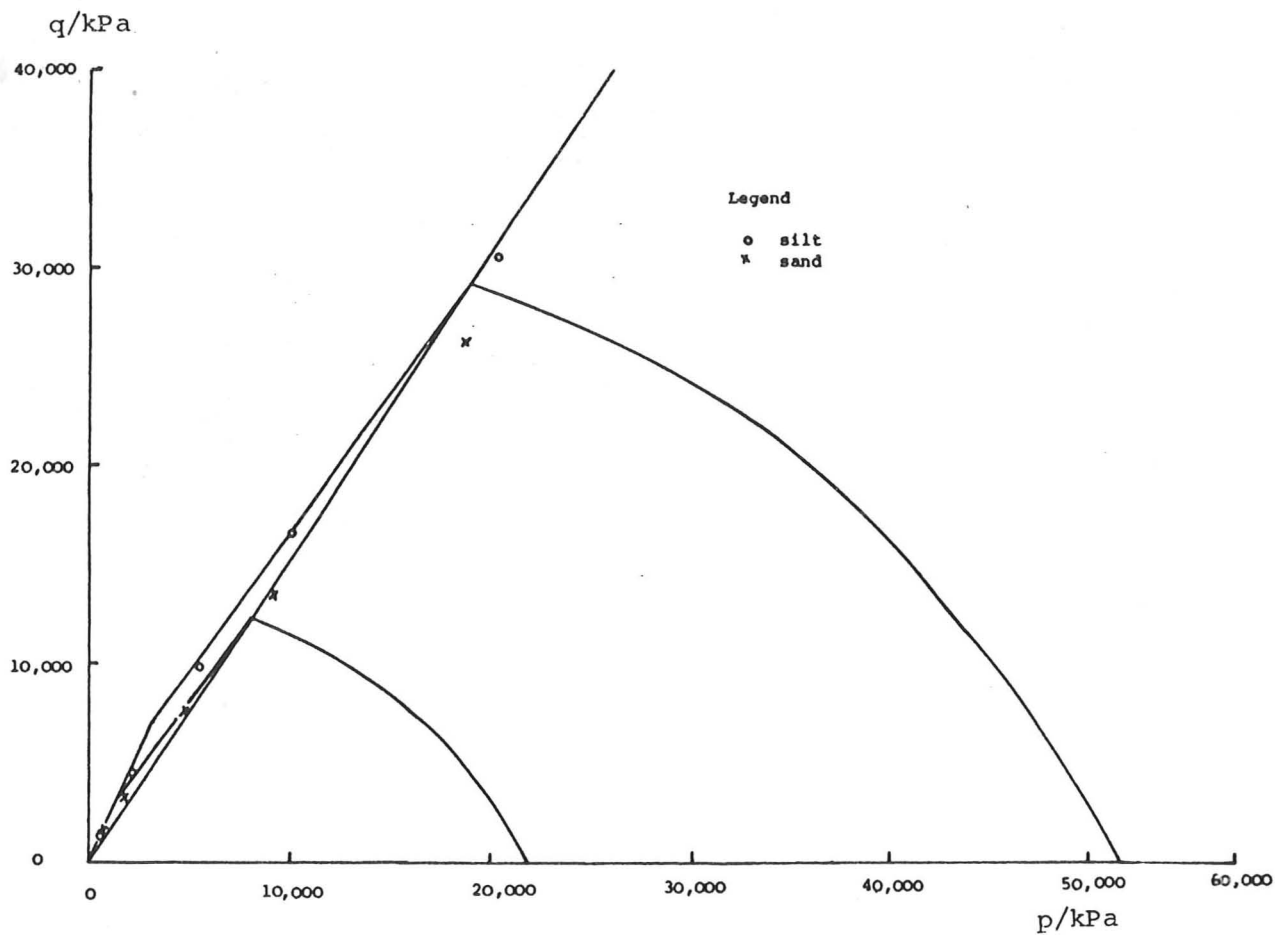
Fig 5.10 Idealization of behaviour of sand and silt
in a p,q,v space
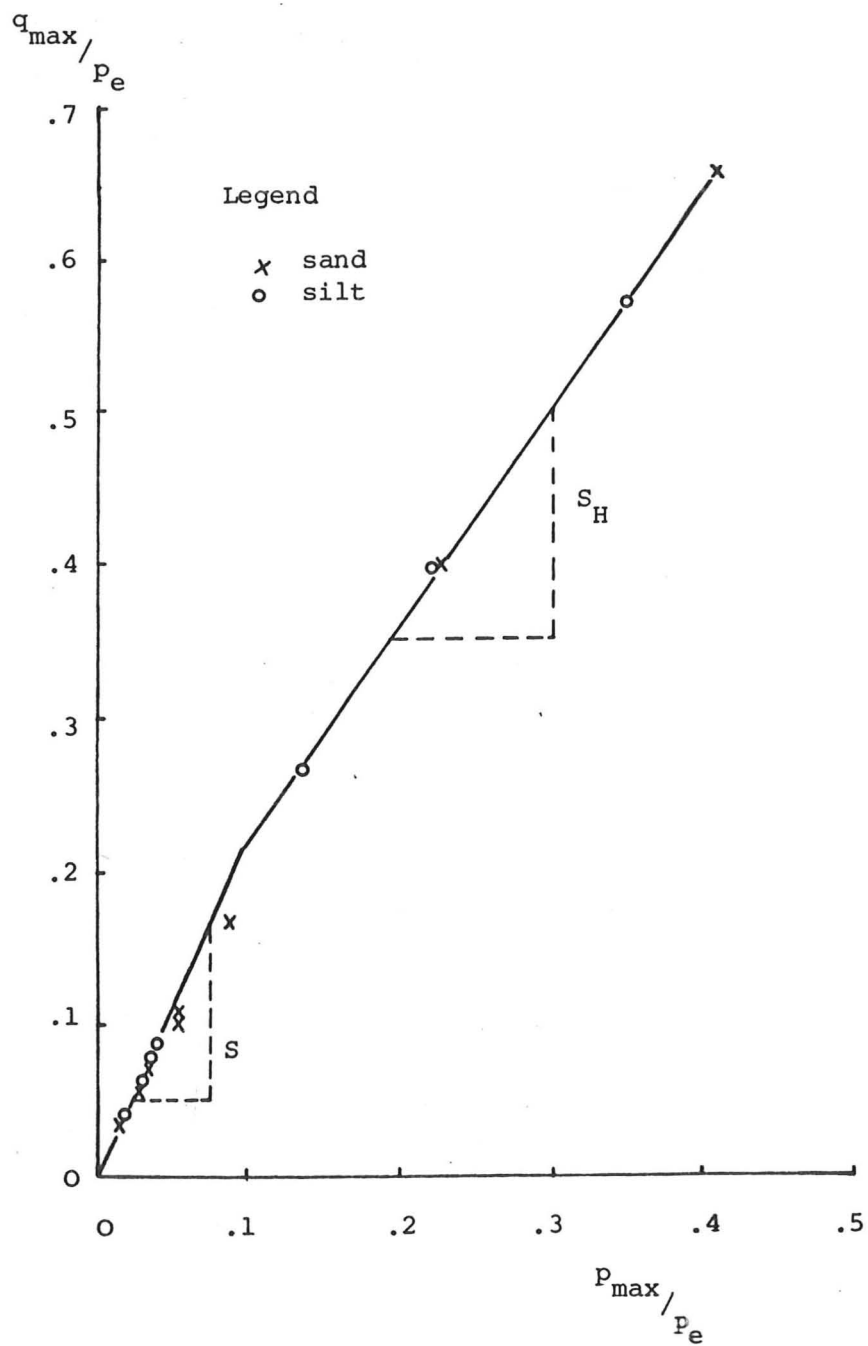
Fig 5.11 Normalized peak stress states on a
constant ν section

$$e_{cs} = e_{init} + (\lambda - \kappa)\ln p_{crit} + \kappa \ln p_{init}$$

Fig 5.12a   Method of determining Γ
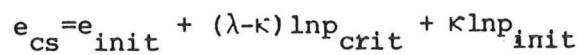
$$\nu_H = (1 + e_{init}) - \kappa(\ln p_{max} - \ln 100)$$

$$p_e = \exp\left(\frac{\Gamma - \nu}{\lambda} + 0.724\right)$$

Fig 5.12b   Method of determining p_e
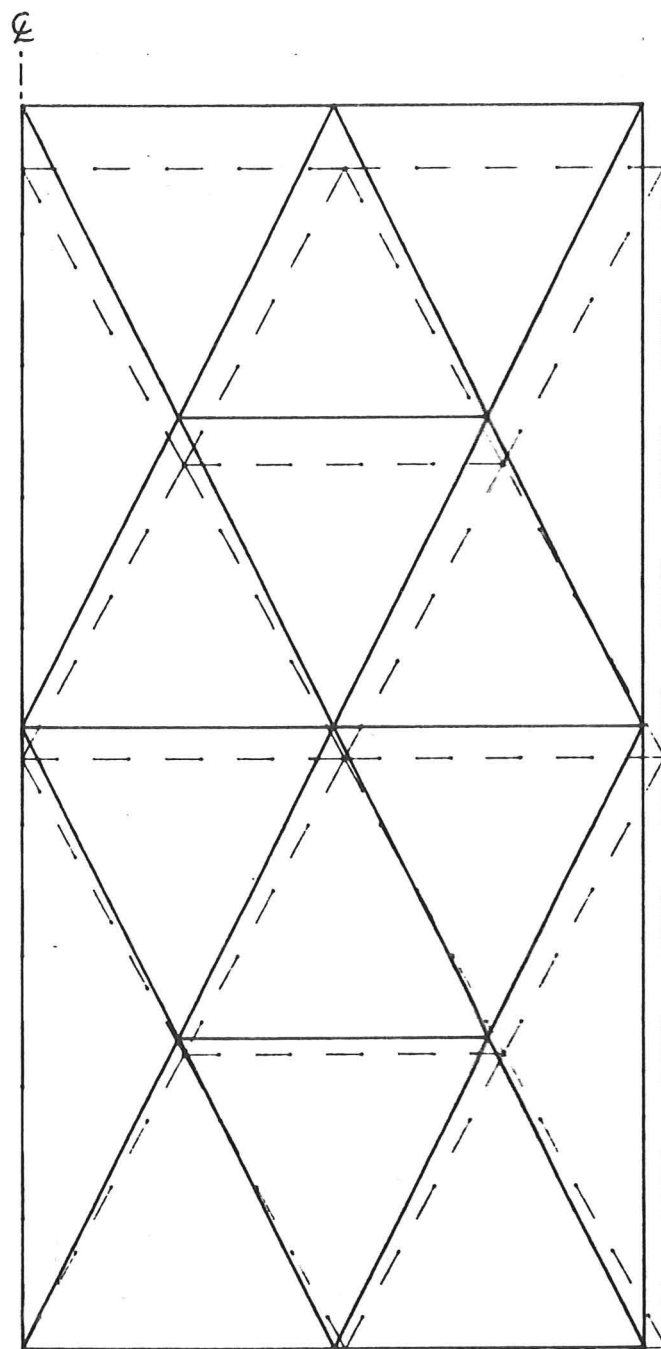
Fig 5.13   Deformed mesh of CRISP1 after
           180 increments when ε_a=5%
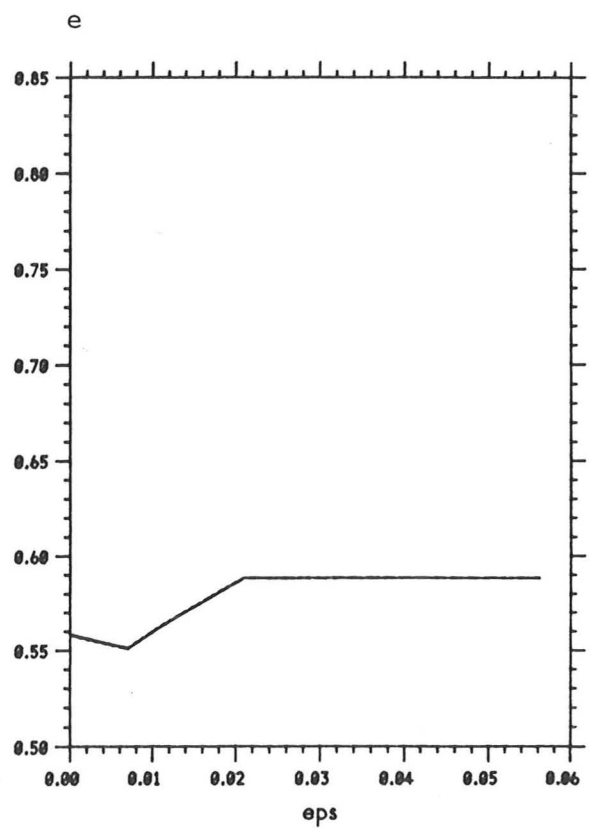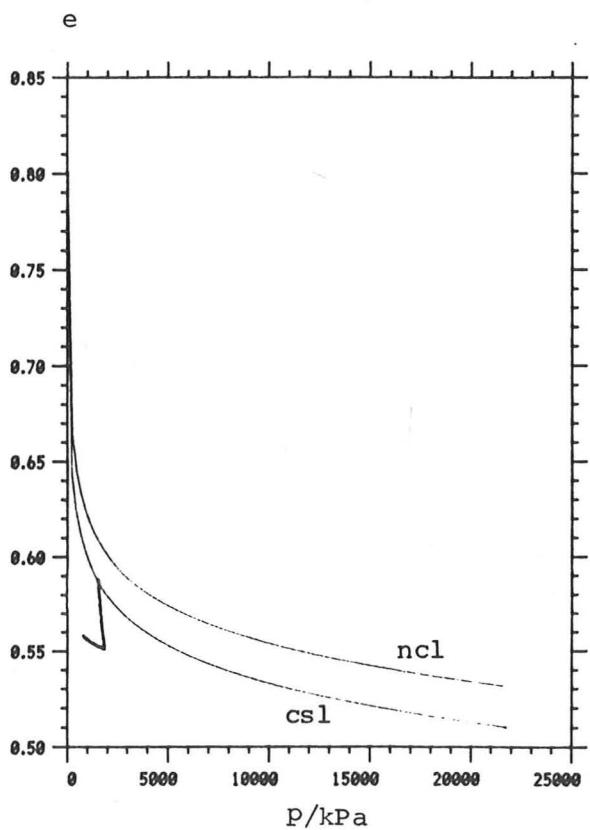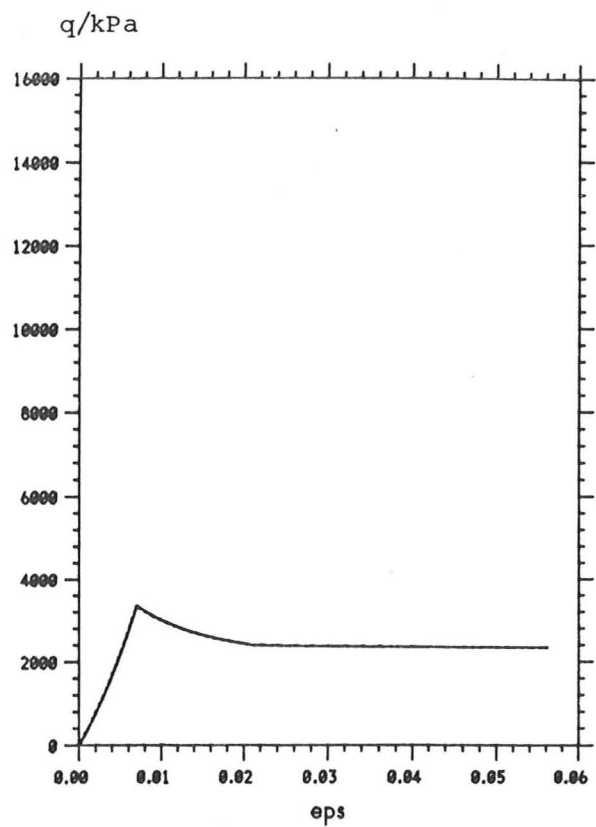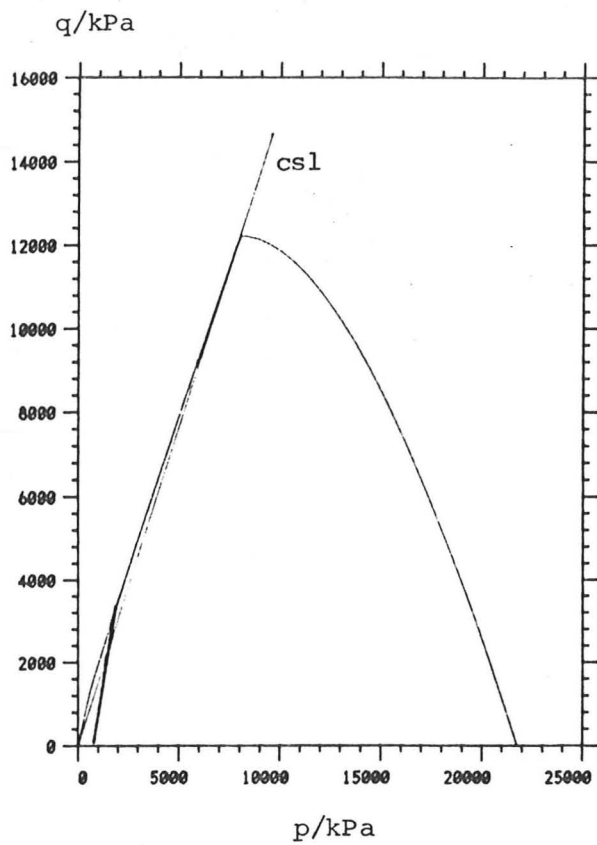
Fig 5.14 Stress-strain history of test CRISP1
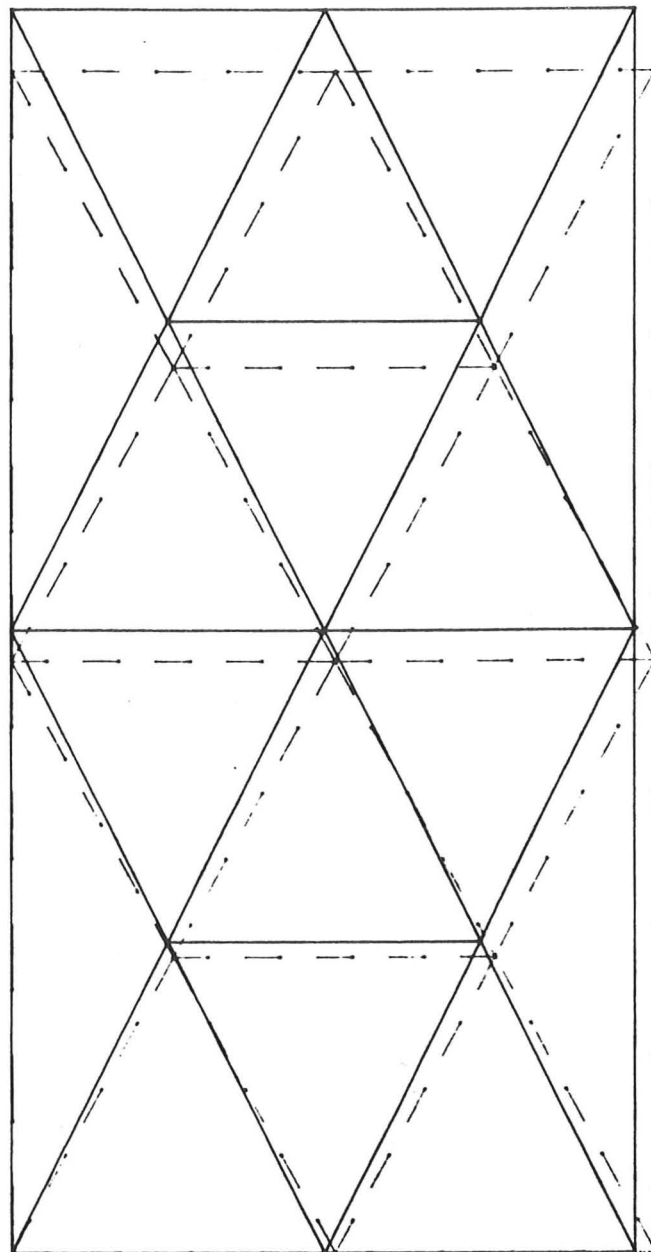
Fig 5.15   Deformed mesh of CRISP2 after
180 increments when ε_a=5%
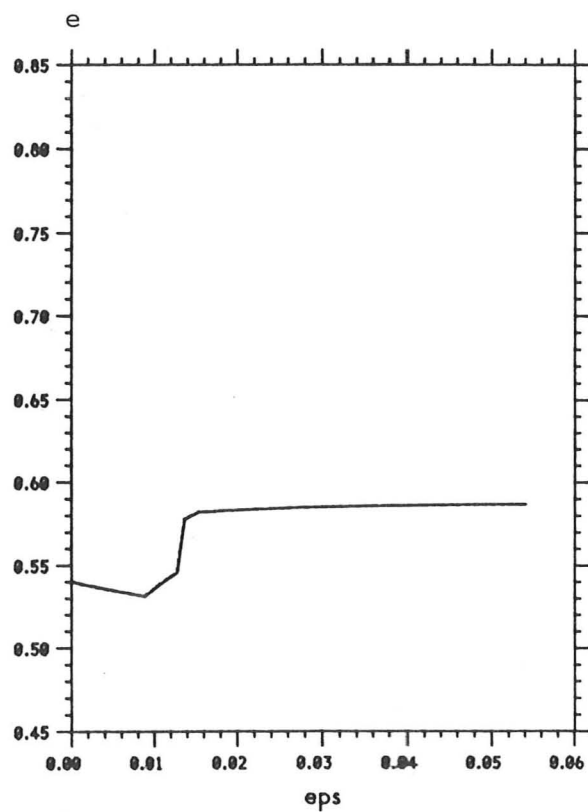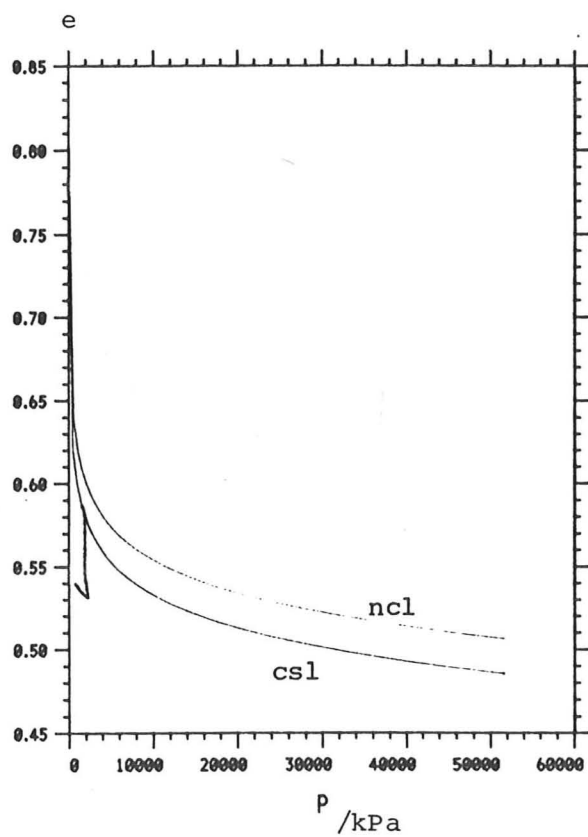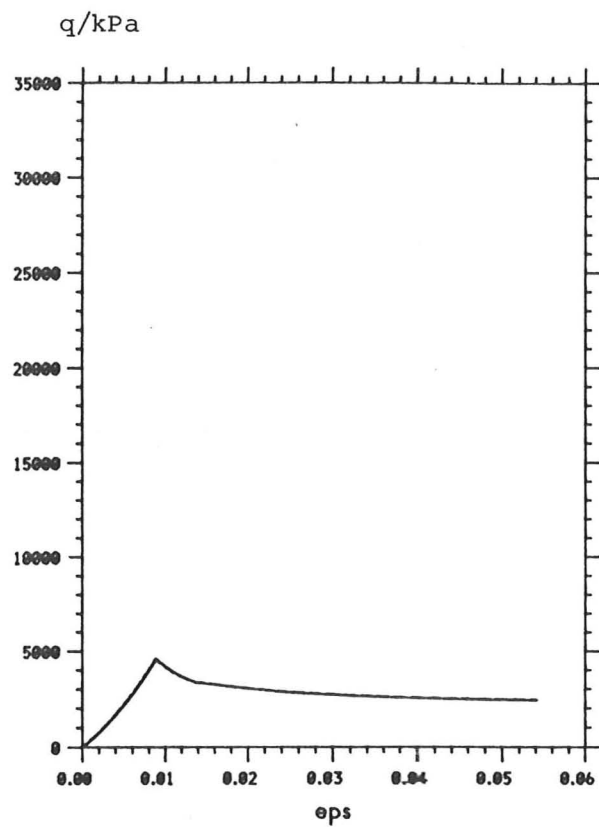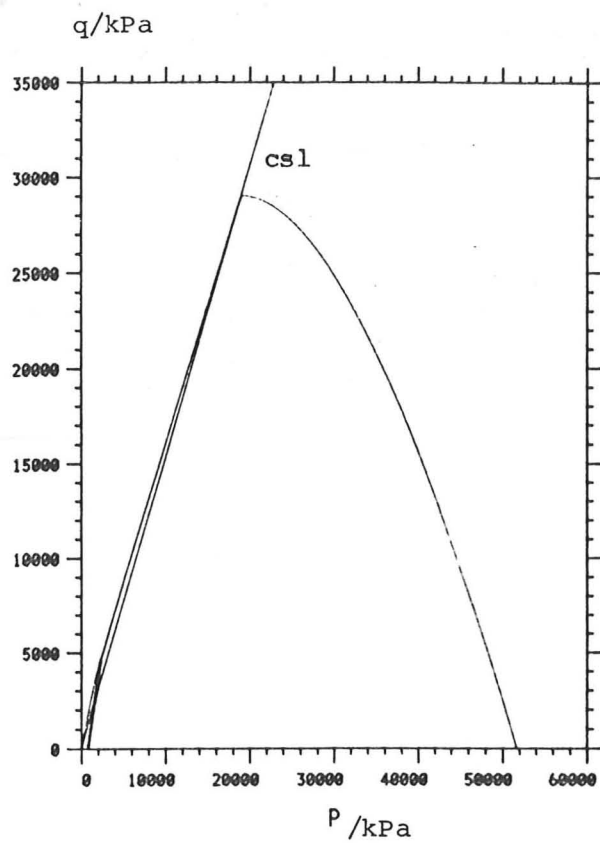
Fig 5.16 Stress-strain history of test CRISP2
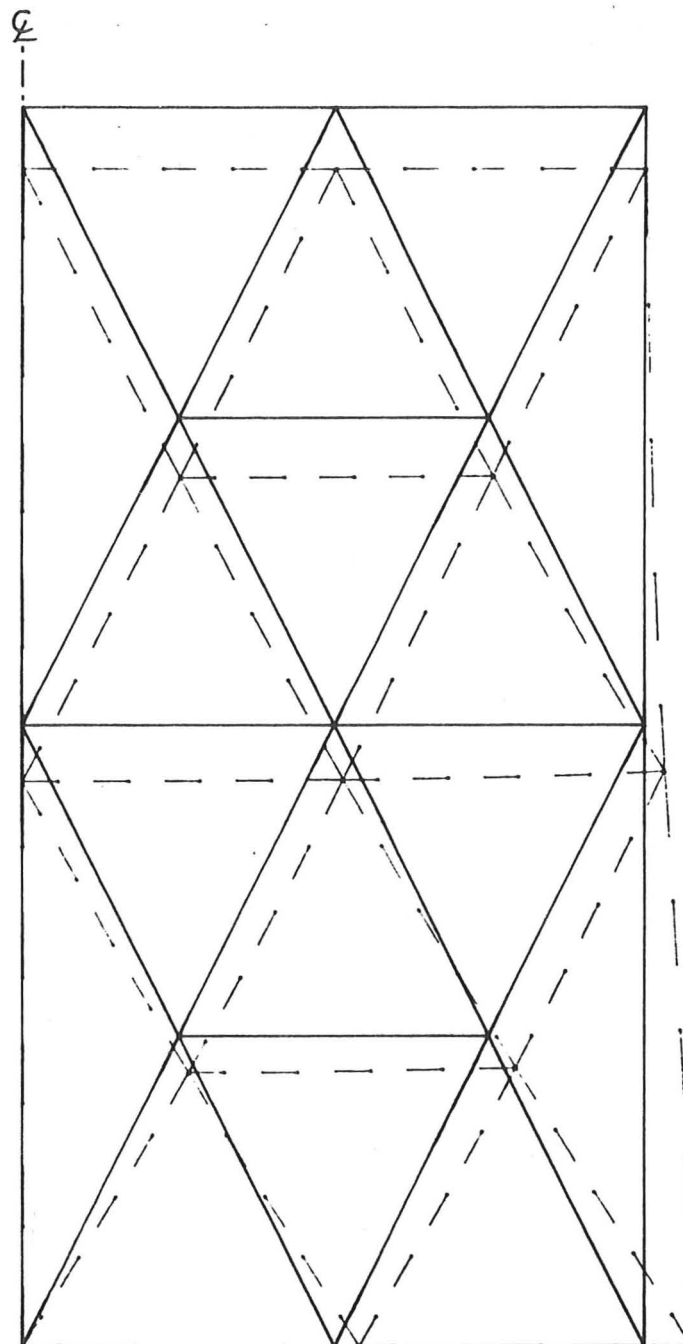
Fig 5.17   Deformed mesh of CRISP3 after
            180 increments when $\varepsilon_a = 5\%$

q/kPa

q/kPa

Legend (see fig 5.2)

data point 1 ———
data point 2 ············
data point 3 - - - - - -

e

ncl

csl

e
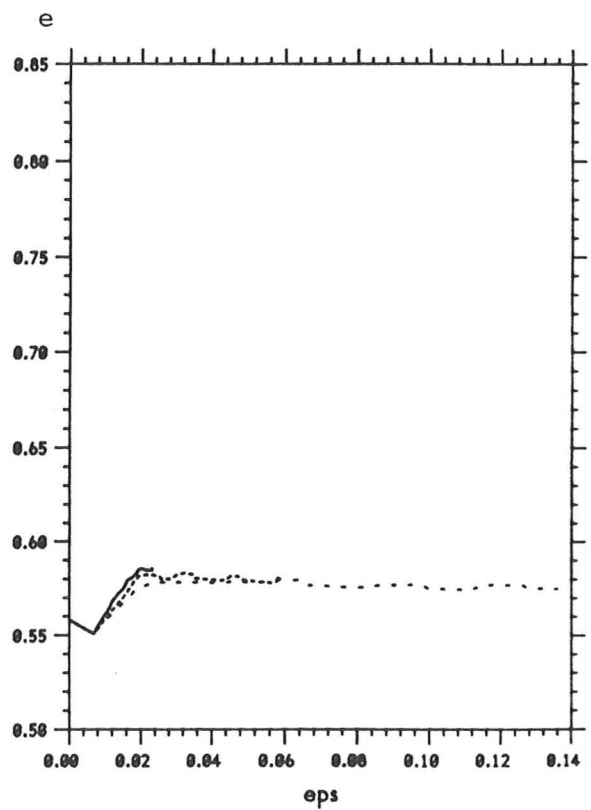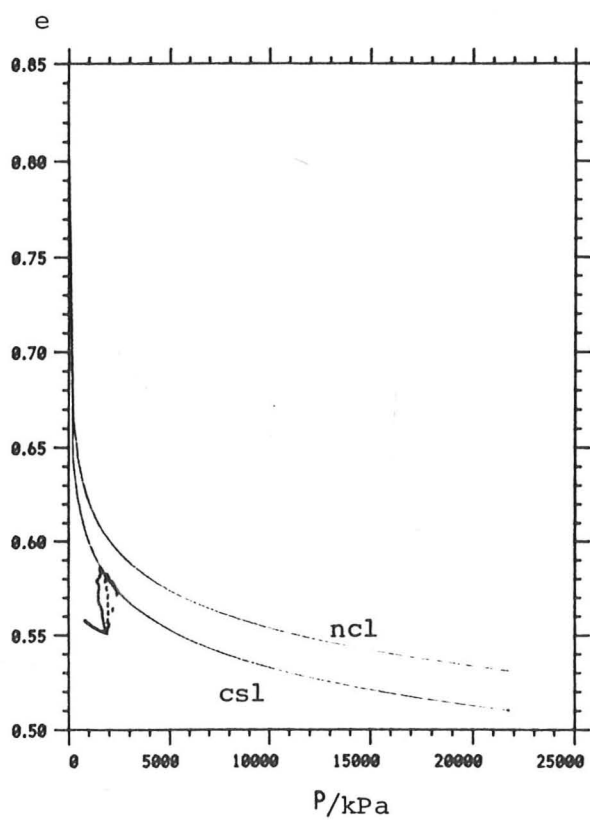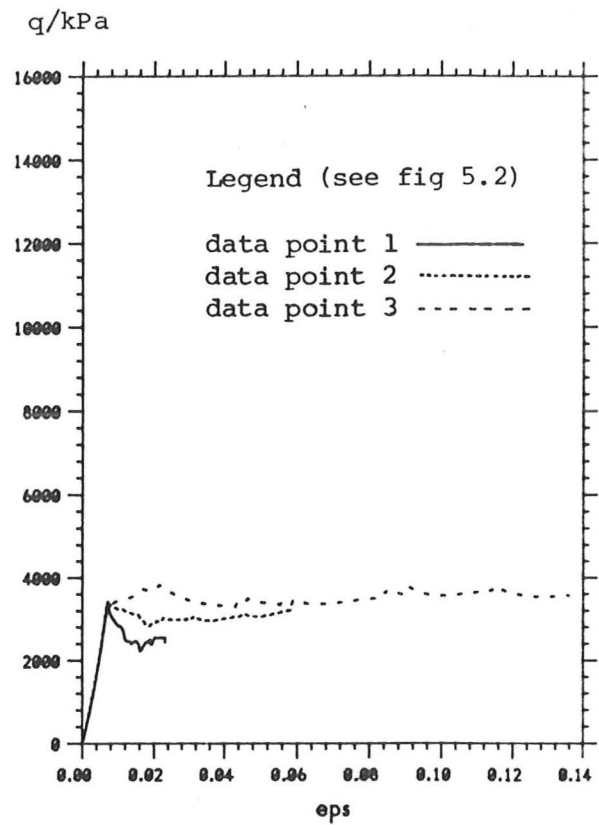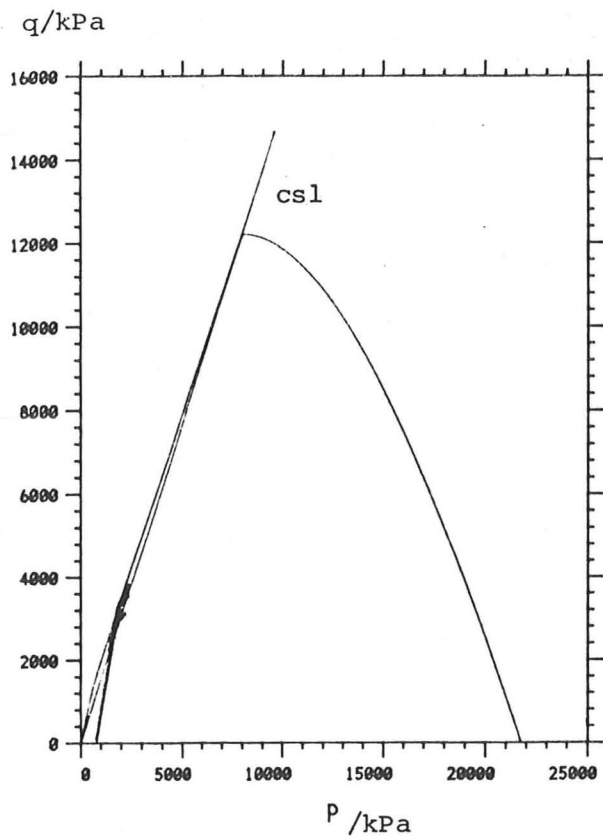
Fig 5.18   Stress-strain history of test CRISP3
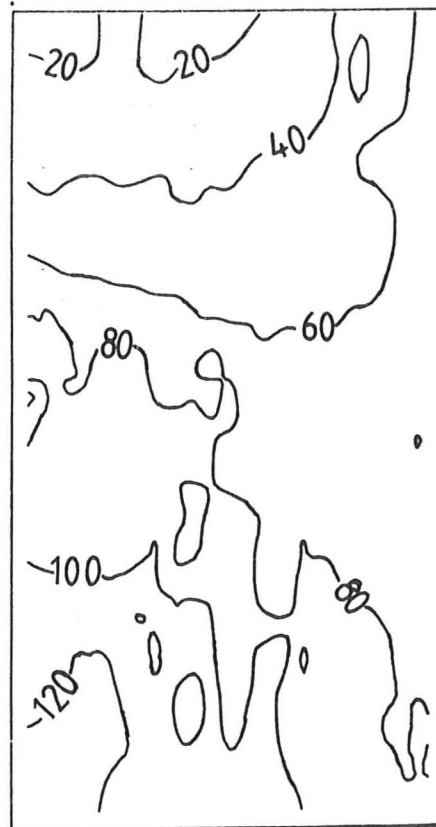
(a) Minor principal stress
contour (1 unit = 10 kPa)
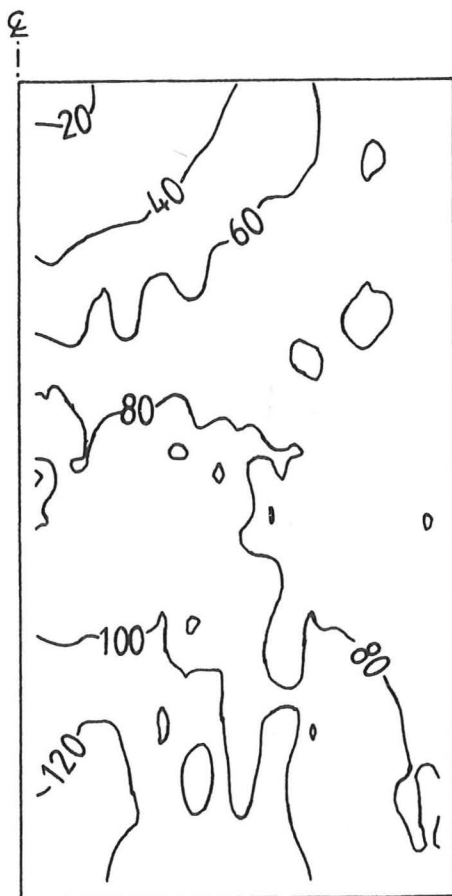
(b) Radial stress contour
(1 unit = 10 kPa)
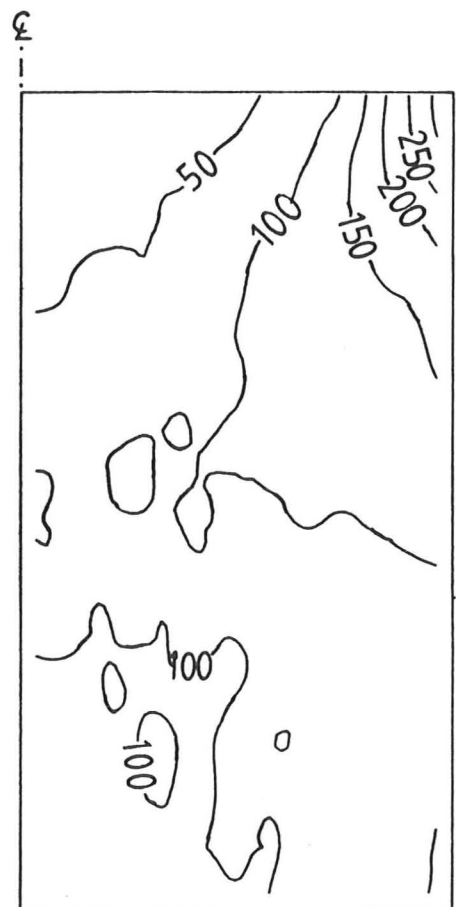
(c) Circumferential stress
(1 unit = 10 kPa)

Fig 5.19 Regional variation of stresses in a triaxial
specimen for test CRISP3 when ε_a=5%
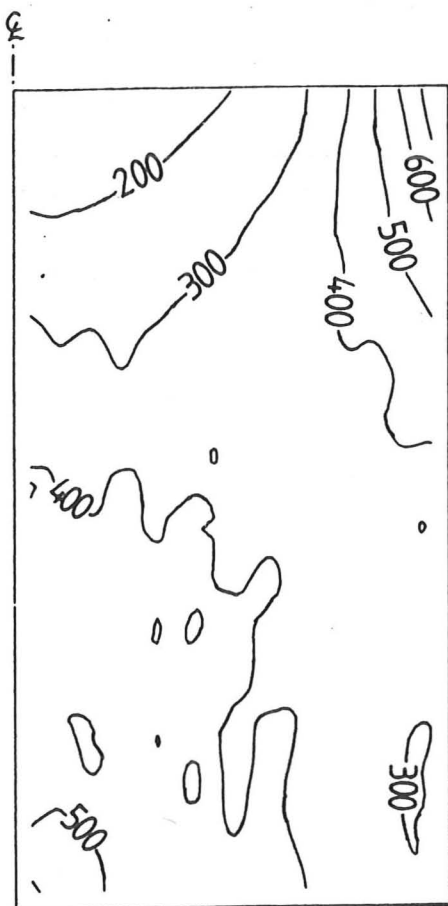
(a) Major principal stress
     contour (1 unit = 10 kPa)
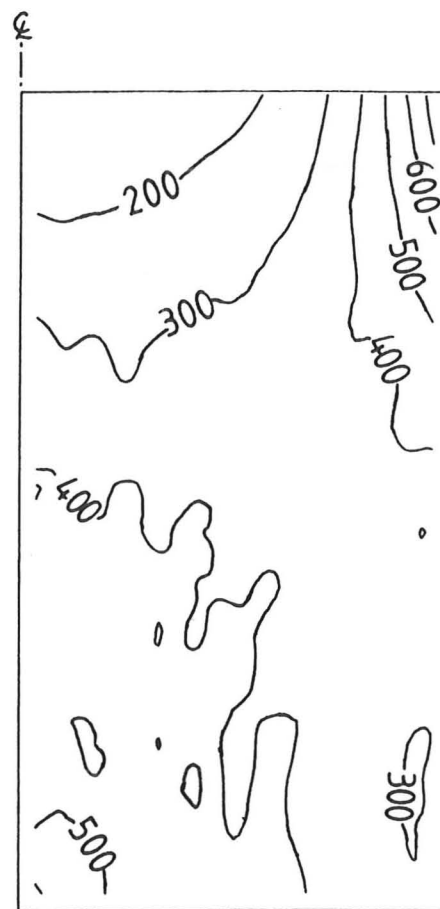
(b) Vertical stress contour
     (1 unit = 10 kPa)

Fig 5.20   Regional variation of stresses
           in a triaxial specimen for test
           CRISP3 when ε_a=5%
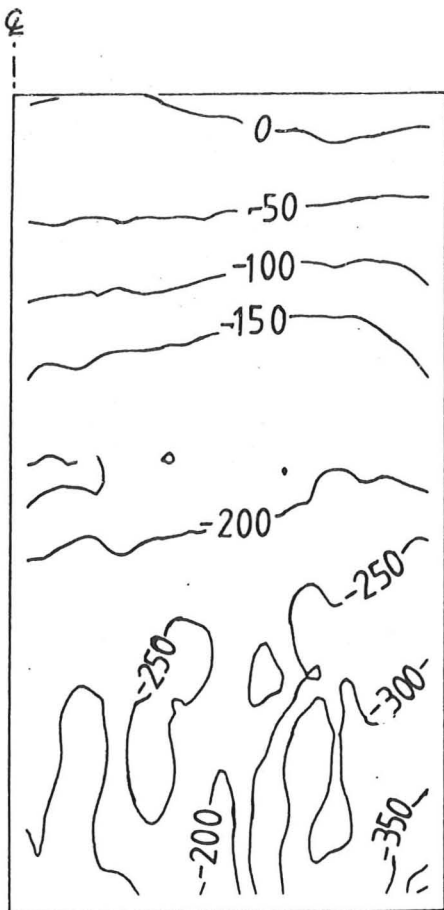
(a)   Volumetric strain
      contour (100 unit = 1%)
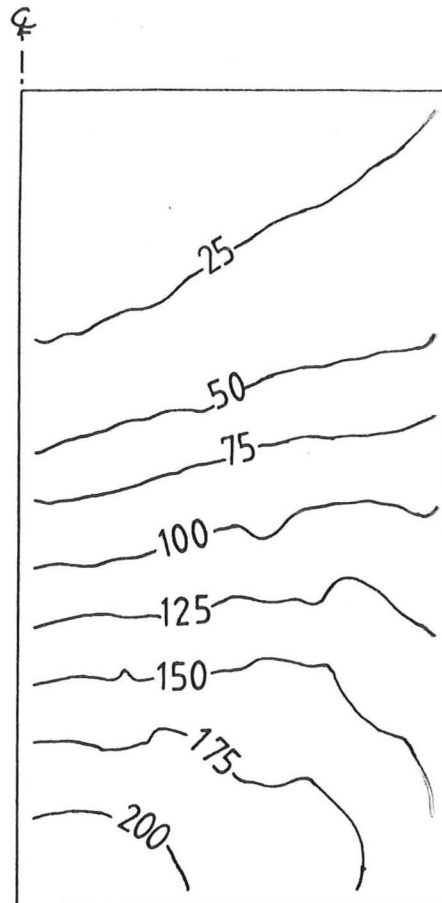
(b)   Maximum shear strain
      contour (10 unit = 1%)
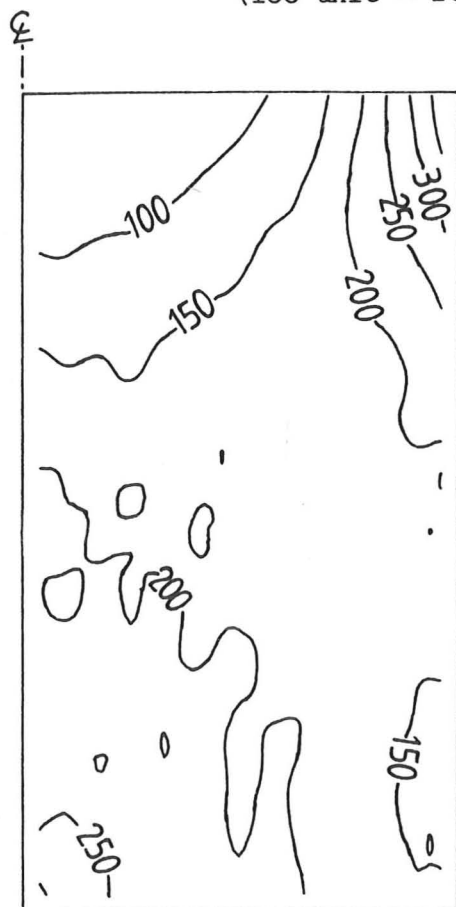
(c)   Mean stress contour
      (1 unit = 10 kPa)
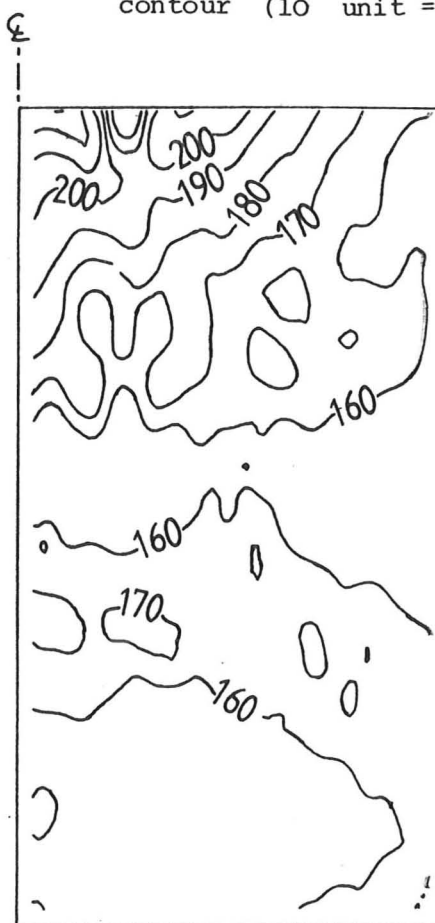
(d)   Stress ratio   q/p
      (100 unit = 1)

Fig 5.21   Regional variation of stresses and strains in
           a triaxial specimen for test CRISP3 when ε_a =5%
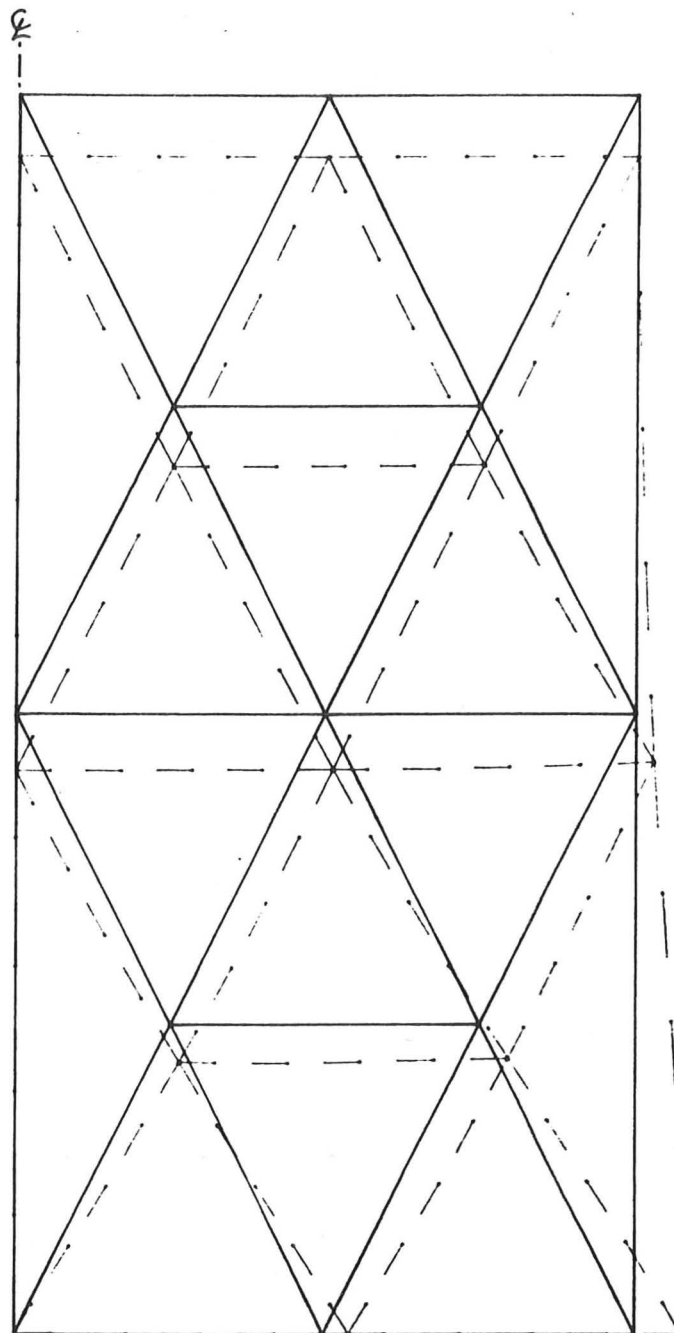
Fig 5.22   Deformed mesh of CRISP4 after
180 increments when ε_a =5%
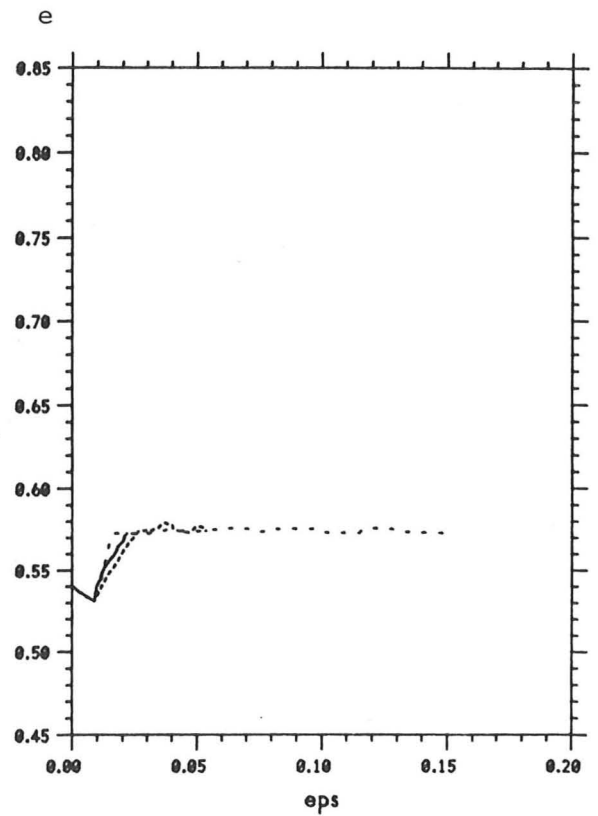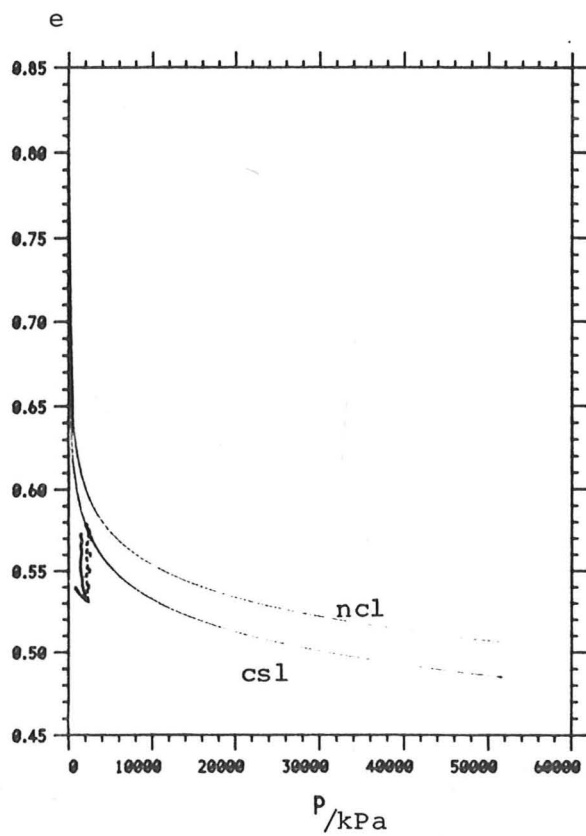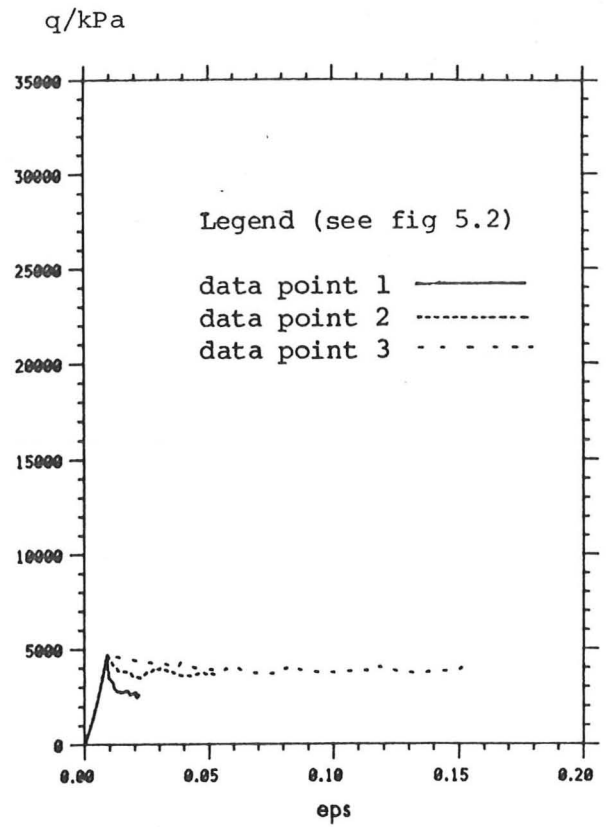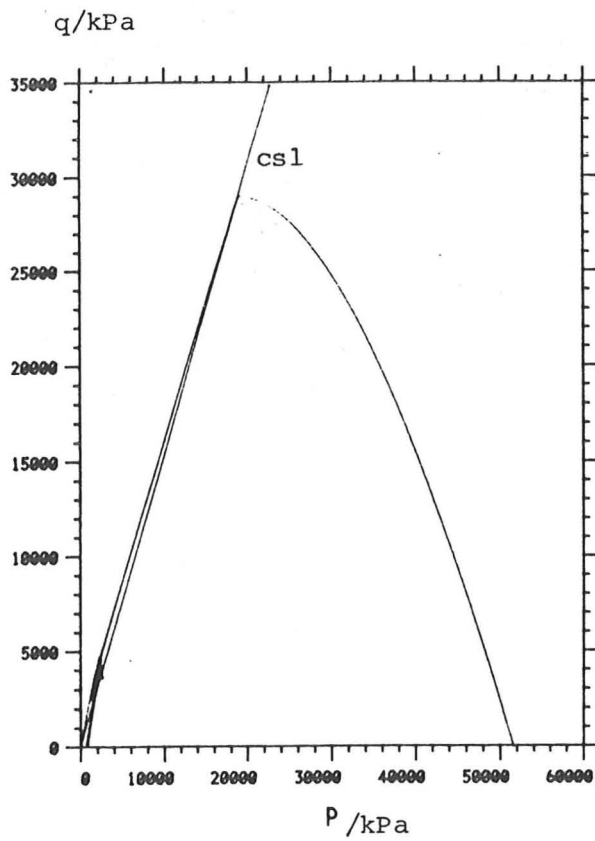
Fig 5.23   Stress-strain history of test CRISP4
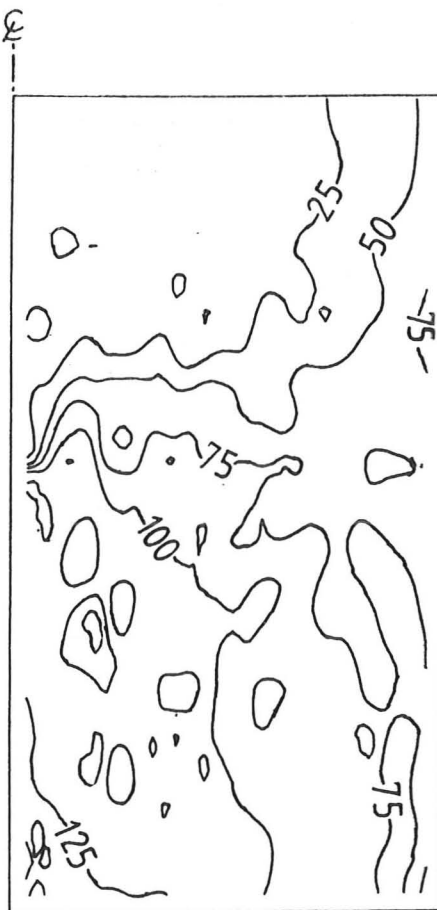
(a)　Minor principal stress
　　　contour (1 unit = 10 kPa)
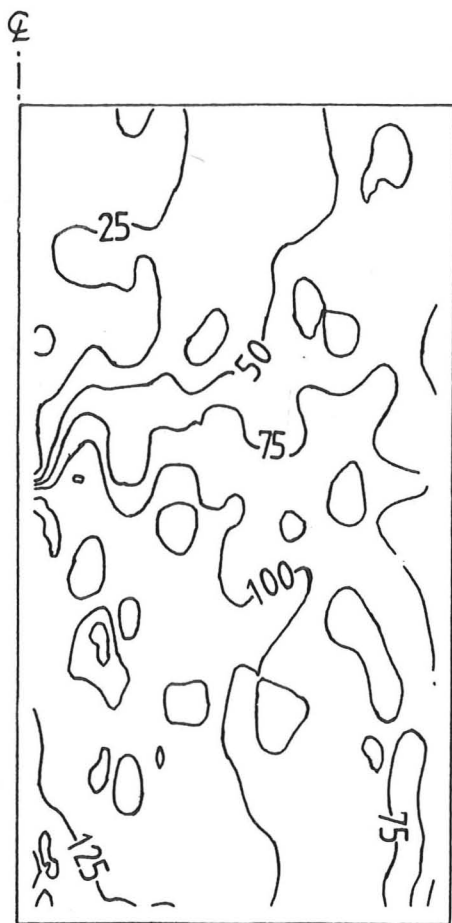
(b)　Radial stress contour
　　　(1 unit = 10 kPa)
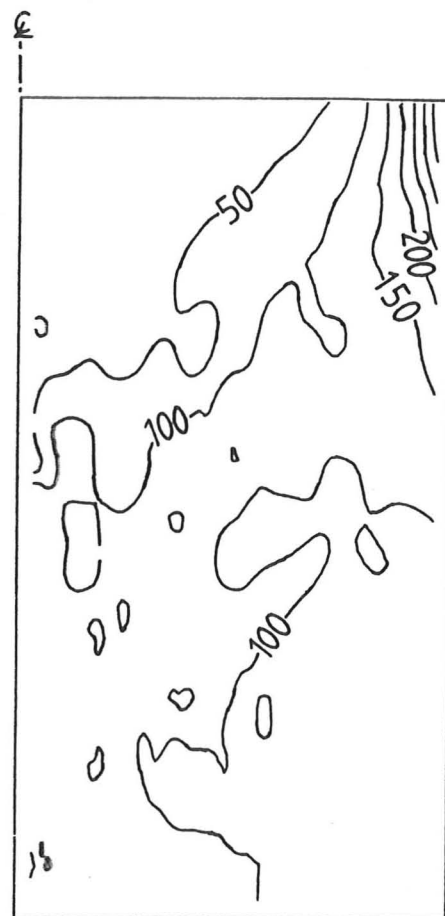
(c)　Circumferential stress
　　　contour (1 unit = 10 kPa)

Fig 5.24　Regional variation of stresses in a triaxial test
　　　　　specimen for test CRISP4 when ε_a=5%
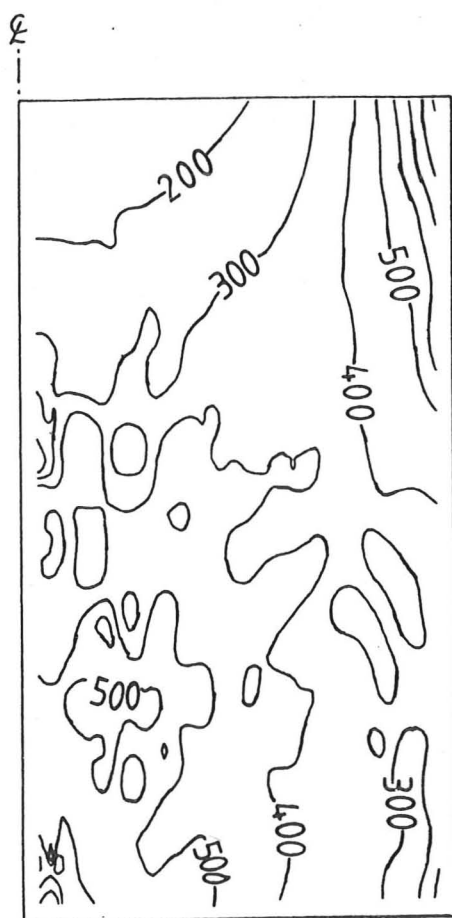
(a) Major principal stress
     contour (1 unit = 10 kPa)
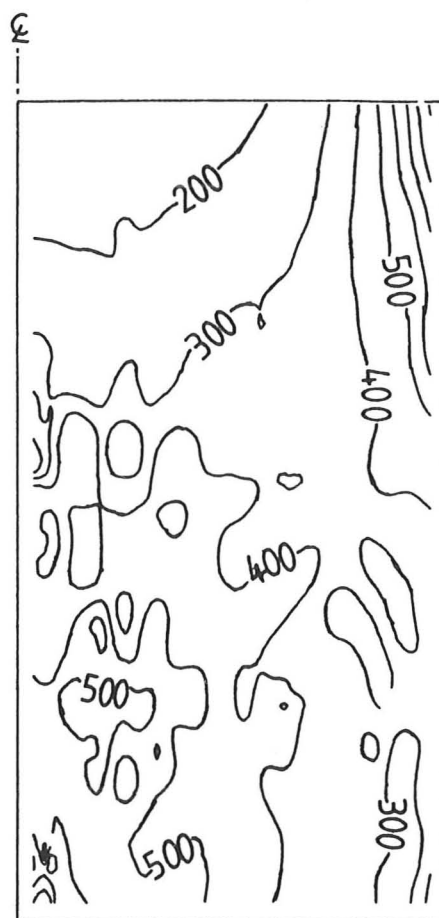
(b) Vertical stress contour
     (1 unit = 10 kPa)

Fig 5.25 Regional variation of stresses in a triaxial
         specimen for test CRISP4 when $\varepsilon_a = 5\%$
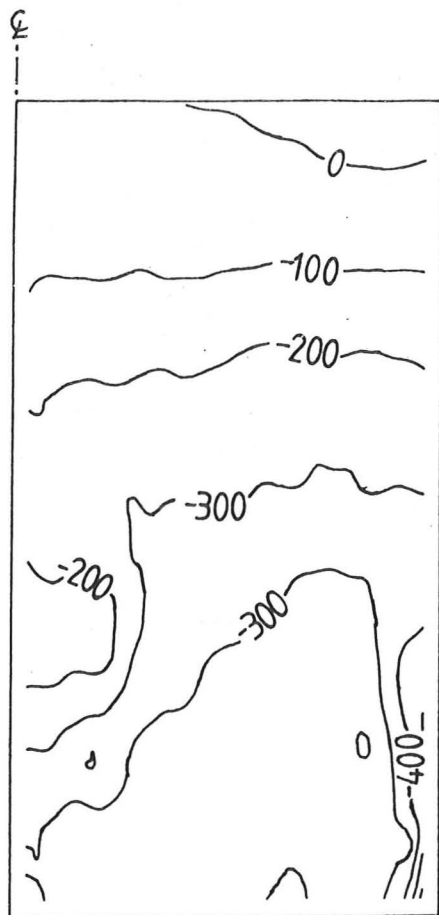
(a) Volumetric strain
     contour (100 unit = 1%)
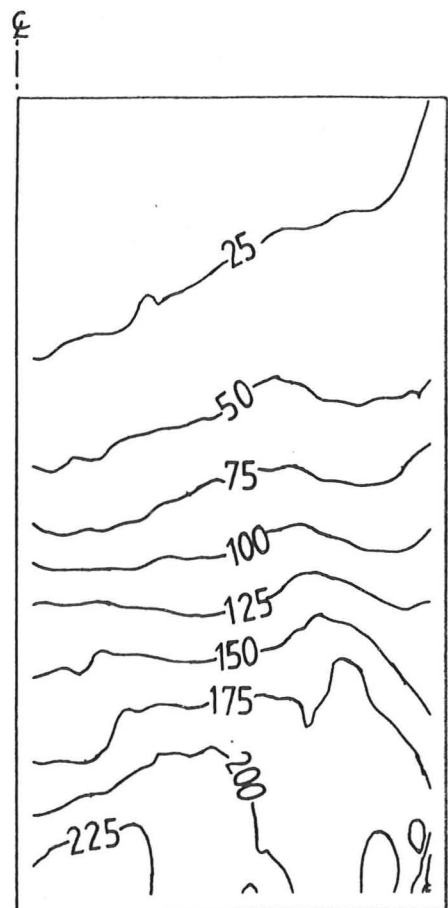
(b) Maximum shear strain
     contour (10 unit = 1%)
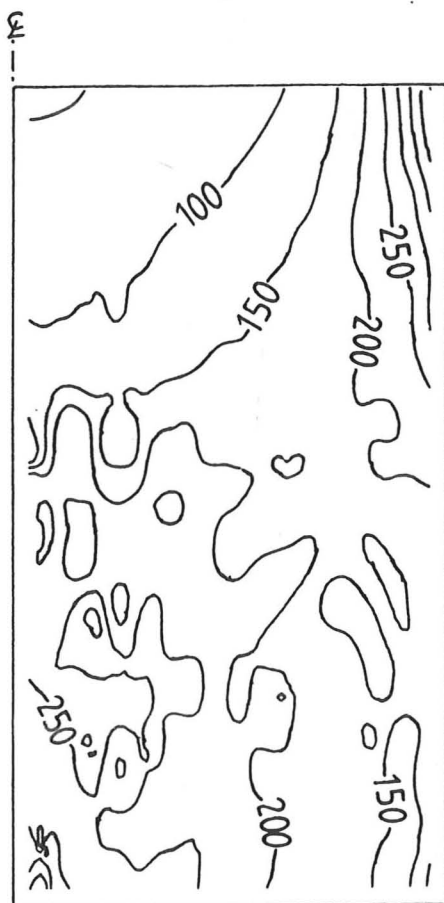
(c) Mean stress contour
     (1 unit = 10 kPa)
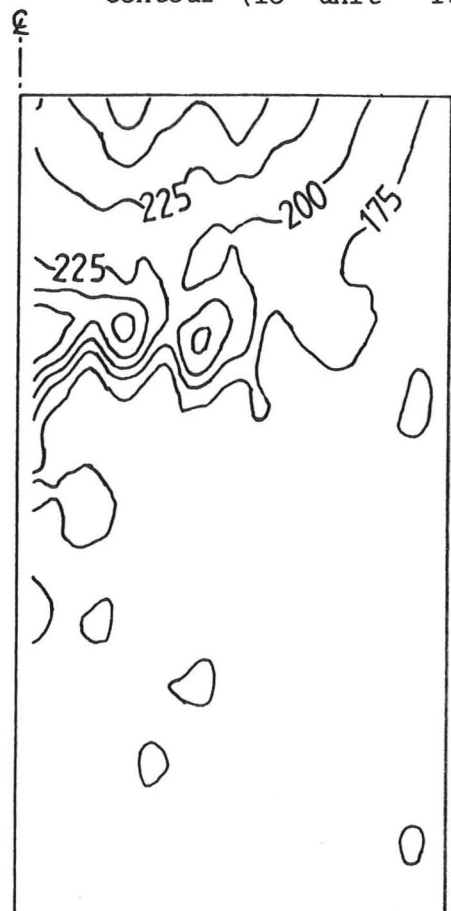
(d) Stress ratio contour q/p
     (100 unit = 1)

· Fig 5.26   Regional variation of stresses and strains in a triaxial
             specimen for test CKL4 when ε_a =5%
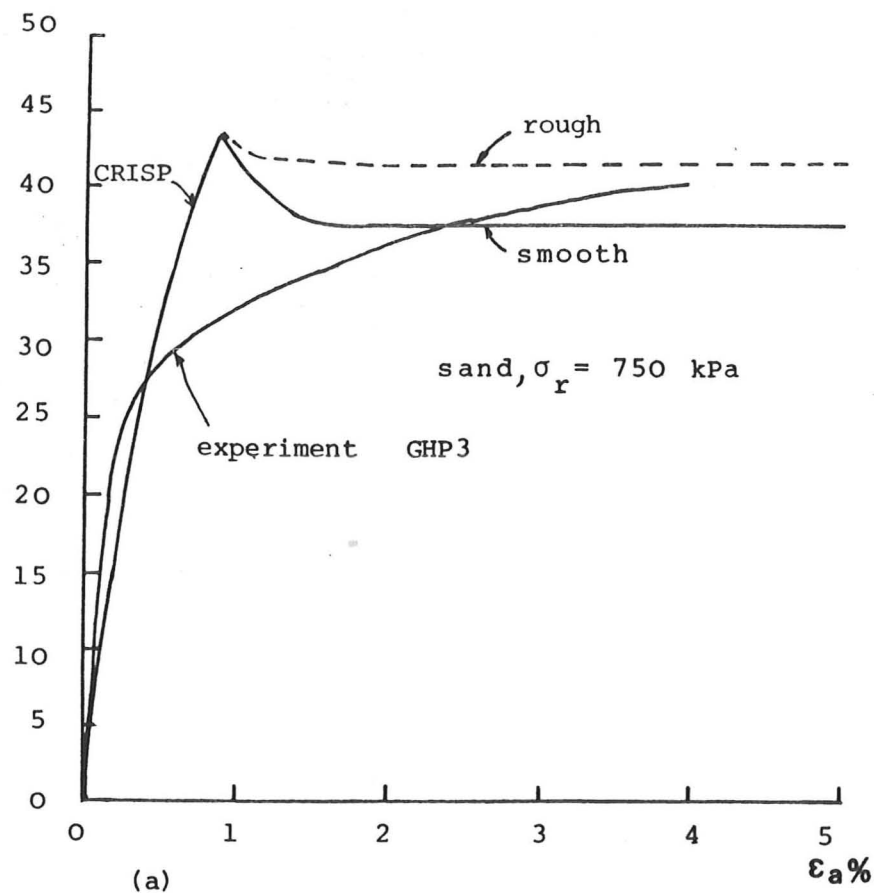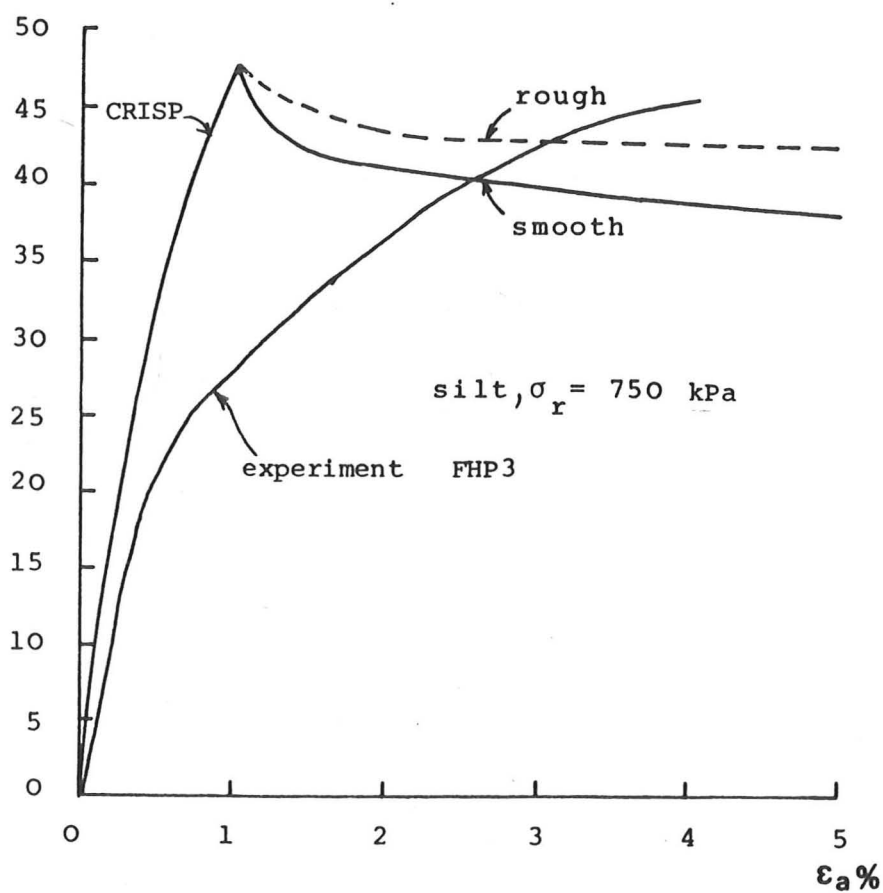
Fig 5.27   Effects of roughness of end platens on ϕ_{max}
measured in a triaxial test
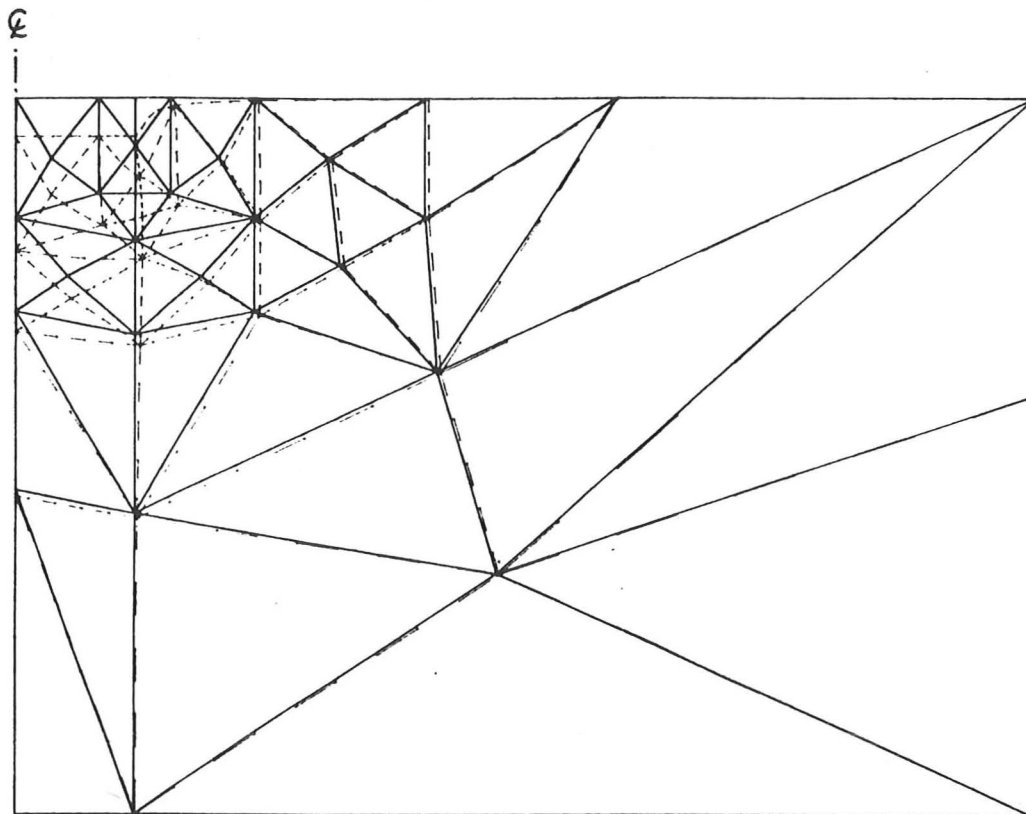
Fig 5.28 Deformed mesh of CRISP5 after 480 increments
when $W/B=16\%$
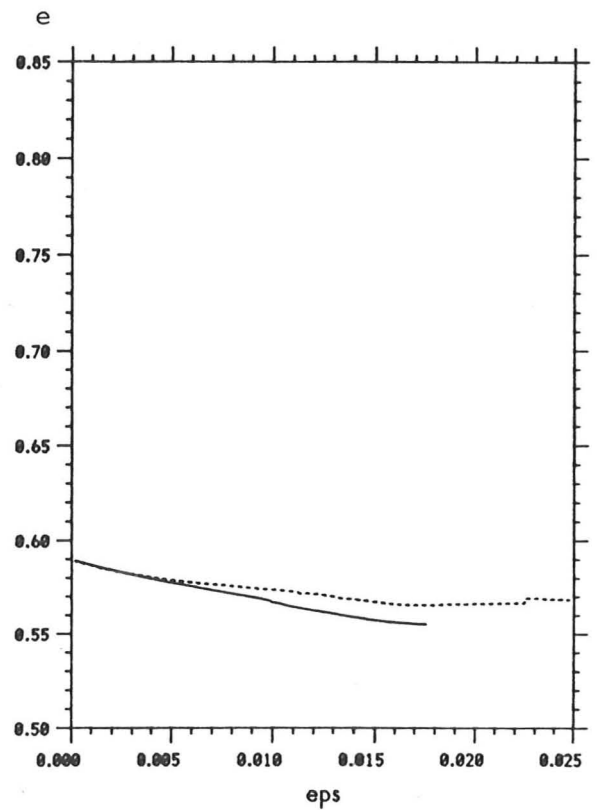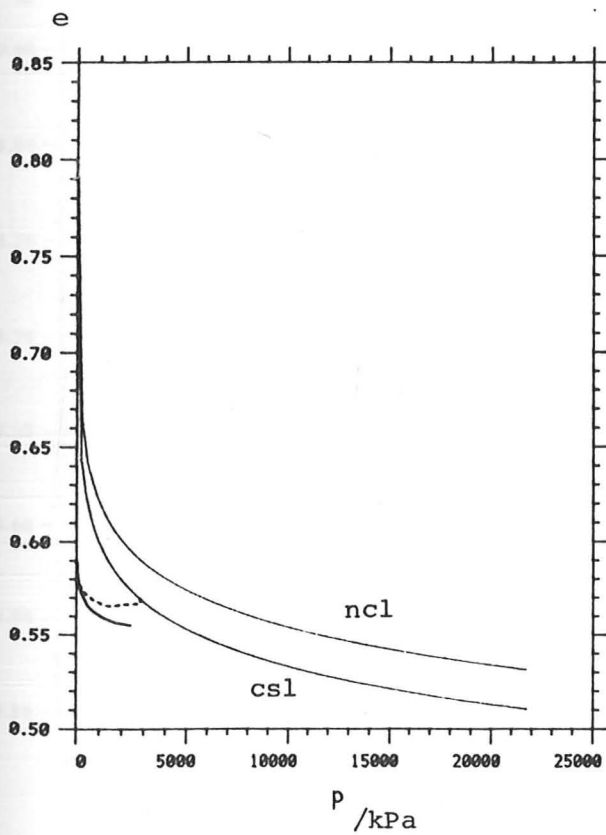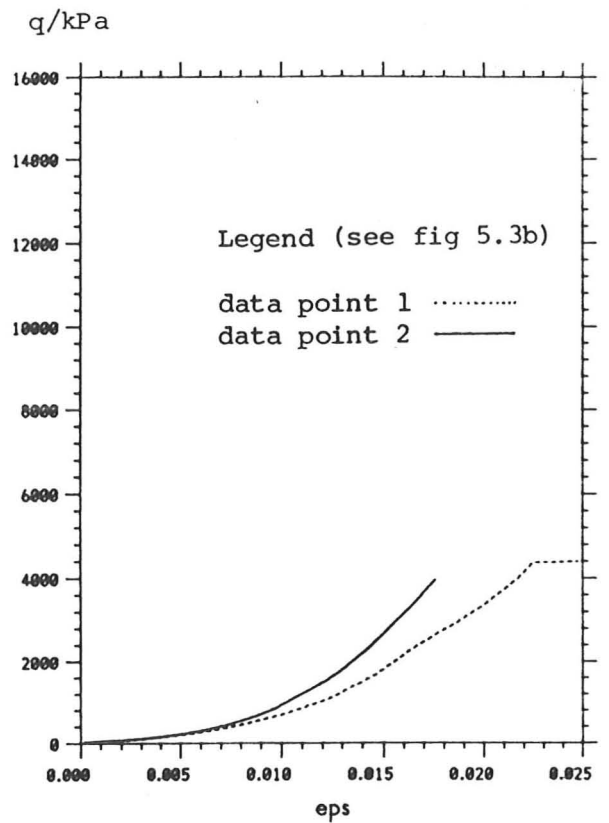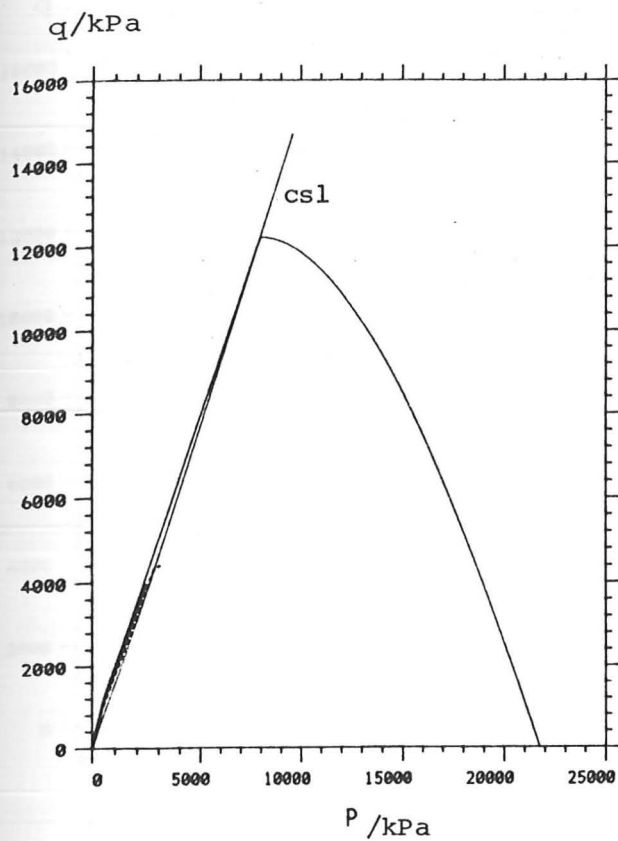
Fig 5.29   Stress-strain history of test CRISP5
           in the active zone
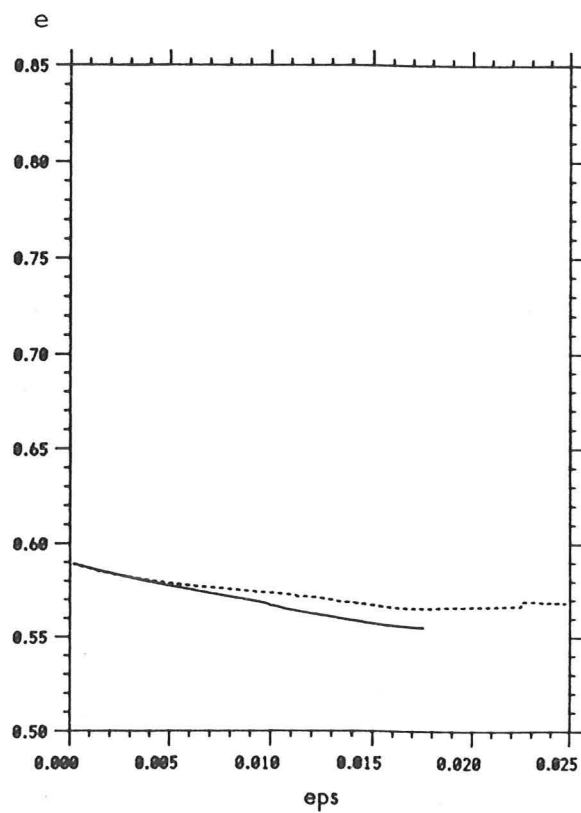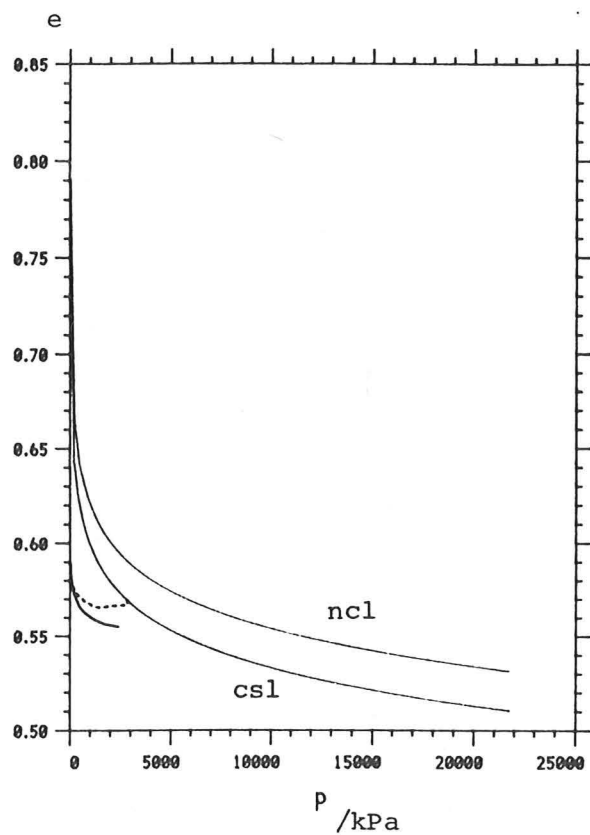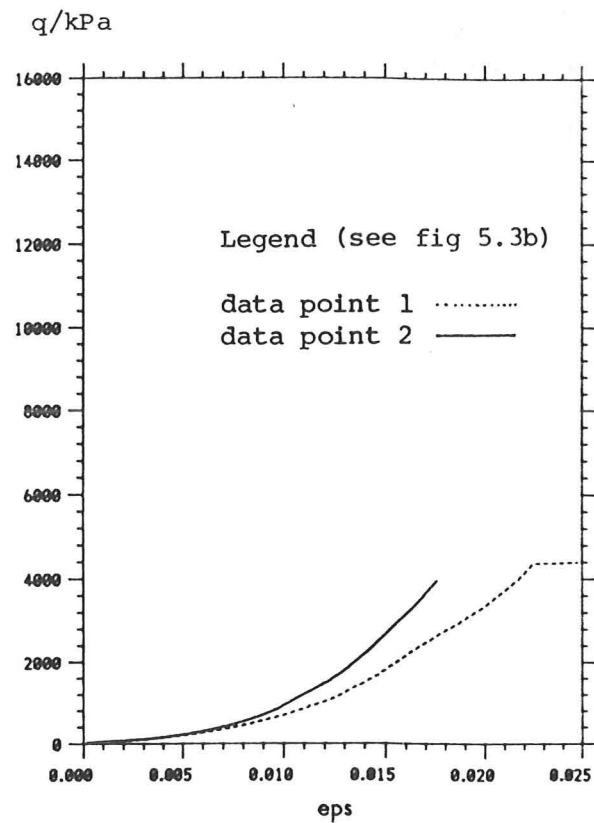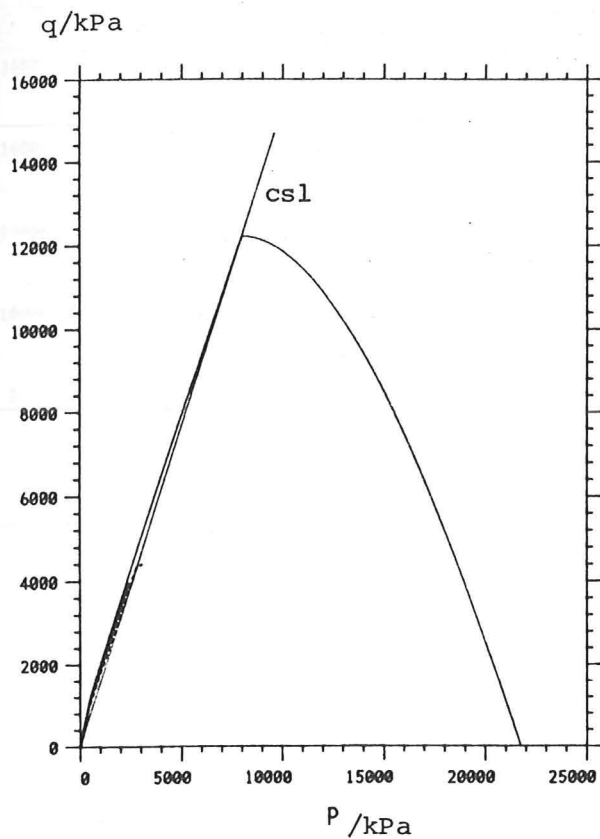
Fig 5.29   Stress-strain history of test CRISP5
in the active zone
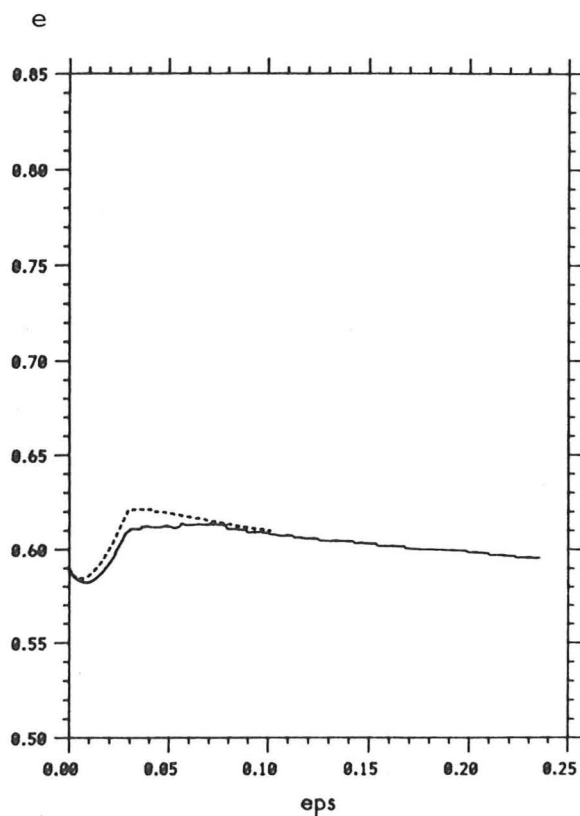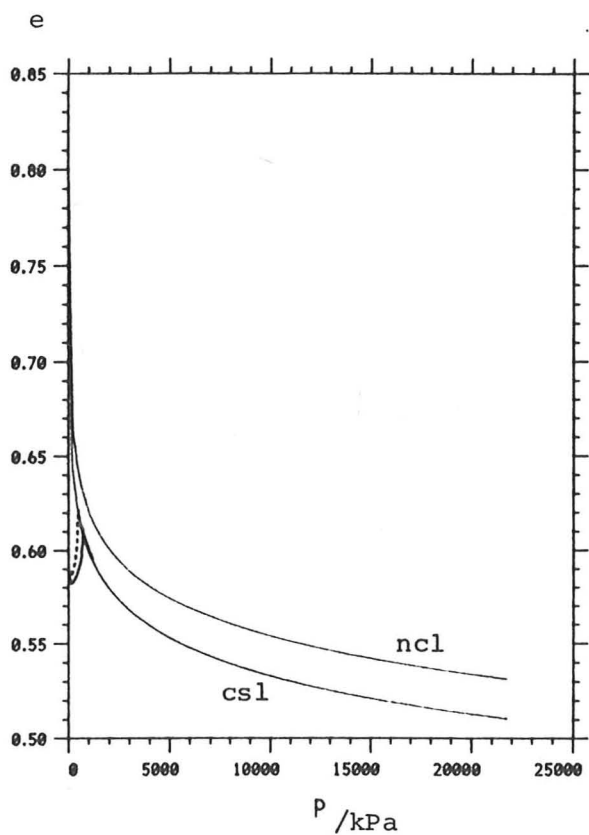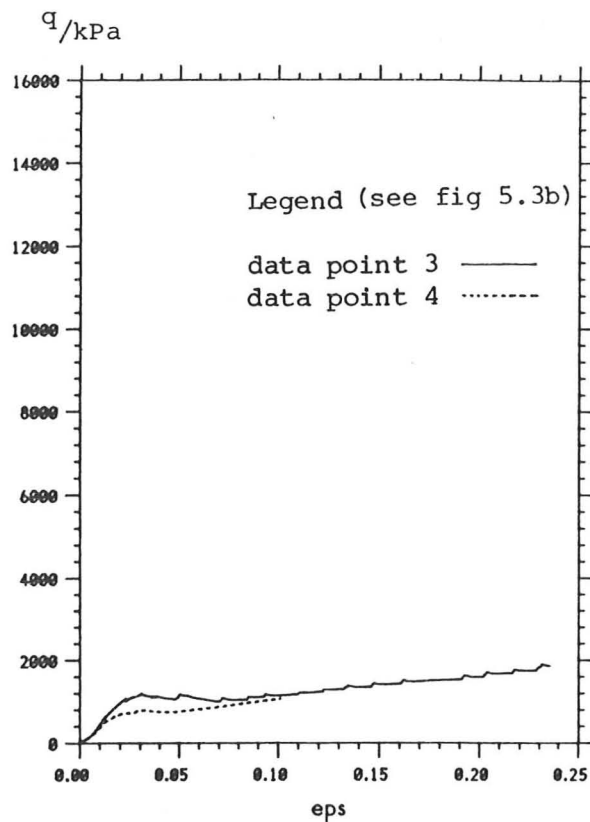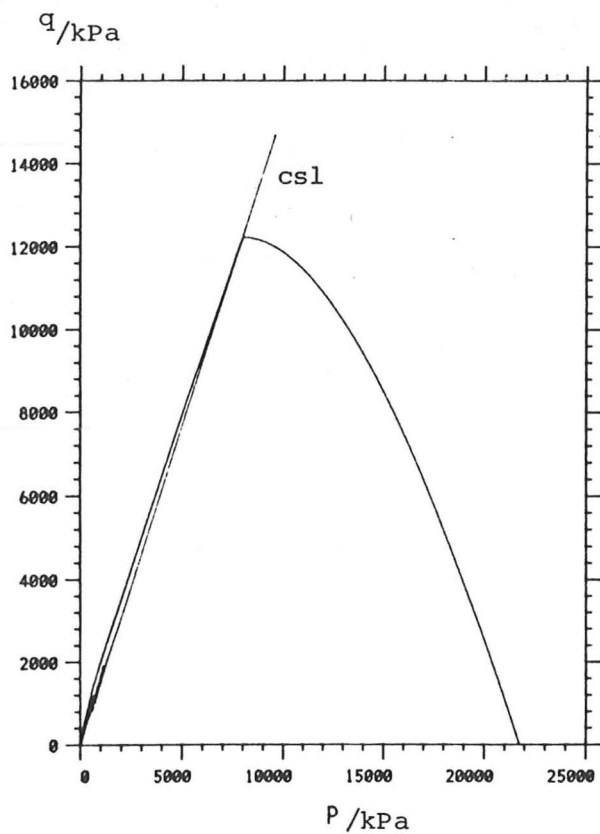
Fig 5.30   Stress-strain history of test CRISP5
in the fan zone
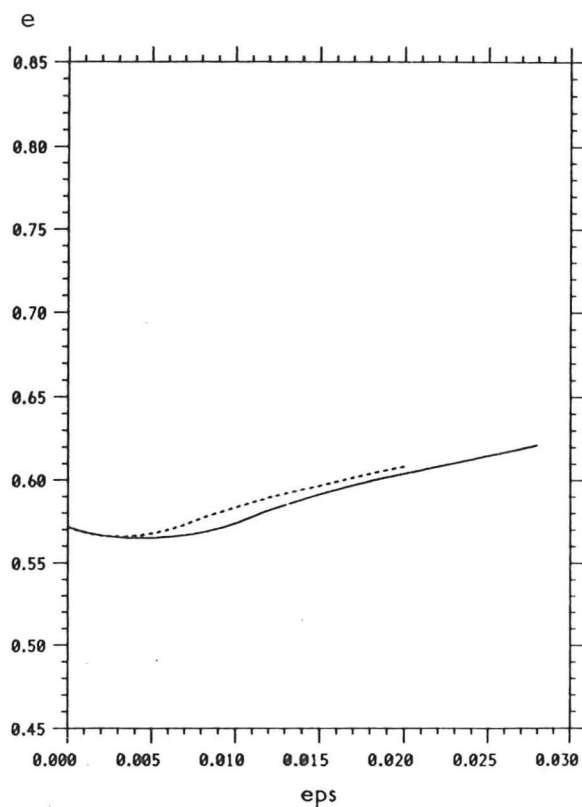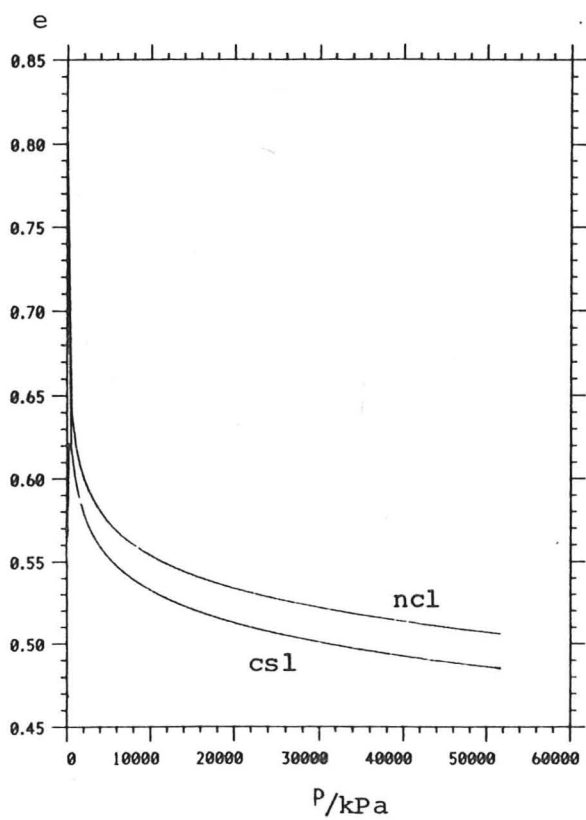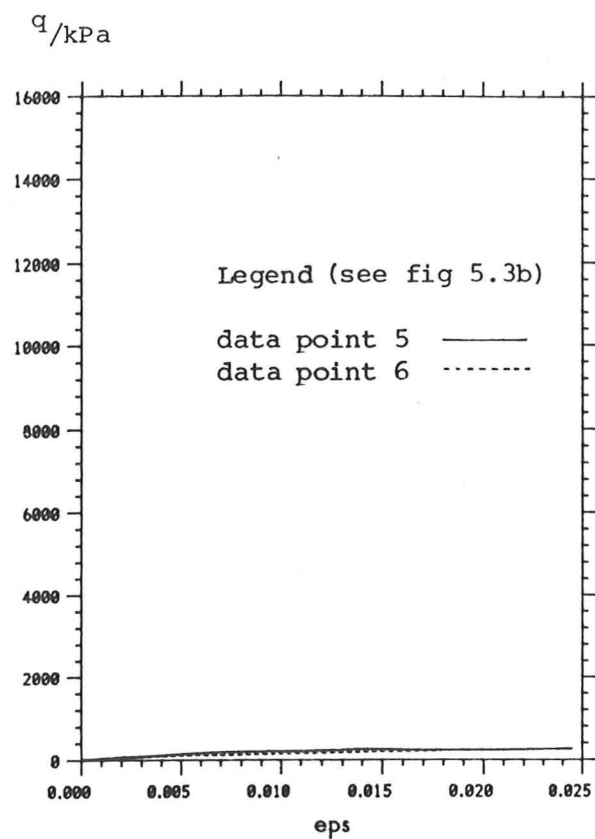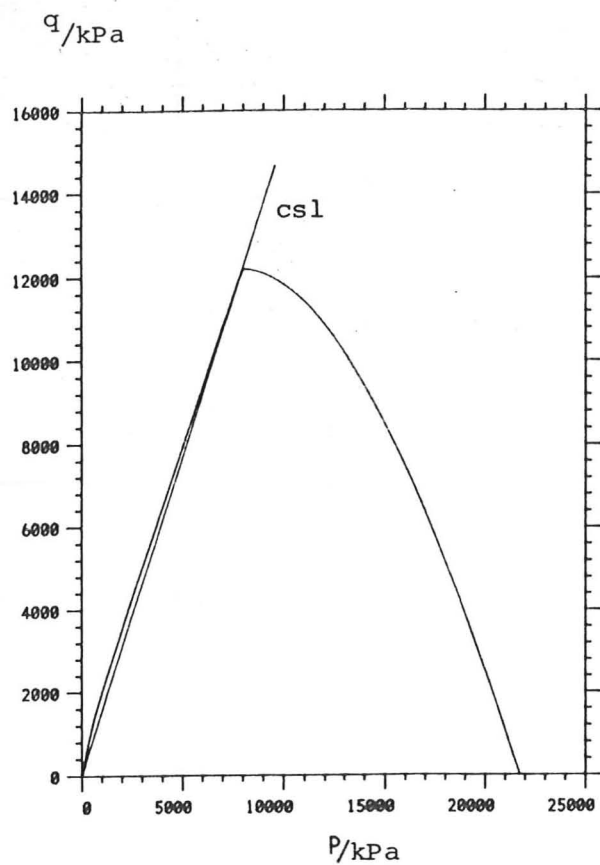
Fig 5.31   Stress-strain history of test CRISP5
in the passive zone
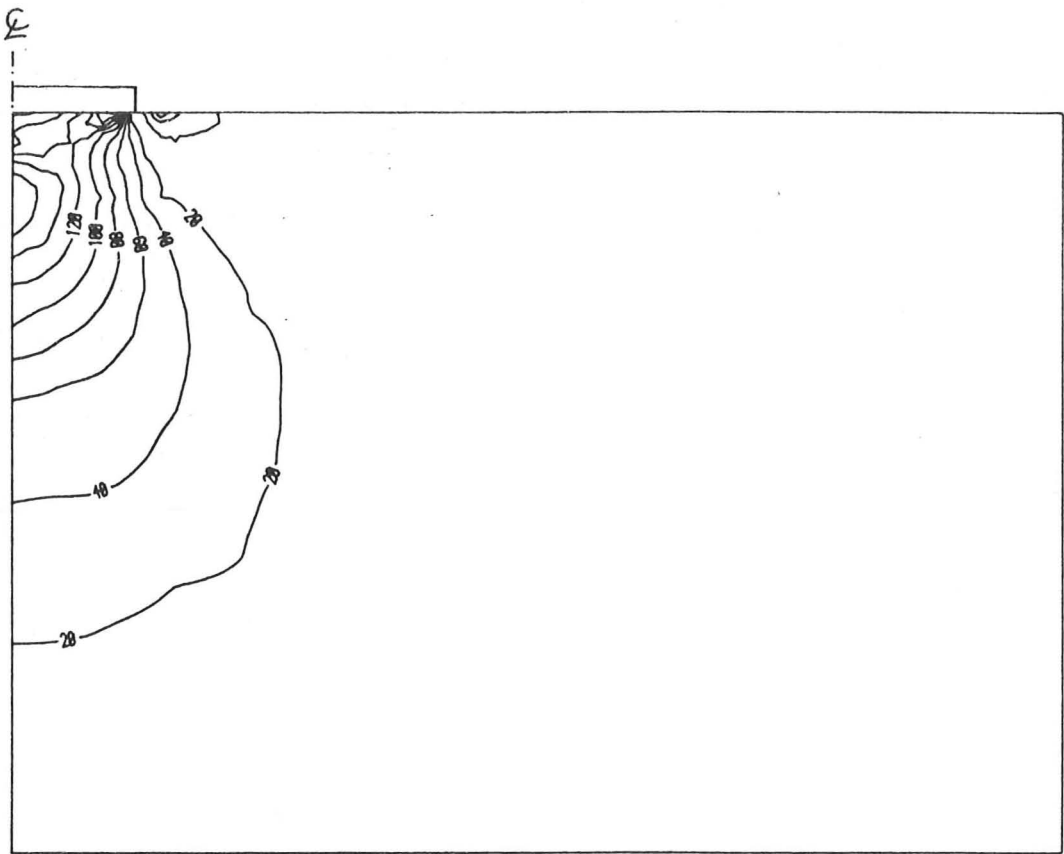
(a)   Minor principal stress contour   (1 unit = 10 kPa)
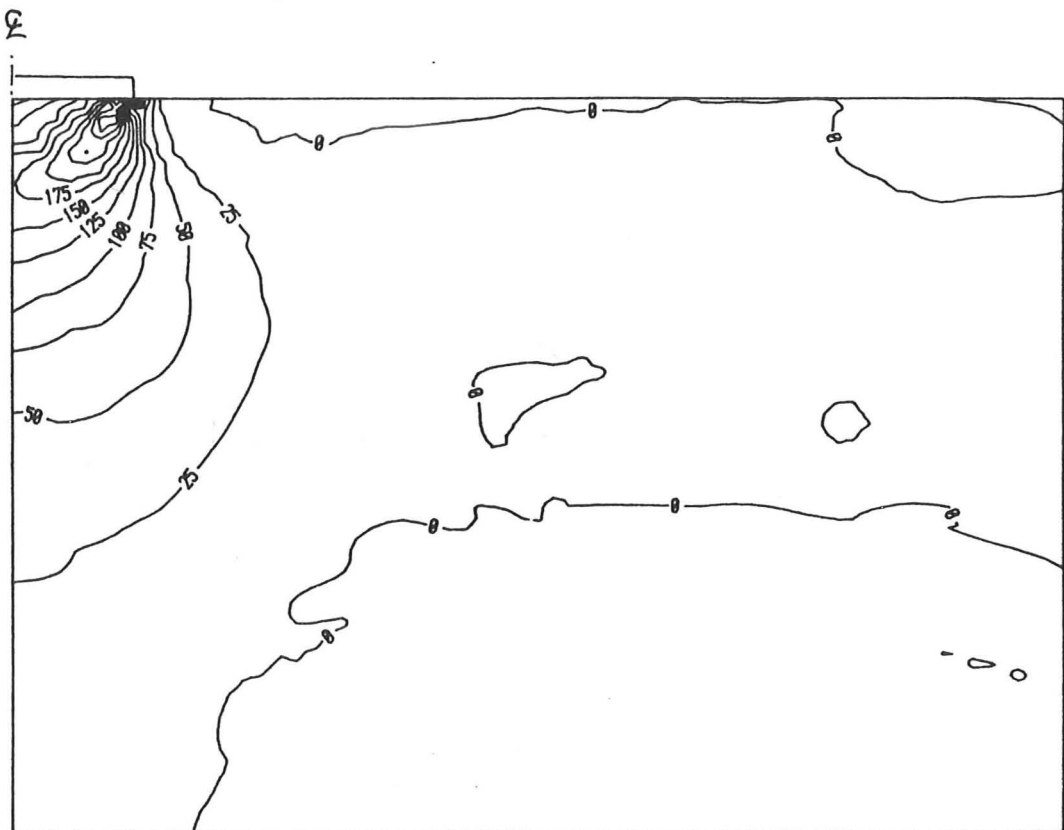
(b)   Circumferential stress contour (1 unit = 10 kPa)

Fig 5.32   Regional variation of stresses in the supporting
           soil for test CRISP5 when W/B=16%
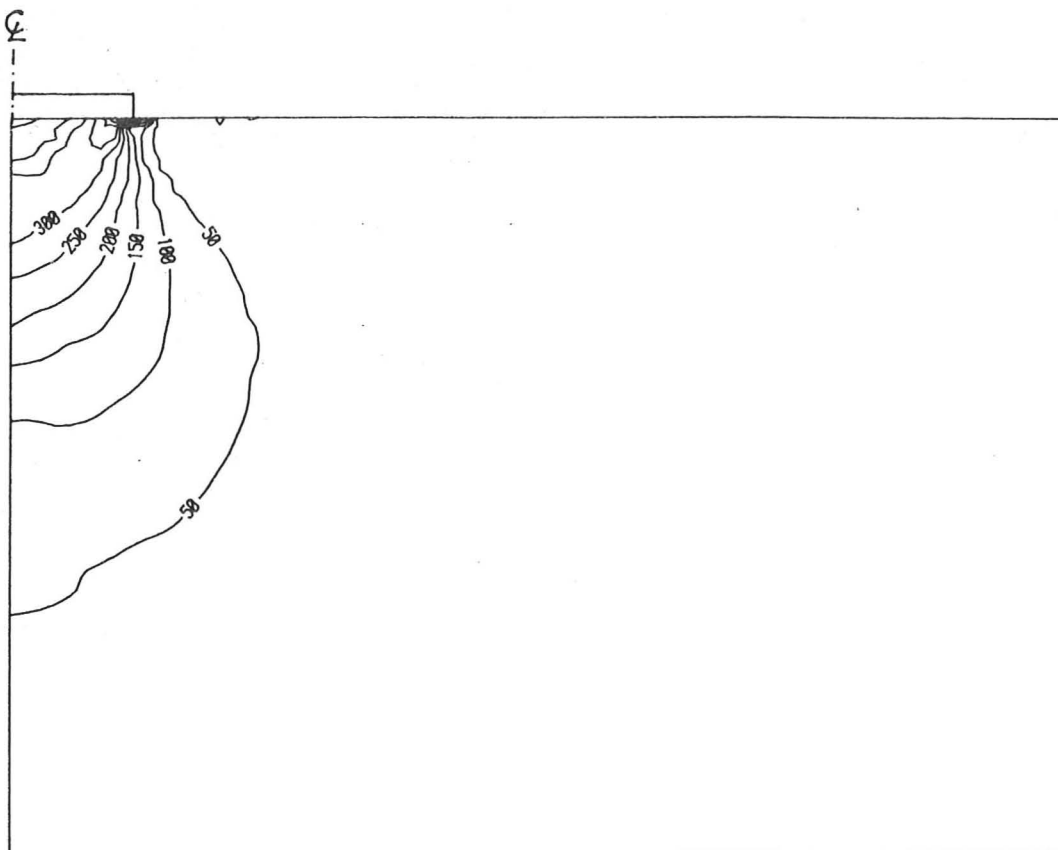
(a)   Mean stress contour (1 unit = 10 kPa)
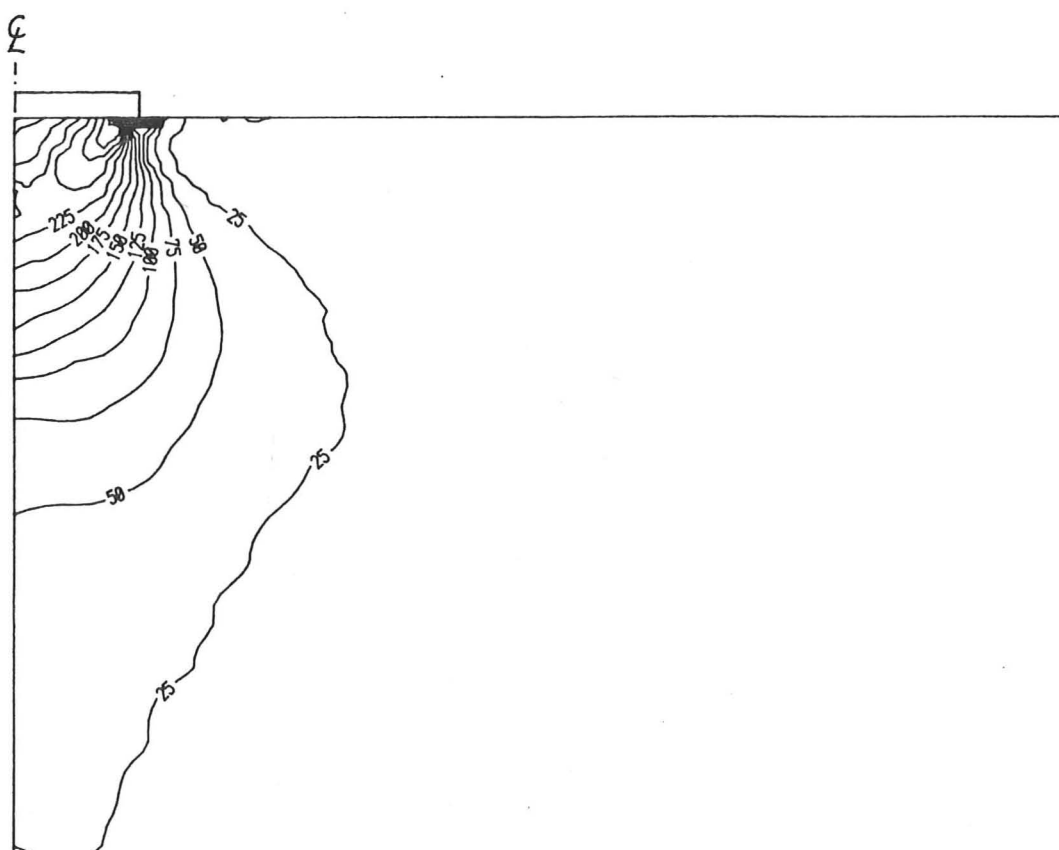
(b)   Maximum shear stress contour (1 unit = 10 kPa)

Fig 5.33 Regional variation of stresses in the supporting soil
          for test CRISP5 when $^W/B=16\%$
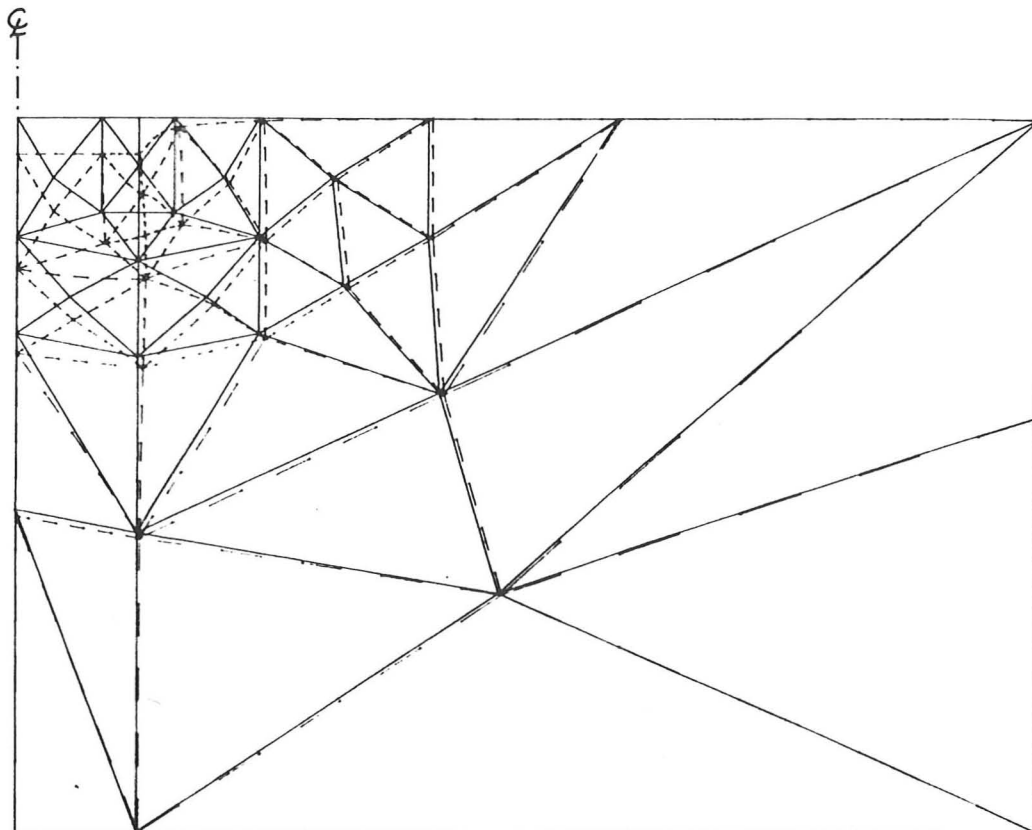
Fig 5.34   Deformed mesh of CRISP6 after 600 increments
          when w /B=15%
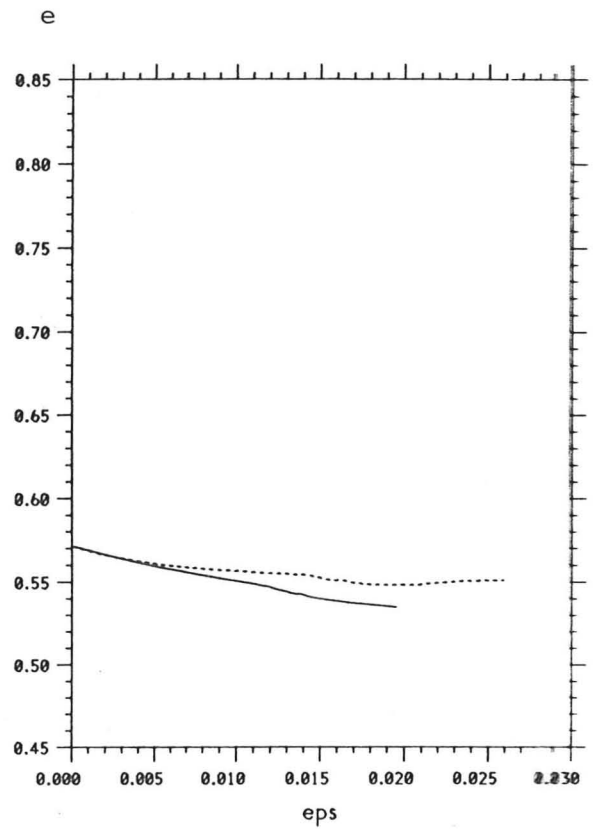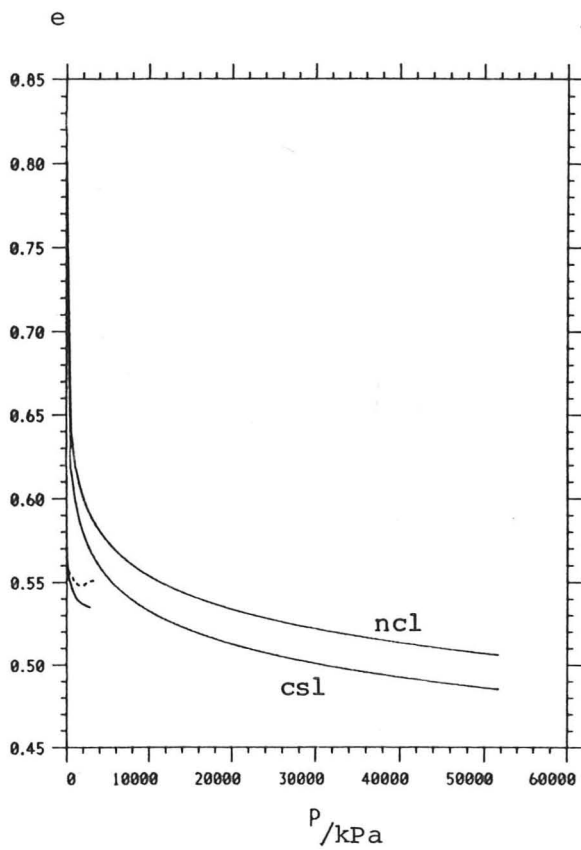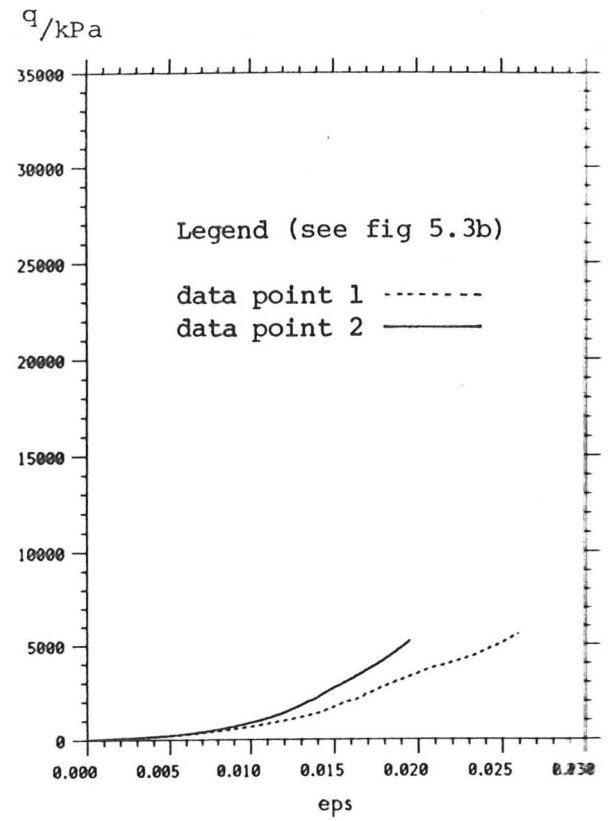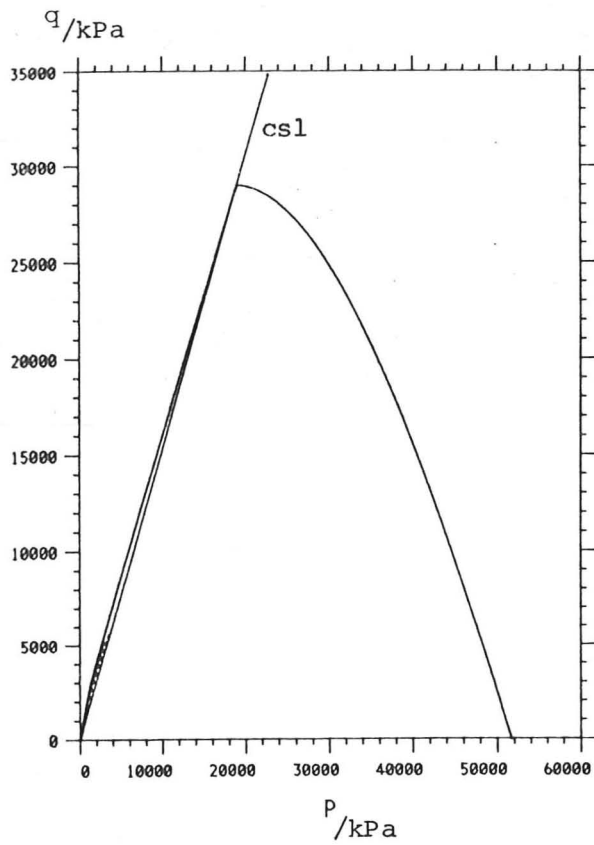
Fig 5.35   Stress-strain history of test CRISP6 in the active zone
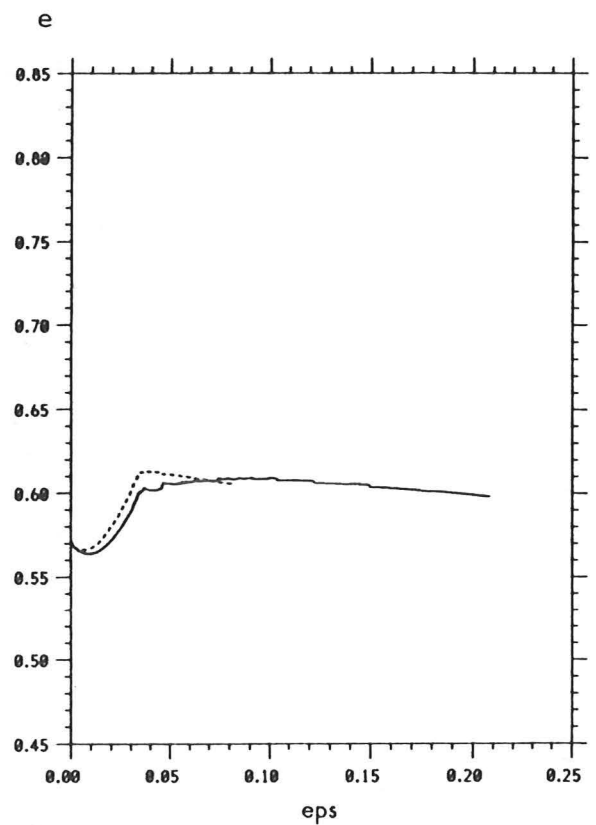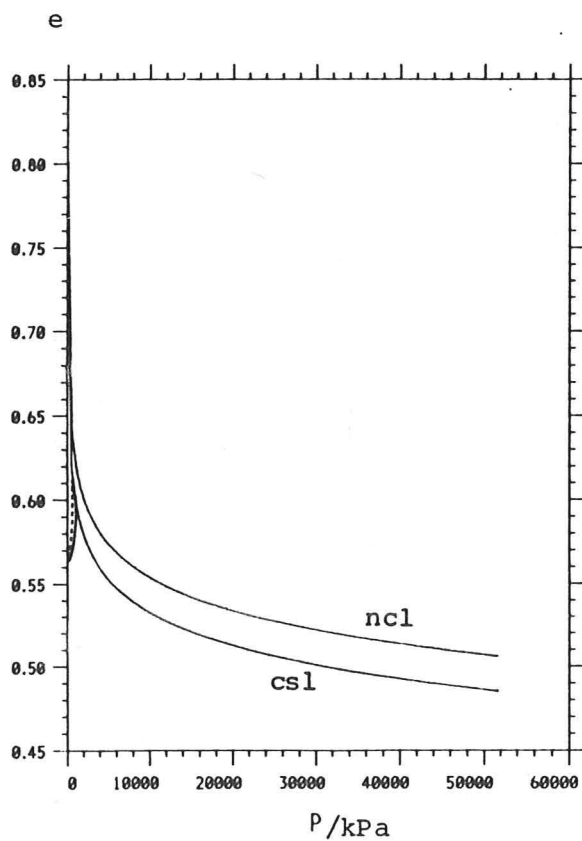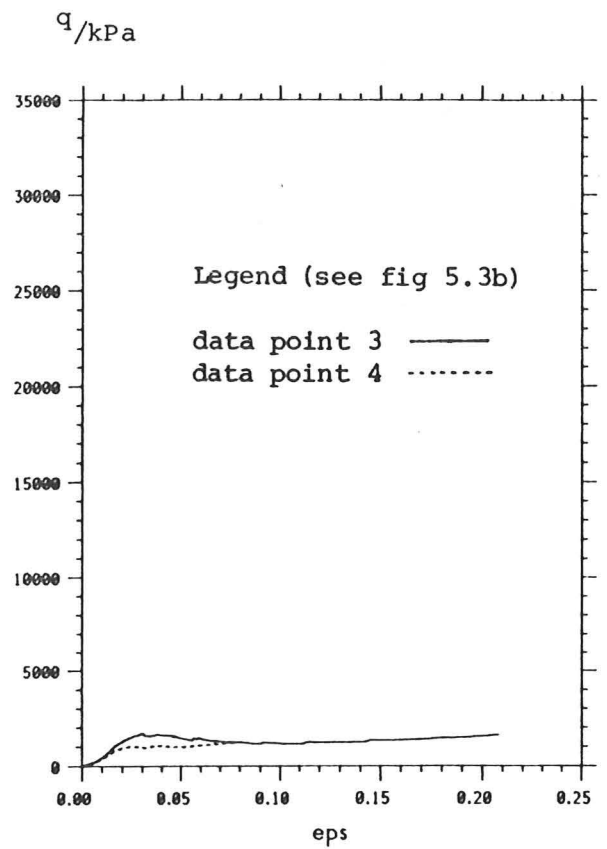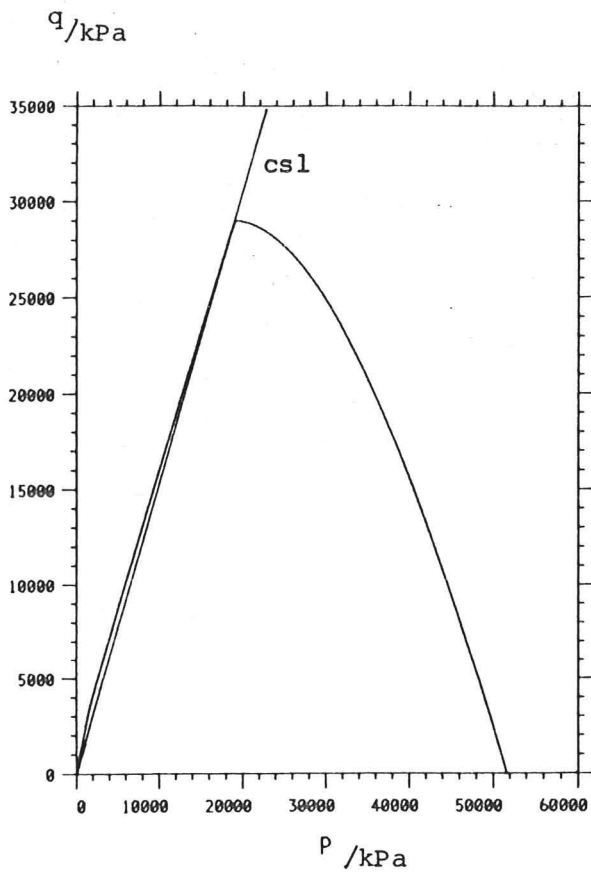
Fig 5.36   Stress-strain history of test CRISP6 in the fan
          zone
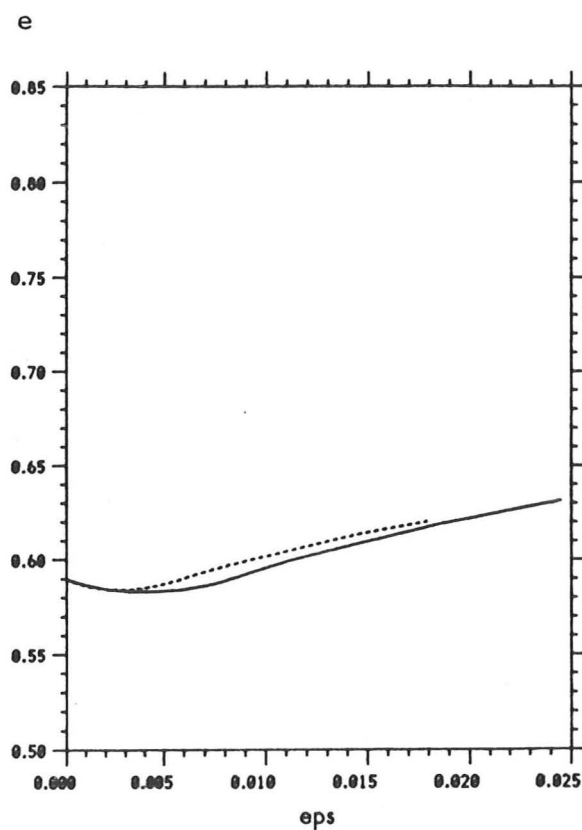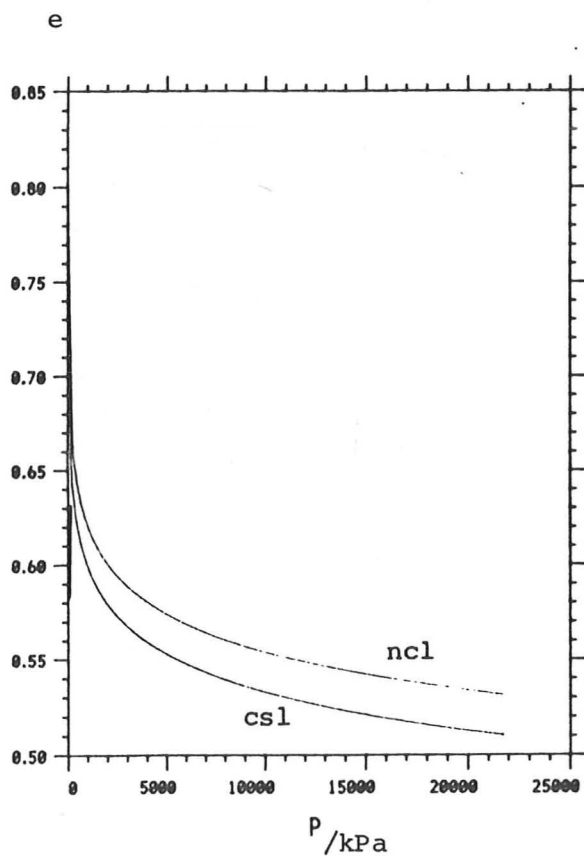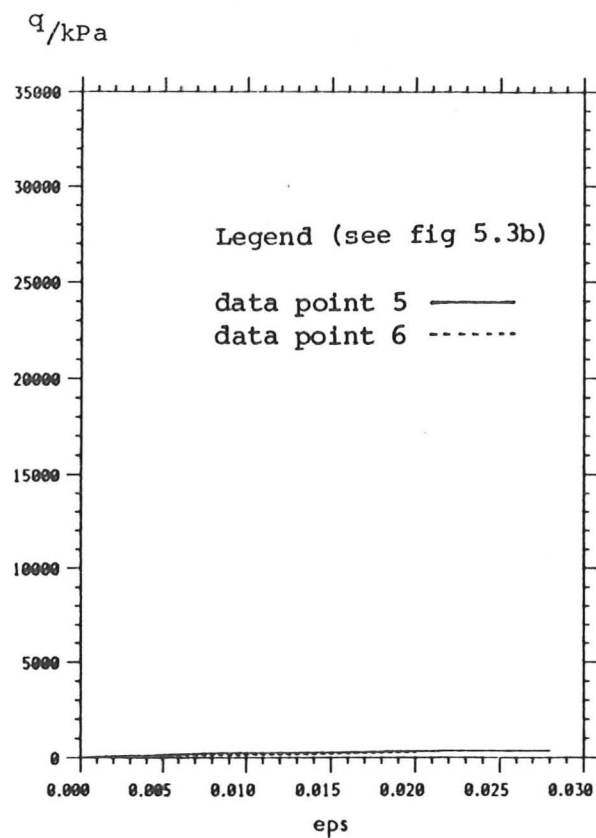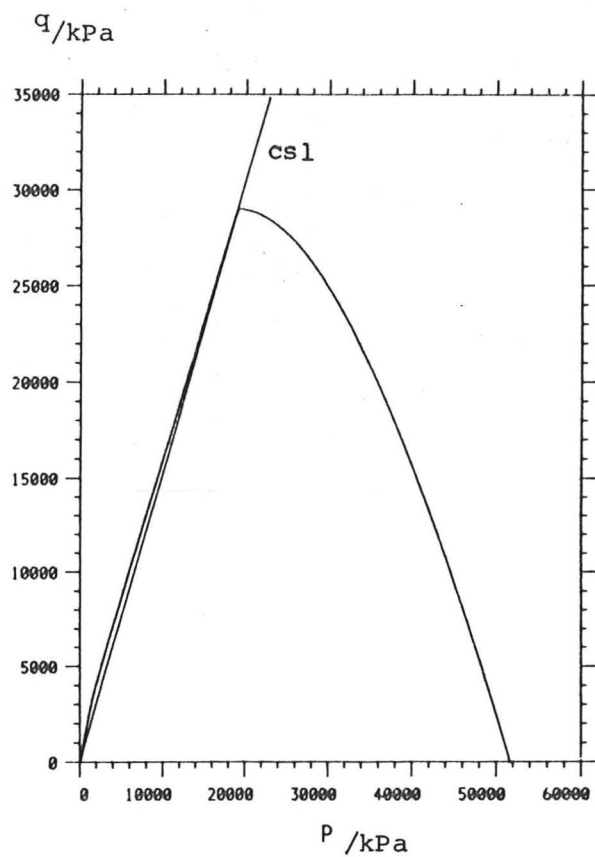
Fig 5.37   Stress-strain history of CRISP6 in the passive zone
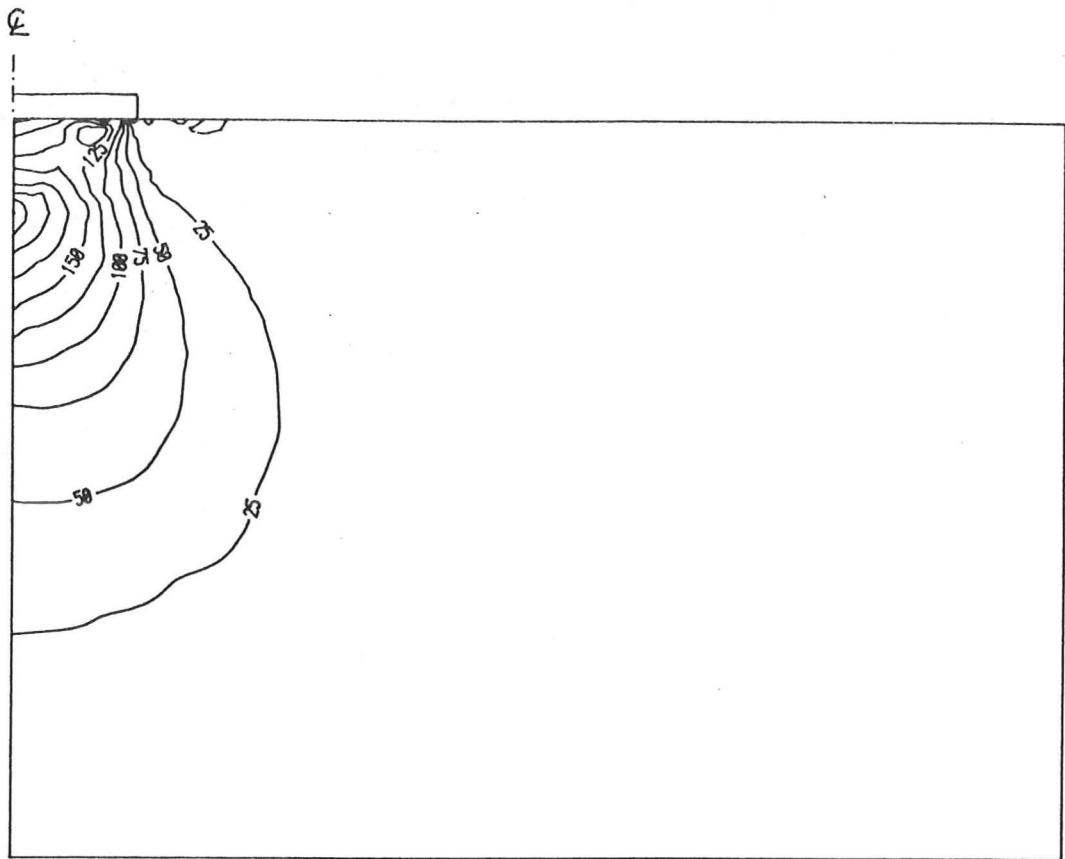
(a)   Minor principal stress contour **(1 unit = 10 kPa)**
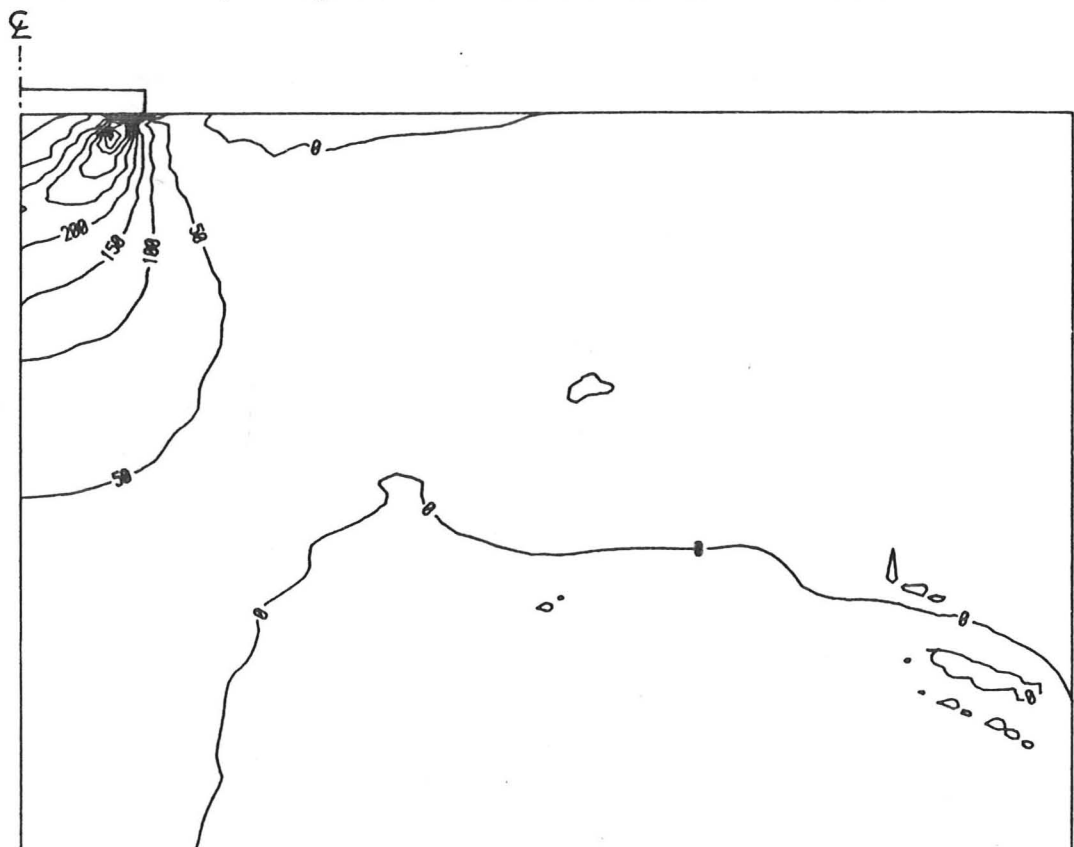
(b)   Circumferential stress contour **(1 unit = 10 kPa)**

Fig 5.38   Regional variation of stresses in the supporting soil
for CRISP6 when $^W/B=15\%$
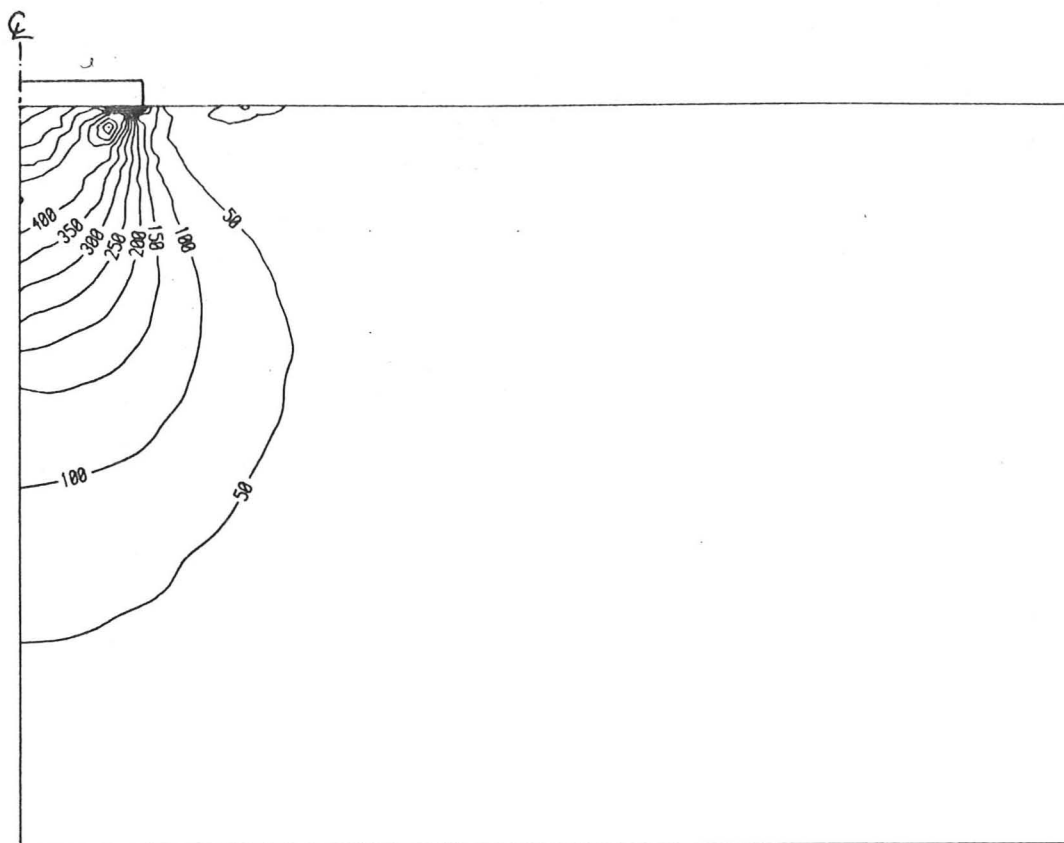
(a) Mean stress contour (1 unit = 10 kPa)
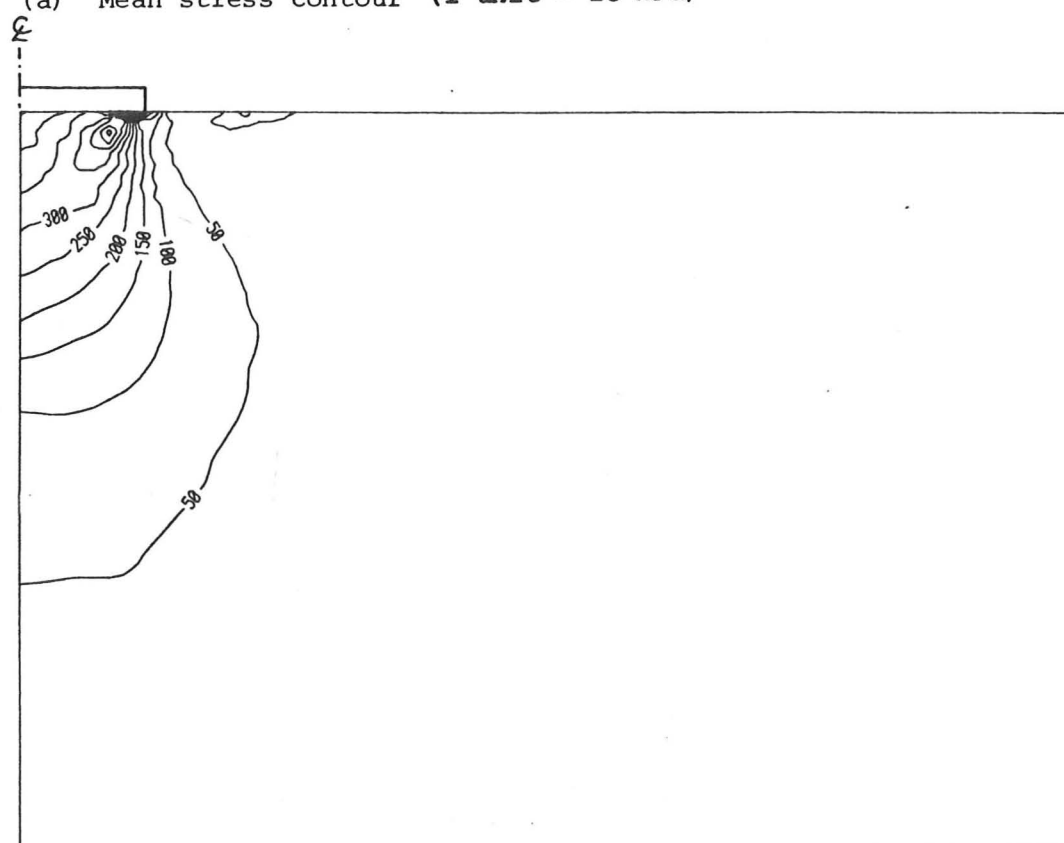
(b) Maximum shear stress contour (1 unit = 10 kPa)

Fig 5.39 Regional variation of stresses in the supporting soil
for test CRISP6 when W/B=15%
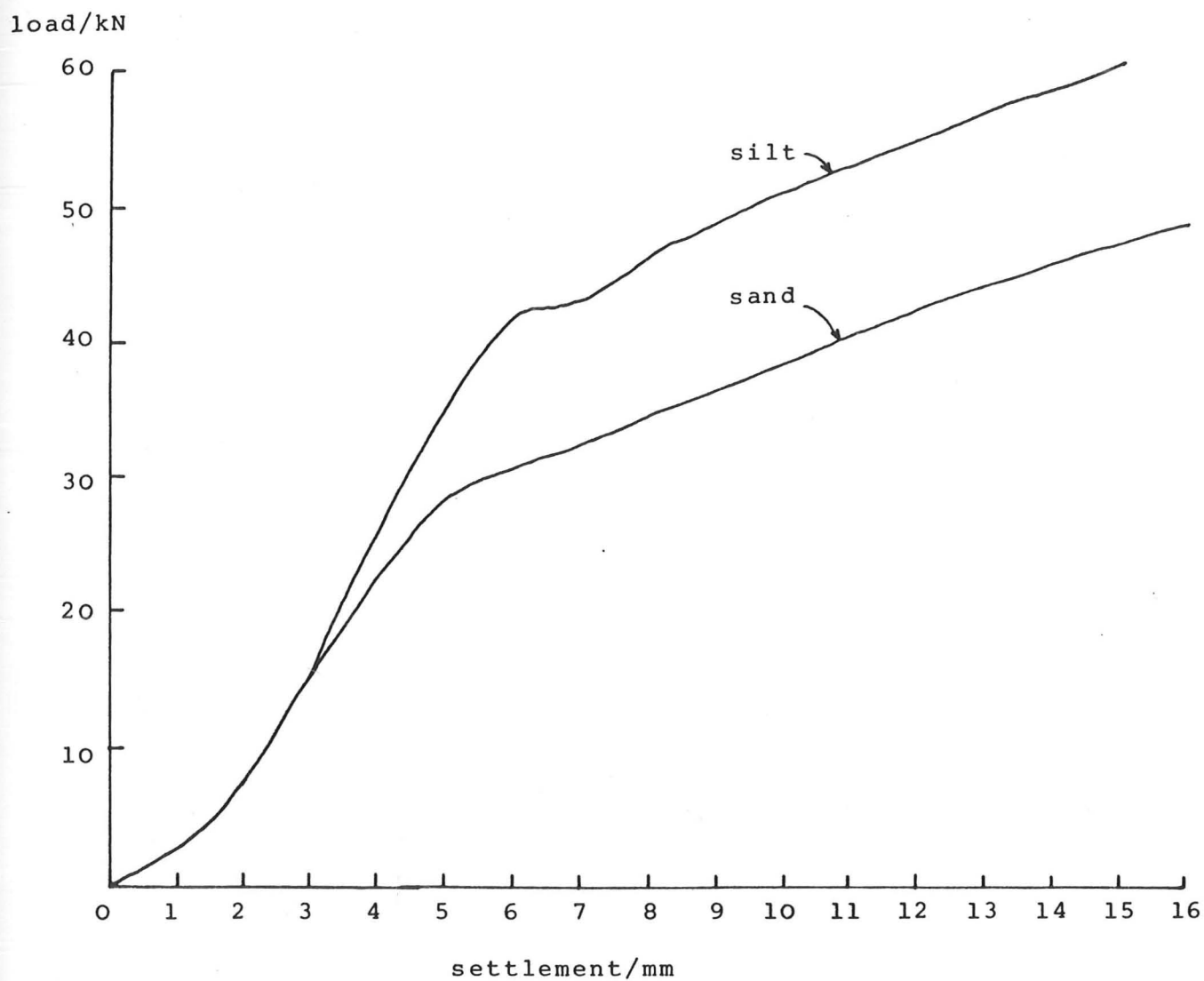
Fig 5.40   Finite element prediction of 1-g tests with B=100mm
and σ_o =25 kPa
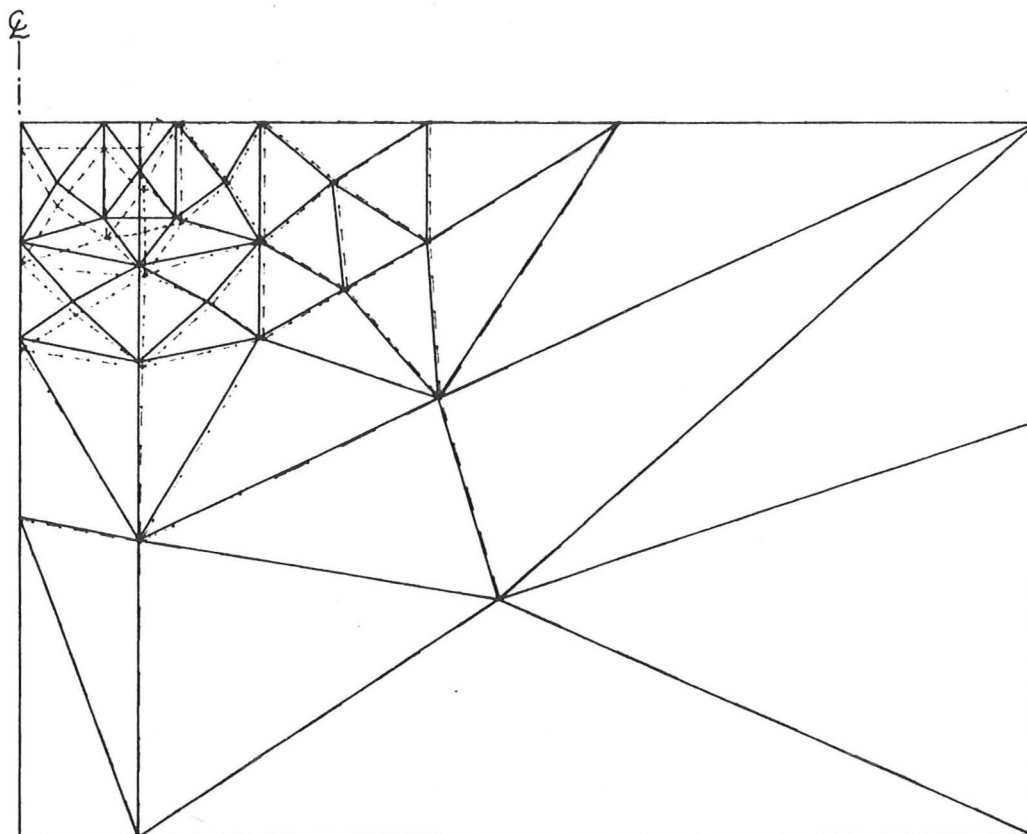
Fig 5.41   Deformed mesh of CRISP7 after 440 increments
           when w/B=11%
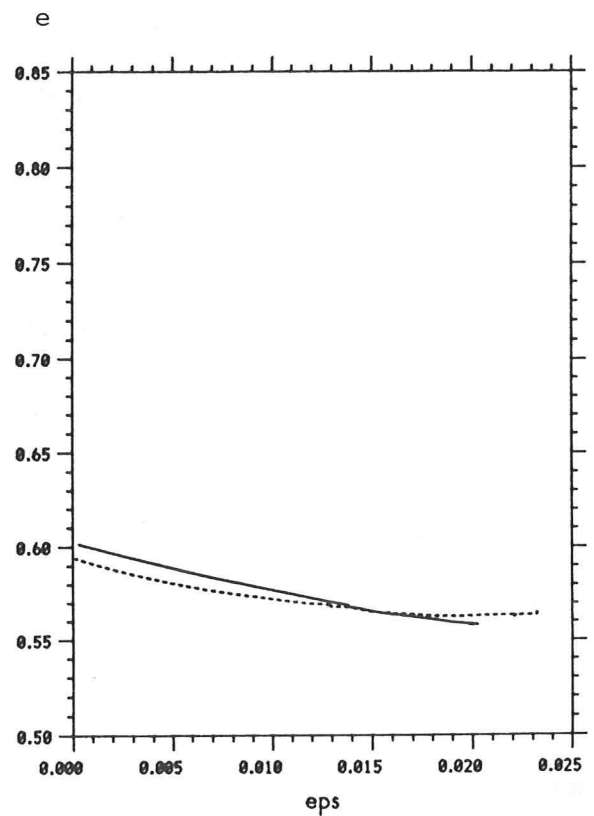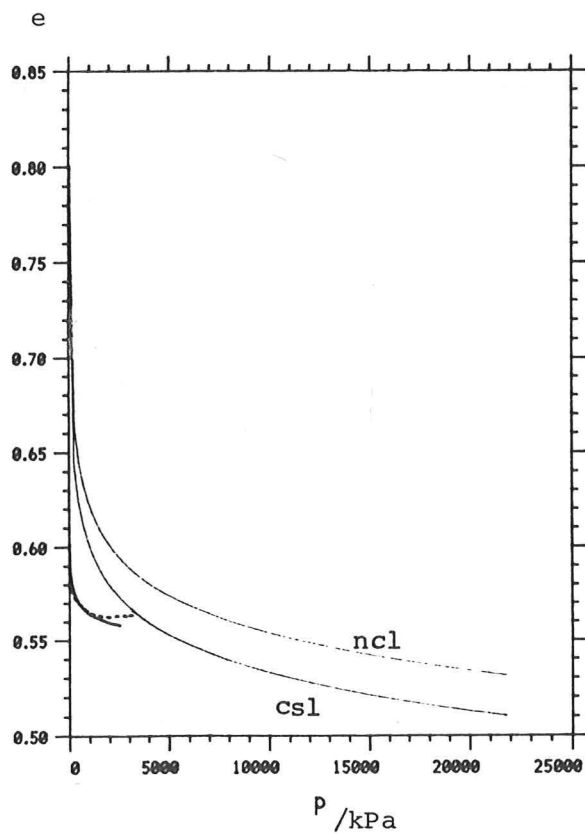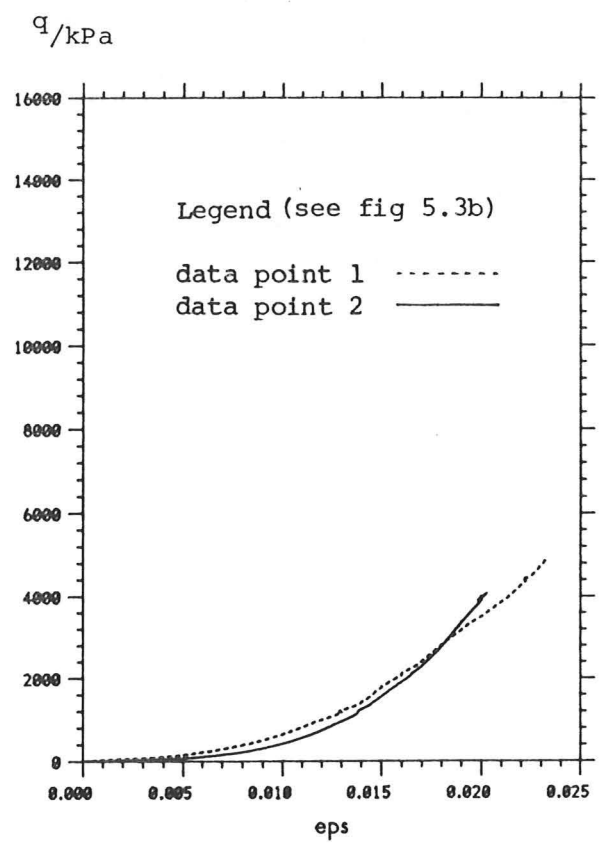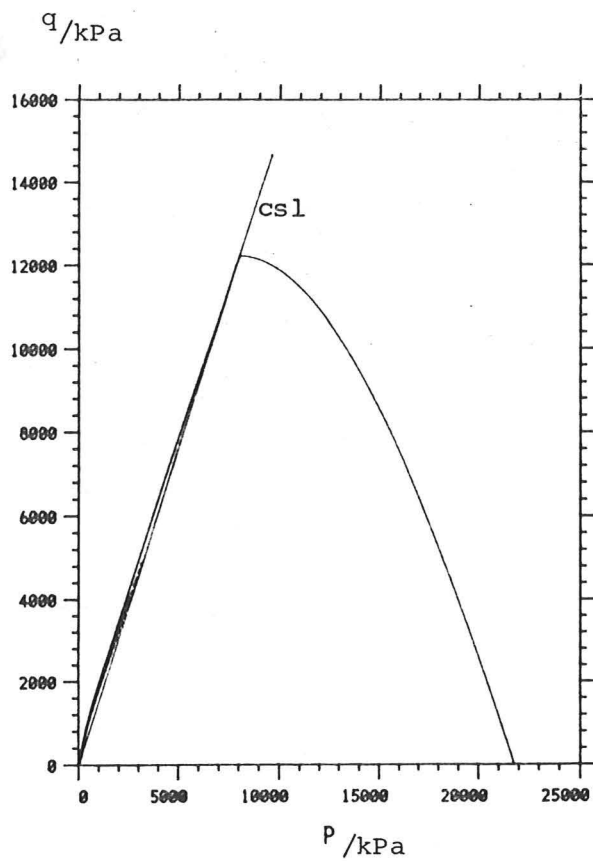
Fig 5.42   Stress-strain history of test CRISP7 in the active zone
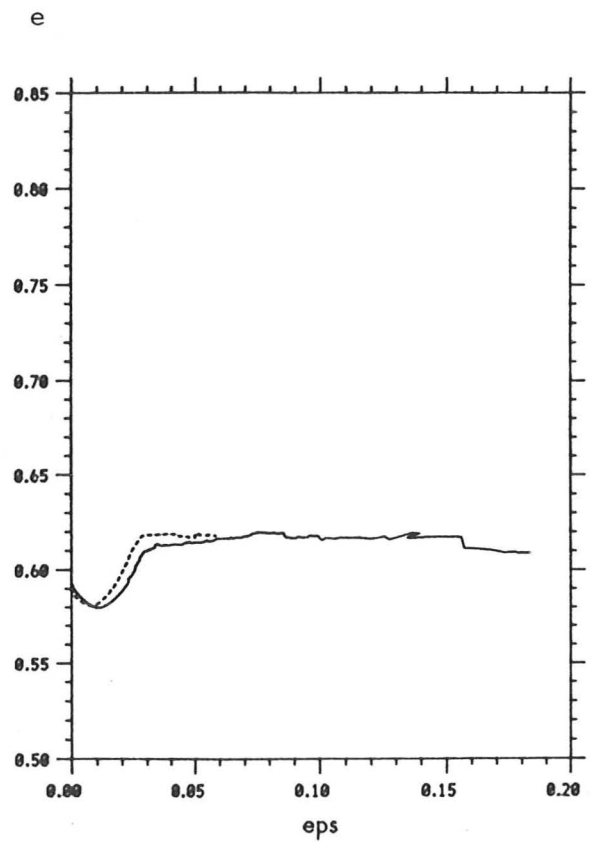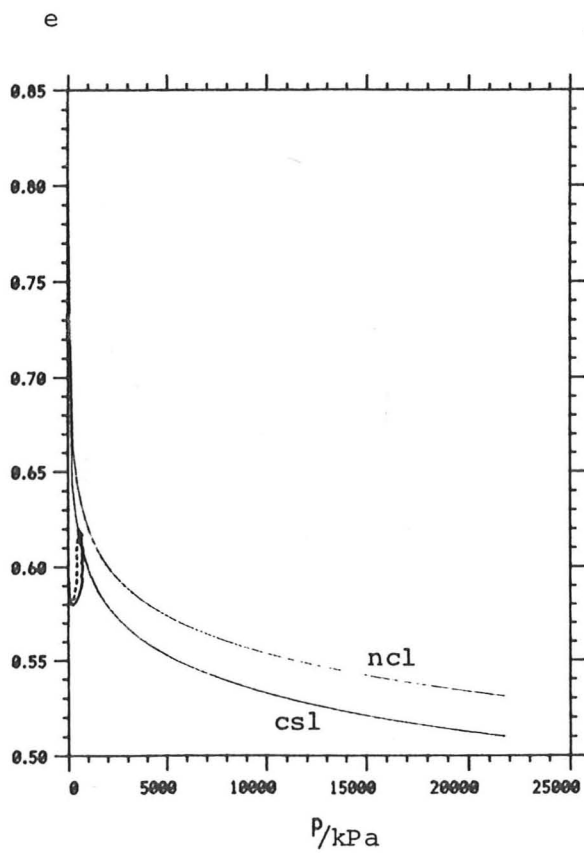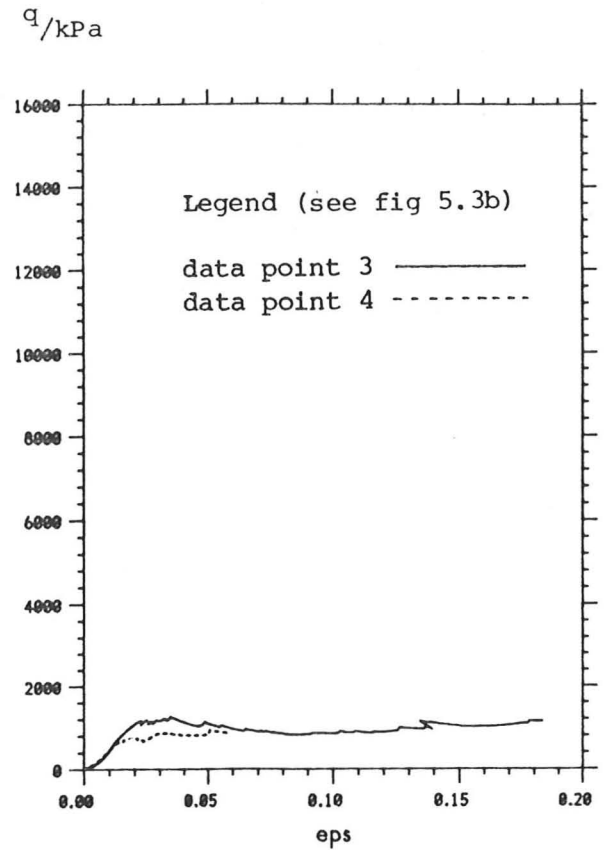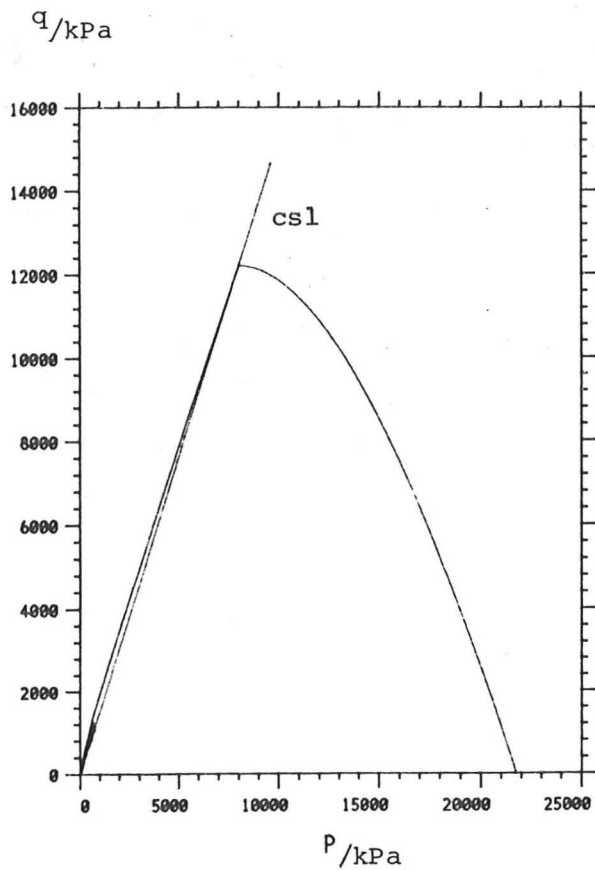
Fig 5.43 Stress-strain history of test CRISP7 in the fan zone
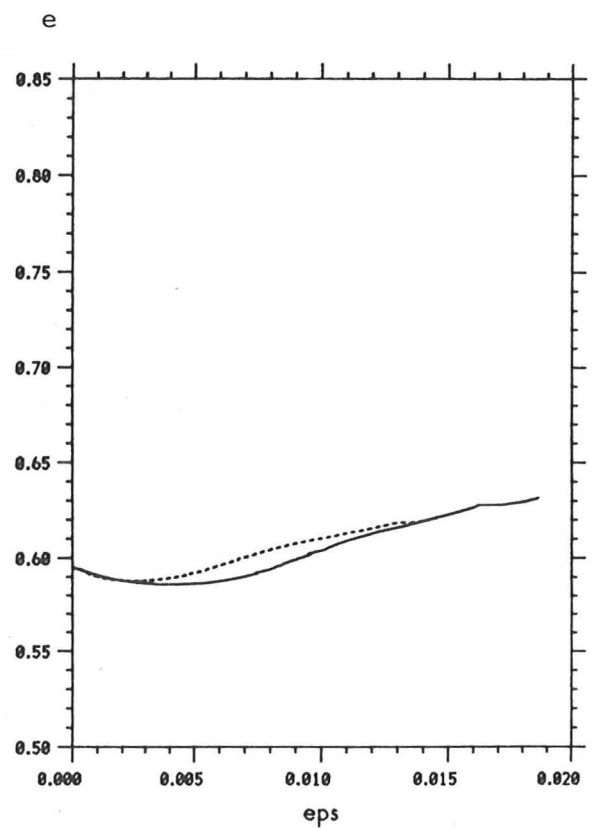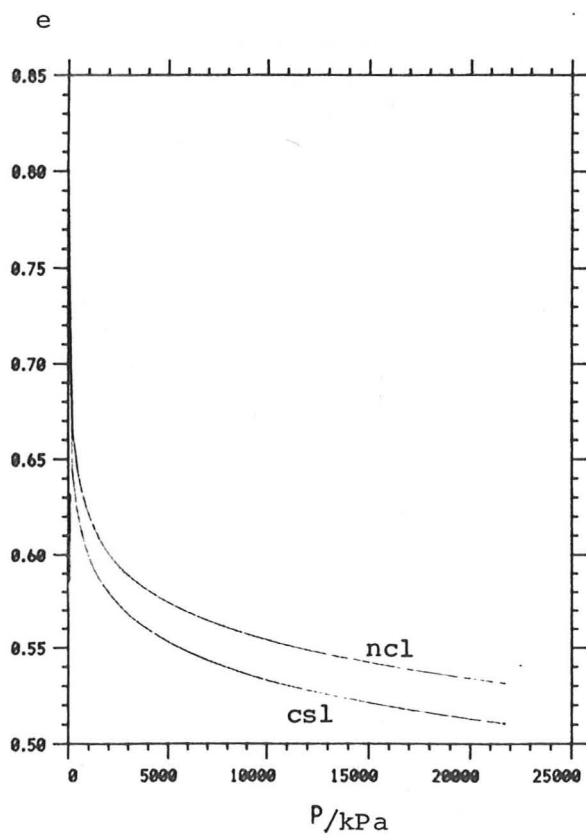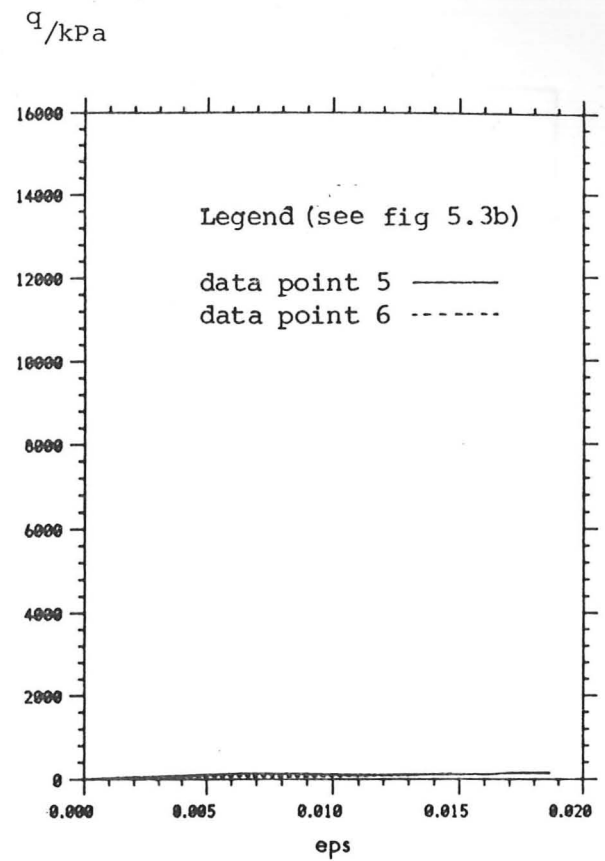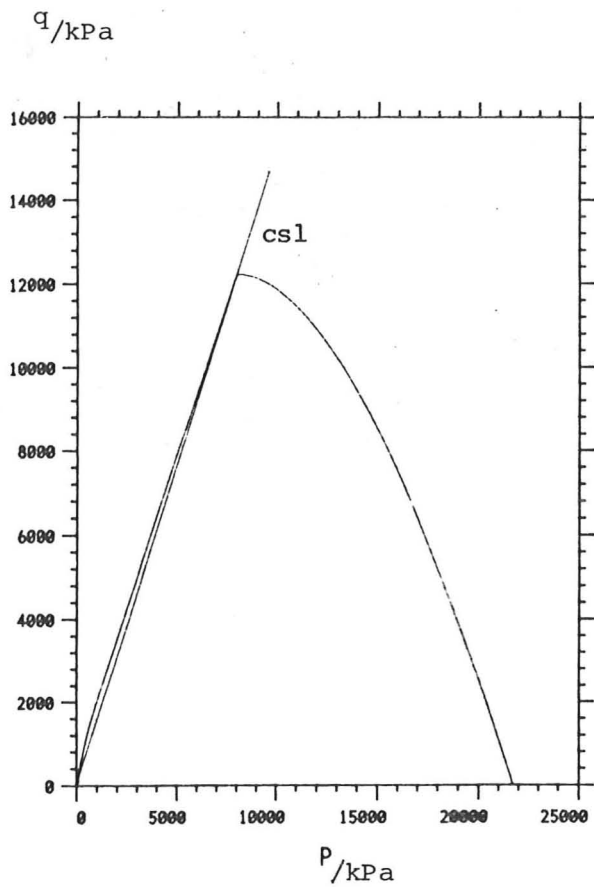
Fig 5.44 Stress-strain history of CRISP in the passive zone
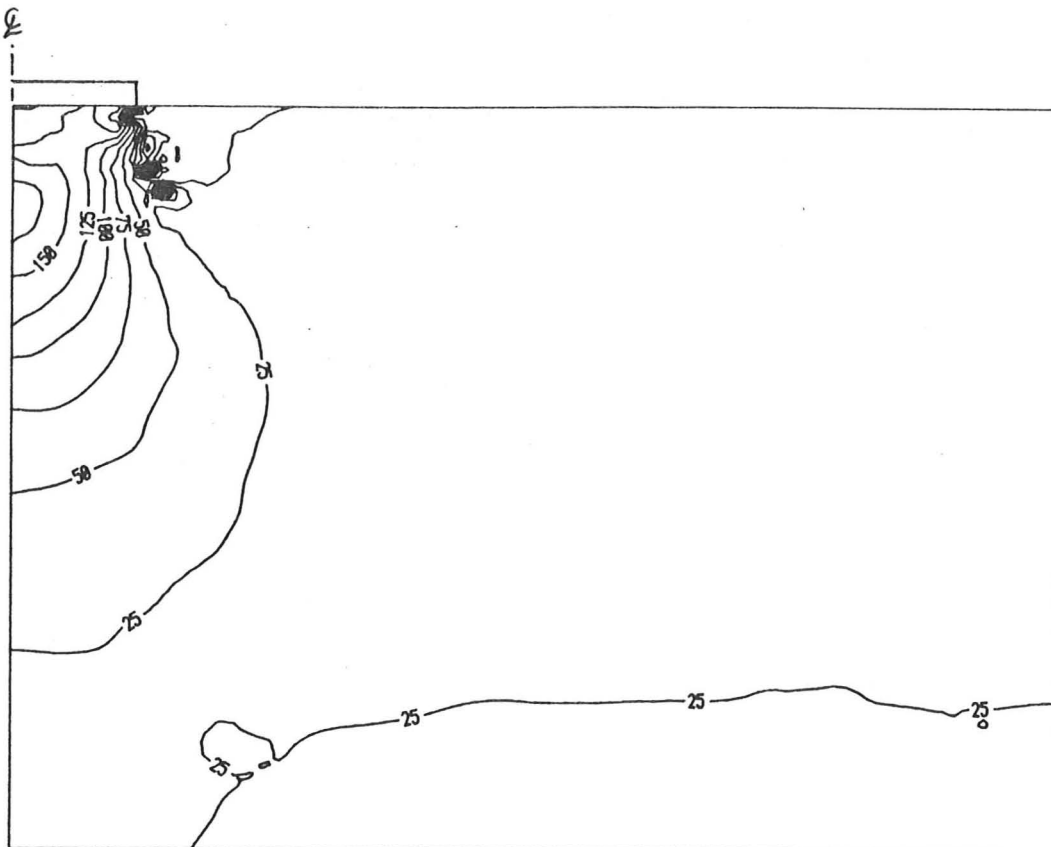
(a)   Minor principal stress contour (1 unit = 10 kPa)
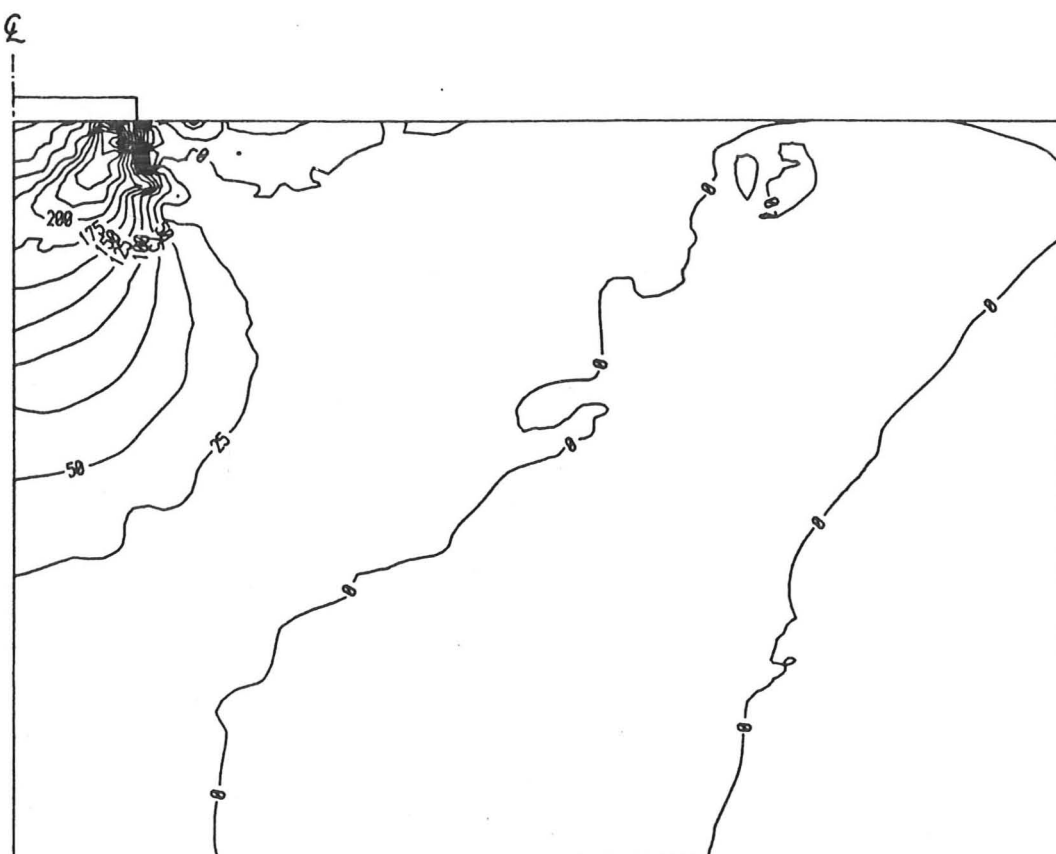
(b)   Circumferential stress contour (1 unit = 10 kPa)

Fig 5.45   Regional variation of stresses in the supporting soil
for CRISP7 when w/B=11%
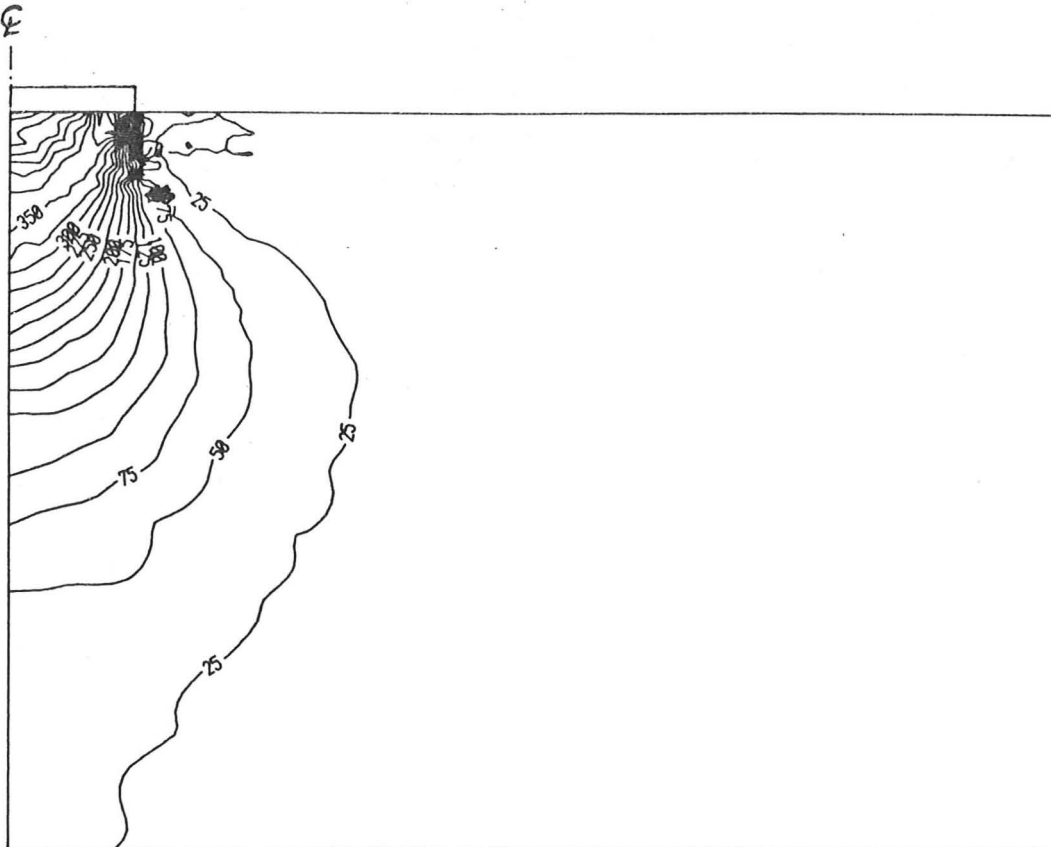
(a) Mean stress contour (1 unit = 10 kPa)
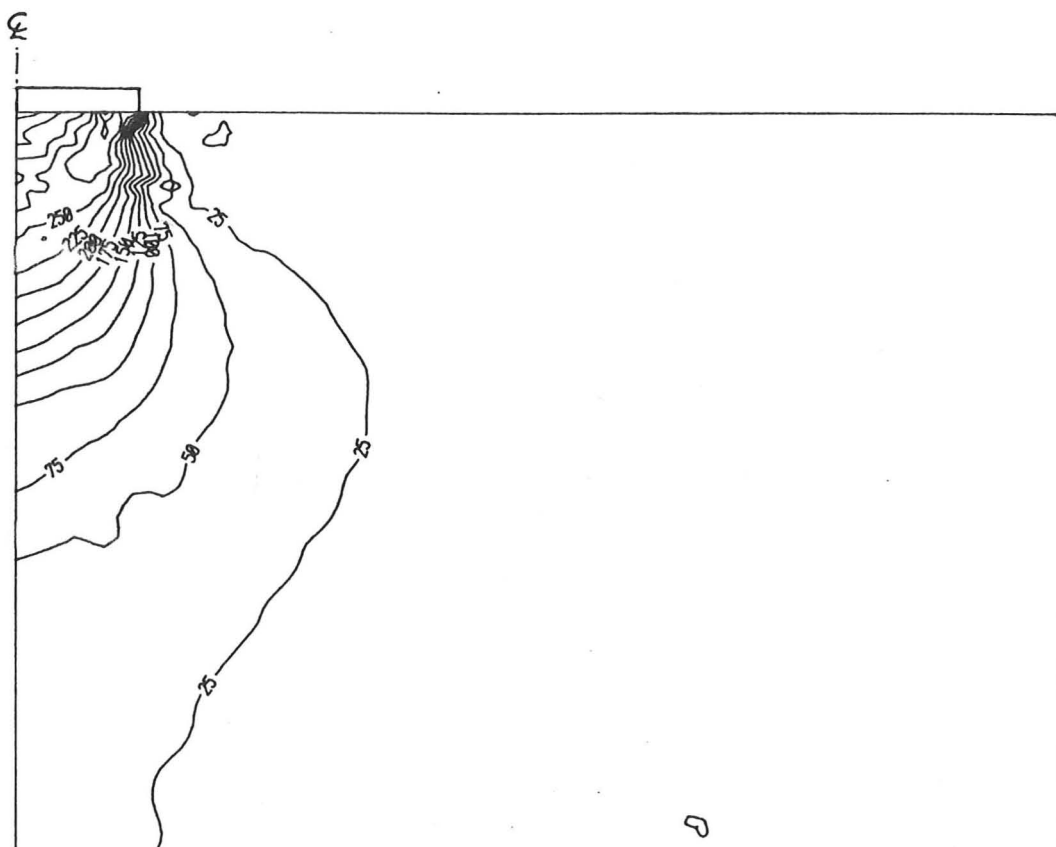
(b)   Maximum shear stress contour (1 unit = 10 kPa)

Fig 5.46   Regional variation of stresses in the supporting
soil for CRISP7 when ^{W}/B=11%
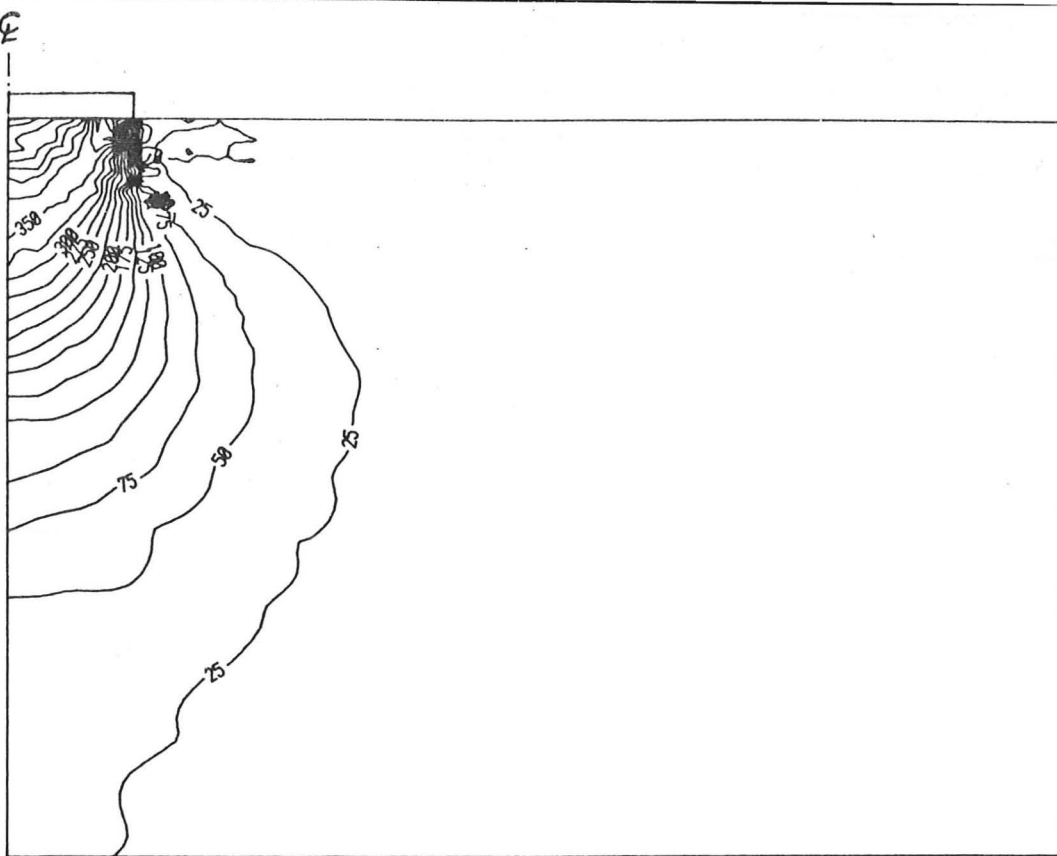
(a) Mean stress contour (1 unit = 10 kPa)
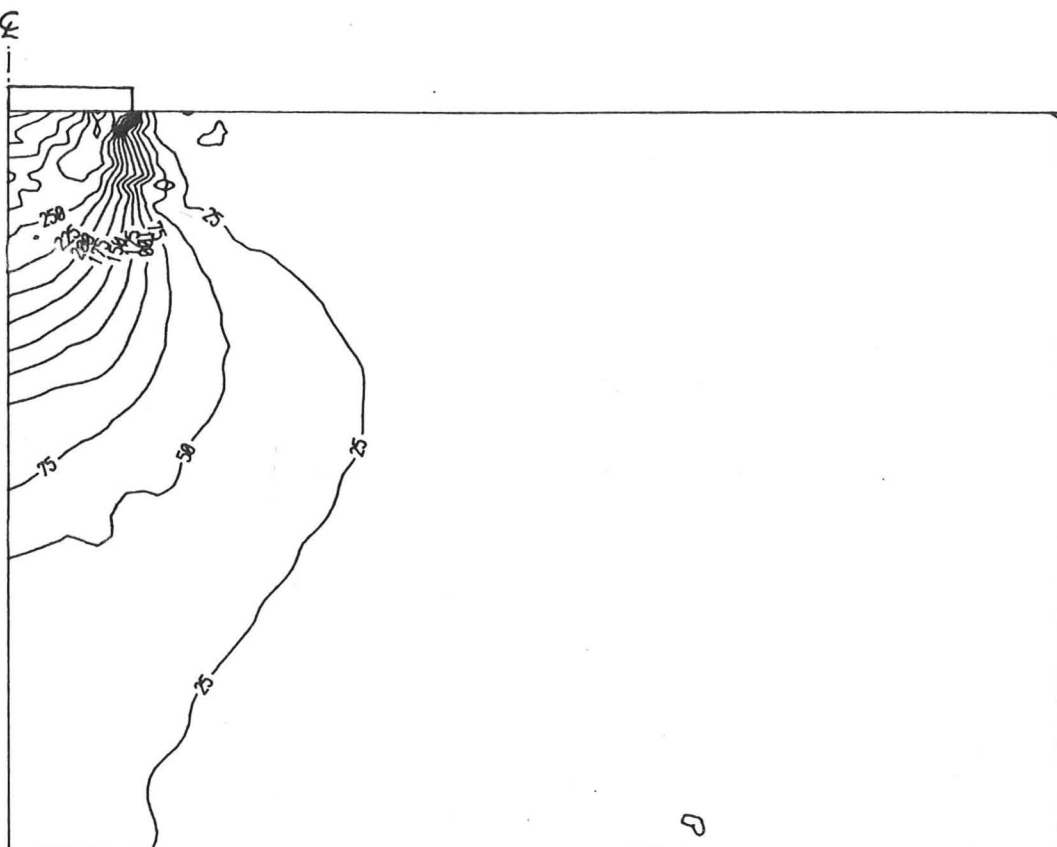
(b)   Maximum shear stress contour (1 unit = 10 kPa)

Fig 5.46   Regional variation of stresses in the supporting
           soil for CRISP7 when $^W/B=11$%
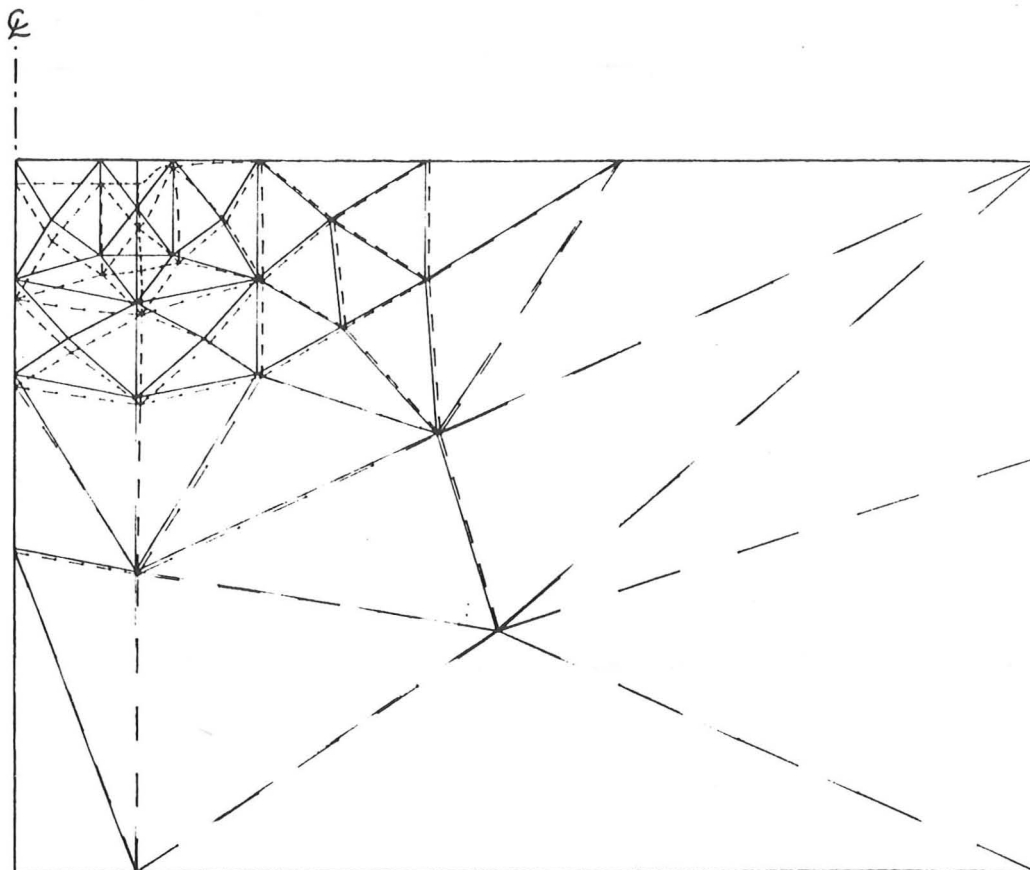
Fig 5.47   Deformed mesh of CRISP8 after 600 increments
           when w/B=10%
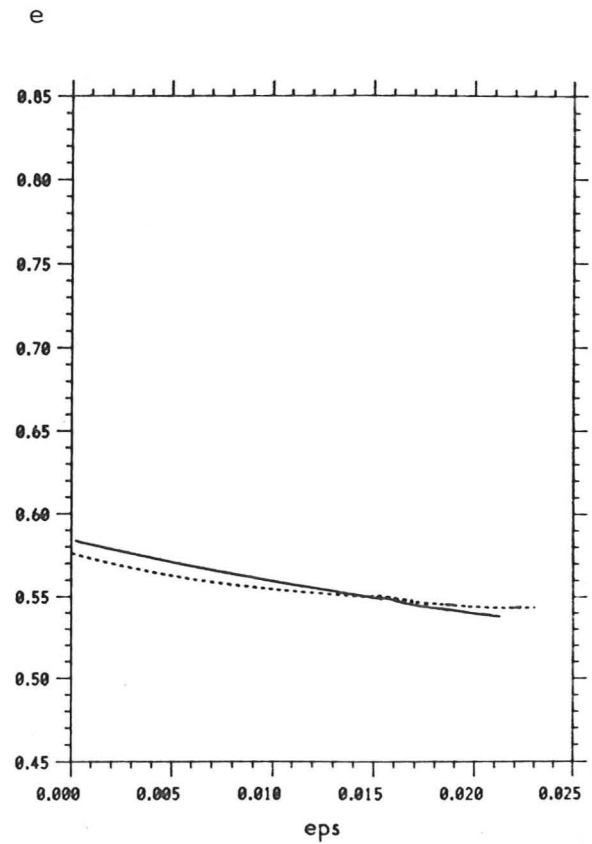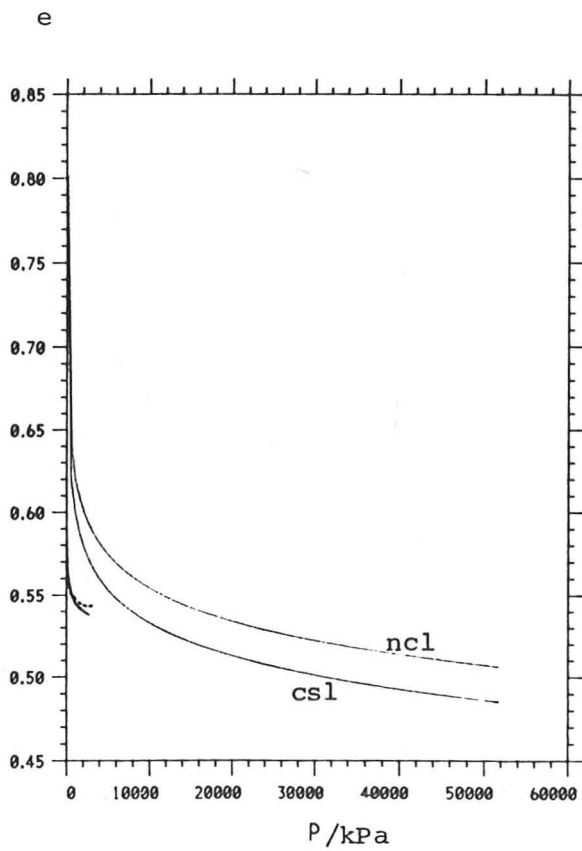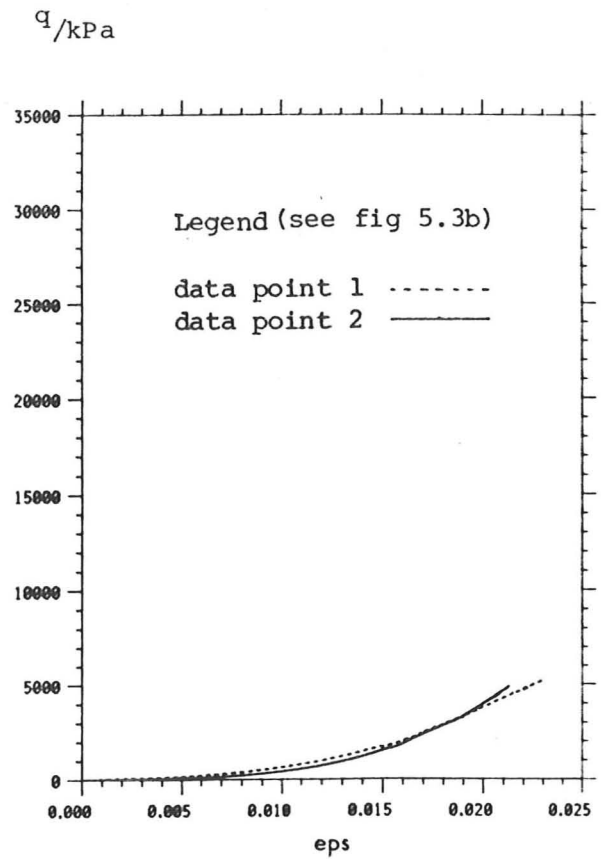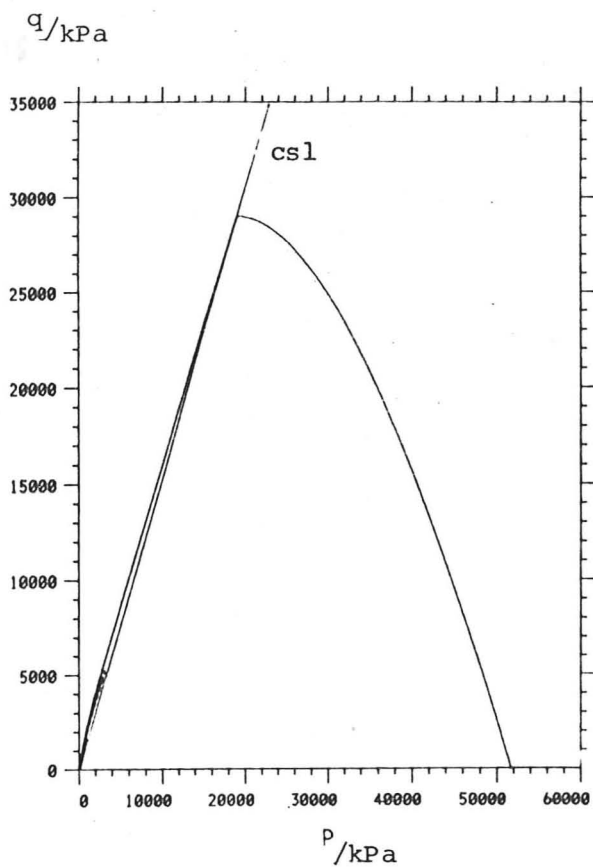
Fig 5.48   Stress-strain history of CRISP8 in the active zone
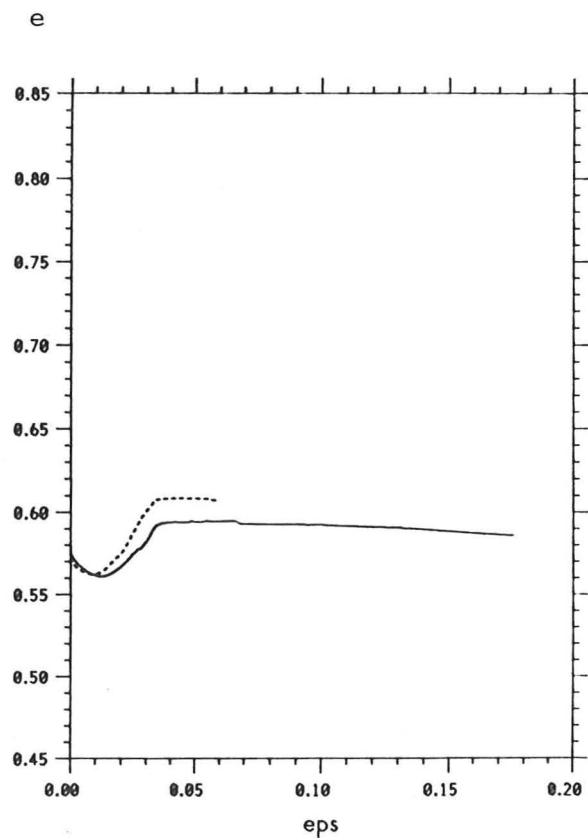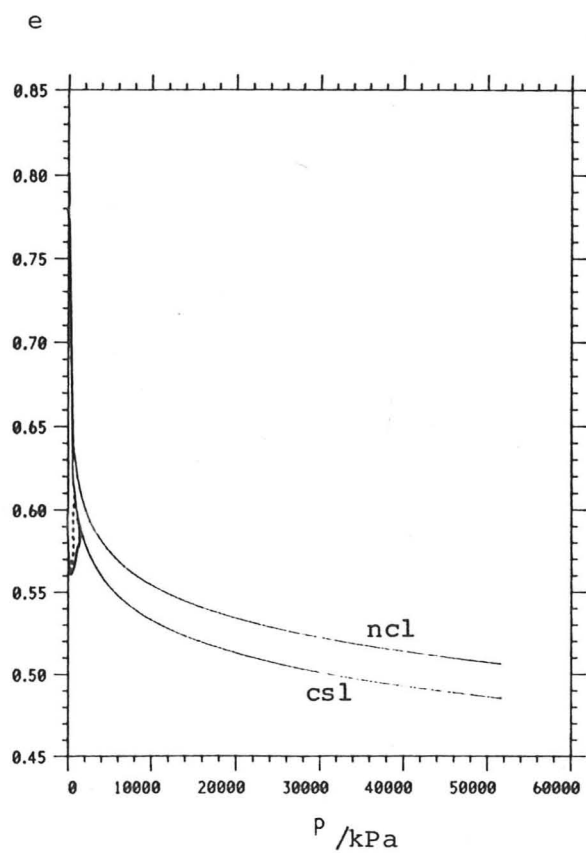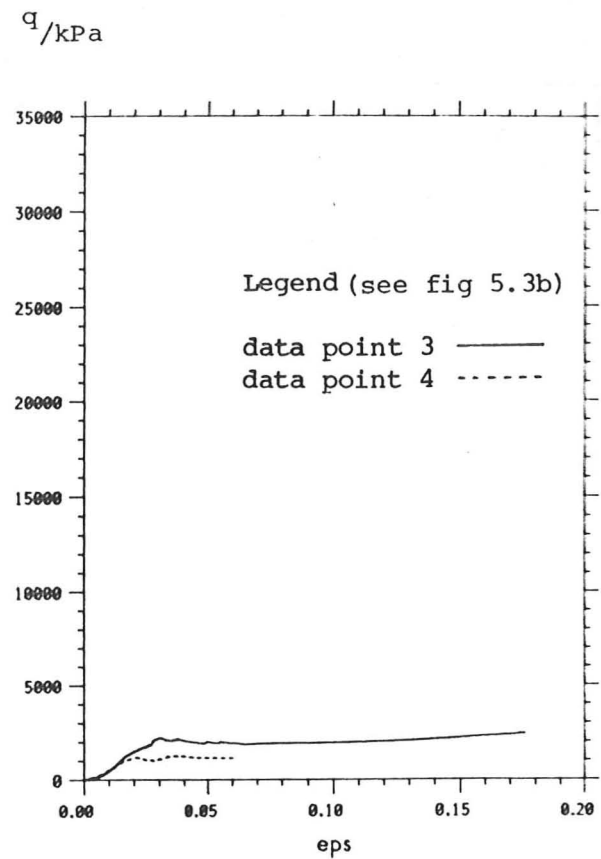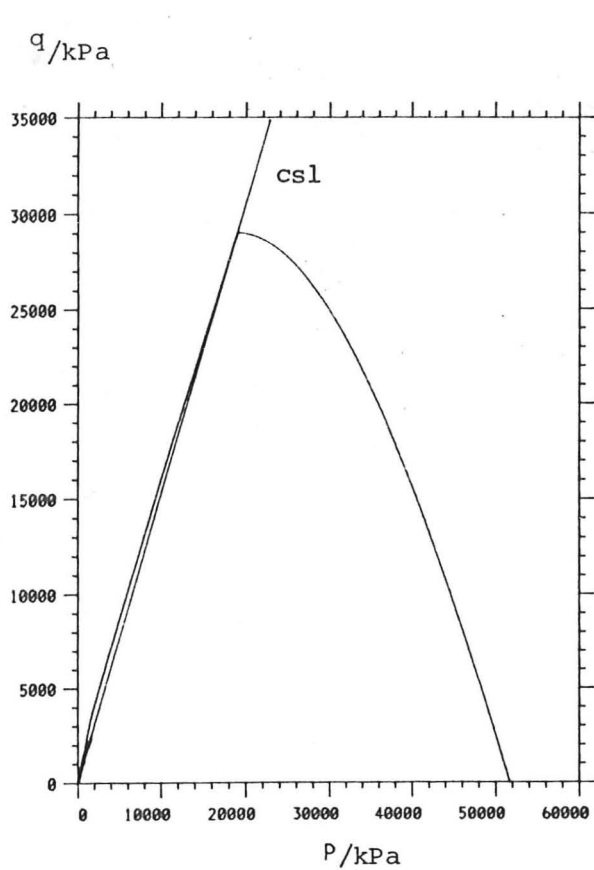
Fig 5.49   Stress-strain history of CRISP8 in the fan zone
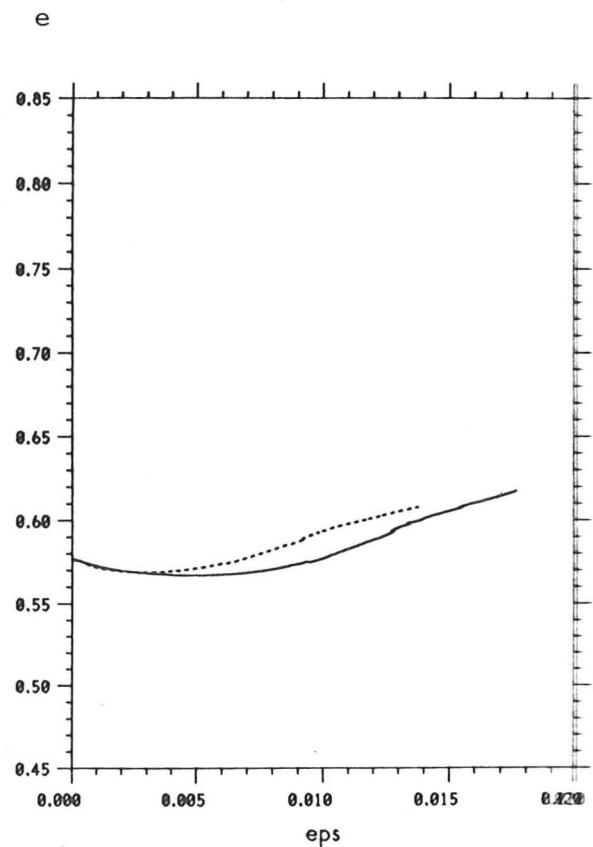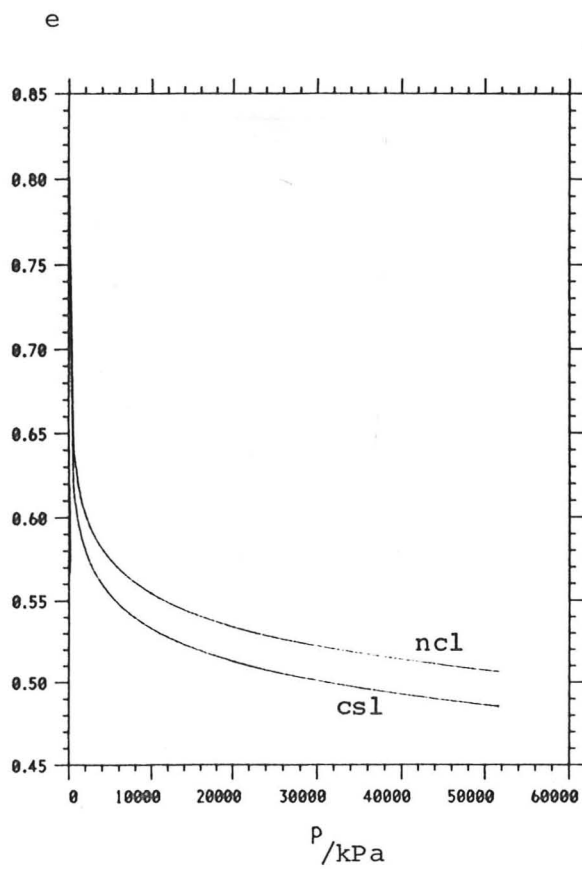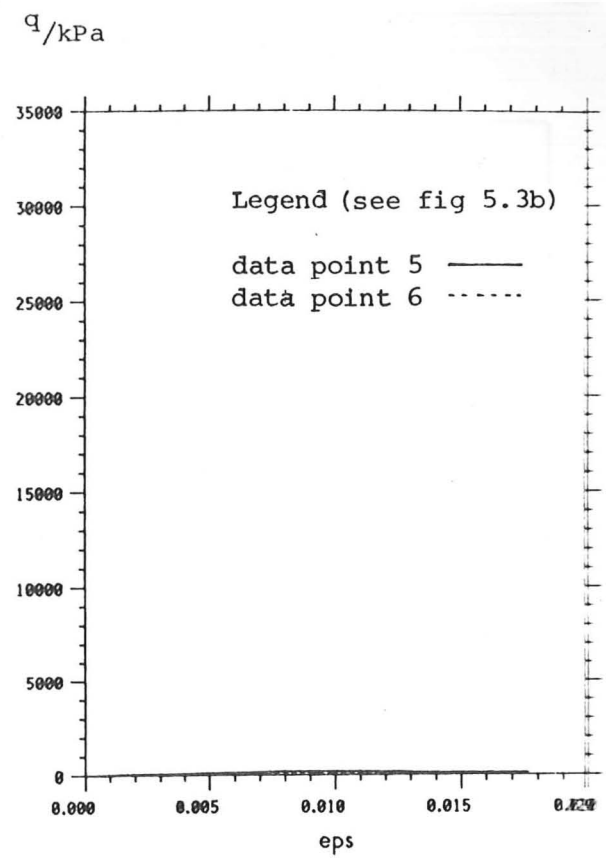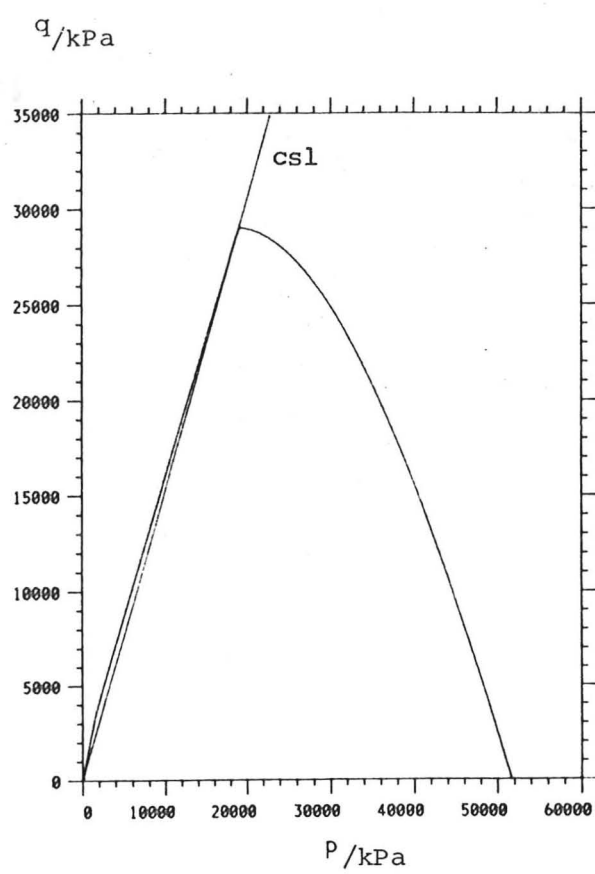
Fig 5.50   Stress-strain history of CRISP8 in the passive zone
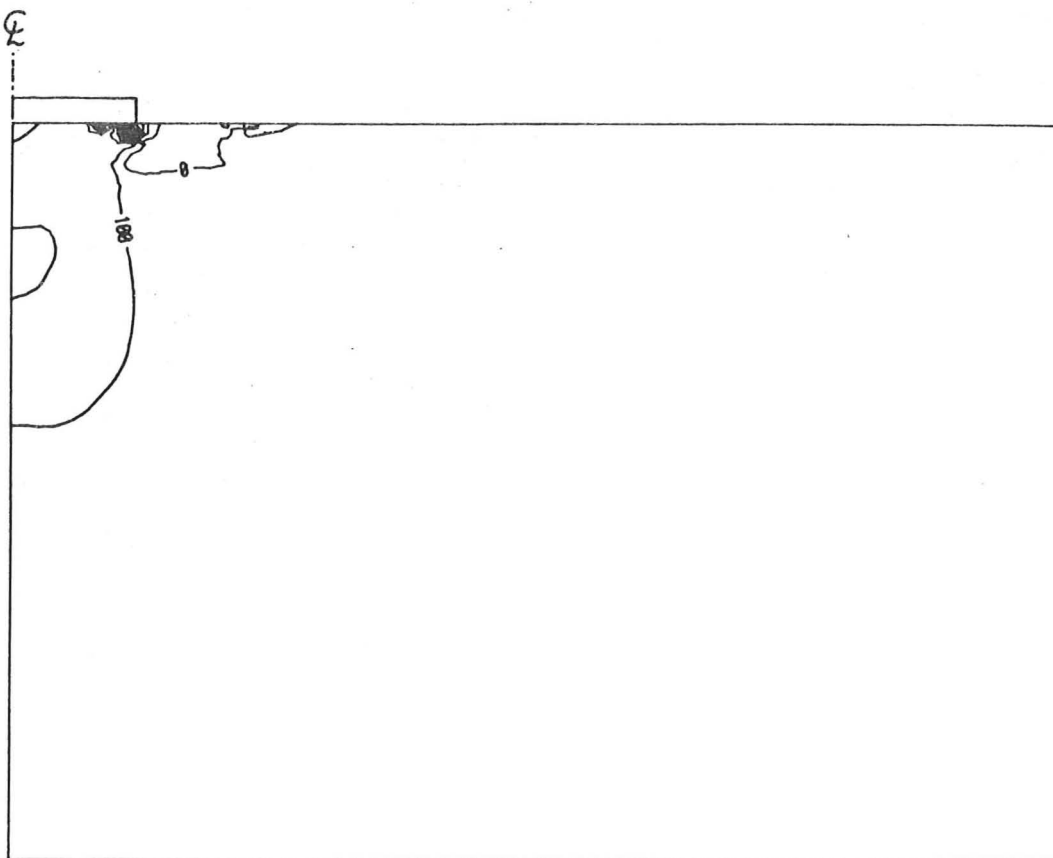
(a)   Minor principal stress contour   (1 unit = 10 kPa)
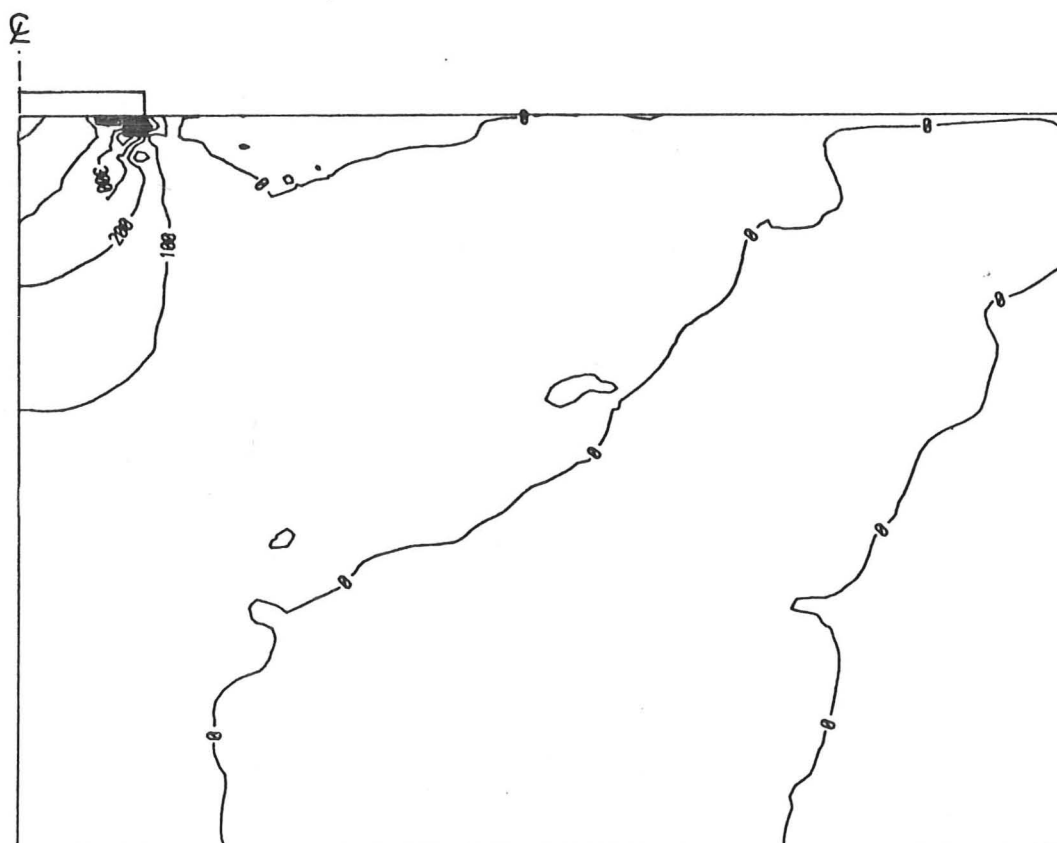
(b)   Circumferential stress contour   (1 unit = 10 kPa)

Fig 5.51   Regional variation of stresses in the supporting soil
           for CRISP8 when w/B=10%
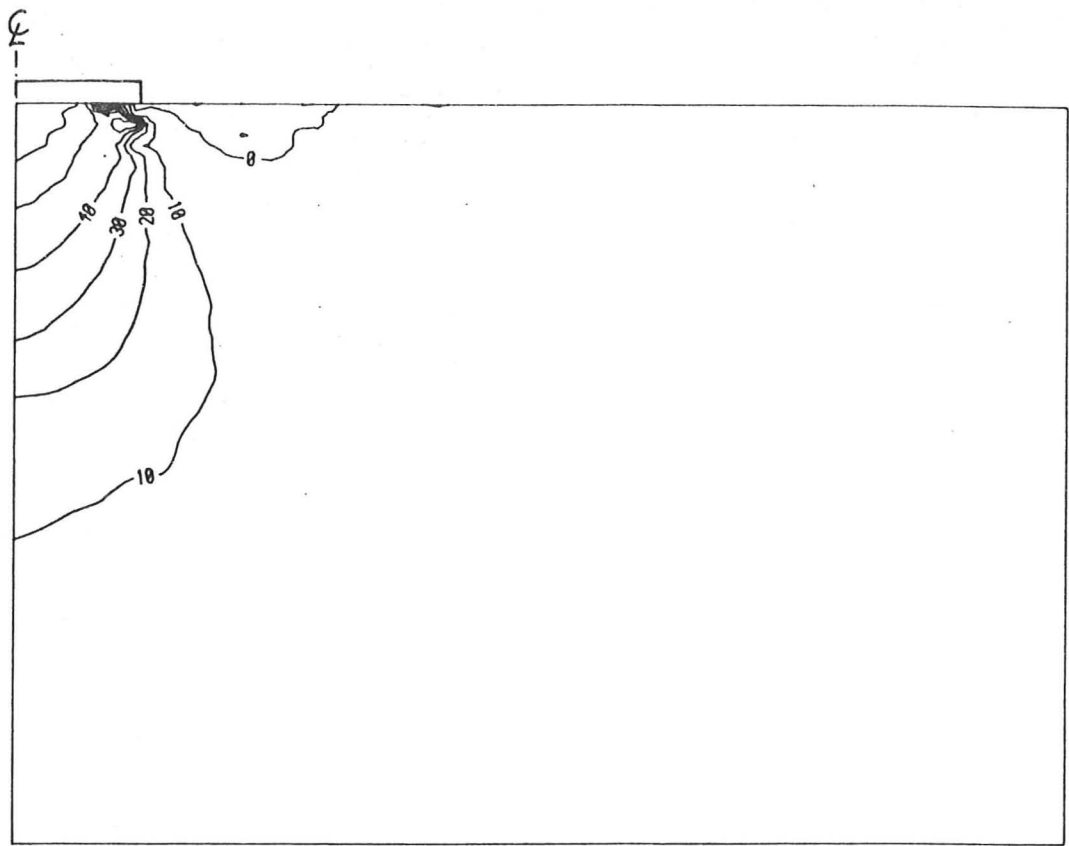
(a) Mean stress contour (1 unit = 10 kPa)
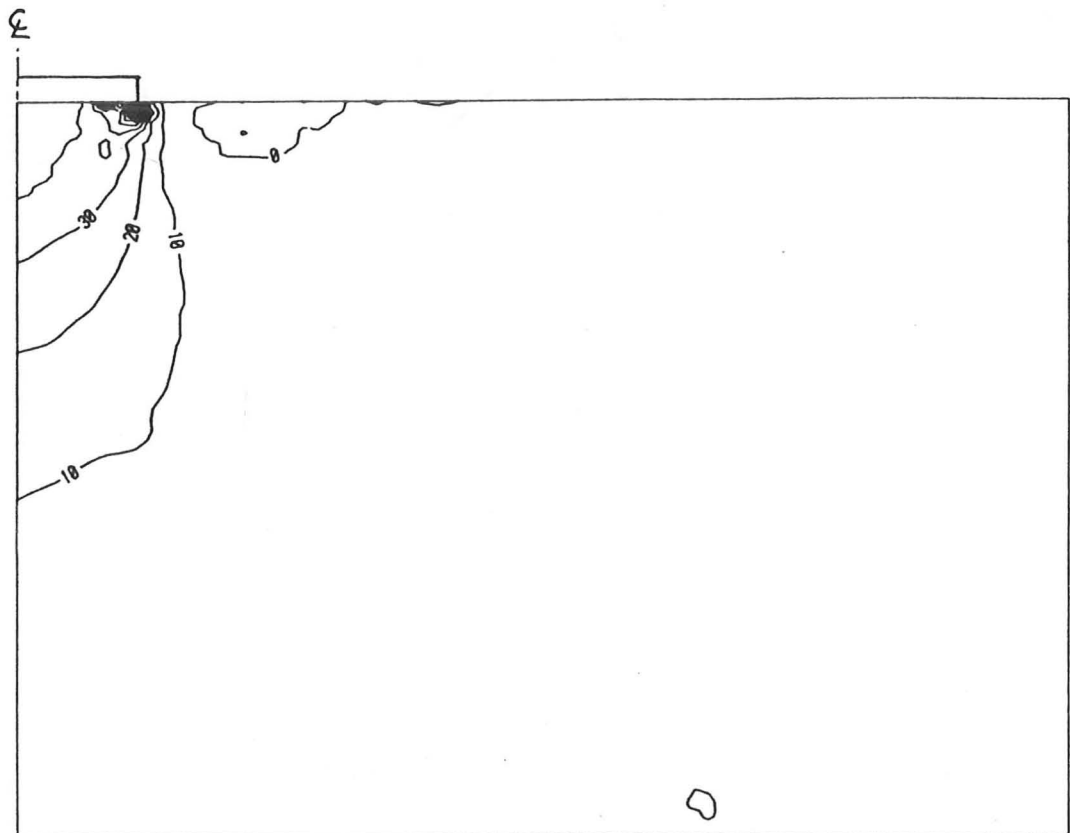
(b) Maximum shear stress contour (1 unit = 10 kPa)

Fig 5.52 Regional variation of stresses in the supporting
          soil for CRISP8 when w/B=10%
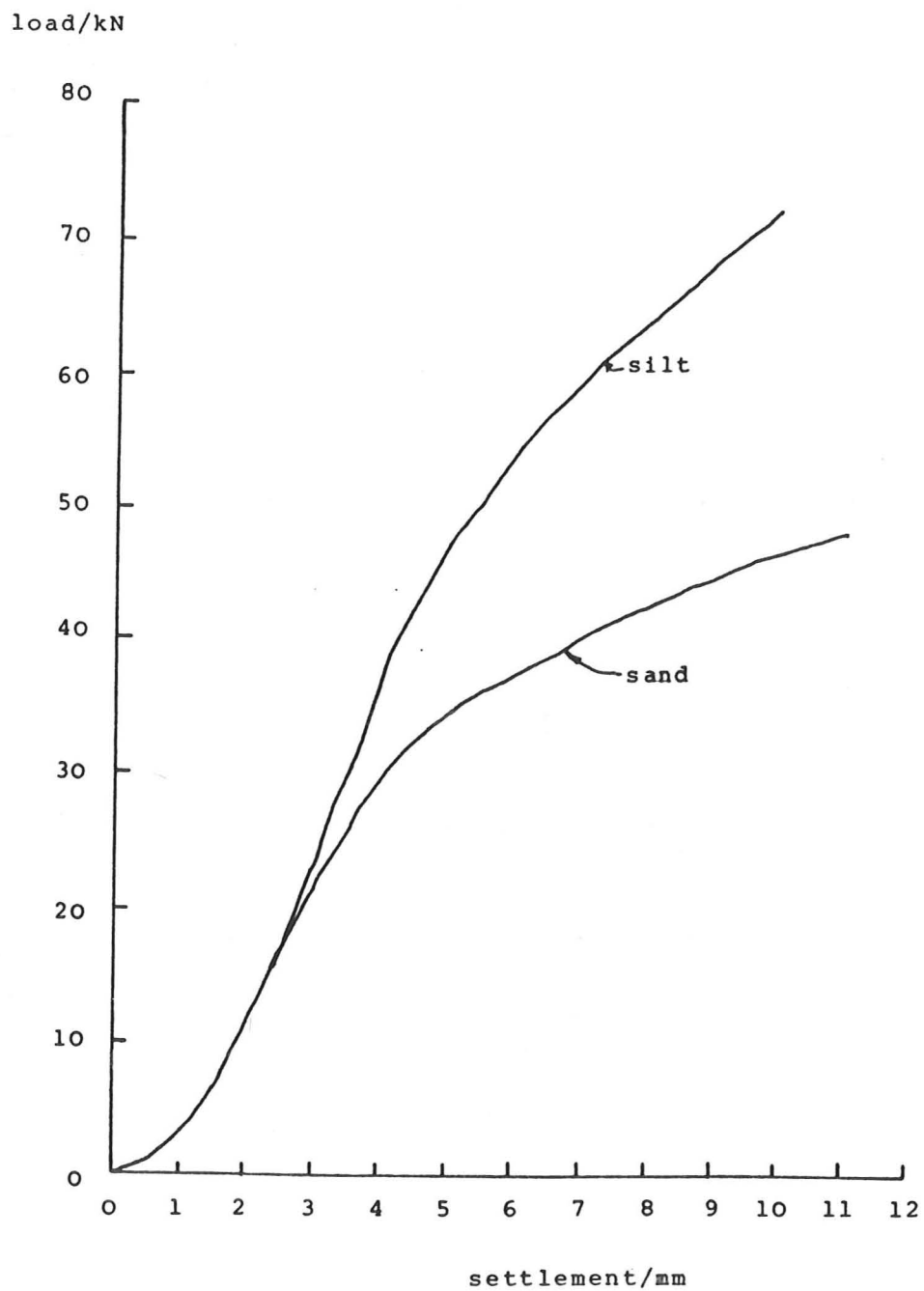
Fig 5.53   Finite element prediction of centrifuge tests
with B=100mm at 50g
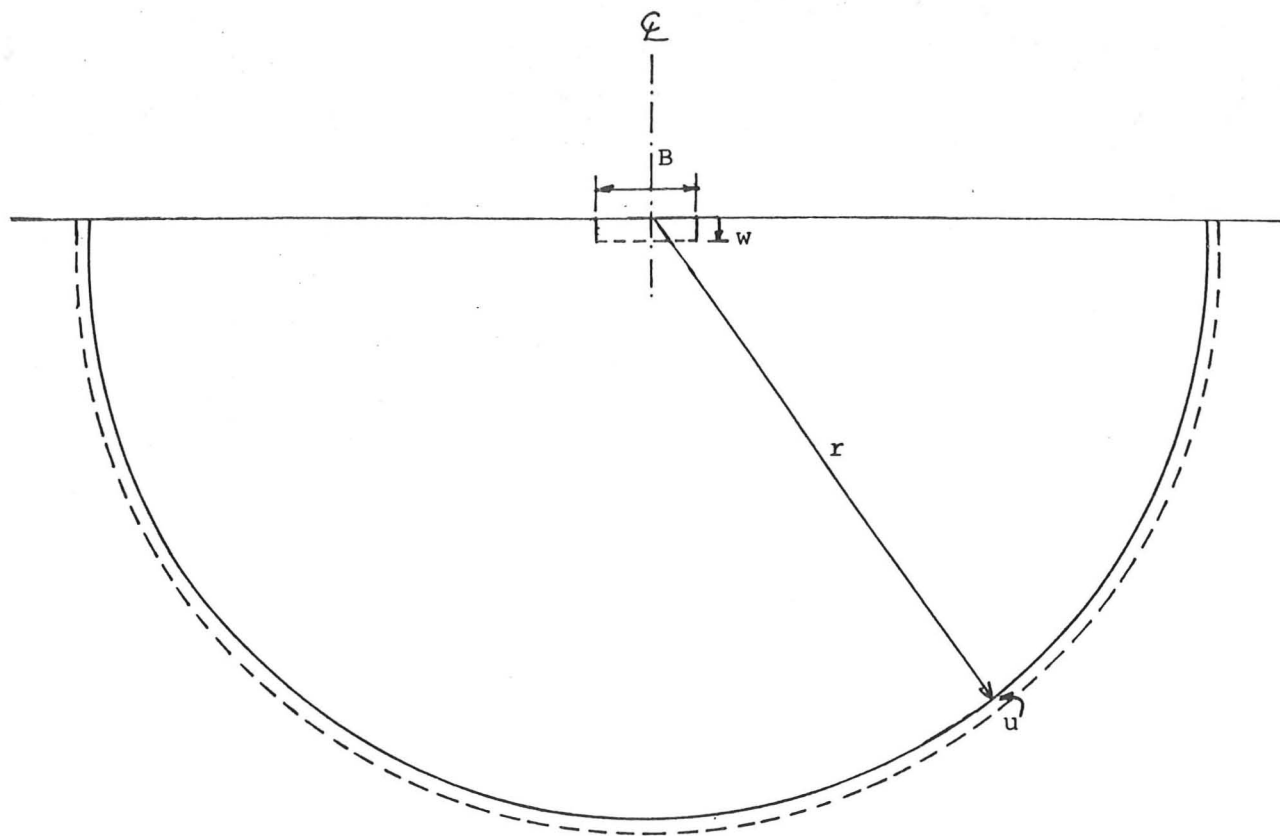
(a) Semi-spherical cavity expansion
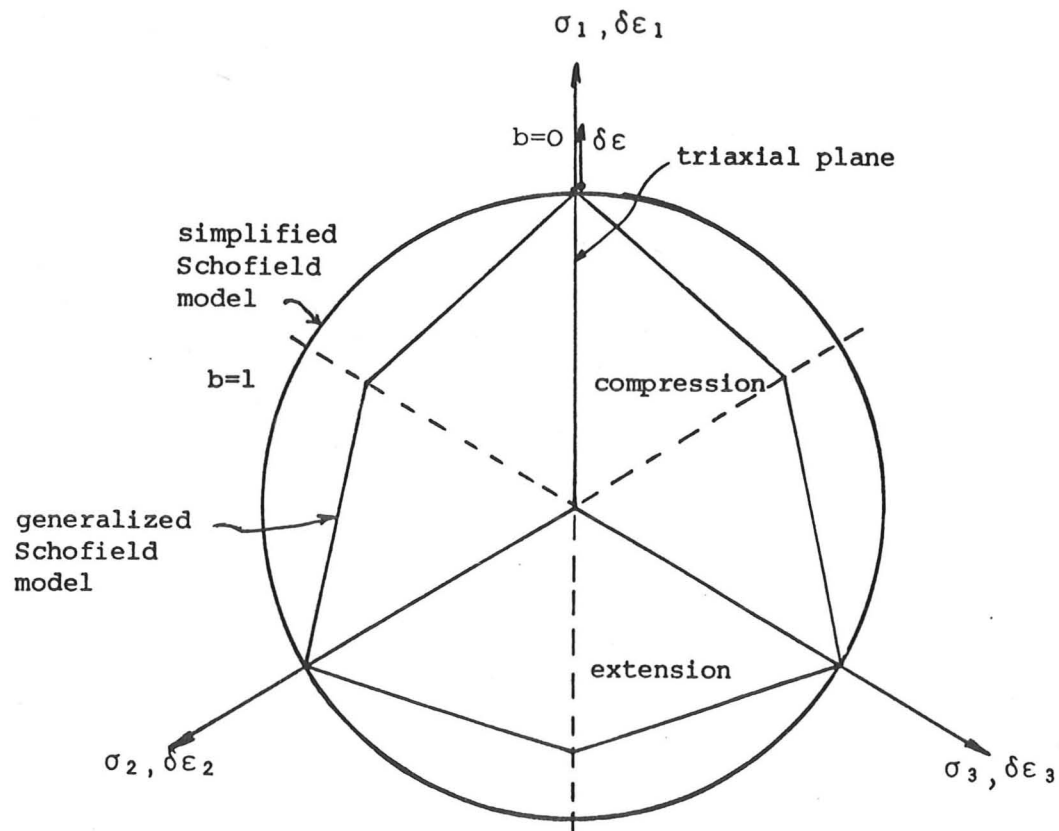
(b) Co-axiality of stresses and strain increments (π-plane)
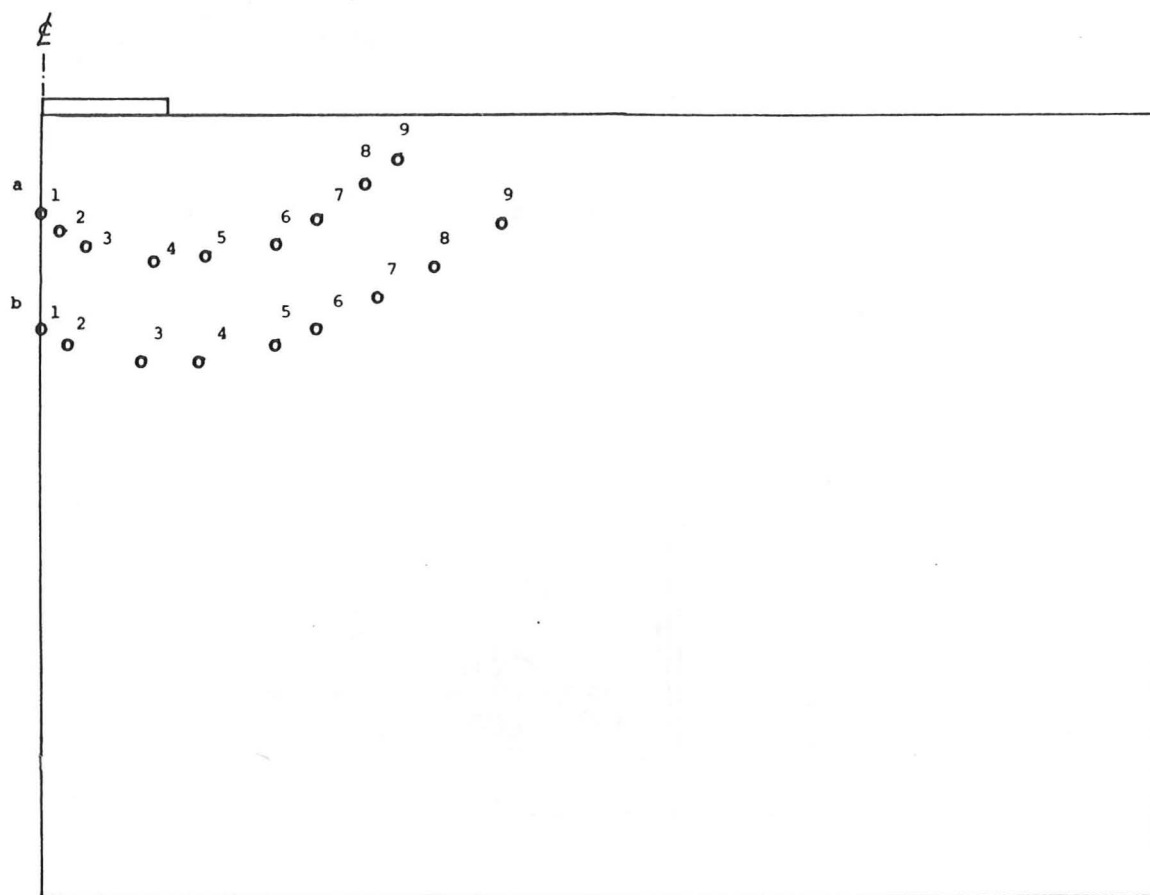
Fig 5.54

Fig 5.55   Location of sampling points for checking intermediate
           stress parameter b and direction of principal stress ψ
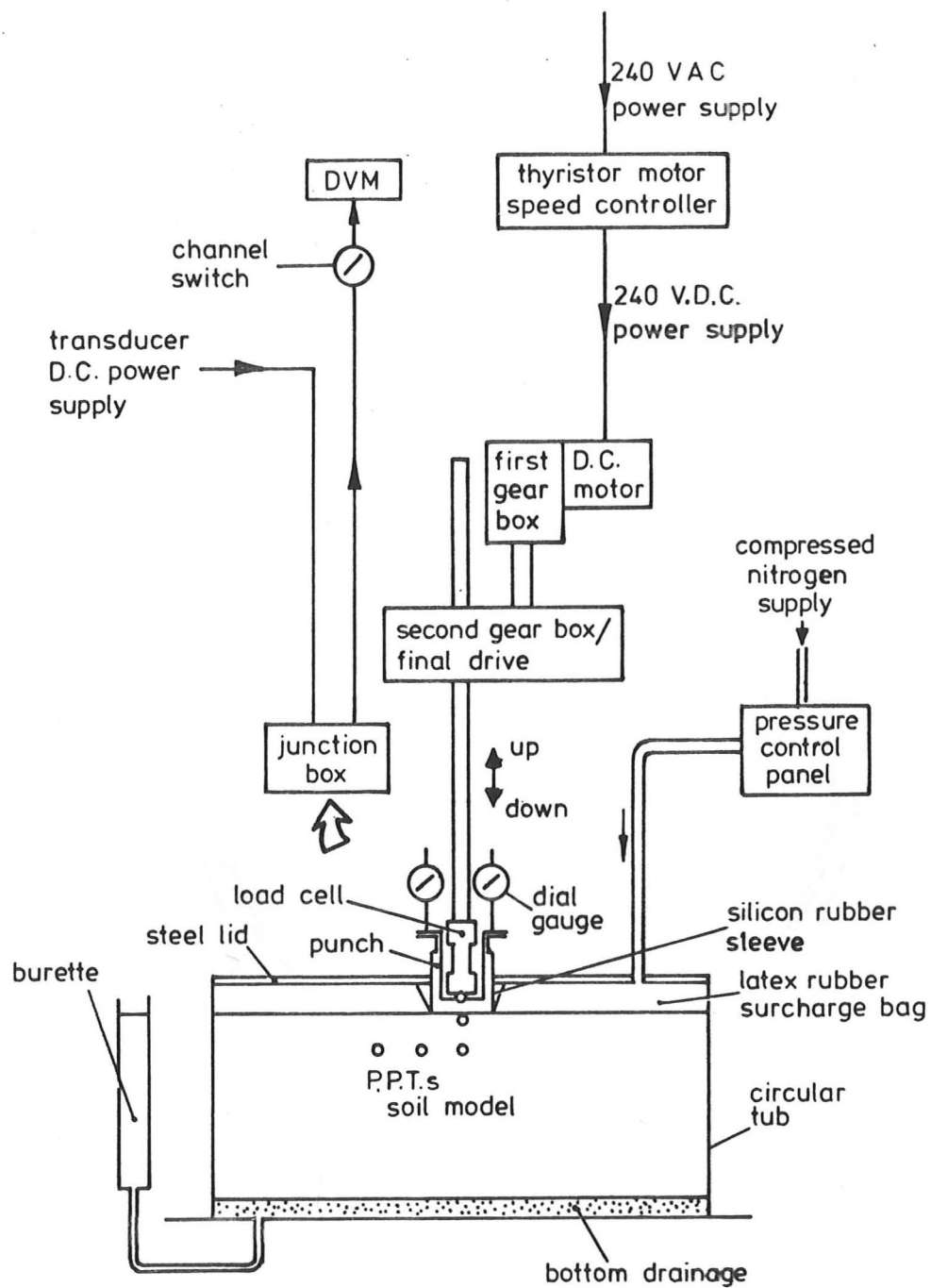
Fig 6.1 Schematic layout of the 1-g test rig
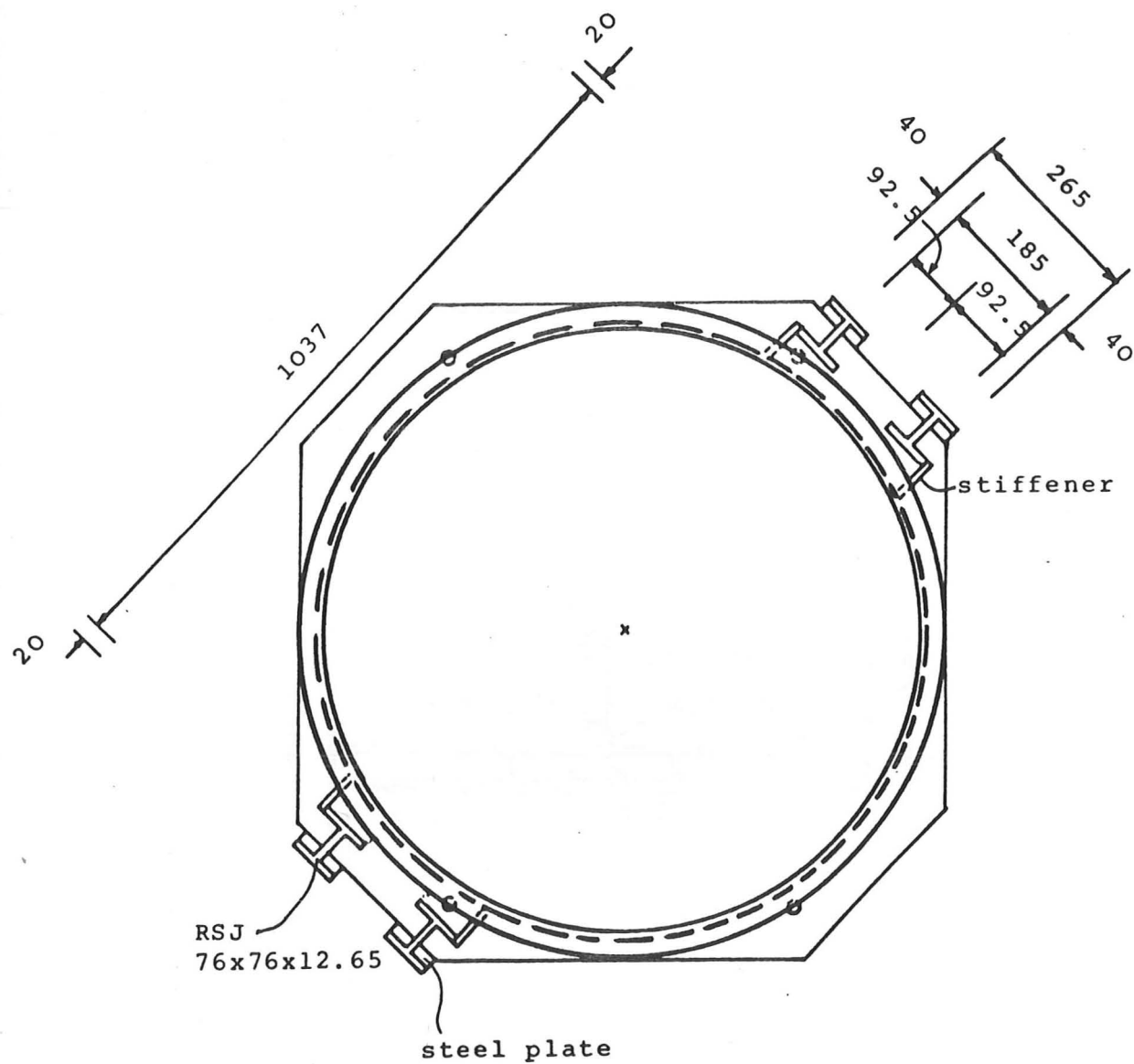
Fig 6.2   Modification details for a standard 850 mm tub
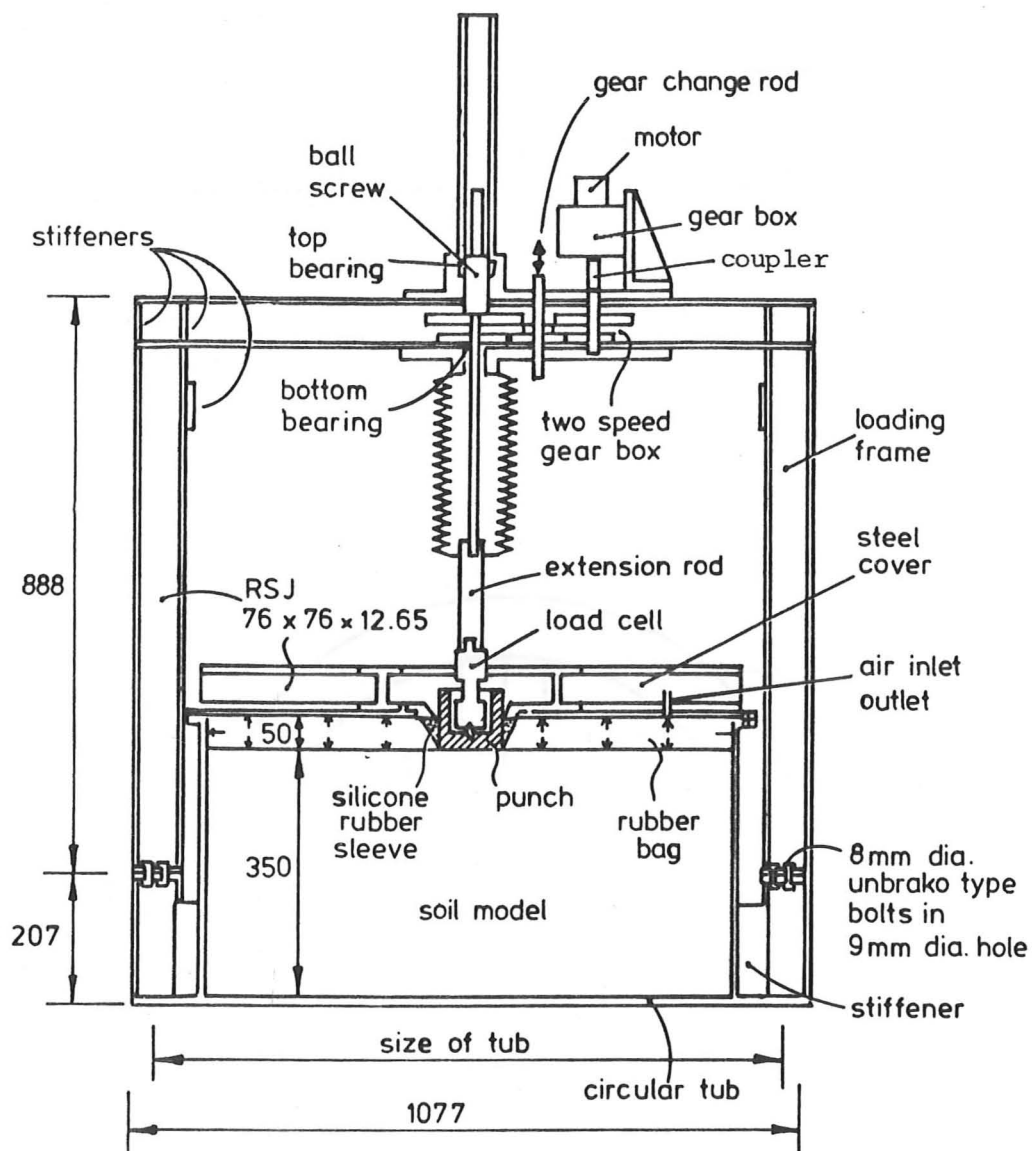
Fig 6.3   General layout of test rig at 1-g

section x-x

100 dia

plan
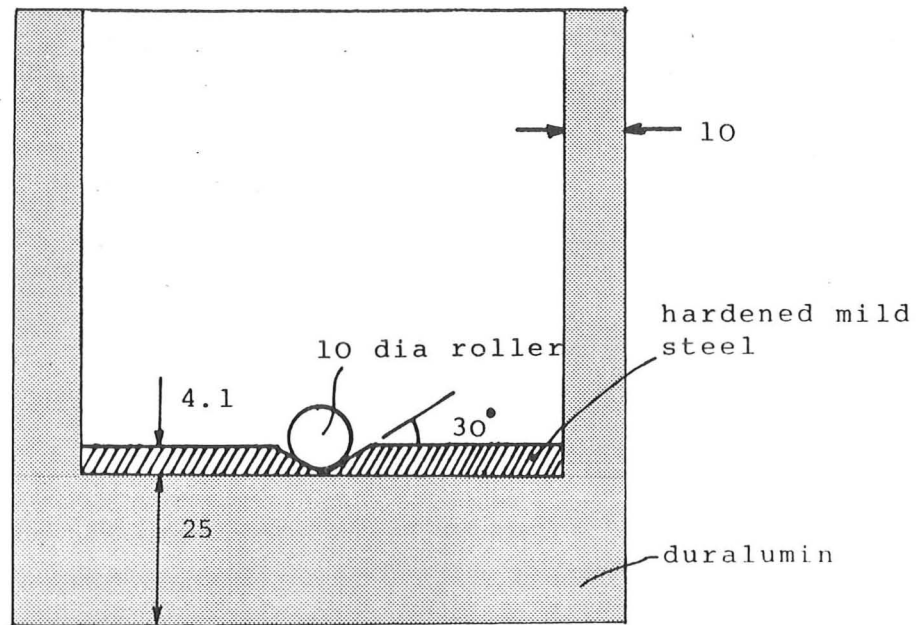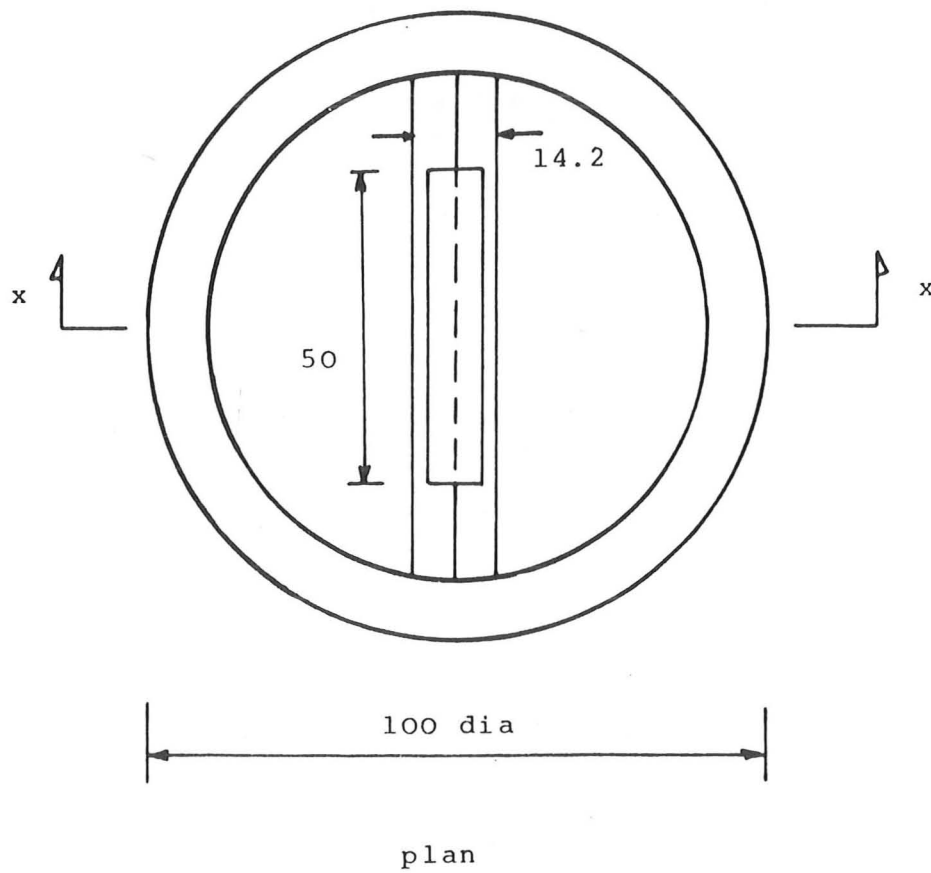
Fig 6.4   Details of 100mm diameter punch

₡

loader

mild steel

50

10 dia

1.42R tip

150°

hardened
mild steel

30°

duralumin

3.55

14.2 dia

section x-x

groove

30 plane

x

x

1

14.2 dia

plan
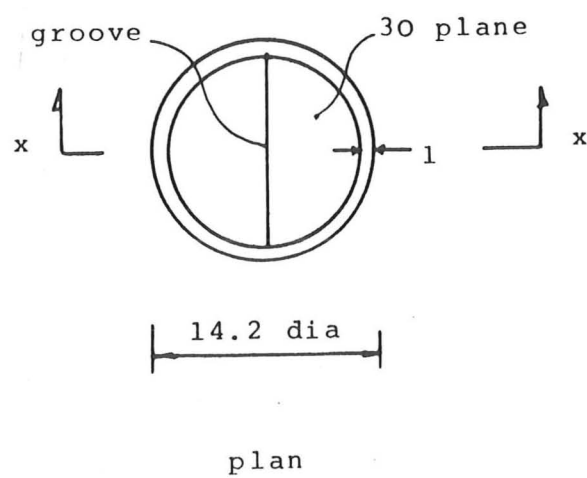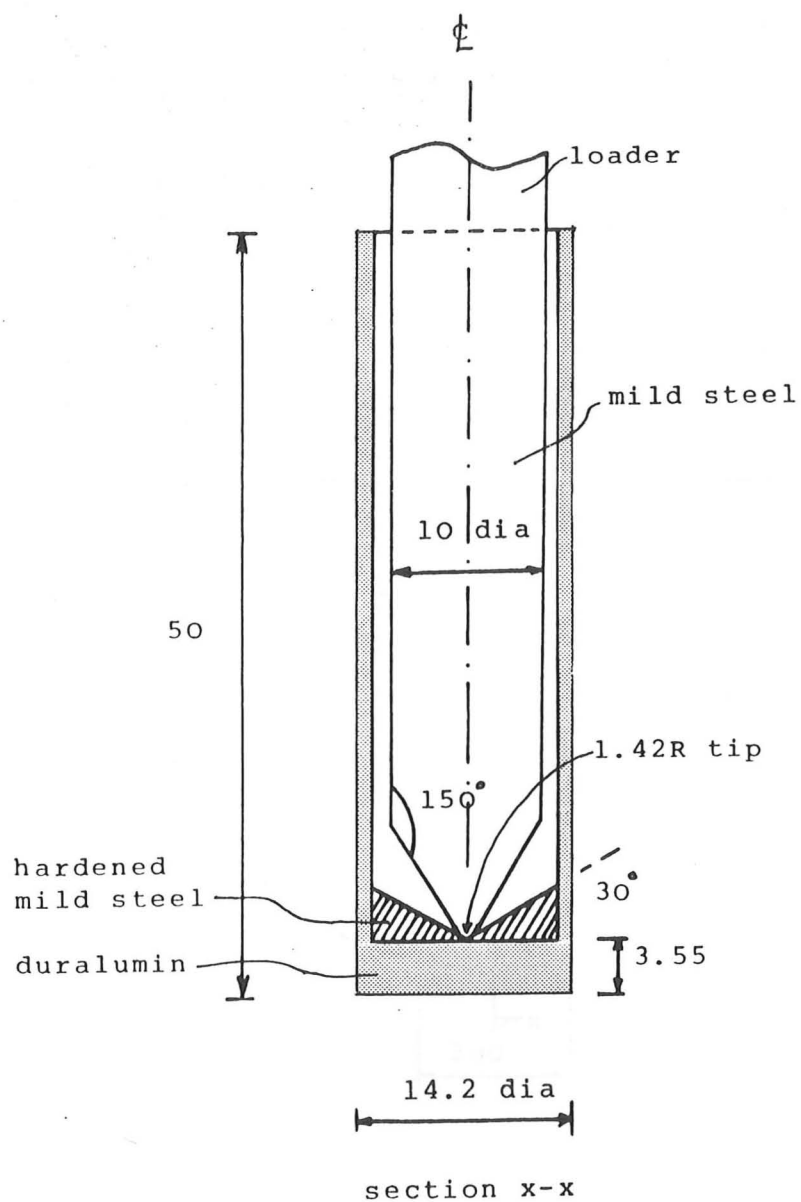
Fig 6.5 Details of 14.2mm diameter punch

Plan view

RSJ 76x76x12.65

Section x-x
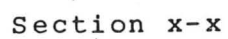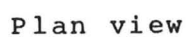
Fig 6.6 Details of the steel lid

burette for surcharge
(use only when $\sigma_o = 5$ kPa)

load cell

punch

lid

sleeve

water in
rubber bag

burette
connected
to bottom
drainage

soil bed
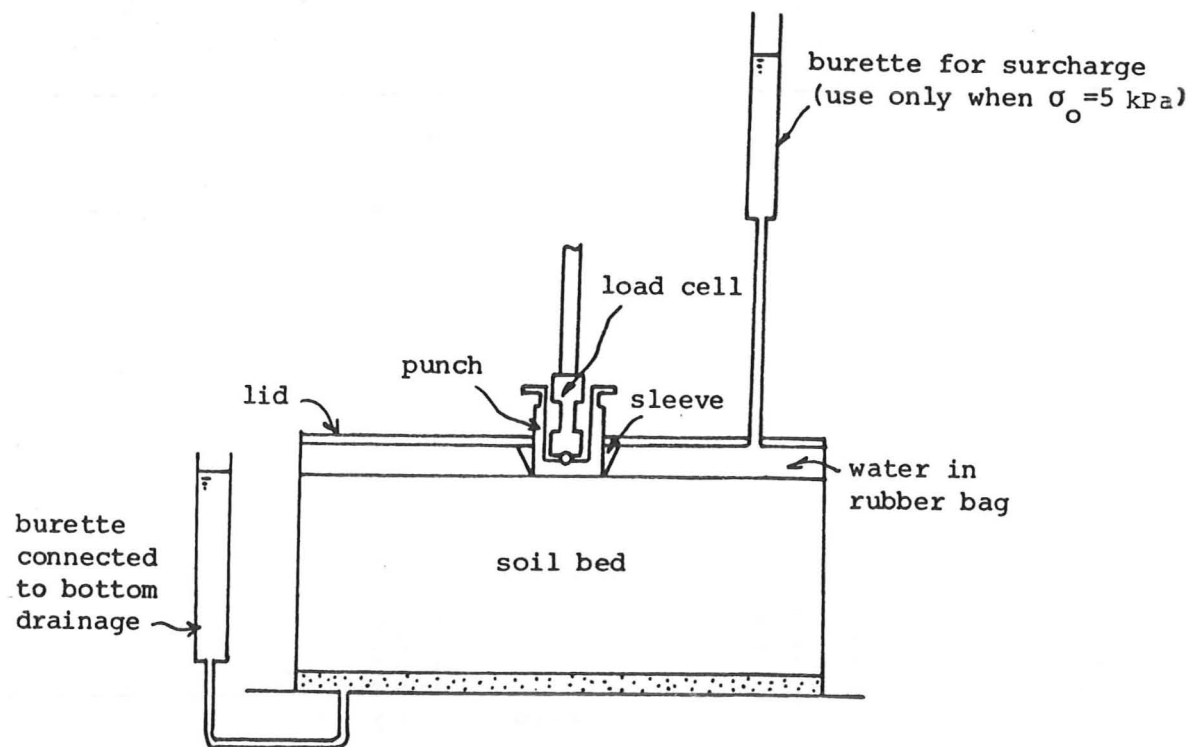
Fig 6.7 Details of using static water head to provide
surcharge
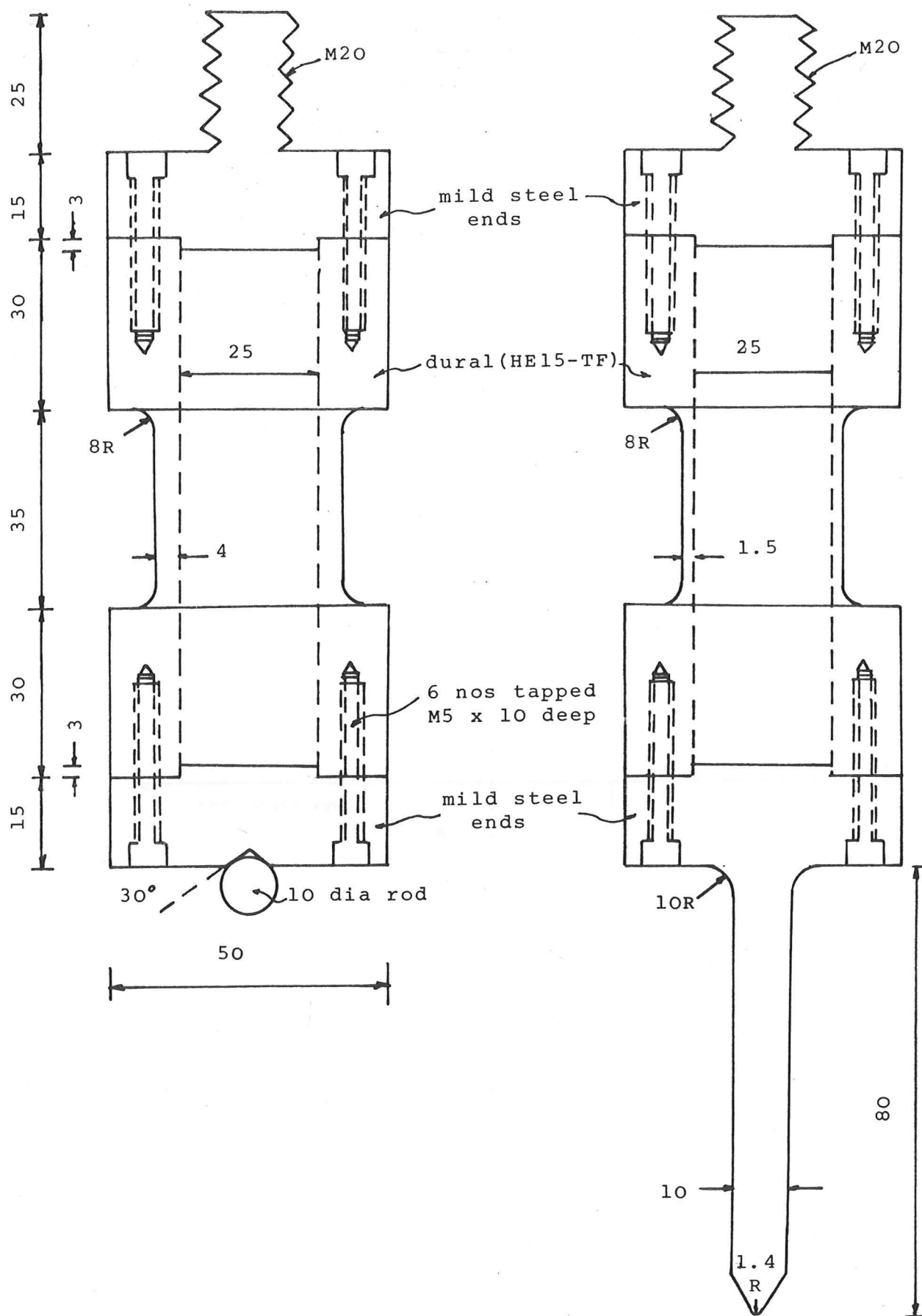
Fig 6.8 Details of load cells
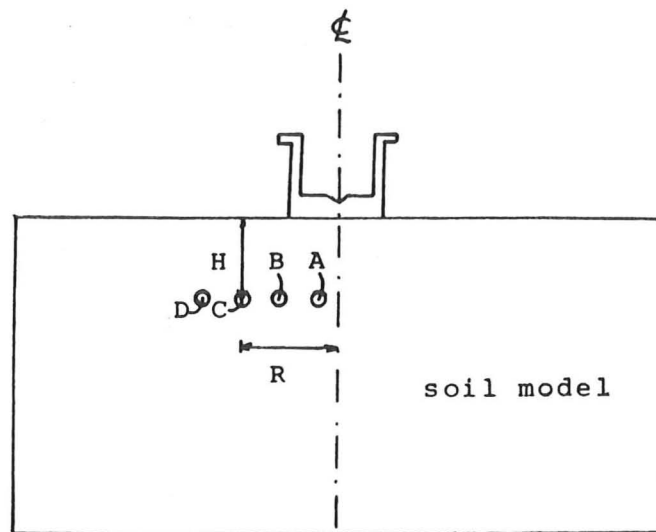
ppt position no. / test no.	A		B		C		D	
	R	H	R	H	R	H	R	H
1GT11	0	100	72	100	180	100	–	–
1GT29	40	125	90	70	145	135	250	104

Fig 6.9   Location plan of PPTs

$\sigma_{f}/$ kPa

8000

7000   1GT21(dry) ,σ_o=50 kPa   e=0.58
                                        1GT23(sat) ,σ_o=50 kPa
6000   e=0.57   1GT17(dry) ,σ_o=25 kPa
                                                   e=0.58
5000   1GT25(sat) ,σ_o=25 kPa
                                                 e=0.64
4000

3000

2000

1000

0
   0   4   8   12   16   20   24   28   32   36   40   44

                                                        w /mm
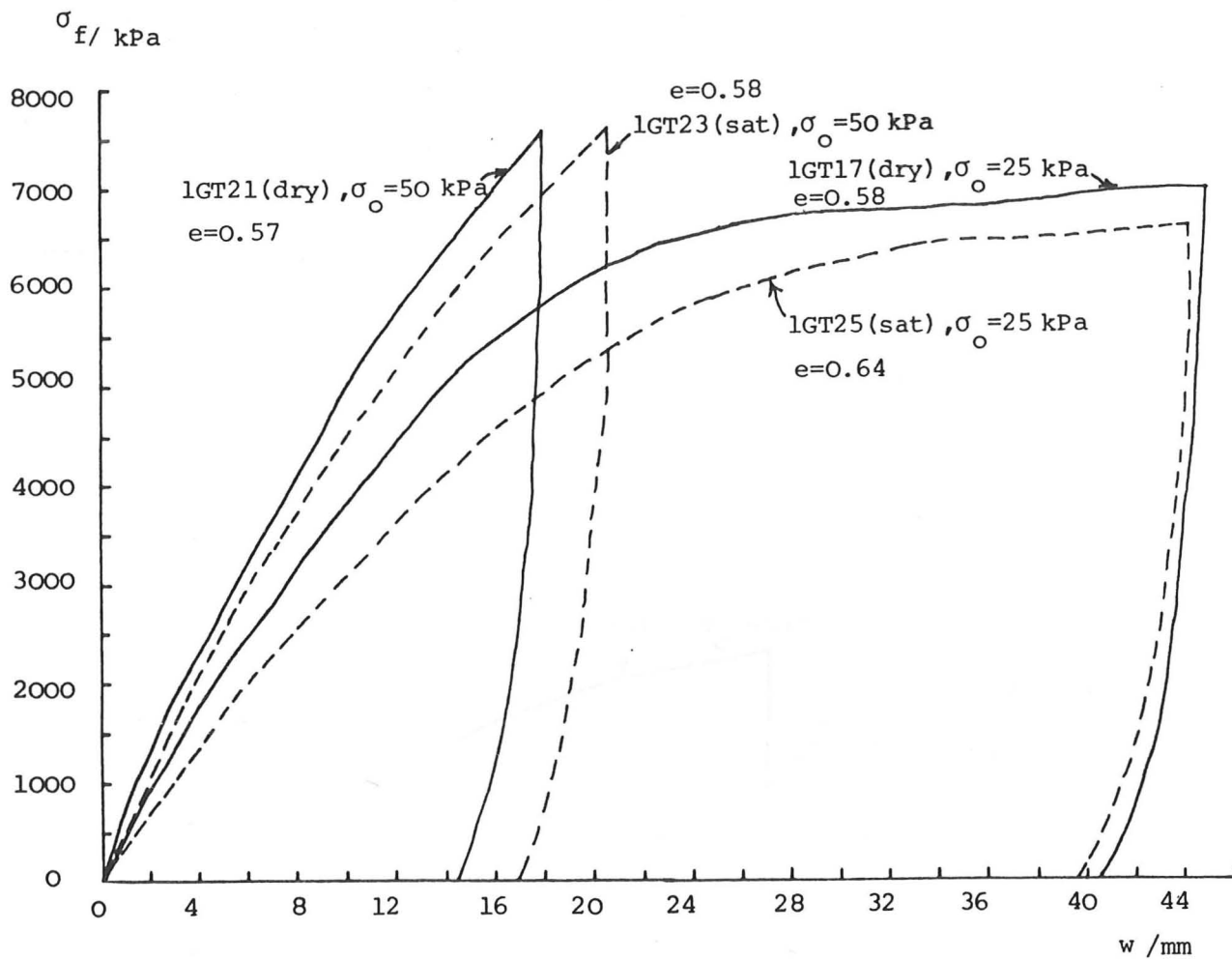
Fig 6.10   Effects of saturation on footing test on sand
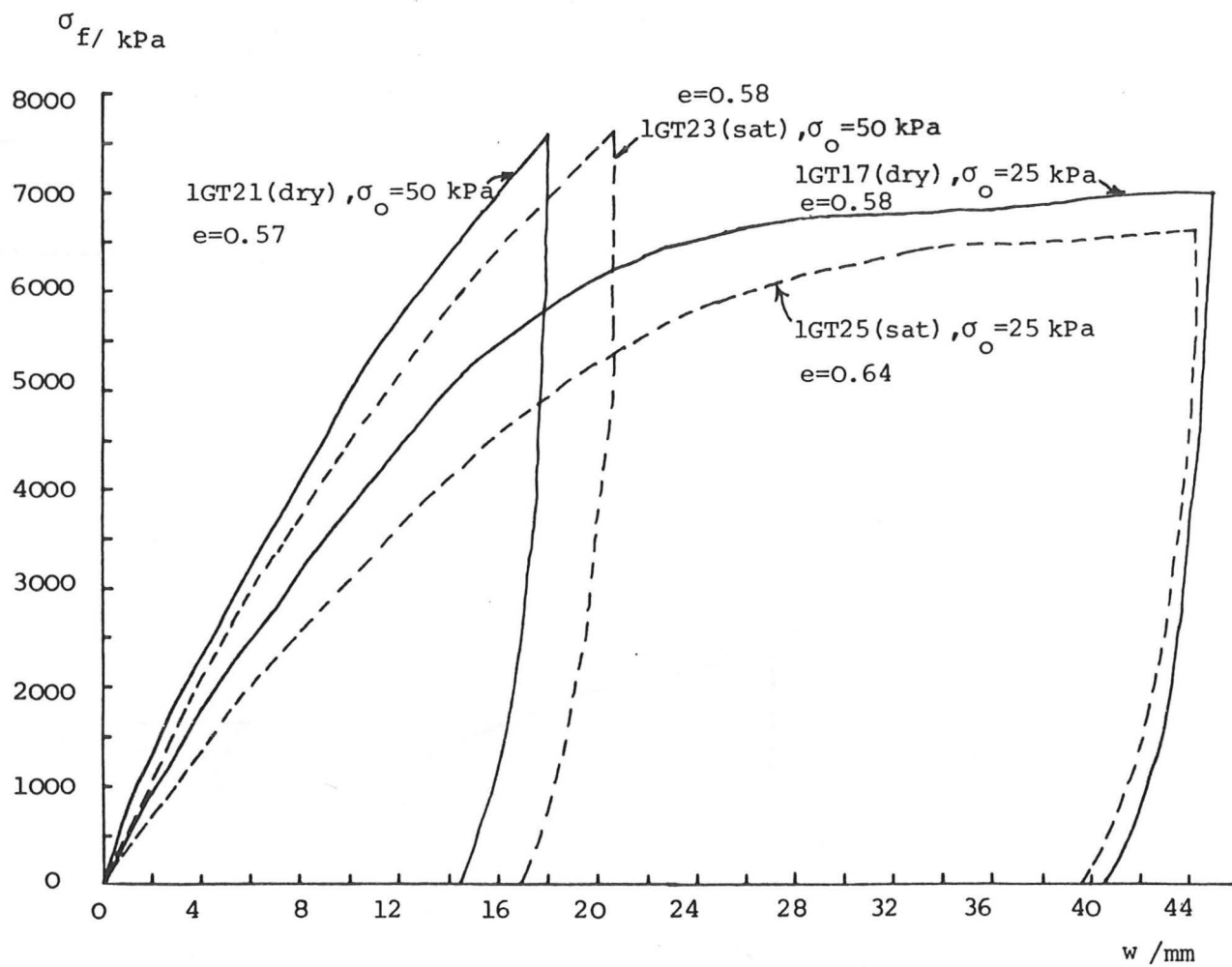
Fig 6.10   Effects of saturation on fóoting test on sand
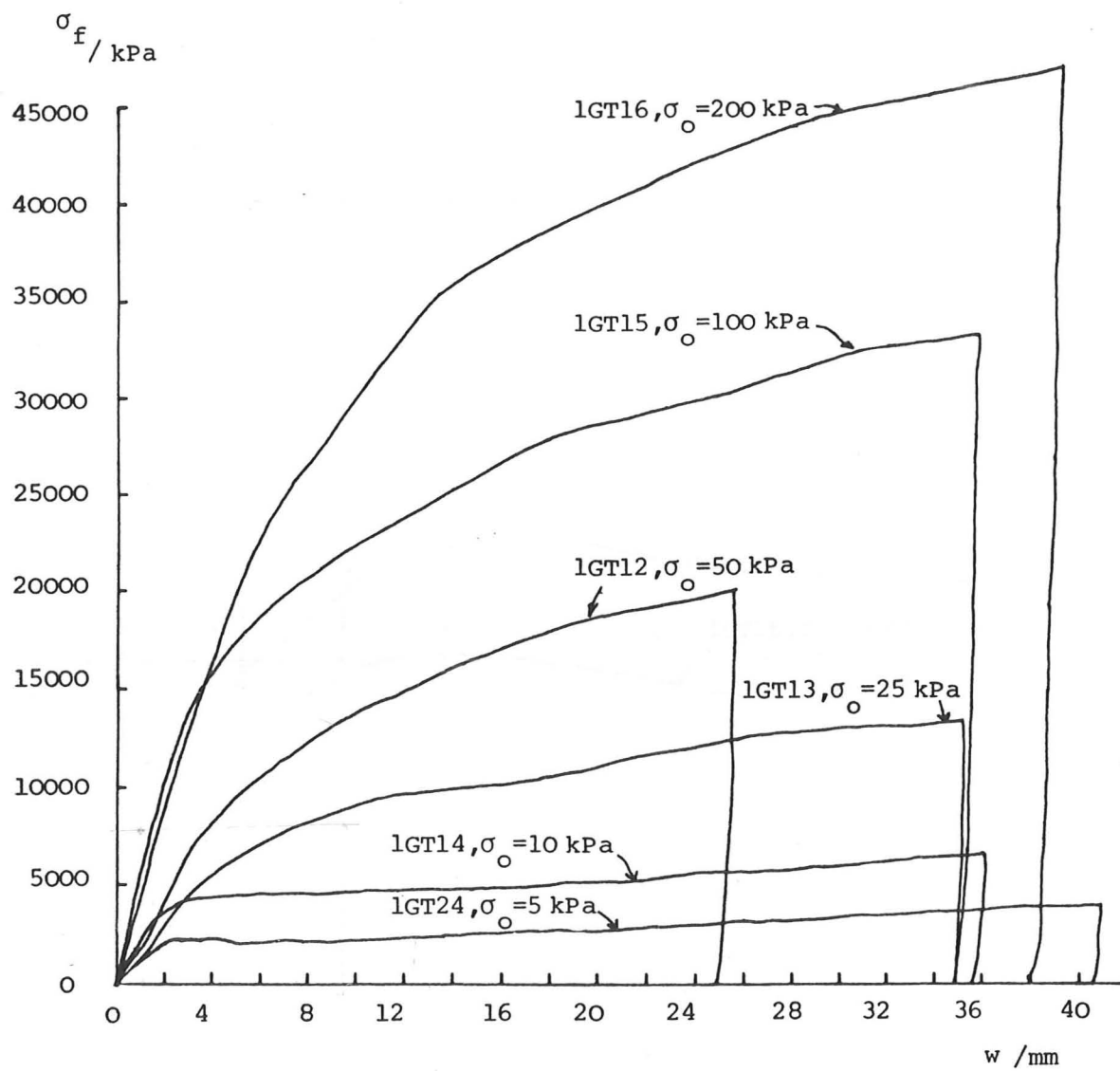
Fig 6.11   Effects of surcharge on the load/settlement
response of 1-g tests (sand, B=14.2mm)
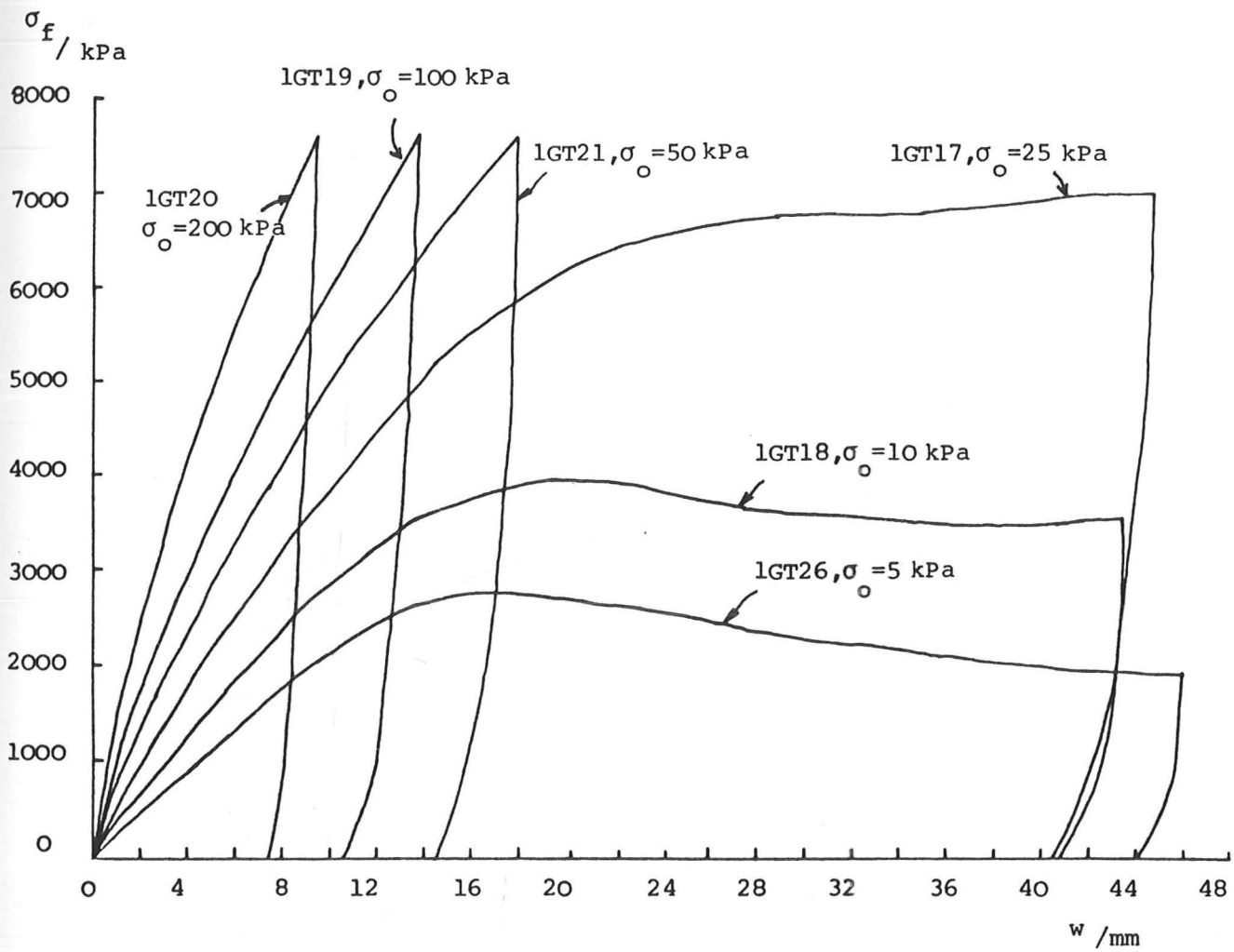
Fig 6.12   Effects of surcharge on the load/settlement
response of 1-g tests (sand,B=100mm)
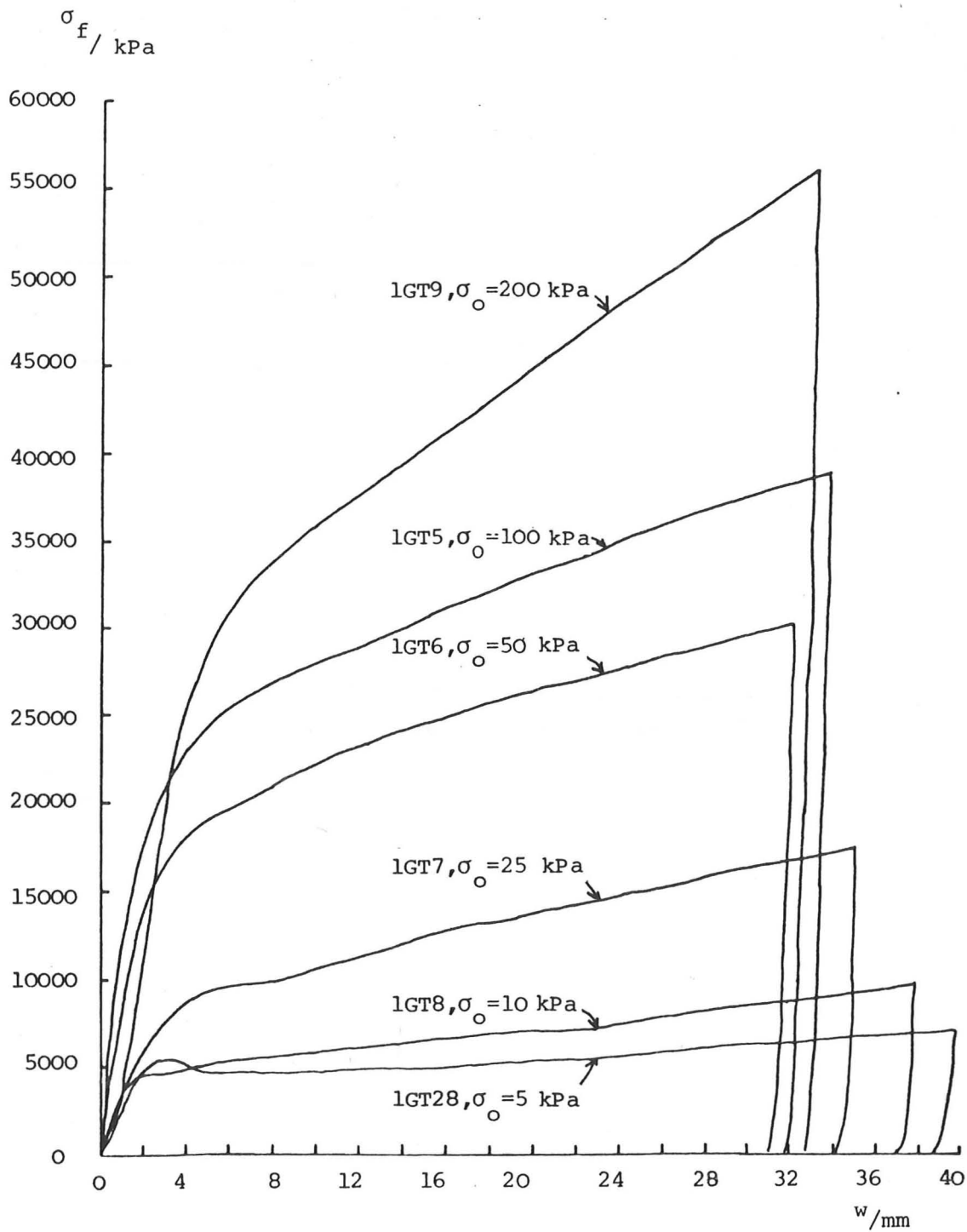
Fig 6.13 Effects of surcharge on the load/settlement response
of 1-g tests (silt, B=14.2mm)
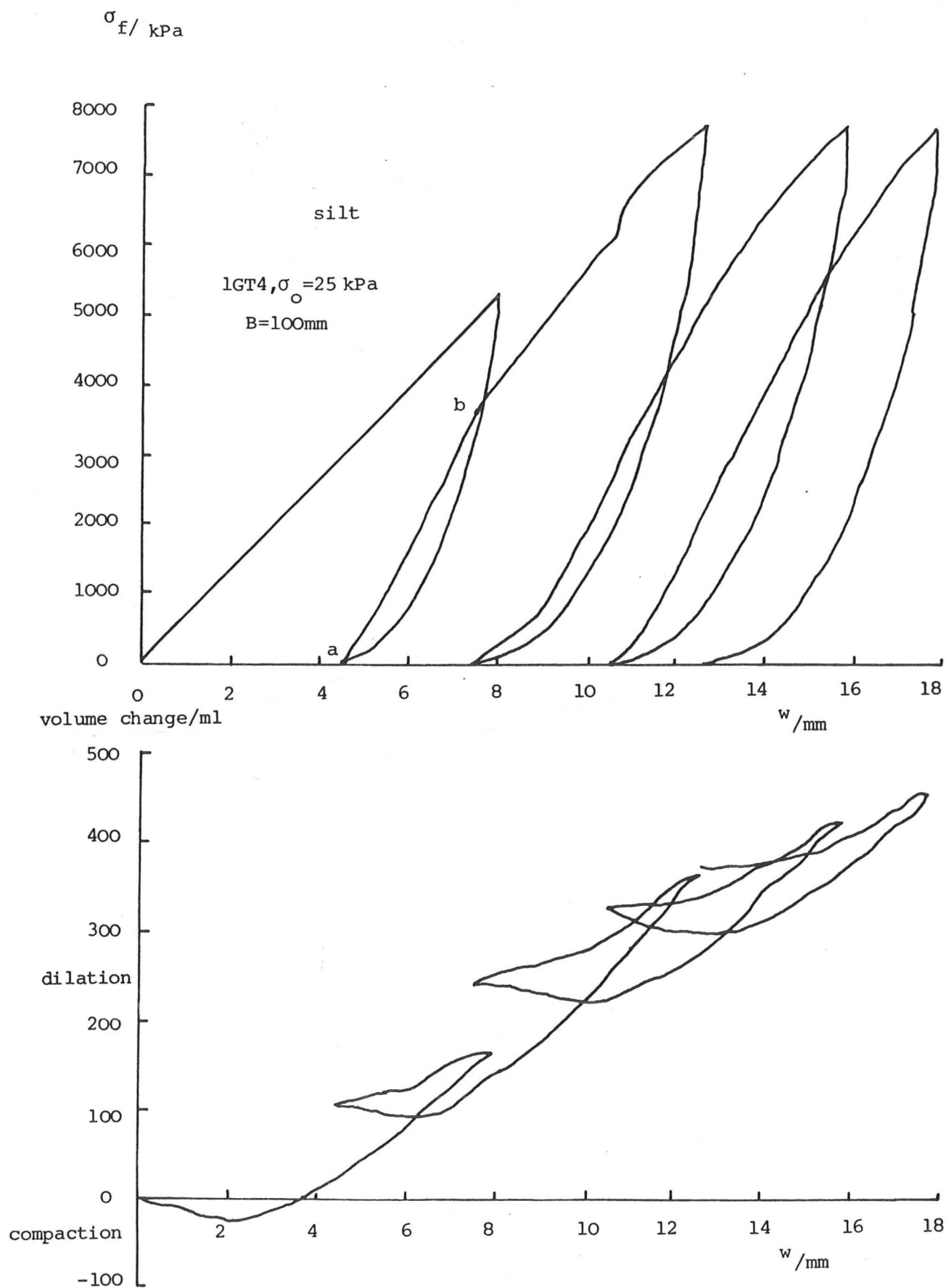
Fig 6.14   Load/settlement response of 1-g test (with volume
change measurement)
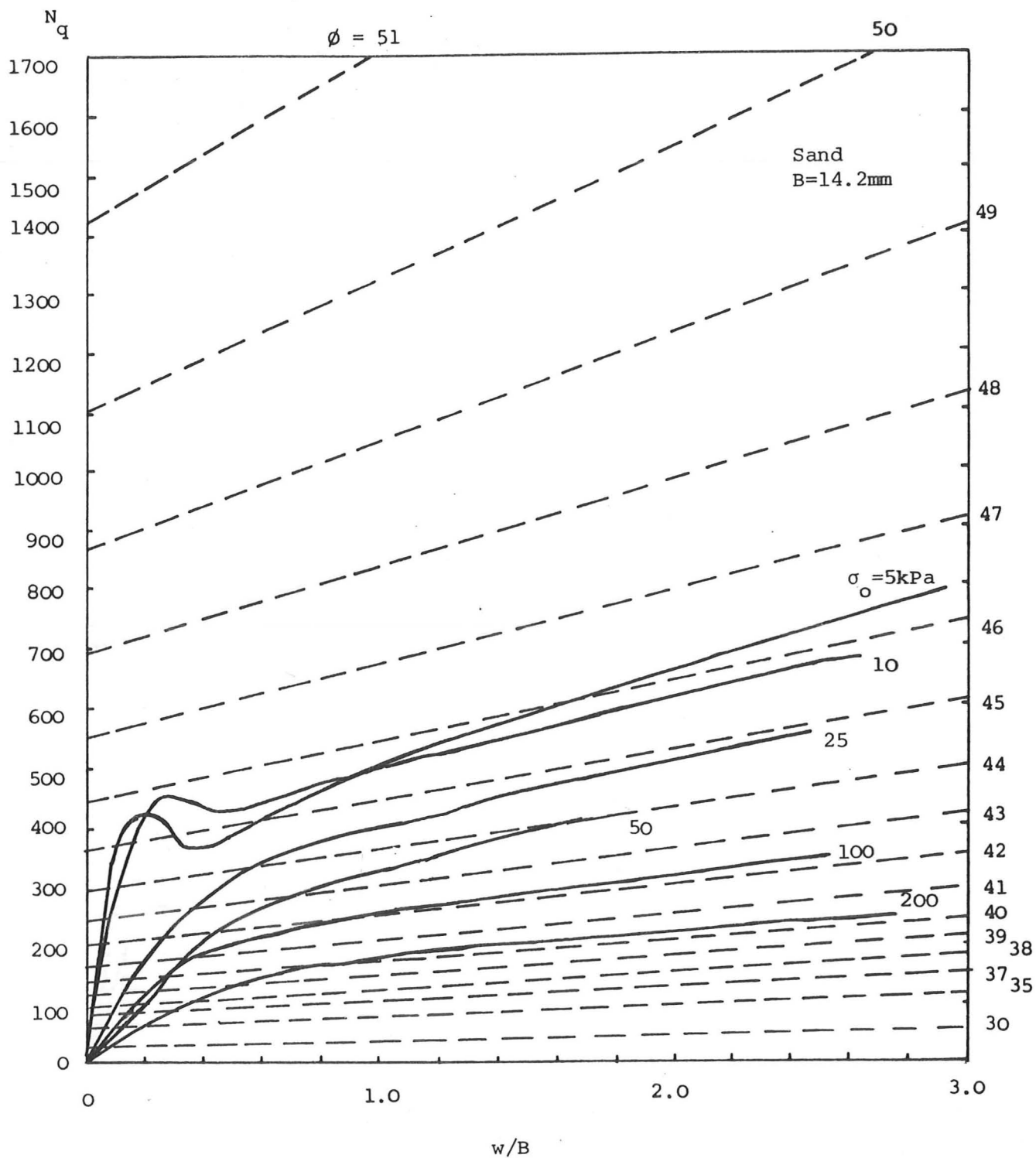
Fig 6.15 Interpretation of 1-g test data by superposing the
normalized theoretical and experimental curves
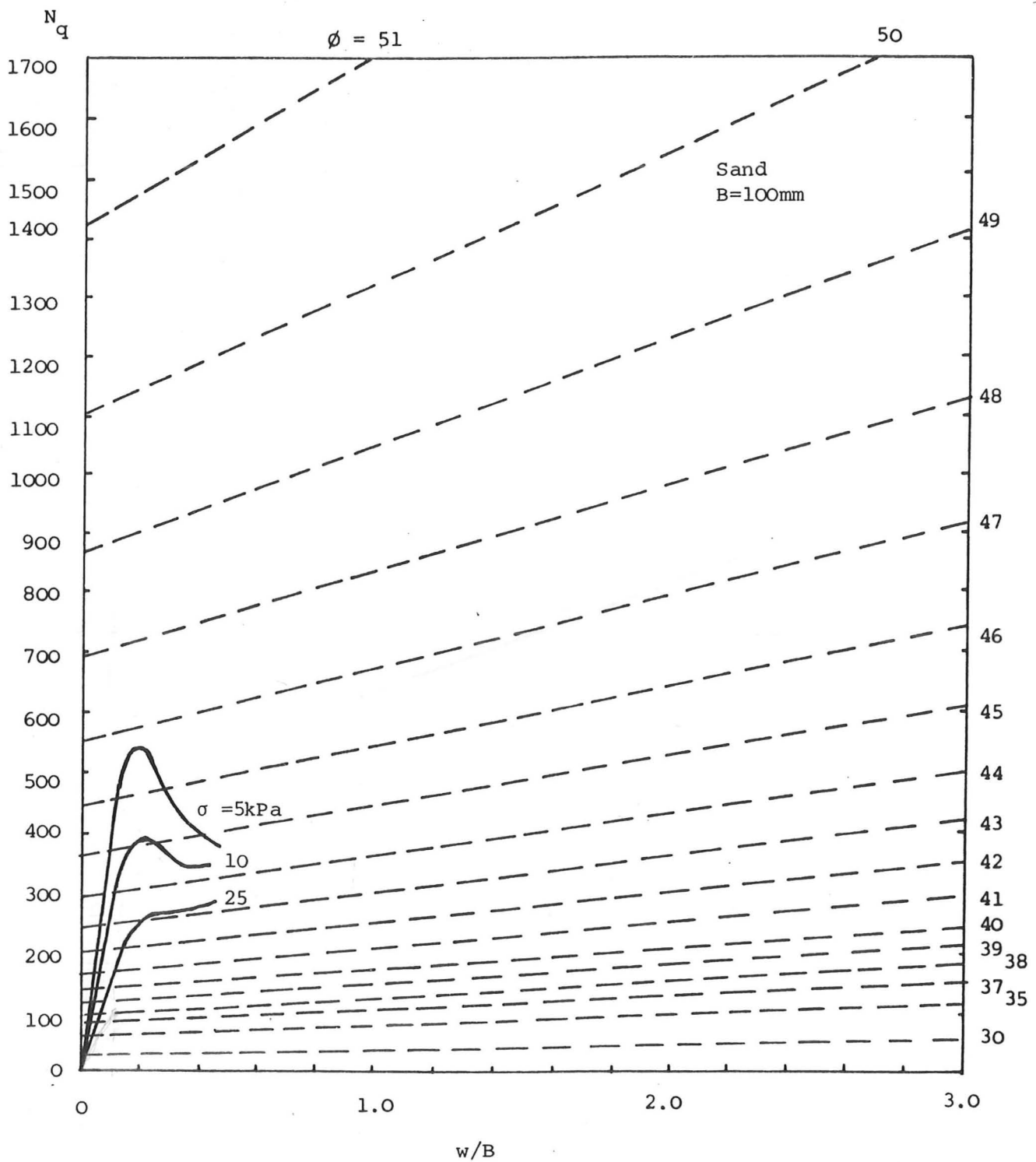
Fig 6.16 Interpretation of 1-g test data by superposing the
normalized theoretical and experimental curves
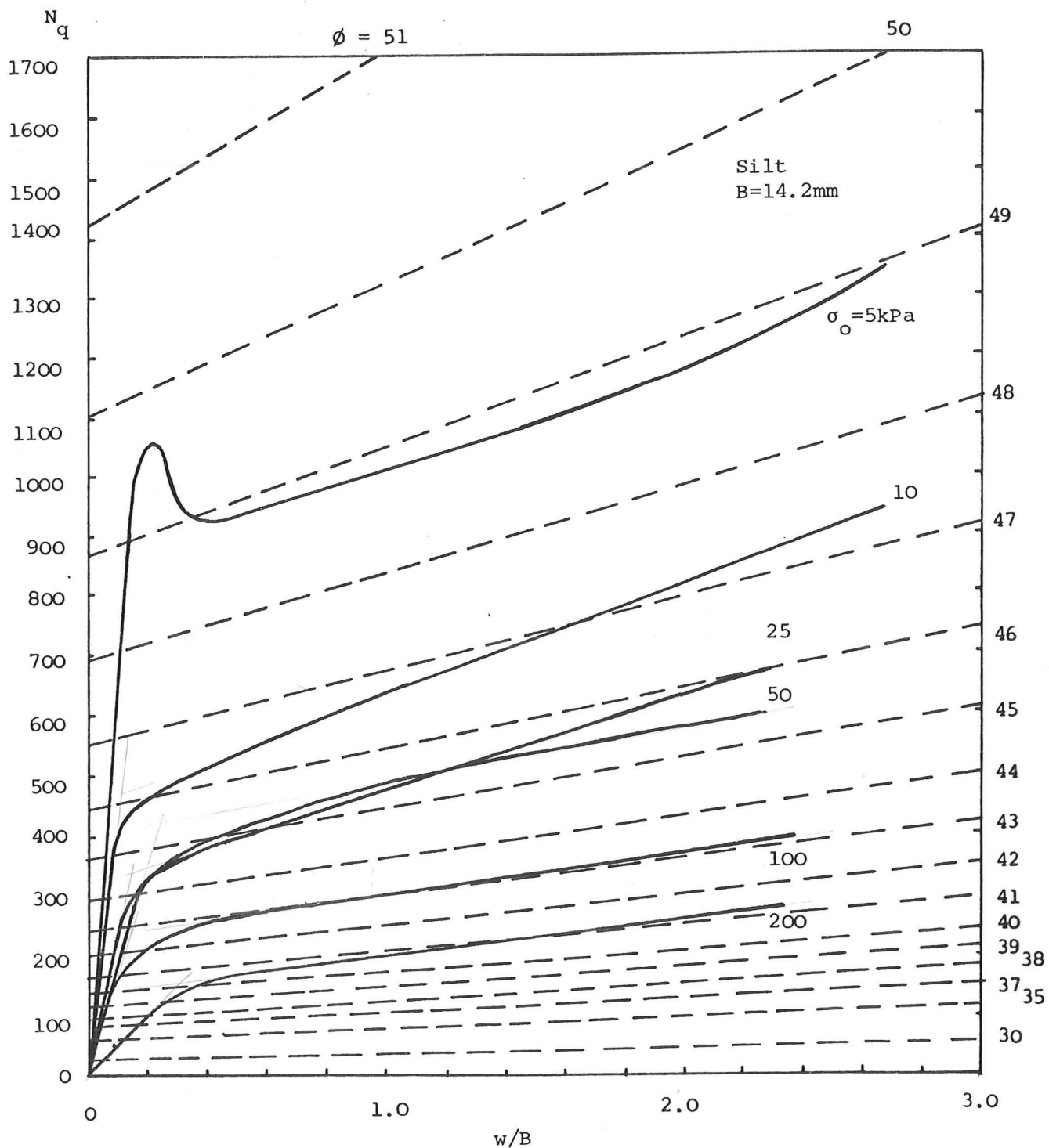
Fig 6.17   Interpretation of 1-g test data by superposing the
            normalized theoretical and experimental curves
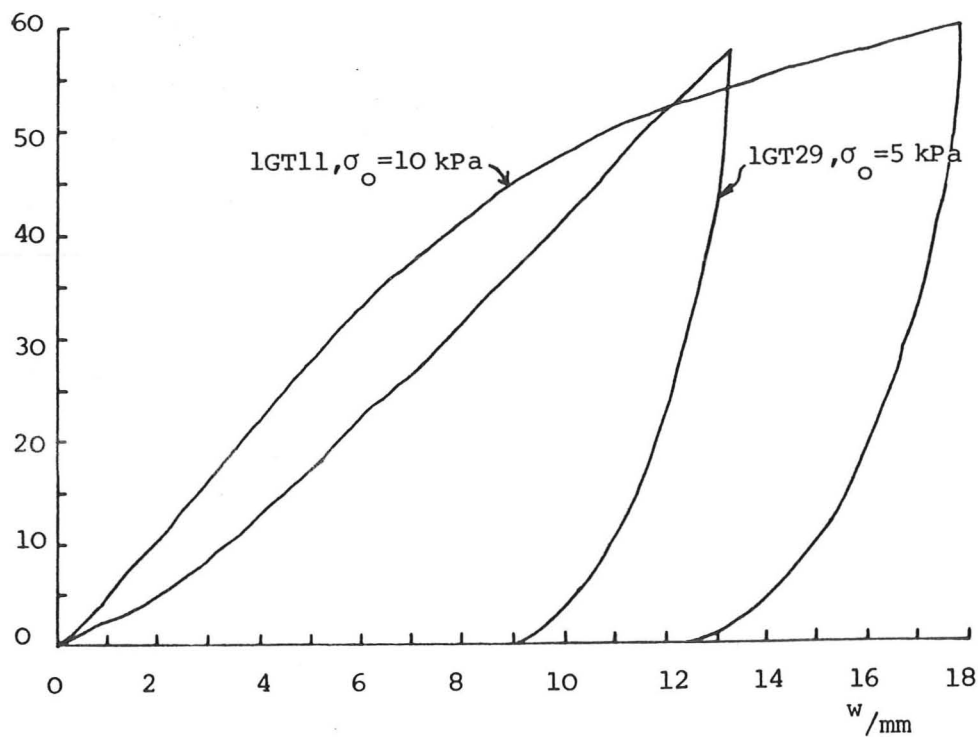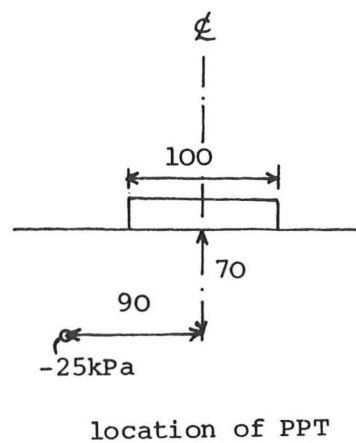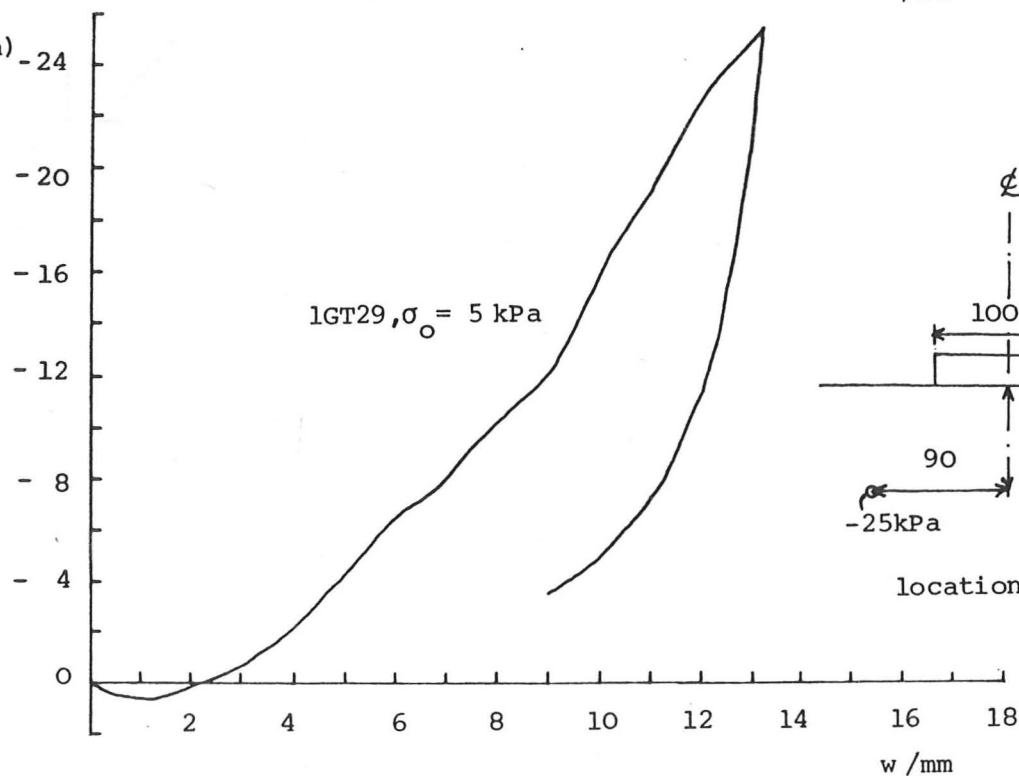
Fig 6.18   Effects of loading rate on stiffness and strength
           as a result of negative pore pressure build-up
           (rate: 0.1mm/min)
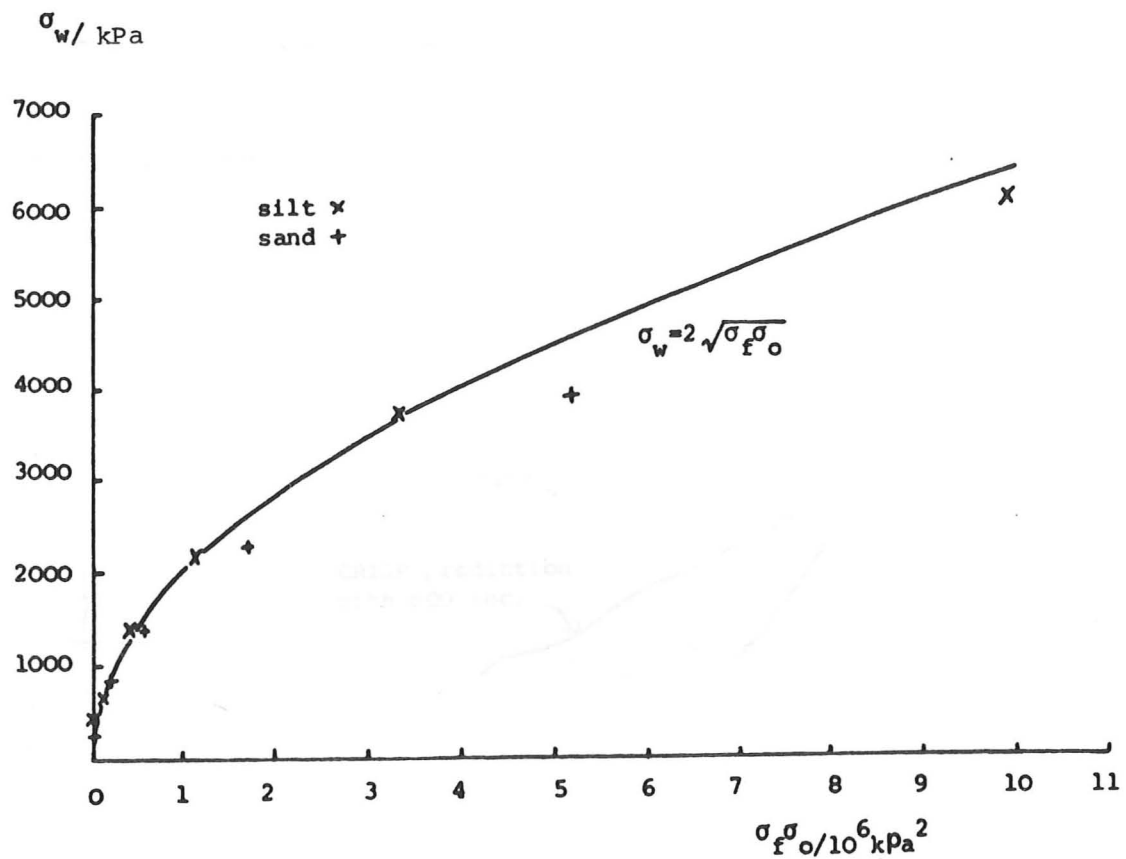
Fig 6.19 Empirical rule to find the working mean stress in
weightless soil supporting a circular surface footing

Vertical load/kN

sand,B=100mm,σ_o=25 kPa

CRISP prediction
with 480 inc.

experiment
1GT17

(a)

$^W/_{mm}$

silt,B=100mm,σ_o=25 kPa

CRISP prediction
with 600 inc.

experiment
1GT4

(b)

$^W/_{mm}$
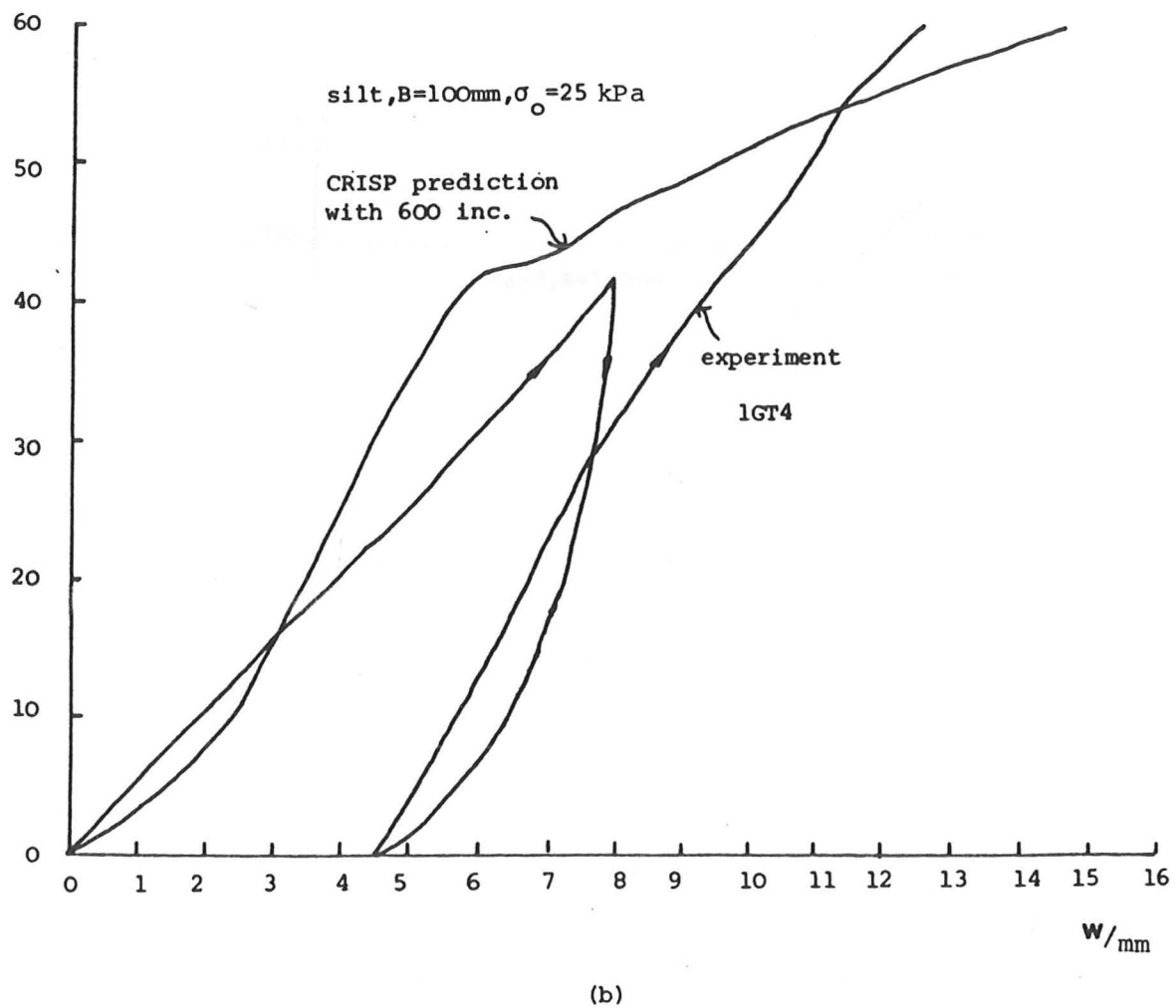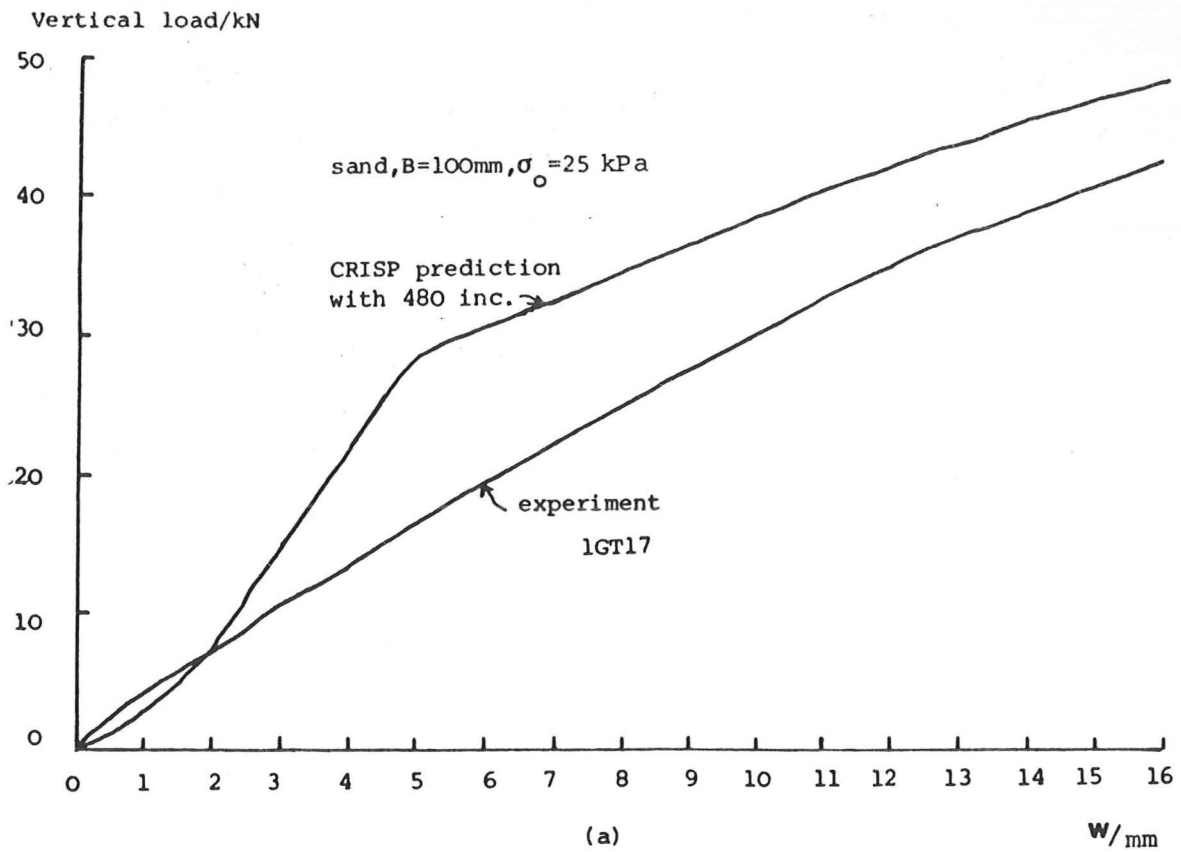
Fig 6.20 Comparison between theoretical and experimental load/
settlement curves

Assume this portion of the soil behaves like a triaxial specimen
$\varepsilon_a = 0.5 \Delta w / B$
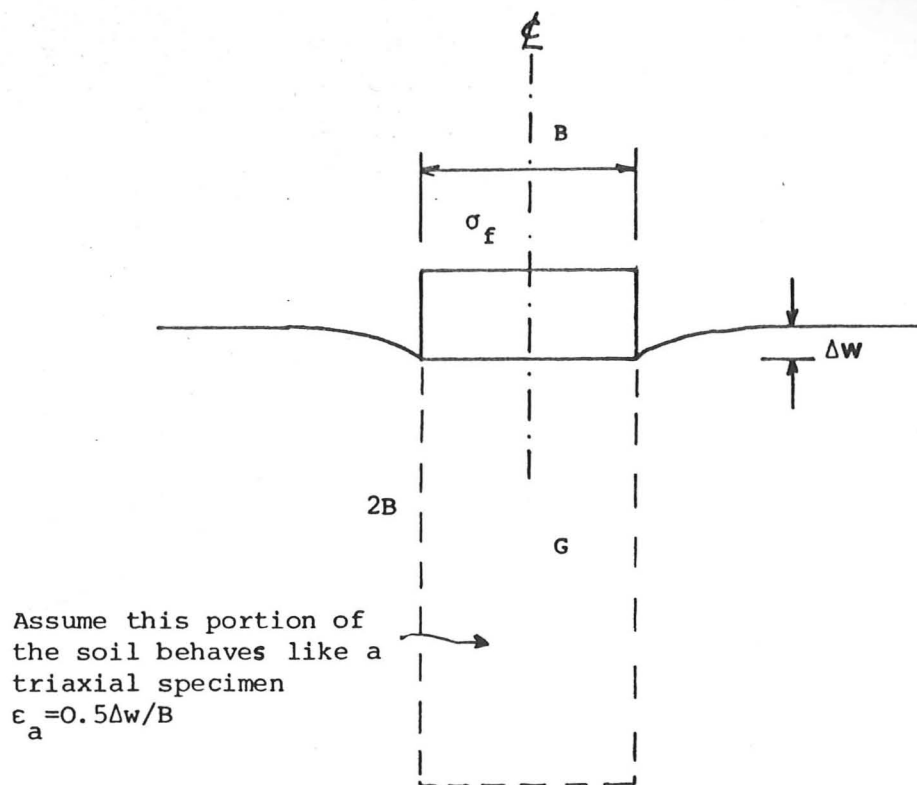
Fig 6.21 Elastic settlement of a circular surface footing

sand, B=100mm

1GT19, σ_o=100 kPa
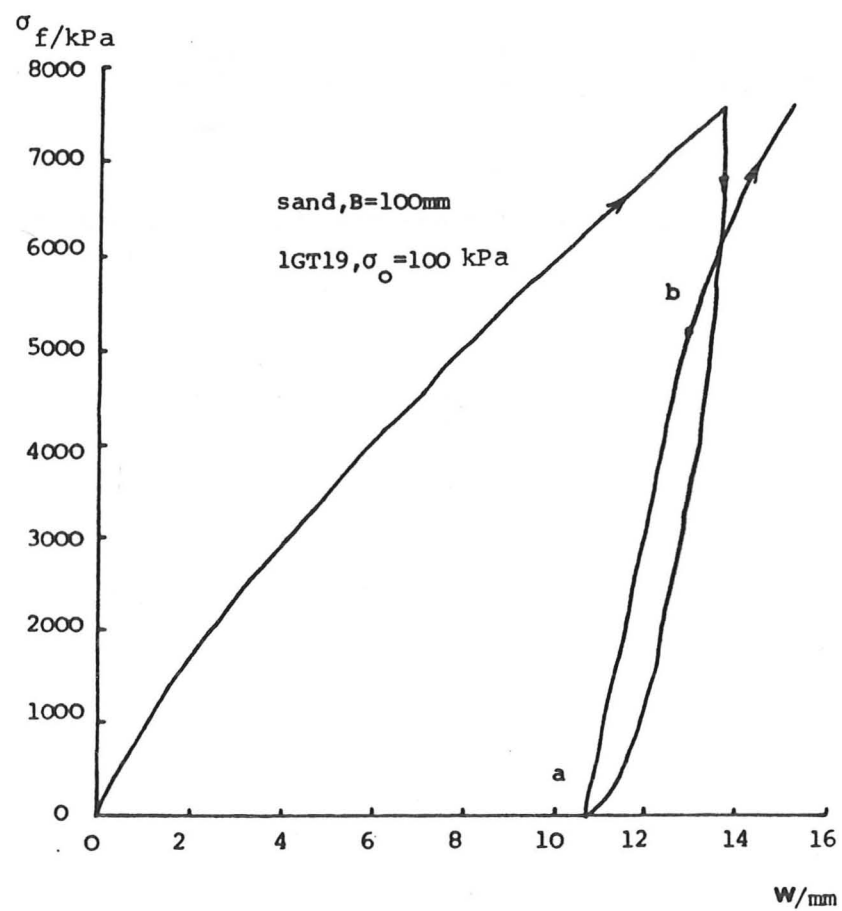
Fig 6.22 Load/settlement response of a footing involving
a cycle of unloading/reloading
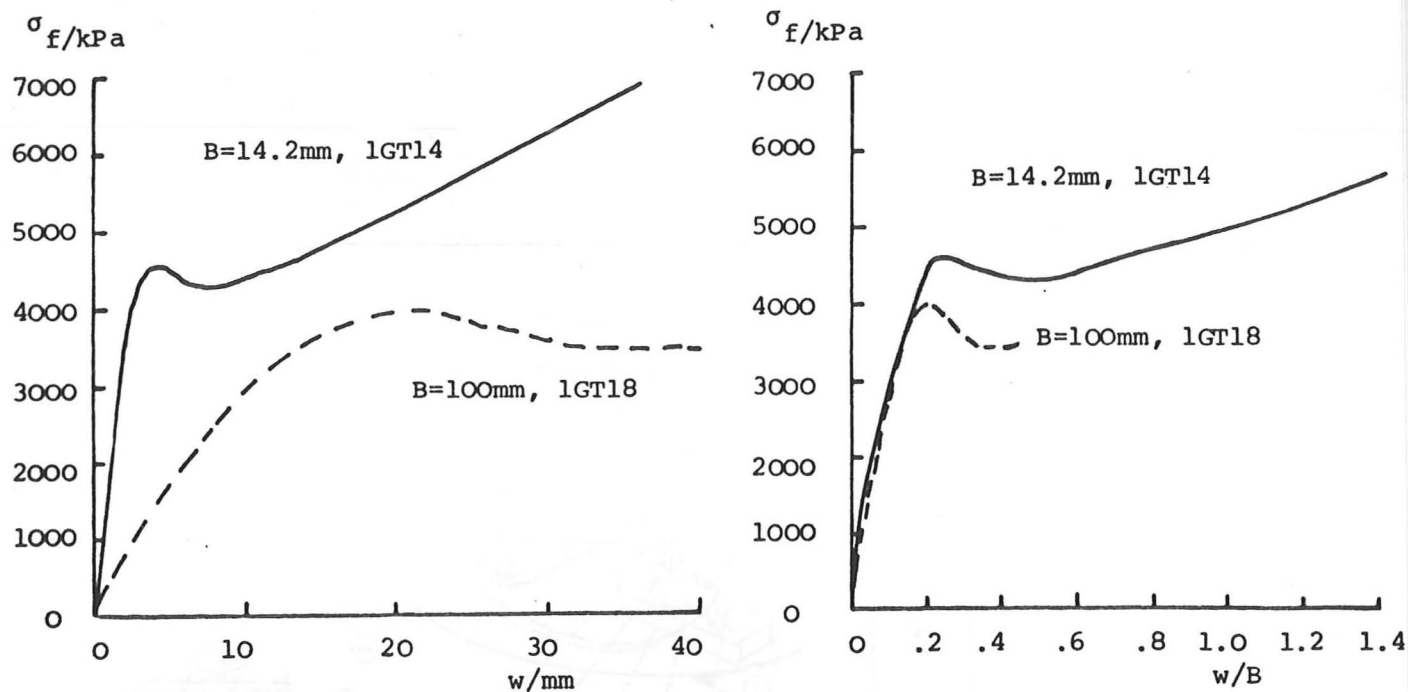
Fig 6.23   Comparison between load/settlement response with
            load/relative settlement response of a footing on
            sand at 1-g with $\sigma_o = 10 kPa$
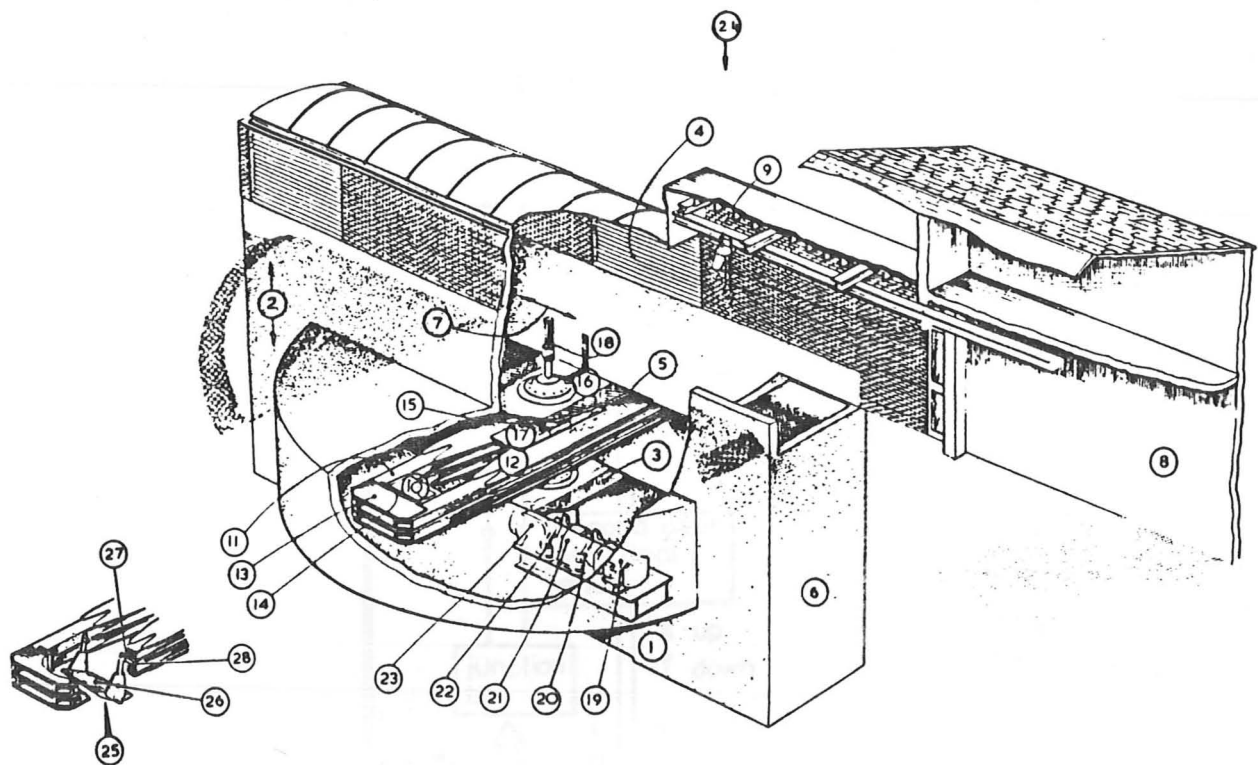
①	TUNNEL	⑧	OBSERVATION ROOM	⑮	BEARING SHAFT	㉒	ELECTROMAGNETIC BRAKE
②	AIR DUCT	⑨	CRANE	⑯	HORIZONTAL PLATE	㉓	GEARBOX
③	AIR VENT	⑩	SPECIMEN BOX	⑰	BEARING PLATE	㉔	WATER TOWER (POSITION OF)
④	LOUVRES	⑪	SPOKES	⑱	SLIP RING STACK	㉕	SWINGING CARRIAGE
⑤	AIR VENT	⑫	GUSSET PLATES	⑲	DRIVE MOTOR	㉖	PLATFORM
⑥	SHAFT	⑬	BRIDGING STRUCTURES	⑳	ELECTROMAGNETIC BRAKE	㉗	SWING ARM PIVOTS
⑦	CORRIDOR	⑭	MOUNTING PLATE	㉑	EDDY CURRENT COUPLING	㉘	TORSION BARS

Fig 7.1 Cambridge Geotechnical Centrifuge (After Schofield, 1980)

Fig 7.2   Schematic layout of the centrifuge test set-up

72

120

R=445

20⁰

Plan

₵

B ⸸ C ⸸

B C

916

Section A-A

180

180

Section B-B Section C-C
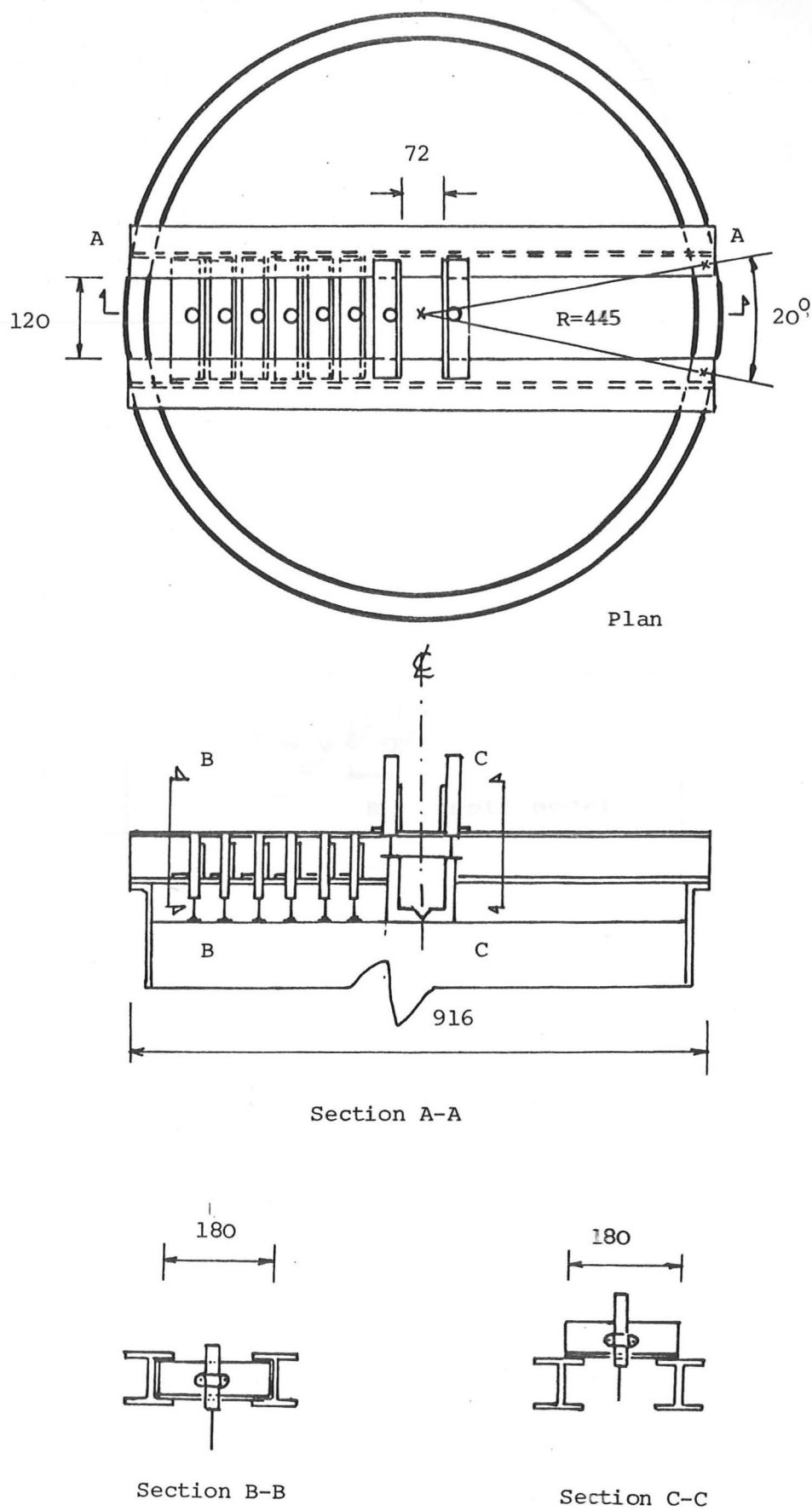
Fig 7.3 Details of cross beam for supporting LVDTs

plan view

```
x                                              x
                                                  top
11    7    3         6   10   14
 .  .  .  .  .    x    .  .  .  .  .
13    9    5         4    8   12

bottom

              soil model
```

section x-x

```
5@50c/o    40  120  40    5@50c/c
                    ¢

              1 : 2

              H
           B | A
        D      C
bottom                              top

        R    soil model
```
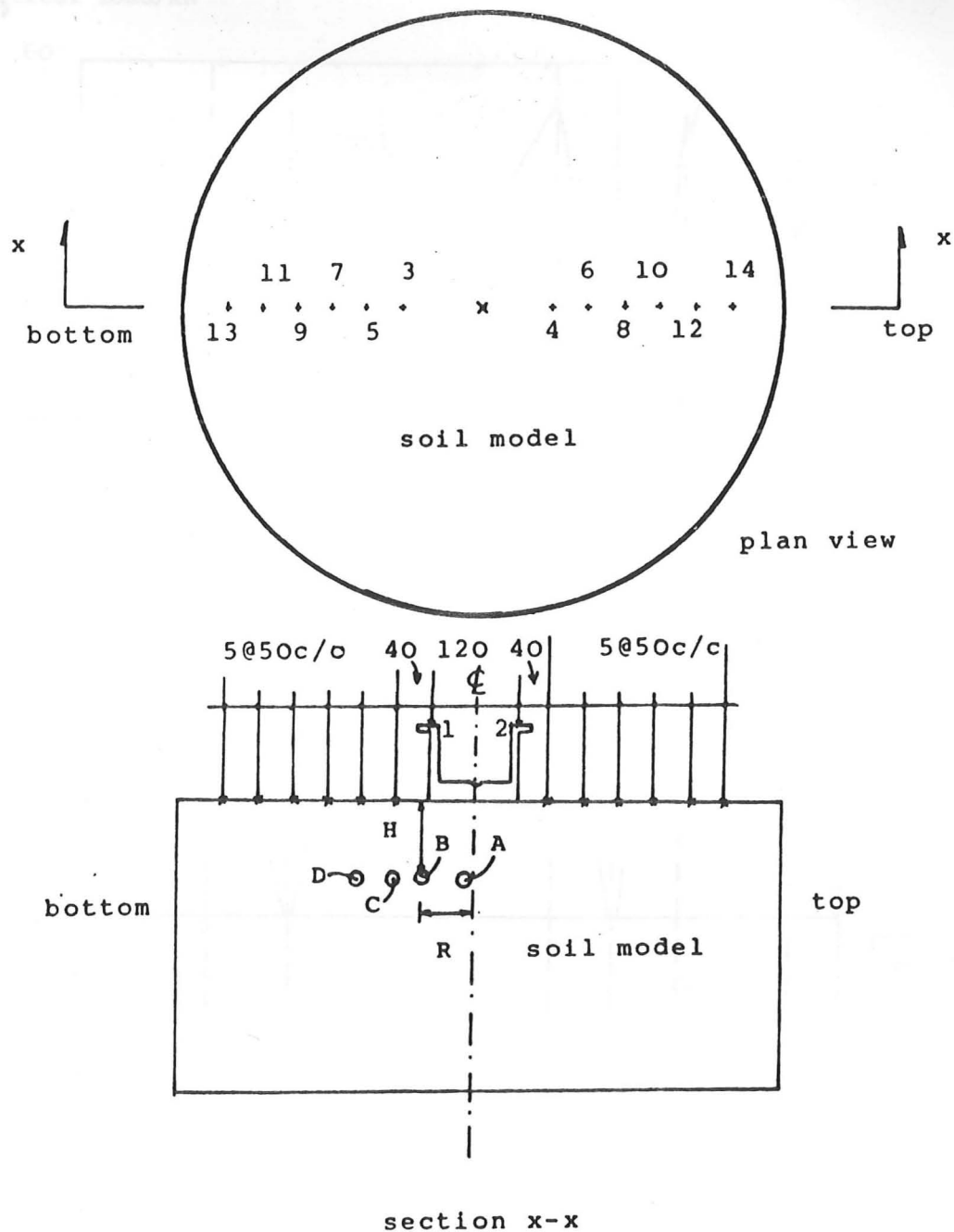
ppt position test no.	A		B		C		D	
	R	H	R	H	R	H	R	H
CKL1	0	0	75	95	145	111	185	91
CKL2	–	–	–	–	–	–	–	–
CKL3	5	102	171	76	189	122	–	–
CKL4	20	105	110	105	180	105	–	–

Fig 7.4   Vertical movement check point and PPT location plan

Vertical load/kN

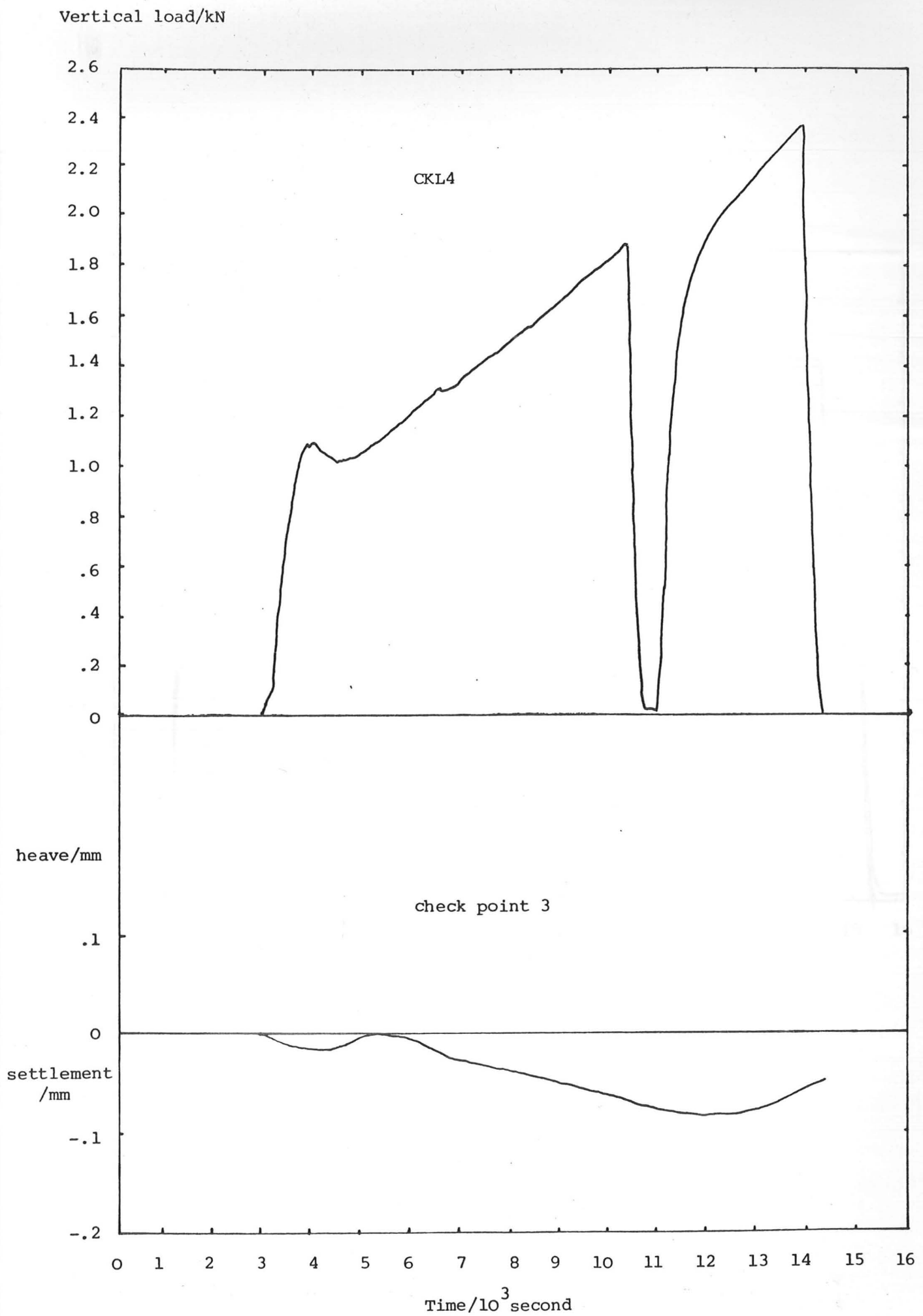| check point	ratio
3	1.00
4	0.47
5	0.53
6	0.32
7	0.37
8	0.19
9	0.18
10	0.10
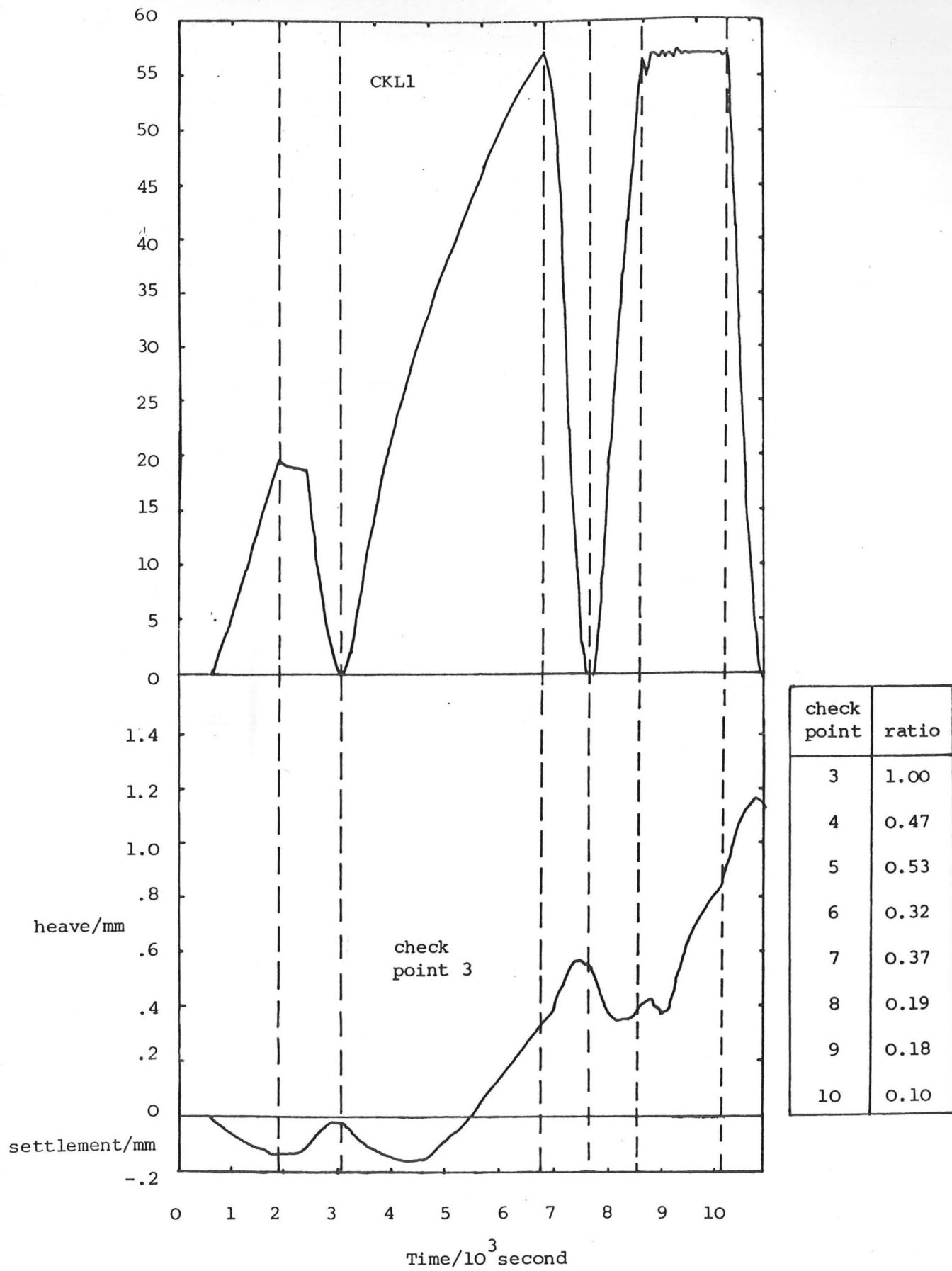
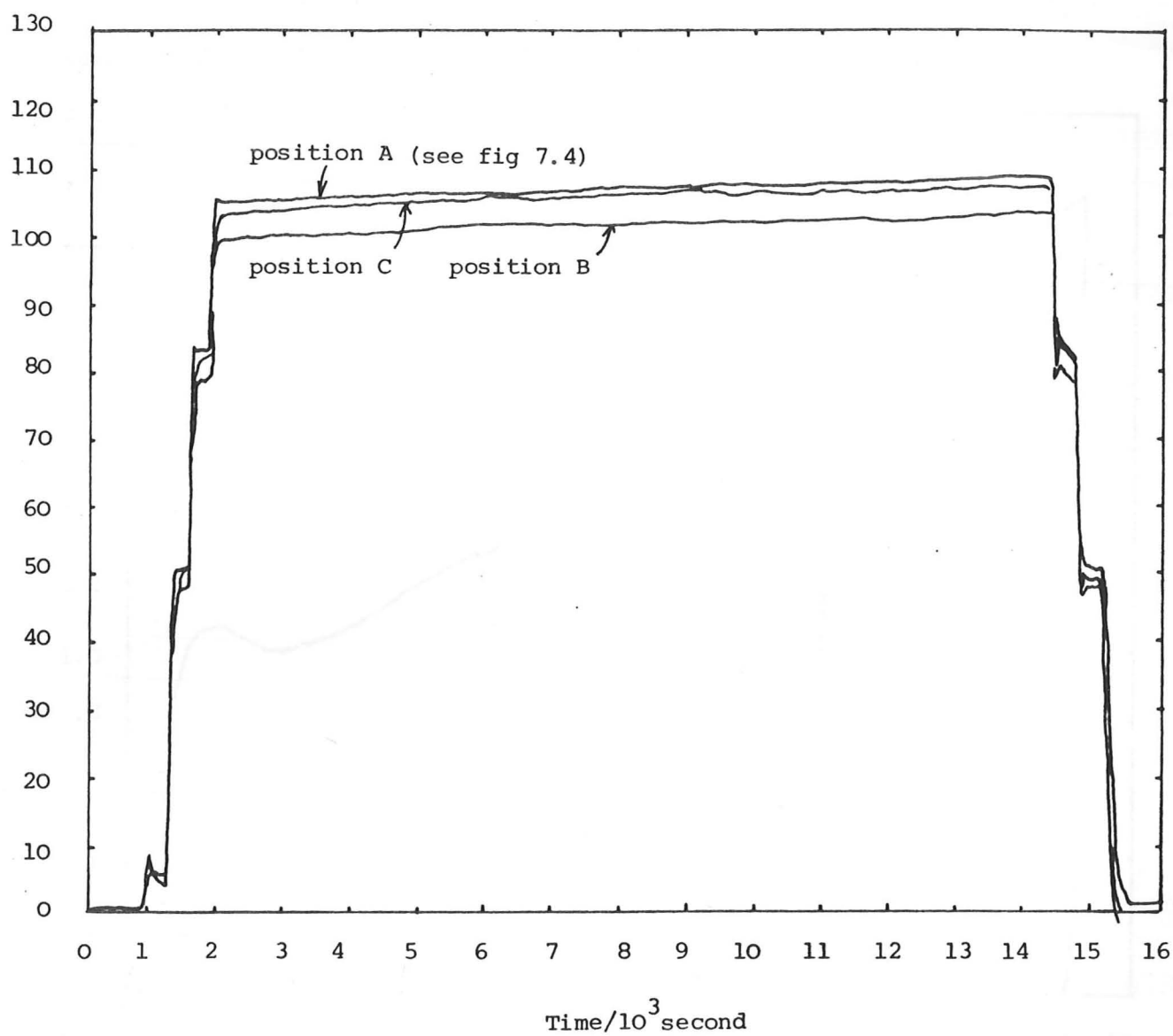Fig 7.5 Vertical load and check point movement during test CKL1

pore pressure/ kPa
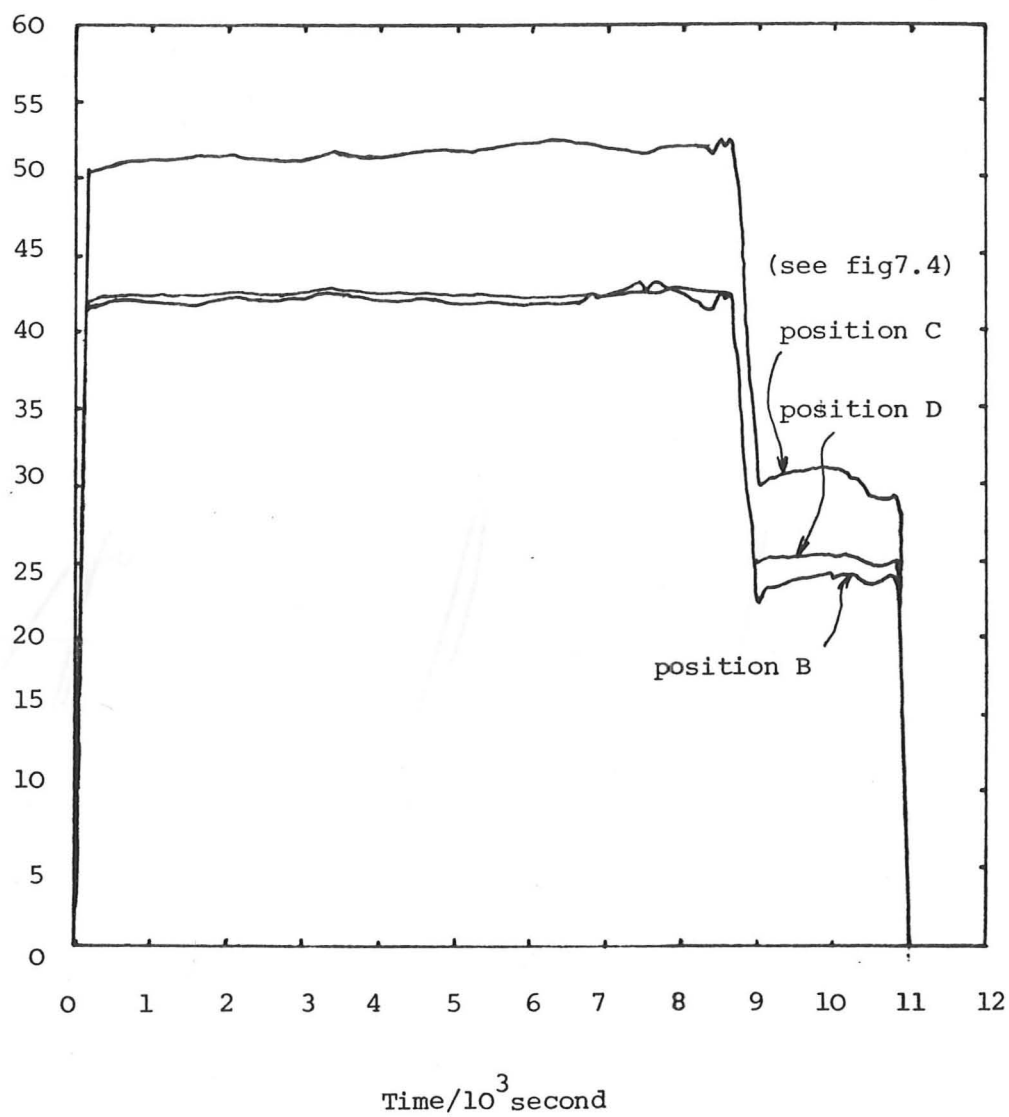
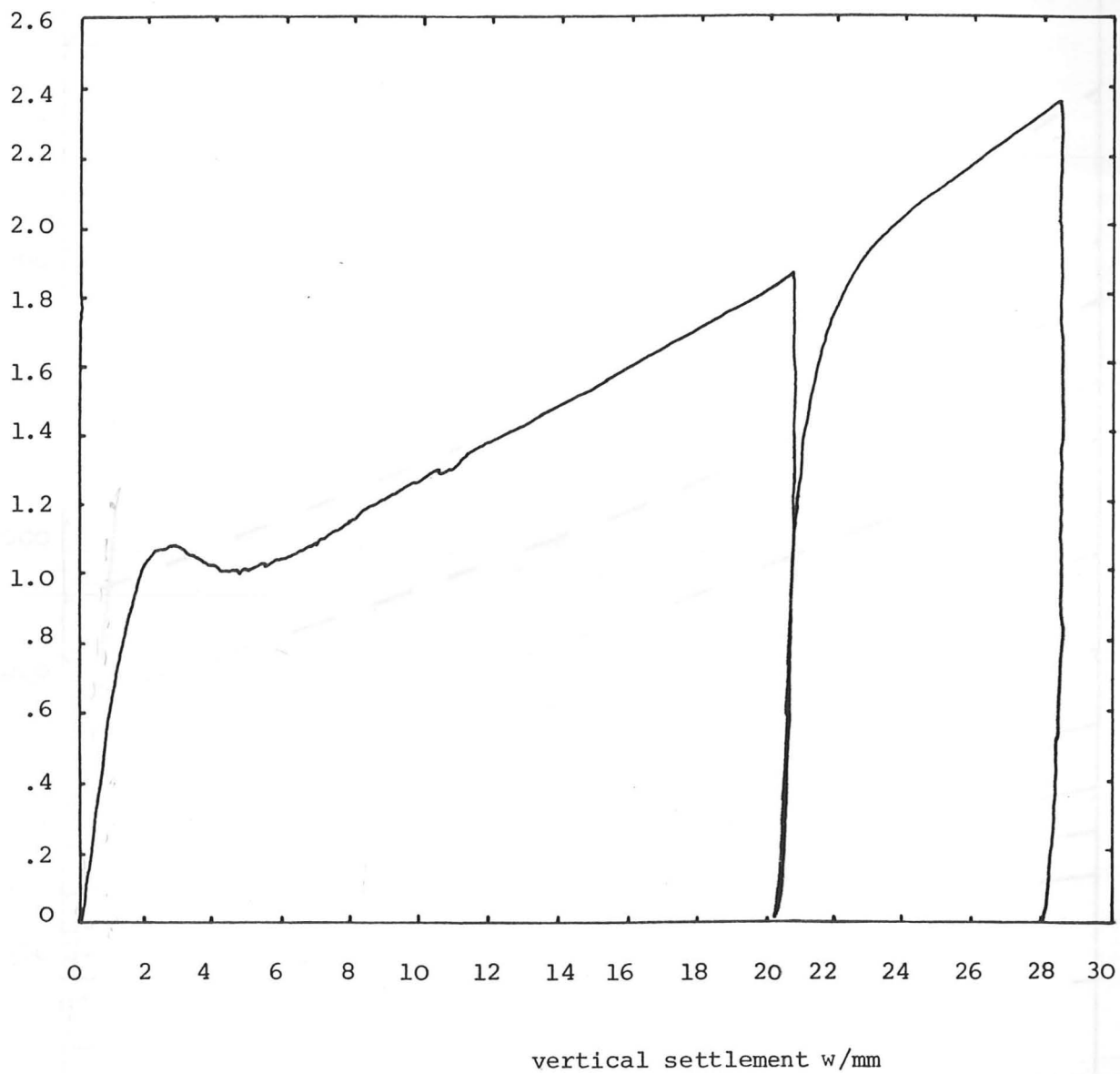Fig 7.6   Pore water pressure response during test CKL1
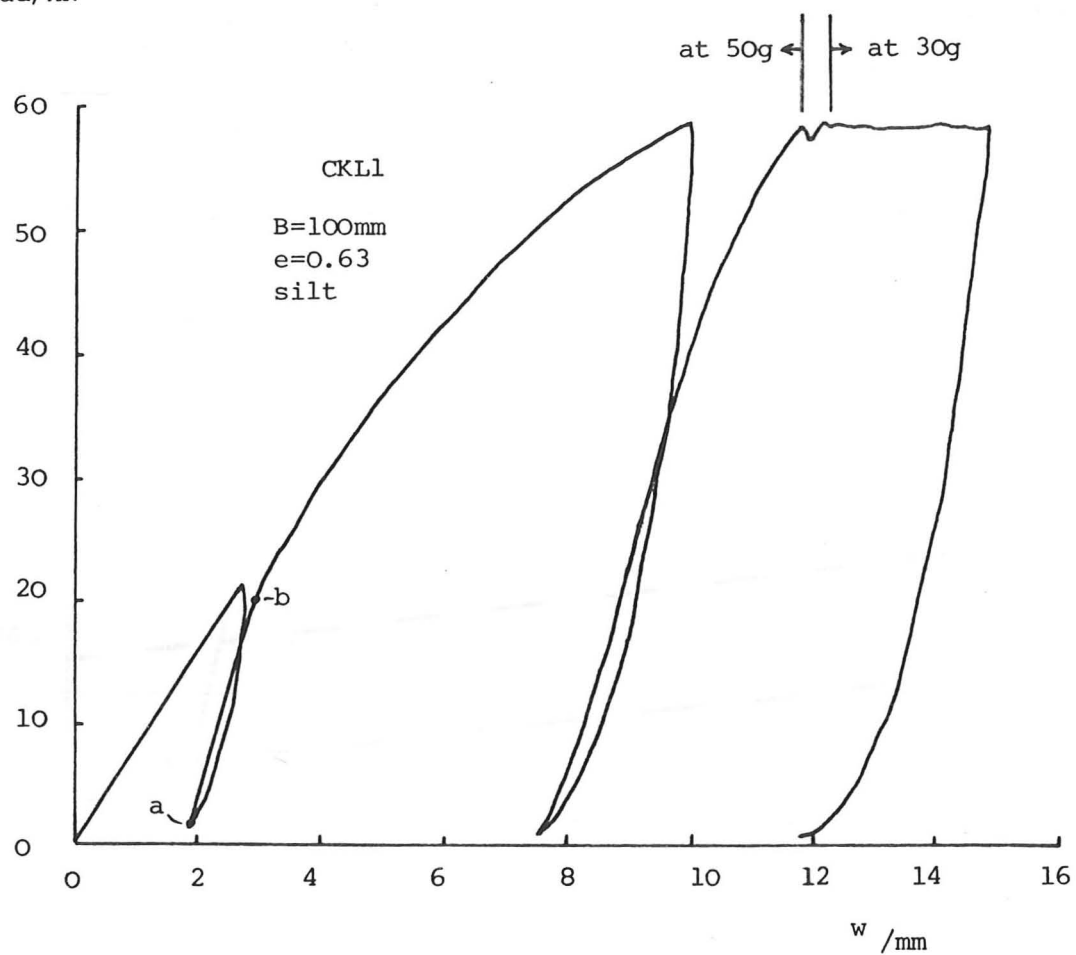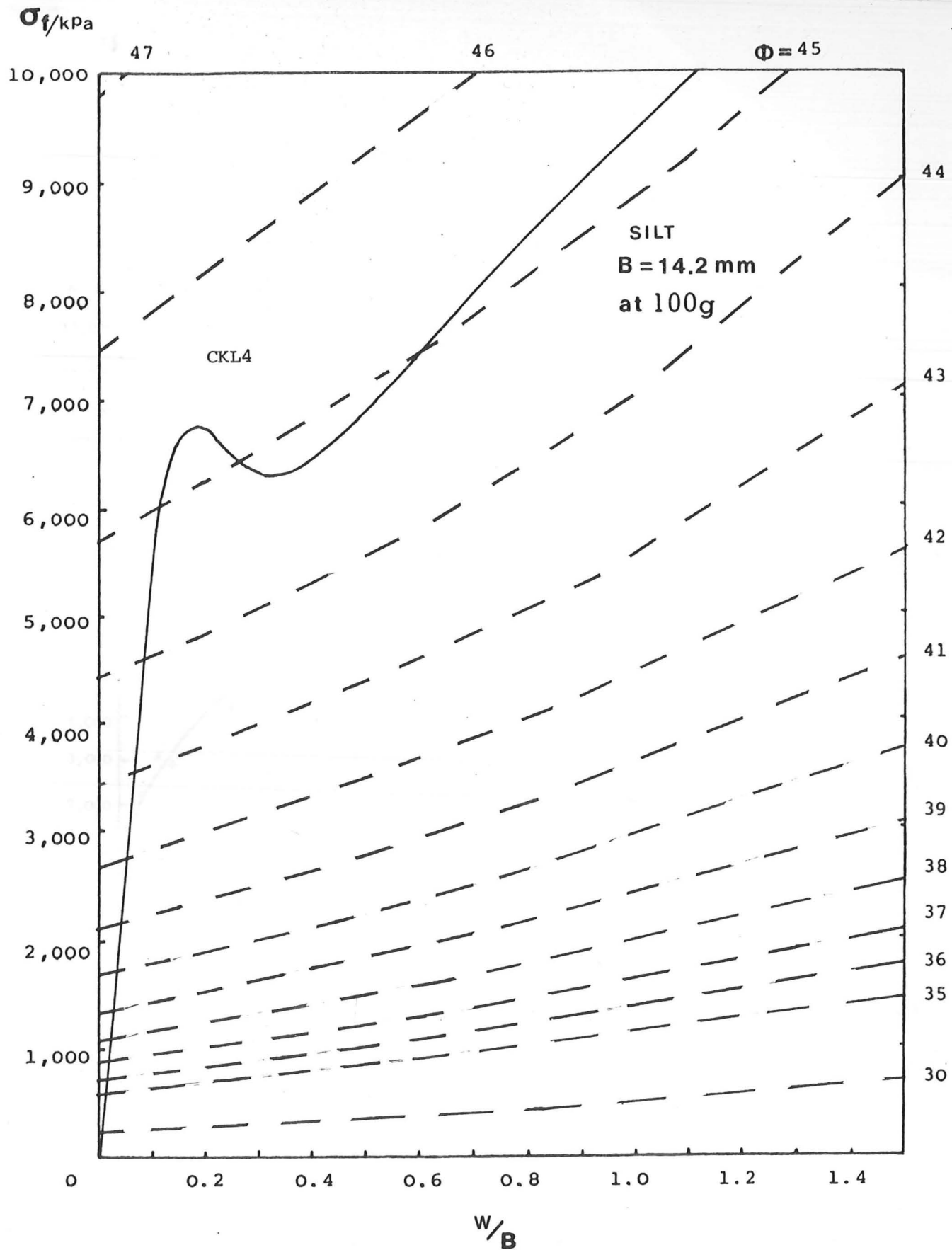
Fig 7.7   Load/settlement response of centrifuge test CKL1
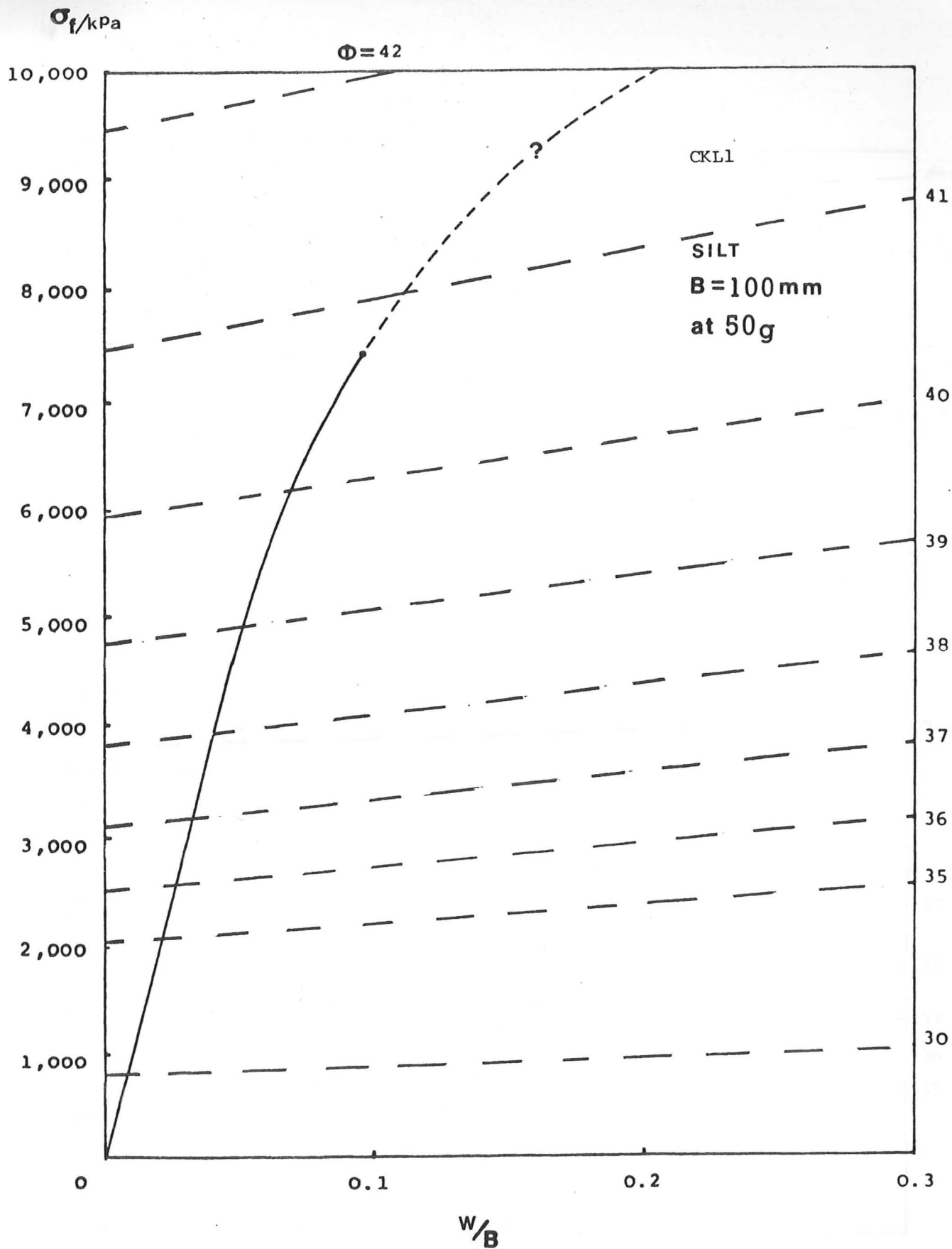
Fig 7.8   Interpretation of the centrifuge test data by superposing
the theoretical and experimental curves
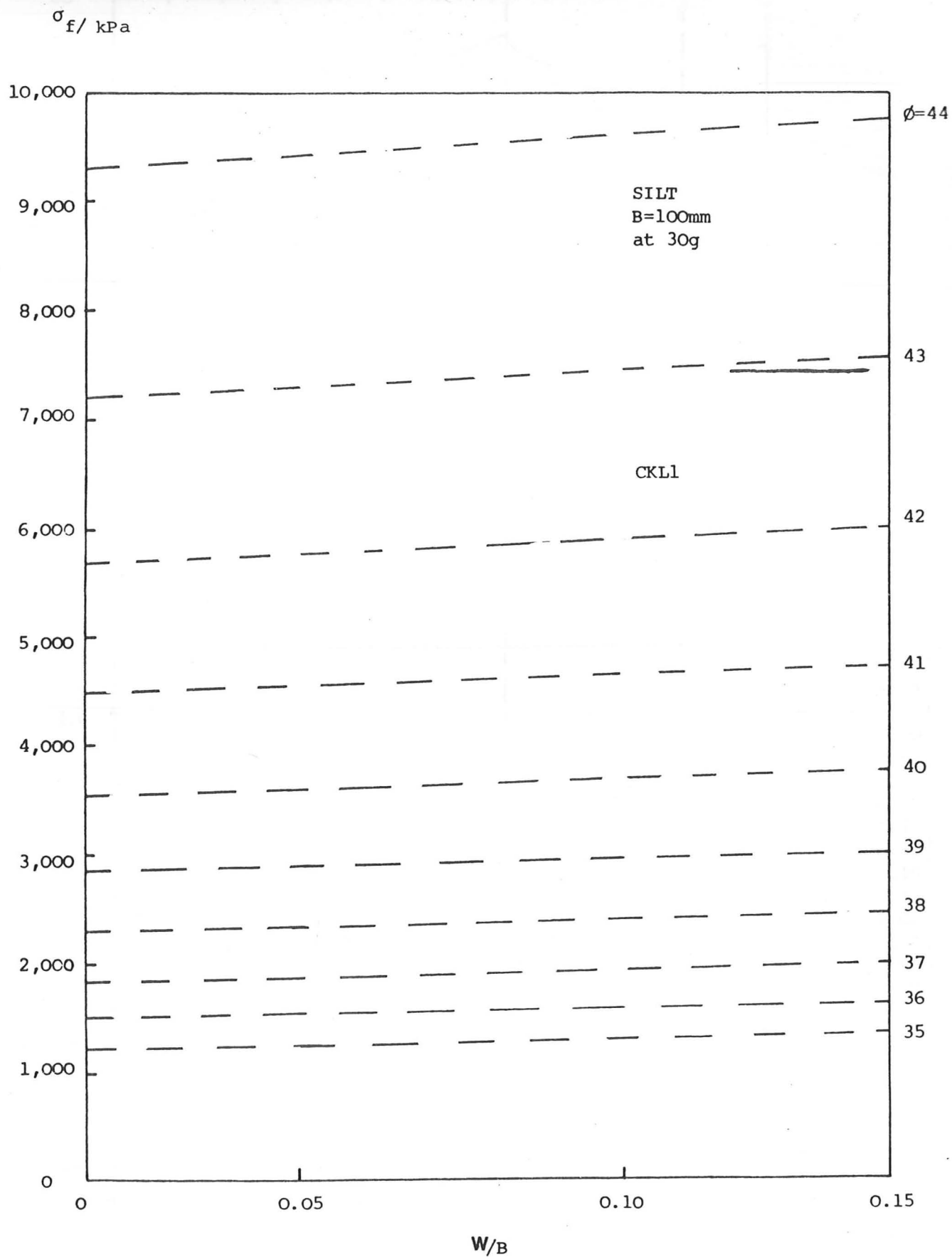
Fig 7.9   Interpretation of centrifuge test data by superposing the
theoretical and experimental curves
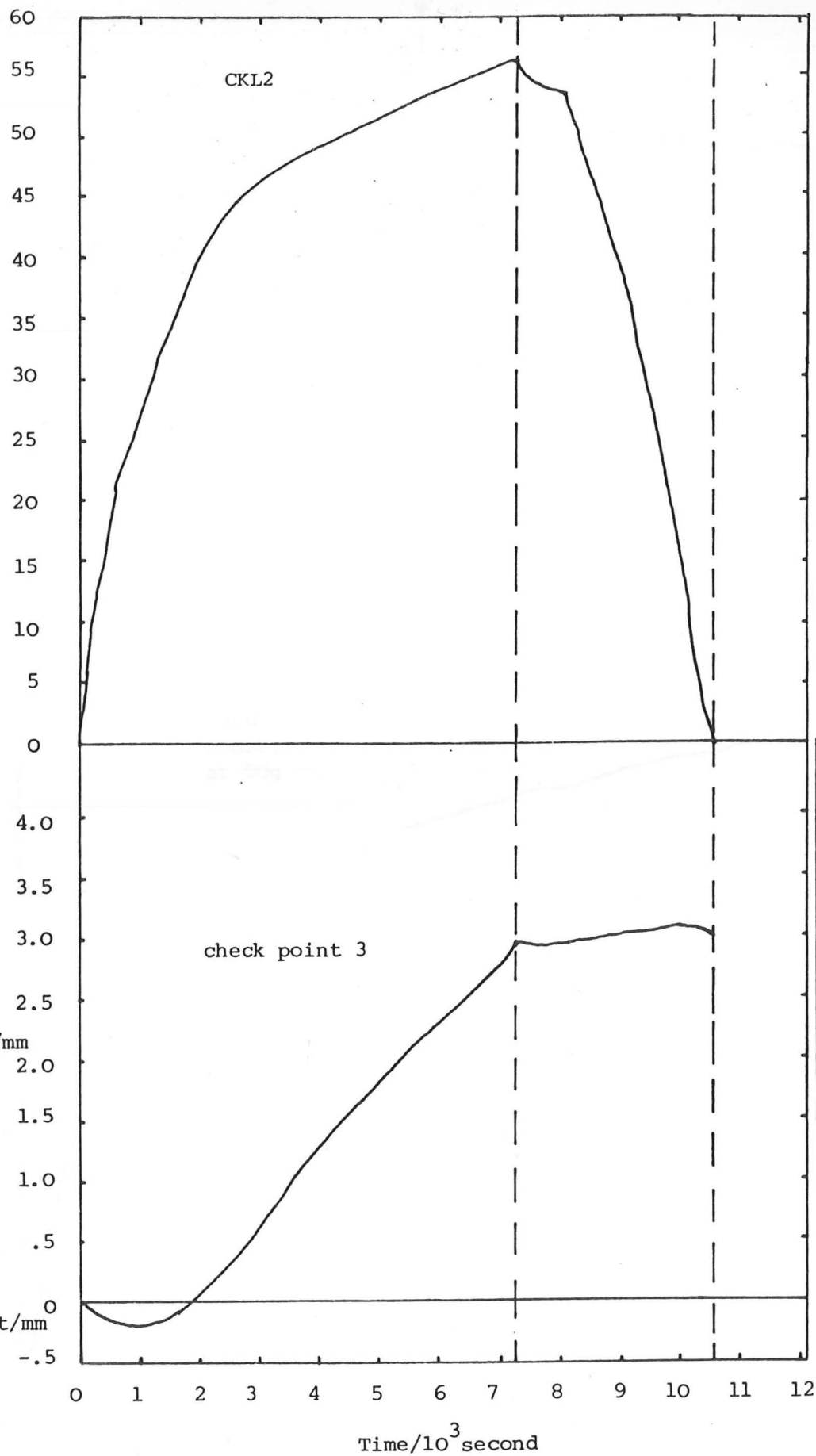
Fig 7.10   Vertical load and check point movement during test CKL2
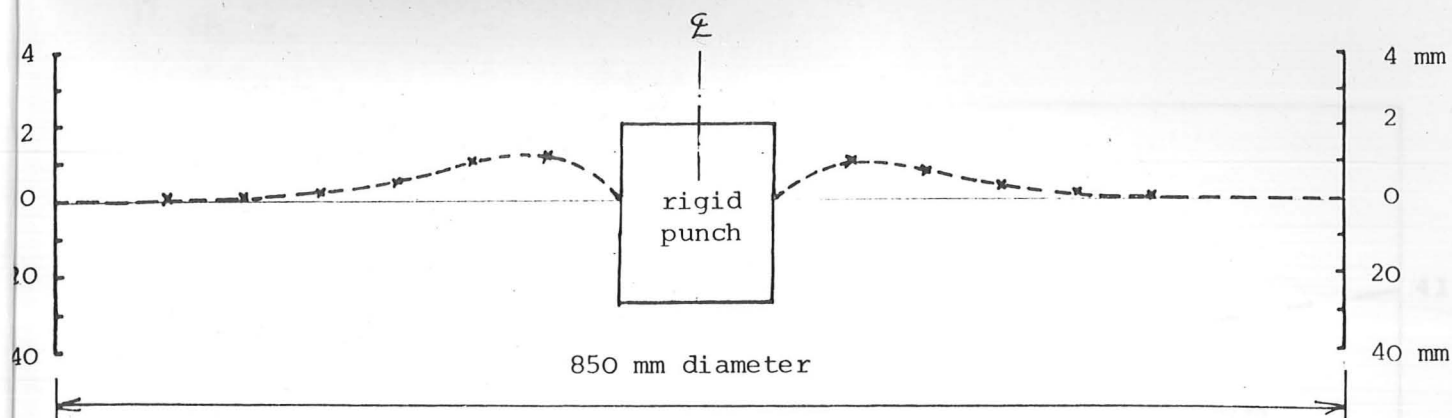
Fig 7.11a   Top profile of model when σ_f was maximum (CKL2)
(note: x10 scale factor on heave)
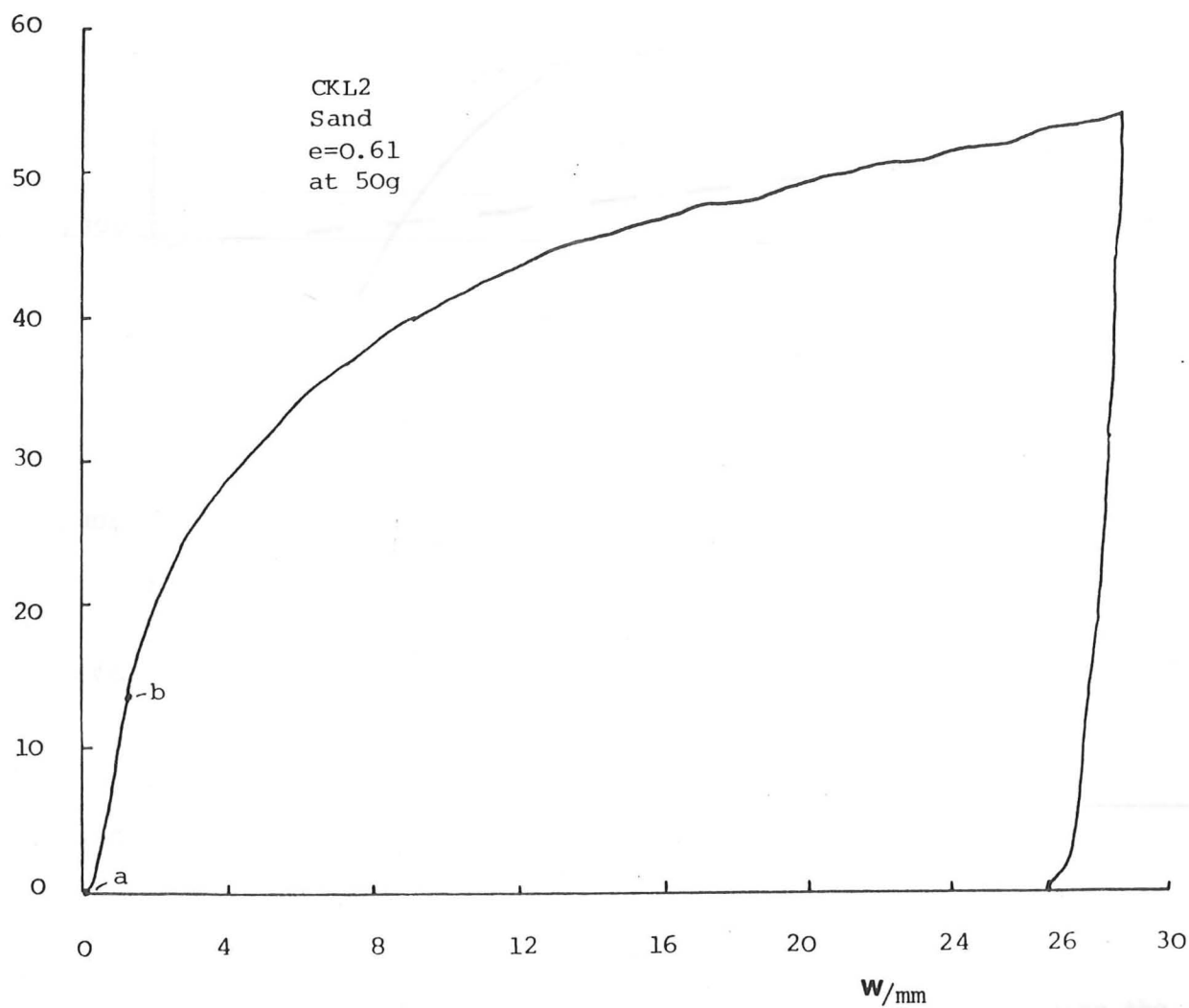
Fig 7.11b Load/settlement response of centrifuge test CKL2
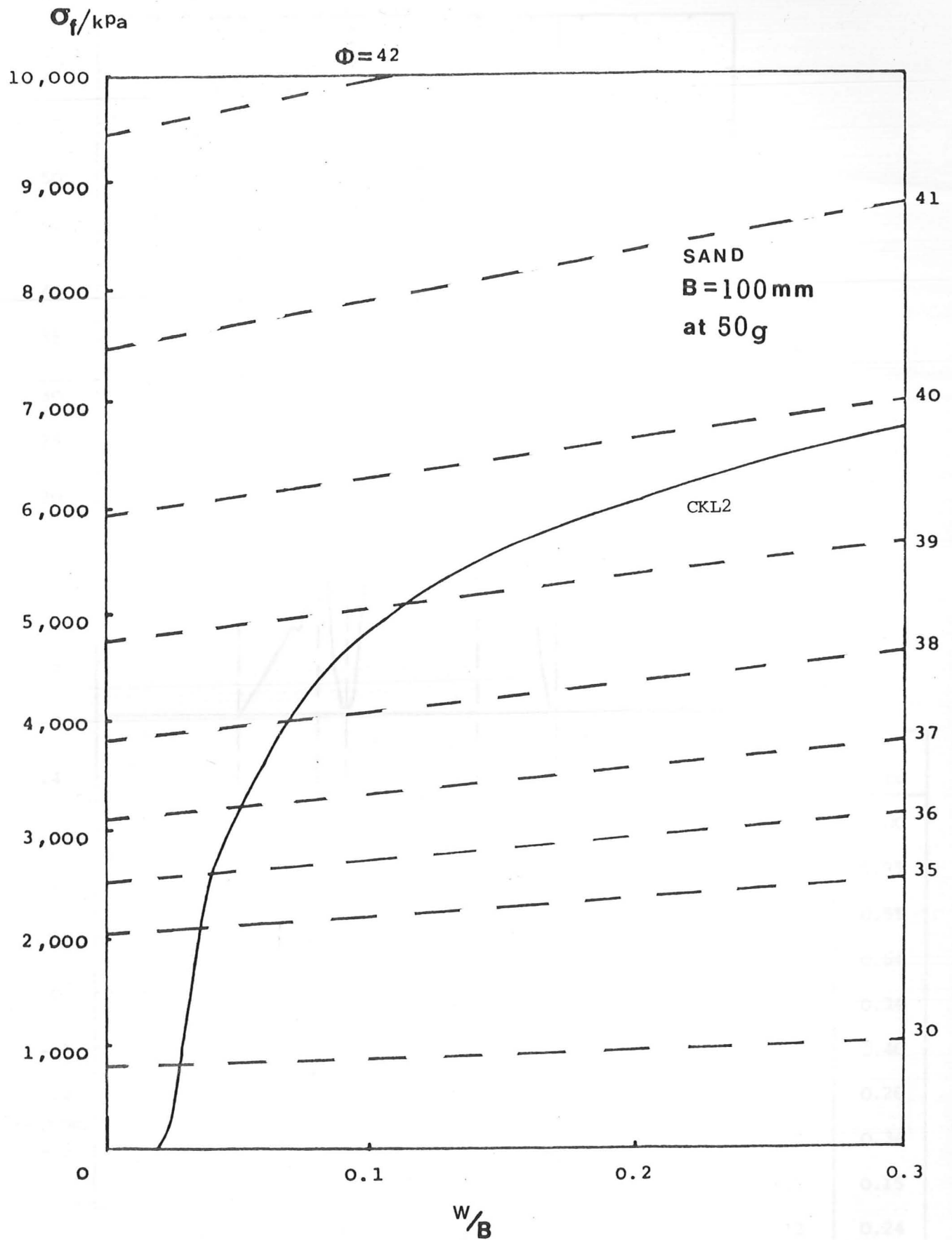
Fig 7.12 Interpretation of centrifuge test data by superposing the theoretical and experimental curves

Fig 7.13   Vertical load and check point movement during
test CKL3
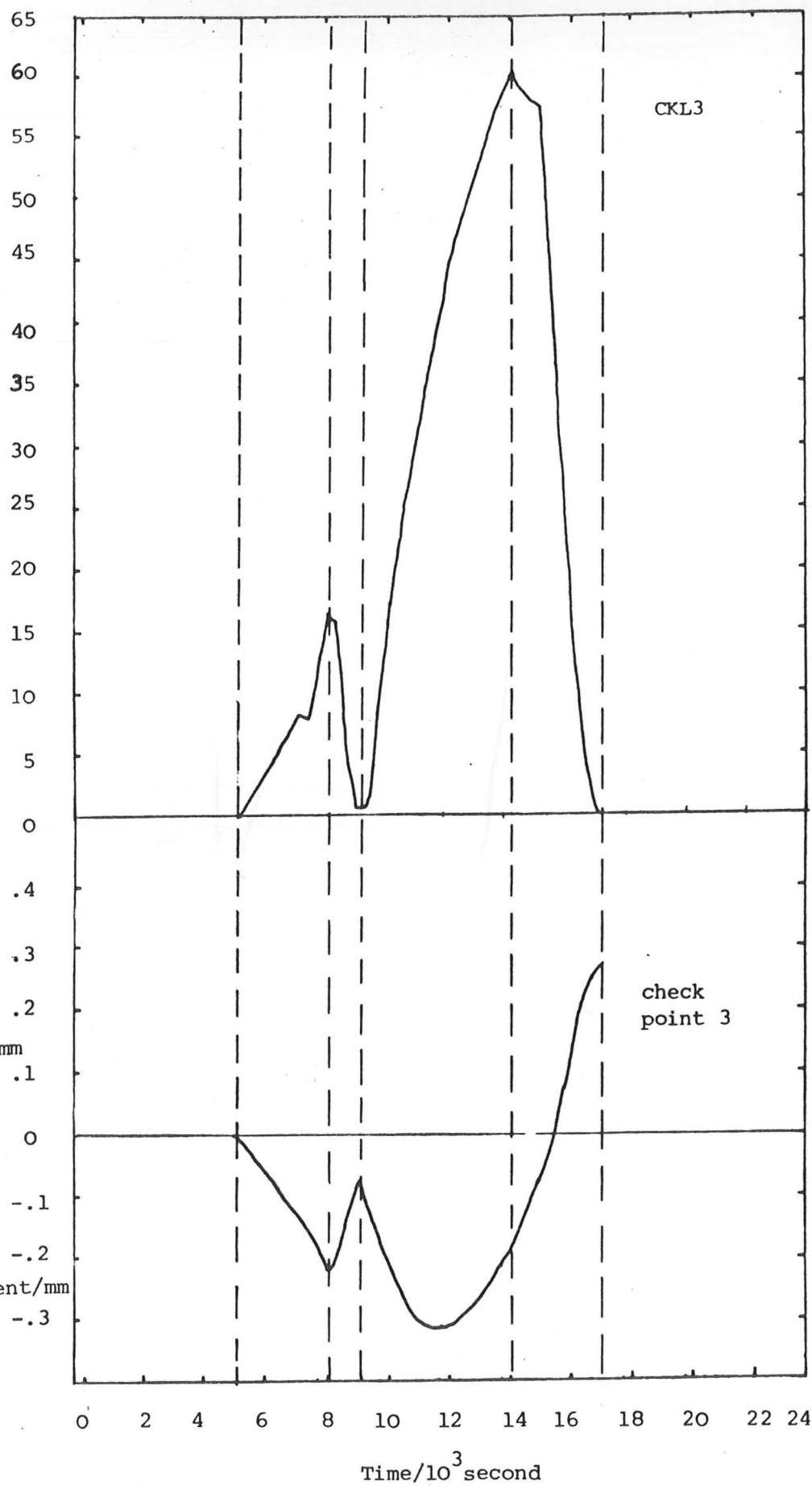
check point	ratio
3	1.00
4	0.95
5	0.55
6	0.64
7	0.34
8	0.46
9	0.26
10	0.34
11	0.15
12	0.24
13	0.11
14	0.11
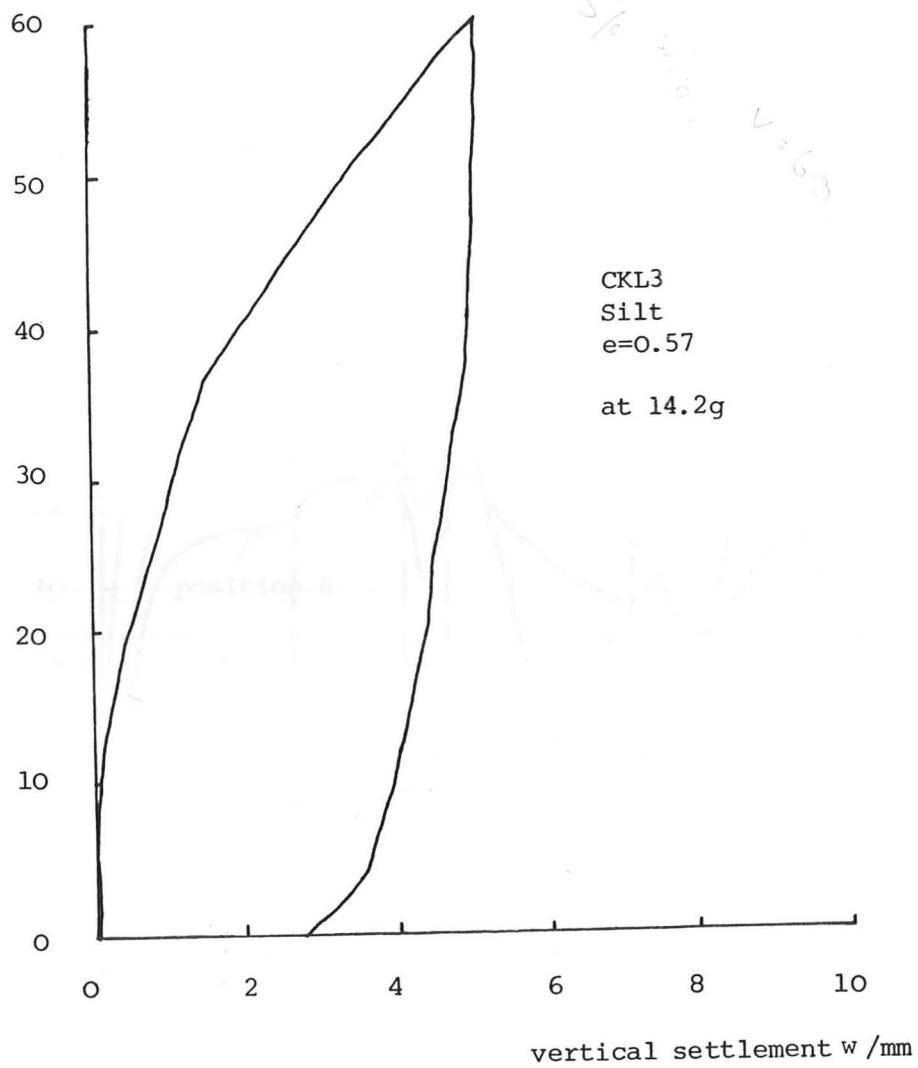
Fig 7.14   Load/settlement response of centrifuge
test CKL3

Location of PPTs
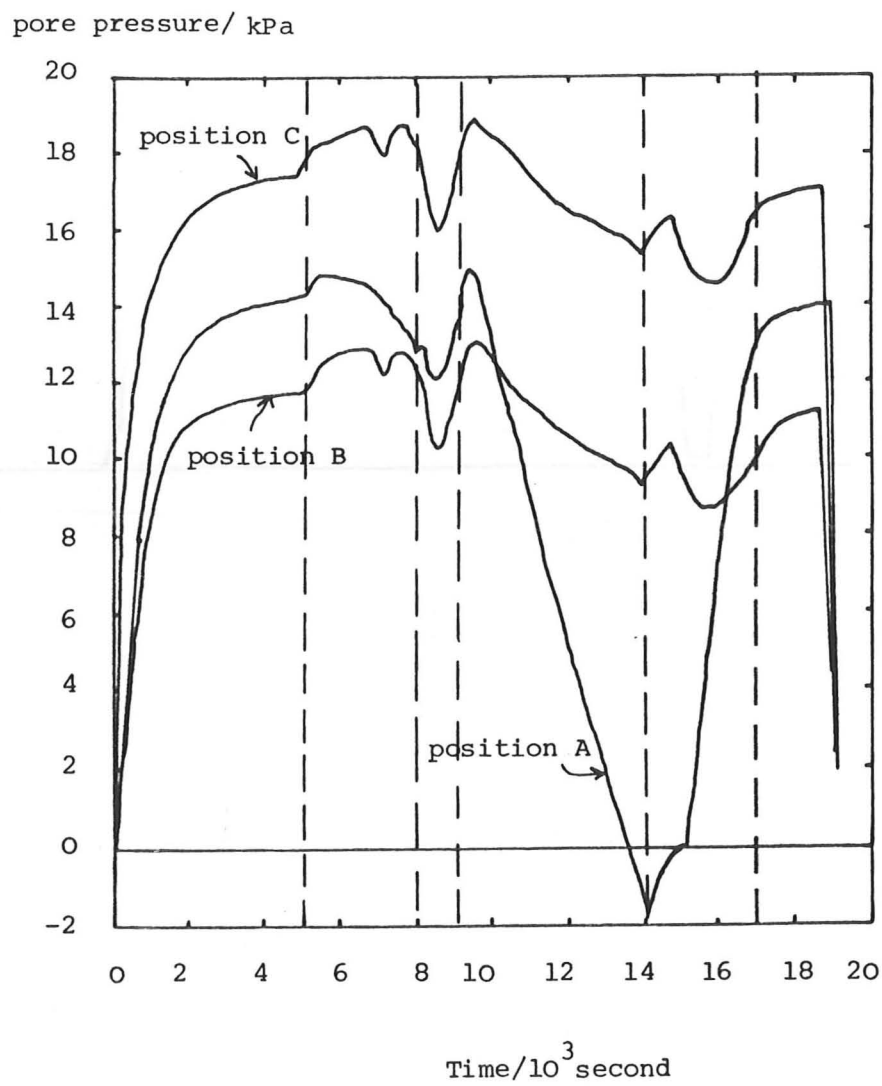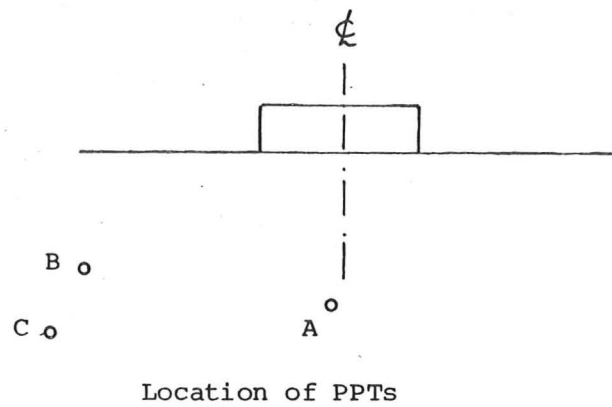
Fig 7.15   Pore water pressure response during test CKL3

Fig 7.16 Vertical load and check point movement during test CKL4

Pore pressure/ kPa

Fig 7.17 Pore water pressure response during test CKL4

vertical load/kN

vertical settlement w/mm

Fig 7.18   Load/settlement response of centrifuge test CKL4

Fig 7.19 Interpretation of centrifuge test data by superposing the theoretical and experimental curves

average working stress σ_w/kPa
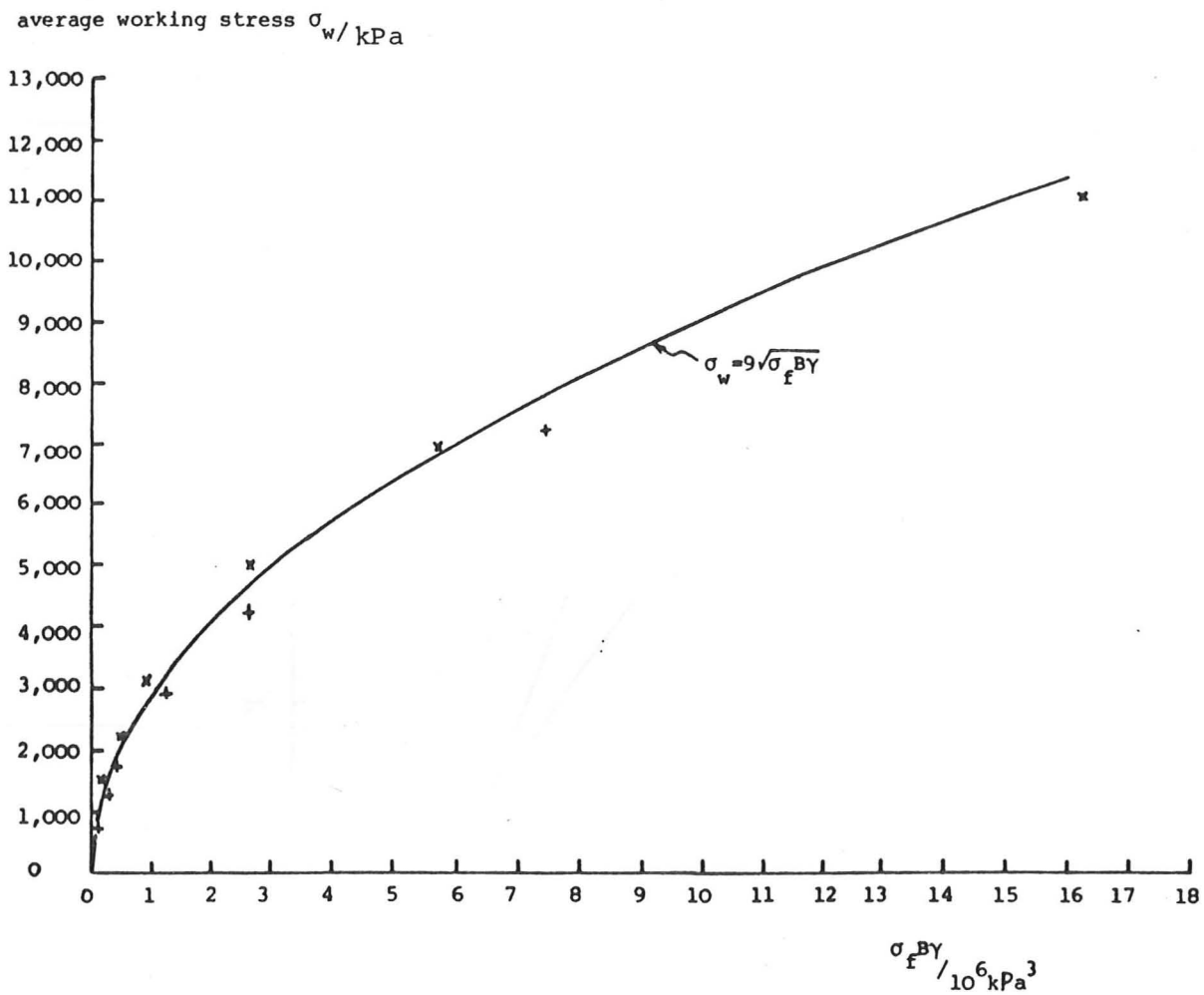
Fig 7.20 Empirical rule to find the average working stress σ_w, in the soil supporting a circular surface footing

Vertical
load/kN

80

Silt, B=100mm at 50g

70

CRISP prediction
with 600 inc.

60

50

40 — experiment (CKL1)

30

20

10

0

0   1   2   3   4   5   6   7   8   9   10 11 12

W/mm
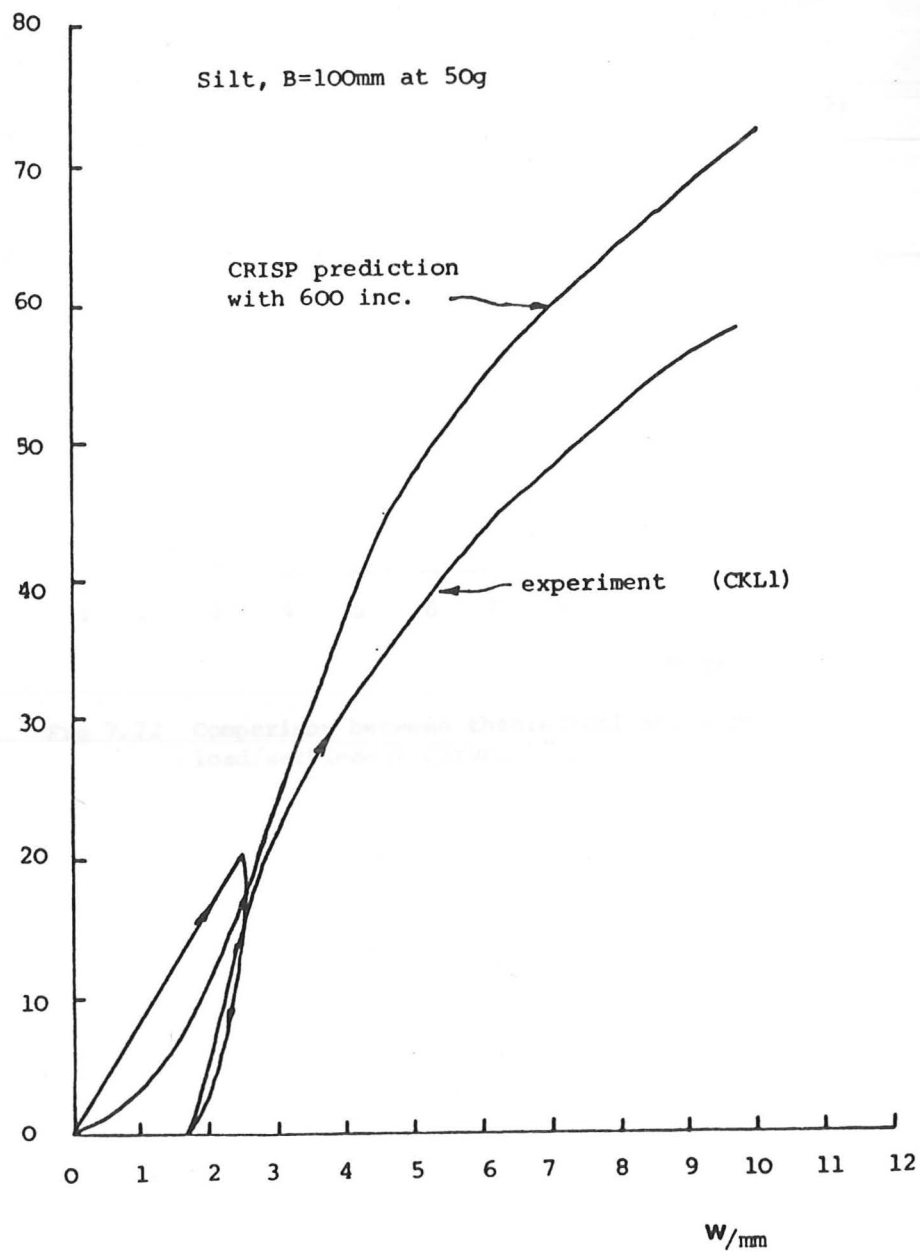
Fig 7.21   Comparison between theoretical and experimental
load/settlement curves

Vertical
load/kN

60

Sand,B=100mm,at 50g

50

CRISP prediction
with 440 inc.

40

experiment   (CKL2)

30

20

10

0

0   1   2   3   4   5   6   7   8   9   10   11   12

W/mm
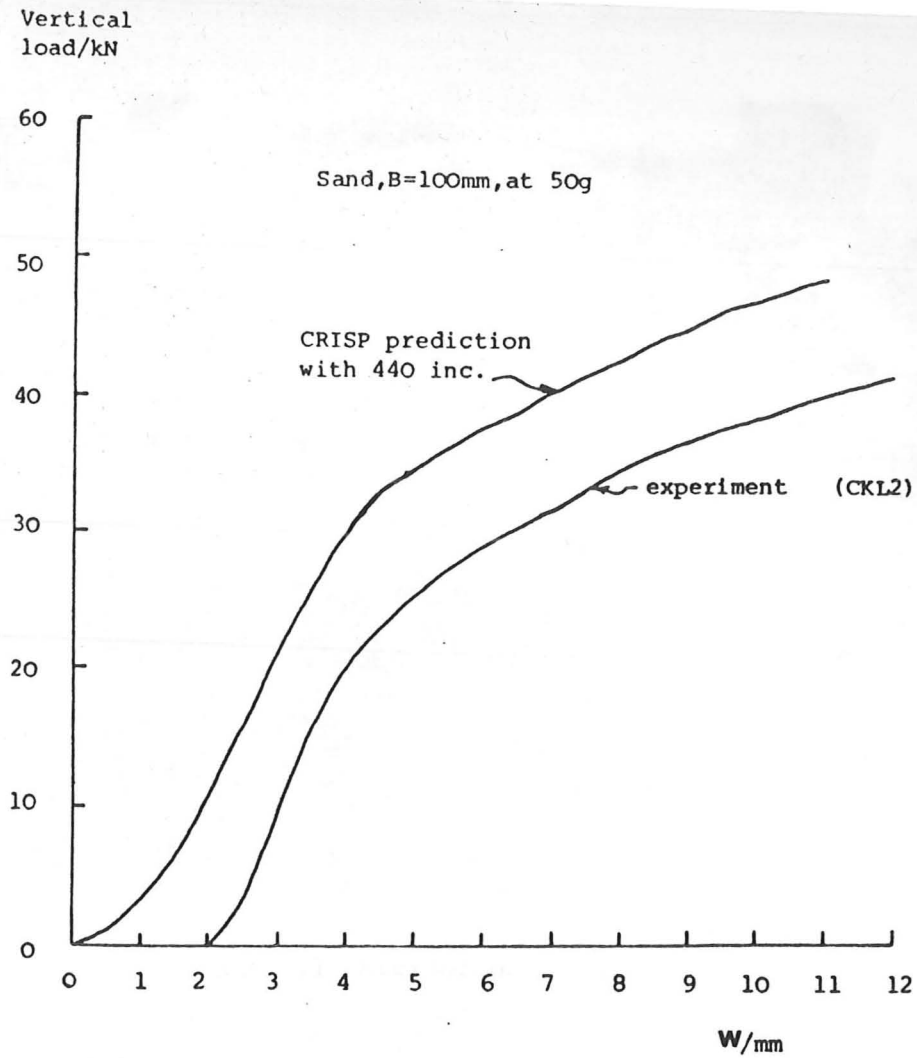
Fig 7.22   Comparison between theoretical and experimental
load/settlement curves

ø

γ
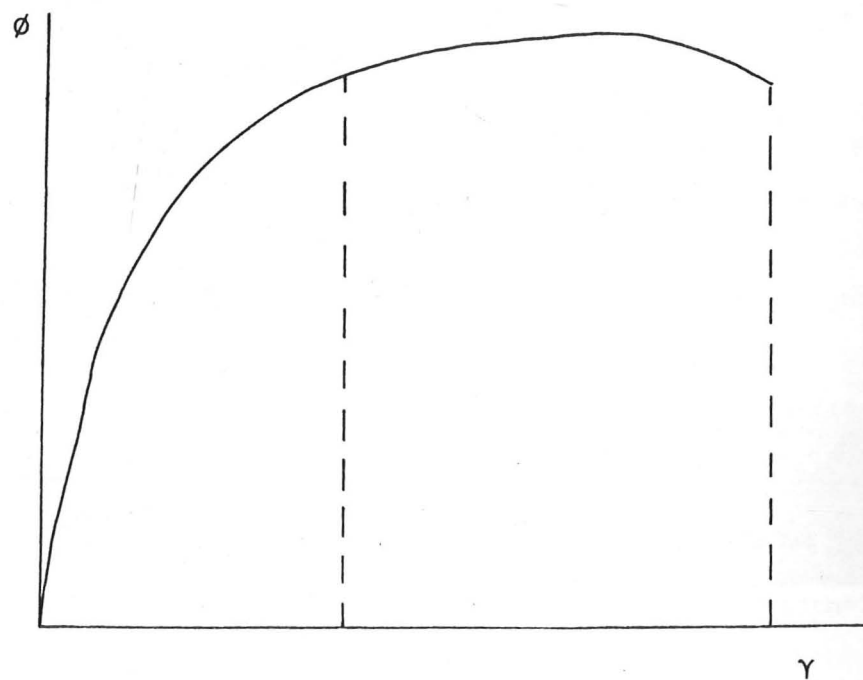
Fig 7.23   Typical effects of strain on the secant
angle of friction

picture width=2.32mm

Plate 2.1 Micrograph of sand

picture width=56μm
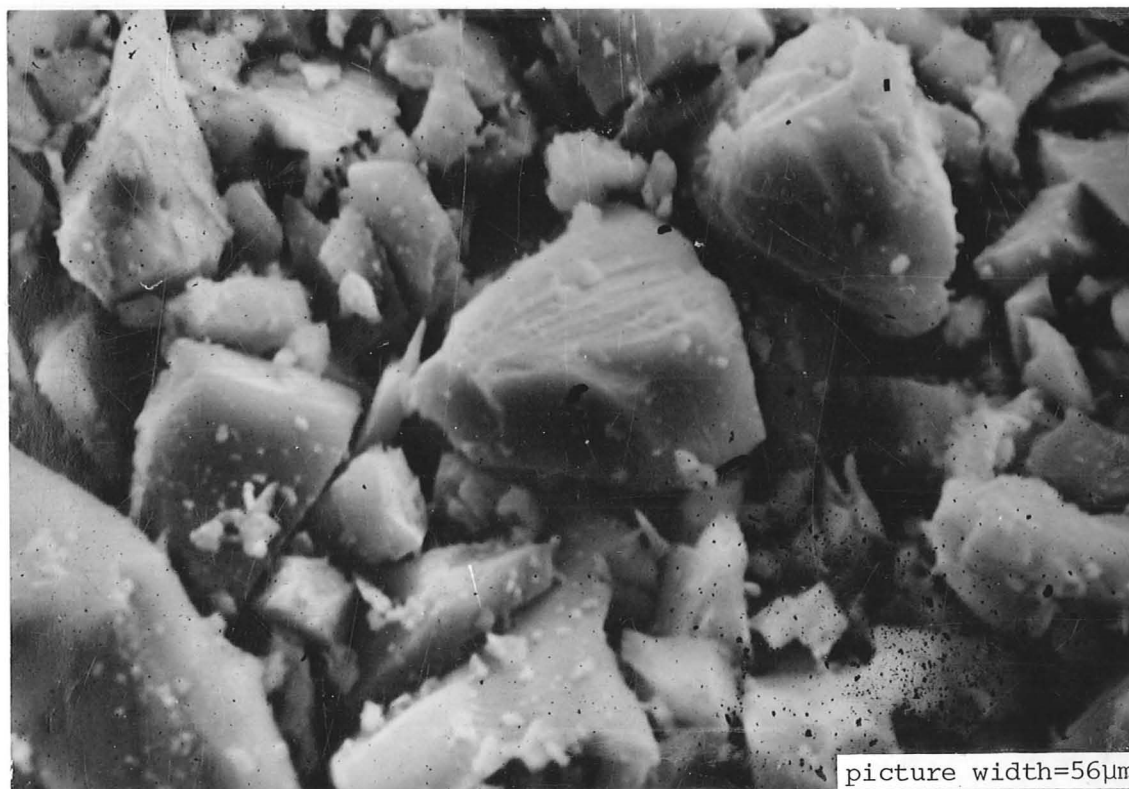
Plate 2.2 Micrograph of silt
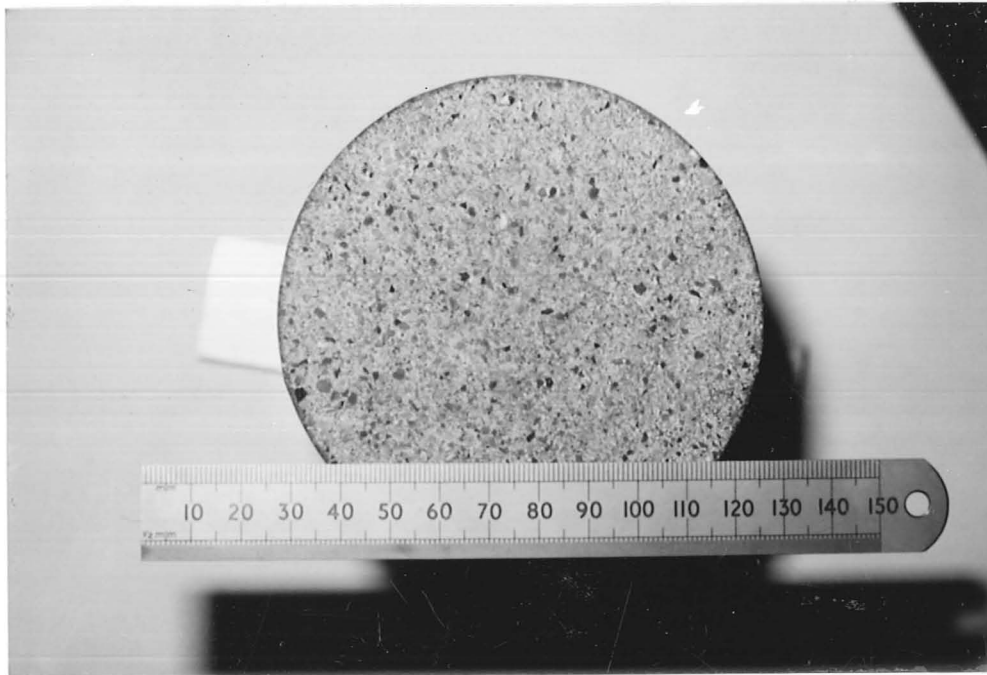
Plate 6.1   Close-up view of punch base
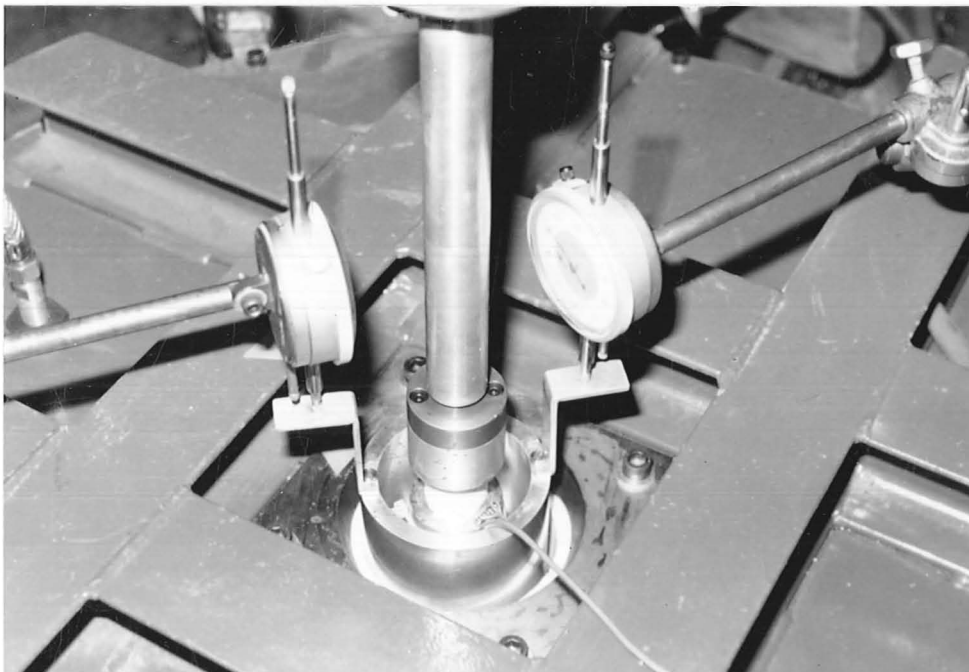
Plate 6.2   Close-up view of 1-g test rig
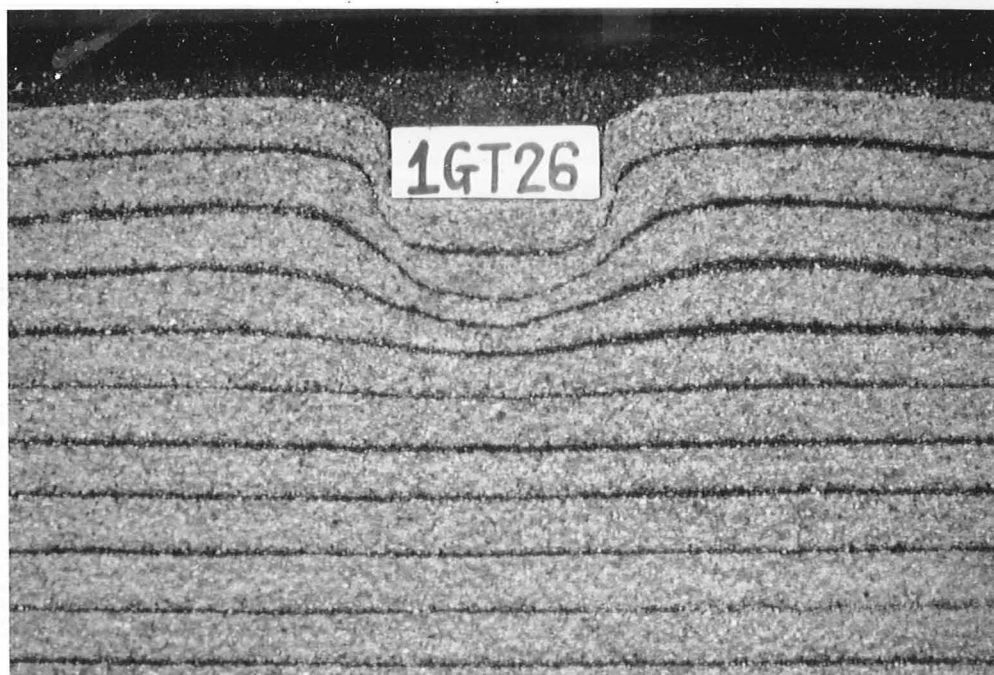
Plate 6.3   Photograph record of vertical section
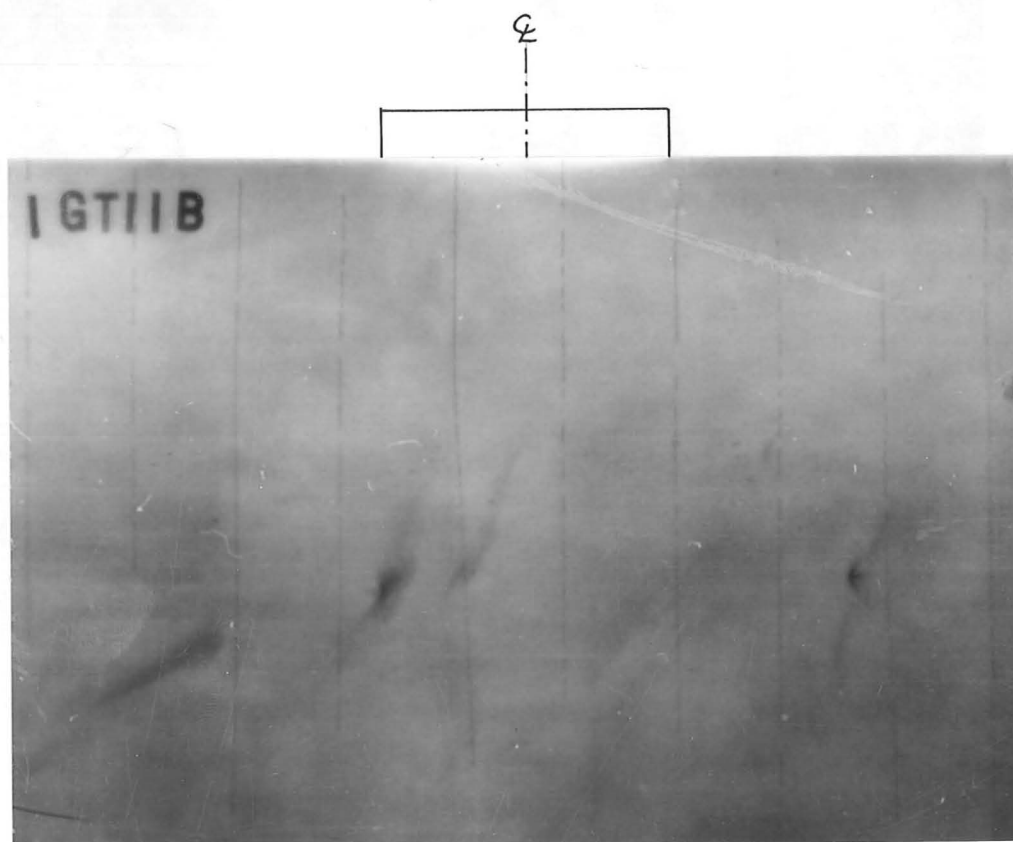of sand model after test 1GT26, σ_o=5kPa

Plate 6.4   Radiograph of vertical section of
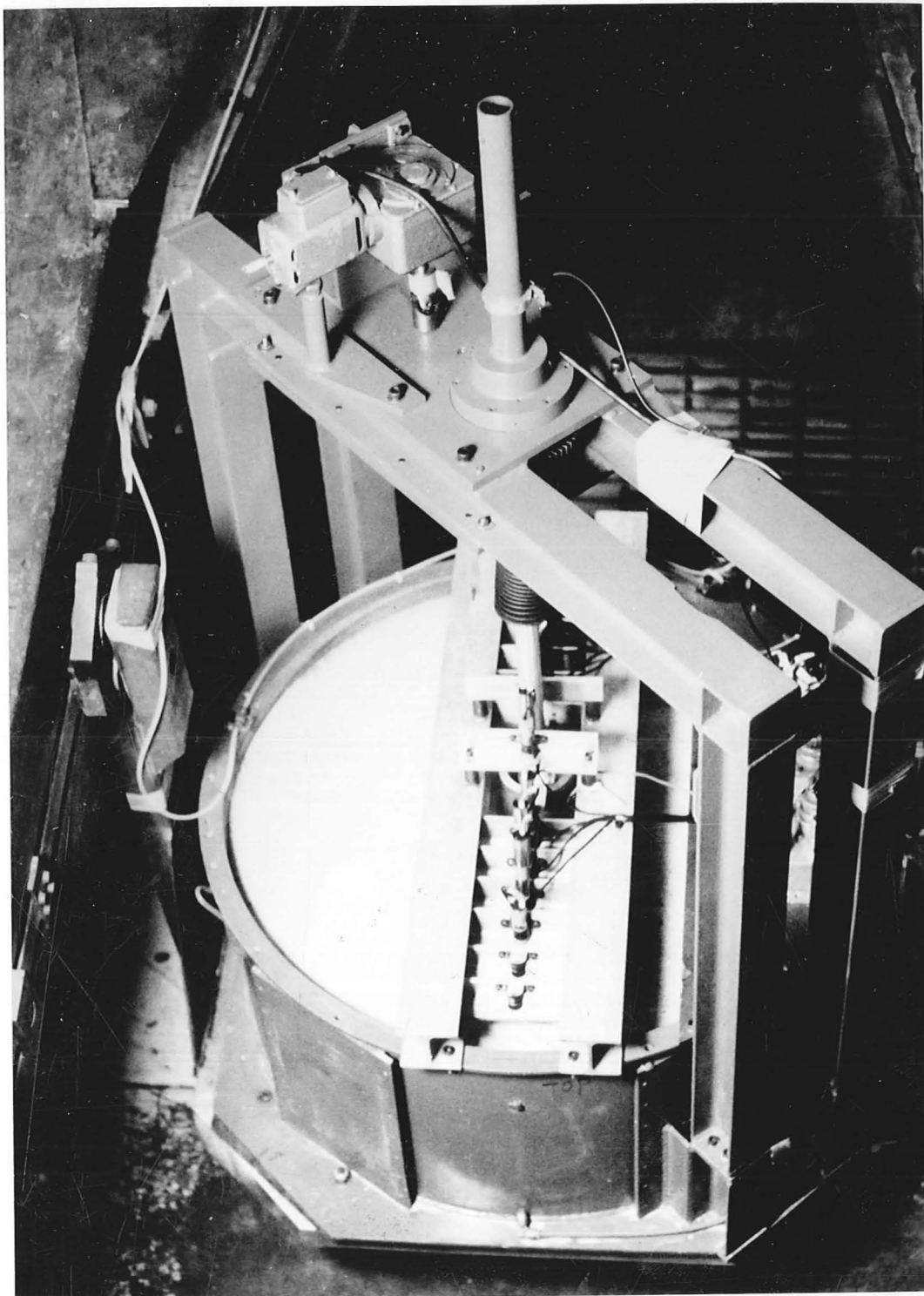silt model after test 1GT11, σ_o=10kPa
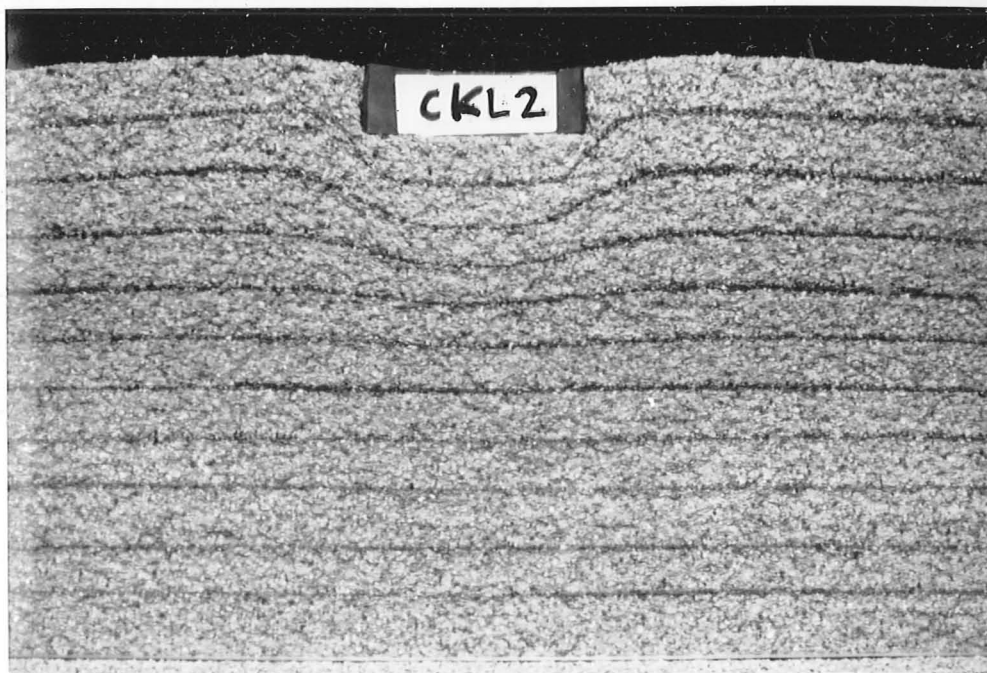
Plate 7.1 The centrifuge package

Plate 7.2 Photograph record of vertical section of sand
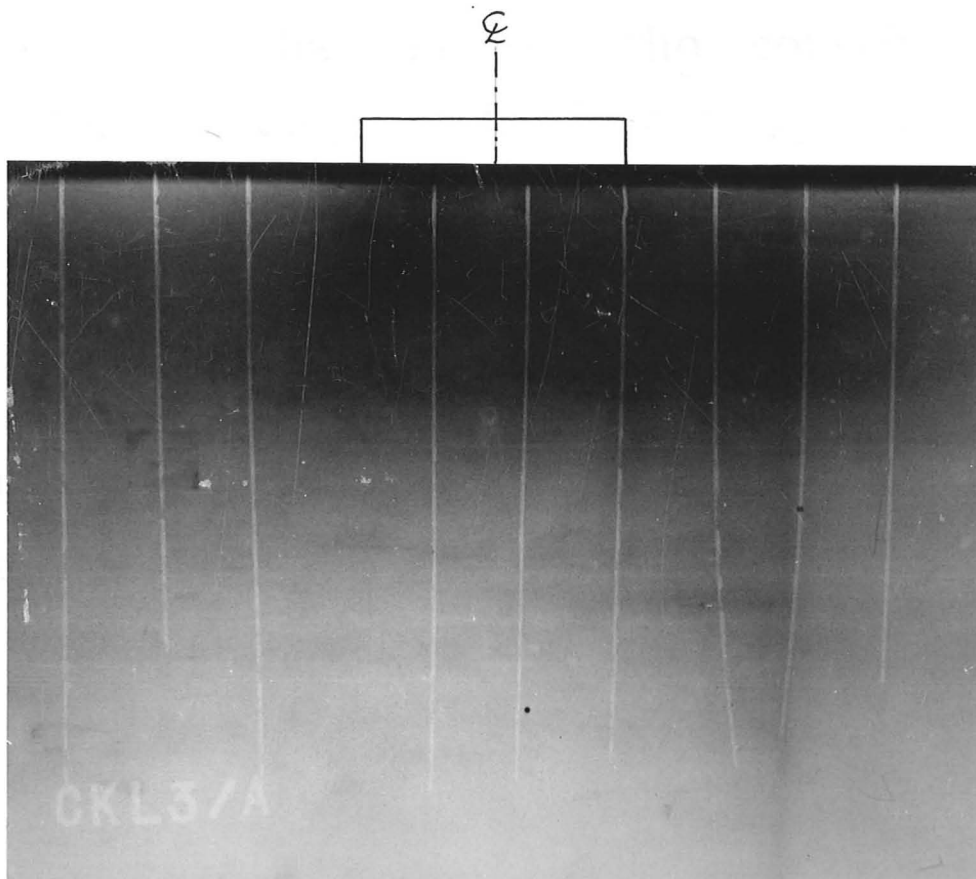model after test CKL2 at 50g, B=100mm

Plate 7.3 Radiograph of vertical section of silt model
after test CKL3 at 14.2g, B=100mm